1999

Evaluation of a friction component for a post-tensioned steel connection

Garrick D. Petty
Lehigh University

Petty, Garrick D.

Evaluation of a Friction Component for a Post-Tensioned Steel Connection

January 2000

Evaluation of a Friction Component for a Post-Tensioned Steel Connection

by

Garrick D. Petty

A Thesis
Presented to the Graduate and Research Committee
of Lehigh University
in Candidacy for the Degree of
Master of Science

in
the Department of Civil and Environmental Engineering

Lehigh University
July 30, 1999

Certificate of Approval

This thesis is accepted and approved in partial fulfillment of the requirements for the Master of Science.

7/30/99

Date

Dr. James M. Ricles, Thesis Advisor

Dr. Richard Sause, Thesis Advisor

Dr. Arup Sengupta, Department Chairperson

Acknowledgments

Psalms 50:15 says "And call upon me (God) in the day of trouble: I will deliver thee, and thou shalt glorify me." First giving honor and thanks to my heavenly father, who has provided me with this opportunity, establishing a greater purpose for every situation I encountered during my graduate studies, and working everything out for my good.

I would like to thank my research advisors, Dr. James Ricles, and Dr. Richard Sause, for giving me the opportunity to work with them on this research project. Both advisors provide opportunities for me to gain a deeper understanding of engineering concepts, and were also willing to share there knowledge with me. I would especially like to thank Dr. Sause for pushing me above and beyond my perceived capabilities, during the development of my thesis. Not only was this a learning experience, but a character building one as well.

I would like to thank everyone at the Advanced Technology for Large Structural Systems (ATLSS) Center for providing me with place to perform this research. I would like to thank the ATLSS laboratory technicians for their unrelenting assistance in tackling problem after problem during my experimental testing. I would like to thank Peter Bryan, the ATLSS Information Systems Manager, for his patience during the preparation of this thesis, and helping out of a lot of "sticky situations".

I would like to thank Dr. Henry Odi, Assistant Provost of Lehigh University, for providing financial means for me to pursue my graduate degree, and for direction and guidance during my studies.

I would like to thank my fellow graduate students at Lehigh for their encouragement, and making everyday exciting. I would especially like to thank Maria Garlock and Shih-Wei Peng for being my friends, and encouraging me.

I would like to thank my Church family, and especially the Singles Ministry of Union Baptist Church, for helping me to press on when times were tough, and keeping me in pray.

I would like to thank my parents, Tanks, Dad and mom, and my grandmother for keeping me motivated and focused throughout my studies. And lastly I would like to thank my fiancee' Janet, for being there for me when my back was against the wall. Being patient with me, and helping me to come out each day purposing to fight a good fight.

Table of Contents

List of Tables

Chapter 6

List of Figures

Chapter 3

Chapter 4

Chapter 5

Chapter 6

Abstract

Unexpected failures of conventional welded beam-to-column connections in seismic-resistant moment resisting frames (MRFs) occurred during recent earthquakes. Improved details for welded connections have improved the behavior of welded MRF connections, but these connections still require inelastic deformation (yielding and buckling) in the beams that results in permanent lateral drift of a MRF after a major earthquake. Thus, there is a need for innovative connections that soften and dissipate energy without significant inelastic deformation of the beams (or columns) of a MRF. Previous research has developed a post-tensioned (PT) steel connection, which provides the stiffness of a fully-rigid connection; the deformation capacity required for major seismic events; and a self-centering capability without permanent deformation. This was achieved by clamping the beam to the column with post-tensioned stands, and using the inelastic deformation of top and seat angles in the connection to dissipate energy.

In this thesis, a friction component is proposed as an alternative way to dissipate energy in a PT steel connection. A double angle friction connection component (FCC) was developed. The PT connection with a FCC provides strength, stiffness, energy dissipation capacity, and deformation capacity, without requiring significant inelastic deformation of the beams (or columns). In the double angle FCC, brass shims are placed between the double angles and beam web to provide a controlled level of friction. Clamping bolts through the beam web provide the

normal force on the brass-steel tribo (friction) surfaces. Oversized holes in the beam web allow the beam to rotate with respect to the column without the clamping bolts going into bearing on the beam web.

Two types of FCC tests were conducted. The first series of nine tests evaluated the brass-steel tribo surfaces. The parameters varied were the initial wear of the brass tribo surface, the normal force on the friction surfaces, and the imposed displacement rate. The second series of sixteen tests evaluated the double angle FCC. The parameters varied were the assembly sequence, the initial wear of the brass tribo surface, the imposed displacement rate, and the use of stiffeners on the angles. The results of the tests show that the FCC is a viable way to dissipate energy in a PT steel connection. A relatively consistent and durable friction behavior was obtained.

1. Introduction

This thesis presents research conducted on an innovative connection for steel moment resisting frames called the post-tensioned friction-damped connection (PFC). In particular, this research focused on an experimental evaluation of the friction component of this type of connection. This chapter introduces the motivation for developing the PFC, introduces the PFC and its components, and presents the objectives and scope of the research.

1.1 Welded Steel Moment Resisting Frame Connections

During the 1994 Northridge earthquake, over one hundred buildings with welded moment resisting frames (MRFs) were damaged. A typical welded beam-to-column connection for a steel MRF is shown in Figure 1.1. Investigations determined that the majority of the damage to the steel frames resulted from brittle fracture of the welded MRF connections (NIST, 1995). Brittle fracture of welded MRF connections was found in buildings of various configurations, story heights, and age. Failures were also detected in MRFs that were recently erected. The damaged MRFs were found over a wide geographical area, including sites where only moderate ground motions occurred (FEMA 267, 1995). Connection fractures were also found to occur at relatively low levels of seismic loads. The brittle fractures of the MRF connections reduced the confidence of engineers in what was believed to be a reliable seismic-resistant connection.

Most MRFs are designed to have strong column-weak beam behavior, in which energy introduced into the MRF is dissipated by inelastic deformation in the beams. This inelastic deformation is characterized by yielding and localized buckling in the beams. The beam-to-column connections should have sufficient strength to develop the plastic moment of the beams. Inelastic behavior is concentrated in the beams to avoid damage in the columns, because the columns must maintain resistance to gravity loads. The design strength of the connection elements (i.e., welds and bolts) is usually greater than that of the beams and columns, to avoid damage to these elements which are not usually very ductile. In a properly designed MRF, inelastic behavior of the beams should not be accompanied by a significant loss in resistance.

The welded MRF connections did not consistently achieve the desired inelastic behavior during the Northridge earthquake. In some cases brittle fracture appears to have occurred during elastic response of the MRF. Figure 1.1 shows a typical welded connection fracture in the weld between the lower beam flange and the column flange. The typical beam flange weld was a complete penetration weld with the backing bar left in place. The welded MRF connection fractures have been attributed to several factors (NIST, 1995), including the following: (1) the notch resulting from leaving the backing bar in place; (2) poor weld quality including slag inclusions and porosity; (3) lack of fusion defects in the weld; (4) post welding cracking; and (5) low fracture toughness of the weld metal.

Studies of retrofit details for existing welded MRF connections have been conducted. Retrofit is usually expensive. Improved details for new connections have also been developed. These new details improve the ductility of welded MRF connections but do not prevent the beams from being damaged from inelastic deformation (yielding and buckling). The permanent inelastic deformation of the beams will result in permanent lateral drift of a steel MRF building after a major earthquake.

1.2 Post-Tensioned Steel Moment Resisting Frame Connections

Concerns about the performance of welded moment resisting frame (MRF) connections during the Northridge earthquake has lead to research on a post-tensioned steel MRF connection (i.e., the PT connection) at Lehigh University (Chen, 1998; Garlock et al., 1998; and Peng et al., 1999). The PT connection (Figure 1.2) provides both the rigidity desired for minor seismic events and wind loads, as well as the deformation capacity required for major seismic events.

The PT connection is shown in Figure 1.2. Angles are used to attach the beams to the column. Post-tensioned (PT) strands are anchored at the flanges of the column that define the ends of the MRF (i.e., at the exterior columns of a planar MRF). These columns are anticipated to be within the building. The PT strands, when tensioned, compress the beams against bearing plates that are welded to the column flanges. This provides the connection with a significant flexural strength. Shear

forces are resisted by the friction generated between the portion of beam flange and web that bear against the bearing plates, and by the angles. The bearing plates separate the beam web from the column flange, and prevent yielding of the beam web. Yielding of the beam flanges is reduced by the use of beam flange cover plates.

The rigidity of the PT connection (Figure 1.2) is provided by clamping the beam flanges to the column flanges with PT strands. The rigidity of the PT connection is similar to that of a fully-rigid connection, as described in the AISC specifications (AISC-LRFD, 1995). By using relatively long PT stands between anchor points, significant rotation of the connection can occur without yielding the strands. As the connection rotates (i.e., the beam rotates relative to the column flange), inelastic behavior can occur in the top and seat angles (Figure 1.2). This inelastic behavior dissipates energy. The top and seat angles can be replaced if they are seriously damaged during a seismic event. However, tests have shown that the angles can be designed to have a low-cycle fatigue life sufficient to allow them to be perform well over several earthquake events (Chen, 1998). The force in the PT strands provides the connection with a significant self-centering capability, even after the angles have been pushed into the inelastic range. High-strength bolts are used to attach the angles and field welding is not needed

Tests of cruciform beam-column subassemblies with PT connections have been conducted by Chen (1998) and Peng et al. (1999). Each subassembly corresponded to the region between assumed locations of inflection points in a typical MRF. The tests investigated the behavior of PT connections and varied parameters such as the properties of the angles and the use of cover plates. Each test specimen was subjected to cyclic lateral loading up 3% story drift.

The results of Tests PC2-A and PC4 (Table 1.1) will be used to demonstrate the behavior of the PT connection. The PT test results are shown in Table 1.2 (Peng et al., 1999). Test PC2-A studied a PT connection without angles, and Test PC4 studied a connection with L8x8x5/8 inch angles. In Test PC2-A the PT connection developed 59% of the plastic moment (M_p) of the beam at 3% drift. In Test PC4 the PT connection developed 89% of M_p. For PC4 at 3% drift, the maximum PT strand force ($T_{exp,3\%}$) was 55% of the strand ultimate strength (T_u). Thus favorable flexural strength of a PT connection can be achieved while maintaining safe levels of force in the PT strands. The permanent drift was less than 0.07% and 0.04% for PC2-A and PC4, respectively. The load-displacement curves From Tests PC2-A and PC4 are presented in Figure 1.3 (Chen, 1998). The results show the self-centering and energy dissipating capability of the connection.

1.3 Motivation for Post-Tensioned Friction-Damped Connection

The post-tensioned friction damped connection was developed as an alternative to the post-tensioned (PT) steel MRF connection discussed in the previous section. In the post-tensioned friction-damped connection (PFC), structural damage (to the angles) is not required to produce energy dissipation. Energy dissipation occurs as friction is generated due to the relative motion between two tribo (friction) surfaces. By controlling the clamping force on the tribo surfaces, the friction force can be controlled. This research is aimed at developing a double angle friction connection component (FCC) for use in the post-tensioned friction-damped connection (PFC).

The PFC has characteristics similar to those of the PT connection presented in the previous section: (1) the initial stiffness of a fully-rigid connection; (2) the required deformation capacity; and (3) self centering capability due to the restoring force of the PT strands. Furthermore, structural damage is not required for energy dissipation.

A brass-steel tribo surface was selected for the FCC based on previous research by Grigorian and Popov (1994). The behavior of the steel-steel tribo surfaces studied by Grigorian and Popov (1994) was undesirable because the friction force was not consistent. More consistent behavior was observed with the use of brass-steel surfaces that produced a stable friction force which is necessary to control the energy dissipating capability of the FCC in design.

1.4 Research Objectives and Scope

The objective of this research are:

(1) to develop preliminary analytical and design procedures for a post-tensioned steel connection with a friction damping component; and

(2) to evaluate the friction connection component, as an energy dissipater for the post-tensioned steel connection.

To conduct accomplish these objectives, the behavior of brass-steel tribo surfaces, and the behavior of a double angle friction connection component (FCC) with brass-steel tribo surfaces were evaluated. The research involved the following areas of work.

Development of the post-tensioned friction-damped connection (PFC) concept:

(1) Development of the expected moment-rotation behavior of the PFC; and

(2) Development of a model for the PFC.

Design of the double angle friction connection component (FCC) of a PFC:

(1) Identification of the design parameters of the double angle FCC;

(2) Design of a double angle FCC as the basis for the specimens used in the tests.

Development of experimental procedures to investigate key parameters:

(1) Identification of key parameters related to friction behavior;

(2) Development of experimental test procedures to investigate identified parameters; and

(3) Design of experimental test frame and test specimens.

Evaluation of the friction behavior of brass-steel tribo surfaces:

(1) Tests of the friction behavior of unworn and unworn brass tribo surfaces;

(2) Studies of the variation in friction behavior due to wear of the brass tribo surfaces, and the use of various slip displacements rates.

Evaluation of the double angle friction connection component (FCC):

(1) Investigation of the friction behavior of the double angle FCC;

(2) Investigation of the repeatability of the friction behavior of the FCC, and the durability of the brass-steel tribo surfaces of the FCC; and

(3) Examination of the influence of the assembly sequence of the FCC on the friction behavior.

The research involved two types of tests. The first series of tests (double plate friction tests) was intended to evaluate the brass-steel tribo surfaces. Nine of these tests were conducted. The parameters varied were the initial wear of the brass tribo surface, the normal force on the tribo surfaces, and the imposed displacement rate.

The second series of tests was conducted on double angle friction connection components. Sixteen tests were conducted. The parameters varied were the assembly sequence, the initial wear of the brass tribo surface, the imposed displacement rate, and the use of stiffeners on the angles.

1.5 Scope of Thesis

The remainder of the thesis is organized as follows. Chapter 2 provides a simple model for the post-tensioned friction-damped connection (PFC) and outlines the expected moment-rotation behavior. Chapter 3 presents the design of the friction connection component of a PFC. Chapter 4 describes the experimental set-up and procedures used in the research. Chapter 5 provides detailed results of the double plate friction tests that were conducted to evaluate the friction behavior of the brass-steel tribo surfaces. Chapter 6 provides detailed results of the tests that were conducted to evaluate the friction behavior of the double angle friction connection with brass-steel tribo surfaces. Chapter 7 summarizes the research and presents conclusions.

1.6 Notation:

A = cross-sectional area
A_B = cross-sectional area of bolt
A_c = contact area
A_{ts} = tribo surface area
A_i = arbitrary surface area of ply i
A_{str} = cross-sectional area of PT strand
a = outer plate radius
b = width; inner plate radius
C_i = plate constant, i

c1 = moment arm of the force due to friction from the COR
c2 = moment arm of the force due to prestressing of the spring from the COR
c3 = moment arm of the reaction from the COR
D = plate constant
d_b = beam depth
d_j = distance of PT strand centerline from COR
E = modulus of elasticity
E_B = modulus of elasticity of bolt
E_{str} = modulus of elasticity of PT strand
F = force acting a tribo surface
F_f = friction force
F_{fk} = kinetic friction force
F_{fs} = static friction force
F_{fx} = horizontal component of the friction force
F_{fy} = vertical component of the friction force
f_f = friction stress
f_{fxi} = horizontal friction stress component at an arbitrary point
f_{fyi} = vertical friction stress component at an arbitrary point
G = shear modulus
g = gage length
K_s = deflection coefficient
k = length of angle fillet region
k_s = stiffness of the spring
L = length
L1 = length of angle vertical leg which decompresses
L2 = length of angle horizontal leg which decompresses
L_{BG} = grip length of bolt
L_i = radial location function, i
L_{str} = length of PT strand
l_x = horizontal distance of bolt from COR
l_y = vertical distance of bolt from COR
M = applied moment
$M_{add}(\theta)$ = additional moment due to elongation of PT strands due to the gap opening rotation
M_{Ff} = moment due to friction
M_{pst} = moment due to post-tension force in PT strands
$M_{\theta i}$ = moment required initiate motion
m_1= internal moment in vertical angle leg
m_2 = internal moment in angle horizontal leg
N = normal force
N_i = initial clamping force
N1 = normal force on tribo surfaces
n = number of PT strands
n_{ts} = number of tribo surfaces
PT = post-tension

P_{add} = additional PT strand force
$P_{add}(\theta)$ = additional force in PT strand due to gap opening rotation
P_{bolt} = bolt force
$P_{bolt,meas}$ = measured bolt force
P_i = bolt preload
P_{LRFD} = code specified bolt unfactored nominal tensile strength
P_s = prestressing force in the spring
P_{pst} = post-tension force in the PT strands
P_u = ultimate (maximum) load before failure
P_y = load at yield
R = reaction force
r = distance of arbitrary point of stress on tribo surface to COR
r_o = radial location of the unit line load
S = section modulus
T = period
t = thickness
t_i = thickness of ply i
V = shear force
x = horizontal distance of an arbitrary point from the COR
y = vertical distance of an arbitrary point from the COR
$y_c = d_b/2$
α = angle which gives the direction of slip or location of an arbitrary point on the tribo surfaces; coefficient of thermal expansion
α_B = coefficient of thermal expansion of bolt grip length
α_i = coefficient of thermal expansion of ply i
δ = deformation; displacement amplitude
δ_P = deformation due to applied load
δ_{str} = elastic deformation of the PT strands
δ_T = deformation due to thermal effects
δ_v = vertical displacement
δ_h = horizontal displacement
ε = strain
$\varepsilon_{total,meas}$ = total measured strain
$\varepsilon_{initial}$ = strain before thermal effects
ε_{total} = strain due to mechanical and thermal effects
Δ = elongation, deformation
$\Delta\varepsilon_B$ = change in strain in bolt
$\Delta\varepsilon_p$ = change in mechanical strain
$\Delta\varepsilon_T$ = change in thermal strain
$\Delta\varepsilon_{total}$ = total change in strain due to mechanical and thermal effects
ΔL_{BG} = change in bolt grip length
ΔP = change in applied force
ΔP_{bolt} = change in bolt force
$\Delta\sigma$ = change in stress

$\Delta\sigma_B$ = change in stress in the grip length of the bolt
$\Delta\sigma_i$ = change in stress of ply i
ΔT = change in temperature
ΔT_B = change in temperature in the grip length of the bolt
ΔT_i = change in temperature of ply i
Δt = change in thickness of plies
Δt_i = change in thickness of ply i
Δx = horizontal displacement of an arbitrary point
Δy = vertical displacement of an arbitrary point, total deflection
Δy_b = deformation due to bending
Δy_s = deformation due to shear
μ = coefficient of friction
$\mu N1$ = friction force on tribo surface
$\mu\varepsilon$ = micro-strain ($\varepsilon*10^{-6}$)
μ_k = kinetic coefficient of friction
μ_s = static coefficient of friction
ν = Poisson's ration
ϕR_n = factored resistance
θ = rotation, gap opening angle
θ_s = story drift rotation
σ_{a+b} = axial and bending stresses
σ_u = ultimate stress
σ_y = yield stress
ω = unit line load

Table 1.1: Post-Tensioned Connection Test Matrix

Test	Angle (F_y=36)	g/t*	Number of PT Strands —	ΣPT Strand Force*** (kips)
PC2-A	none	—	8	173
PC4	L8x8x5/8	4.0	8	153

* g/t = horizontal bolt gage to angle thickness ratio

** PC2A and PC4 had the cover plates on the underside of the flanges.

*** measured PT Strand Force (Chen, 1998)

Table 1.2: Post-Tensioned Connection Test Results

Test	$M_{exp,3\%}$ M_p	M_{design} M_p	$T_{exp,3\%}$ T_u	$\theta_{r,exp,3\%}$ (rad)	Residual Offset* (Permanent Drift)
PC2-A	0.59	0.7	N/A	0.03	0.07%
PC4	0.89	0.84	0.55	0.025	0.04%

* Residual drift after 3%

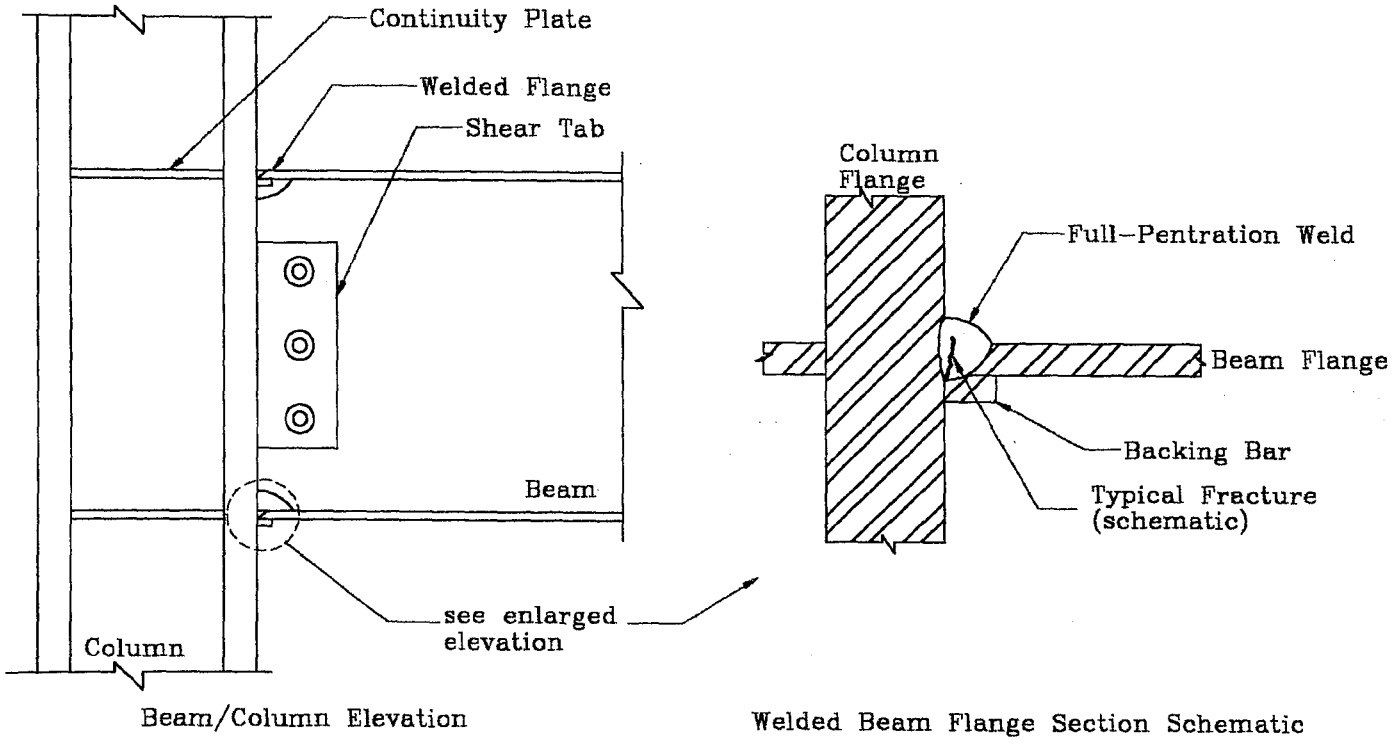

Figure 1.1. Typical Welded Steel Moment Resisting Frame Connection

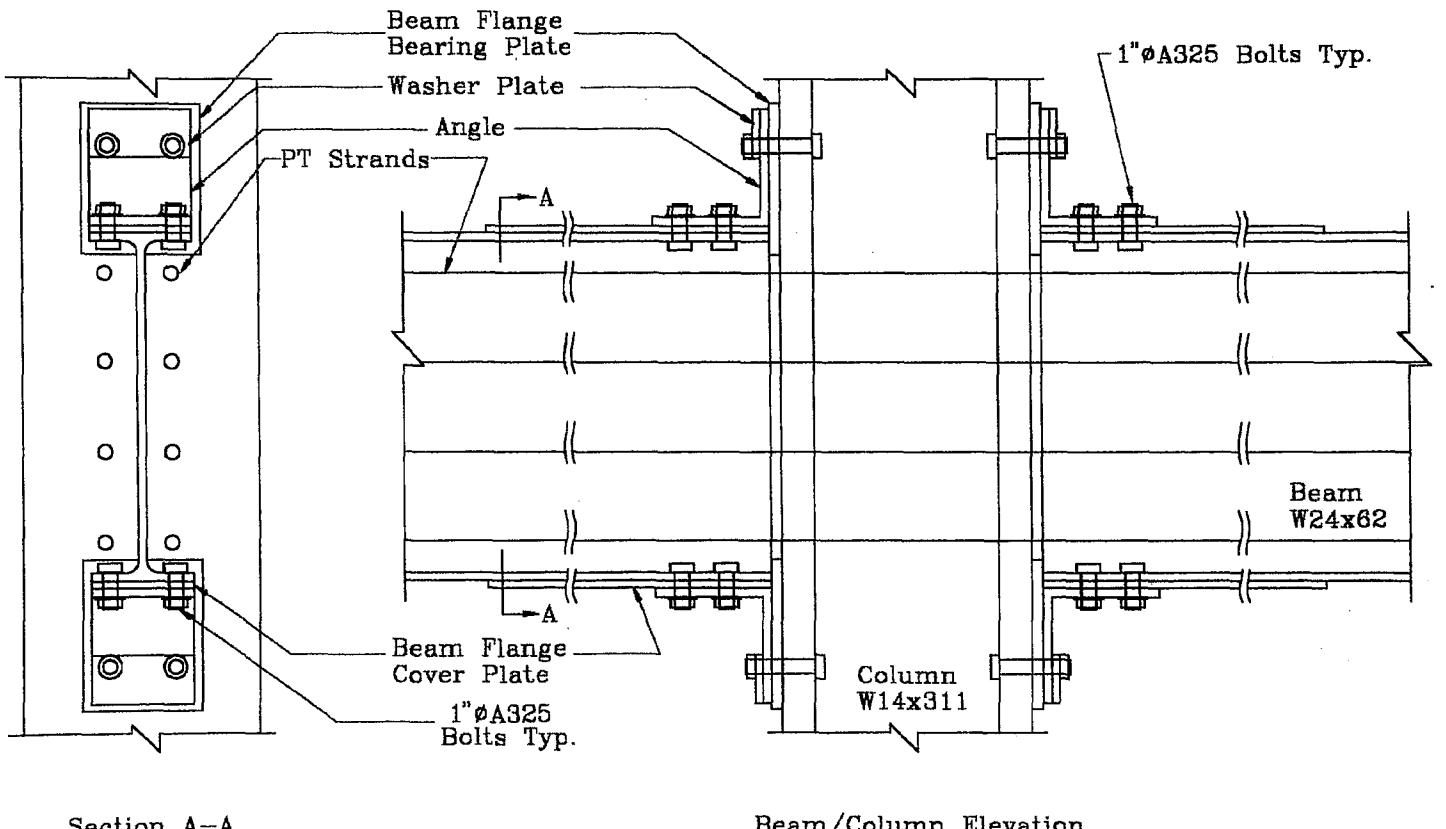

Figure 1.2. Post-Tensioned Top and Seat Angle Connection Details

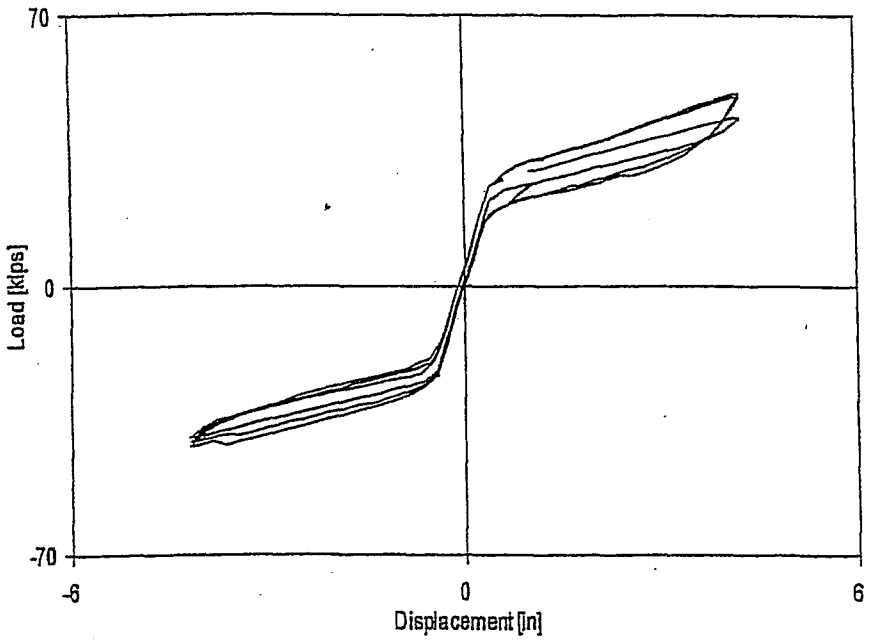

(a)

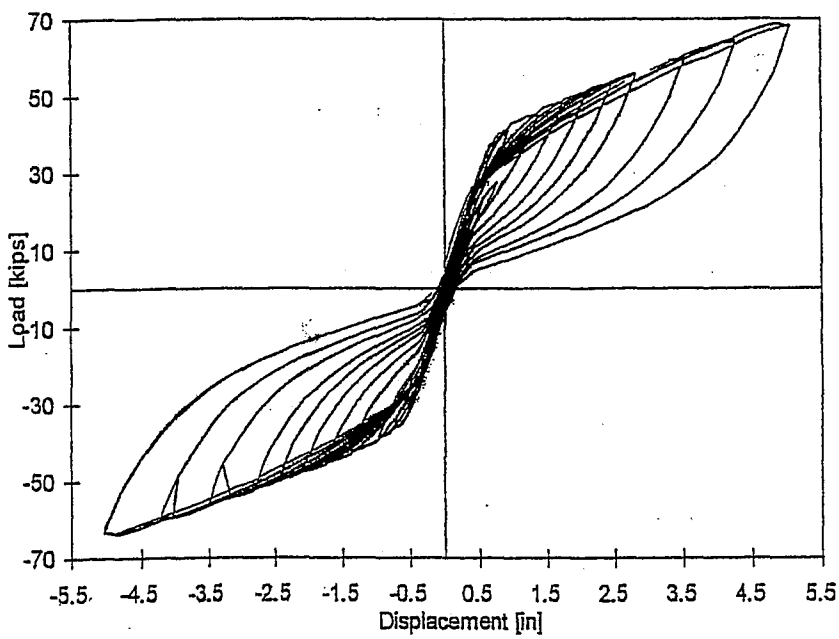

(b)

Figure 1.3. Load Displacement Response Curves; (a) PC2-A; and (b) PC4 (Chen, 1998)

2. Conceptual Development of the Post-Tensioned Friction-Damped Connection

The objective of this chapter is to present the expected behavior of the post-tensioned friction-damped connection (PFC). A model for the PFC is developed and used to study the moment-rotation (M-θ) behavior of the connection. The behavior of the friction component and post-tensioned (PT) components are studied independently. The two components are combined into one system, and the expected M-θ behavior of the PFC is analyzed and discussed.

2.1 Simple Model for Post-Tensioned Friction-Damped Connection

A typical post-tensioned friction-damped connection (PFC) is shown in Figure 2.1. As discussed in Chapter 3, the member sizes used in this study were adopted from previously studied post-tensioned steel moment resisting connections (Chen, 1998; Garlock et al., 1989; and Peng et al., 1999). Some of the details shown in Figure 2.1 vary from the details used in previously studied post-tensioned moment resisting connection shown in Figure 1.1.

Figure 2.1 shows that the PFC has two specific components of interest, namely the friction surfaces between the brass shims and the beam web, and the post-tensioned (PT) strands. To develop an understanding of the moment-rotation behavior of the PFC connection, a rigid block model will be used to idealize the moment-rotation response of the PFC (see Figure 2.2). The rigid block rotates counter-clockwise

about a center-of-rotation (COR). The COR is represented by a clevis with a frictionless pin. The rigid block is supported by a rigid bearing surface at the corner opposite to the COR. This allows unrestricted, counter-clockwise rotation of the block. The mass of the rigid block is neglected. Mechanical devices are added to the model to represent the friction and PT components. The rigid block in the undisplaced (unrotated) position is shown in Figure 2.2, with subsequent figures showing the rigid block in rotated positions. Free-body diagrams (FBDs) will be used to show the contribution of the friction and PT components to the resistance of applied moment. A summation of moments is taken with respect to the COR. Thus, the forces occurring at the frictionless pin located at the COR do not contribute to the moment, and therefore the clevis is shown on the FBDs. A horizontal reference line is used to show the rotation of the rigid block with respect to the COR. The rotations (in radians) are assumed to be small which allows for the use of small angle theory.

2.1.1 Contribution of the Friction Component

The energy dissipating component of the PFC utilizes friction to dissipate energy input to a structure by seismic loading. *Friction* can be defined as a force that resists the relative sliding motion of two *tribo surfaces*, where tribo surfaces are defined as "surfaces in mechanical contact under relative motion" (Vingsbo, 1988). The force that develops on the tribo surfaces under relative motion is referred to as the friction force (F_f). Friction is a function of the tribo surface conditions, the

properties of the tribo surface materials, and the relative rate of sliding between the tribo surfaces (Flaherty and Petach, 1957). For simplicity, the basic friction theory developed by Coulomb will be used in the design of the friction component. Although this may oversimplify the actual friction behavior, Coulomb friction theory is widely accepted and commonly used. When needed, additional tribology concepts will be used to further explain the friction and wear behavior of the tribo surfaces. Tribology terminology is presented in Appendix 1.

Coulomb friction theory describes the friction force that resist relative motion between two tribo surfaces under relative motion. According to Coulomb friction theory, the friction force is a function of the normal force (N), or force perpendicular to the tribo surfaces, and the coefficient of friction (μ). The resulting equation for the friction force is:

$$F_f = \mu \cdot N \tag{2.1}$$

The coefficient of friction varies with the tribo surface conditions, the tribo surface material properties, and the relative velocity of the tribo surfaces. When the relative velocity (i.e., incipient motion) is zero, the static coefficient of friction (μ_s) is used. The kinetic coefficient of friction (μ_k) is applicable when the relative velocity is not zero. The change from the static to kinetic coefficient occurs after the relative displacement of the tribo surfaces exceeds the *asperity junction size*, and the shearing of the bonds between adjacent tribo surfaces occurs (Rabinowicz, 1991). *Asperities* are the high points or irregularities that exist on a surface at the microscopic level

(Flaherty and Petach, 1957). The kinetic coefficient of friction has an inverse relationship with the relative velocity. As the relative velocity increases, μ_k decreases (Grigorian and Popov, 1994).

The friction forces which correspond to μ_s and μ_k are F_{fs} and F_{fk}, respectively. Theoretically the static friction force (F_{fs}) is independent of the direction of incipient motion and is assumed constant. F_{fs} can be determined using Equation 2.1. In actuality, F_{fs} is a function of stick time, or time interval between zero relative velocity and sliding of the tribo surfaces. This variation in F_{fs} is only significant if the stick time is less than approximately 1/10 second (Grigorian and Popov, 1994). Because the stick time between seismic loading events on a structure is sufficient for the full static friction force to develop, the variations in F_{fs} due to limited stick time are neglected. Relative motion or sliding along the tribo surfaces is referred to as slip. Slip is incipient when the applied force reaches F_{fs}.

After slip, the kinetic friction force (F_{fk}) is the force required to maintain motion. F_{fk} is a function of the relative velocity between the two tribo surfaces, and is difficult to accurately determine using Coulomb friction theory (Grigorian and Popov, 1994). Although differences exist between F_{fs} and F_{fk}, previous research conducted by Grigorian and Popov (1994) has shown that these differences are small after initial wear of the tribo surfaces occurs and can be ignored in design. Therefore, F_{fs} is

assumed to be equivalent to F_{fk} in the following discussion, and the term F_f will be used to refer to the force under both conditions.

A friction device consisting of two friction strips in contact with the rigid block was used to model the friction component of the PFC. Elevations of the rigid block with friction device are shown in Figure 2.3. The two friction strips sandwich the rigid block, and are attached to the foundation. The friction forces act perpendicular to the foundation. The contact surfaces of the rigid block and friction strips are the tribo surfaces. A distributed clamping force is exerted on the friction strips to clamp the tribo surfaces. This force is represented by the resultant force N. The coefficient of friction between the two surfaces is μ.

Figure 2.3(b) shows a FBD of the rigid block model with the friction component. An external counter-clockwise moment (M) is applied. The friction forces are at a distance of c1 from the COR. M produces counter-clockwise rotation, therefore F_f acts downward on the tribo surface of the block to oppose this rotation. As shown on Figure 2.3(b), the force at the tribo surfaces is F, which is less than or equal to F_f.

The moment-rotation (M-θ) response of the rigid block model with the friction component is similar to a rigid-perfectly plastic (RPP) system. An RPP system displays both the initial rigidity of a friction system until F_f has been reached, and the continuous deformation (or slip) at a constant force (i.e., plastic behavior). The

M-θ behavior of the rigid block model with the friction component is shown in Figure 2.4(i). An explanation of the M-θ behavior is as follows, with corresponding illustrations also shown in Figure 2.4. The behavior starts with the block at rest (θ=0) and no applied moment (event A shown in Figure 2.4(a)). A counter-clockwise, or positive, moment (M) is applied to the block. M incrementally increases in magnitude without rotating the block. The magnitude of the moment is less than F_f times the moment arm (c1) (event B shown in Figure 2.4(b)). At this event, M is increasing along the moment axis of Figure 2.4(i), with zero rotation (see event (B) on Figure 2.4(i)). The rotation is zero until M reaches M_{Ff}, which is the moment at which relative motion occurs. M_{Ff} is equal to F_f•c1 (event C in Figures 2.5(c) and (2.5(i)). This event corresponds to a limit on the increase in M, and the beginning of rotation of the block. M is constant as the rigid block rotates about the COR, and is equal to M_{Ff}. As long as M equals M_{Ff} (i.e., M equals F_f•c1), rotation will occur as shown by the horizontal line through event D in Figure 2.4(i). If M is decreased to a value less than F_f•c1, the block ceases to rotate as shown by event E in Figures 2.4(e) and 2.4(i)). When the applied moment is reduced to zero, as shown by event F in Figures 2.4(f) and 2.4(i), a residual rotation results. As shown in Figure 2.4(i), the rotation does not change as the moment is reduced to zero as shown by the vertical decline from event E to F. The rotation does not change because M is less than F_f•c1. If a clockwise or negative moment (M) is applied, M can be increased in magnitude between (events F and G as shown (Figure2.4(i)) without rotation while M is less than F_f•c1. At event G (Figure 2.4(g)), M equals

$F_f \cdot c1$ and the block begins to rotate. Again, M is constant and equal to M_{Ff}. This corresponds to the change in θ without change in M as shown in Figure 2.4(i). Rotation will occur as long as M equals M_{Ff} (i.e., equals $F_f \cdot c1$) as shown by event H (Figure 2.4(h)). Figure 2.4(i) shows that the friction component dissipates energy during load reversals.

2.1.2 Contribution of Post-Tensioned Component

The post-tensioned (PT) strands are the component of the PFC that provides most of the moment resistance. The PT strands provide the PFC with stiffness, strength, and self-centering capability (Chen, 1998; Garlock et al., 1989; and Peng et al., 1999). Yielding of the PT strands is prevented in order to maintain the self-centering capability of the connection (Chen, 1998; Garlock et al., 1989; and Peng et al., 1999). Thus, only linear elastic behavior of the PT strand is considered.

A prestressed spring was used in the rigid block model to model the effect of the PT strands on the M-θ response of the PFC. Figure 2.5(i) shows the rigid block with the spring, prestressed in tension, attached underneath the rigid block and attached to the foundation. The spring is located a distance c2 from the COR. The prestressing of the spring is equivalent to the prestressing of the PT strands. As shown in Figure 2.5(a), the prestress is represented by a force (P_s), which compresses the rigid block against the rigid bearing surface. A reaction force (R) develops between the block and bearing surface as shown in Figure 2.5(a). R is assumed to occur at a distance

c3 from the COR. As rotation of the block occurs, the spring elongates. The force in the spring acts vertically and resists the rotation of the block. The stiffness of the spring (k_s) represents the elastic behavior of the strands. The M-θ behavior of the block is described below. Corresponding FBDs are shown in Figure 2.5.

The M-θ behavior starts with the block at rest with the spring prestressed as shown by event A in Figures 2.5(a) and 2.5(ii). A moment (M) is applied to the block, gradually increasing in magnitude. The motion of the rigid block is restrained by the prestressing of the block against the bearing surface. Between events A and B in Figure 2.5(ii), M is equal to $P_s \cdot c2 - R \cdot c3$. As M increases, the rotation is zero until R goes to zero (event B in Figures 2.5(b) and 2.5(ii). R goes to zero when the M reaches M_{pst}, which is the restraining moment due to the prestressing of the spring (or the post-tensioning of the PT strands). M_{pst} is equal to $P_s \cdot c2$ as shown in Figure 2.5(b). The increase in M without rotation corresponds to the vertical rise between events A and B on the M-θ response curve shown in Figure 2.5(ii). After M reaches M_{pst} (i.e., M equals $P_s \cdot c2$), the block decompresses from the bearing surface, and is able to rotate. This event, event B, is referred to as decompression. After decompression the spring begins to deform elastically as shown in Figure 2.5(c), and the moment increases linearly (Figure 2.5(ii)). The linear increase in moment is proportional to the stiffness of the spring (k_s). The elongation of the spring (δ) is directly related to the rotation of the rigid block, and is equal to $c2 \cdot \theta$. The additional force in the spring (beyond Ps) is equal to $k_s \cdot \delta = k_s \cdot c2 \cdot \theta$. The additional

moment (M_{add}) due to the spring (or PT strand) elongation is $k_s \bullet \delta \bullet c2 = k_s \bullet c2^2 \bullet \theta$. The total moment is the decompression moment plus the moment due to the elongation of the spring as shown by event C in Figures 2.5(c) and 2.5(ii). Since the system is elastic, the loading and unloading behavior follow the same curve. Thus, when M is decreased, the M-θ curve unloads along the curve it followed under loading. When the block comes into contact with the bearing surface, the spring force returns to its initial prestressed condition with a force equal to P_s. This event is similar to event B. As M decreases further, R increases with zero rotation. The initial condition is reached with P_s compressing the block against the bearing surface which is similar to event A. Thus the PT component allows the system to avoid residual rotation (i.e., the spring provides self-centering capability) after a loading event.

2.1.3 Behavior of the Post-Tensioned Friction-Damped Connection

The M-θ behavior of the post-tensioned friction-damped connection (PFC) is a function of both the friction and post-tensioned components. The behavior of the PFC can be understood be superimposing the contribution of its two components. A rigid block model for the PFC is shown in Figure 2.6. The model is comprised of the friction device and prestressed spring spaced at a distance c1 and c2 from the COR, respectively. The bearing surface reaction (R) occurs at a distance c3 from the COR.

The M-θ behavior of the rigid block model of the PFC is described as a series of events, shown in Figure 2.7. The behavior shown in Figure 2.7 assumes that the moment resistance of to the friction component is less than the moment resistance of the post-tensioned component. This prevents residual rotation of the rigid block after the applied moment is removed because the prestress of the spring forces the block back to its original position (θ=0). FBDs corresponding to the events along the M-θ curve in Figure 2.7 are shown in Figure 2.8.

The rigid block is initially at rest before the moment (M) is applied (event A in Figure 2.8(a)). P_s compresses the block against the bearing surface. As M is gradually increased in magnitude, the rotation of the block is restrained by P_s. Rotation of the block cannot occur until event B, when the reaction from the bearing surface (R) is equal to zero and M is equal to $P_s \bullet c2$, as shown in Figure 2.8(b). The moment at event B is the decompression moment. The force at the tribo surfaces (F) is assumed negligible between events A and B, as shown in Figure 2.7, because the rotation of the block is restrained. After the decompression moment is reached, additional resistance to rotation is provided by F. M continues to increase until it reaches $P_s \bullet c2+F_f \bullet c1$. This corresponds to event C in Figures 2.7 and 2.8(c). At event C, rotation begins. The spring is assumed to remain elastic, and therefore, the M-θ curve (Figure 2.7) is linear elastic after event C. The moment during rotation is a function of: (1) the initial prestress of the spring (P_s); (2) the friction force (F_f); and

(3) the force required to elongate the spring ($k_s \cdot c2 \cdot \theta$). That is, M is equal to $[P_s+(k_s \cdot c2 \cdot \theta)] \cdot c2+(F_f \cdot c1)$ between events C and D in Figure 2.7.

At event D, it is assumed that the applied moment is held constant and then decreased, and the block begins to return to its original position as follows. At event D, the force at the tribo surfaces (F) is equal to F_f, but no rotation occurs because the applied moment is held constant. The initial decrease in M from the moment at event D (M_D) to that corresponding to event E is equivalent to $F_f \cdot c1$ as shown in Figures 2.7 and 2.8(e). This decrease in M occurs as the force at the tribo surfaces (F) changes from the value at incipient slip (F_f), to zero.

Between events D and E, the total spring force ($P_s+k_s \cdot c2 \cdot \theta$) and rotation of the block remain constant, as shown in Figure 2.7. As M decreases beyond event E, the rotation is now opposed by $F_f \cdot c1$ which has changed direction due to the change in direction of incipient rotation. The applied moment (M) must decrease in magnitude equivalent to $F_f \cdot c1$ between events E and F (Figure 2.7) before rotation occurs. The total change in moment from event D to F is equal $2 \cdot (F_f \cdot c1)$ as shown in Figures 2.7 and 2.8(f).

After event F, the deformation in the spring is reduced as a clockwise rotation of the block occurs. The force in the spring decreases as the elongation of the spring decreases. Thus, the moment between events F and G (Figure 2.7) is $M_D-[2 \cdot (F_f \cdot c1)]$-

$(k_s \cdot c2 \cdot \theta) \cdot c2$. The moment at event G, as the block initially contacts the bearing surface (R=0), is $M_D-[2 \cdot (F_f \cdot c1)]-(k_s \cdot c2 \cdot \theta_D) \cdot c2$ as shown in Figure 2.8(g). The block is compressed against the bearing surface between events G and H in Figure 2.7. When the moment reaches zero at event H there is a residual friction force, and thus the reaction is less than it was at event A, as shown in Figure 2.8. The moment which occurs as the block is fully-compressed against the bearing surface is $M_D-[2 \cdot (F_f \cdot c1)]-(k_s \cdot c2 \cdot \theta) \cdot c2-[(P_s \cdot c2)-(F_f \cdot c1)]=0$ as shown event H in Figure 2.7 and Figure 2.8(h). Figure 2.7 shows the energy dissipation and self centering capabilities of the friction and PT components.

2.2 Post-Tensioned Friction-Damped Connection Moment-Rotation Model

Based on the behavior of the simple model for the post-tensioned friction-damped connection (PFC) presented in section 2.1, a moment-rotation (M-θ) model for the PFC connection was developed. The model is based on the PFC shown in Figure 2.9. The model consists of a beam compressed against the flange bearing plates. The exterior face of the column flange is shown as a single vertical line. The friction component is represented by a rectangular, arbitrary friction surface centered on the centroidal axis of the beam. PT strands are located above and below the arbitrary friction surface. The strand locations are symmetrical with respect to the centroidal axis. The resultant friction force and the total PT strand force are shown acting at the centroidal axis of the beam, which is at half the beam depth from the

bottom of the beam. As shown in Figure 2.9, the beam is able to rotate about either of its flanges. Therefore, two centers of rotation (COR1 and COR2) are shown.

The M-θ response of the PFC is shown in Figure 2.10. The M-θ response is discussed using FBDs shown in Figure 2.11. Each FBD corresponds to a specific event on the M-θ curve, or to states between specific events.

The M-θ response curve begins with the applied moment (M) and the rotation (θ) equal to zero as shown by event 1 in Figure 2.10. The post-tension force in the PT strands (P_{pst}) compresses the beam flanges against the flange bearing plates. The force at the tribo surface (F) is assumed equal to zero, and the compressive force in each flange is half the total post-tension force because of the symmetry of the strands at M=0. Reaction forces acting on each flange are equal to the force in each flange. A clockwise moment is applied to the beam, and the magnitude of the moment increases gradually. The reaction force (R2) on the flange opposite the center of rotation (COR1) decreases as the applied moment increases. The reaction force on the flange at COR1 (R1) increases. Between events 1 and 2 as shown in Figure 2.11(a), the applied moment is decompressing one flange and increasing the compression in the flange at the COR. However, the flanges remain in contact with the bearing plates. Once the magnitude of the applied moment (M) reaches the moment resistance due to the post-tension force in the PT strands (M_{pst}),

decompression of the beam occurs. However, at event 2 in Figure 2.10, the rotation of the beam is still restrained by the moment resistance of the friction component.

The moment resistance due to the post-tension force is a function of the location of the strands and the post-tension force in the strands, as follows:

$$M_{pst} = \sum_{j}^{n} \left(P_{pstj} \cdot d_j \right) \tag{2.2}$$

where: P_{pstj} = the post-tension force in PT strand j,

d_j = the distance of PT strand j from the COR, and

n = the number of PT strands.

M_{pst} can be expressed in terms of the resultant of the post-tension force in the strands. With symmetrical placement of the PT strands, M_{pstr} is the same for either COR. Thus, M_{pst} is now determined as follows:

$$M_{pst} = \left(\sum_{j}^{n} P_{pstj} \right) \cdot \frac{d_b}{2} = \sum P_{pst} \cdot \frac{d_b}{2} \tag{2.3}$$

where: d_b = the beam depth, and

$$\sum P_{pst} = \sum_{j}^{n} P_{pstj}$$

Event 2 in Figure 2.10 corresponds to decompression of the top flange which occurs as M reaches M_{pst} (i.e., $\Sigma P_{pst} \bullet (d_b/2)$). This is similar to event B in Figures 2.5(ii) and 2.5(b) of the rigid block model with the PT component.

The applied moment continues to increase between events 2 and 3 as shown in Figure 2.10 as the rotation of the block is restrained by the moment resistance of the friction component. The total applied moment between event 2 and 3 is a function of the post-tension and friction forces as shown in Figure 2.11. The force in the compression flange (R1) continues to increase. The force in the decompressed flange is zero. Once the applied moment (M) reaches the moment resistance due to friction (M_{Ff}) plus M_{pst}, rotation of the beam initiates as shown by event 3, which is the point of incipient rotation, in Figure 2.10. M_{Ff} is a function of the coefficient of friction (μ), the normal force (N), the surface area of the tribo surfaces, and corresponding distance of the tribo surface to the COR, as shown by the following equation. Here, M_{Ff} is assumed to be equal to $F_f \bullet (db/2)$, however, the moment due to friction will be discussed in further detail later in this chapter.

$$M_{Ff} = f(\mu, N, A_{ts}, d) \cong F_f \cdot \left(\frac{d_b}{2}\right) \tag{2.4}$$

At the onset of rotation, the beam rotates away from the decompressed bearing plate. The moment corresponding to event 3 in Figure 2.10 is the moment required to initiate rotation of the beam ($M_{\theta i}$) as follows:

$$M_{\theta i} = M_{Ff} + M_{pst} \tag{2.5}$$

The beam rotates away from the decompressed bearing plate about the COR as shown in Figure 2.11(c). The angle of rotation between the beam and the bearing plates is the gap opening angle (θ). As θ increases, the PT strands are elongated. Additional force develops in the strands as this elastic deformation occurs. Thus,

the applied moment (M) will increase, as shown between events 3 and 4 in Figure 2.10, as the beam rotates about the COR. This increase in moment is a function of the PT strand stiffness.

The expected rotation is small which allows the use of small angle theory. Assuming a small rotation, the additional force in the strands is:

$$P_{add} = \frac{A_{str} \cdot E_{str}}{L_{str}} \cdot \delta_{str} \tag{2.6}$$

where: P_{add} = the additional force in the strands due to elongation,

L_{str} = the length of the strands,

A_{str} = the cross sectional area of the strands,

E_{str} = the modulus of elasticity of the strands, and

δ_{str} = the elastic deformation of the strands at the centroid of the strands.

The elastic deformation of the strand can be determined using similar triangles from the rotated beam configuration shown in Figure 2.12. δ_{str} is shown with respect to the centroid of the PT strands, because for a symmetric interior beam-column joint, all strands undergo the same elongation (El-Sheikh et al., 1997).

$$\delta_{str} = \left(\frac{d_b}{2}\right) \cdot \theta \tag{2.7}$$

where: θ = the gap opening angle between beam and the bearing plates.

Substituting Equation 2.7 into Equation 2.6, the additional PT strand force is as follows:

$$P_{add}(\theta) = \left(\frac{A_{str} \cdot E_{str} \cdot d_b}{2 \cdot L_{str}}\right) \cdot \theta \tag{2.8}$$

Therefore, assuming the strands are symmetric, the additional moment ($M_{add}(\theta)$) due to the elongation of the strands is as follows:

$$M_{add}(\theta) = \left[\left(\frac{A_{str} \cdot E_{str} \cdot d_b}{2 \cdot L_{str}}\right) \cdot \theta\right] \cdot \frac{d_b}{2} \tag{2.9}$$

As shown in Figure 2.11(c), M is the sum of the moment resistance due to friction (M_{Ff}), the moment resistance due to the post-tension force in the PT strands (M_{pst}), and the moment due to the additional force in the strands due to elongation of the strands ($M_{add}(\theta)$). Thus, M is a function of the rotation θ, as follows:

$$M(\theta) = M_{Ff} + M_{pst} + M_{add}(\theta) = M_{\theta i} + M_{add}(\theta) \tag{2.10}$$

At event 4, $M(\theta)$ is equal to M_4 as shown in Figure 2.10. At event 4 (Figure 2.10), it is assumed that the applied moment is held constant instantaneously and then decreased. As the applied moment decreases, θ remains constant at θ_4 as shown between events 4 and 6 in Figure 2.10. This behavior is similar to that between events D and E in Figure 2.1. The reduction in M between events 4 and 5 is equal to M_{Ff} as shown in Figure 2.10. At event 5 in Figure 2.11(d), F is zero and M is a function of the PT strand force. M continues to decrease in magnitude, while θ is

constant, between events 5 and 6 as shown in Figure 2.10. As shown in Figure 2.11(e), the force at the tribo surface (F) has changed direction as the post-tensioning force in PT strands tries to rotate the beam counter-clockwise. The total change in M between events 4 and 6 is $2 \cdot M_{Ff}$ as shown in Figure 2.10.

Between events 6 and 7 in Figure 2.10, the beam rotates until the beam top flange is back in contact with the bearing plate. Between events 6 and 7, F is equal to F_f as shown in Figure 2.11(f). At event 7 (Figures 2.10 and 2.11(g)), the top flange of the beam is in contact with the bearing plate, but not compressed. Because the top flange is not compressed against the bearing plate, R2 is equal to 0 as shown in Figure 2.11(g). The compression of the top flange occurs between events 7 and 8 as shown in Figures 2.11(g) and 2.11(h). Between events 7 and 8, F is not equal to zero, as shown in Figure 2.11(h). M decreases as the reaction force (R2) increases, as shown in Figure 2.10. Event 8 in Figure 2.10 corresponds to the beam being compressed against the bearing plates and M equal zero. The sum of R1 and R2 is equal to $\Sigma P_{pst} - F_f$ at event 8, as shown in Figure 2.11(i).

A counter-clockwise moment is now applied to the beam as shown in Figure 2.11(j). Because a residual friction force exists at event 8 as shown in Figure 2.11(i), the forces in the system are indeterminate until event 9 is reached. That is, R1+R2 is equal to ΣP_{pst}-F and the values of F, R1 and R2 cannot be determined. Thus there is no clear point of decompression on the curve as shown in Figure 2.10. The moment

at event 9 in Figure 2.11(j) is equal to $M_{\theta i}$. Event 9 is similar to event 3 in Figure 2.10. Events 10, 11, 12 and 13 corresponds events 4, 5, 6 and 7, respectively. Event 8 in Figure 2.11(i) again describes the behavior of the beam at M equal to 0.

As shown in Figure 2.10, the response of the PFC to a counter-clockwise moment is similar to the response to a clockwise moment due to the symmetry of the components about the centroidal axis of the beam as shown in Figures 2.9. The self-centering capability, rigidity, and ductility of the connection are shown in Figure 2.10.

2.3 Moment Resistance of the Friction Component of the PFC

As previously stated, the total applied moment between events 3 and 4 in Figure 2.10 is the sum of the moment resistance due to friction, and the moment resistance due to the post-tension force in the PT strands, and the moment due to the additional force in the strands due to the elongation of the strands. Due to the rotation of the beam, the friction force on the friction component has both a horizontal and vertical component as shown in Figure 2.13. The horizontal and vertical friction force components, F_{fx} and F_{fy} are not located at the center of the tribo surface, but at some eccentricity of e_y and e_x, respectively, as shown in Figure 2.13.

To quantify the friction force components, the friction force was converted into a friction stress (f_f) acting over the tribo surface area (A_{ts}). A small angle of relative rotation about the COR was assumed, and thus only the original geometry of the tribo surface area was considered. As the beam rotates θ, the relative slip at an arbitrary point on the tribo surfaces has a direction given by the angle α, as shown in Figure 2.14. The horizontal and vertical slip at the arbitrary point are noted as Δx and Δy, respectively. The horizontal and vertical friction stress components resulting from slip at an arbitrary point are as follows:

$$f_{fx} = f_f \cdot \cos\alpha = f_f \cdot \left(\frac{\Delta x}{\sqrt{\Delta x^2 + \Delta y^2}} \right) \tag{2.11}$$

$$f_{fy} = f_f \cdot \sin\alpha = f_f \cdot \left(\frac{\Delta y}{\sqrt{\Delta x^2 + \Delta y^2}} \right) \tag{2.12}$$

where: f_f = the friction stress, and

α = the angle which gives the direction of slip which depends on the location of the arbitrary point on the tribo surfaces.

Δx and Δy are a function of position of the tribo surface relative to the COR as shown in Figure 2.14. Assuming the gap opening angle (θ) to be small, the following relationships can be used:

$$\Delta x = y \cdot \theta \tag{2.13}$$

$$\Delta y = x \cdot \theta \tag{2.14}$$

where: y = the vertical distance of the arbitrary point from the COR, and

x = the horizontal distance of the arbitrary point from the COR.

Δx and Δy are both treated as positive when in the direction shown in Figure 2.14.

The friction stresses can be integrated with respect to the area of the tribo surface as shown in the following equations. The resulting factors, F_{fx} and F_{fy}, are the horizontal and vertical friction force components acting on each tribo surface.

$$F_{fx} = \int_{A_{ts}} f_f \cdot \left(\frac{y}{\sqrt{y^2 + x^2}} \right) dA \tag{2.15}$$

$$F_{fy} = \int_{A_{ts}} f_f \cdot \left(\frac{x}{\sqrt{y^2 + x^2}} \right) dA \tag{2.16}$$

where: A_{ts} = the tribo surface area.

Because F_{fx} and F_{fy} are a function of the geometry of the tribo surfaces with respect to the COR, the tribo surface geometry is defined with respect to the COR as shown in Figure 2.15. The horizontal boundaries of the tribo surfaces from the COR are defined by y_2 and y_1, and x_2 and x_1 define the vertical boundaries as shown in Figure 2.15. Thus Equations 2.15 and 2.16 can be rewritten as follows:

$$F_{fx} = \int_{x_1}^{x_2}\left(\int_{y_1}^{y_2} f_f \cdot \left(\frac{y}{\sqrt{y^2+x^2}}\right)dy\right)dx \tag{2.17}$$

$$F_{fx} = \int_{x_1}^{x_2}\left(\int_{y_1}^{y_2} f_f \cdot \left(\frac{x}{\sqrt{y^2+x^2}}\right)dy\right)dx \tag{2.18}$$

Equations 2.17 and 2.18 are applicable for any rectangular tribo surface at θ some location with respect to the COR. The total moment due to friction (M_{Ff}) for the friction device is a function of the horizontal and vertical distances from the COR. As shown in Figure 2.14 the friction stress varies with location on the tribo surface, and therefore, F_{fx} and F_{fy} do not act at the centroid of the tribo surfaces. Thus F_{fx} and F_{fy} were not used to determine M_{Ff}.

The moment due to friction (M_{Ff}) was determined by integrating the product of the friction stresses with the distance to the COR as shown in Figure 2.16 as follows:

$$M_{Ff} = \left[\int_{A_{ts}} f_{fx} \cdot y \cdot dA + \int_{A_{ts}} f_{fy} \cdot x \cdot dA\right] = f_f \int_{A_{ts}} r dA \tag{2.19}$$

where: r = the distance from the arbitrary point of stress on the tribo surface to the COR.

To carryout the integral of Equation 2.18 in polar coordinates, the tribo surface area previously defined using Cartesian coordinates (x and y), as shown in Figure 2.15,

is now defined by using r and α as shown in Figure 2.16. The integral of Equation 2.18 is now expressed as:

$$M_{Ff} = \int_{\alpha}\left(\int_{r} r\,dr\right)d\alpha \tag{2.20}$$

where: α = the angle which describes the location of the arbitrary point on the tribo surface with respect to the COR.

The following equation is the result of the integration of Equation 2.20, and can be used to determine the moment due to friction on any tribo surfaces at some location with respect to the COR..

$$\begin{aligned} M_{Ff} = -\frac{1}{6}\mu N\cdot[&-2x_2y_2\sqrt{x_2^{\,2}+y_2^{\,2}} - x_2^{\,3}\sinh^{-1}\left(\frac{y_2}{x_2}\right) + 2x_2y_1\sqrt{x_2^{\,2}+y_1^{\,2}} \\ &+ x_2^{\,3}\sinh^{-1}\left[\frac{y_1}{x_2}\right] + 2x_1y_2\sqrt{x_1^{\,2}+y_2^{\,2}} + x_1\sinh^{-1}\left(\frac{y_2}{x_1}\right) - 2x_1y_1\sqrt{x_1^{\,2}+y_1^{\,2}} \\ &- x_1^{\,3}\sinh^{-1}\left(\frac{y_1}{x_1}\right) + y_1^{\,3}\sinh^{-1}\left(\frac{x_2}{y_1}\right) - y_2^{\,3}\sinh^{-1}\left(\frac{x_2}{y_2}\right) - y_1^{\,3}\sinh\left(\frac{x_1}{y_1}\right) \\ &+ y_2^{\,3}\sinh^{-1}\left(\frac{x_1}{y_2}\right)]/((-x_2+x_1)\cdot(-y_2+y_1)) \end{aligned} \tag{2.21}$$

Equation 2.21 can be simplified for a tribo surface with a vertical edge in the same vertical plane as the COR ($x_1 = 0$) as follows:

$$\begin{aligned} M_{Ff}(x_1=0) = -\frac{1}{6}\mu N\cdot[&-2x_2y_2\sqrt{x_2^{\,2}+y_2^{\,2}} - x_2^{\,3}\sinh^{-1}\left(\frac{y_2}{x_2}\right) + 2x_2y_1\sqrt{x_2^{\,2}+y_1^{\,2}} \\ &+ x_2^{\,3}\sinh^{-1}\left(\frac{y_1}{x_2}\right) + y_1^{\,3}\sinh^{-1}\left(\frac{x_2}{y_1}\right) - y_2^{\,3}\sinh^{-1}\left(\frac{x_2}{y_2}\right)]/((-x_2+x_1)\cdot(-y_2+y_1)) \end{aligned} \tag{2.22}$$

Figure 2.17 shows the comparison of M_{Ff} to $\mu \bullet N \bullet (d_b/2)$ (i.e., the moment resistance due to friction assumed in Equation 2.4). To generate Figure 2.17, Equation 2.20 was non-dimensionalized as follows:

$$\frac{M_{Ff}}{\mu N y_c} = \left[\frac{2}{3}\sqrt{a^2+1} + 2a^2 \sinh^{-1}\left(\frac{1}{a}\right) + \frac{1}{3}\frac{\sqrt{a^2+\left(\frac{1}{c}\right)^2}}{c} - \frac{1}{3}a^2 \sinh^{-1}\left(\frac{1}{b}\right) - \frac{1}{108}\frac{\sinh^{-1}(b)}{c^3 a}\right] \Big/ \left(1-\left(\frac{1}{c}\right)^2\right) \qquad (2.23)$$

where: $a = x_2/y_2$,

$b = x_2/y_1$,

$c = y_2/y_1$, and

$y_c = (y_1+y_2)/2$, therefore, assuming y_c is at half the beam depth

$y_c = (d_b/2)$.

In generating Figure 2.17, the ratio c was constant at 3.875. The value of y_2 was 18.87 inches, and the value of y_c was 11.87 inches. The value of y_c corresponds to $d_b/2$ for a W24x62 beam. Table 2.1 shows data corresponding to Figure 2.17. To generate this table, N was assumed to be 23 kips/bolt and μ was assumed to be 0.3.

Table 2.1. Moment due to F_f as a Function of Tribo Surface Dimensions

$a = (x_2/y_2)$ ---	$\mu \cdot N \cdot y_c$ (kips•inch)	[multiplier] ---	M_{Ff} (kips•inch)
0	245.7090	1.0000	245.7090
0.0530	245.7090	1.0425	256.1590
0.1060	245.7090	1.0867	267.0069
0.1590	245.7090	1.1484	282.1796
0.2120	245.7090	1.2231	300.5316
0.2650	245.7090	1.3082	321.4365
0.3180	245.7090	1.4017	344.4103
0.3710	245.7090	1.5019	369.0303
0.3842	245.7090	1.5279	375.4188
0.4240	245.7090	1.6077	395.0264
0.4769	245.7090	1.7179	422.1035
0.5299	245.7090	1.8319	450.1143
0.5829	245.7090	1.9450	477.9040
0.6359	245.7090	2.0685	508.2491
0.6889	245.7090	2.1902	538.1519
0.7419	245.7090	2.3136	568.4723
0.7949	245.7090	2.4384	599.1368
0.8479	245.7090	2.5645	630.1207
0.9009	245.7090	2.6916	661.3503
0.9539	245.7090	2.8195	692.7765
1.0069	245.7090	2.9483	724.4238
1.0599	245.7090	3.0776	756.1940

Assuming: y2 = 18.87 inches
$c = y_2/y_1 = 3.875$

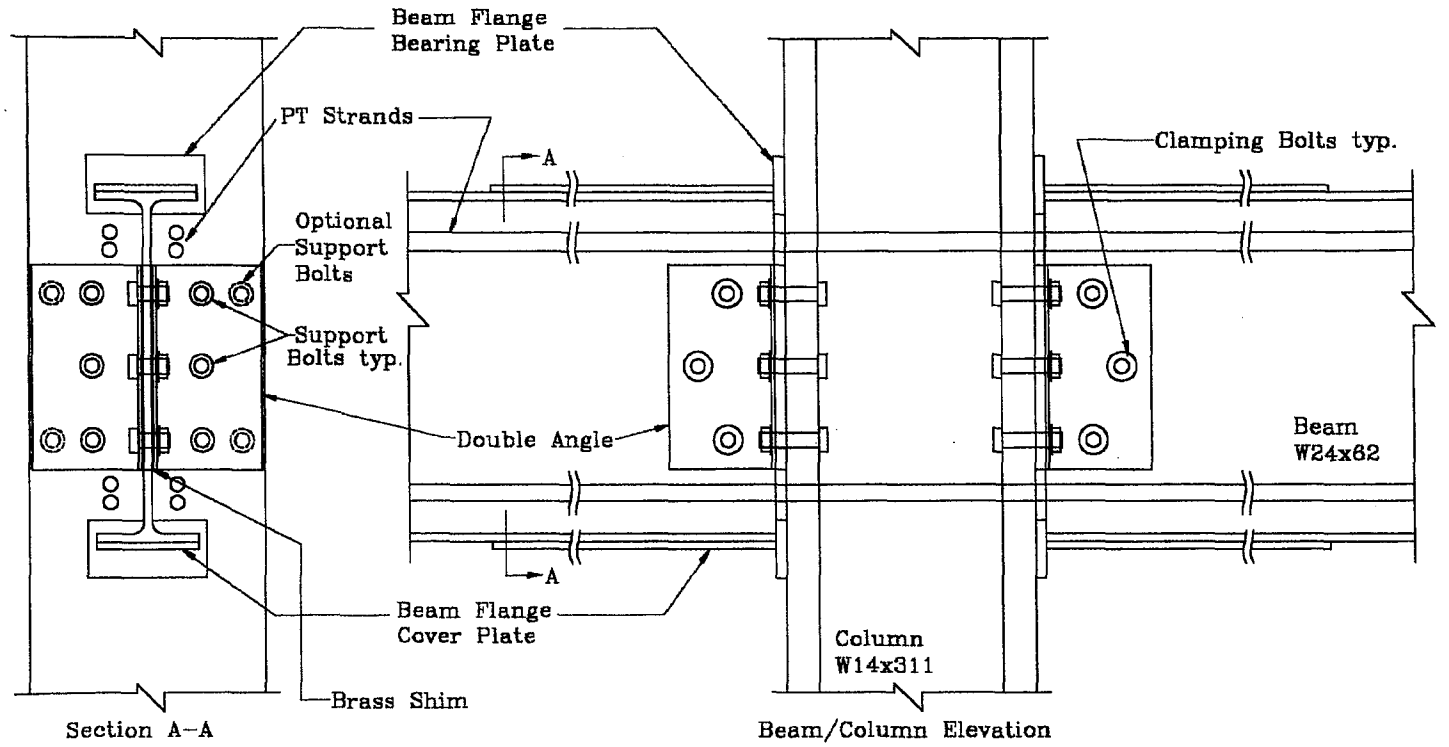

Figure 2.1. Typical Post-Tensioned Friction-Damped Connection Details

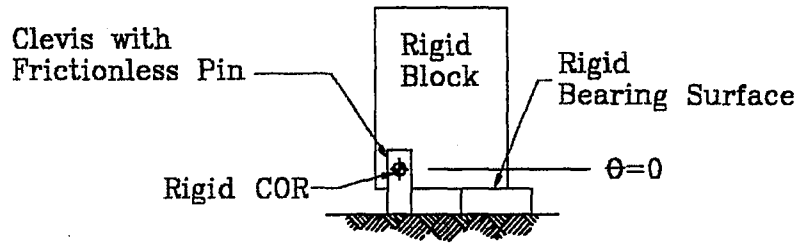

Figure 2.2. Rigid Block Model

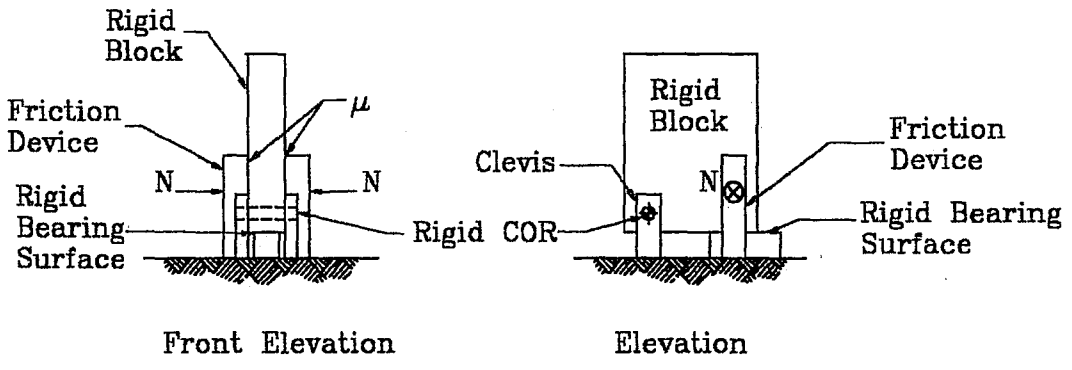

(a)

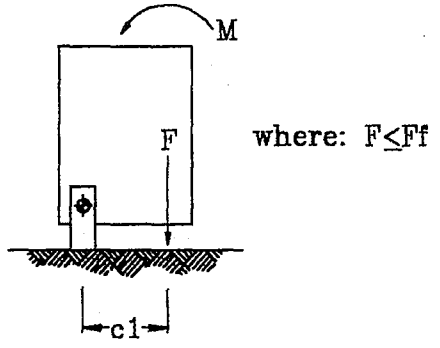

(b)

Figure 2.3. Rigid Block Model with Friction Component
(a) Elevations and (b) FBD

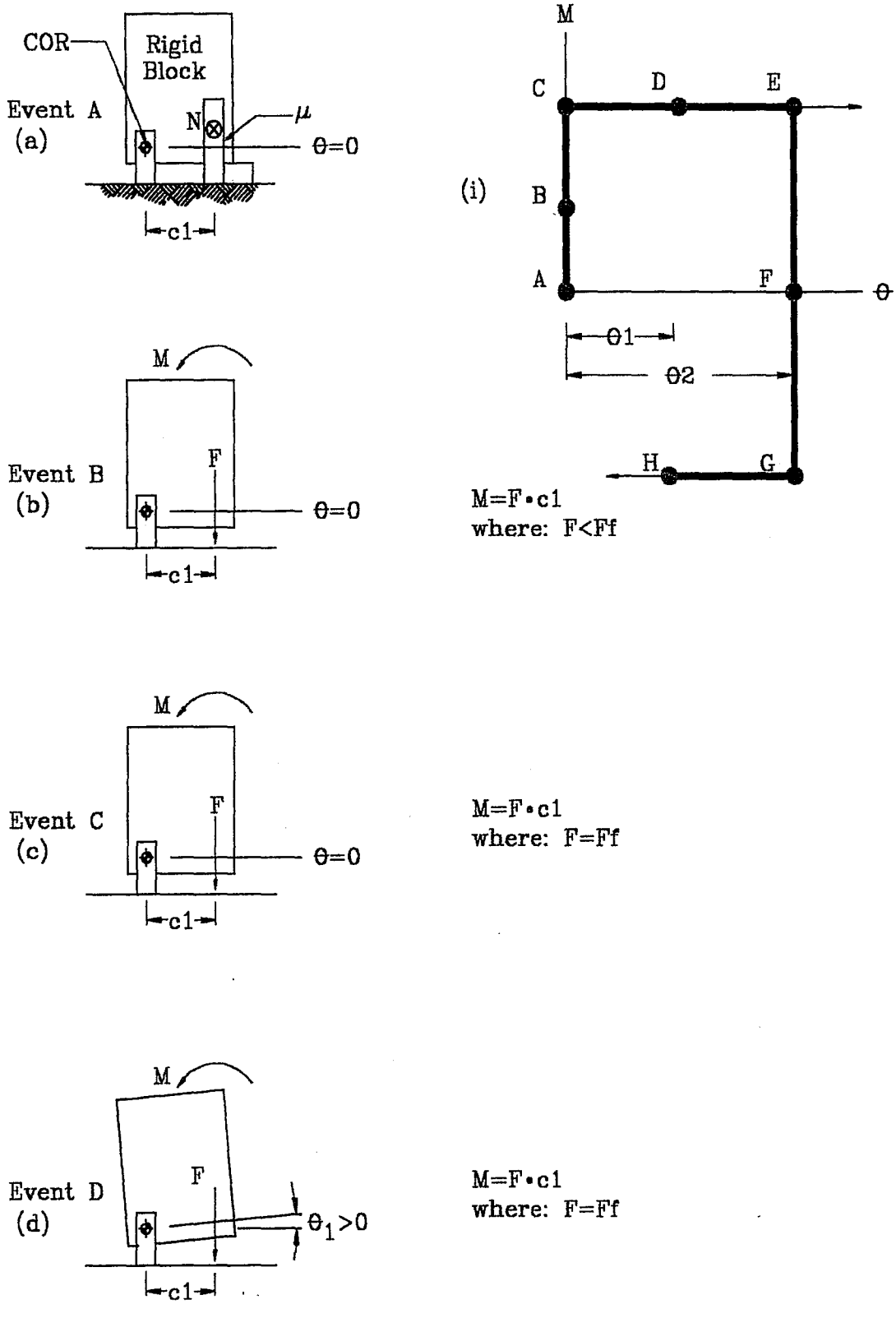

Figure 2.4. M–θ Behavior of Rigid Block Model with Friction Component

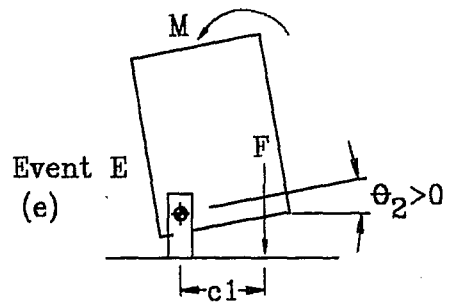

Event E
(e)

M=F•c1
where: F<Ff

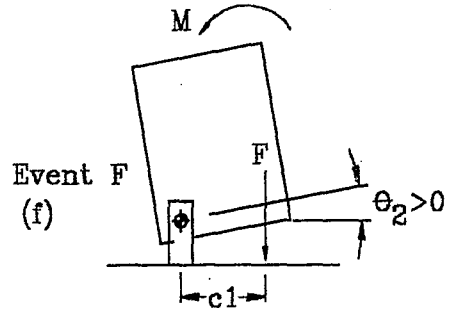

Event F
(f)

M=0
F=0

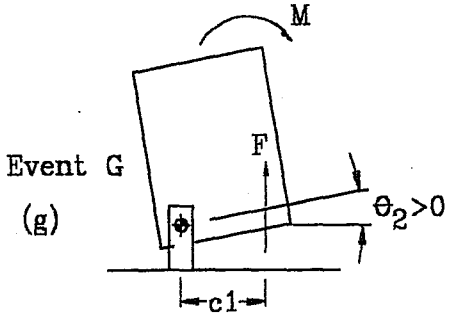

Event G
(g)

M=F•c1
where: F=Ff

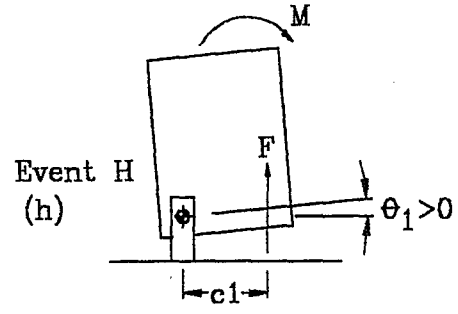

Event H
(h)

M=F•c1
where: F=Ff

Figure 2.4(continued). M–θ Behavior of Rigid Block Model with Friction Component

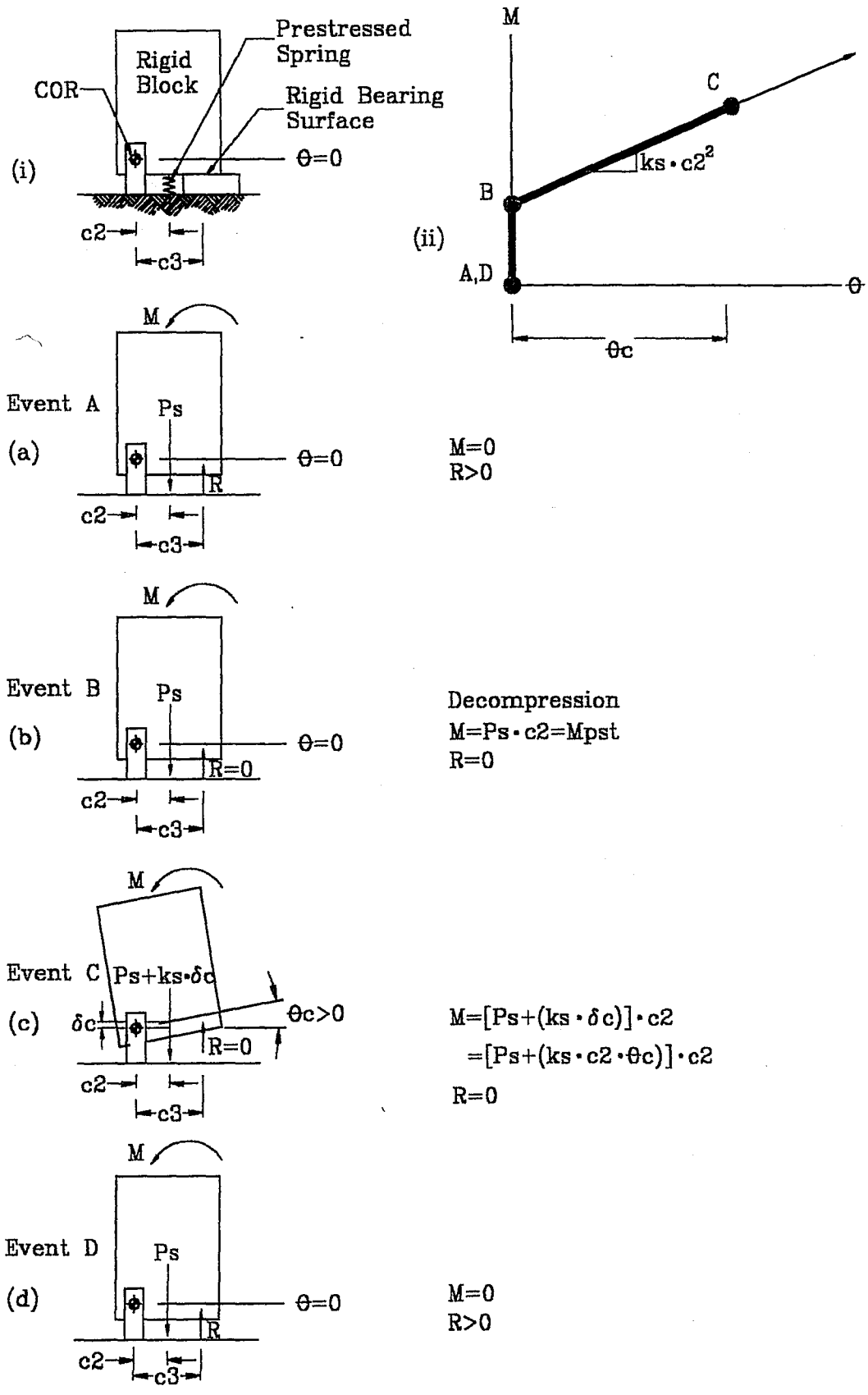

Figure 2.5. M–θ Behavior of Rigid Block with Post-Tensioned Component

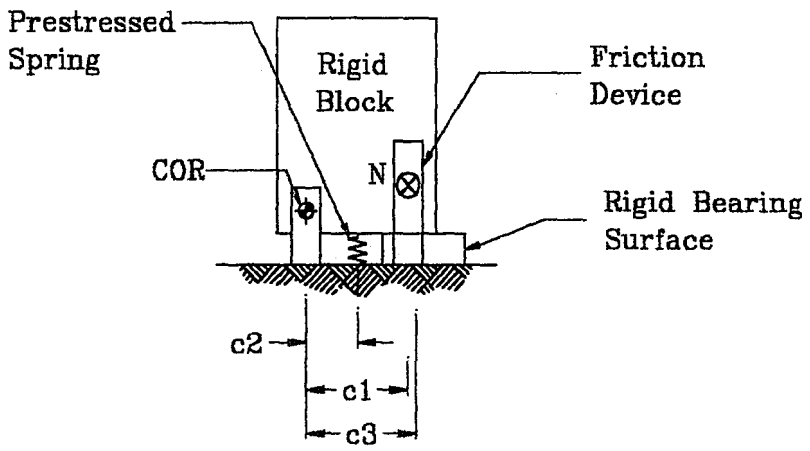

Figure 2.6. Rigid Block PFC Model

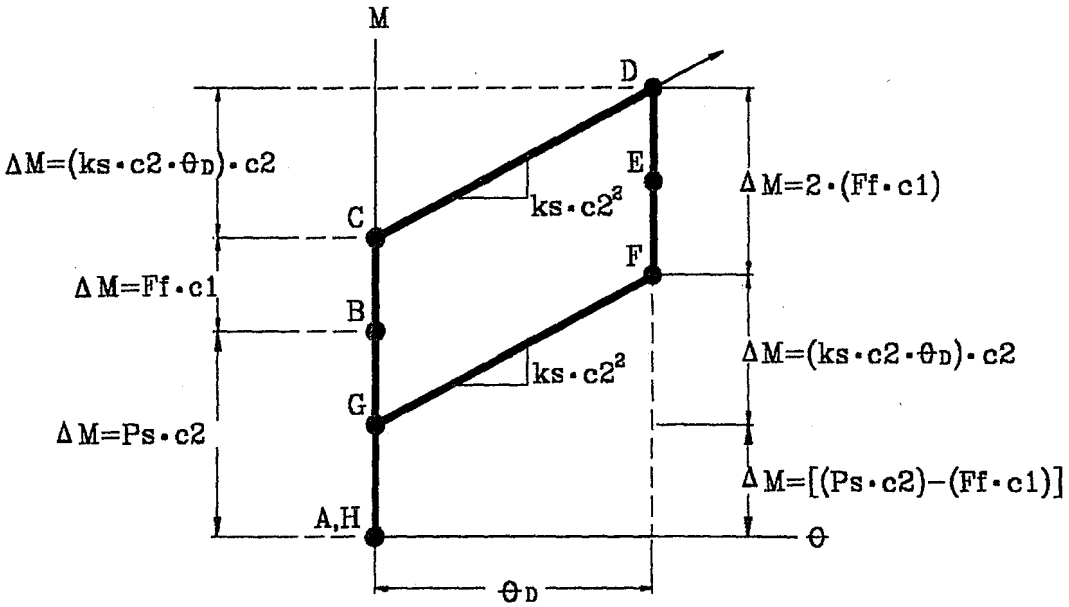

Figure 2.7. M–θ Curve of Rigid Block Model of PFC

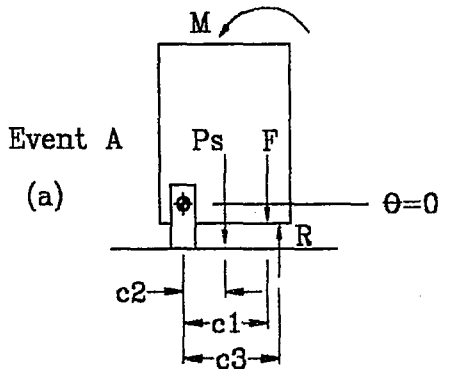

M=0
R=(Ps·c2)/c3
F=0

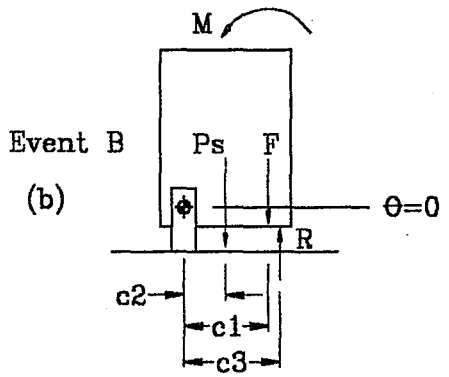

Decompression
M=(Ps·c2)
R=0
F=0

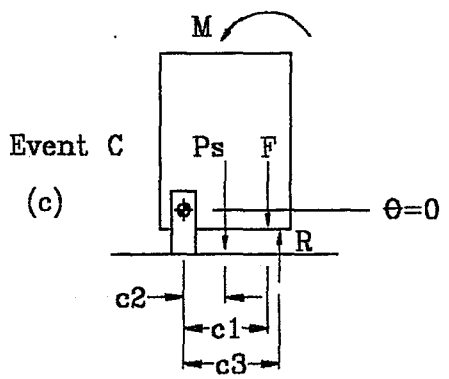

M=(Ps·c2)+(F·c1)
R=0
F=Ff

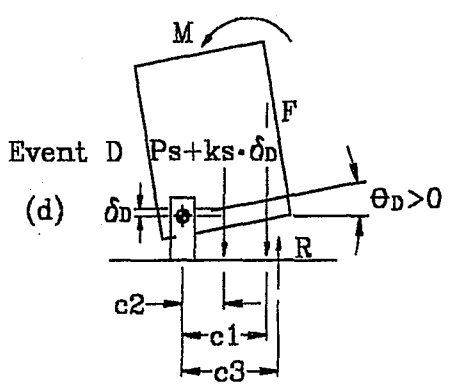

M=[Ps+(ks·c2·θD)]·c2+(F·c1)=MD
R=0
F=Ff

Figure 2.8. M–θ Behavior of Rigid Block Model of PFC

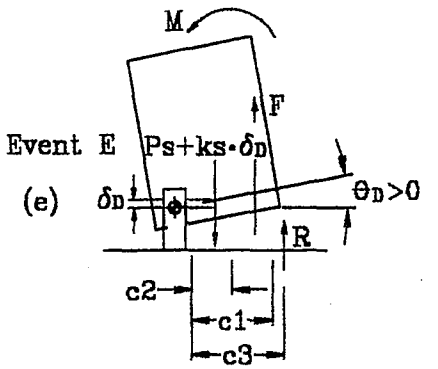

$M=M_D-(Ff\cdot c1)$
$R=0$
$F=0$

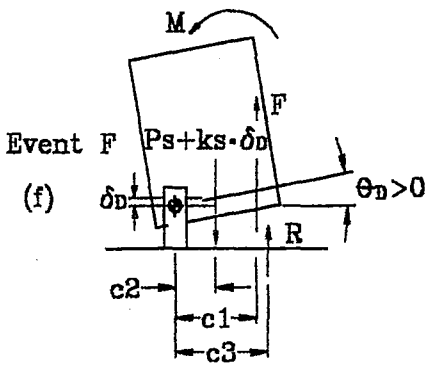

$M=M_D-[2\cdot(Ff\cdot c1)]$
$R=0$
$F=Ff$

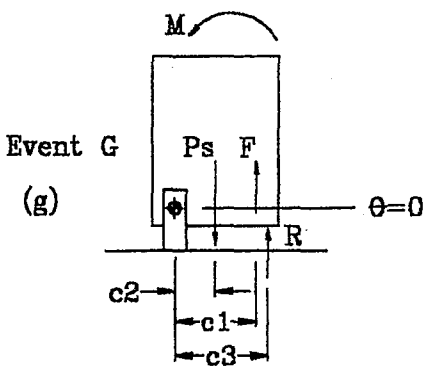

$M=M_D-[2\cdot(Ff\cdot c1)]-(ks\cdot c2\cdot\theta_D)\cdot c2$
$R=0$
$F=Ff$

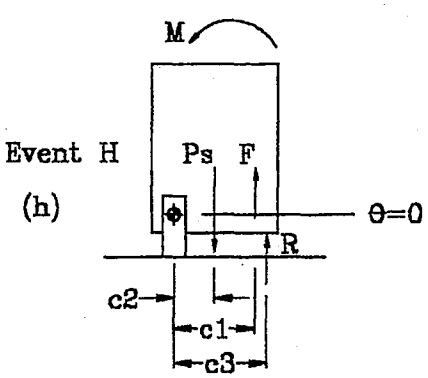

$M=M_D-[2\cdot(Ff\cdot c1)]-(ks\cdot c2\cdot\theta_D)\cdot c2$
$-[Ps\cdot c2)-(Ff\cdot c1)]=0$
$R=[Ps\cdot c2)-(Ff\cdot c1)]/c3=0$
$F=Ff$

Figure 2.8(continued). M—θ Behavior of Rigid Block Model of PFC

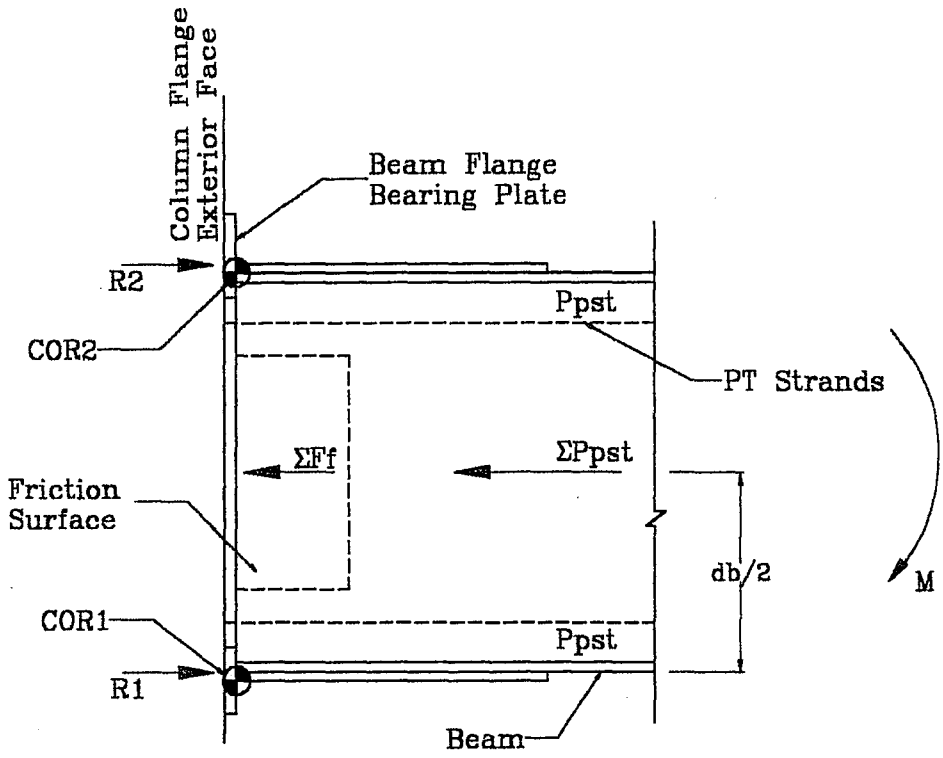

Figure 2.9. Beam Model for PFC M–θ Response Curve

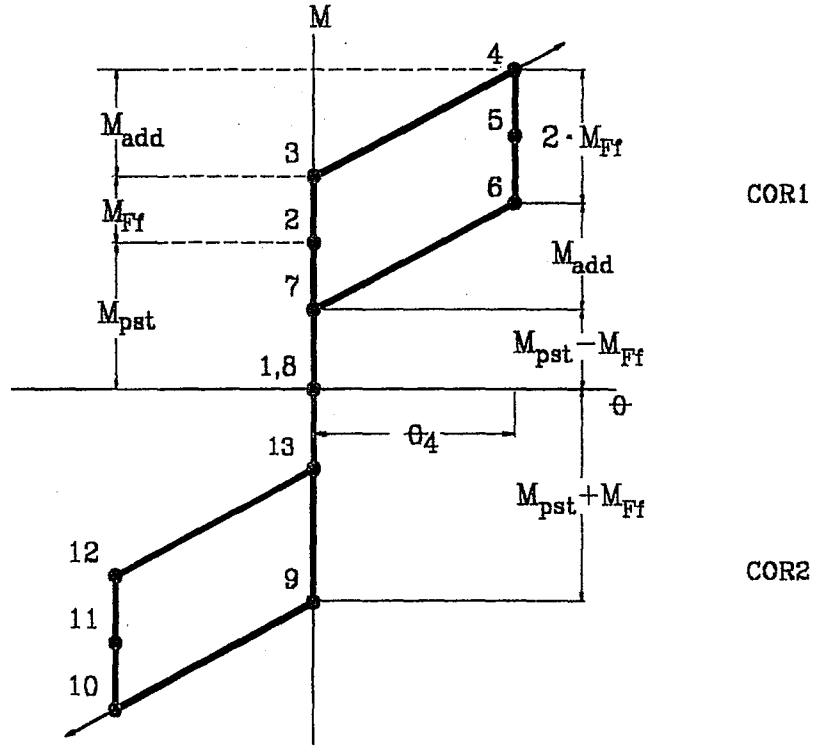

Figure 2.10. PFC M–θ Curve

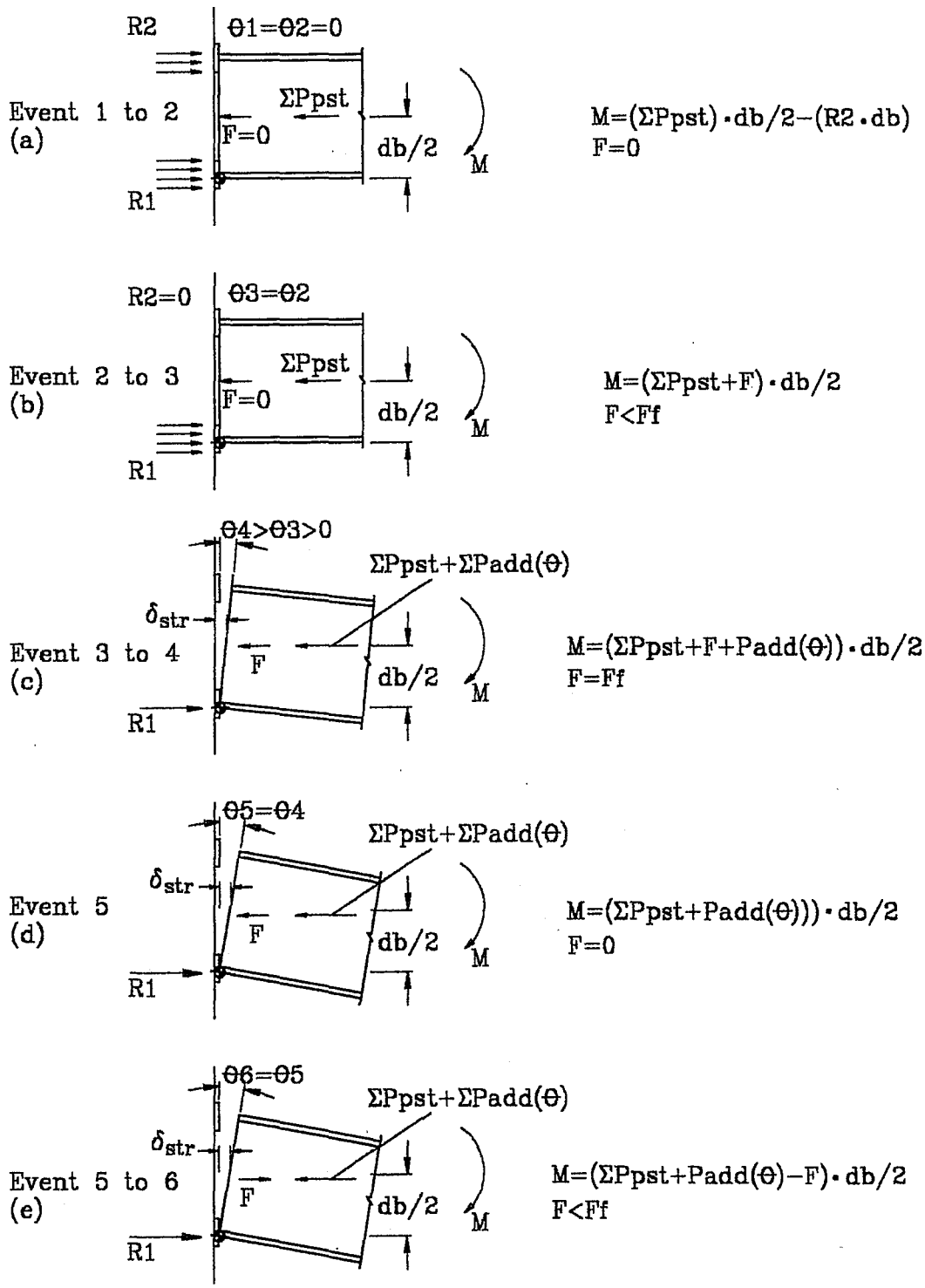

Figure 2.11. M−θ Behavior of PFC

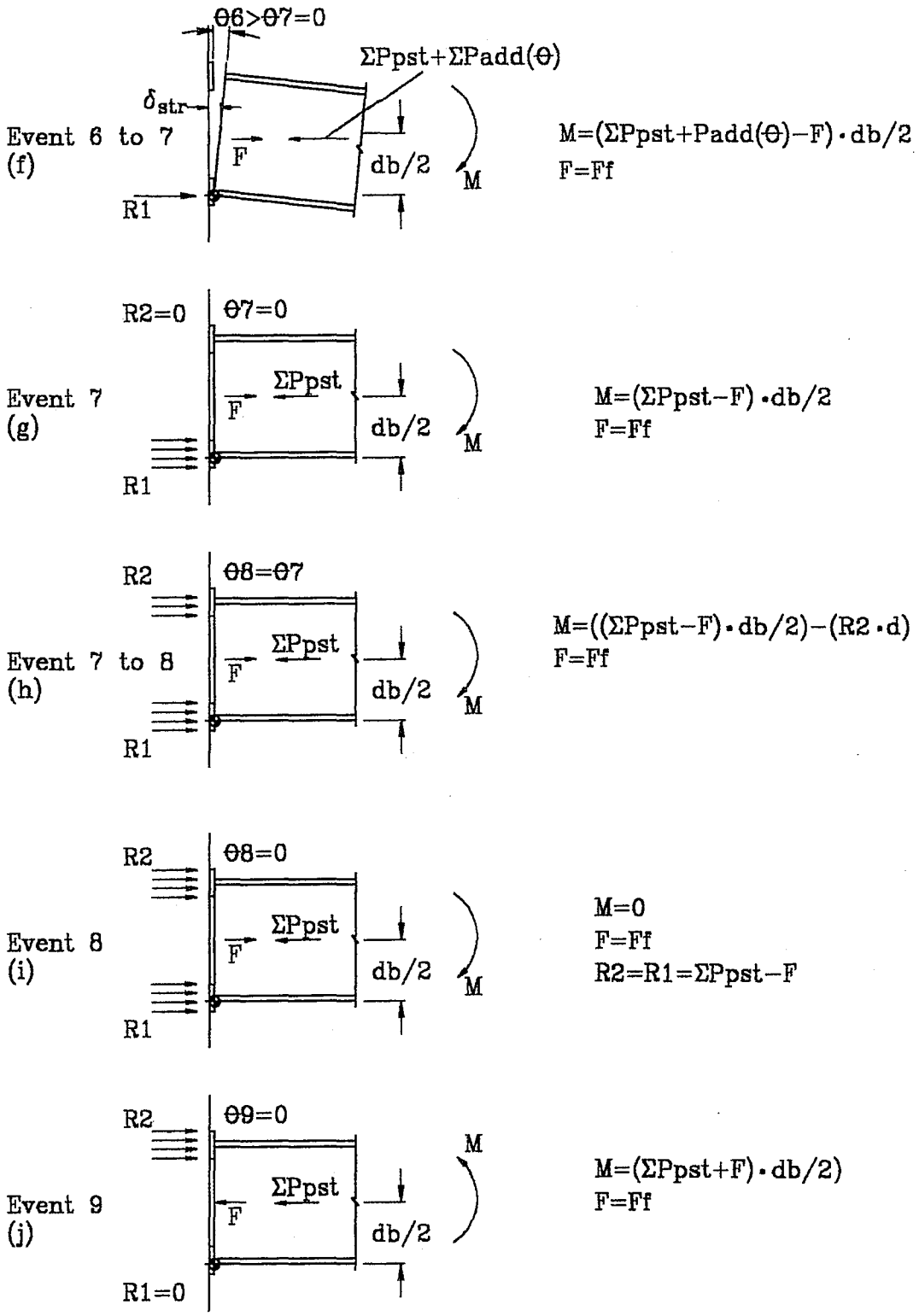

Figure 2.11(continued). M−θ Behavior of PFC

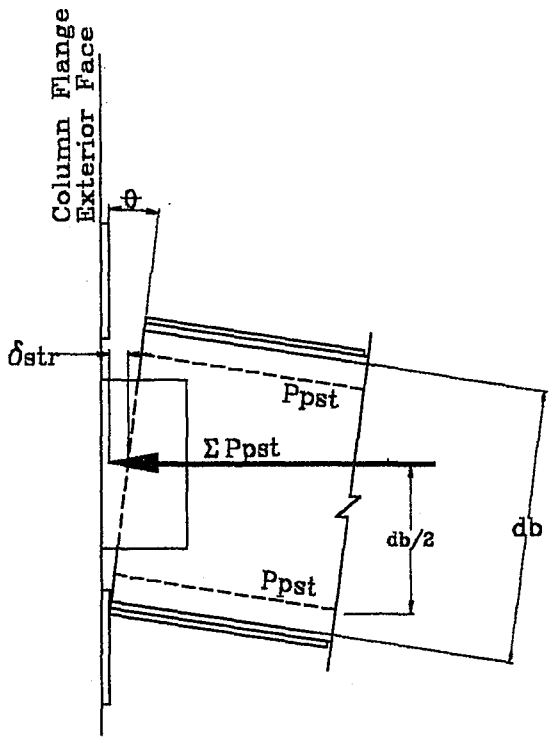

Figure 2.12. Elongation of Post-Tensioned Strands

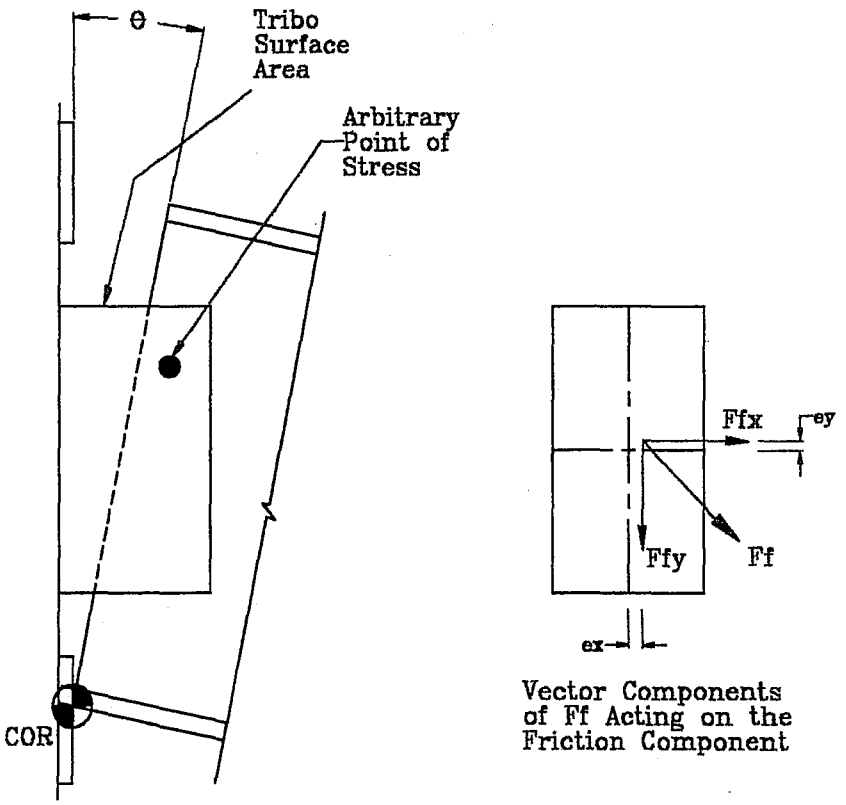

Figure 2.13. Vector Components of Friction Force

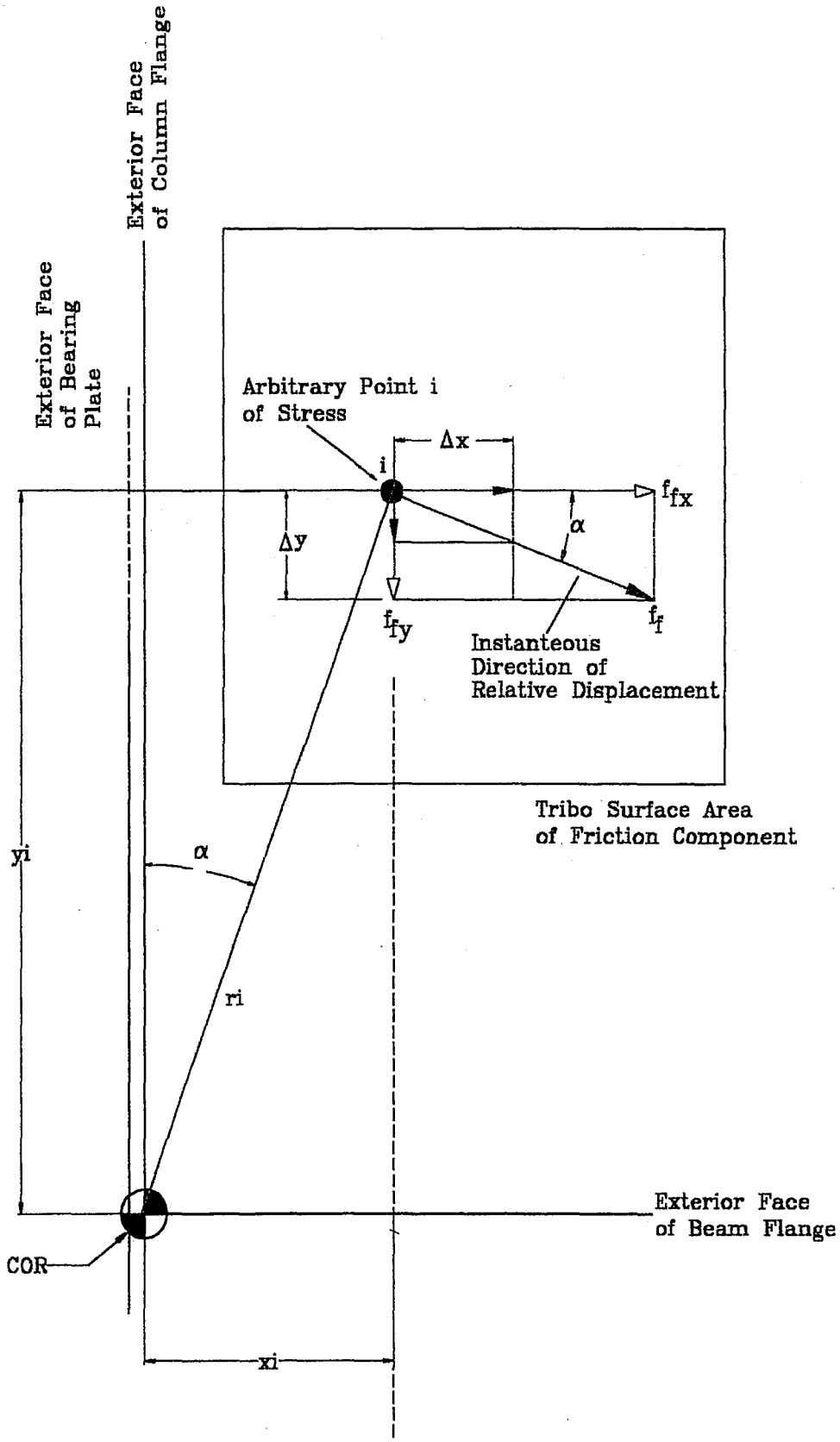

Figure 2.14. Analysis of Relative Displacement at an Arbitrary Point on Tribo Surfaces

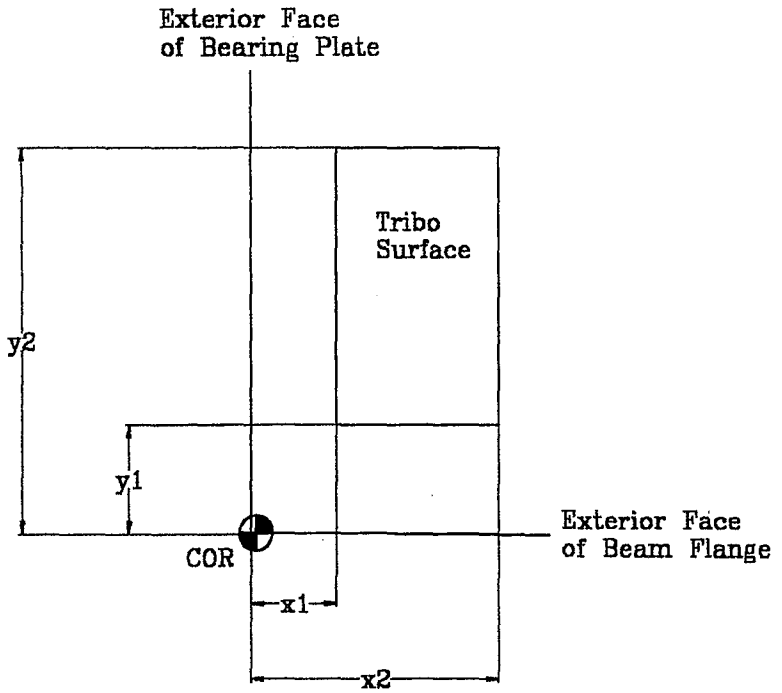

Figure 2.15. Defining of Tribo Surface with Respect to COR

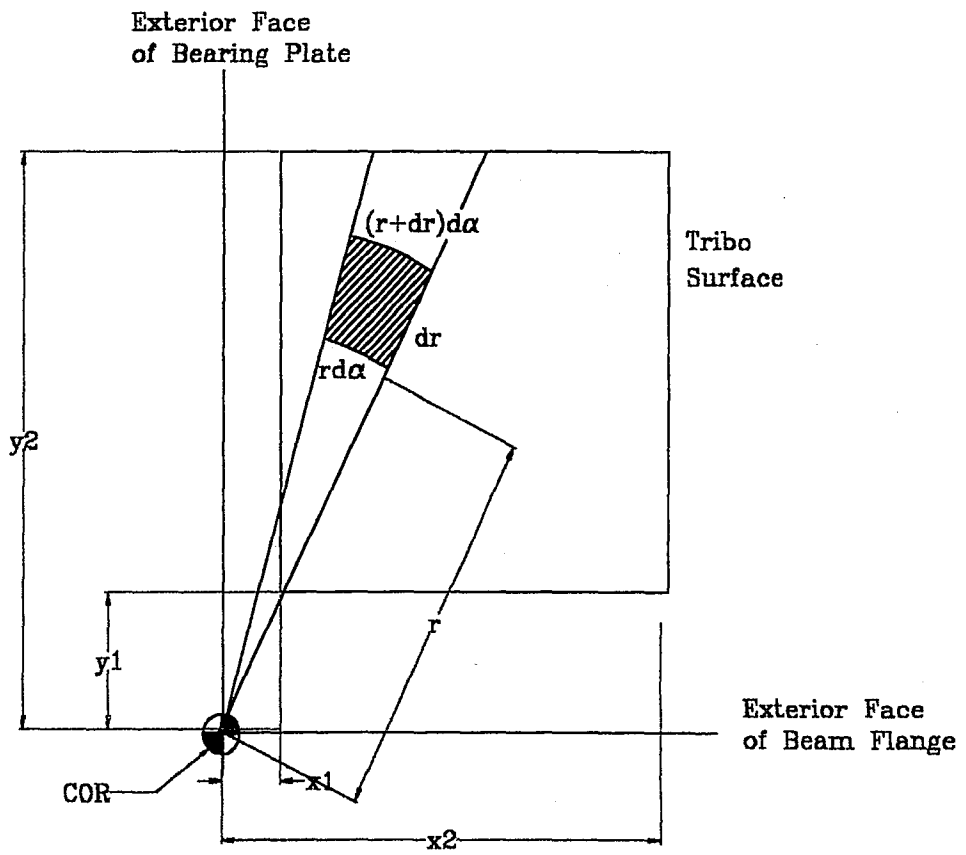

Figure 2.16. Integration Model used to Determine the Theoretical Moment due to Friction

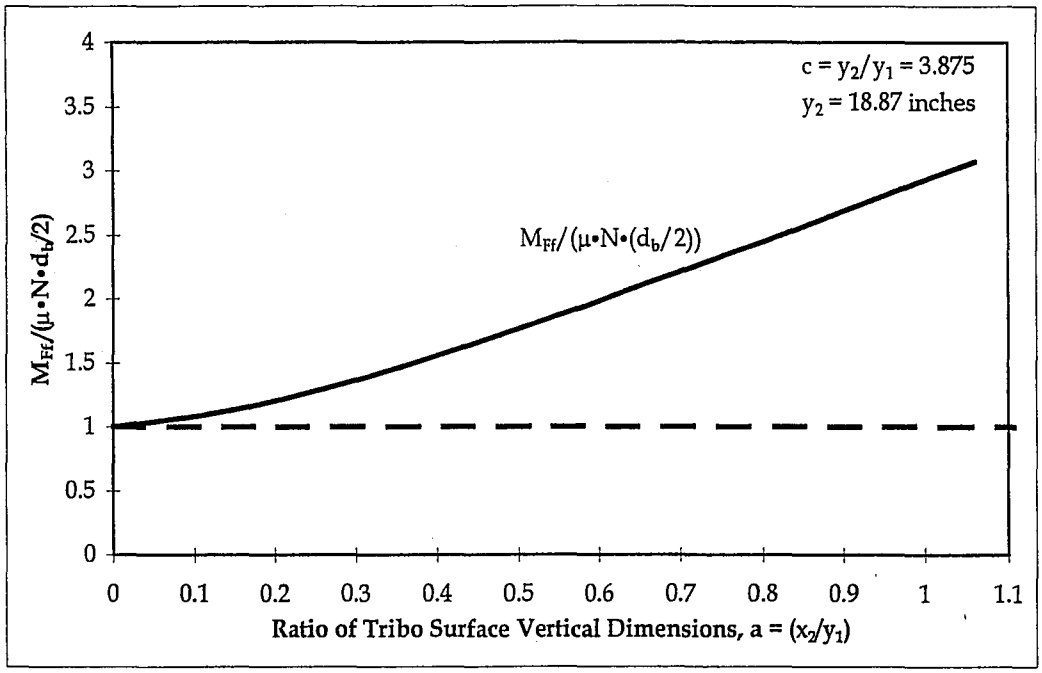

Figure 2.17. $M_{Ff}/(\mu \bullet N \bullet d_b/2)$ vs. Tribo Surface Horizontal Length

3. Design of the Friction Component of a Post-Tensioned Friction-Damped Connection

This chapter presents the design of the friction connection component (FCC) of the post-tensioned friction-damped connection (PFC). The design addresses aspects of the FCC such as the initial design parameters, and detailing of the FCC.

3.1 Relevant Components of Post-Tensioned Steel Connection

The post-tensioned friction-damped connection (PFC) developed in this chapter is based on a post-tensioned steel connection studied in previous research. Some of the components of the PFC are the same as those of Specimen PC4 tested by Chen (1998) and Peng et al. (1999). The dimensions of the beam, column, PT strands, flange bearing plates, and flange reinforcing plates are similar to those of Specimen PC4 shown in Figure 3.1(a). The connections tested by Chen (1998) and Peng et al., (1999) included top and bottom seat angles, which are not included in the PFC, as shown in Figure 3.1(b). Specimen details for Specimen PC4 are given in Table 1.1.

The beam shown in Figure 3.1 is a W24x62 wide flange section with a specified yield strength of 36 ksi. The column is a W14x311, with a specified yield strength of 36 ksi. The beam flange reinforcing plates and beam flange bearing plates are high strength steel with a specified yield strength of 100 ksi. The bearing plates are welded to the exterior face of the column flange. The purpose of these plates is to

prevent contact of the beam web with the column flange. As shown in Figure 3.1(a), the beam flange reinforcing plates were welded to the interior of the beam flange for Specimen PC4, because of constraints created by the initial design of the post-tensioned connections tested by Chen (1998) and Peng et al., (1999). In practice the plates would be on the outside of the beam flanges as shown in Figure 3.1(b) for the PFC. The purpose of these plates is to prevent yielding of the flanges in compression.

The post-tensioned strands are 7-wire strands, protected by a corrosion inhibiting grease and encased in a polypropylene sheath. Each strand had a nominal diameter and cross-sectional area of 0.6 inch and 0.217 inch^2 respectively. The specified ultimate strength for the strand is 270 ksi, and the nominal modulus of elasticity is 28800 ksi. As shown in Figure 3.1(a), four PT strands were equally spaced along each side of the beam web symmetrically about the centroidal axis of the beam for the post-tensioned steel connection. For the PFC, the PT strands were repositioned to avoid interface with the friction component of the connection. To avoid interference, the inner strands were moved to be adjacent to the outer strands. The difference in strand arrangement can be seen by comparing the post-tensioned steel connection and the PFC shown in Figures 3.1(a) and 3.1(b) respectively.

3.2 Selection of Elements of the Friction Component

The friction connection component (FCC) of the PFC developed in this chapter is comprised of a brass-steel tribo surface, double angle connection, clamping bolts and support bolts. Each of these elements of the FCC is discussed below.

Brass-Steel Tribo Surfaces

As mentioned in Chapter 2, one of the determining factors of the friction force is the conditions of the tribo surfaces. Steel-steel tribo surfaces have produced undesirable results in previous tests. The friction force increased rapidly, and then decreased rapidly (Grigorian and Popov, 1994). To avoid this problem, brass-steel tribo surfaces are used for the FCC. Wear theory from Vingsbo (1988), Grigorian and Popov (1994), and others will be used below to explain why brass-steel tribo surfaces are selected instead of steel-steel tribo surfaces.

During relative motion of two tribo surfaces, shear deformation occurs at asperity junctions. This shear deformation eventually leads to *tribo fracture*. *Wear fragments* are produced as particles are removed from the parent material. Two types of *wear mechanisms* that can occur on the steel-steel and brass-steel tribo surfaces, are *abrasive wear* and *adhesive wear*.

Abrasive wear is characterized by elasto-plastic friction conditions at the tribo surfaces. This is expected for steel-steel tribo surfaces, especially if the surfaces are

untreated and mill scale remains. Wear fragments are fractured from the parent tribo surfaces. It has been hypothesized that the wear fragment layer between the tribo surfaces forces the surfaces to separate (Grigorian and Popov, 1994). This causes a rise in the friction force, compared to the initial friction force, if the plates are clamped by bolts. As cycling continues, wear fragments are rejected from the tribo system, decreasing the volume of the wear fragment layer and ultimately, decreasing the friction force (Grigorian and Popov, 1994).

Adhesive wear of brass-steel tribo surfaces occurs because of the ductility of the brass asperities. As sliding occurs between the two surfaces, the brass which is a softer material, is worn by the steel, which is a harder material. As asperities slide relative to one another, shearing of the weaker asperities occurs. As local temperature rises accompany the shearing of asperities in contact, welding or adhesion of the brass (softer) wear fragments to the steel (harder) asperities occurs (Petach and White, 1957). A wear fragment layer is produced which may cause an increase in the friction force. Although some wear fragments fall free from the tribo surfaces, the majority of brass wear fragments remain adhered to the steel surface, producing a relatively constant friction force.

Double Angle Connection

Several different ways of connecting the friction surfaces to the beam and column were investigated. A double angle connection was selected for the FCC. In the

double angle connection, the beam web slides between two stationary angles which are connected to the column. The beam slides between the angles as the beam rotates about two centers of rotation which are where the beam flanges meets the bearing plates. The double angle connection was selected for the following reasons: (1) a similar connection is currently used in practice; (2) the connection can provide a high friction force capacity; (3) the connection provides redundancy; (4) the connection does not require welding; and (5) the connection does not interfere with the attachment of composite slabs. In addition, design specifications for double angle construction have been developed by the American Institute of Steel Construction (AISC), and documented in the Manual of Steel Construction (AISC-LRFD, 1995).

The double angle connection has a high friction force capacity because the connection has large tribo surfaces. The tribo surfaces are between the angle legs extending from the column face and the beam web. Two surfaces are provided because the double angles are connected to both sides of the beam web.

With appropriate detailing, the double angle provides redundancy. The shear capacity of the double angle connection is enough to support significant beam end reactions (shear forces). If the strands of the PFC lose their post-tensioning force the double angle can perform as a simple shear connection.

The desired behavior of the double angle connection can be achieved using high strength structural bolts, thus welding is avoided. The double angle connection has no special design details related to the placement of a composite slab. In comparison, if the FCC was attached to the beam flanges, avoiding interference with a composite slab would require special details. The double angle is placed along the centroidal axis of the beam, thus the composite slab which is placed above the top beam flange, is not affected.

Clamping and Support Bolts

The clamping bolts are the horizontal bolts which fasten the double angle connection to the beam web. These bolts provide the normal (or clamping) force necessary to produce the desired friction force. The support bolts attach the friction component (i.e., the double angles) to the column flange. The support bolts resist the tension and bending of the double angles which result from friction forces that develop as the beam rotates about a center of rotation, and resist vertical forces through shear.

3.3 Design of the Elements of the Friction Component

This section describes the design of the elements of the friction connection component (FCC) of the PFC. The FCC consists of brass-steel tribo surfaces clamped between double angles attached to the beam web (Figure 3.1). Although the double angle connection is capable of supporting gravity loads, emphasis is

placed only on the behavior of the connection when to the frame is subject to lateral loads. AISC specifications are used when appropriate (AISC-LRFD, 1995).

Selection of the Friction Force

The friction force (F_f) of the FCC is related to the moment capacity of the PFC. Thus, the PFC should be designed to have the maximum possible F_f. However, the magnitude of F_f is limited by several limit-states of the associated beam and double angle connection including: (1) failure of beam flange and reinforcing plates in compression; (2) net section failure of the beam web; (3) yielding of the angles; (4) combined bending and tension failure of the support bolts; and (5) failure of the connection to close after the moment is removed which occurs when the moment due to friction (M_{Ff}) exceeds the moment resistance due to the post-tension force in the PT strands (M_{pst}). A discussion of all but the first limit-state is presented below.

If M_{Ff} exceeds M_{pstr}, the PFC does not close after the applied moment is removed, and this results in permanent rotation of the connection. A frame with PFCs will not self-center after the lateral loads are removed, if the PFCs prevent rotation. Thus, the following equation was used in design.

$$M_{Ff} \leq 0.5 \cdot M_{pst} \tag{3.1}$$

The factor of safety of 0.5 covers variations in M_{Ff} and M_{pst}, such as: (1) loss of the post-tension force in the strands; and (2) uncertainties in M_{Ff}.

The total initial post-tension force in the strands in Specimen PC4 was 153 kips, with an average of 19.1 kips/strand. Using Equation 2.3, the moment due to the post-tension force in the strands for Specimen PC4 is as follows:

$$M_{pst} = \Sigma P_{pst} \cdot \frac{d_b}{2}$$

where: P_{pst} = 153 kips; and

d_b = 23.74 inches for a W24x62 beam.

Therefore, M_{pst} is equal to 1816.1 kips•inch. Based on Equation 3.1, the maximum allowable value of M_{Ff} for design is equal to 908.05 kips•inch. With M_{Ff} equal to 908.05 kips•inch, the corresponding friction force can be determined from Equation 2.18 as follows:

$$M_{Ff} = F_f \cdot \frac{d_b}{2} \therefore F_f = \frac{M_{Ff}}{\left(\frac{d_b}{2}\right)}$$

The corresponding F_f is 76.5 kips. Assuming Coulomb Friction theory with μ equal to 0.3, as suggested by Grigorian and Popov (1994), the corresponding total initial clamping force (N_i) on the tribo surfaces can be determined from Equation 2.1 as follows:

$$N_i = \frac{F_f}{\mu \cdot n_{ts}}$$

where: n_{ts} = 2 because the FCC has two tribo surfaces.

The corresponding N_i is 127.5 kips. The tensile design strength for a 1 inch diameter A325 bolt is 53 kips. Thus, the required N_i could be supplied by three 1

inch diameter clamping bolts preloaded to 42.5 kips (i.e., $N_i/3$ bolts), which is 80% (i.e., 42.5 kips/53 kips) of the design tensile strength.

The thickness of the angles was determined based on the beam model shown in Figure 3.2. The model assumes that the angle leg attached to the column flange bends like a beam. As shown in Figure 3.2(c), the moment in the leg of the angle (M) is equal to $1/2 \bullet (1/2 \bullet F_f) \bullet g$, where g is the gage length of the angle, as shown in Figure 3.2(a). To prevent yielding of the angle, M is compared to the yield moment of the angle (M_y), which is calculated as follows:

$$M_y = \sigma_y \cdot S = \left(\frac{b \cdot t^2}{6}\right) \cdot \sigma_y$$

where: S = the section modulus,

b = the width of the angle,

t = the thickness of the angle, and

σ_y = the yield stress.

Equating M to M_y and solving for F_f, the friction force at yield can be determined as follows:

$$F_f = \frac{2 \cdot \sigma_y \cdot b \cdot t^2}{3 \cdot g} \qquad (3.2)$$

An 8x8x3/4 inch angle, 14 inches long (i.e., b=14 inches) with a nominal yield stress of 50 ksi was selected. To estimate the F_f at yield, a gage length of 2.5 inches was used based on AISC bolt spacing specifications (AISC-LRFD, 1995). The estimated

F_f at yield was 105 kips. (Note that if the average measured yield stress for the angles used in the tests described in Chapter 6 (55.6 ksi) is considered, the corresponding F_f at yield is equal to 117 kips.) The F_f at yield of the angles (105 kips) is greater than the F_f corresponding to M_{Ff} equal to $0.5 \bullet M_{pst}$, which was 76.5 kips. Thus, the value of F_f for M_{Ff} equal to $0.5 \bullet M_{pst}$ controls. The corresponding clamping force (N_i) to provide a F_f of 76.5 kips is 127.5 kips. For three bolts, the corresponding bolt tension is 42.5 kips per bolt. The above calculation provides no factor of safety against yielding of the angles. To prevent yielding of the angles, two values of bolt tensions were selected, 23 and 35 kips per bolt, providing a factor of safety of 1.8 and 1.2 respectively.

Based on the moment-rotation model for the PFC presented in section 2.2, the moment at a rotation (θ) equal to 0.03 radians was determined for various bolt preloads using Equation 2.10. The beam is a W24x62, the total post-tension force in strands is assumed to be 153 kips, and a friction coefficient of 0.3 was assumed. The resulting $M(\theta=0.03)$ and $M(\theta=0.03)/M_p$ ratios are shown in Table 3.1. The contributing moment for the various elements are also shown. With bolt preloads of 23 and 35 kips, the connection moment at 0.03 radians is $0.73 \bullet M_p$ and $0.80 \bullet M_p$, respectively.

Brass-Steel Tribo Surface

The brass shims used to create the brass-steel tribo surfaces are shown in Figure 3.3(a). The brass shim is inserted between the interior faces of the double angle and the beam web. A commonly available brass, UNS 260 Half-Hard Cartridge Brass (ASTM B-19), was selected. This type of brass was used by Grigorian and Popov (1994). The brass shim was designed to slide against the beam was, not against the double angles. This required oversized holes in the beam web, as discussed later. Standard bolt holes were used in the legs of the double angles, and similar holes were used in the brass shims. The dimensions of the shims were 7-1/4x14 inches. The thickness of the shim was 1/8 inch. The bolt holes were similar to those in the double angle leg attached to the beam web.

Clamping Bolt Configuration

The configuration of the clamping bolts was based on three considerations: (1) to provide a nearly uniform clamping stress; (2) to provide travel clearances during beam rotation; and (3) to prevent failure of the beam web. Three clamping bolts were used as previously discussed.

A triangular arrangement of bolts was selected to better distribute the clamping force over the angle leg. Coulomb friction theory assumes that the tribo surfaces are rigid and the normal force is independent of the contact area. However, if the tribo surfaces are not rigid, the friction force may be influenced by the area of the

tribo surfaces that are actually in contact (Vingsbo, 1988). The leg of the angle will deform locally around the bolts and concentrate the bolt clamping force onto a contact area around the bolt. If the three bolts were in a single row, the clamping force would be concentrated in a line along the bolts. Therefore, only a portion of the tribo surfaces would be in contact. The triangular pattern of the bolts was selected to reduce the concentration of the bolt clamping force, and create larger contact areas.

The spacing of the clamping bolts depends on the oversized bolt holes needed to avoid contact of the bolts with the bolt holes. The need for oversized bolt holes is based on the relative rotation between the beam web and the bolts. The bolts are designed to remain with the double angles (and brass shims), and the beam moves relative to the bolts, angles, and shims. The rotation of the beam is about the center of rotation (COR) as shown in Figure 3.4. As the beam web moves relative to the COR, it moves relative to the bolts which pass through the web. The bolt holes are oversized to avoid bearing of the bolts on the web. Bearing of the clamping bolts would produce a much larger force than the design friction force and produce damage to the double angles and web.

The required clearance for each bolt was determined from Figure 3.4. The total relative displacement of the bolts with respect to the beam was the vector sum of the horizontal and vertical relative displacement, δ_{hi} and δ_{vi} respectively. As shown in Figure 3.4, the amount of travel or relative motion between the bolt and beam

web varies with location of the bolt with respect to the COR. The maximum relative displacement occurs at the bolt furthest from the COR, at a distance l_{xi} and l_{yi} as shown in Figure 3.4. An irregular shaped hole was needed based on the relative displacement between the bolt and the beam web as discussed below. However, oversized round holes were used as shown in Figure 3.5.

As shown in Figure 3.5, the bolt is positioned toward the edge of the oversized hole furthest from the column. A clearance is provides to prevent bearing as will be discussed later. As the beam rotates, the oversized hole displaces relative to the bolt as shown in Figure 3.5.

The relative displacement between the bolts and the oversized holes in the web was studied as a function of beam rotation, as shown in Figure 3.6. The beam is able to rotate in a clockwise or counter-clockwise. The displacement of the bolts relative to the holes varies with the direction of rotation. Small rotation angles are assumed, and therefore, the bolt is assumed to displace (relative to the oversized holes) in a straight line. Two slotted holes could be used to allow for relative displacement of the beam relative to the bolt, as shown in Figure 3.6, but this solution is uneconomical.

To simplify fabrication, an oversized bolt hole was selected as shown in Figure 3.7. One oversized hole could be designed to work for all the bolts. The oversize hole is

a standard fabrication procedure, and is therefore more economical than two slotted holes. A comparison of the slotted bolt hole with the oversized bolt hole is shown in Figure 3.7.

To determine the actual required dimensions for the oversized hole, the beam configuration shown in Figure 3.1(b), is used as shown in Figure 3.8(a). The critical bolt has a l_x and l_y equal to 17 inches and 3-5/8 inches, respectively, from the bottom beam flange (COR1). The bolt is also 2 inches below the top of the double angle (Figure 3.8(a)). Rotating the beam about each flange, first COR1 followed by COR2, results in two sets of required horizontal and vertical displacements. A beam rotation of 0.05 radians (i.e., a 5% story drift assuming rigid columns) is used. The relative displacement between the bolt and the oversized hole in the web is shown in Figure 3.8(b). For the rotation about COR1, δ_h and δ_v are 17/20 (0.85) and 29/160 (0.18125) inch respectively (Figure 3.8(b)). For rotation about COR2, δ_h and δ_v were 2/5 (0.4) and 29/160 (0.18125) inch respectively (Figure 3.8(b)). The displacements are with respect to the center of the bolt. To account for the remaining bolt cross-section 1/2 inch must be added in each direction (Figure 3.8(b)). The total horizontal and vertical clearance required are 1.85 and 1.3625 inches as shown in Figure 3.8(b). A minimum additional clearance of 1/16 inch (i.e., 1/32 inch in each direction), is recommended to prevent bearing of the bolts. In the details developed in this chapter, a recommended clearance of 2/5 inch was used to be conservative. Thus, a 2-1/4 inch oversized hole was selected.

Based on the 2-1/4 inch oversized hole in the beam web, a 5 inch bolt spacing was used as shown in Figure 3.3(b). The following objectives were considered in the selection of the bolt spacing as previously mentioned: (1) to provide a nearly uniform distribution of the clamping stress; (2) to prevent failure of the beam web; (3) to prevent local clamping stress concentrations; and (4) attempt to maintain a relatively flat (uniform) clamping surface over the tribo surfaces.

Other limit states of the beam web were checked according to AISC specifications. Neglecting bolt bearing, the critical limit state was block shear rupture of the web through the two bolt holes in a single, vertical row, as shown in Figure 3.3(b). The factored resistance (ϕR_n) for block shear failure was 165.2 kips. If bolt bearing on the web is considered, the limiting value of ϕR_n decreases to 134.7 kips. However, ϕR_n equal to 134.7 kips is greater than the theoretical maximum expected F_f equal to 63 kips, based on Coulomb friction, using the larger value of N_i equal to 35 kips per bolt and μ equal to 0.3.

Support Bolts

The support bolts are shown in Figure 3.3(c). The support bolts for the double angle FCC of the PFC should be designed to prevent decompression of the angle from the column flange due to the friction forces acting on a single angle (F_{fx} and F_{fy}) as shown in Figure 3.9. The preload of the support bolts (P_i) produces a

compressive stress (σ_a) on the contact surface between the angle and the column, which fastens the angle to the column as shown in Figure 3.9(a). The forces F_{fx} and F_{fy} produce stresses on the contact surface (σ_b) as shown in Figure 3.9(b). If σ_b exceeds the initial compressive stress, the angle will decompress from the column flange as shown in Figure 3.9(c). Tensile stresses are assumed positive and compressive stresses assumed negative. Therefore, based on the stress distributions, to avoid decompression;

$$\frac{\Sigma P_i}{A_c} > \frac{F_{fx}}{A_c} + \frac{\left(F_{fx} \cdot e_y + F_{fy} \cdot e_x\right)}{S} \tag{3.3}$$

where A_c = the contact area,

ΣP_i = the sum of the preloads of the support bolts, and

S = the section modulus of the contact area.

If decompression occurs, additional support bolts are needed, and should be placed at the top and bottom of the angle as shown in Figure 3.3(c) due to load reversals.

Double Angles

The bolt holes in the double angles for the clamping bolts are shown in Figure 3.3(c). Standard bolt hole sizes for a 1 inch diameter bolt were used (AISC-LRFD, 1995). The spacing of the holes for the support bolts was consistent with the 5 inch spacing used for the clamping bolts as shown in Figure 3.3(c). Two vertical rows of bolts were used. The row closest to the fillet of the angle had 3 bolts. The second vertical row is spaced 2-3/4 inches from the row closest to the fillet with an edge

distance of 1-3/8 inches. These dimensions satisfy the minimum spacing for bolts given by the AISC specifications (AISC-LRFD, 1995).

Table 3.1. Moment Capacity of PFC Connection at a Beam Rotation of 0.003 Radians

Total PT Post-Tension Force (kips)	Clamping Bolt Preload (kips/bolt)	Beam Rotation, θ (rad)	M_{pst} (kips•in)	$M_{add}(\theta)$ (kips•in)	M_{Ff} (kips•in)	$M(\theta)$ (kips•in)	$M(\theta)/M_p$ —
153	0	0.003	1816.1	1444.0	0.0	3260.138	0.59
153	20	0.003	1816.1	1444.0	652.9	3912.9975	0.71
153	23	0.003	1816.1	1444.0	750.8	4010.9264	0.73
153	30	0.003	1816.1	1444.0	979.3	4239.4272	0.77
153	35	0.003	1816.1	1444.0	1142.5	4402.6421	0.80
153	40	0.003	1816.1	1444.0	1305.7	4565.857	0.83
153	50	0.003	1816.1	1444.0	1632.1	4892.2867	0.89
153	51	0.003	1816.1	1444.0	1664.8	4924.9297	0.89

Beam: W24x62

M_p beam = 5508 kips•in

Friction Coefficient, $\mu = 0.3$

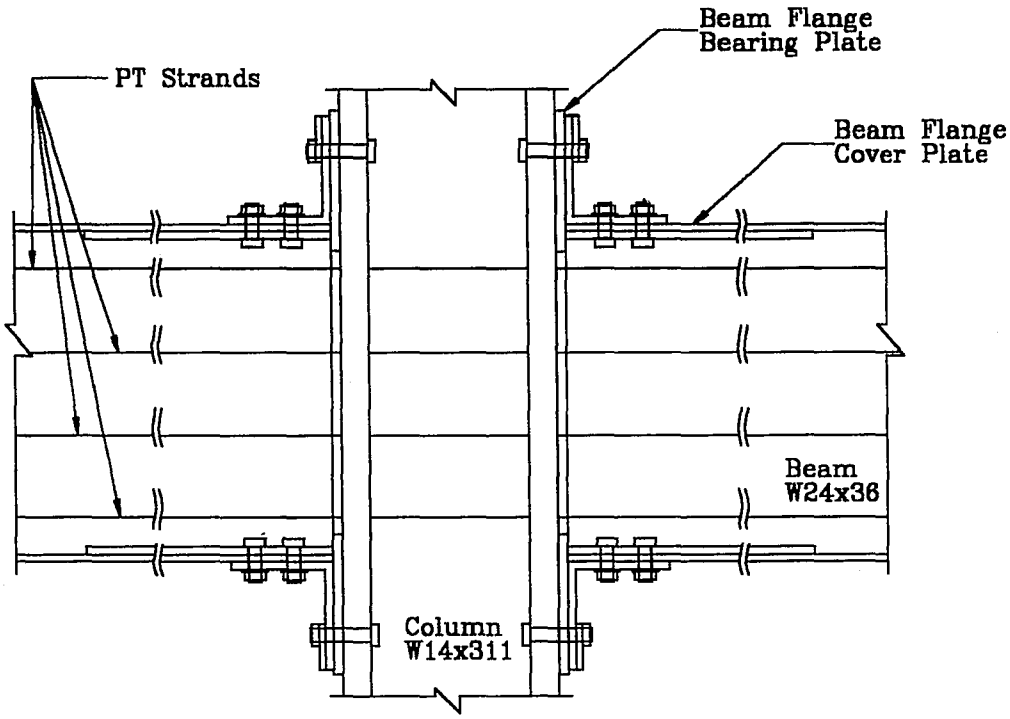

(a) Post-Tensioned Steel Connection

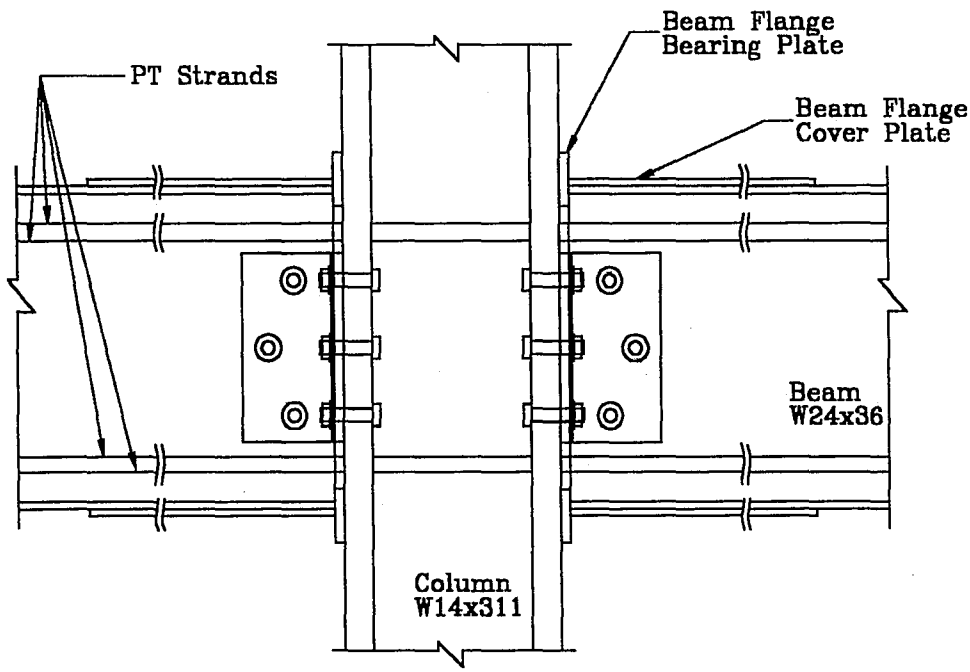

(b) Post-Tensioned Friction Damped Connection

Figure 3.1. Typical Components of Post-Tensioned Connections

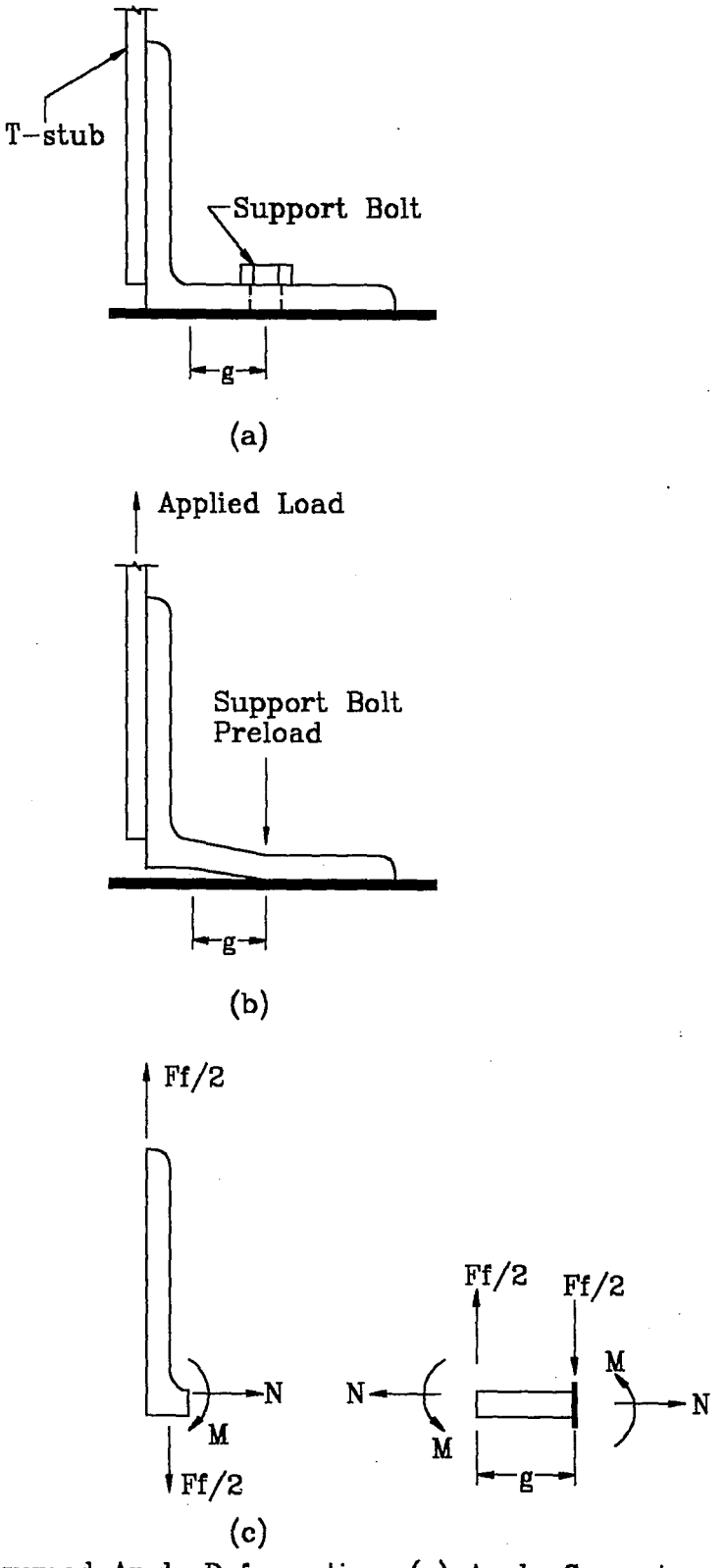

Figure 3.2. Assumed Angle Deformation: (a) Angle Geometry; (b) Deformed Shape; and (c) Angle FBD

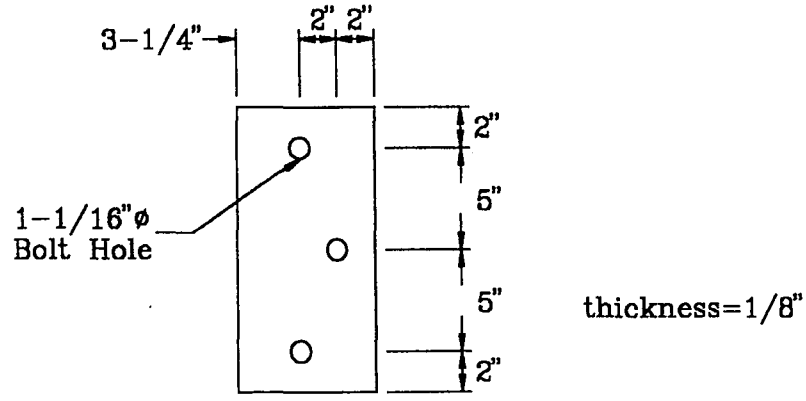

(a) Brass Shim

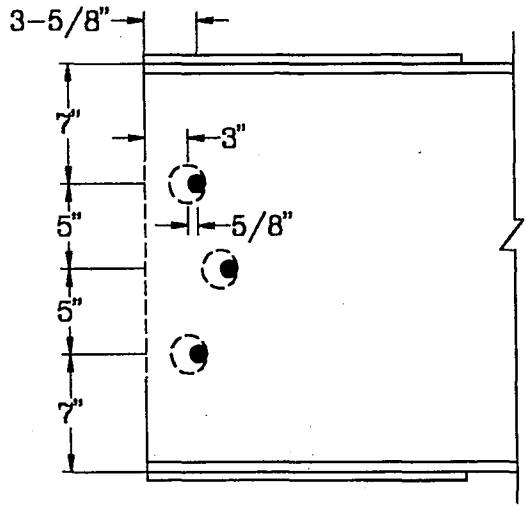

(b) Beam Web

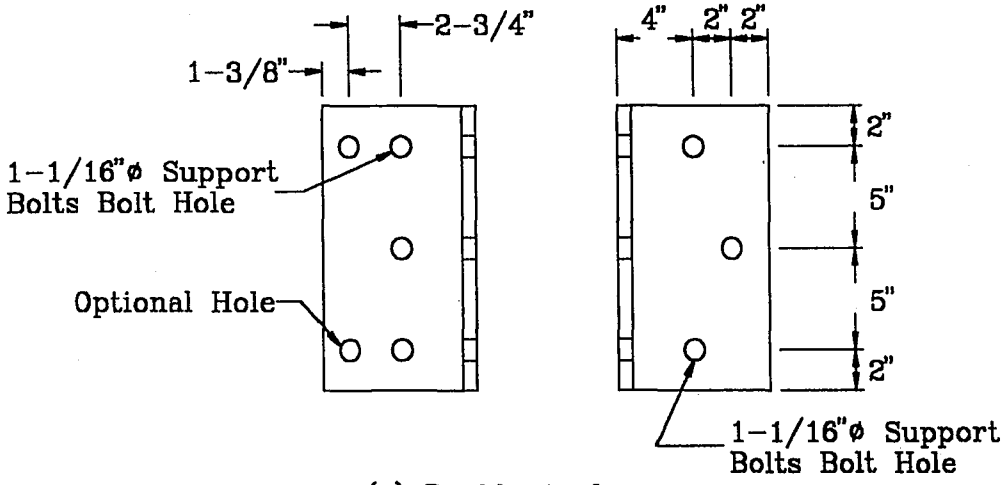

(c) Double Angle

Figure 3.3. Friction System Details

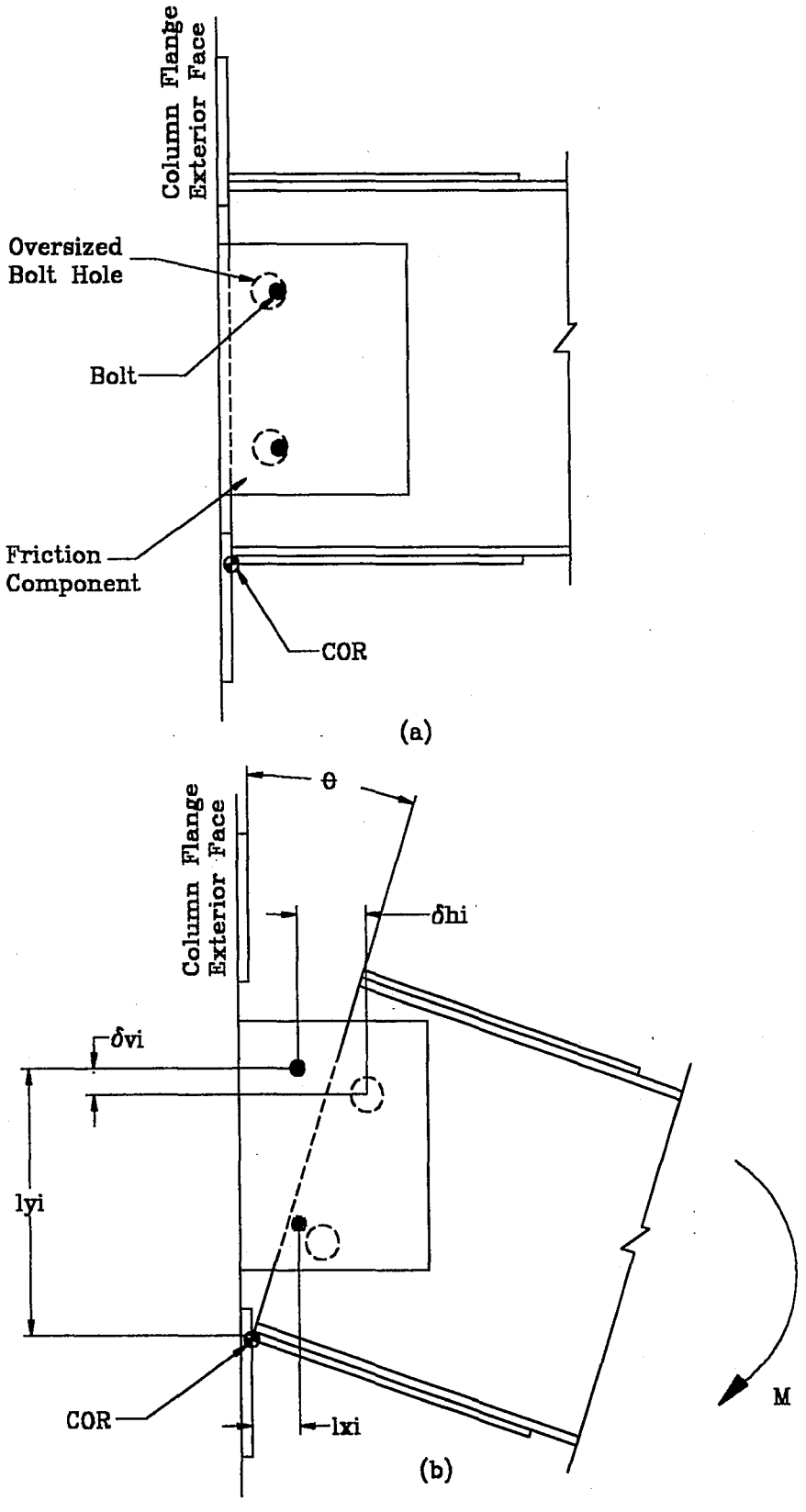

Figure 3.4. Determination of Bolt Relative Displacement: Undisplaced Beam; and (b) Displaced Beam

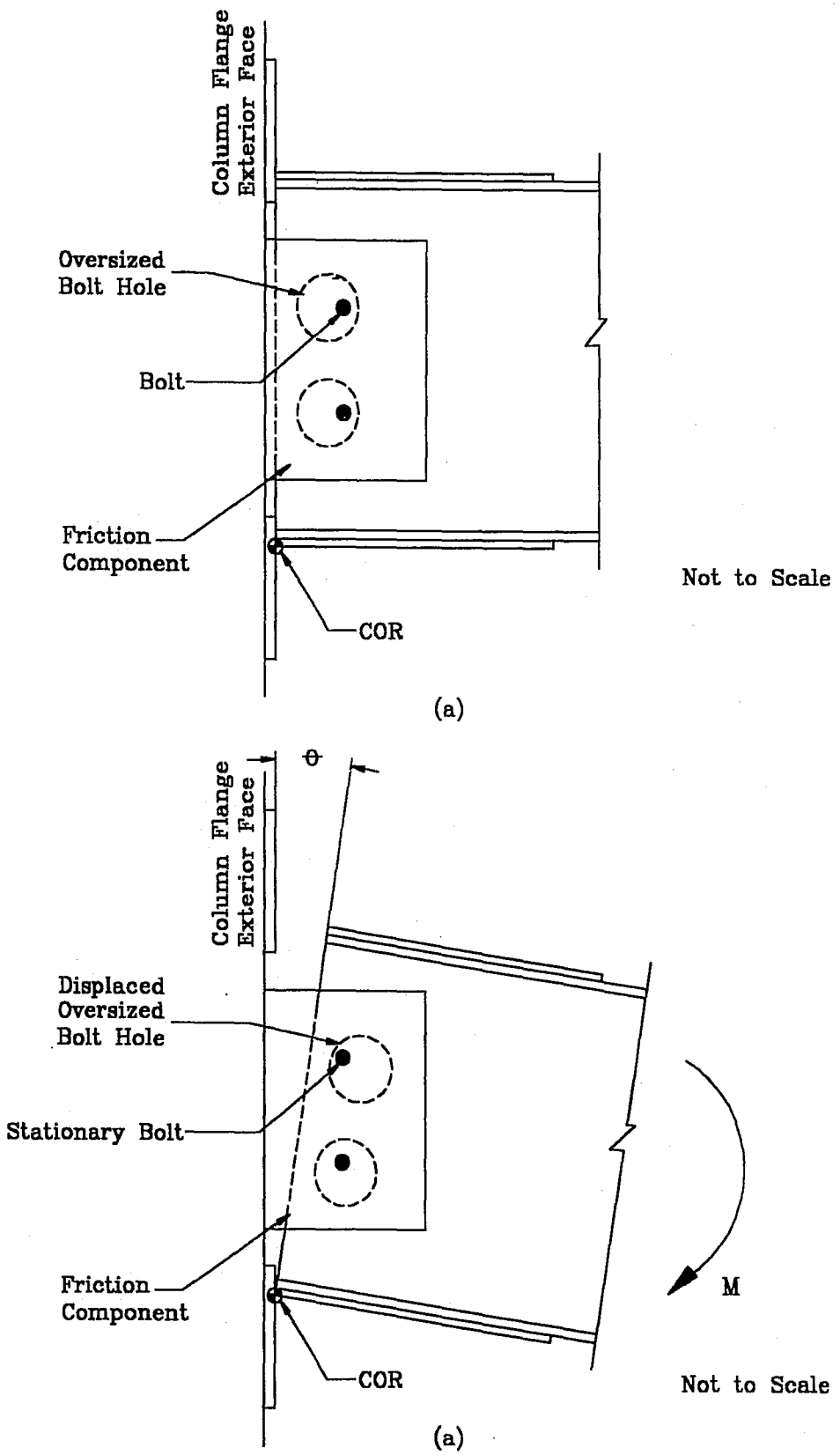

Figure 3.5. Beam with Oversized Holes: (a) Beam Undisplaced and (b) Displaced Beam

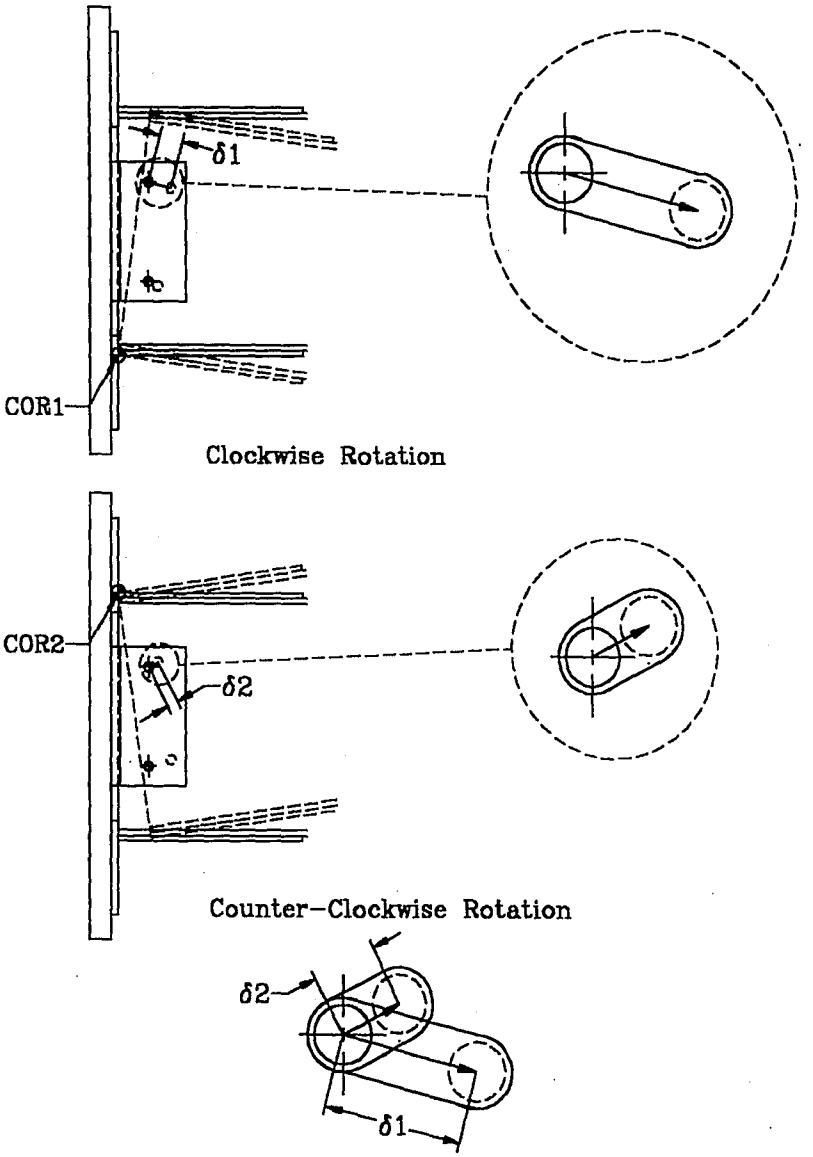

Irregular Slotted Bolt Hole
Figure 3.6. Irregular Slotted Bolt Hole

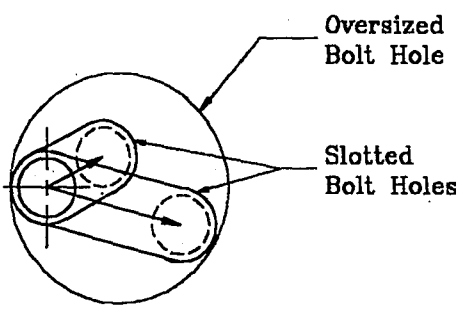

Figure 3.7. Comparison of Irregular Slotted Bolt Hole with Oversized Bolt Hole

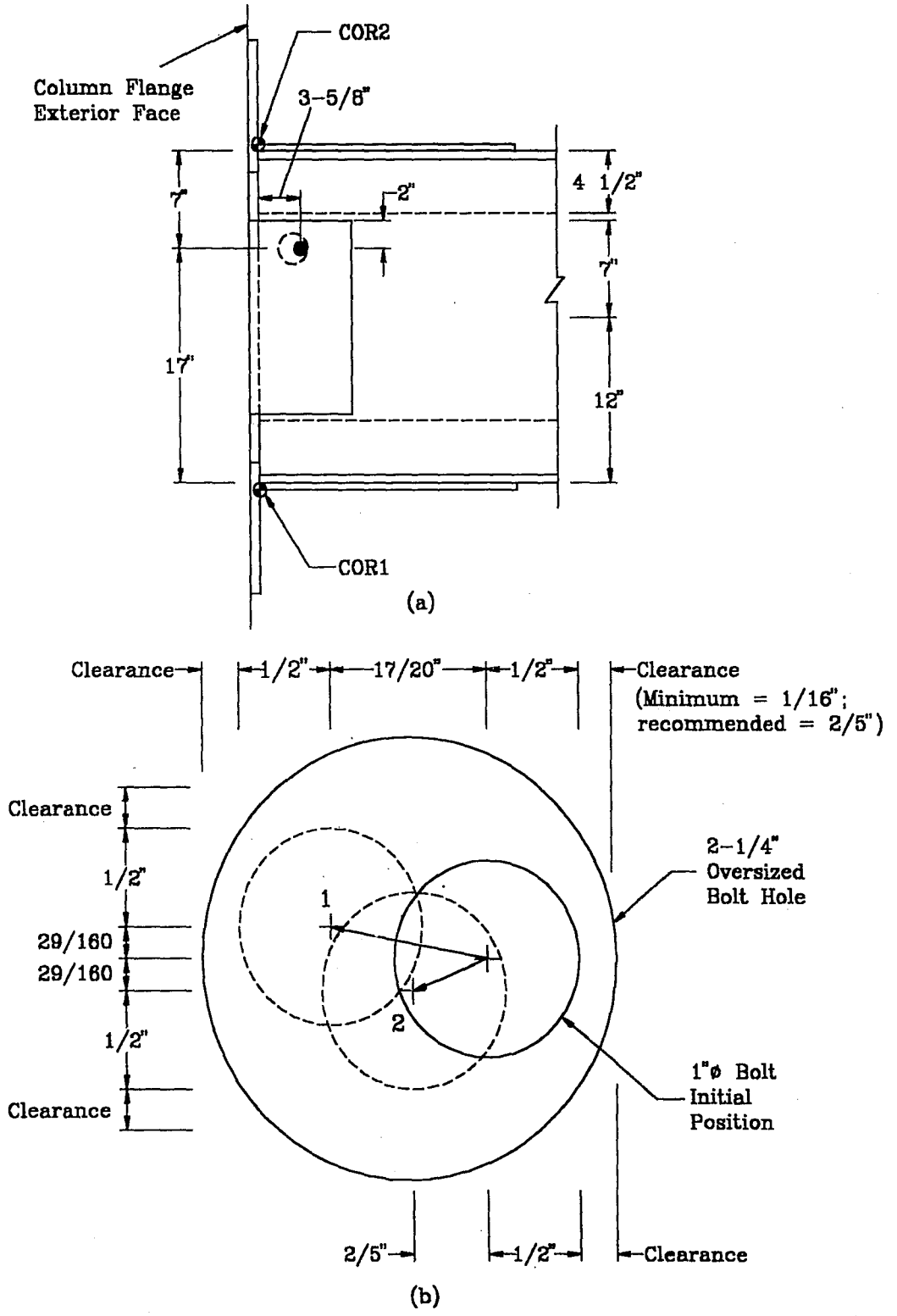

Figure 3.8. Determination of Oversized Bolt Hole Size:
(a) Undisplaced Beam; and
(b) Required Clearance for 5% Story Drift

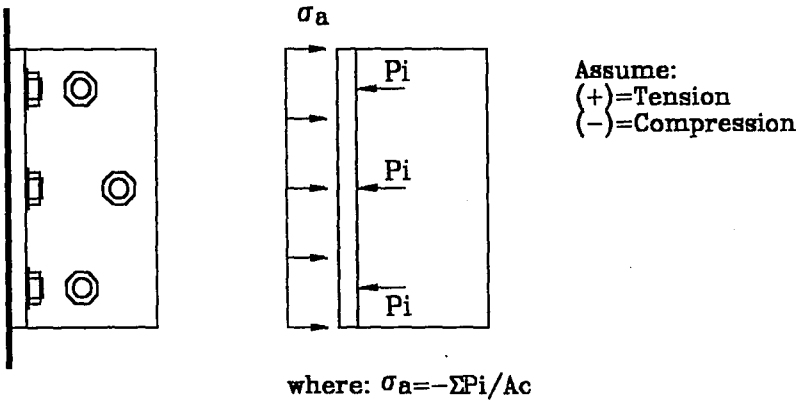

where: $\sigma a = -\Sigma Pi/Ac$

(a) Stress due to Support Bolt Preload

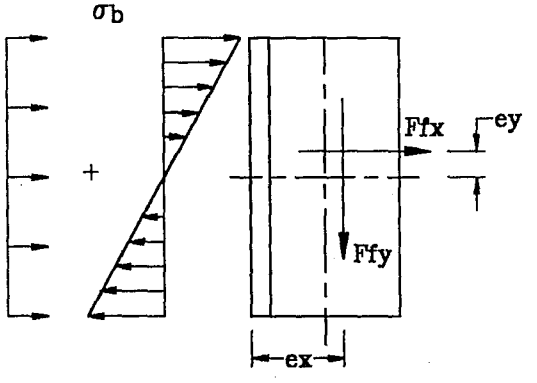

where: $\sigma b = Ffx/Ac + (Ffx \cdot ey + Ffy\ ex)/S$

(b) Stress from
Moment due to Friction

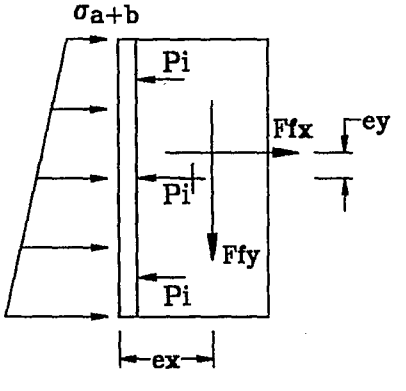

where: $\sigma a+b = \sigma b + \sigma a$

(c) Resulting Stress at the
Contact Surface due to
Compression+Bending Stresses

Figure 3.9. Stress at Double Angle–Column Contact Surface

4. Friction Component Experimental Procedures

This chapter describes the experimental set-up and testing procedures used to investigate the friction connection component (FCC) of the post-tensioned friction connection (PFC). The experimental procedures were designed to investigate four key parameters: (1) the friction behavior of the friction connection component; (2) the repeatability of the friction behavior; (3) the effects of the slip rate on the friction behavior; and (4) the durability of the brass-steel tribo surfaces.

4.1 Test Frame

The test frame used in the experiments is shown in Figure 4.1. The main members include two W12x190 columns connected by upper and lower cross-beams. As shown in Figure 4.1, the columns were spaced 5 feet apart, center-to-center. The clear span of the cross-beams was 47 inches. Each cross-beam was built from two wide flange beams with an approximate depth, length, and width of 21, 72 and 27 inches, respectively. A portion of each of the interior flanges of each wide flange beam was removed to allow the columns to fit between the two wide flange beams. A 200 kip capacity, 10 inch stroke, actuator was suspended from the center of the upper cross-beam, providing a clear distance of 45 inches with the actuator fully retracted. Four 1 inch diameter threaded steel rods were used to suspend the actuator, and steel channels were used to restrain transverse movement of the actuator as shown in Figure 4.1. The lower clevis of the actuator was restrained from rotation by the use of shims.

A 71 inches W14x193 spreader beam was attached to the lower clevis to provide a surface for the attachment of the test specimens. The beam was centered on the actuator. The beam had 1 inch thick bearing stiffeners at mid-span on each side of the web, which was also the centerline of the actuator and test specimens. Additional stiffeners were spaced 29 inches from the center stiffener. Each test specimen was centered with respect to the actuator centerline and attached to both the lower cross-beam and the spreader beam.

4.2 Double Plate Friction Tests

4.2.1 Test Set-up

The double plate friction test specimens consisted of a single plate sliding between two stationary plates as shown in Figure 4.2. The upper T-stub was attached to the actuator via the spreader beam. The lower T-stub was attached to the lower cross-beam. The two T-stubs were cut from a W36x150 A36 steel section. The depth and width of each T-stub was 16 inches and 18 inches, respectively. Three 1 inch diameter A325 bolts on each flange were used to fasten the T-stub to the spreader beam as shown in Figure 4.2. Four 5x5x1/2 inch stiffeners were fillet welded to each side of each T-stub. The T-stubs were positioned plumb (one directly above the other) with a 3/4 inch separation in between the web of each T-stub.

The lower T-stub was welded to a 21x21x1 inch steel plate using a 5/16 inch fillet weld all around. The steel plate was welded to the lower cross beam using a 4 inch long, 3/8 inch fillet weld at the corners. In addition, four large wrench clamps were used to clamp the T-stub to the lower cross beam.

Bolt holes in the outer steel plates were aligned with the corresponding holes in the webs of the T-stubs as shown in Figure 4.3. The hole pattern in the upper T-stub consisted of three oversized (2-1/4 inch) holes. The holes allowed for the translation of the upper T-stub relative to outer plate without bolt bearing. The bolt holes in the lower T-stub were standard (1-1/16 inch) holes for a 1 inch bolt. A triangular bolt hole pattern, as discussed in the Chapter 3, was used in the upper T-stub as shown in Figure 4.3. The hole pattern in the lower T-stub consisted of four bolts in two rows as shown in Figure 4.3.

The two outer plates had a thickness of 1 inch and a specified yield strength of 50 ksi. The plates were 14 inches by 17-1/2 inches as shown in Figure 4.2. The tribo surface area in the upper portion of the plate was similar to that of the proposed double angle friction connection component presented in Chapter 3. The bolt holes in the outer plates were standard (1-1/16 inch) holes for 1 inch bolts as shown in Figure 4.3.

The clamping bolts were 1 inch diameter A325 bolts, 5 inches in length. The three bolts in the upper plate provided a predetermined initial clamping force (bolt preload) for each test. The typical clamping bolt assembly is shown in Figure 4.4. This assembly was previously used by Grigorian and Popov (1994). A single standard washer was placed under the bolt head and the bolt nut. A Belleville washer was used to help maintain the bolt preload (Grigorian and Popov, 1994).

The four bolts in the lower plate were used to restrain the movement of the outer plates. These bolts were not pretensioned. Pretensioning of these bolts made it difficult to control the normal force on the tribo surfaces between the outer plates and the upper T-stub. Therefore, the bolts in the lower T-stub worked in bearing. When the actuator moved in the upper T-stub, the bearing of the bolts in the lower T-stub prevented the movement of the outer plates and forced the upper T-stub to slide relative to the outer plates.

The brass-steel tribo surfaces were created between the upper T-stub web and the brass shims as shown in Figure 4.2. A 1/8 inch thick alloy, 260 half-hard cartridge brass shim was placed between each outer plate and the upper T-stub. The brass shims were to remain stationary with the plates. The holes in the shims were the same as those in the outer plates. Before erecting the test specimen, several applications of Magnaflux Spotcheck SKC-S, a common degreasing spray, were applied to the tribo surfaces to remove grease and loose debris. A single set of T-

stubs and outer plates was used for multiple tests because of the non-destructive nature of the friction tests.

4.2.2 Instrumentation

A schematic of the instrumentation is shown in Figure 4.5. The purpose of the instrumentation used in the double plate friction tests was to record the applied force-displacement response of each test. The instrumentation plan was the same for each test.

A load cell attached to the actuator was used to measure the applied force as shown in Figure 4.1. A linear variable displacement transducer (LVDT), attached to the actuator, was used to control and measure the travel of the actuator.

Three Micro Measurements BTM-6C bolt gauges were used to measure the tensile strain in each of the three clamping bolts as shown in Figure 4.5. The gauges allowed for accurate pretensioning of each bolt to a predetermined clamping force. Reference numbers for the gauged bolts are shown in Figure 4.5.

Four linear potentiometer displacement transducers, with a 1-1/2 inch travel, were attached as shown in Figure 4.5. A linear potentiometer was attached to each side of the lower T-stub web to measure the relative displacement of the upper T-stub as shown in Figure 4.5. A 2x2x1/4 inch angle was attached to each side of the upper

T-stub web, and the shaft of the linear potentiometer was placed in contact with this angle. A linear potentiometer was also attached to each face of the upper T-stub web to measure the relative displacement between the T-stub and the outer plate as shown in Figure 4.5. This displacement was taken as the slip of the tribo surfaces. An angle was attached to each outer plate and the shaft of the linear potentiometer was placed in contact with the angle. The slip of the tribo surfaces was measured in this way to avoid including any simultaneous slip between the outer plates and the lower T-stub when the lower set of bolts shifted into bearing.

4.3 Double Angle Friction Connection Component Tests

4.3.1 Test Set-up

The double angle friction connection component (FCC) tests were conducted to study the behavior of the friction connection component at full scale. The test set-up, shown in Figures 4.6, was used for all of these tests.

The test specimen consisted of a pair of 8x8x3/4 14 inch long A572 Grade 50 double angles fastened to an upper W36x50 T-stub and a lower spreader beam. The upper T-stub was attached to the upper spreader beam as shown in Figure 4.6 The lower spreader beam simulated the column at a beam-column connection. The lower spreader beam was attached to the lower cross-beam, shown in Figure 4.1, and ran perpendicular to the plane of the test frame. The lower spreader beam was a 42 inch long W14x193 steel beam. The lower spreader beam was fastened to the lower

cross-beam using six dogs. Two full-depth bearing stiffeners, 1 inch in thickness, were located at each end of the lower spreader beam on each side of the web. A 21x21x1 inch plate was placed in between the lower spreader beam and the double angles because the tips of the angles extended 9/16 inch beyond the flanges of the lower spreader beam.

For clarity in the following description of the double angle friction connection component test specimens, the angle leg connected to the T-stub will be referred to as the vertical leg, and the angle leg connected to the steel plate and the lower spreader beam will be referred to as the horizontal leg. Three 1 inch diameter A325 bolts, 4-1/2 inches long, were used to connect each horizontal angle leg to the lower spreader beam. The bolt assembly shown in Figure 4.4 was used. Three 1 inch diameter A325 bolts, 4 inches long, were used as clamping bolts through the vertical legs of the angles. Standard (1-1/16 inch) bolt holes were used in both legs of the angle. The clamping and support bolt patterns are shown in Figure 4.6. The clamping bolt pattern was similar to the pattern used in the double plate friction test.

The brass-steel tribo surfaces were created using 1/8 inch thick, alloy 260 half hard cartridge brass shims. The shims were placed between the vertical angle legs and the T-stub web. The brass-steel tribo surface was between the T-stub and the brass

shim, as shown in Figure 4.6. The bolt holes and the tribo surfaces were prepared for testing as discussed above for the double plate friction tests.

4.3.2 Instrumentation

The instrumentation scheme used for the double angle friction connection component tests is shown in Figure 4.7 and 4.8. The instrumentation plan remained the same for each test. The load cell and LVDT used with the actuator are as described for the double plate friction tests.

A total of 24 Texas Measurements EA-06-250BG-120 strain gauges were used on the T-stub and double angles as shown in Figure 4.7. Ten gauges were located on each angle. There were two rows of three gauges on the vertical angle leg. The bottom row of gauges was 1/4 inch from the toe of the fillet, with the center gauge aligned with the centerline of the vertical angle leg in the horizontal direction. The spacing of the two outer gauges at each row was 3-1/2 inches. Two rows of two gauges were also used on the horizontal angle leg as shown in Figure 4.7. The first row was 1/4 inch from the fillet toe. The second row was 1-3/4 inch from the centerline of the first row of gauges. The gauges were spaced 2-1/2 inches from the angle centerline.

Two gauges were also placed on each face of the T-stub web in similar locations. The gauges were 7-1/2 inches from the exterior face of the T-stub flange as shown

in Figure 4.7. The gauges were spaced 4 inches from the centerline of the T-stub in the horizontal direction.

Micro Measurements BTM-6C bolt gauges were used to measure the tensile strain in seven specific bolts shown in Figure 4.7. Bolt gauges were used in the three clamping bolts, and the southern and center support bolts as shown in Figure 4.7. Reference numbers for the gauged bolts are shown in Figure 4.7.

Two types of displacement transducers were used to measure displacements as shown in Figure 4.8. Four linear potentiometers, with a 1-1/2 inch travel, were attached to the specimen. A linear potentiometer was attached to each side of the T-stub web to measure the relative displacement of the T-stub with respect to the steel plate as shown in Figure 4.8. A linear potentiometer was also attached to each face of the T-stub web to measure relative displacement between the T-stub and angle as shown in Figure 4.8. This displacement was taken as the slip displacement of the tribo surfaces. A 2x2x1/4 inch angle was attached to the tip of each angle leg and the shaft of the linear potentiometer was placed in contact with these small angles. A 1-1/2 inch travel LVDT was mounted from the interior face of the lower spreader beam flange as shown in Figure 4.8. Its purpose was to measure uplift of the angle heel off the lower spreader beam flange. A 1/2 inch diameter hole was drilled through the flange of the lower spreader beam and steel plate to allow the rod of the LVDT to reach the heel of the angle.

4.4 Material Properties

Material tests were conducted on samples of 8x8x3/4 inch angle material, and a 1 inch diameter A325 bolt, 4 inches in length. The material test were conducted according to ASTM E8-83 (1997). A 600 kip capacity Satec (tension/compression) machine was used to conduct both tests.

4.4.1 Clamping Bolts

A tensile test was conducted on a 1 inch diameter A325 bolt, 4 inches in length. According to the AISC specifications (AISC-LRFD, 1995), the factored and unfactored nominal tensile strengths for a 1 inch diameter A325 bolt are 53.0 and 70.67 kips, respectively. The bolt had a yield load (P_y) of 70 kips, and a peak load (P_u) of 92.1 kips, as shown in Figure 4.9. The test results show that the 1 in diameter A325 bolt yield load corresponds to the nominal unfactored tensile strength. These test results were comparable to previous test results for 1 inch diameter bolts from the same bolt supplier conducted at Lehigh University (Peng et al., 1997).

4.4.2 Angle

Four standard 0.505 round coupons were cut from the 8x8x3/4 inch angle material. Two coupons were taken out of each leg of the angle. The coupons were cut in the transverse direction of the angle (from the heel of the angle to the tip of the angle leg), which is the direction of the applied force. The angle was A572 Grade 50 material, with a specified minimal yield strength and ultimate strength of 50 ksi and 65 ksi, respectively. Each coupon had an approximate diameter of 1/2 inch,

and an initial gage length of 2 inches. The test procedure followed ASTM E8-83 with the addition of several sustained pauses after yielding of the coupon. The pauses were used to determine the static yield strength by holding the strain of the specimen constant when the stress was on the yield plateau (Galambos, 1999). The test results are shown in Table 4.1. Test results indicate that the average yield stress and ultimate stress are 55.6 ksi and 79.0 ksi, respectively. The average yield to tensile ratio was 0.7.

4.5 Testing Procedures

Displacement History

Both the double plate friction test specimens and the double angle friction connection component test specimens were tested under imposed displacement. The displacement history was sinusoidal. The selected amplitudes of displacements, and corresponding levels of story drift for a frame with W24x36 beams are shown in Figure 4.10. The largest of these displacement amplitudes corresponds to a level of story drift which would result in serious damage to a typical moment resisting frame. To determine the story drift, it was assumed that the beams and columns are rigid, and the story drift angle (θ_s) is equal to the gap opening angle of the PFC (θ).

The amplitudes of displacement were combined into a series of imposed sinusoidal displacements as shown in Figure 4.11. The displacement history consisted of 63

cycles separated into three cycle sets as shown in Figure 4.11. The selected displacement amplitudes, given in Figure 4.10, were used for cycle set 1 and cycle set 2. The average displacement rate (or the maximum displacement rate of the sinusoidal displacement) for cycle sets 1 and 2 was constant. This was done by varying the period of the sinusoidal displacement with the displacement amplitude.

The sinusoidal displacements were arranged into seven subsets, and imposed on the test specimens in the following manner: (1) 1/8; (2) 3/16; (3) 5/16; (4) 7/16; (5) 5/16; (6) 3/16; and (7) 1/8 inch displacement amplitudes. Each subset consisted of four sinusoidal displacement histories (four sinusoidal waves) that were imposed continuously without stopping. A momentary pause occurred before the ensuing displacement amplitude subset began. This displacement pattern was consistent throughout cycle sets 1 and 2 for each test specimen.

Cycle set 3 consisted of seven consecutive sinusoidal displacements at the maximum displacement amplitude of 7/16 inch. The cycles were imposed on the test specimens without pausing between successive cycles. The first three cycles were imposed at the same displacement rate as the previous sinusoidal displacements. The next two cycles were imposed at twice the displacement rate as the previous three cycles. The remaining two cycles were imposed at the original displacement rate. This displacement history was used for most of the tests. The

total travel of the displacement history was 66-1/4 inches, which exceeds the demands of a design level earthquake on the friction component of a PFC.

In the following chapters, the terms push cycle and pull cycle will be used to refer to the applied force in the actuator, and the direction of the increement relative displacement of the upper T-stub to the remaining portion of the test specimen. During a push cycle, the T-stub slips downward relative to the remaining portion of the test specimen. The applied force of the actuator is negative, and pushes downward on the T-stub. During the push cycle, the displacements measured by the slip linear potentiometers are decreasing, and therefore, negative displacement increment is said to occur. During the pull cycle, the upper T-stub slip upward relative to the remaining portion of the test specimen. The applied force in the actuator is positive, and pulling the T-stub upward. During the pull cycle, the displacement measured distance of the slip linear potentiometers are decreasing, and thus positive displacement increment is said to occur.

Loading History

Three displacement histories, GWAVE, GWAVEX2, and GDYN, were developed to load the test specimens. The displacement histories are described in Table 4.3. The first two displacement histories, GWAVE and GWAVEX2, had essentially static displacement rates. This allowed for observation of the specimens during testing. The average displacement rates for GWAVE and GWAVEX2 were 0.00625

inch/second and 0.0125 inch/second, respectively as shown in Table 4.2(a) and (b). The GDYN displacement history was developed to study the friction connection component behavior at displacement rates similar to those that occur during the actual response of a building to an earthquake. The average displacement rate for GYDN was 0.5 inch/second as shown in Table 4.2. This rate was comparable the displacement rates used by Grigorian and Popov (1994), as shown in Table 4.2(d).

The displacement histories shown in Figure 4.11 and Table 4.3 describe the specified displacement of the actuator. The relative displacement of the upper and lower T-stubs was measured by liner potentiometers placed on the each side of the web of the T-stubs as shown in Figure 4.5. It was found that the relative displacement of the T-stubs fell short of the specified actuator displacement in the pull cycle as shown in Figure 4.12. This error was more noticeable as the amplitude of the displacement history increased. The error in the T-stub relative displacement at a specified displacement amplitude of 7/16 inch was 1/48 inch.

Temperature Measurement

At the tribo surfaces, mechanical energy is converted to heat generated due to friction. A thermal probe was used to measure the change in temperature (ΔT) of the test specimens during each test.

The temperature of the outer steel plates or angles was measured before the start of each test, and immediately after the completion of the test. The temperature was

measured between bolts 1 and 2 on the east and west elevation of the test specimen. The change in temperature was the final temperature minus the initial temperature of the test specimen.

Table 4.1. Tensile Coupon Test Results for 8x8x3/4" Angle

Angle Size	Coupon Identification	σ_y (ksi)	σ_u (ksi)	E (ksi)	Elongation (%)
L8x8x3/4"	A-1	55.2	78.8	28294	27.7
	A-2	56.1	79.1	25664	29.2
	A-3	55.3	78.9	34134	29.2
	A-4	55.6	79	30466	26.3
Average		**55.6**	**79**	**29640**	**28.1**

Table 4.2. Experimental Displacement Histories

(a) GWAVE

Amplitude, δ (in)	Period, T (sec)	Frequency, f (Hz)	Avg. Displ. Rate (in/sec)	Max. Displ. Rate (in/sec)	W24 Story Drift* (rad)	Gap Opening Angular Velocity (rad/sec)
1/8	20	0.05000	0.00625	0.0393	0.0104	0.006
3/16	30	0.03333	0.00625	0.0393	0.0156	0.006
5/16	50	0.02000	0.00625	0.0393	0.0260	0.006
7/16	70	0.01429	0.00625	0.0393	0.0365	0.006

(b) GWAVEX2

Amplitude, δ (in)	Period, T (sec)	Frequency, f (Hz)	Avg. Displ. Rate (in/sec)	Max. Displ. Rate (in/sec)	W24 Story Drift* (rad)	Gap Opening Angular Velocity (rad/sec)
1/8	10	0.10000	0.0125	0.0785	0.0104	0.013
3/16	15	0.06667	0.0125	0.0785	0.0156	0.013
5/16	25	0.04000	0.0125	0.0785	0.0260	0.013
7/16	35	0.02857	0.0125	0.0785	0.0365	0.013

Table 4.2(continued). Experimental Displacement Histories

(c) GDYN

Amplitude, δ (in)	Period, T (sec)	Frequency, f (Hz)	Avg. Displ. Rate (in/sec)	Max. Displ. Rate (in/sec)	W24 Story Drift* (rad)	Gap Opening Angular Velocit (rad/sec)
1/8	0	4.00000	0.5	3.1416	0.0104	0.500
3/16	0	2.66667	0.5	3.1416	0.0156	0.500
5/16	1	1.60000	0.5	3.1416	0.0260	0.500
7/16	1	1.14286	0.5	3.1416	0.0365	0.500

(d) Grigorian and Popov (1994)

Amplitude, δ (in)	Period, T (sec)	Frequency, f (Hz)	Avg. Displ. Rate (in/sec)	Max. Displ. Rate (in/sec)	W24 Story Drift* (rad)	Gap Opening Angular Velocit (rad/sec)
0.40	1.00	1.00	0.4	2.5133	0.0333	0.400
0.70	1.49	0.67	0.469	2.9468	0.0583	0.469
1.10	2.00	0.50	0.55	3.4558	0.0917	0.550
1.60	4.00	0.25	0.4	2.5133	0.1333	0.400

*Note: Story drift calculated assuming beams and columns rigid.

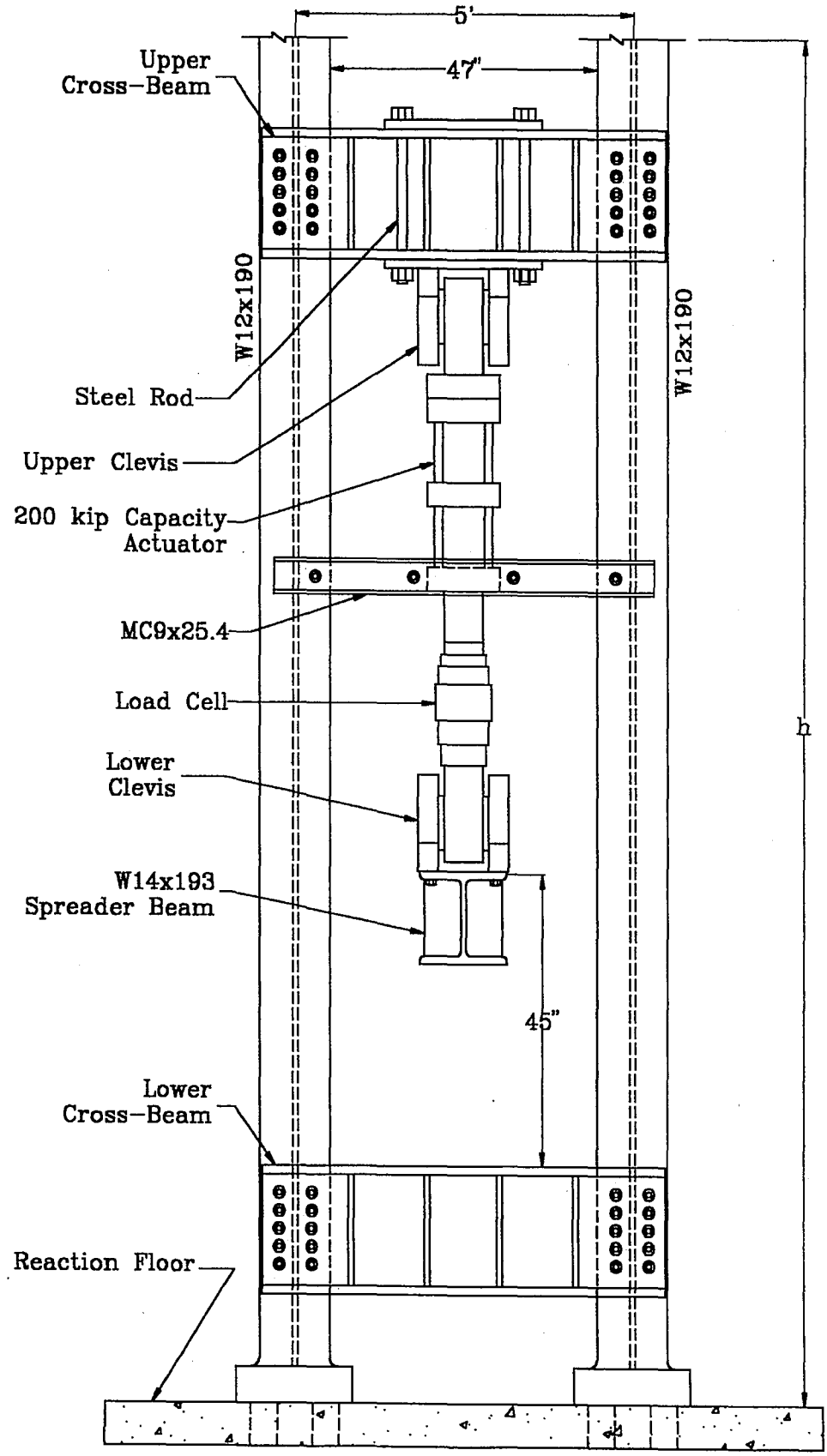

Figure 4.1. Experimental Test Frame – South Elevation

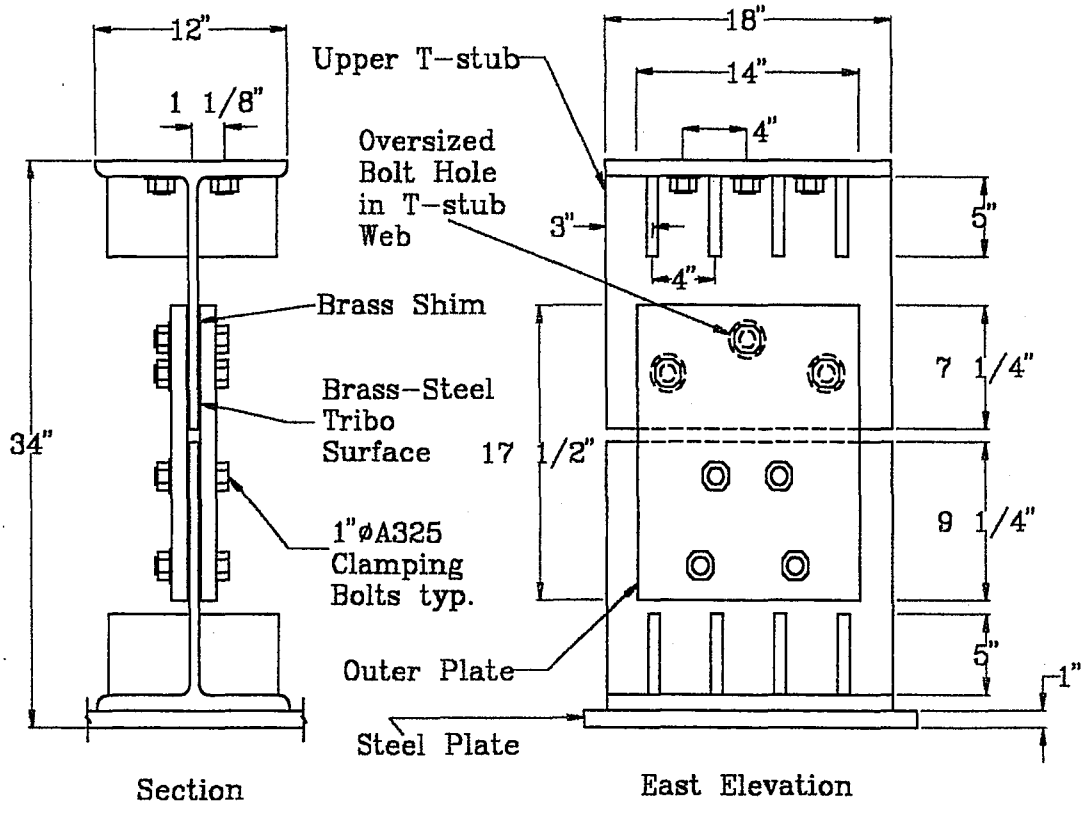

Figure 4.2. Double Plate Friction Test Specimen

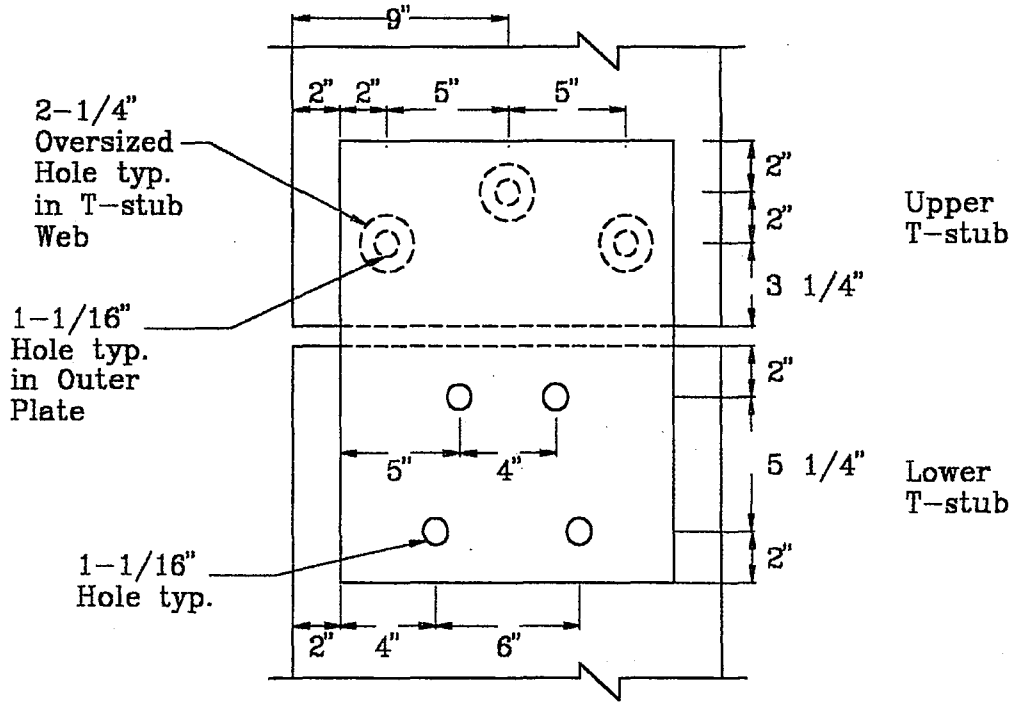

Figure 4.3. Double Plate Test Specimen Bolt Pattern

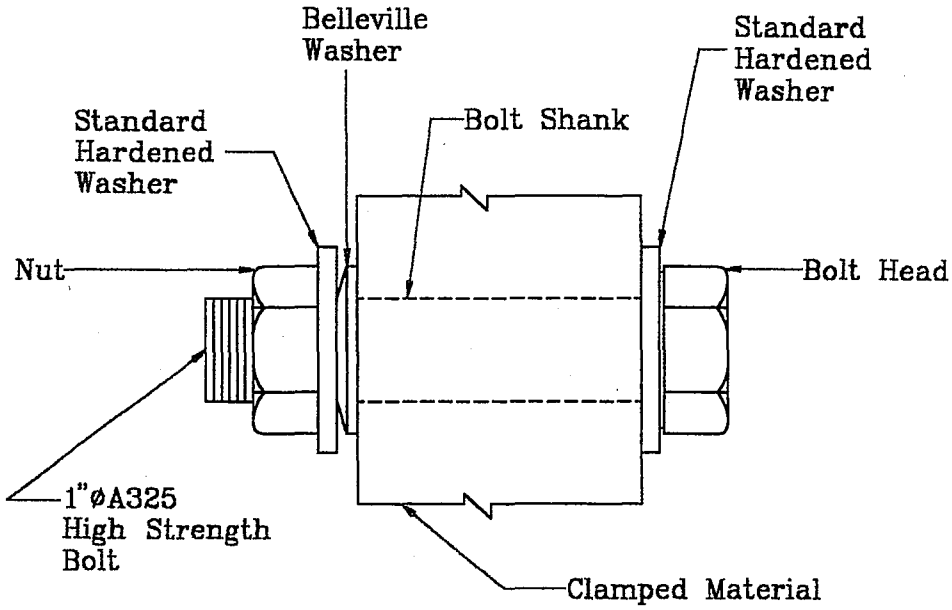

Figure 4.4. Typical Clamping Bolt Assembly
(Grigorian and Popov, 1994)

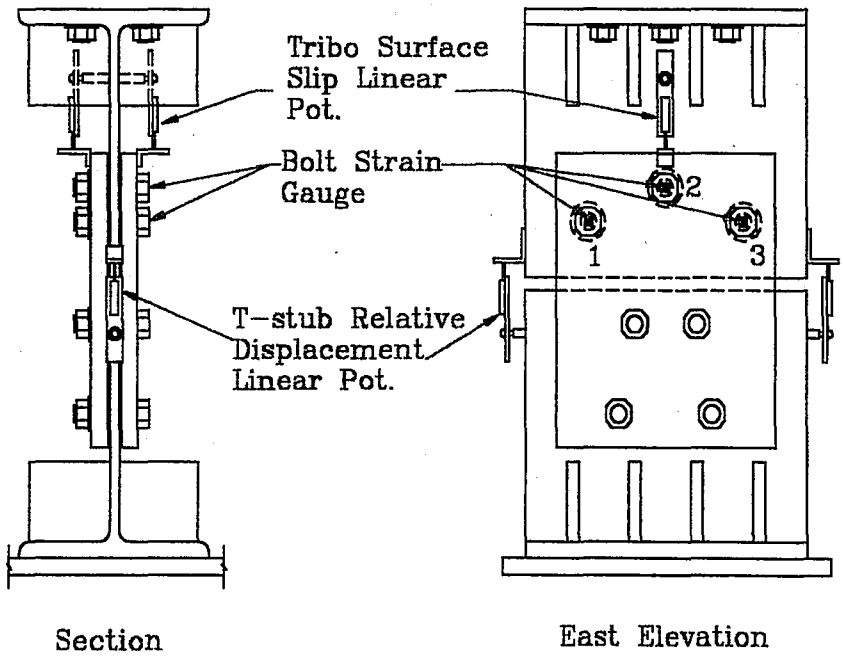

Figure 4.5. Double Plate Friction Specimen Instrumentation Plan

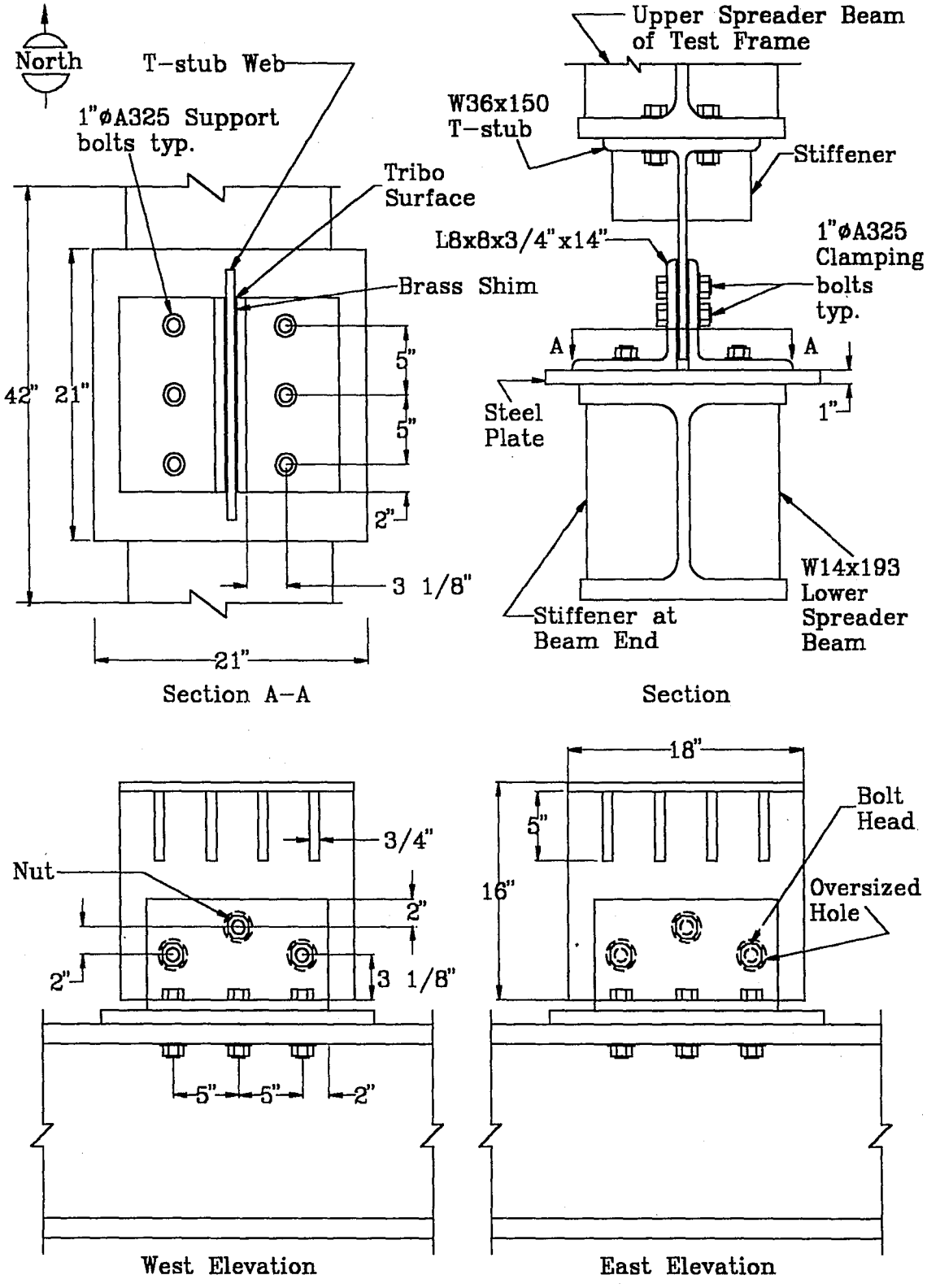

*Note: Upper Spreader Beam not Shown

Figure 4.6. Double Angle Friction Component Test Specimen

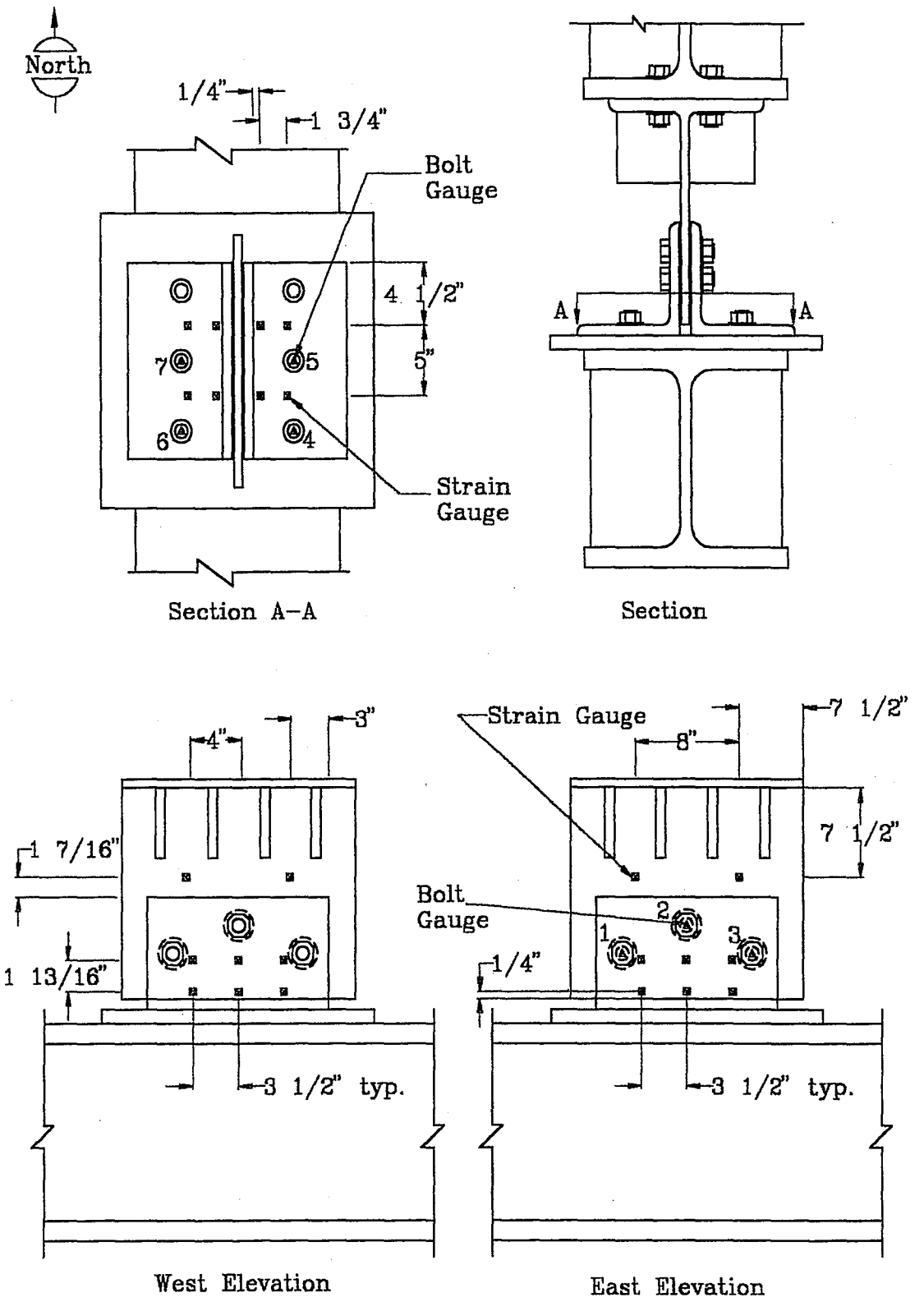

Figure 4.7. Double Angle Friction Component Test Specimen
Strain Gauge Instrumentation Plan

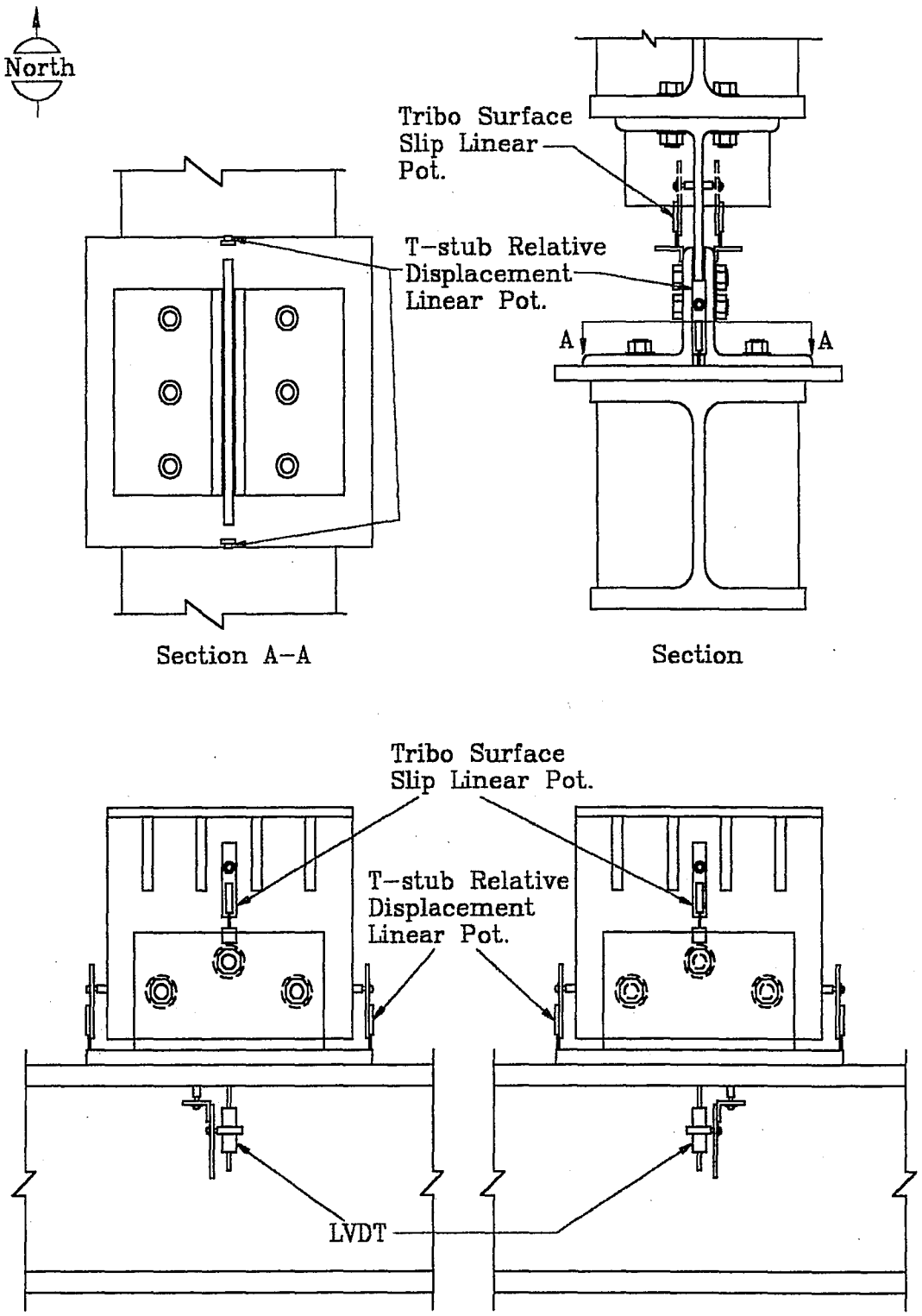

Figure 4.8. Double Angle Friction Component Test Specimen Voltage Device Instrumentation Plan

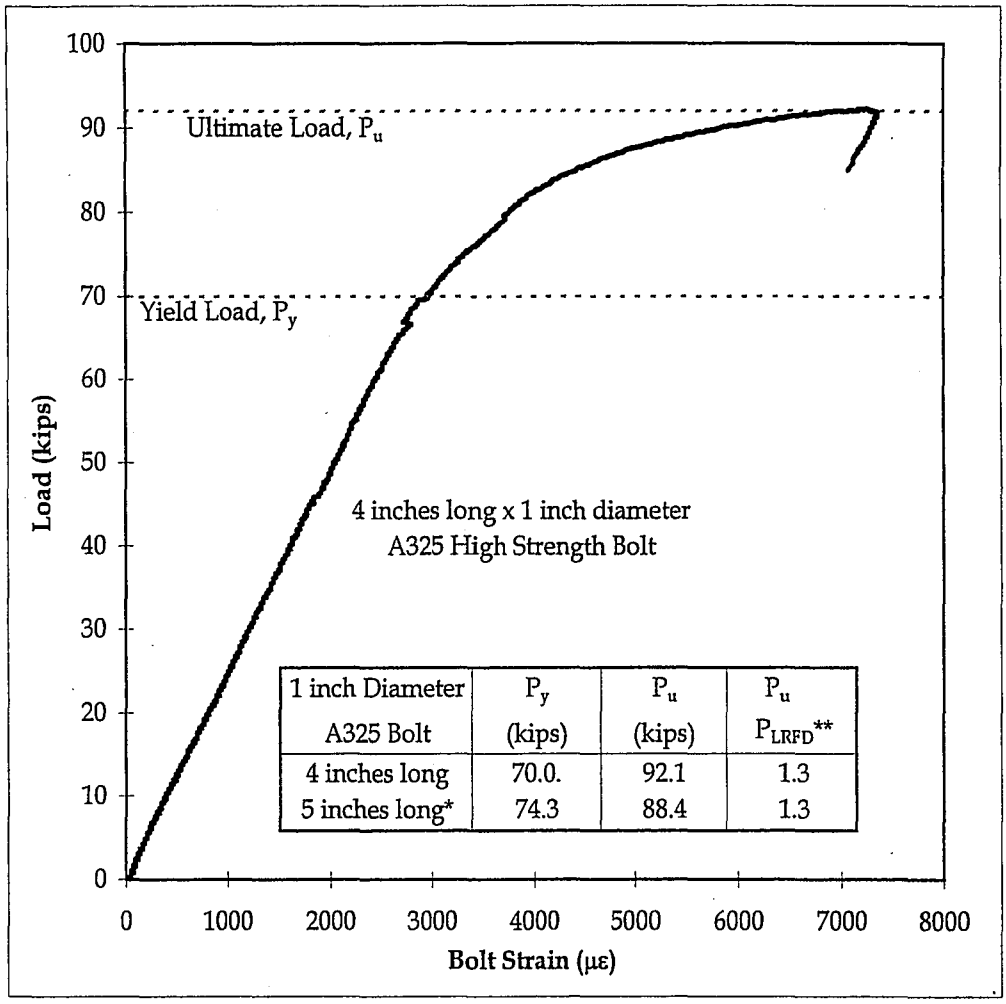

1 inch Diameter A325 Bolt	P_y (kips)	P_u (kips)	P_u P_{LRFD}**
4 inches long	70.0.	92.1	1.3
5 inches long*	74.3	88.4	1.3

*Peng, 1997

**Nominal unfactored tensile strength (AISC-LRFD, 1995)

Figure 4.9. Clamping Bolt Tensile Test Results
(4 inches long x 1 inch Diameter A325 High Strength Bolt)

Amplitude, δ_h (inch)	Story Drift, θ_s (radians)
1/8	0.0104
3/16	0.0156
5/16	0.0260
7/16	0.0365

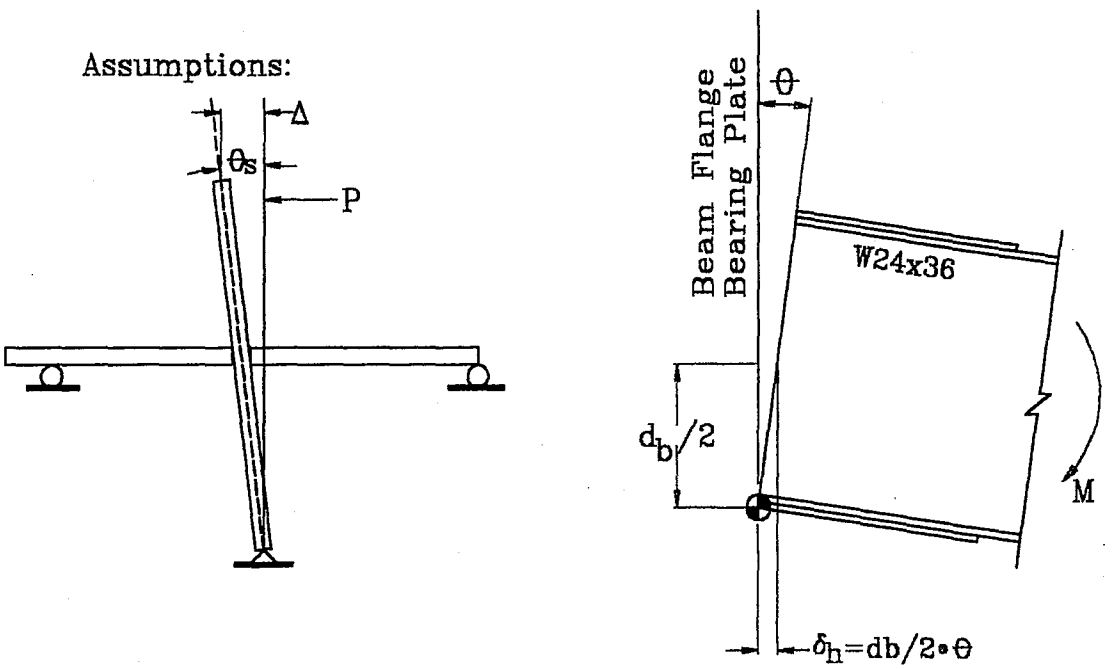

Displaced Beam–Column Cruciform

Displaced Connection

$\theta=\theta_s$, assuming Beams and Column Rigid

Figure 4.10. Story Drift Corresponding to Displacement Amplitude

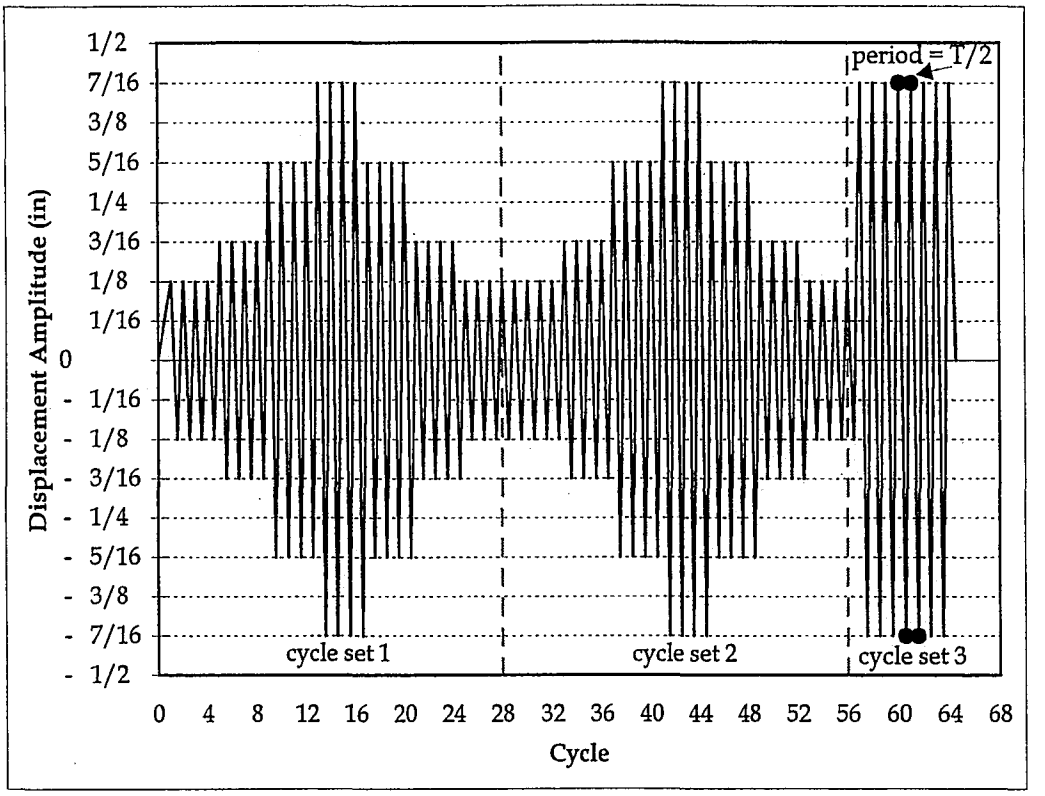

Total Travel for Cycle Set 1 and Total Travel for Cycle Set 2 = 27 inches
Total Travel for Cycle Set 3 = 12-1/4 inches
Total Travel for Cycle Sets 1, 2, and 3 = 66-1/4 inches

Figure 4.11. Displacement History for Experimental Testing

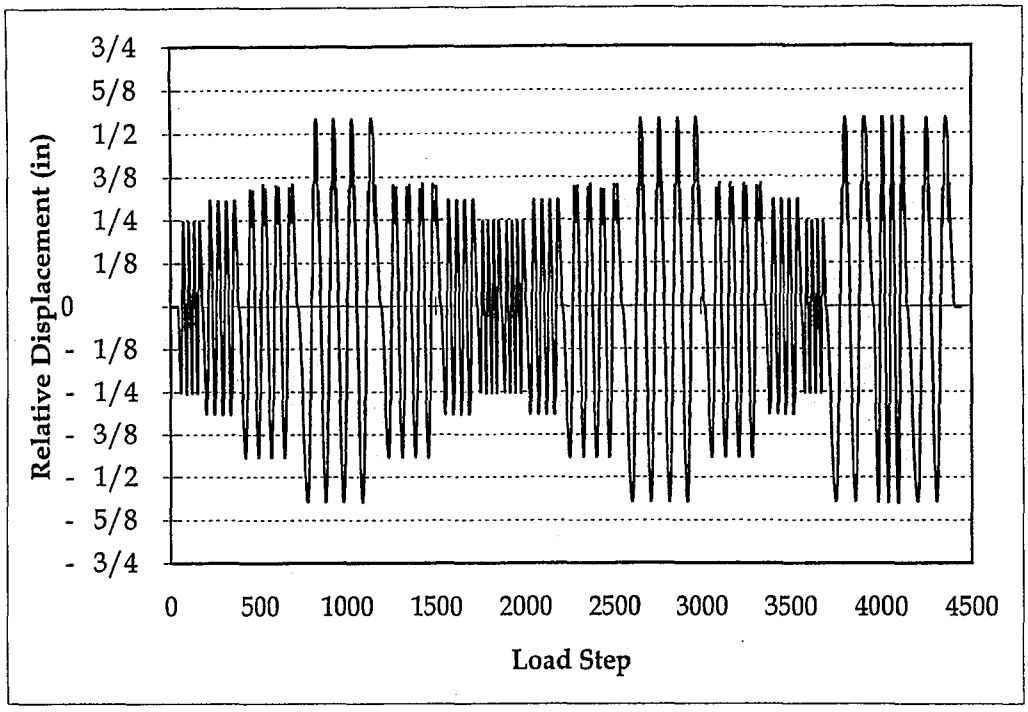

(a)

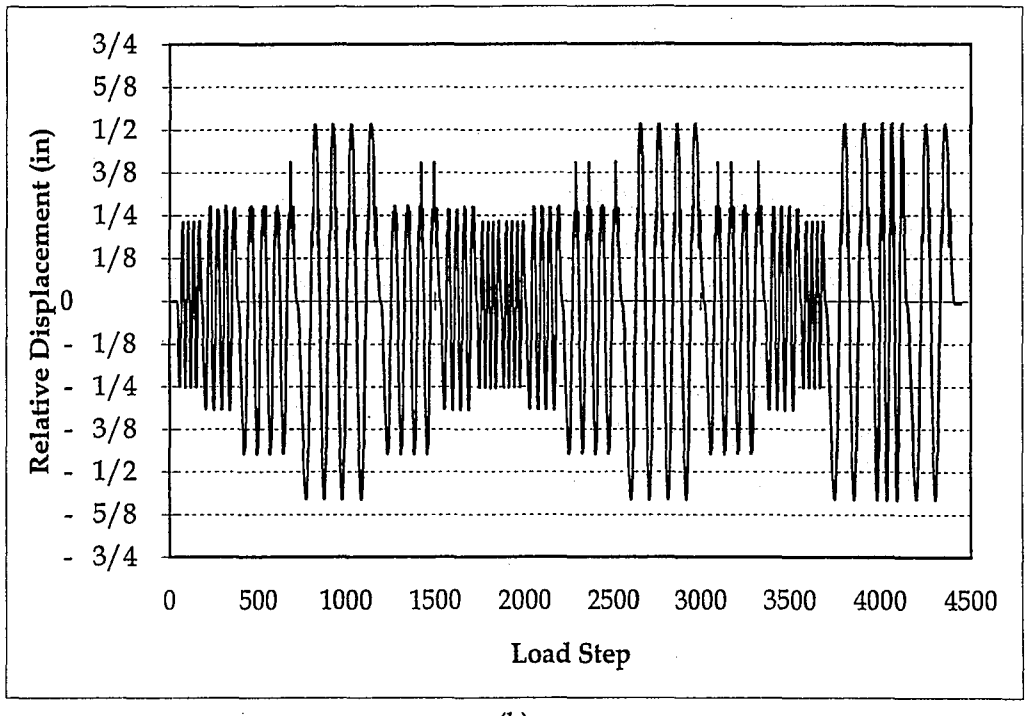

(b)

Figure 4.12. Measured Unrestrained Actuator Displacement from (a) North and (b) South Linear Potentiometers

5. Double Plate Friction Tests

The purpose of this chapter is to present the experimental results of the double plate friction tests. Experimental phenomena observed during the test are also discussed. Nine double plate friction tests were used to investigate the parameters shown in Table 5.1. One set of two brass shims was used for the first series of four test (F1 to F4), and one set of shims was used for the second series of four test (F5 to F8). Each series of four tests was conducted using a single level of clamping bolt preload. The first test studied the friction behavior for an unworn brass shim. The second test studied the variation in the friction behavior after the brass shims were worn. The third test evaluated the consistency of the friction behavior when the displacement rate was doubled. A dynamic displacement rate was used for the fourth test to compare the friction behavior under nearly static displacement rates and under dynamic displacement rates, as discussed in Chapter 4. One final test (F9) investigated the durability of the brass-steel tribo surfaces.

For the first series of tests (F1 to F4), a clamping bolt preload of 23 kips/bolt was used. With three clamping bolts, 2 tribo surfaces, and an assumed μ of 0.3, the preload results in a theoretical friction force of 41.4 kips. The second series of tests (F5 to F8) used a clamping bolt preload of 35 kips/bolt. The corresponding theoretical friction force was 63 kips. The imposed displacement histories used in the tests were discussed previously in Chapter 4.

5.1 Experimentally Observed Behavior

5.1.1 Wear of the Brass Shim Tribo Surfaces

Tribo surfaces sliding relative to one another undergo wear. The brass-steel tribo surfaces were not thoroughly inspected until a series of tests (e.g., F1 to F4) was completed. Thus, the observations discussed below pertain to the cumulative wear after a series of tests at a specific level of bolt preload.

Adhesive wear occurred at the tribo surface due to the differences in hardness of the brass and steel as shown in Figures 5.1 and 5.2. Each tribo surface on the T-stub web was examined after tests F1 to F4 were completed. Adhesion of brass particles above and below the oversized holes in the T-stub web was observed. The amount of brass particles on the two tribo surfaces of the T-stub web appeared to be similar. The brass adhesion was concentrated around the oversized holes in the direction of slip displacement between the brass shim and web (i.e., above and below the oversized holes) because of the increase in compressive contact stress due to the deformation of the outer plates, as discussed in Section 5.1.2. The amount of brass adhesion in the direction perpendicular to the direction of slip displacement from the oversize holes was significantly less.

The steel T-stub is a harder than the brass shims, therefore wear is expected on the tribo surfaces of the brass shims. Figure 5.3 and Figure 5.4 show the east and west brass shim tribo surfaces, respectively. The figures show that the majority of wear

occurred in the direction of slip displacement. The large darkened areas indicate typical wearing. The darken color is a result of mill scale from the tribo surfaces of the T-stub which has adhered to the brass tribo surface. It appears that mill scale wear fragments were formed and adhered to the brass surface.

The wear of each brass shim is not uniform over the entire tribo surface, but is concentrated over an area around each bolt hole as shown in Figure 5.3. Thus, the force in the clamping bolts does not appear to be uniformly distributed over the tribo surface area. The worn area around bolt hole 3 is approximately rectangular, with an area of approximately 25 in^2, including the bolt hole. An area of severe wear occurred between bolt hole 1 and bolt hole 2, on both brass shims as shown in Figure 5.3. This area of severe wear is believed to have occurred because of a local irregularity in the thickness of the T-stub web.

Abrasive wear of the brass shim tribo surfaces also occurred as shown in Figure 5.3. Abrasive wear is characterized by the "machined" appearance of the worn surface (Lansdown and Price, 1986), as evident in the direction of relative displacement on the tribo surfaces of the brass shims in Figure 5.3. Under close visual examination, groove-like patterns running parallel to the direction of slip displacement were observed. The formation of the groove-like patterns is a function of the material and the temperature of the tribo surface. For low temperature wearing of the tribo surfaces, abrasive wear is generally seen in the form of a machined appearance. For

higher temperatures, the worn surface develops a partially melted appearance, and wear fragments may re-attach themselves to the tribo surfaces (Lansdown and Price, 1986). The smallest and largest measured change in temperature (ΔT) for tests F1 to F4 are 18 and 101 degrees Fahrenheit, respectively. The temperature was measured using the procedure presented in Chapter 4. No apparent melting of the brass surface occurred. The reduction of the thickness of the shims, due to the abrasive wearing, had negligible effects on the friction behavior as will be discussed later.

The machined appearance of the brass shim above and below the bolt holes can be attributed to abrasive wear, but an additional form of wear took place due to the deformation of the outer plates. As a result of the bolt hole drilling process, a sharp edge was produced at the edge of the oversized bolt hole in the web of the T-stub. When the friction test specimen is assembled, the brass shim is placed in contact with the sharp edge of the oversized hole at approximately 1-1/8 inch, in the radial direction, from the hole center, as shown in Figure 5.4. The oversized bolt hole edge is located 19/32 inch away from the edge of the brass shim bolt hole. During the preloading of each clamping bolt, the areas of the outer plates which protruded into the area of the oversized hole were deformed into the oversized hole, as discussed in Section 5.1.2. Although this lateral deformation is small, it causes the sharp edge of the oversized bolt hole to be pushed into the brass shim tribo surfaces.

As slip displacement between the brass shims and T-stub occurs, a portion of the edge of the oversized bolt hole in the T-stub is pushed closer to the bolt and gouges the surface of the brass shims. *Gouging wear* is a form of wear in which "lumps or particles rub against a surface with sufficient force to gouge out material" (Lansdown and Price, 1986). It appears that the depth of the gouging increased as the edge of the oversized bolt hole in the web was pushed closer to the bolt, and decreased as it was pushed away. As the web is pushed toward the bolt, it pushes open the inwardly deformed outer plates, while subsequently digging further into the brass shim due to the increase in compressive stress on the plates. As slip displacement between the brass shims and T-stub occurs, a lip or build up of brass material is produced in the direction of motion.

The visible effects of gouging are similar to that of abrasive wear. A machined surface appearance results, but the severity of wear is more intense. Measuring the worn surface areas of the brass shim tribo surface, it was determined that the gouging of the shim started at a distance typically 1/8 to 3/16 inch away from the bolt hole edge of the brass shim in the direction of relative displacement as shown in Figure 5.4. In the direction perpendicular to the relative displacement, gouging of the shim occurred 5/16 to 9/16 inch away from the hole edge (Figure 5.4). The brass shim was initially in contact with the edge of the oversized hole at about 19/32 inch from the edge of the brass shim bolt hole as previously stated. The

displacement of the oversized hole edge in the direction of to slip displacement can be determined by subtracting the width of the ungouged surface of the brass shim (1/8 to 3/16 inch) from the distance between the edge of the oversized hole and the edge of the brass shim bolt hole (19/32 inch). The slip displacement calculated from these measurements is approximately 13/32 to 15/32 inch as shown in Figure 5.4, which directly corresponds to the largest imposed displacement of 14/32 (7/16) inch. The gouging process is believed to occur during the test until the depth of material removed by gouging equals the depth that the oversized hole edge is pushed into the brass shim surface. Once this gouging is complete, only abrasive wear occurs.

Tests F5 to F8 included similar but more severe, wear phenomena of the brass shim tribo surfaces, as shown in Figure 5.5. The approximate wear surface area is similar to that of the shims used for Tests F1 to F4 (Figure 5.3), but the abrasive wear was greater. The transfer of mill scale from the steel T-stub web to the brass shim tribo surfaces was decreased due to the increase in abrasive wear. Adhesive wear of the T-stub surface was increased, as shown in Figures 5.6 and 5.7, compared to the adhesive wear during Tests F1 to F4 (Figures 5.1 and 5.2).

A decrease in the measured bolt force in the clamping bolts during slip displacement in the first cycle is also attributed to wear of the surfaces of the brass shims. This drop in force is caused by yielding of the asperity peaks which were

placed in contact during the initial assembly of the test specimens. Yielding of the asperities is caused by shear forces at the asperity peaks produced as slip occurs. Yielding of the asperities in contact at assembly causes a reduction in the thickness of the tribo surfaces, which results in a decrease in bolt force.

5.1.2 Deformation of the Outer Plates

The test results shown later, indicate that the force in the clamping bolts varied from the preload force during the tests. The variation in the force in each clamping bolt was cyclic, with increases and decreases that appear to depend upon the location of the clamping bolt relative to the oversized bolt hole in the T-stub web. When the bolt was aligned with the centerline of the oversized bolt hole, the minimum bolt force occurred. When the edge of the oversized hole approached the bolt, the bolt force increased. When the oversized hole edge was closer to the bolt (i.e., the amplitude of slip displacement was larger), the increase in the bolt force was greater.

This variation in bolt force is attributed to deformation of the outer plates. The undeformed clamping bolt cross section is shown in Figure 5.8. The outer plates extend beyond the edges of the oversized hole in the T-stub web. Initially, the bolt holes in the outer plates and shims are aligned with respect to the oversized hole. The head of the bolt and nut have a maximum diameter of 1-5/8 inches. The washer has a diameter of 2 inches. Thus, the bolt assembly fits entirely within the

2-1/4 inch oversized hole diameter. As the preload is applied to the bolt, the outer plates and brass shims are deformed into the oversized bolt hole by the bolt, as shown in Figure 5.9.

The magnitude of the deformation of the outer plates into the oversized hole was estimated using an analytical model for a flat circular plate with constant thickness, as shown in Figure 5.10 (Young, 1989). The restraint of the outer plates at the edge of the oversized hole was unknown, therefore the analysis considered both fixed and pinned support conditions. These two support conditions, respectively, provide an upper bound (maximum) and lower bound (minimum) to the estimated plate deformation. Bending and shear deformations were included. The bending deformation with fixed support conditions, is as follows:

$$\Delta y_b = -\frac{\omega \cdot a^3}{D} \cdot \left(\frac{C_1 \cdot L_6}{C_4} - L_3 \right) \tag{5.1}$$

where: ω = the unit line load (force per circumferential length),

a = the outer plate radius, which is taken as the radius of the oversized bolt hole in the T-stub,

D = the plate constant, which is $=E \bullet t^3/(12 \bullet (1-\nu^2))$,

E = the modulus of elasticity of the plate material,

t = the thickness of the plate, and

ν = Poisson's ratio of the plate material.

The bending deformation with pinned support conditions is as follows:

$$\Delta y_b = -\frac{\omega \cdot a^3}{D} \cdot \left(\frac{C_1 \cdot L_9}{C_7} - L_3 \right) \tag{5.2}$$

The plate constants (C_i) and radial location functions (L_i) used in the previous equations are as follows:

$$C_1 = \frac{1+\nu}{2} \cdot \frac{b}{a} \cdot \ln\frac{a}{b} + \frac{1-\nu}{4} \cdot \left(\frac{a}{b} - \frac{b}{a} \right)$$

$$L_3 = \frac{r_o}{4 \cdot a} \left\{ \left[\left(\frac{r_o}{a} \right)^2 + 1 \right] \cdot \ln\frac{a}{r_o} + \left(\frac{r_o}{a} \right)^2 - 1 \right\}$$

$$C_4 = \frac{1}{2} \left[(1+\nu) \cdot \frac{b}{a} + (1-\nu) \cdot \frac{a}{b} \right]$$

$$L_6 = \frac{r_o}{4 \cdot a} \left[\left(\frac{r_o}{a} \right)^2 - 1 + 2 \cdot \ln\left(\frac{a}{r_o} \right) \right]$$

$$L_9 = \frac{r_o}{a} \left\{ \frac{1+\nu}{2} \cdot \ln\left(\frac{a}{r_o} \right) + \frac{1-\nu}{4} \cdot \left[1 - \left(\frac{r_o}{a} \right)^2 \right] \right\}$$

$$C_7 = \frac{1}{2} \cdot (1-\nu^2) \cdot \left(\frac{a}{b} - \frac{b}{a} \right)$$

where: r_o = the radial location of the unit line load, and

b = the inner plate radius, which is taken as the radius of the standard bolt in the outer plate.

The shear deformation with either fixed or pinned support conditions is as follows:

$$\Delta y_s = \frac{K_s \cdot \omega \cdot a}{t \cdot G} \tag{5.3}$$

where: K_s = the deflection coefficient, and

G = the shear modulus.

K_s is calculated as follows:

$$K_s = -1.2\left(\frac{r_o}{a}\right) \cdot \ln\left(\frac{a}{r_o}\right)$$

The total deformation (Δy) is the sum of the bending and shear deformations.

$$\Delta y = \Delta y_b + \Delta y_s \tag{5.4}$$

The analysis of the outer plate deformation used the following assumptions, as shown in Figure 5.11: (1) the supports of the outer plate were located at the edge of the oversized holes in the T-stub web; (2) the outer plate radius (a) was the radius of the oversized bolt hole; (3) the inner radius (b) was the radius of the standard bolt hole in the outer plate; (4) the unit line load (ω) was imposed at a radius (r_o) of 43/64, which is halfway between the radius of the standard bolt hole in the outer plates ((1-1/16)/2 inch) and the radius of the bolt head ((1-5/8)/2 inch); and (5) the deformation of the outer plate was calculated at a distance of r_o from the hole centerline.

Although the nominal clamping bolt preloads were 23 and 35 kips/bolt as shown in Table 5.1, the actual bolt preload varied between 23 and 24 kips/bolt, and 35 and 36 kips/bolt, respectively. Therefore, bolt preload values in the middle of these ranges were used for the analysis. The maximum and minimum plate deformation (Δy) for a bolt preload of 23.5 kips/bolt is 0.00095 inch and 0.00035 inch respectively. For a bolt preload of 35.5 kips/bolt, the maximum and minimum plate deformation is 0.00143 inch and 0.00053 inch, respectively.

Reasonable evidence to support the hypothesis that outer plate deformation causes the variation in the clamping bolt force comes from comparing data from Tests F1 and F5 with the analytical results, in Figure 5.12. Figure 5.12 shows the deformation of the outer plates plotted versus the slip displacement during the test. For the initial condition, at zero slip displacement, the outer plates are deformed inward due to the bolt preload. The inward deformed condition is taken as zero outer plate deformation. The straight lines are analytical estimates of how the initially inward deformed plates will be pushed outward by the T-stub web (i.e., how much outward deformation of the outer plates will occur) as slip displacement occurs. For the clamping bolt assembly shown in Figure 5.9, the total outward deformation of the outer plates can be as much as two times the analytical estimated (i.e., $2 \cdot \Delta y$). The solid square symbols in Figure 5.12 represent the case when the entire inward deformation ($2 \cdot \Delta y$) is recovered (as outward deformation) when the maximum slip displacement of 7/16 inch is reached.

The measured data shown in Figure 5.12, is an estimate of the outward deformation of the outer plates assuming the deformation is equal to the change in the grip length of the clamping bolts (ΔL_{BG}). ΔL_{BG} is equal to the measured change in strain in the bolt ($\Delta\varepsilon_B$) times the length of the bolt grip (L_{BG}). Changes in the bolt grip length are comparable to changes in the thickness of the assembly clamped by the bolts. In this case, the change in assembly thickness is assumed to be due to outward deformation of the outer plates. The change in the grip length occurring during the tests also corresponds to the variation of the bolt force.

The data for the change in grip length versus the slip displacement is shown for each clamping bolt in Figure 5.12. Figures 5.12(a) to (c) and (e) to (f) are for Tests F1 and Test F5, respectively. The change in grip length (ΔL_{BG}) for one complete cycle of slip displacement, at a displacement amplitude of 7/16 inch, is shown. As shown in Figure 5.12, the estimates of the outward deformation of the outer plates from ΔL_{BG} with falls near the analytical estimates for the fixed (minimum) conditions, in most cases, and below the analytical estimates for the pinned conditions. The estimates of plate deformation from ΔL_{BG} should fall below the analytical estimates, because the entire inward deformation ($2 \bullet \Delta y$) will not be recovered even if the bolt reaches the edge of the oversized hole, which does not happen at a slip displacement of 7/16 inch.

The variation in bolt grip length (ΔL_{BG}) is not symmetric because the bolt is not initially at the centerline of the oversized hole in the T-stub web. In the analysis of the outer plate deformation, the bolt is assumed to be aligned with the centerline of the oversize hole, but some initial offset may exist due to fabrication and assembly tolerances. If the bolt is initially offset from the oversize hole centerline, the bolt deformation in one direction may be greater than the other.

5.1.3 Clamping Bolt Force Variations

As discussed in the previous section, the clamping bolt force fluctuates throughout each test in a consistent cycling motion as shown in Figures 5.13 and 5.14. The magnitude of the bolt force depends on its location within the oversized hole in the T-stub web. Alignment of the bolt with the centerline of the oversized hole produces the minimum bolt force. As the edge of the oversized hole is pushed towards the bolt, the bolt force increases. The magnitude of the increase depends on the proximity of the edge of the oversized hole to the bolt. Thus for the smaller amplitudes of slip displacement, the increase in bolt force is less than that for the larger amplitudes of slip displacement.

The variation in the bolt force is directly related the change in the bolt grip length, as discussed in the previous section. The change in the bolt grip length (ΔL_{BG}) is related to the deformation of the outer plates. The bolt is linear elastic under the preload. As the outer plates are pushed outward by the T-stub, and the initially

inward deformation of the outer plates is recovered, the bolt is forced to elongate. The elongation of the bolt from its initial condition after preloading is measured by a change in bolt strain ($\Delta\varepsilon_B$). As the web pushes the outer plates outward, a change in bolt strain is measured, and the bolt force increases. As the oversized hole returns to its original position and the bolt moves closer to the centerline of the oversized hole (i.e., the slip displacement is equal to zero), the bolt returns to its original length (ΔL_{BG} goes to zero), and the increased bolt force is removed.

Figures 5.13 shows the applied force measured by the load cell of the actuator versus the average cumulative travel as well as the bolt force versus average cumulative travel for one cycle with a slip displacement amplitude of 7/16 inch, during Tests F1. Figure 5.15 shows the same results for Test F5. The slip displacement is the relative displacement between the upper T-stub and outer plates, and is measured by the slip linear potentiometers shown in Figure 4.5. The slip displacement is averaged for the two potentiometers and accumulated from the beginning of the each test to obtain the average cumulative travel. The change in bolt force depends on the slip displacement, and is largest at the largest slip displacement. The points of zero slip displacement, shown in Figures 5.13 and 5.14, are the slip displacement measured by the instrumentation at the beginning of each test. At zero slip displacement, the bolt is not necessarily centered in the oversized hole, although at the beginning of each test, the bolts were loose and the T-stub web was positioned so that the bolts were close to the center of the oversized hole. The

zero slip displacement points are shown at the beginning, middle, and end of the cycle in Figures 5.13 and 5.14.

As shown in Figures 5.13 and 5.14, the bolt force increases during the push and pull cycles, as slip displacement occurs between the tribo surfaces. The push cycle refers to the portion of one cycle when the actuator pushes the T-stub downward between the outer plates. During the push cycles, the top edge of the oversized hole in the T-stub web is pushed closer to the bolt, as shown in Figures 5.13 and 5.14. The pull cycle refers to the remaining portion of the same cycle when the actuator pulls the T-stub upward relative to the outer plates. During the pull cycles, the upper edge of the oversized hole is pulled away from the bolt and the lower edge of the oversized hole is pulled towards the bolt, as shown in Figures 5.13 and 5.14.

Figure 5.14(a) shows the force variation in bolt 1 for Test F5. The bolt is aligned close to the centerline of the oversized hole. The zero displacement points all occur at relatively the same bolt force for both the push and pull cycles of relative displacement. Some variation exists in the maximum bolt force for the push and pull cycles due to the unequal stroke of the actuator, which was discussed in Chapter 4.

As shown in Figures 5.13 and 5.14, the maximum bolt force occurs at zero applied force, because the zero applied force occurs at the maximum slip displacement for either the push or pull cycles. Therefore, at zero force the T-stub web has been pushed toward the bolt and pushing open the outer plates.

At zero slip displacement the bolt is assumed to be in the center of the oversized hole, as previously discussed in this section, and the minimum bolt force occurs. As the slip occurs, the T-stub web moves relative to the bolt, pushing open the inwardly deformed outer plates. As shown in Figures 5.13 and 5.14, the force in each bolt increases as slip occurs during the push cycle due to outer plate deformation. The maximum force in each bolt occurs at the maximum slip displacement for the cycle (7/16 inch in Figures 5.13 and 5.14). As shown in Figures 5.13 and 5.14, the maximum force in each bolt occurs near zero applied force during the push cycle, because zero applied force occurs close to the maximum slip displacement.

As shown in Figures 5.13 and 5.14, as slip occurs and the bottom of the oversized hole is pull towards the bolt, the bolt force decreases as it nears the center of the oversized hole. At zero displacement after the push cycle, the bolt force begins to increases during the pull cycle. As shown in Figures 5.13 and 5.14, the force in each bolt increase due to outer plate deformation during the pull cycle. The maximum bolt force in the pull cycle occurs near zero applied force, similar to the previously

described push cycle. A decrease in applied force occurs during the transition from the pull to push cycles, and the bolt force decrease as zero displacement is approached.

5.1.4 Thermal Effects

During the tests, energy dissipation occurs as the brass-steel tribo surfaces undergo relative displacement. The energy dissipation occurs as mechanical energy (from the friction force acting through slip displacement) is converted into heat, which dissipates into the surrounding environment.

The introduction of heat into a friction test specimen can influence the friction behavior due to thermal effects (i.e., thermal expansion). Thermal expansion of material at or near the tribo surfaces can cause the clamping bolt force to increase as the clamped material expands. The rise in bolt force then causes an increase in friction force. Excessive heating may result in melting of one or both of the tribo surfaces.

Thermal effects were clearly observed Tests F4 and F8, which were conducted using a dynamic displacement rate. A model of the thermal effects is developed in this section. A schematic of the clamping bolt assembly is shown in Figure 5.15. The deformation of the assembly due to bolt preload was neglected, because this mechanical action (i.e., the variation of the bolt force due to outer plate

deformation) was addressed in the previous section. As shown in Figure 5.16, it was assumed that the change in thickness of the plies (or layers), material clamped by the bolt, is equal to the change the length of the bolt grip. The following compatibility equation is used to express this assumption:

$$\Delta L_{BG} = \Delta t = \Sigma \Delta t_i \tag{5.5}$$

where: ΔL_{BG} = the change in bolt grip length,

Δt = total change in thickness of plies clamped by the bolt, and

Δt_i = the change in thickness of ply i.

The change in the length (i.e., the deformation) of the bolt grip and the change in the thickness of one ply is attributed to two factors. The first being the thermal deformation (δ_T) caused by the temperature change, expressed as follows:

$$\delta_T = \alpha \cdot \Delta T \cdot L \tag{5.6}$$

where: α = the coefficient of thermal expansion (for steel α=6.5x10^{-6}in/in/°F; for brass α = 11.1x10^{-6} in/in/°F),

ΔT = the change in temperature, and

L = the length of material in direction of expansion.

The second is the mechanical deformation of the material due to changes in the applied force from the clamping bolts (δ_P), as follows:

$$\delta_P = \frac{\Delta P \cdot L}{A \cdot E} = \frac{\Delta \sigma \cdot L}{E} \tag{5.7}$$

where: ΔP = the change in bolt force,

A = area of the bolt or tributary area around bolt,

E = the modulus of elasticity (for steel $E \cong 29500$ ksi;

for brass $E = 16000$ ksi INCO, 1968), and

$\Delta \sigma$ = the change in stress.

Combining these equations, the total deformation can be expressed as follows:

$$\delta = \delta_T + \delta_P = (\alpha \cdot \Delta T \cdot L) + \left(\frac{\Delta \sigma \cdot L}{E}\right) \tag{5.8}$$

The total deformation (i.e., change in the grip length) of the bolt is:

$$\Delta L_{BG} = (\alpha_B \cdot \Delta T_B \cdot L_{BG}) + \left(\frac{\Delta \sigma_B \cdot L_{BG}}{E_B}\right) \tag{5.9}$$

where: α_B = the thermal expansion coefficient of the bolt,

ΔT_B = change in temperature in the bolt,

L_{BG} = the grip length of the bolt,

$\Delta \sigma_B$ = the change in stress in the bolt, and

E_B = the modulus of elasticity of bolt.

The total change in thickness of the plies is:

$$\Delta t = \Sigma \Delta t_i = \sum \left[(\alpha_i \cdot \Delta T_i \cdot t_i) + \left(\frac{\Delta \sigma_i \cdot t_i}{E_i} \right) \right] \tag{5.10}$$

where: Δt_i = the change in thickness of ply i,

α_i = the thermal expansion coefficient for ply i,

ΔT_i = the change in temperature of ply i,

t_i = the thickness of ply i,

$\Delta \sigma_i$ = the change in stress in ply i, and

E_i = the modulus of elasticity of ply i.

For equilibrium to be maintained within the system, the change in the force in a clamping bolt must be equal to the change in force applied by the clamping bolt on the plies. The corresponding change in stress for the bolt and for ply i can be determined, where tension stresses are positive and compression stresses are negative. The change in stress in ply i is:

$$\Delta \sigma_i = \frac{-\Delta P_{bolt}}{A_i} \tag{5.11}$$

where: $\Delta \sigma_i$ = the change in stress in ply i, and

A_i = the tributary around the bolt in ply i.

The change in stress in the bolt grip length is:

$$+\Delta\sigma_B = \frac{+\Delta P_{bolt}}{A_B} \tag{5.12}$$

where: $\Delta\sigma_B$ = the change in stress in the bolt, and

A_B = the area of the bolt (i.e., the area of the bolt shank).

The change in stress in the bolt is a tensile stress, which elongates the bolt. The change in stress in the plies is a compressive stress because the bolt head and nut compress the plies together.

Substituting Equations 5.9 and 5.10 into Equation 5.5, then substituting Equations 5.11 and Equations 5.12 into the resulting equation, and then solving for the change in bolt force, results in the following equation:

$$\Delta P_{bolt} = \left[\frac{\left[\sum\left(\alpha_i \cdot \Delta T_i \cdot t_i\right) - \left(\alpha_B \cdot \Delta T_B \cdot L_{BG}\right)\right]}{\left[\sum\left(\frac{t_i}{A_i \cdot E_i}\right) + \left(\frac{L_{BG}}{A_B \cdot E_B}\right)\right]} \right] \tag{5.13}$$

Equation 5.13 provides the change in bolt force due to mechanical and thermal effects. However, the internal bolt gauge used to measure "bolt force" cannot differentiate between mechanical elongation or thermal elongation of the bolt. Therefore, an expression for the total strain in the bolt, including thermal strain is needed. The total change in strain in the bolt due to thermal effects is as follows:

$$\Delta\varepsilon_{total} = \Delta\varepsilon_P + \Delta\varepsilon_T = \frac{\Delta P_{bolt}}{A_B \cdot E_B} + \alpha_B \cdot \Delta T_B \tag{5.14}$$

where: $\Delta\varepsilon_P$ = the change in mechanical strain,

$\Delta\varepsilon_T$ = the change in thermal strain, and

ΔP_{bolt} = the result from Equation 5.13.

The total strain in the bolt is as follows:

$$\varepsilon_{total} = \varepsilon_{iinitial} + \Delta\varepsilon_{total} \tag{5.15}$$

where: $\varepsilon_{initial}$ = the strain before thermal effects occur.

The measured data from the bolts in the double plate friction tests consists of "bolt force" which is obtained from the bolt gauges as discussed in Chapter 4. The bolt gauges were calibrated so the output was in force units (kips). As noted above, the bolt gauge cannot differentiate between mechanical strain and thermal strain of the bolt. Therefore, the "bolt force" output by the bolt gauges is proportional to the total strain in the bolt. The total measured strain in the tests is as follows:

$$\varepsilon_{total,meas} = \frac{P_{bolt,meas}}{A_B \cdot E_B} \tag{5.16}$$

where: $\varepsilon_{total,meas}$ = the total measured strain in the bolts from the bolt gauges, and

$P_{bolt,meas}$ = the apparent bolt force obtained from the bolt gauges, which includes both mechanical strain and thermal strain.

Figure 5.17 and 5.18 shows the comparison of analytical estimate of the total bolt strain (ε_{total}) due to mechanical and thermal bolt strains versus the measured bolt strain ($\varepsilon_{total,meas}$) for Tests F4 and F8. The measured bolt strains are plotted versus the average cumulated travel for each test and the analytical estimates of the total bolt strain (ε_{total}) are from Equation 5.15. The measured bolt strain is obtained from Equation 5.16 using the bolt force from the gauges in the clamping bolts. The measured initial strain in the bolts is taken after the initial decrease in clamping bolt force occurs due to the shearing of the high points of the asperities after slip begins as discussed in Section 5.1.

The temperature of the outer steel plate between bolts 1 and 2 was recorded at the beginning and end of each test using a thermal probe, as discussed in Chapter 4. The change in temperature (ΔT) due to the generation of heat at the tribo surface is the final temperature minus the initial temperature, and was assumed constant for all the plies. The ΔT of the bolt was assumed to be 25% of the measured ΔT of the outer plate, because heat transfer from the outer plate to the bolt was limited by the small portion of the bolt head and nut that were in direct contact with outer plates through the washers. The analytical estimate of the bolt strain is assumed to occur at the point of maximum average cumulative travel for each test. The analytical estimate of the bolt strain should be compared to the measured bolt strain when the bolt is near the center of the oversized hole to neglect the mechanical variation of the bolt strain (i.e., bolt grip length) due to outer plate deformation.

For Test F4, as shown in Figure 5.17, the initial mechanical strain was 897 με which corresponds to a bolt force of 22 kips. The analytical estimate of the total strain (ε_{total}) was 1247 με for a ΔT of 101 degrees Fahrenheit. The corresponding average cumulative travel was 59.5 inches. As shown in Figure 5.17 for Test F4, ε_{total} was close to the measured bolt strain when the bolt is near the oversized hole center for bolt 1, and slightly higher than the measured strain for bolts 2 and 3. For Test F8, as shown in Figure 5.18, the initial mechanical strain was 1386 με which corresponds to a bolt force of 34 kips. The analytical estimate of strain ε_{total} was 1754 με for a ΔT equal to 106 degrees Fahrenheit. The corresponding average cumulative travel was 48 inches. As shown in Figure 5.18, ε_{total} was close to the measured bolt strain when the bolt is at the center of the oversized hole for bolts 1, 2, and 3. The comparison of the analytical estimate and the measured bolt strain was closest for bolt 2.

The increase in bolt strain due to thermal effects was higher in bolts 1 and 2 than bolt 3 for Tests F4 and F8, as shown in Figures 5.17 and 5.18. This may be due to the additional wear which occurred due to the irregularity in thickness of the T-stub web between bolt hole 1 and bolt hole 2 discussed in Section 5.1. This additional wear may have generated more heat near bolts 1 and 2 which caused a greater increase in bolt strain due to the thermal effects. Thus, by the measured ΔT is the change in temperature throughout the plies, and the change in temperature in the

bolt equal to 25% of the measured ΔT, a conservative estimate of the bolt strain was provided for Tests F4 and F8.

5.2 Experimental Results

Eight test were conducted as shown in Table 5.1. In the following sub-sections, the results for the tests are grouped together according to the bolt preload. Test results for each specimen are presented in a sequence of plots as follows: (1) applied force versus average cumulative travel and the applied force versus the average slip displacement; (2) the bolt force versus the average cumulative travel; (3) the bolt force versus the average slip displacement; and (4) the average friction force per cycle.

5.2.1 Friction Tests F1 to F4

Tests F1 to F4 used the same bolt preload (23 kips/bolt) and the same pair of brass shims, but the displacement rate was varied as shown in Table 5.1. A photo of the test specimen after the completion of this series of tests is shown in Figure 5.19. Figure 5.20(a), 5.24(a), 5.28(a), and 5.32(a) show the applied force versus the average cumulative travel for Tests F1, F2, F3, and F4, respectively. The applied force is obtained from the load cell on the actuator. This force equals the sum of the forces on the two brass-steel tribo surfaces. When the tribo surfaces are under relative motion (slip), the applied force is equal to the sum of the friction forces on the two tribo surfaces (F_f). The average cumulative travel is the slip displacement

accumulated from the beginning to the end of the test. The figures show that the friction force is influenced by the amplitude of displacement as explained in Sections 5.1.2 and 5.1.3. As the displacement amplitude increases, F_f increases due to the effects of the outer plate deformation (i.e., the T-stub web pushing the outer plates outward).

During Test F1 (Figure 5.20(a)), the brass shim was initially unworn. F_f values at incipient slip during the break in cycles of cycle set 1 are approximately 65 kips. *Break-in*, or wearing of the unworn shim surfaces, occurred during the displacement cycles in the first half of cycle set 1, as the displacement amplitude increased. After break-in occurred during cycle set 1, the friction behavior stabilized (i.e., *steady state* was reached).

During Test F1 (Figure 5.20), the values of F_f at steady state are approximately 55 kips for the cycles with a displacement amplitude of 1/8 inch, and between 65 and 70 kips for the cycles with a displacement amplitude of 7/16 inch. During Test F2 (Figure 5.24), F_f was relatively constant throughout the entire test. F_f values at incipient slip are between 55 and 60 kips for the cycles with a displacement amplitude of 1/8 inch, and between 60 and 65 for the cycles with a displacement amplitude of 7/16 inch. For Test F3 (Figure 5.28), F_f values at incipient slip are relatively constant at approximately 60 kips, with the only significant increase during cycles with a displacement amplitude of 7/16 inch. Comparing Tests F1 and

F2, the difference in F_f between the unworn and the worn brass-steel tribo surfaces is 5 to 10 kips for a displacement amplitude of 1/8 inch. Comparing Tests F1 to F3, the effects of the rate increase in Test F3 appear negligible. For Test F4, the values of F_f at incipient slip are 65 kips for the first half of cycle set 1. Due to thermal effects (see Section 5.2.4), F_f increases as the test continues.

The hysteresis loops for Tests F1, F2, and F3, given in Figures 5.20(b), 5.24(b), and 5.28(b), show that the friction behavior of the brass-steel tribo surface is repeatable over a large number of cycles. In these figures, the applied force is plotted versus the average slip displacement, where the average slip displacement is the relative displacement between the outer plates and the upper T-stub. The behavior during Test F4 (Figure 5.32(b)) is not consistent with the behavior during the previous tests because of the thermal effects. During the period of break-in in Test F1 (Figure 5.20), larger values of F_f occur during the horizontal (or slip) regions of the curve, as the maximum positive and negative slip displacements are reached. However, the hysteresis loops after steady state behavior is reached are repeatable throughout each test. The bow-tie shape of the hysteresis loops occurs because of variations in the bolt forces due to the effects of deformation of the outer plates. This behavior is consistent for all four tests. The hysteresis loops for Test F4, Figure 5.32(b), are somewhat more variable when compared to the results for the other tests. As mentioned in Chapter 4, shortening of the displacement amplitudes occurred in the positive displacement direction. The error is not as large in the negative

displacement direction. F_f is repeatable for consecutive cycles, as seen by the grouping of lines in the slip regions of the hysteresis loops (Figure 5.32(b)), but thermal effects cause variation between loops from non-consecutive cycles.

Although the primary brass-steel tribo surfaces are between the brass shims and the T-stub web, the brass shims also slipped relative to the outer plates because of the standard 1/16 inch oversize bolt holes in the brass shims and outer plates. After the shims slip, the bolts go into bearing. The slip between the brass shims and outer plates occurred randomly during the test. When the shims slip relative to the outer plates, a increase in the friction force occurs (i.e., F_f peaks) within the slip regions of the hysteresis loops, as shown in Figures 5.20(b), 5.24(b), 5.28(b), and Figure 5.32(b). The peaks in F_f usually occur after a slip displacement of 1/16 inch from the point of incipient slip near the maximum positive and negative displacement in each cycle.

The magnitude of the increase in F_f is dependent upon the occurrence of one or both shims slipping simultaneously. The increase in F_f as one shim slips into bearing is approximately 3 to 4 kips. During Test F1, the increase in F_f as both shims slipped into bearing is noticeable as shown in Figure 5.20(b). During Test F2 (Figure 5.24(b)), only the east shim slipped and thus the increases in F_f are smaller compared to the increase in F_f during Test F1. No noticeable slip of the shims was observed during Test F3 (Figure 5.28(b)). No visual inspections were made during

Test F4 for safety reasons. An increase in F_f after incipient slip occurred often in Test F4, and may be due to slip of the shims (Figure 5.32(b)).

Plots of force in each clamping bolt versus the average cumulative travel for Tests F1, F2, F3, and F4 are shown in Figures 5.21, 5.25, 5.29, and 5.33. The measured bolt force shows an initial 2 to 3 kips decrease in bolt force during the first cycle of slip displacement. This decrease in bolt force is attributed to an initial yielding of asperity peaks which were brought into contact during the assembly of the test specimens.

For Tests F1 to F3 (Figures 5.21 and 5.29), the minimum bolt force (i.e., the bolt force when the clamping bolt is in the center of the oversized hole) is relatively constant after this point. The increases in bolt force are dependent upon the displacement amplitude. Some variation in the peak bolt force in each cycle exists because the bolt was not initially centered in the oversized hole. During Tests F1 and F2, the bolt force varied between 20 and 25 kips. For Test F3 (Figure 5.29), the range of bolt force is slightly greater. The force in bolt 2 shows some increase in force during Test F3, as shown in Figure 5.29(b). This rise in bolt force is attributed to thermal effects as discussed in Section 5.1.4. As noted in Section 5.1.4, the measured bolt force is obtained from the bolt strain gauges that do not distinguish thermal strain from mechanical strain. Therefore, the increase in force shown in Figure 5.29(b) in bolt 2 in Test F3 is misleading.

Some of this apparent increase is due to a change in bolt force, as given by Equation 5.13, and some of this apparent increase is due to thermal strain in the bolt due to an increase in the bolt temperature. The bolt forces plotted in Figure 5.33 show similar, but greater increases in force during Test F4. Again, part of this apparent increase is due to thermal strain in the bolt, and the rest is due to a true increase in bolt force.

The bolt force versus the average slip displacement plots for Tests F1, F2, F3, and F4, given in Figures 5.22, 5.26, 5.30, and 5.34, respectively, show the measured bolt force is consistent over successive displacement cycles. The maximum and minimum force in each clamping bolt during both Tests F1 and F2 (Figures 5.22 and 5.26) was approximately 25 to 26 kips and 19 to 20 kips, respectively. During Test F3 (Figure 5.30), the behavior of bolt 3 was consistent the previous test. Inconsistent variations in force occurred in bolt 1, and an increase in force occurred in bolt 2 during Test F3. These variations in bolt force were 2 to 3 kips. The increase in bolt force due to thermal effects is dramatic for Test F4 (Figure 5.34). The minimum bolt force is 21 kips, and the maximum force ranged from 40 kips in bolt 1 to 36 kips in bolt 3. The concave upward shape of the plots given Figures 5.22, 5.26, 5.30, and 5.34 show the relationship between an increase in displacement amplitude and an increase in bolt force due to the effects of the outer plate deformation.

The average friction force (average F_f) per cycle in Tests F1, F2, F3, and F4, is shown in Figures 5.23, 5.27, 5.31, and 5.35, respectively. The average F_f per cycle was determined in the following manner. First, the energy dissipated per cycle was determined. The energy dissipated per cycle was normalized by dividing by the total travel for the cycle, to produce the average F_f per cycle. In addition the energy dissipated per cycle was accumulated over the entire test. The accumulated energy dissipation for each test is shown in Table 5.2.

For Tests F1 to F3 (Figures 5.23, 5.27 and 5.31), the average F_f per cycle remained relatively constant. During Test F1 (Figure 5.23), a greater average F_f per cycle occurred during the break-in cycles, but after steady state was reached the average F_f was more constant. During break-in, the average F_f per cycle ranged from 60 to 65 kips, and during the steady state behavior it ranged from 55 to 58 kips. During Test F2 (Figure 5.27), the average F_f per cycle was between 55 and 58 kips. During Test F3 (Figure 5.31), the average F_f per cycle was between 59 and 66 kips. During Test F4 (Figure 5.35), the average F_f per cycle was 60 kips for the first cycle and increased to 95 kips for the last cycle. The rise is directly related to thermal effects which increased the bolt forces and F_f as the test progressed.

5.2.2 Friction Tests F5 to F8

The friction behavior during Tests F5 to F8 was similar to the friction behavior during Tests F1 to F4. A picture of the test specimen used for Tests F5 to F8 is

shown in Figure 5.36. Plots of the applied force versus the average cumulative travel and the applied force versus the average slip displacement for Tests F5, F6, F7, and F8 are shown in Figures 5.37, 5.41, 5.45, and 5.49, respectively.

During Test 5, the break-in of the unworn brass shims occurred during the cycles of increasing displacement amplitude in cycle set 1 (Figure 5.37(a)). The friction force (F_f) during break-in was higher than at steady state. For the first 4 cycles with a displacement amplitude of 1/8 inch, F_f at incipient slip was approximately 85 to 90 kips during the pull cycles and 90 to 95 kips during push cycles. For the remaining cycles during break-in, the values of F_f at incipient slip were approximately 95 kips and 100 kips during the pull and push cycles, respectively.

During the break-in cycles, F_f increased by 10 to 15 kips from the force at incipient slip, as shown in Figure 5.37(b). This behavior decreased as the steady state behavior was approached. For Test F6 (Figure 5.41), the values of F_f at incipient slip ranged from 90 kips for cycles with a displacement amplitude of 1/8 inch to 110 kips for cycles with a displacement amplitude of 7/16 inch. The increase in F_f as the displacement amplitude increased is attributed to the effects of outer plate deformation on the bolt force. The values of F_f at incipient slip for Test F7 (Figure 5.45) ranged from 100 kips for cycles with a displacement amplitude of 1/8 inch to 115 kips for cycles with a displacement amplitude of 7/16 inch. F_f in Test F7 is slightly higher than F_f of Tests F5 and F6 and maybe caused by the increase in

displacement rate in Test F7. During Test F8 (Figure 5.49), the values of F_f at incipient slip were 100 kips for the cycles with a displacement amplitude of 1/8 inch early in the test. F_f increased due to thermal effects, and the values of F_f at incipient slip were 130 kips at the end of the test.

Slip between the brass shims and the outer plates was observed in Test F5. Peaks in F_f when the bolts go into bearing occur after a slip displacement of 1/16 inch from incipient slip, as shown in Figure 5.37(b). Slip of the west shim was observed during Tests F6 and F7 as shown in Figures 5.41(b) and 5.45(b), respectively. During Test F8 (Figure 5.49(b), visual inspection for shim slip was not carried out for safety reasons. It is difficult to identify shim slip from variations in F_f.

The clamping bolt behavior for Tests F5, F6, F7 and F8 is shown in Figures 5.33, 5.42, 5.46, and 5.50, respectively. Similar to the previous tests, the bolt force decreases at the initiation of slip in the first cycle, apparently due to yielding of the asperities. The drop in bolt force was between 4 and 5 kips for each test. For Test F5 (Figure 5.33), a further decline in bolt force occurred during cycle set 1. This drop was probably due to the wearing of the brass shims during break-in, which was more severe in Test F5 (with a greater clamping bolt force) than in Test F1. The measured bolt force in cycle sets 2 and 3 of Test F5 are consistent with those of Test F6, as shown in Figure 5.42. For Test F7 (Figure 5.46), the changes the force in bolts 1 and 3 are similar to those of the previous tests. Bolt 2 had a consistent apparent

increase in bolt force during the test due to thermal effects. As noted earlier, some of this apparent increase in bolt force is due to thermal strain in the bolt. During Test F8 (Figure 5.50), all three bolts were influenced by thermal effects. The increase in force was greater in bolts 1 and 2 than in bolt 3. The variations in bolt force due to the effects of outer plate deformation were also present during each test.

The bolt force versus the average slip displacement for Tests F5, F6, F7, and F8 are shown in Figures 5.34, 5.43, 5.47, and 5.51. The concave up shape reflects the increase in bolt force as slip displacement amplitude increases. The minimum bolt forces during Tests F5 and F6 (Figures 5.34 and 5.43, respectively) were approximately 26 to 30 kips. The maximum bolt forces were 35 to 41 kips. The bolt force was repeatable during the test, as is shown by the overlapping of cycle sets 1 and 2. During Test F7 (Figure 5.47), the minimum forces in bolts 1.and 3 were 30 kips. The minimum force in bolt 2 was 32 kips. The behavior of bolt 1 was similar to the behavior in Tests F5 and F6. The force in bolt 2 increased in cycle set 2 due to thermal effects. The force in bolt 3 was between 44 and 45 kips for a displacement amplitude of 7/16 inch. During Test F8, the constant rise in the forces in each bolt due to thermal effects in each bolt are shown in Figure 5.51. The increase in force is nearly 50 kips in bolts 1 and 2, and 55 kips for bolt 3. The minimum force for each bolt was between 32 and 33 kips.

The average friction force (average F_f) per cycle for Tests F5 to F8 was determined in the same manner as previously discussed for Tests F1 to F4. The average F_f per cycle for Tests F5, F6, F7, and F8 is shown in Figures 5.40, 5.44, 5.48, and 5.52, respectively. The accumulated energy dissipation for each test is shown in Table 5.2.

During Test F5 (Figure 5.40), the average F_f per cycle for the first cycle was 76 kips, during the break-in cycles the average F_f per cycle was between 81 and 95 kips, and during the steady state cycles the average F_f per cycle was between 80 and 86 kips. During Test F6 (Figure 5.44), the average F_f per cycle ranged from 85 to 91 kips. The average F_f per cycle during Test F6 ranged from 85 to 96 kips. During Test F7 (Figure 5.48), the average F_f per cycle ranged from 91 to 108 kips. During Test F8 (Figure 5.52), the average F_f per cycle ranged from 100 kips to 130 kips, with the rise in the average F_f per cycle resulting from thermal effects.

5.2.3 Coefficient of Friction

The coefficient of friction was determined at various points of static and kinetic friction behavior for each test using Coulomb friction theory (i.e., $\mu \cdot N$), where the normal force (N) is assumed to be equal to the sum of the bolt forces. This assumption introduces errors for Tests F4 and F8 where a significant rise in temperature occurred. The errors arise because the bolt gauges used to measure bolt force cannot differentiate between mechanical strain and thermal strain, and

some of the apparent increase in bolt force due to may actually be caused by thermal strain in the bolts.

The static coefficients of friction (μ_s) were determined at the point of incipient slip for the pull and push cycles. The kinetic coefficients of friction (μ_k) were determined at a slip displacement of 0 inches. The displacement rate during each cycle of the test was assumed to be maximum at this point, and the minimum μ_k could be determined. The results for Tests F1 through F8 are shown in Figures 5.53 through 5.60, respectively.

For Test F1 (Figure 5.53), the static coefficient of friction for the unworn shims was 0.43 and 0.37 for the initial pull and push cycles, respectively. The remaining upper and lower values of the static coefficient of friction (μ_s) were 0.5 and 0.44, respectively. For Test F2 (Figure 5.54), similar results were obtained, except for three values of μ_s equaling 0.51. For Test F3 (Figure 5.55), the results were similar to Tests F1 and F2 for cycle set 1, but a decline in μ_s occurred during cycle set 2. The μ_s values for cycle set 2 ranged from 0.4 to 0.48 with one value at 0.37. The results for Test F4 (Figure 5.56) varied significantly during the test. The bulk of the μ_s values ranged from 0.45 to 0.52. Several values ranged from 0.31 to 0.44. For Test F5 (Figure 5.57), the results were similar to Test F2. μ_s was between 0.27 and 0.29 during the first cycle, and 0.45 to 0.46 for the second cycle. A decline in μ_s from 0.52 to 0.44 occurred during the test. This decline may have been caused by abrasive

wear at the tribo surfaces, which produced a smoother tribo surface, which can result in a decrease in the μ. For Tests F6 and F7 (Figures 5.58 and 5.59, respectively) the majority of μ_s values ranged from 0.5 to 0.42. The minimum values of μ_s occurred at the maximum displacement amplitude. For Test F8 (Figure 5.60), μ_s ranged from 0.4 to 0.55 except for four individual values of 0.4, 0.36, 0.34, and 0.31.

The kinetic coefficient of friction (μ_k) for Tests F1 and F2 is shown in Figures 5.53 and 5.54, respectively. At steady state, μ_k for both tests ranged from 0.47 to 0.40, beginning at the upper value and slowly declining. During the break-in cycles for Test F1, μ_k declined from 0.53 to 0.47. For Tests F3 and F4 (Figure 5.55 and 5.56 respectively), μ_k varied from 0.5 to 0.45 throughout most of the test. μ_k dropped at the end of Test F3 to 0.42, and rose at the end of Test F4 to 0.54. For Test F5 (Figure 5.57(b)), μ_k was 0.44 and 0.37 during the first pull and push cycle, respectively. During break-in, μ_k rose to 0.5. At steady state, μ_k varied between 0.5 and 0.43, decreasing as the test progressed. μ_k for Tests F6 and F7 (Figures 5.58 and 5.59, respectively) ranged from 0.49 to 0.41. μ_k was relatively repeatable for both tests. Test F8 (Figure 5.60) displayed varied results similar to F4. The majority of the μ_k values ranged from 0.5 to 0.45, with maximum and minimum values of 0.54 and 0.42, respectively.

Throughout the test, the majority of the μ_s values ranged from 0.45 to 0.5 after

break-in had occurred Before break-in, the initial values were between 0.27 and 0.37. The majority of the μ_k values ranged from 0.43 to 0.5. During a seismic event the structure is under continuous motion, thus the kinetic coefficient is assumed to be more applicable. Both the static and kinetic coefficients of friction have a majority of values in the range between 0.45 and 0.5, and therefore the variation between the two coefficients of friction is small for the brass-steel tribo surfaces.

5.2.4 Friction Test F9

The purpose of Test F9 was to determine the durability of the brass shims under continuous sinusoidal displacement loading at a dynamic displacement rate. The total cumulative travel expected was 218 inches ($\cong$ 18 feet). The behavior of the clamping bolts was similar to that observed during Tests F4 and F8, until an average cumulative travel of approximately 130 to 140 inches, as shown in Figure 5.62. As shown in Figure 5.62(b), the force in bolt 2 began to decrease at this point, and then increased near the end of the test. At a average cumulative travel of 150 inches, the force in bolt 1 began to decrease and increase, repeatedly (Figure 5.62(a)). The behavior of bolt 3 was similar to bolt 1, with decreases and increases in the bolt force beginning at a travel of approximately 185 inches (Figure 5.62(c)). Thermal effects were noticeable in the behavior of bolts 1 and 2, but the force in bolt 3 remained relatively constant until it began to decrease and increase.

During Test F9, the values of the friction force (F_f) at incipient slip were 65 kips in the pull direction and 70 in the push during the first cycle, as shown in Figure 5.61(a). After this, F_f was relatively constant in both directions varying between 65 and 70 kips. The thermal effect became noticeable after a travel of approximately 75 inches. Slipping of the shims occurred throughout the test, as shown by the hump in the hysteresis loops in Figure 5.61(b).

After Test F9 was completed, and the test specimen was allowed to cool, the brass shims were stuck to the upper T-stub as shown in Figure 5.63. After removal of the brass shims, a melted appearance was present in the region adjacent to the previously described irregularity in thickness of the T-stub. Melting of the brass shim tribo surfaces is a result of high temperature abrasive wear as discussed in Section 5.1.1. During cooling, after the test was completed, the melted brass tribo surfaces fused to the steel tribo surfaces. The response of the specimen was not hindered by the partial melting of the brass shim tribo surfaces. Furthermore, seismic loading of a typical building is unlikely to generate a displacement history on a friction connection component as demanding as the displacement history used in the Test F9.

Table 5.1. Double Plate Friction Test Matrix

Test	Tribo Surface Area	Parameter	Initial Brass Shim Condition	Clamping Bolt Preload (kips)	μ (Assumed)*	Friction Force [(μ•N)•2**] (kips)	Displacement Rate (in/sec)
F1	7.25x14"	μ	Unworn	23	0.3	41.4	0.00625
F2	7.25x14"	Repeatability	Worn	23	0.3	41.4	0.00625
F3	7.25x14"	Rate Effects	Worn	23	0.3	41.4	0.0125
F4	7.25x14"	Dynamic	Worn	23	0.3	41.4	0.5
F5	7.25x14"	μ	Unworn	35	0.3	63	0.00625
F6	7.25x14"	Repeatability	Worn	35	0.3	63	0.00625
F7	7.25x14"	Rate Effects	Worn	35	0.3	63	0.0125
F8	7.25x14"	Dynamic	Worn	35	0.3	63	0.5
F9	7.25x14"	Durability	Worn	23	0.3	41.4	0.5

* based on Grigorian and Popov (1994)

** $N = \Sigma P_{bolt}$ and 2 tribo surfaces

Table 5.2. Accumulated Energy Dissipation during Double Angle Friction Tests

Test	Accumulated Energy Dissipation (kips•in)
F1	3662
F2	3667
F3	3981
F4	4516
F5	4602
F6	4813
F7	5013
F8	5245

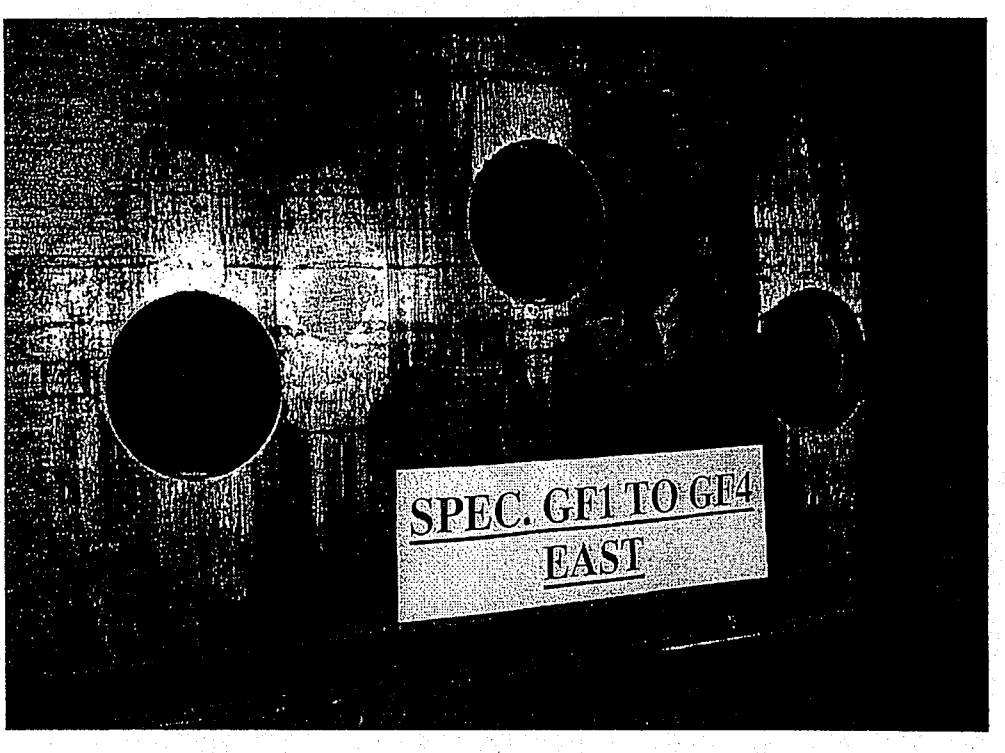

Figure 5.1. Tests F1 to F4 - East Face of T-stub Web

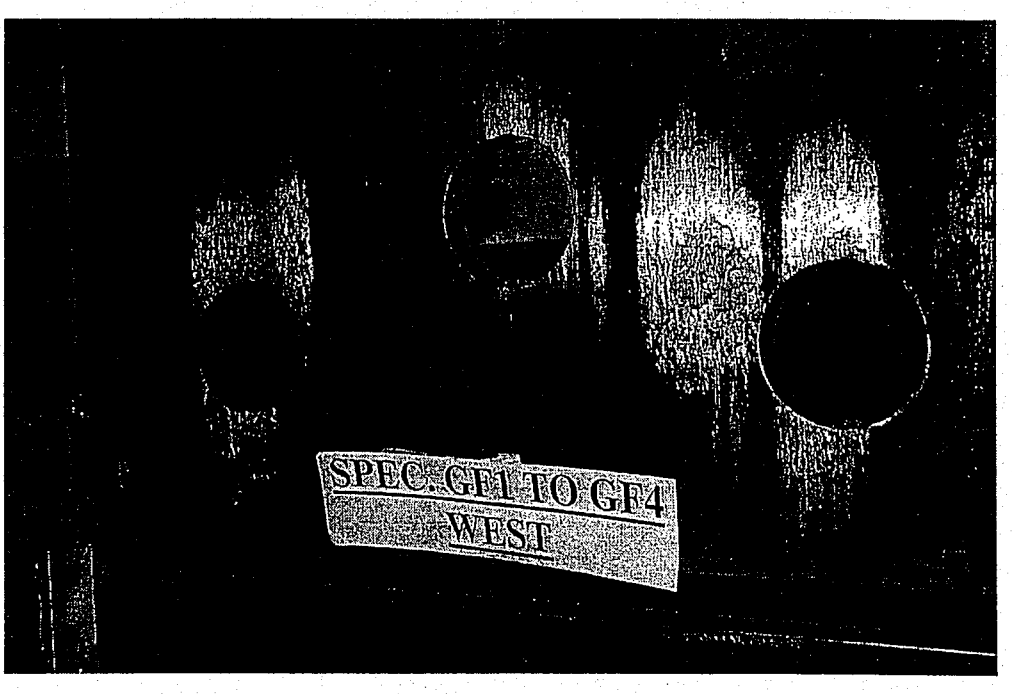

Figure 5.2. Tests F1 to F4: West Face of T-stub Web

Figure 5.1. Tests F1 to F4 - East Face of T-stub Web

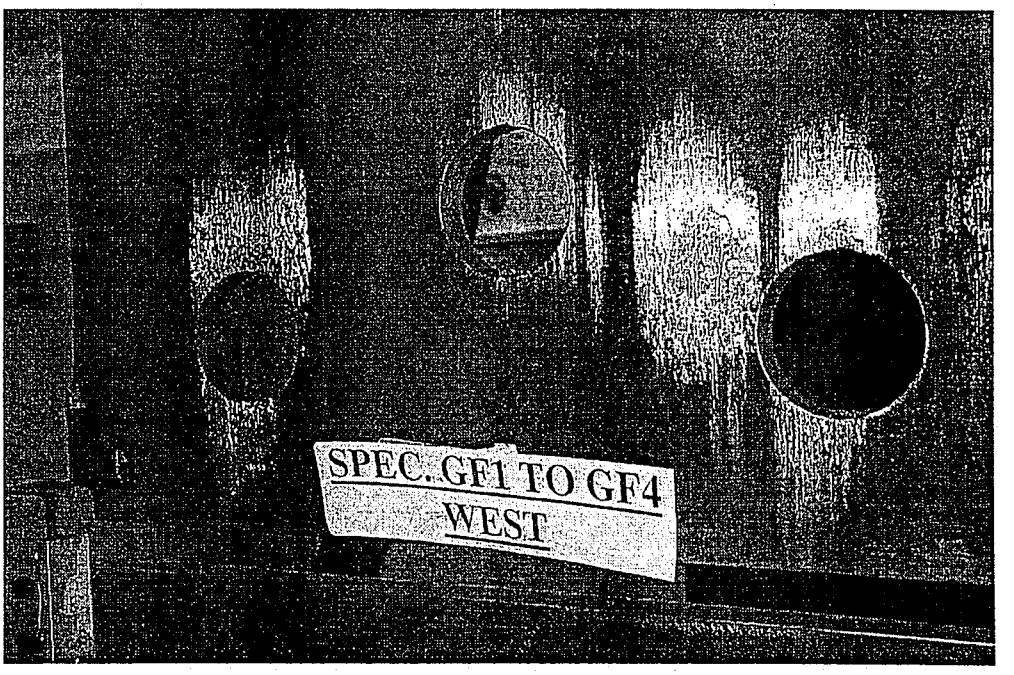

Figure 5.2. Tests F1 to F4: West Face of T-stub Web

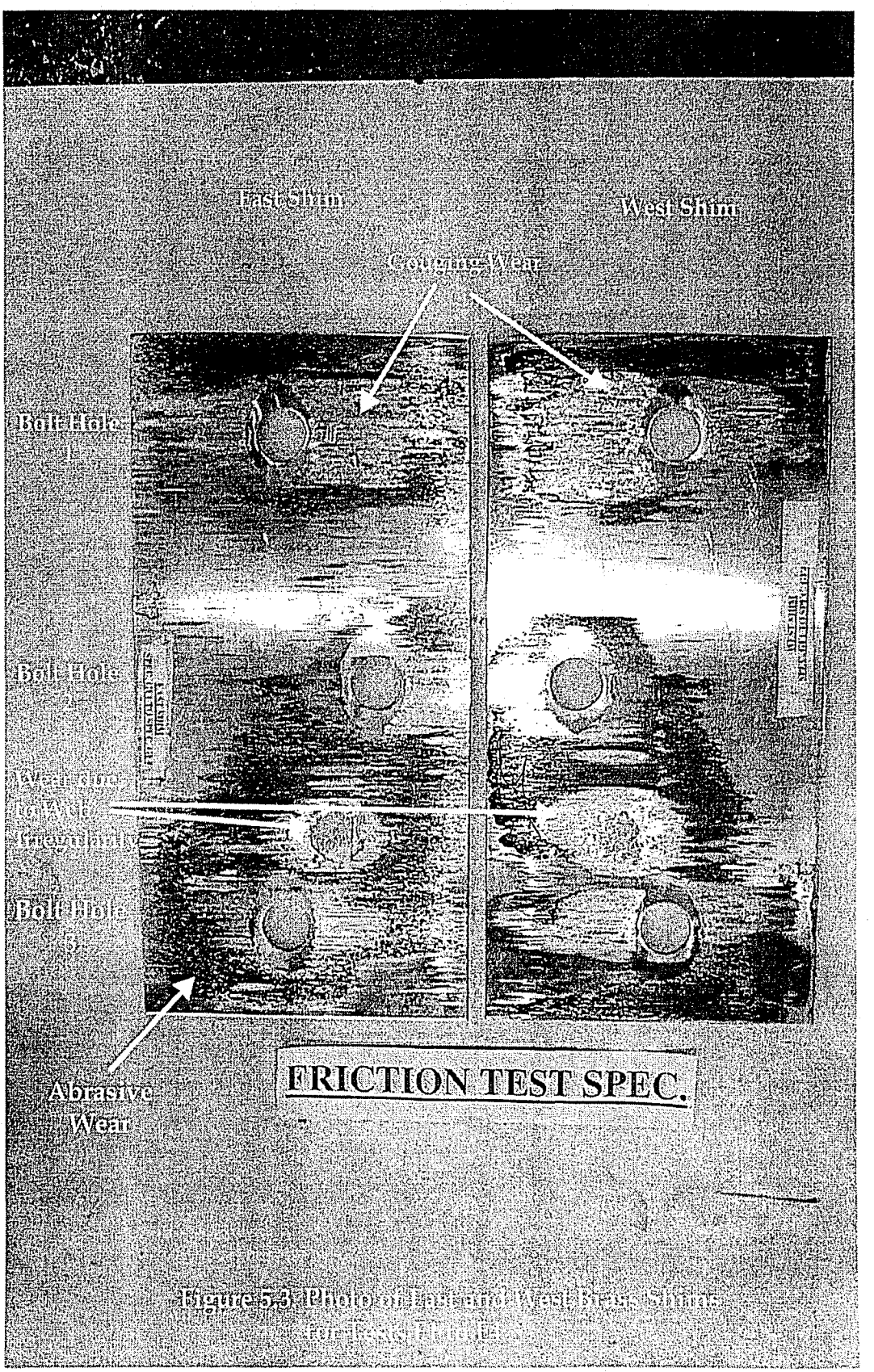

Figure 5.3 Photo of East and West Shims

INTENTIONAL SECOND EXPOSURE

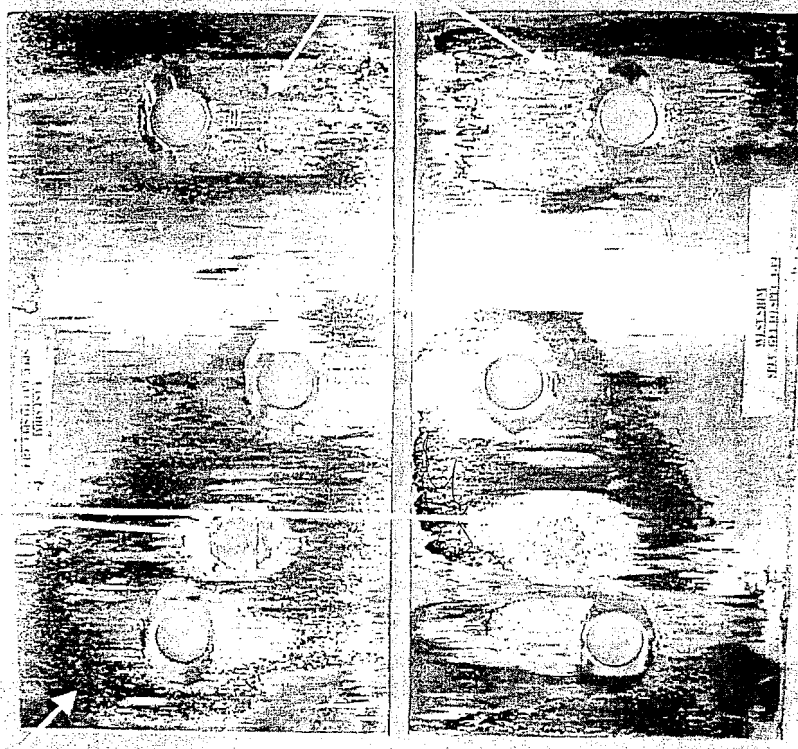

FRICTION TEST SPEC.

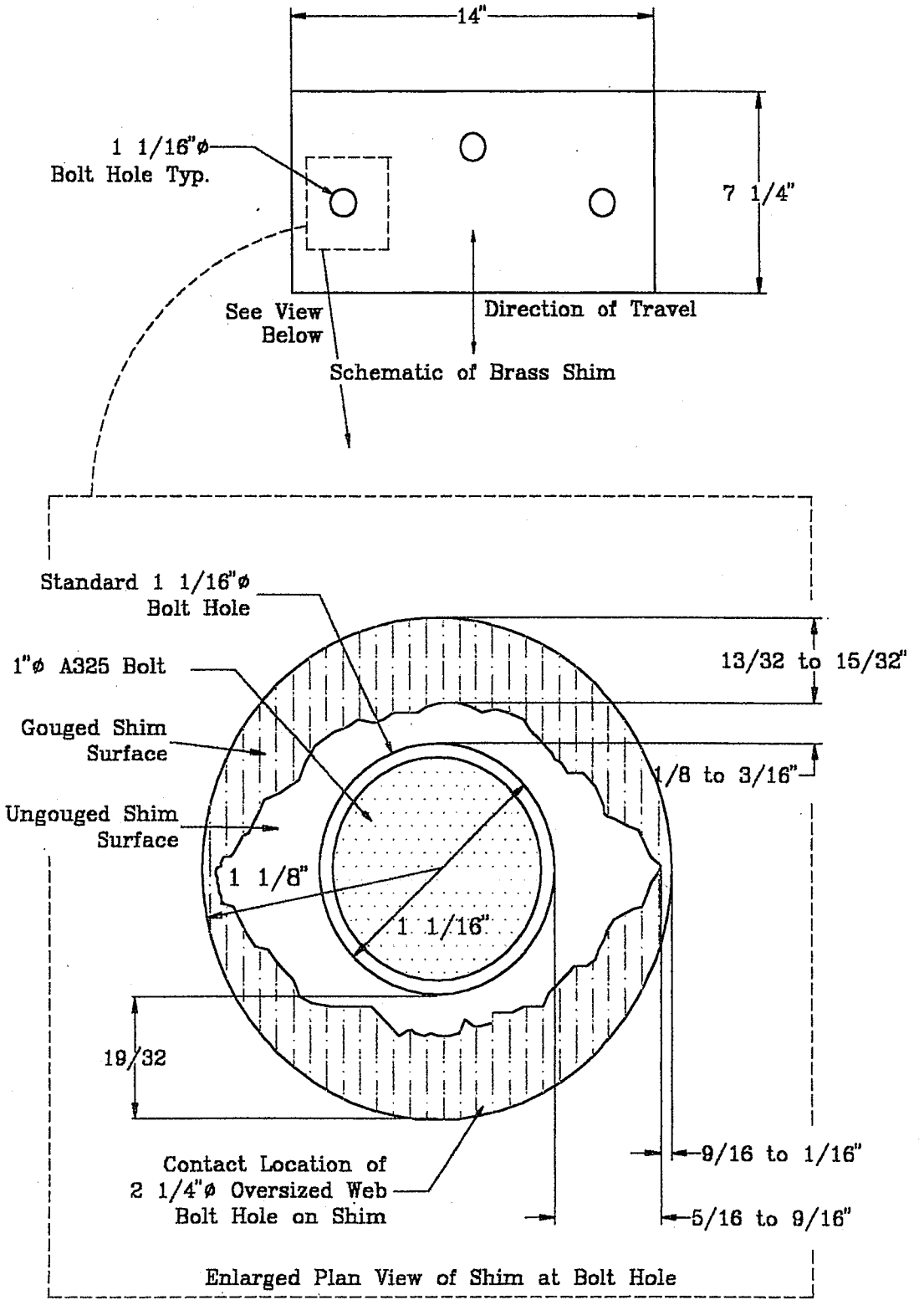

Figure 5.4. Gouging of Brass Shim

Figure 5.5. Photo of East and West Brass Shims for Tests F5 to F8

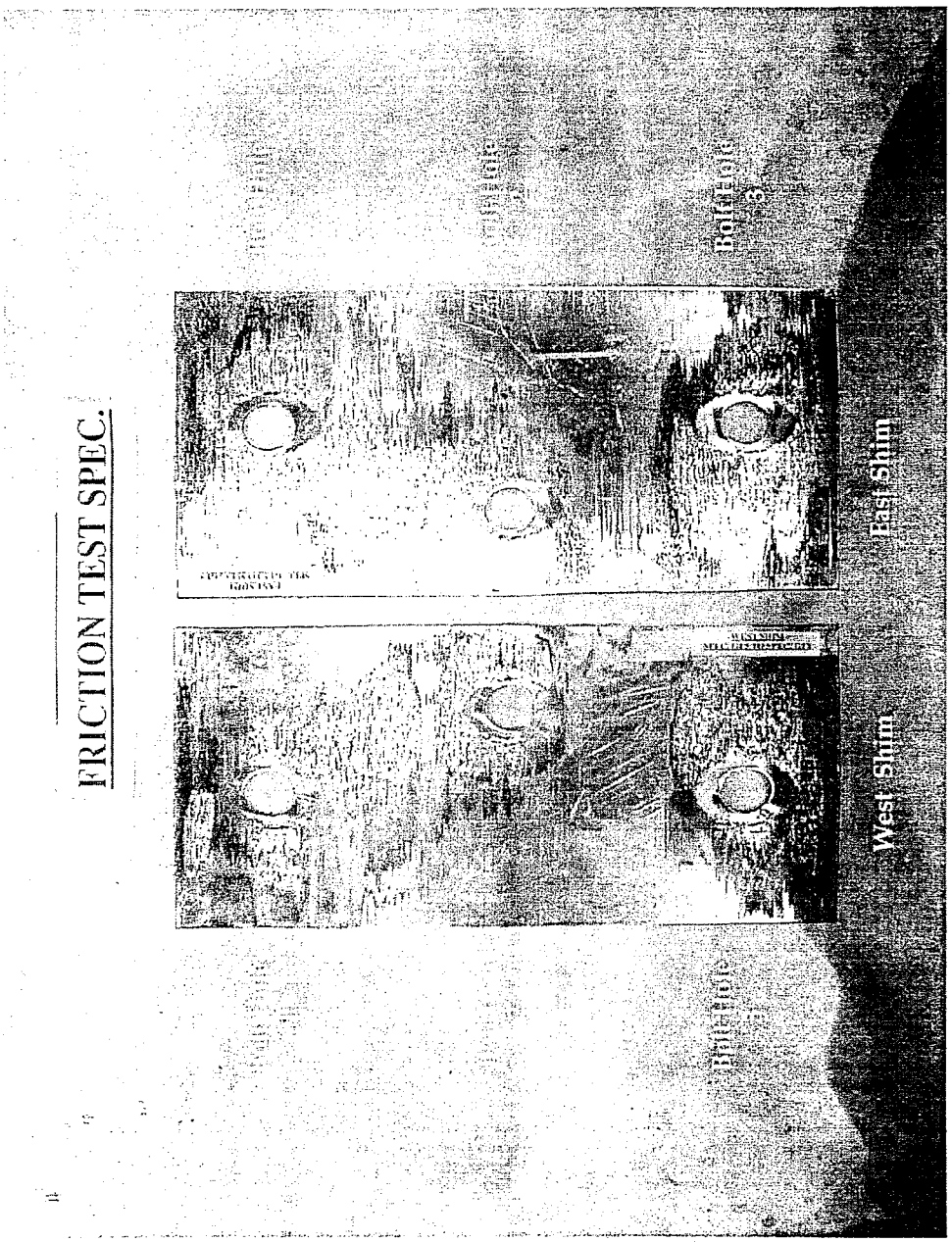

Figure 5.5. Photo of East and West Brass Shims for Tests F5 to F8

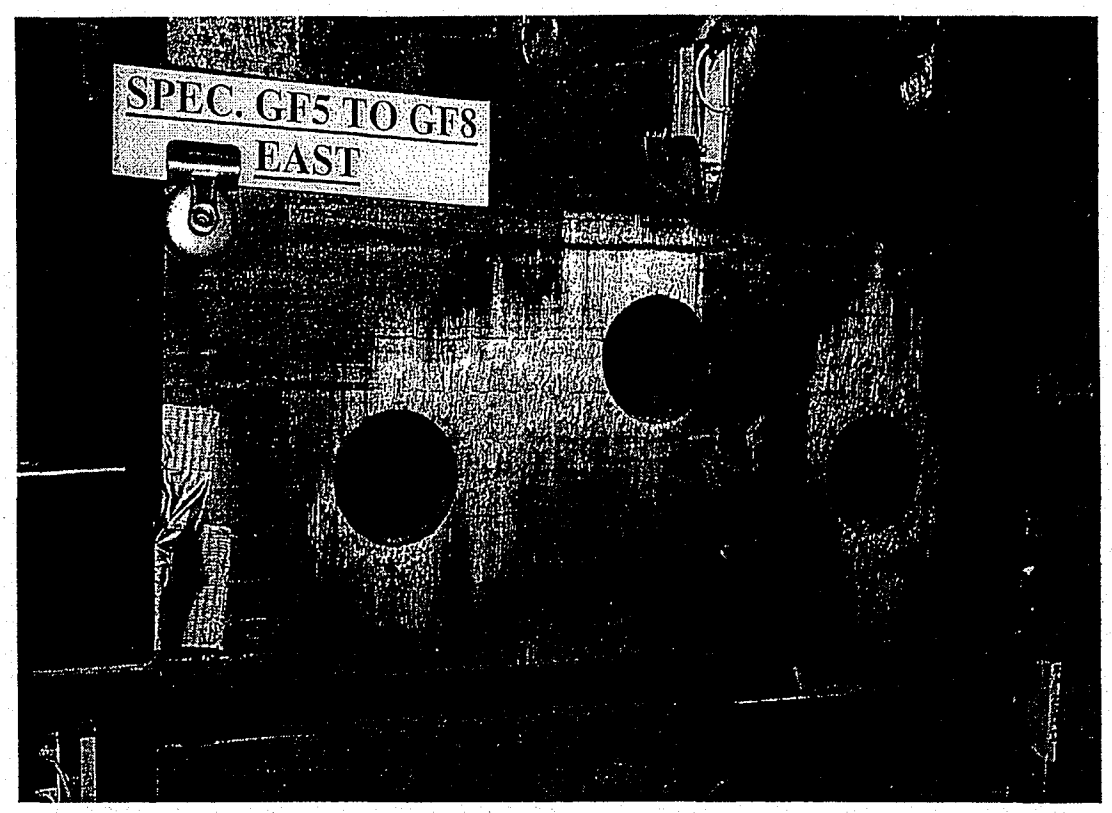

Figure 5.6. Tests F5 to F8 - East Face of T-stub Web

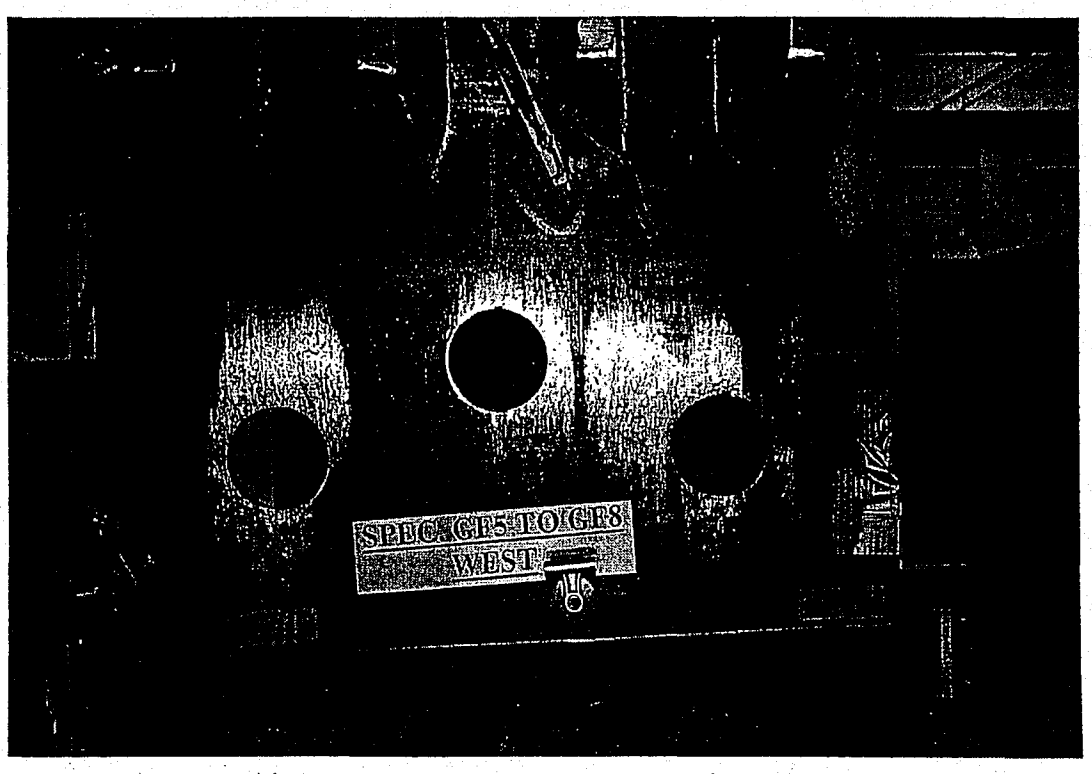

Figure 5.7. Tests F5 to F8 - West Face of T-stub Web

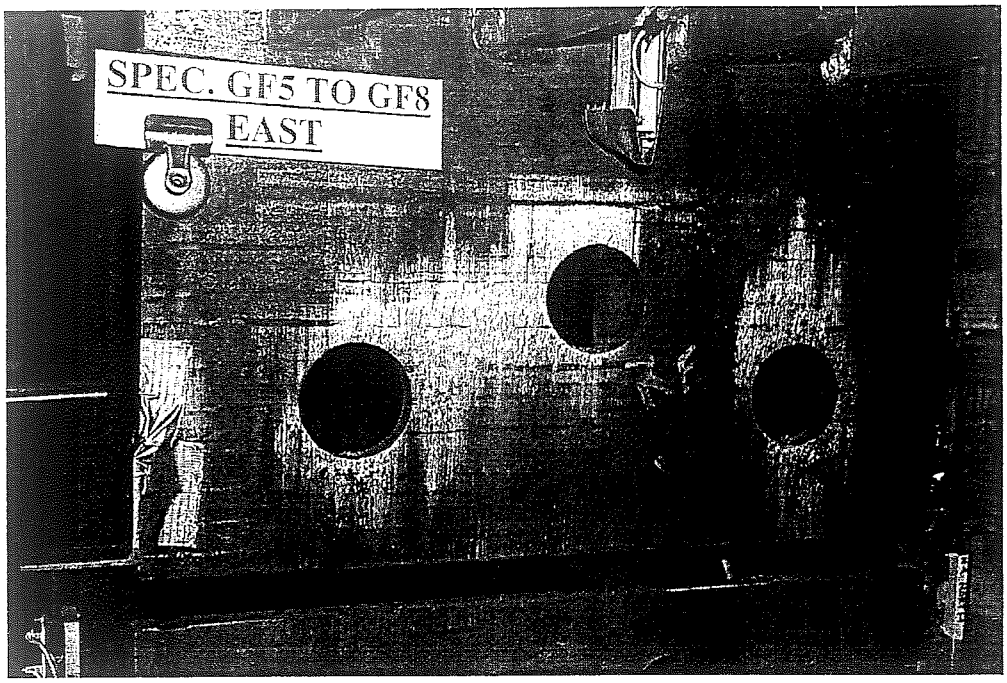

Figure 5.6. Tests F5 to F8 - East Face of T-stub Web

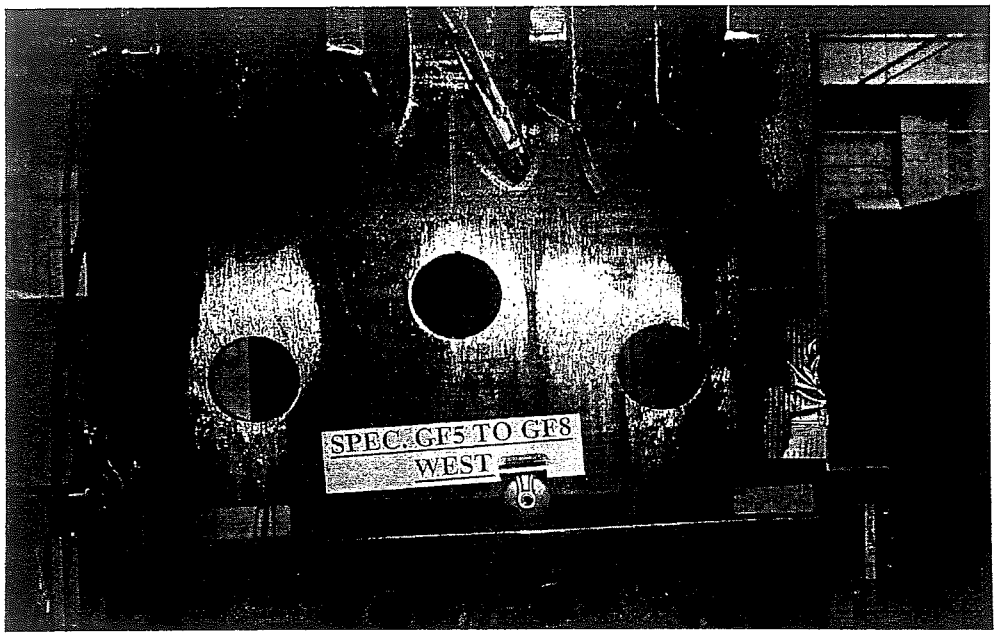

Figure 5.7. Tests F5 to F8 - West Face of T-stub Web

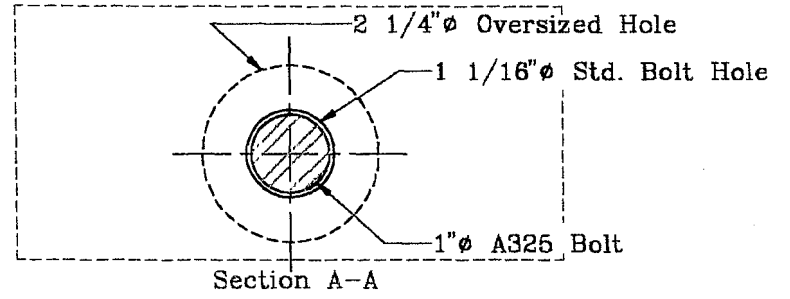

Figure 5.8. Undeformed Clamping Bolt Section (Bolt Not Tightened)

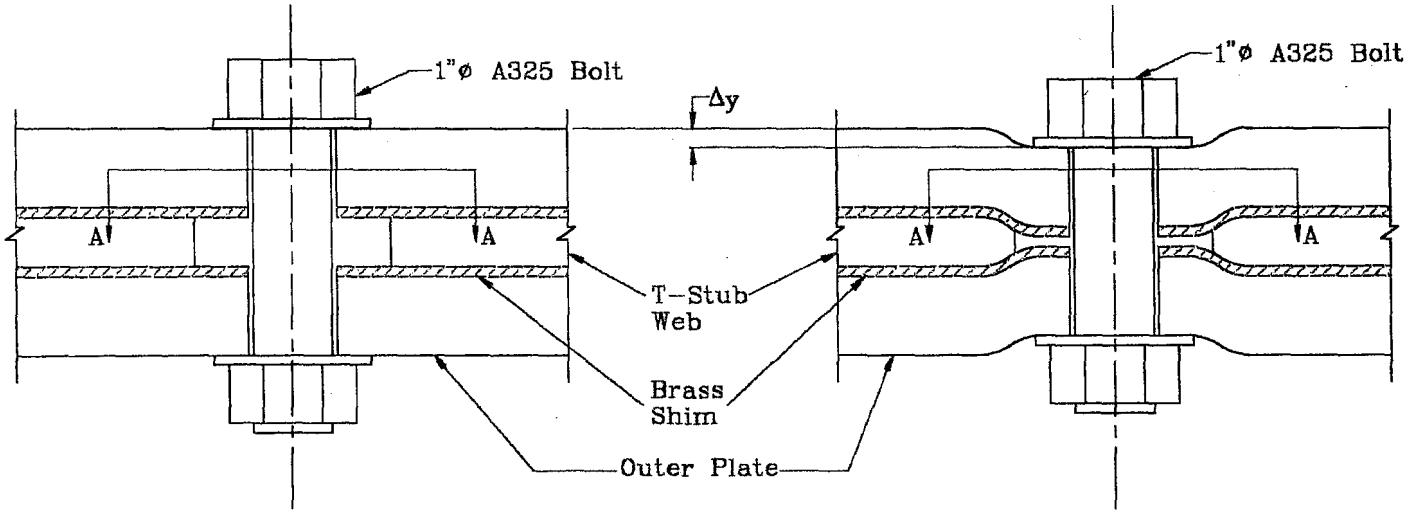

Figure 5.9. Deformed Clamping Bolt Section (Bolt Tightened)

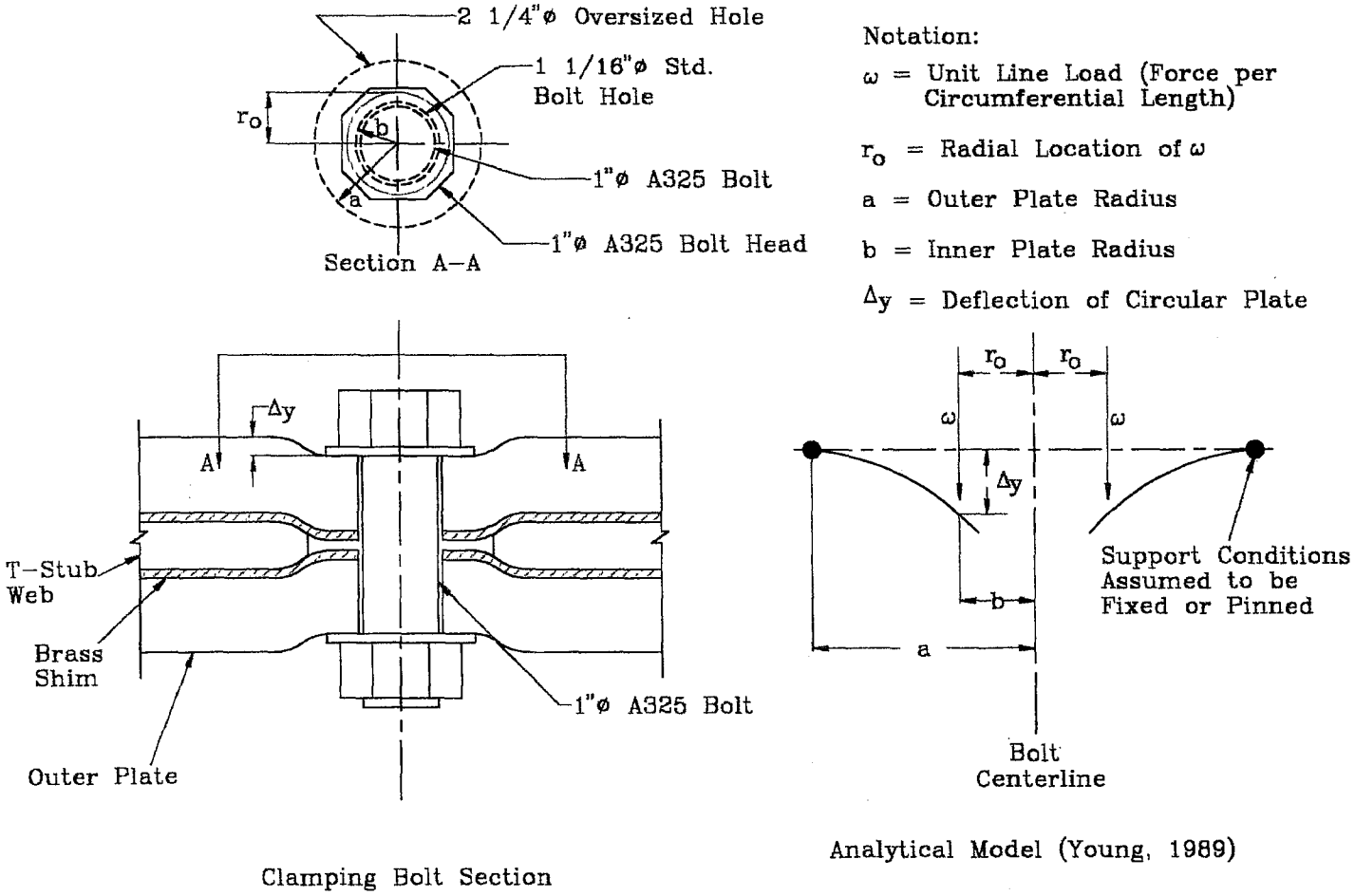

Figure 5.10. Analytical Model

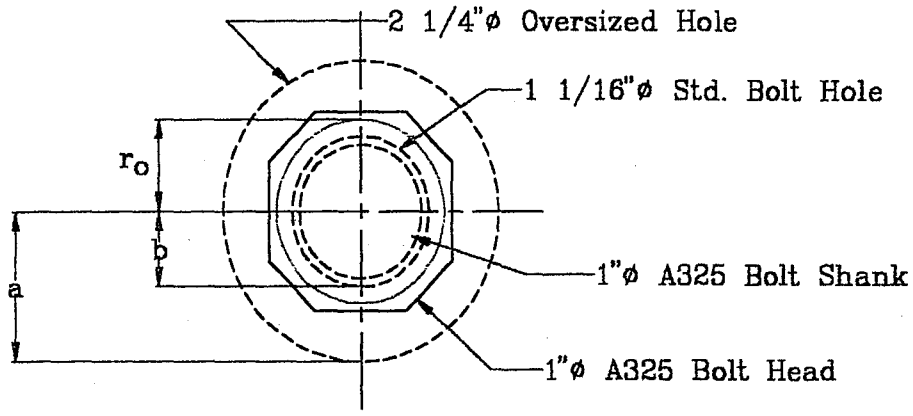

Plan

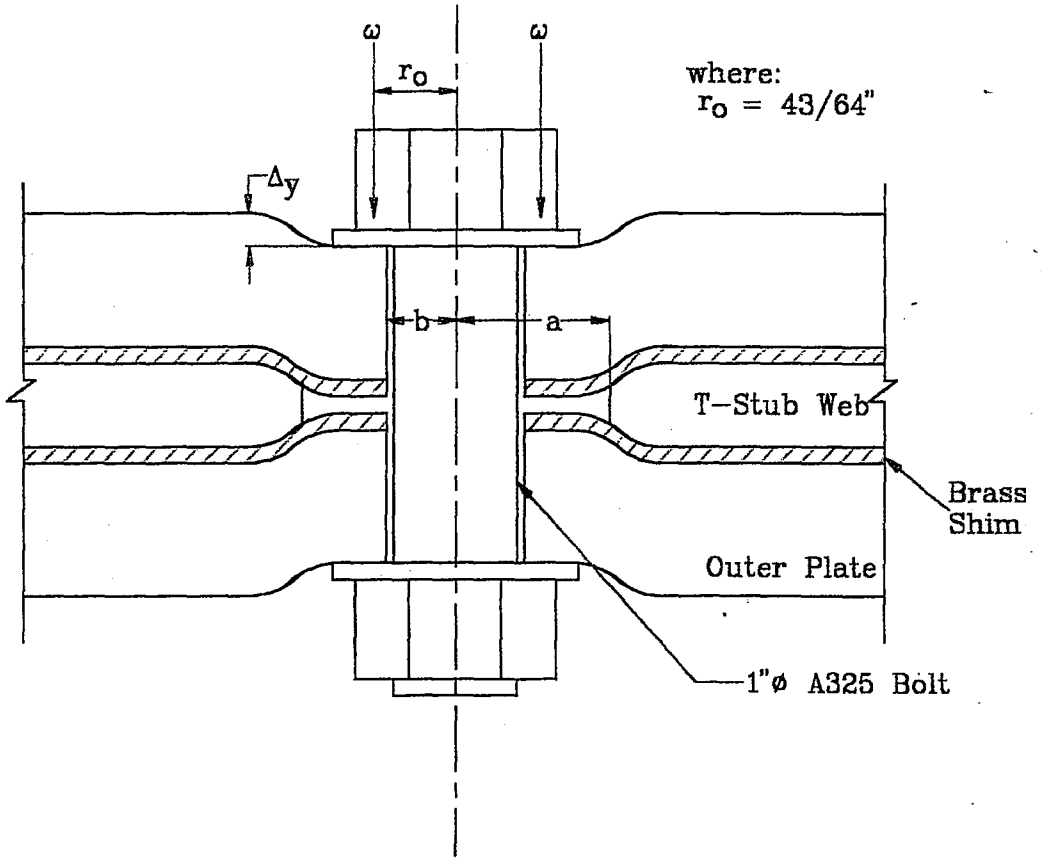

Clamping Bolt Section

Figure 5.11. Outer Plate Deformation Details of Assumptions

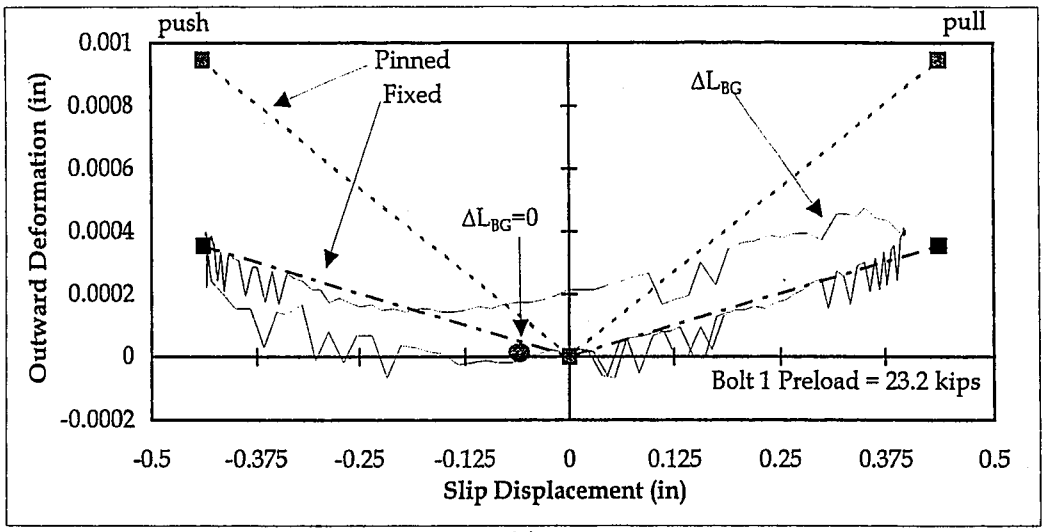

(a)

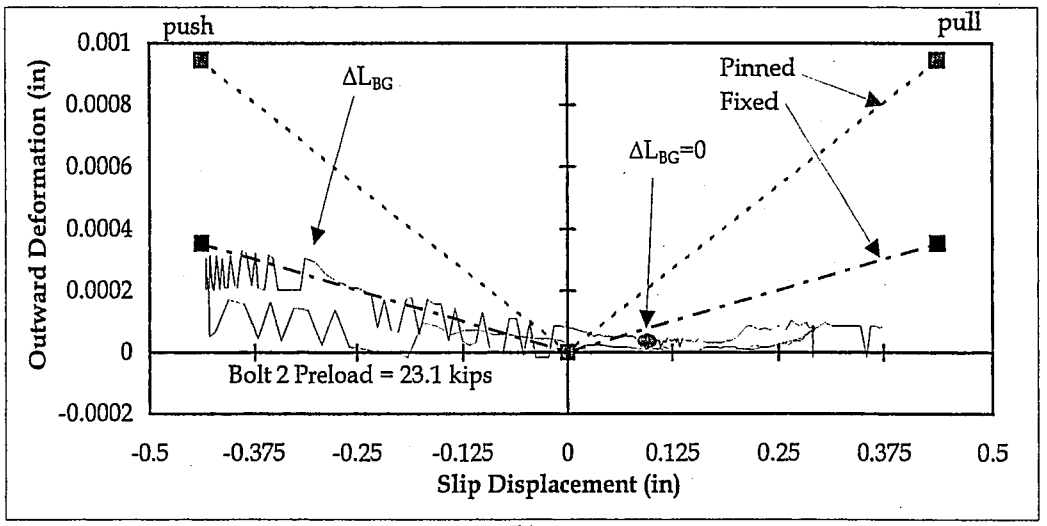

(b)

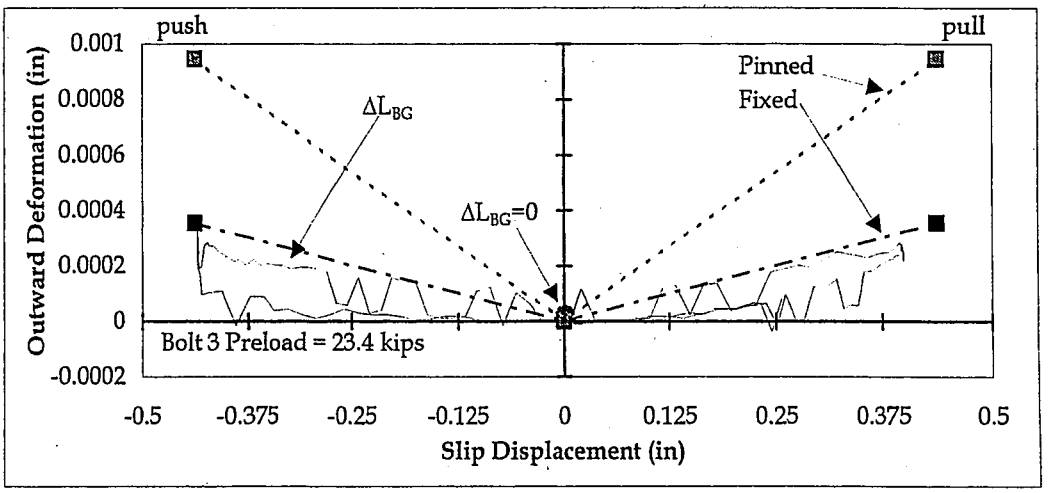

(c)

Figure 5.12. Estimates of Outer Plate Deformation: (a), (b), and (c) Bolts 1, 2, and 3 for Test F1; (d), (e), and (f) Bolts 1, 2, and 3 for Test F5

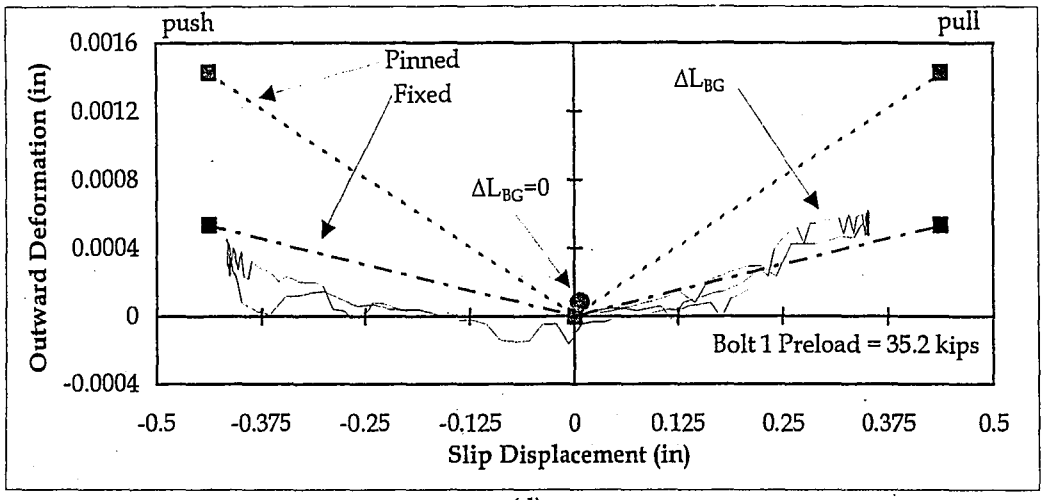

(d)

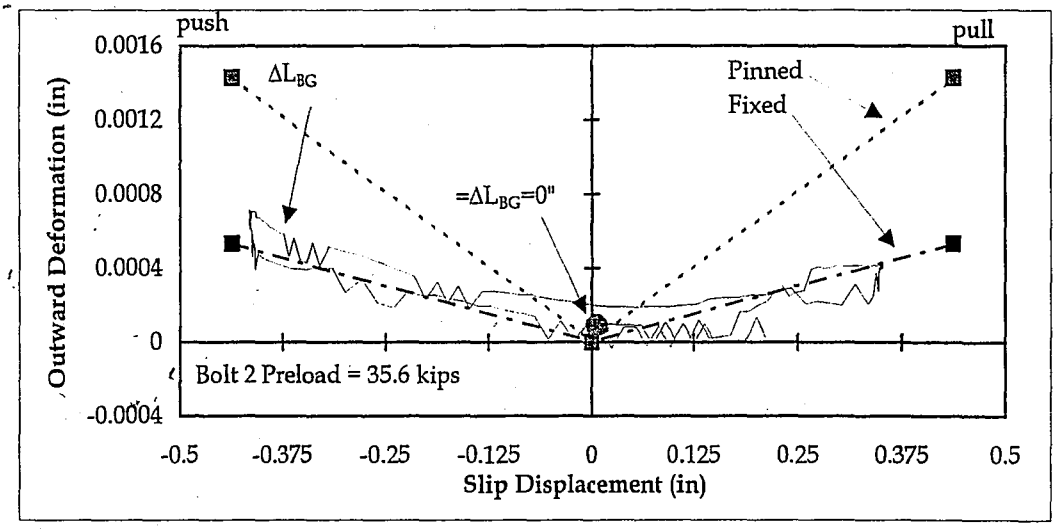

(e)

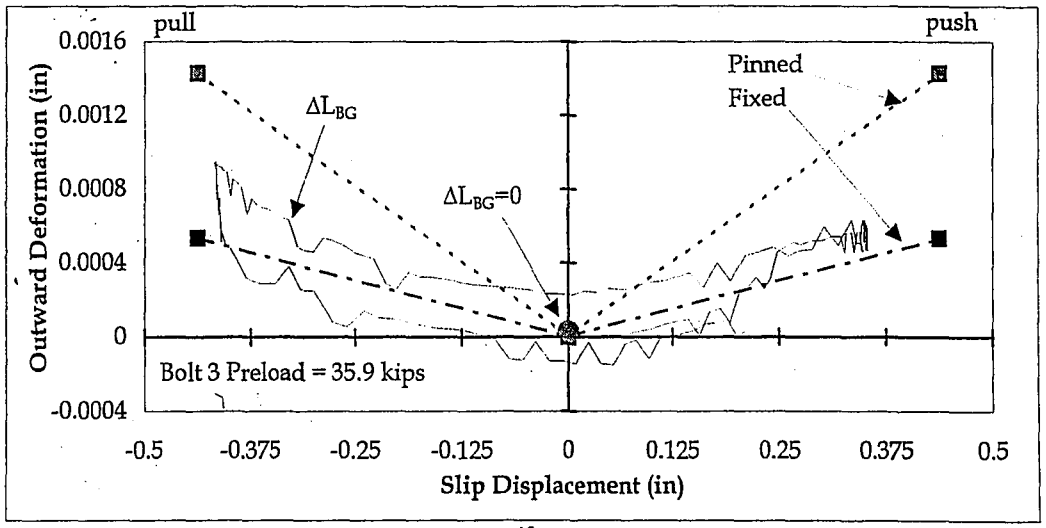

(f)

Figure 5.12(continued). Estimates of Outer Plate Deformation: (a), (b), and (c) Bolts 1, 2, and 3 for Test F1; and (d), (e), and (f) Bolts 1, 2, and 3 for Tests F5

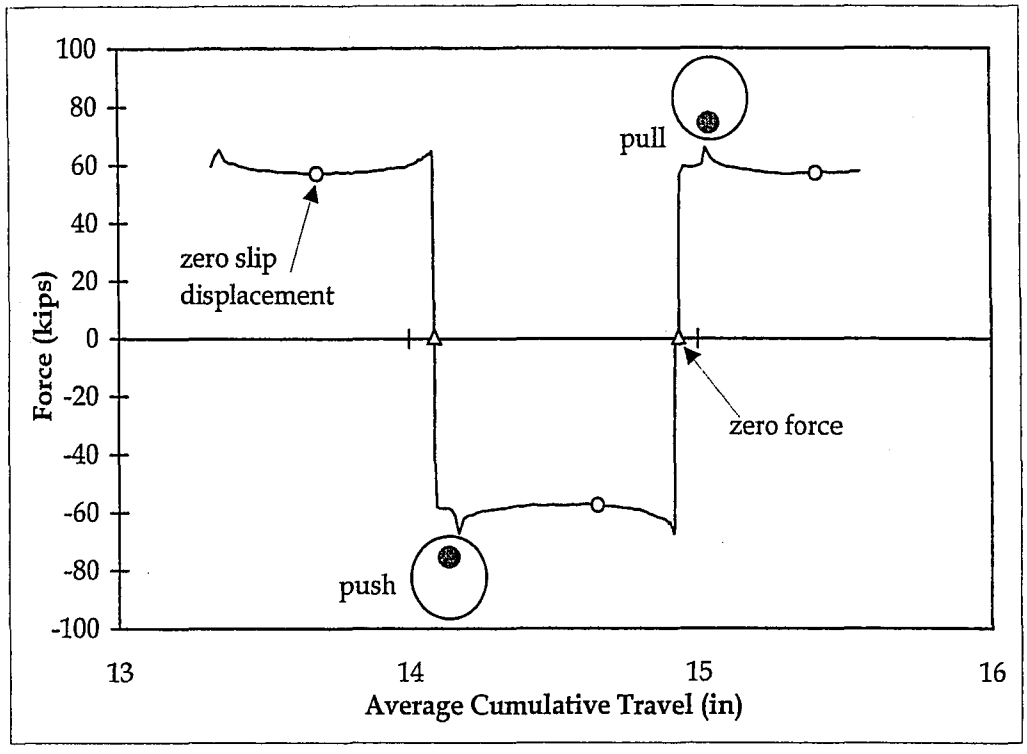

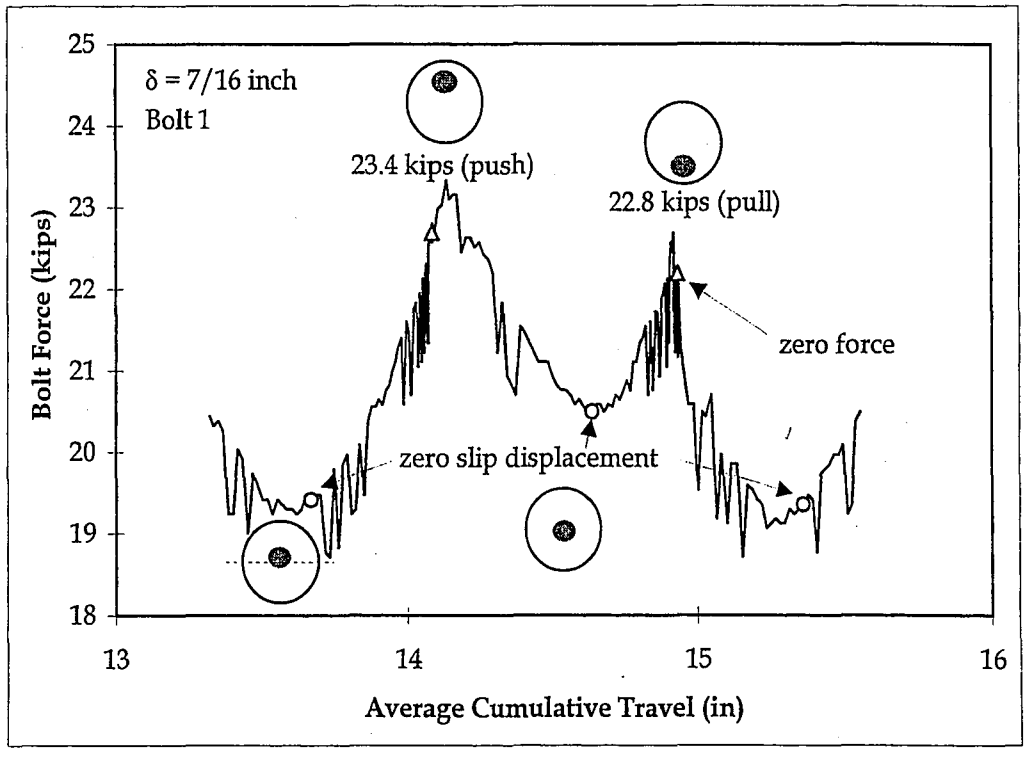

Figure 5.13. Variation in Bolt Force for Test F1: (a) Bolt 1

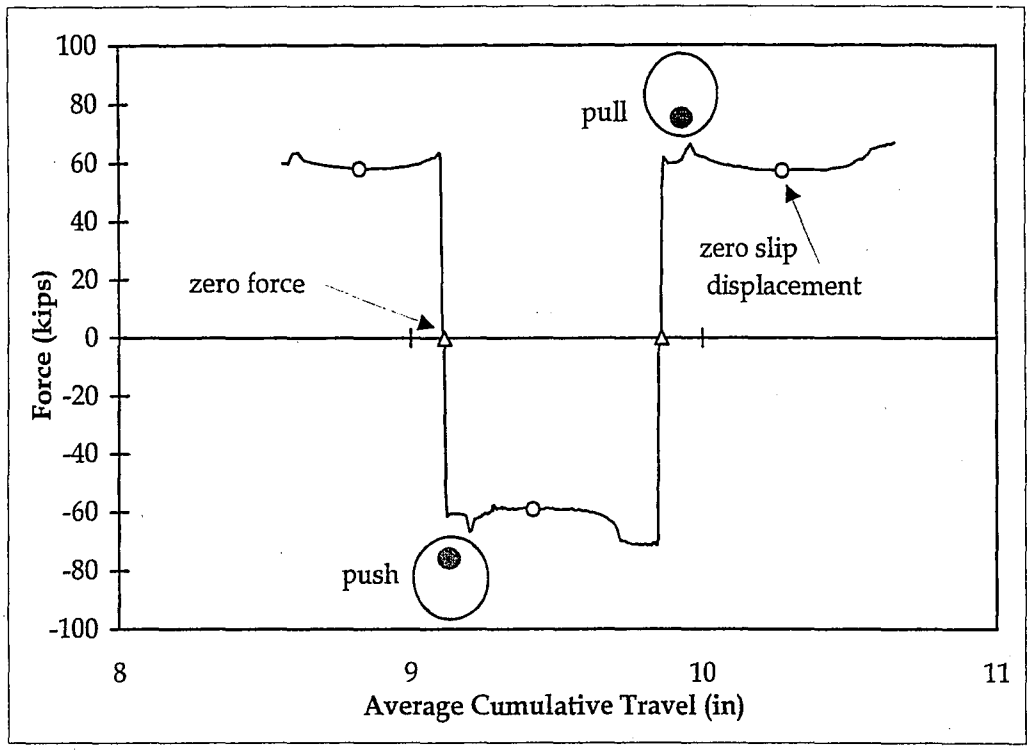

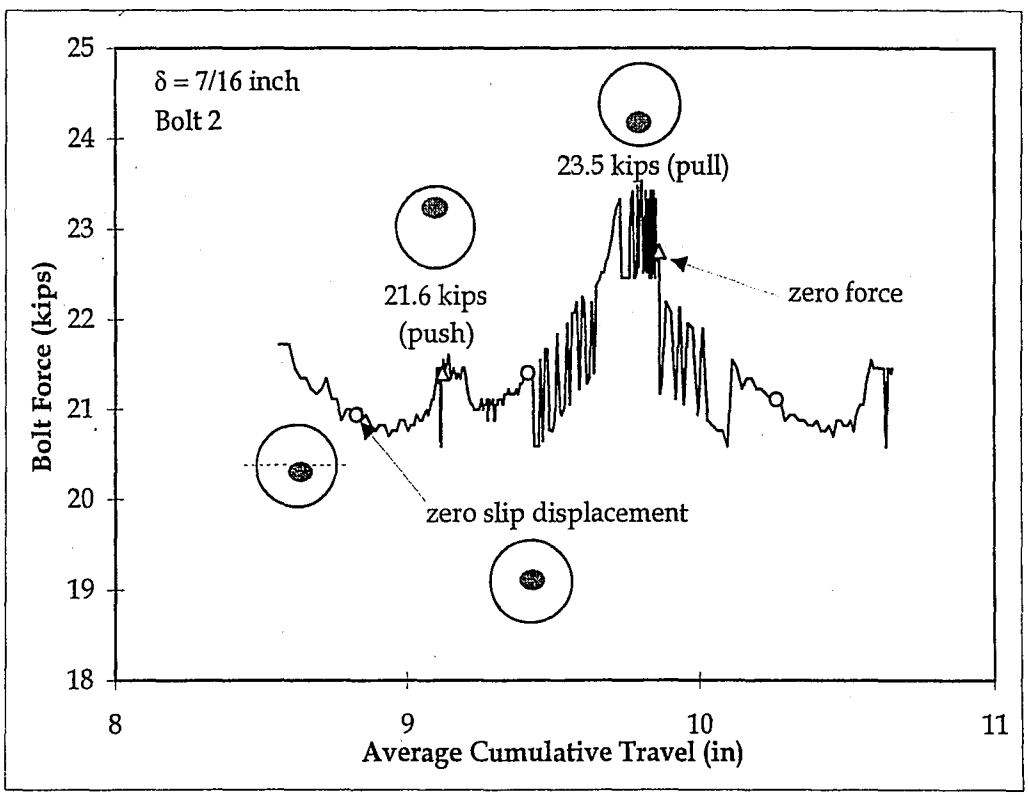

Figure 5.13(continued). Variation in Bolt Force for Test F1: (b) Bolt 2

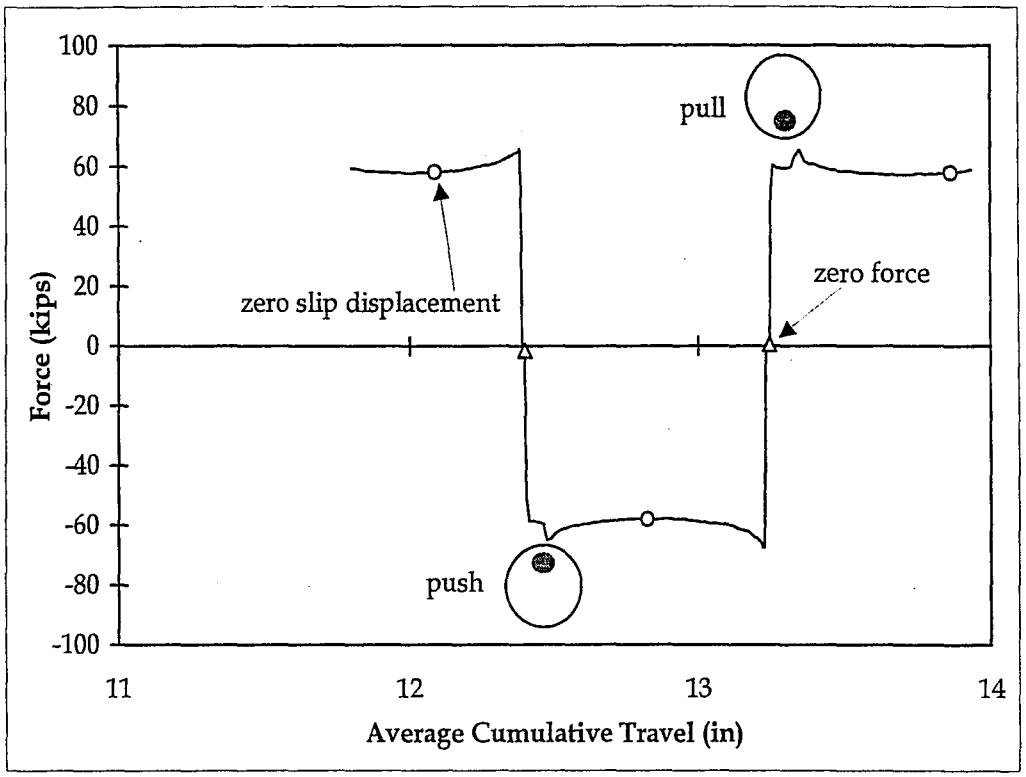

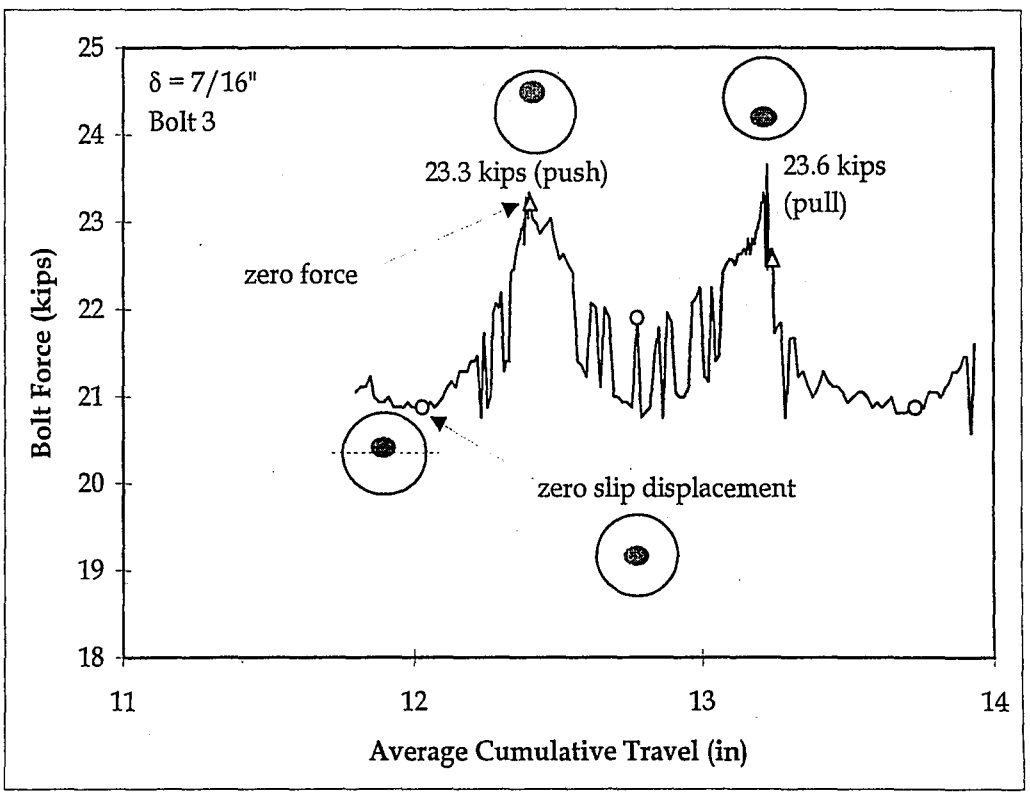

Figure 5.13(continued). Variation in Bolt Force for Test F1: (c) Bolt 3

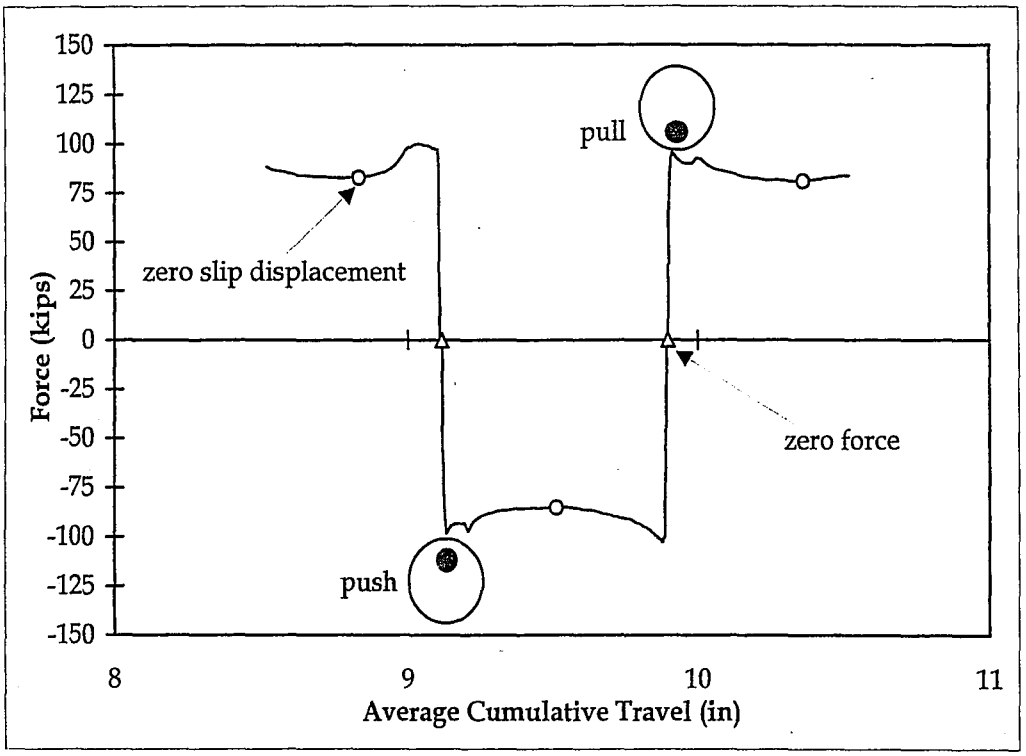

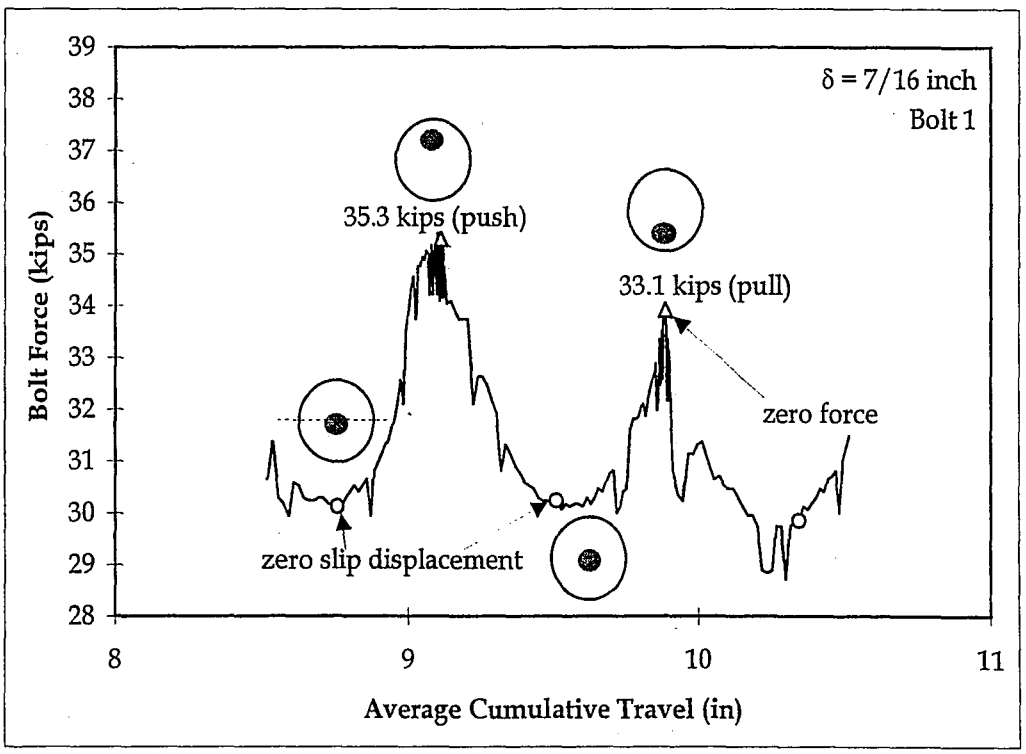

Figure 5.14. Variation in Bolt Force for Test F5: (a) Bolt 1

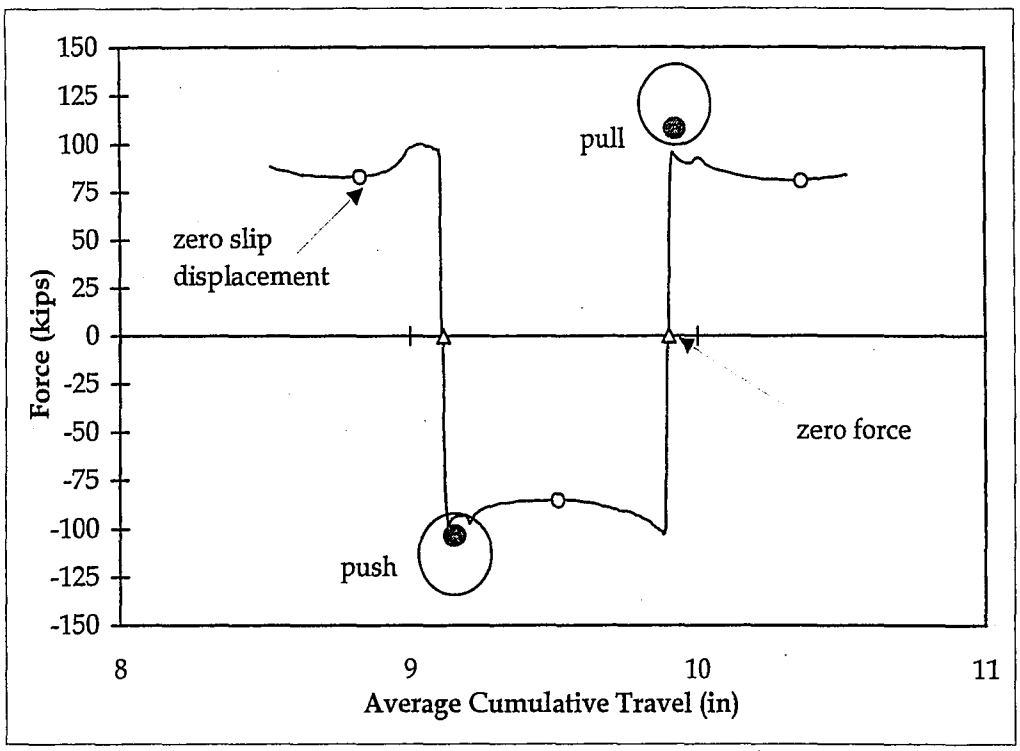

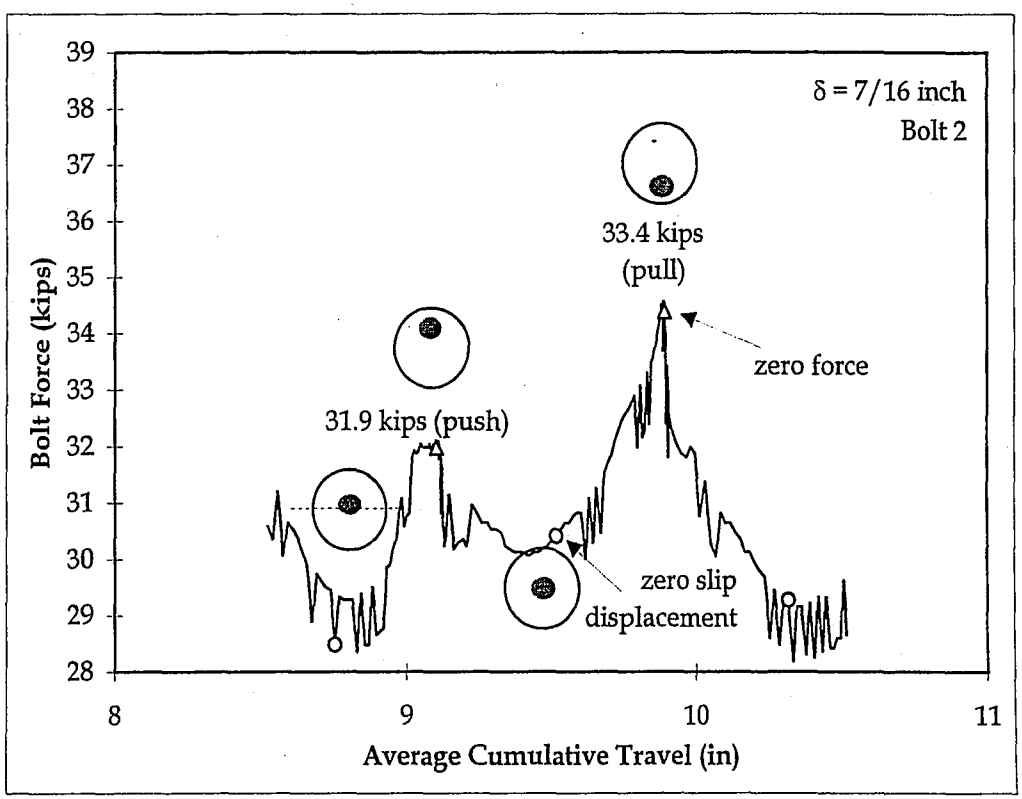

Figure 5.14(continued). Variation in Bolt Force for Test F5: (b) Bolt 2

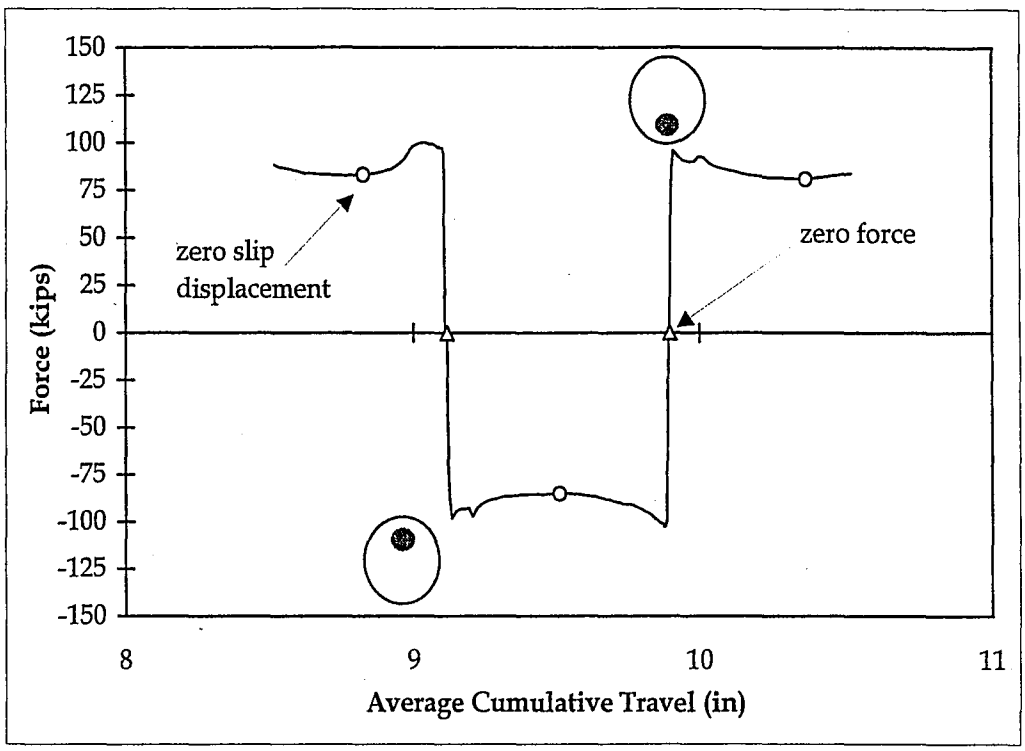

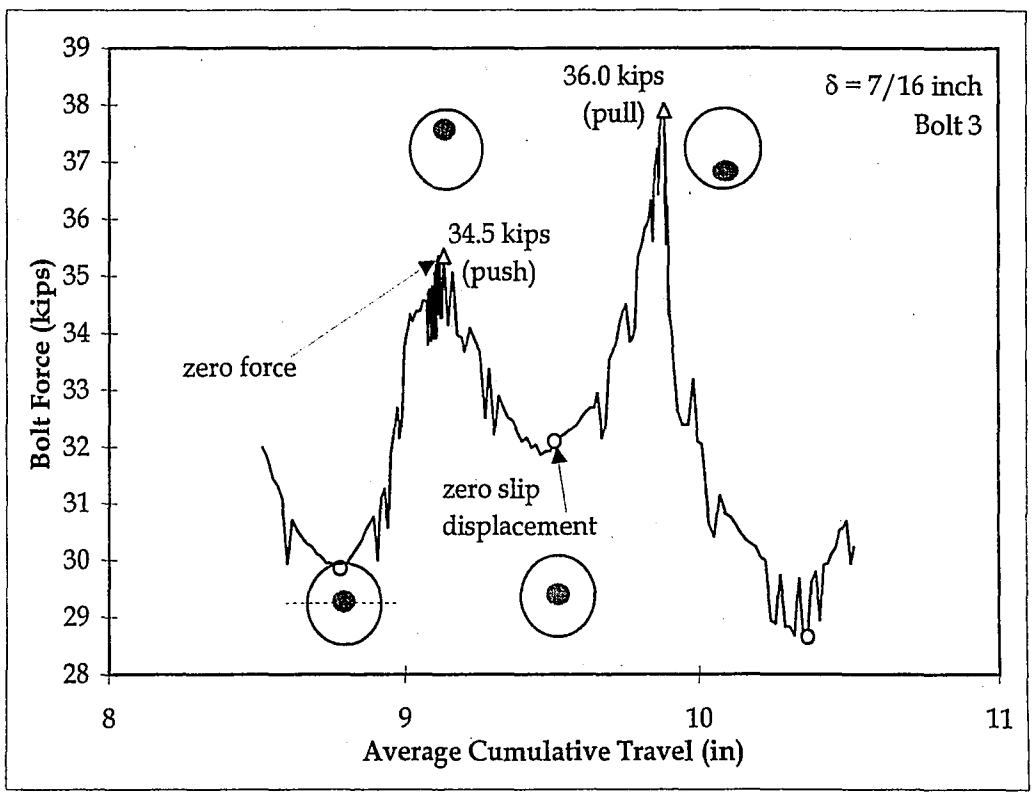

Figure 5.14(continued). Variation in Bolt Force for Test F5: (c) Bolt 3

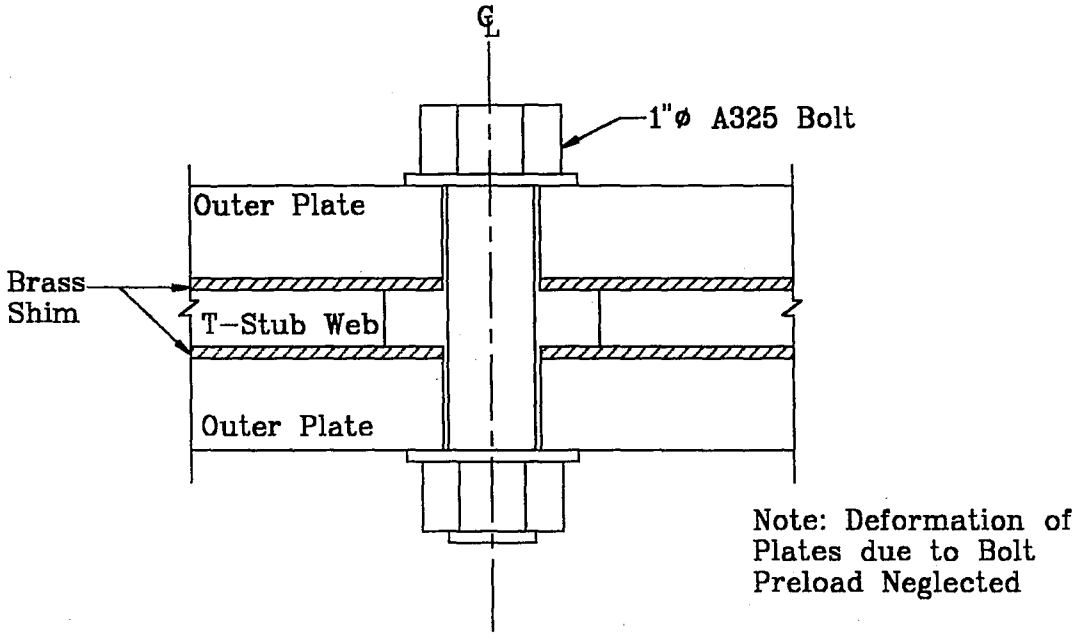

Figure 5.15. Clamping Bolt Assembly

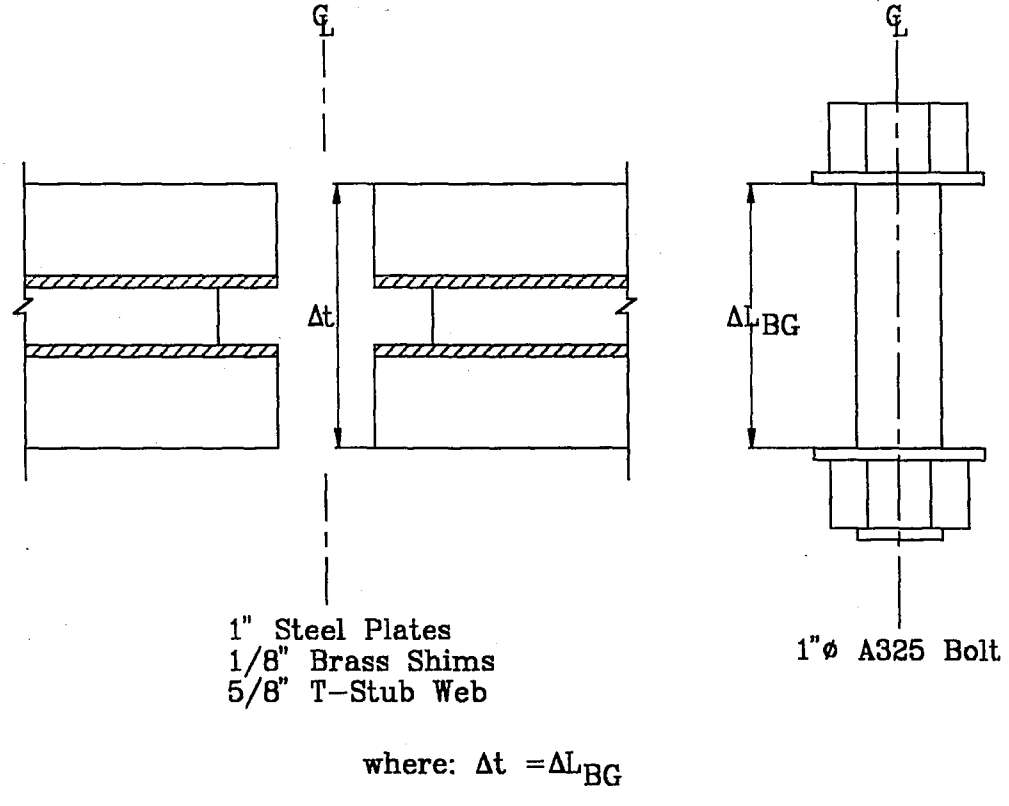

where: $\Delta t = \Delta L_{BG}$

Figure 5.16. Clamping Bolt and Section Compatibiltiy Assumption

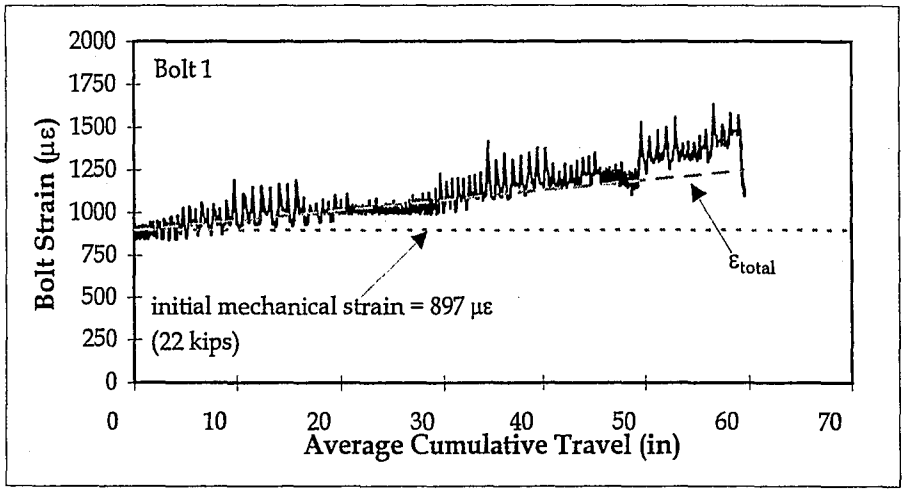

(a)

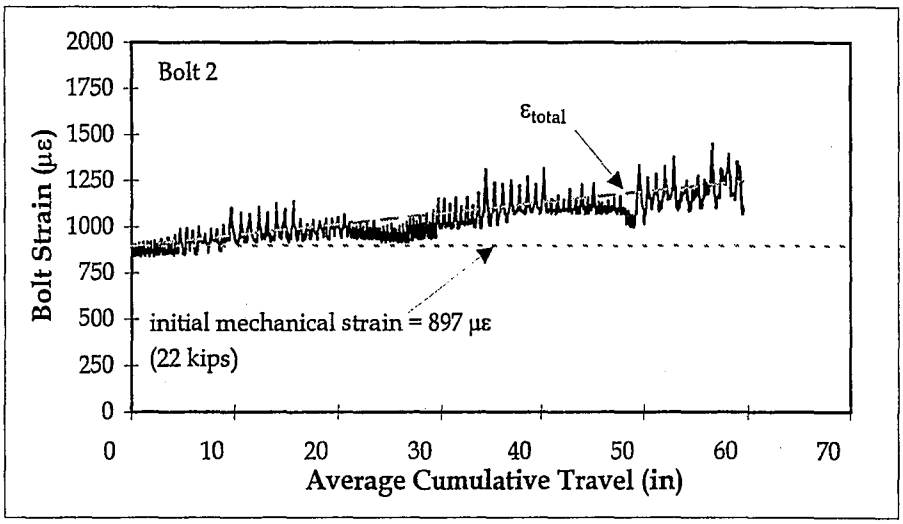

(b)

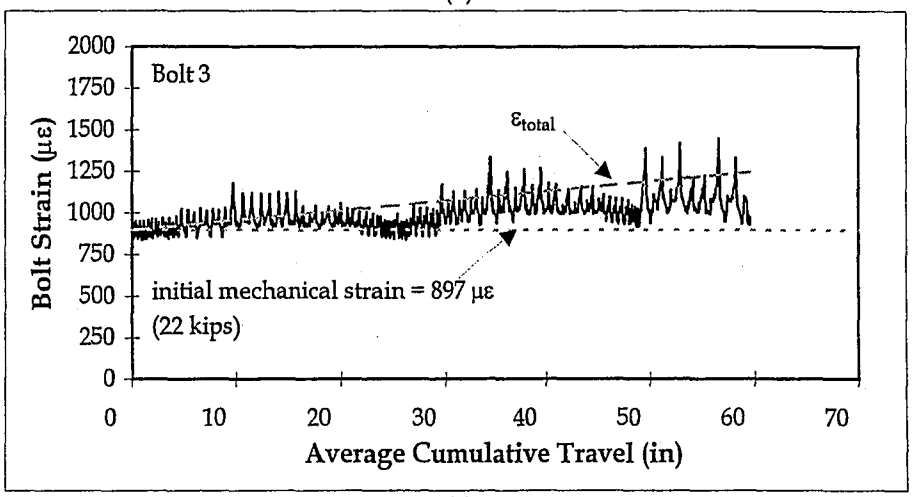

(c)

Figure 5.17. Bolt Strain vs. Average Cumulative Travel for Test F4: (a) Bolt 1; (b) Bolt 2; and (c) Bolt 3

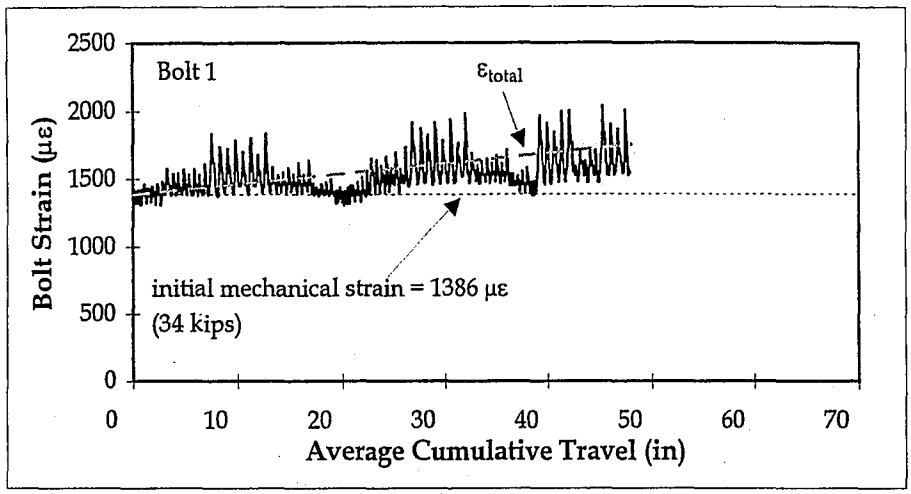

(a)

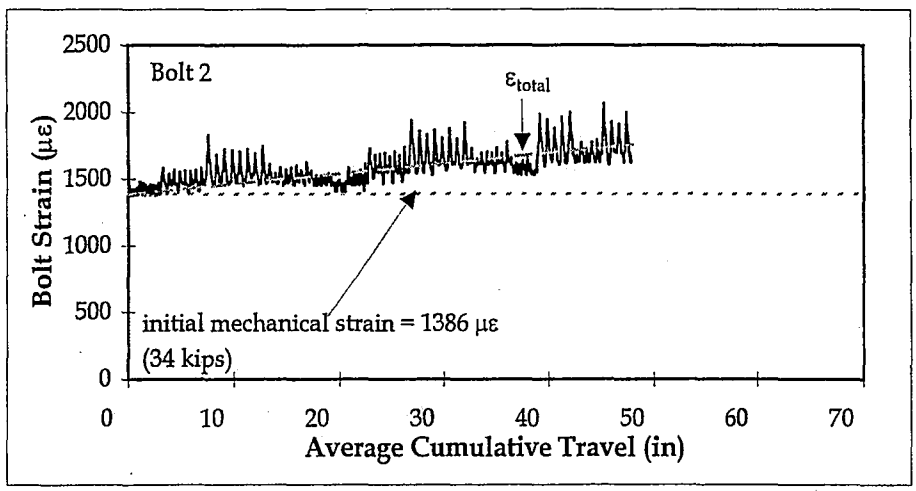

(b)

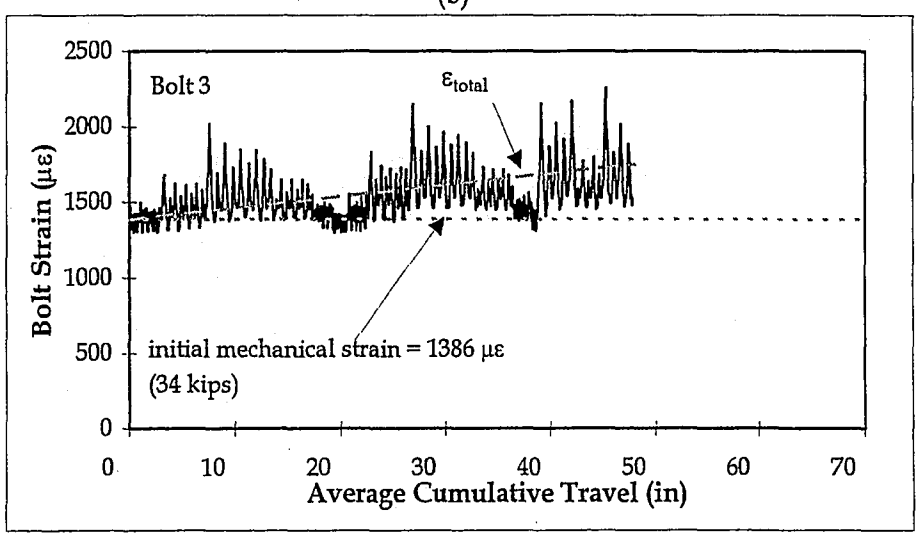

(c)

Figure 5.18. Bolt Strain vs. Average Cumulative Travel for Test F8: (a) Bolt 1; (b) Bolt 2; and (c) Bolt 3

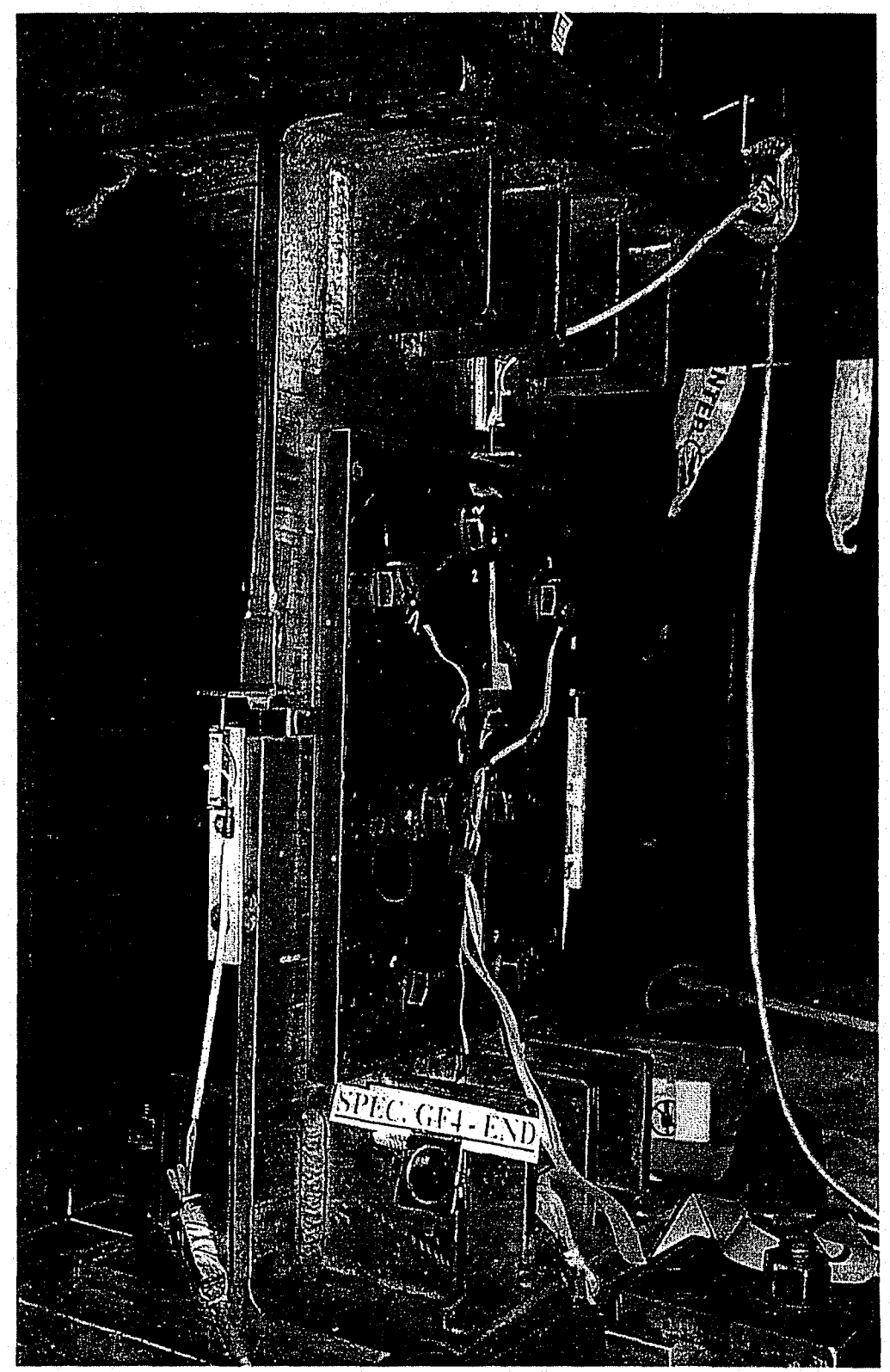

Figure 5:19. Photo of Double Plate Test Specimen for Tests F1 to F4

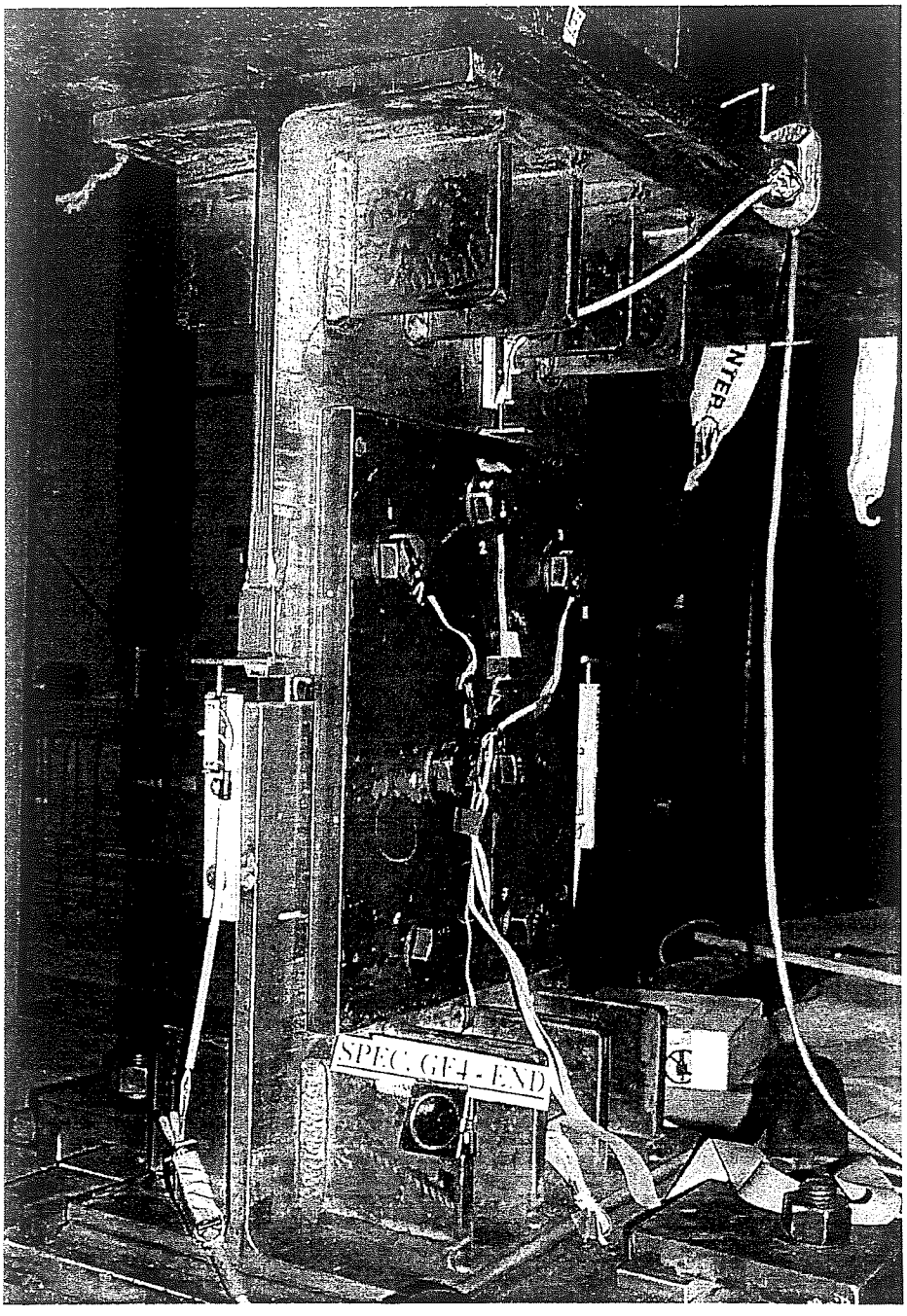

Figure 5:19. Photo of Double Plate Test Specimen for Tests F1 to F4

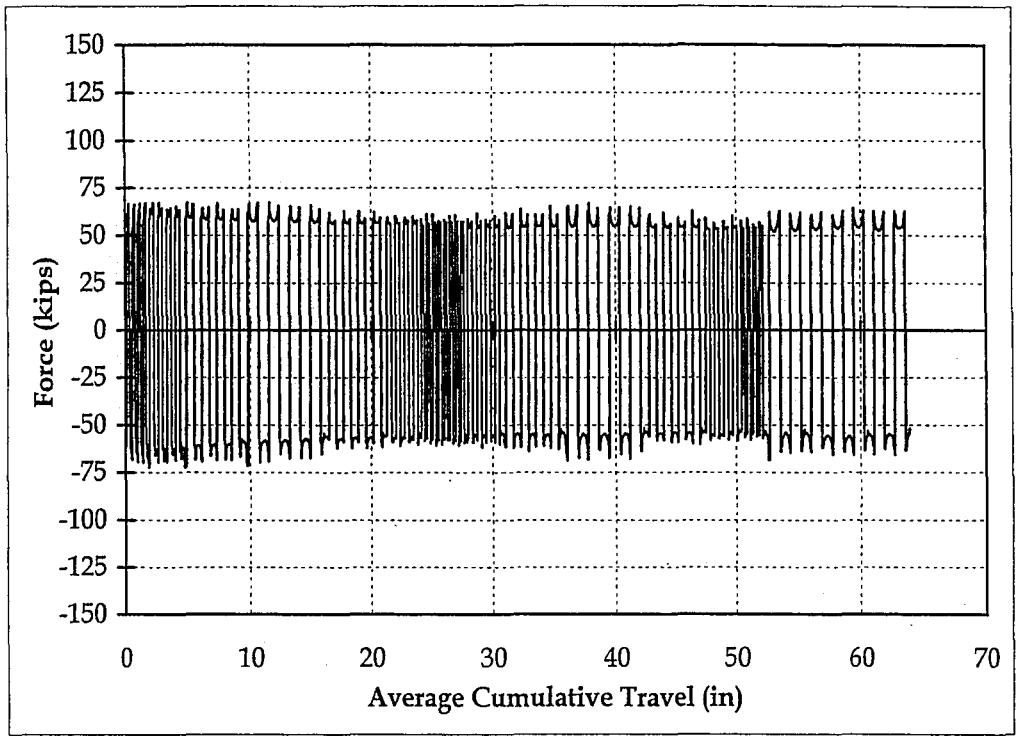

(a)

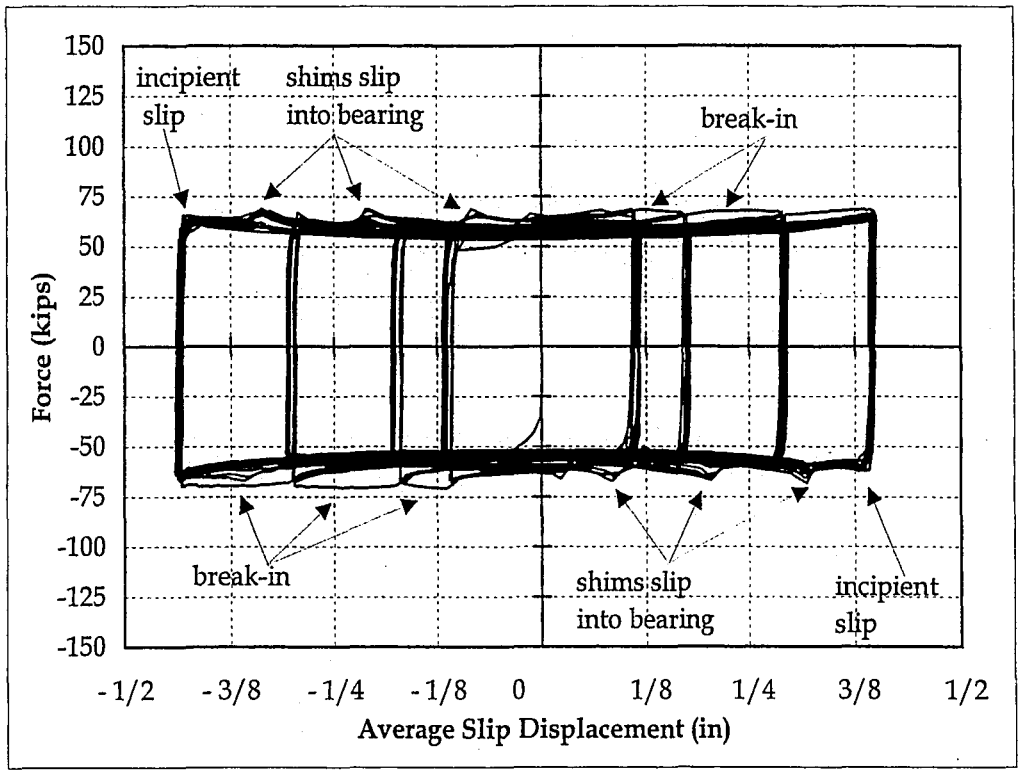

(b)

Figure 5.20. (a) Force vs. Average Cumulative Travel for Test F1; and
(b) Force vs. Average Slip Displacement for Test F1

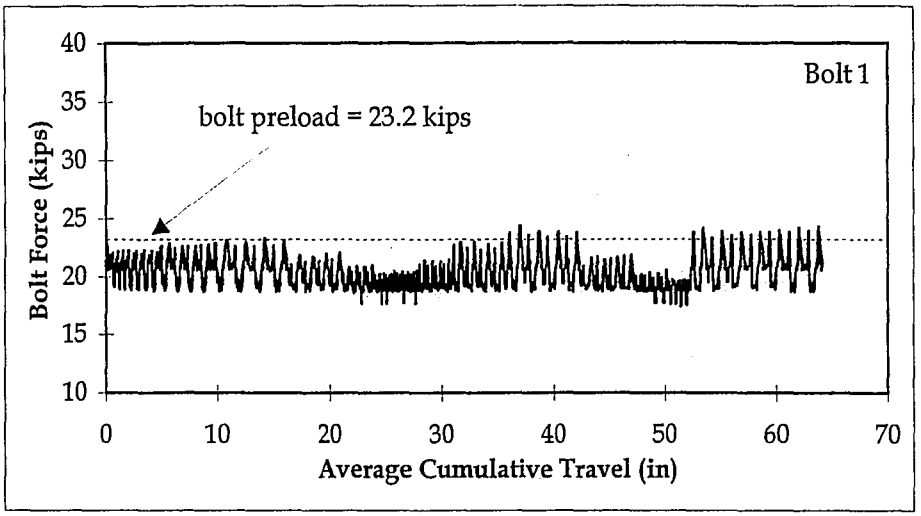

(a)

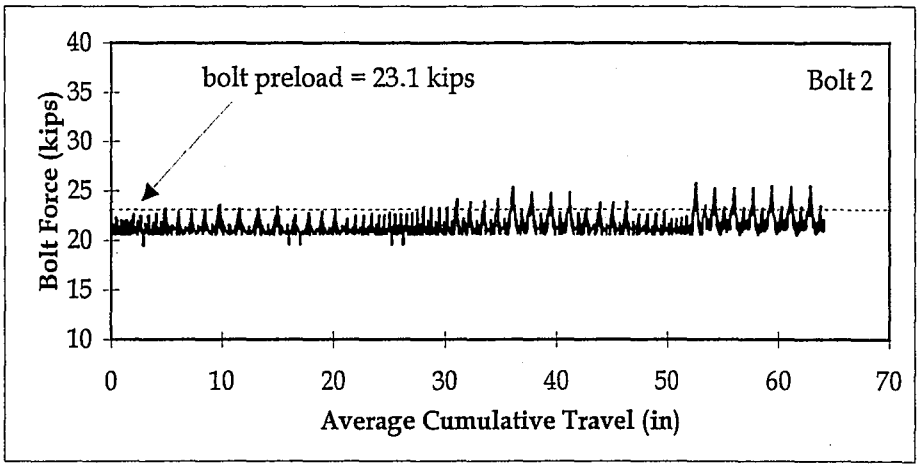

(b)

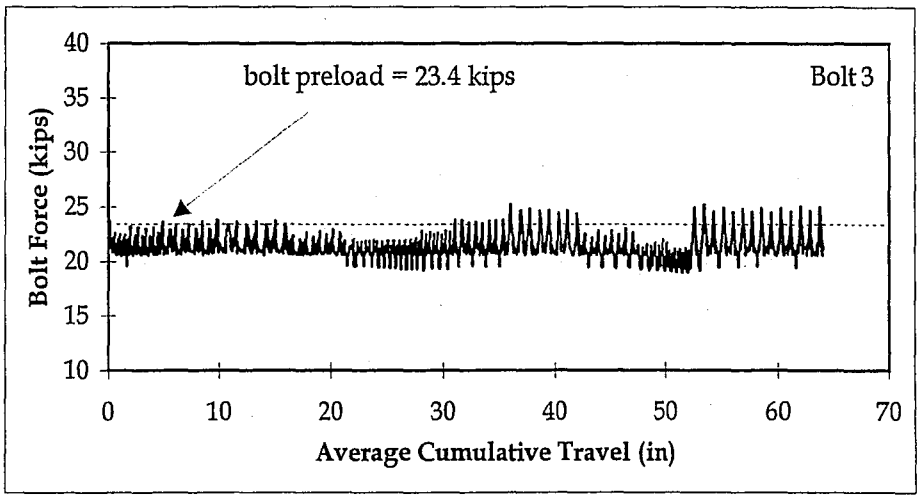

(c)

Figure 5.21. Clamping Bolt Force vs. Average Cumulative Travel for Test F1: (a) Bolt 1; (b) Bolt 2; and (c) Bolt 3

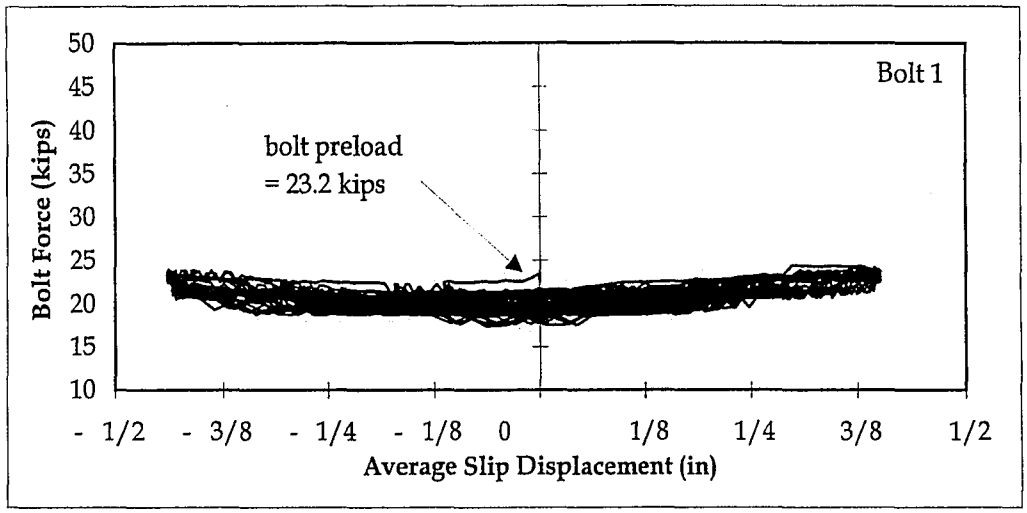

(a)

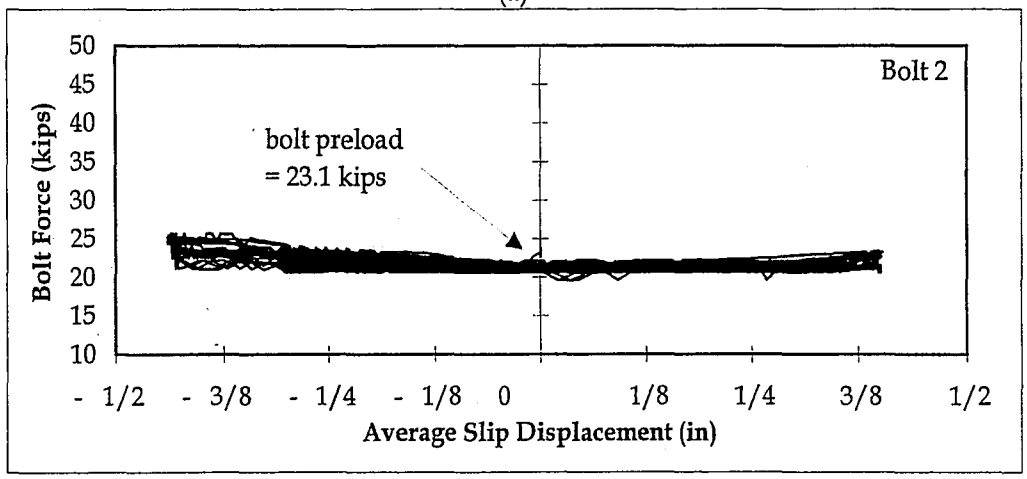

(b)

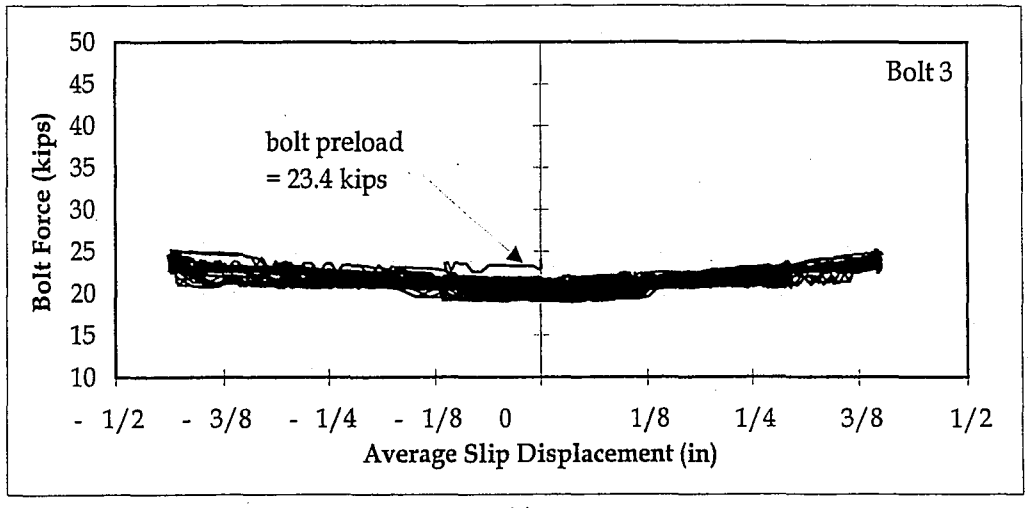

(c)

Figure 5.22. Clamping Bolt Force vs. Average Slip Displacement for Test F1: (a) Bolt 1; (b) Bolt 2; and (c) Bolt 3

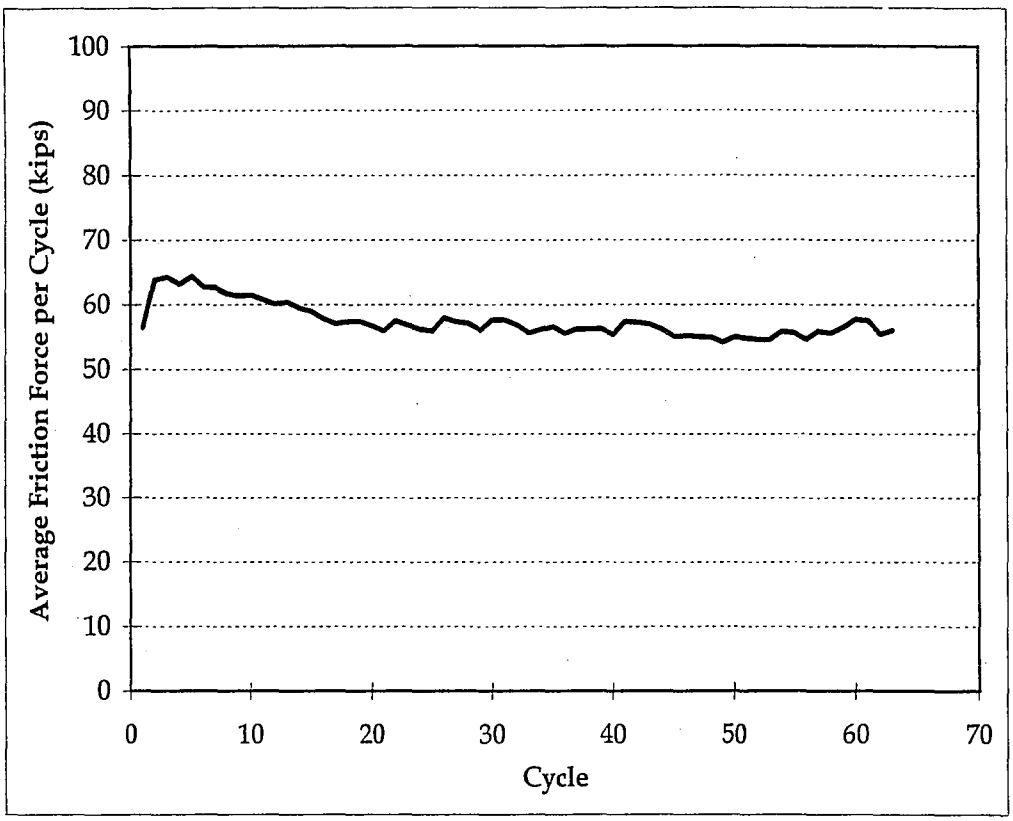

Figure 5.23. Average Friction Force per Cycle for Test F1

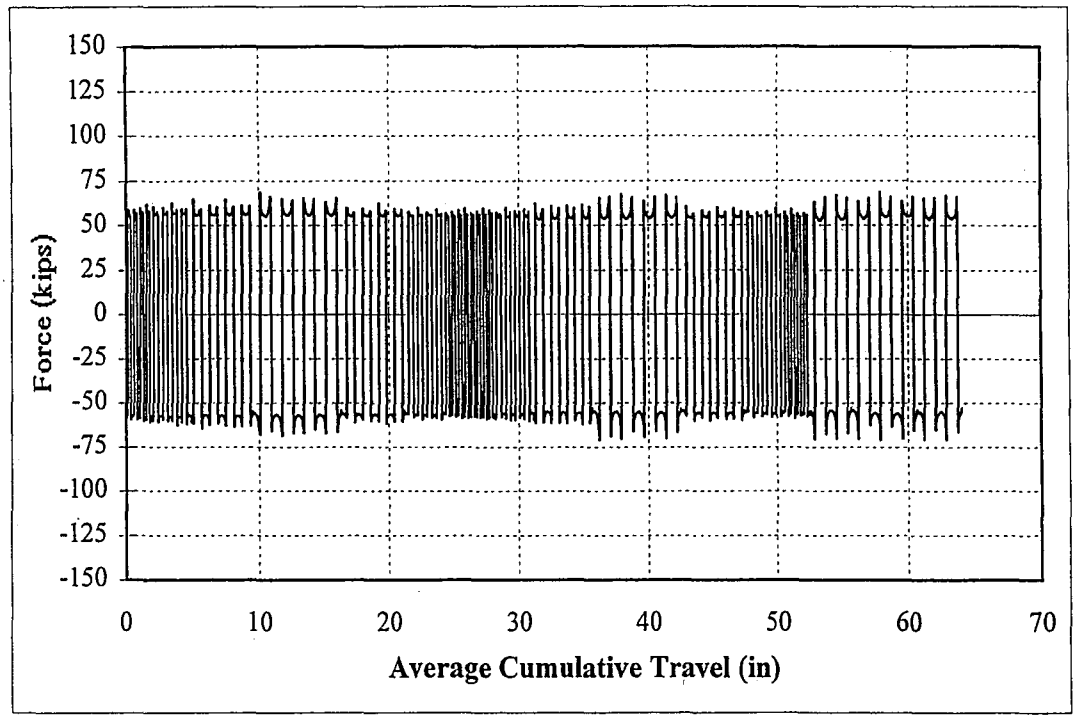

(a)

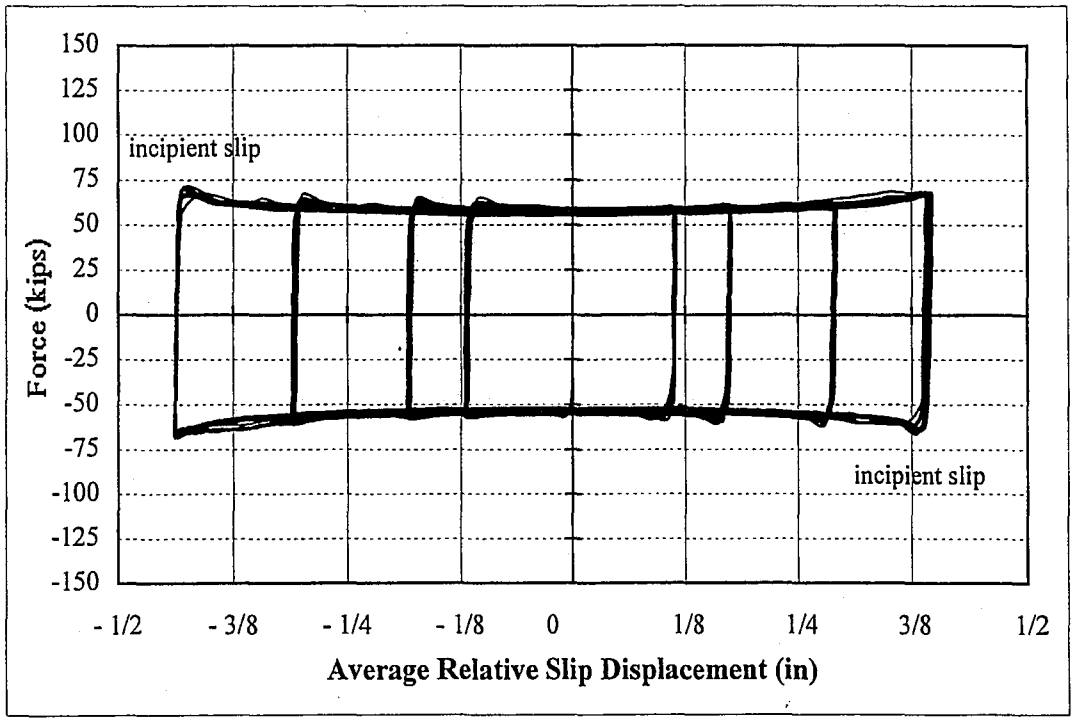

(b)

Figure 5.24. (a) Friction Force vs. Average Cumulative Travel for Test F3; and
(b) Hysteresis Curve for Test F2

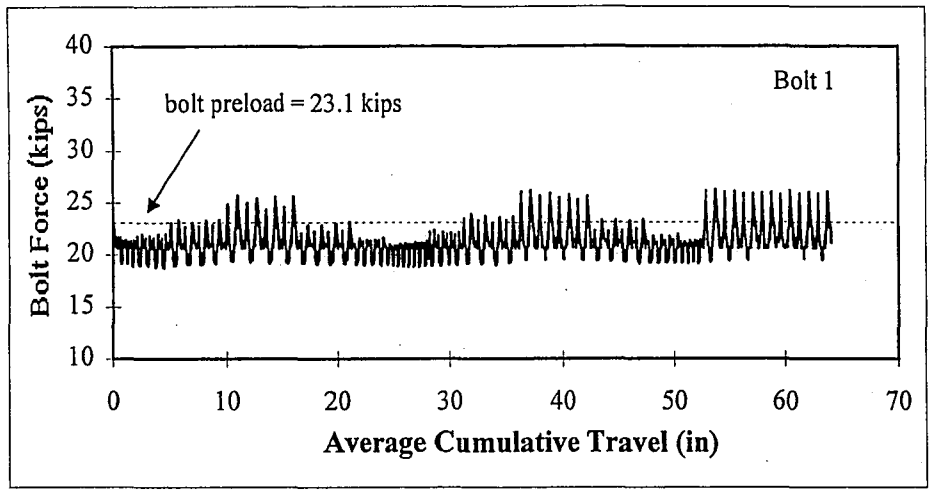

(a)

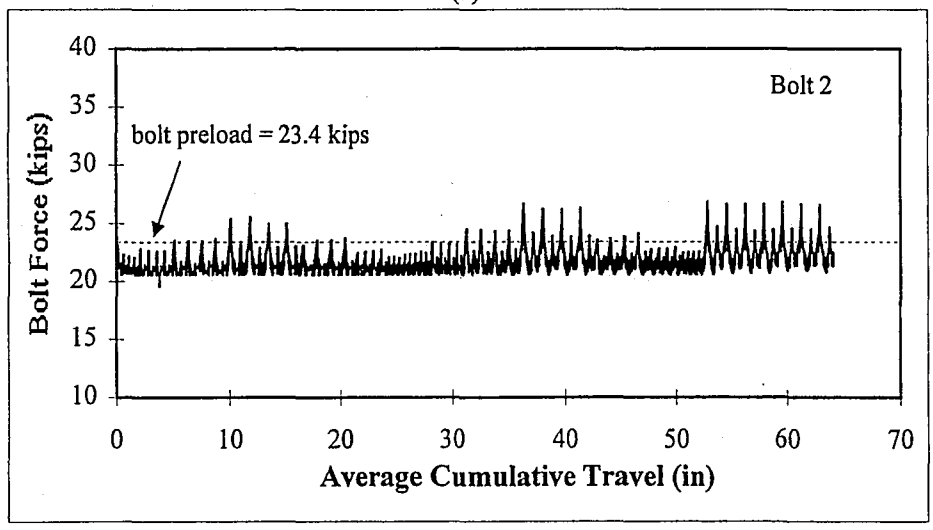

(b)

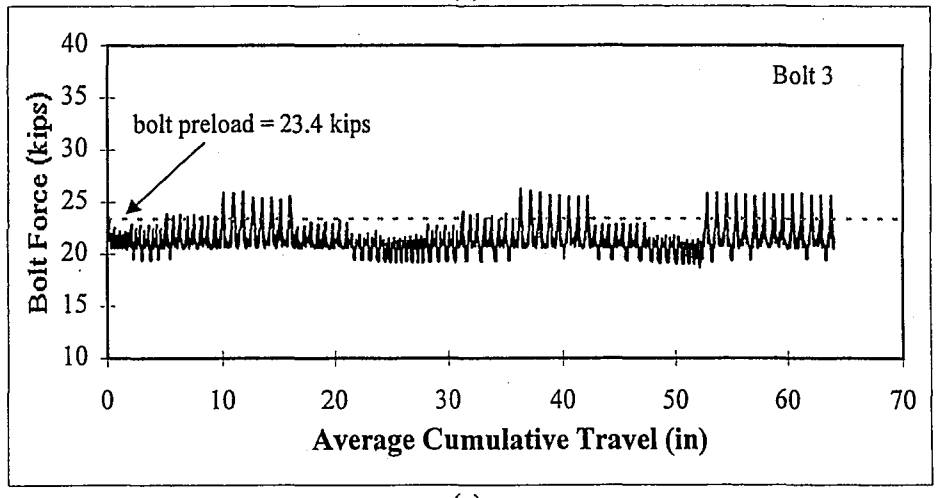

(c)

Figure 5.25. Clamping Bolt Force vs. Average Cumulative Travel for Test F2: (a) Bolt 1; (b) Bolt 2; and (c) Bolt 3

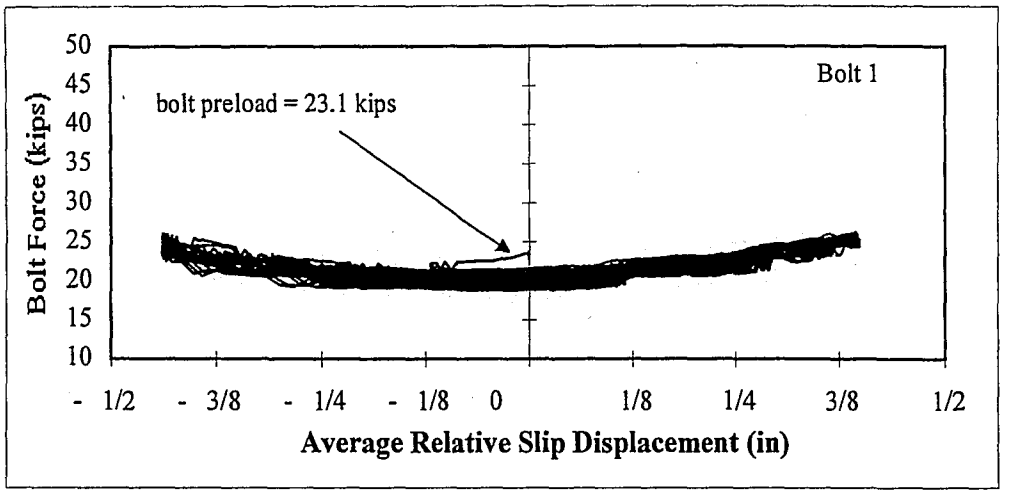

(a)

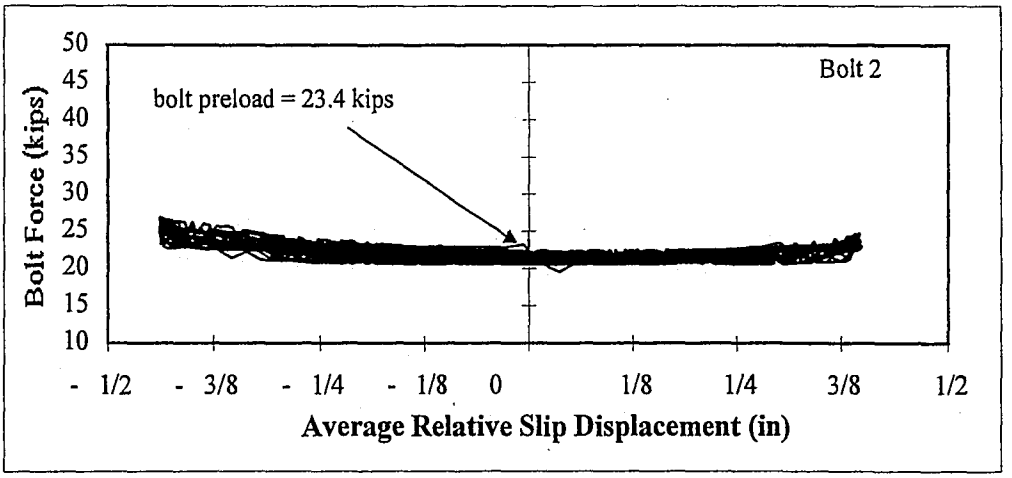

(b)

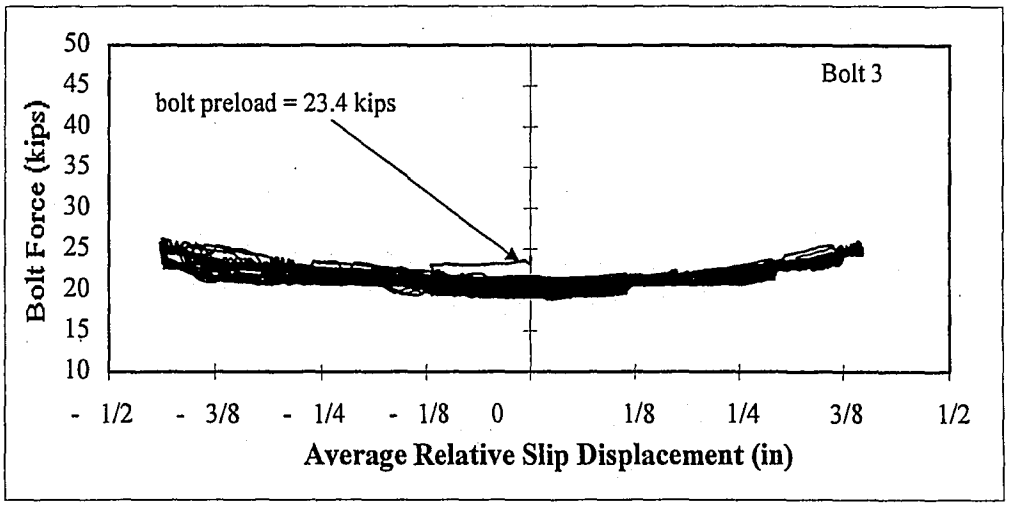

(c)

Figure 5.26. Clamping Bolt Force vs. Average Relative Slip Displacement for Test F2: (a) Bolt 1; (b) Bolt 2; and (c) Bolt 3

Figure 5.27. Average Friction Force per Cycle for Test F2

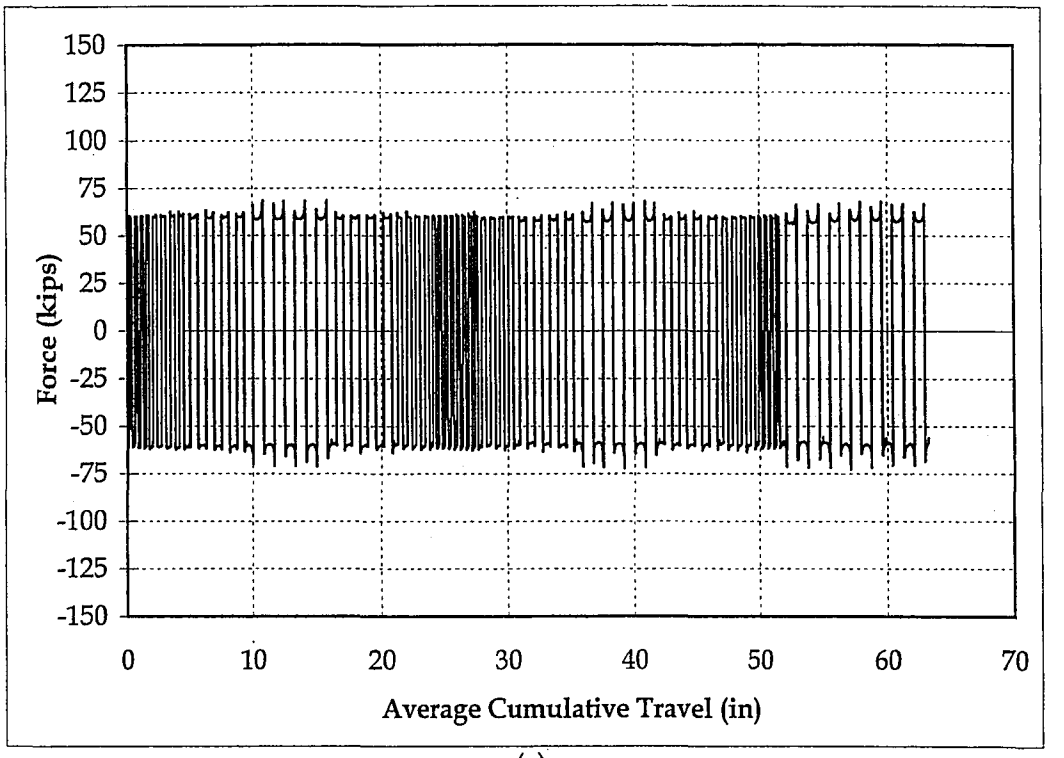

(a)

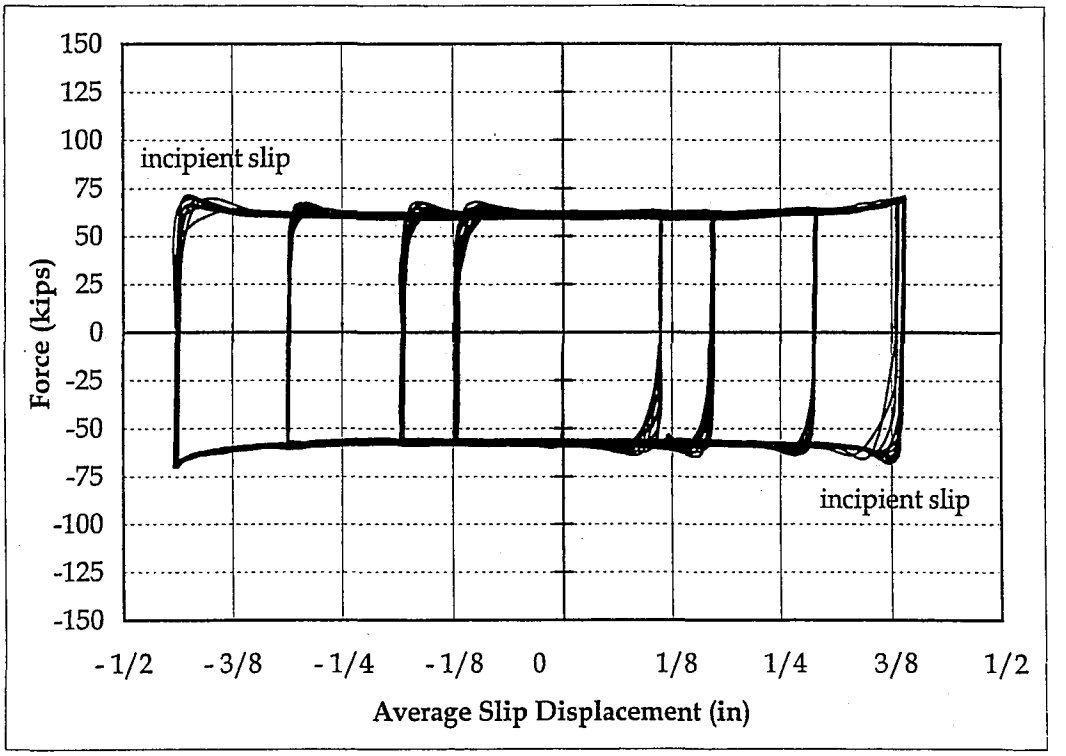

(b)

Figure 5.28. (a) Force vs. Average Cumulative Travel for Test F3; and
(b) Force vs. Average Slip Displacement for Test F3

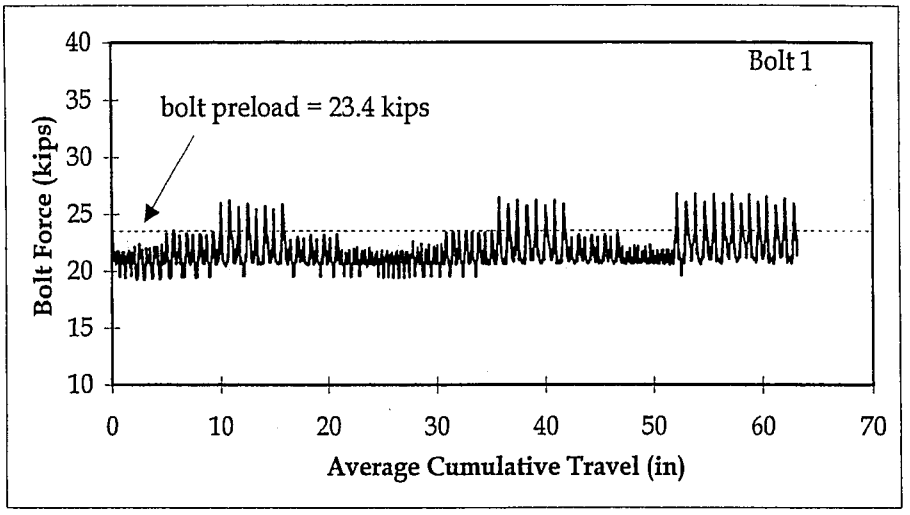

(a)

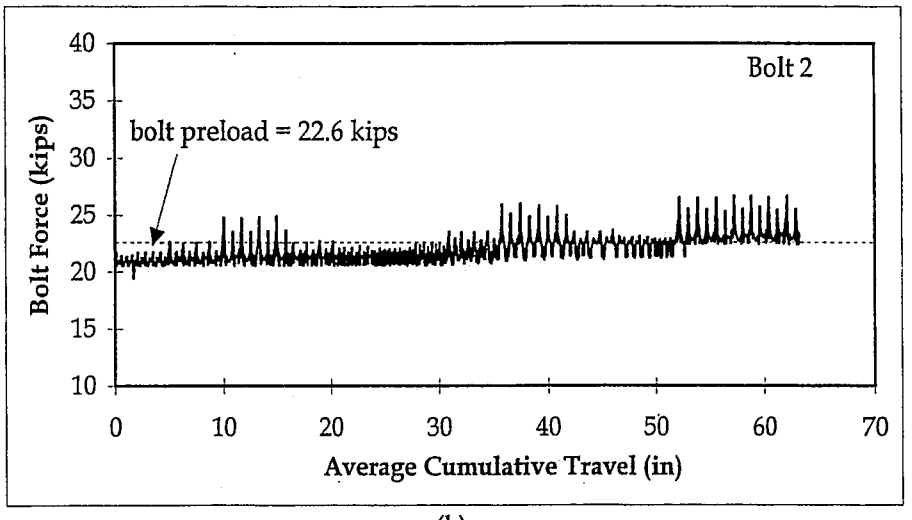

(b)

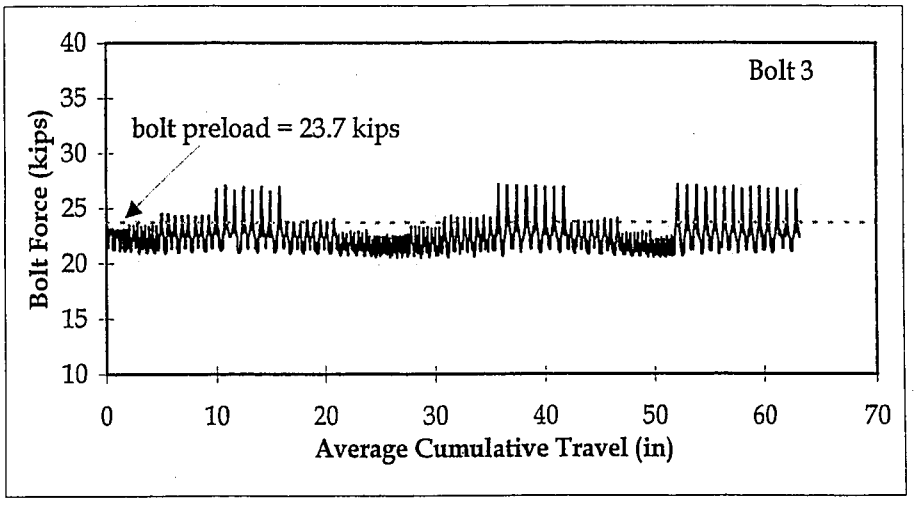

(c)

Figure 5.29. Clamping Bolt Force vs. Average Cumulative Travel for Test F3: (a) Bolt 1; (b) Bolt 2; and (c) Bolt 3

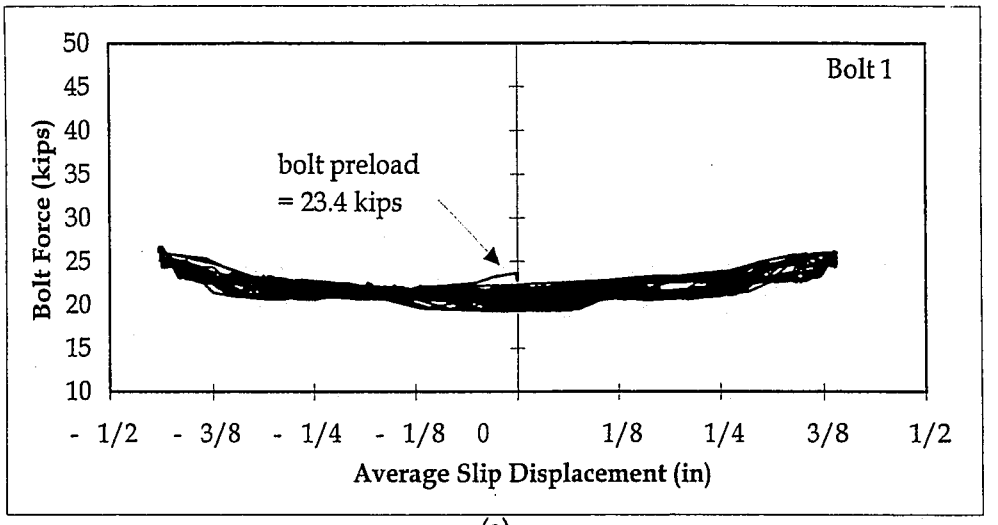

(a)

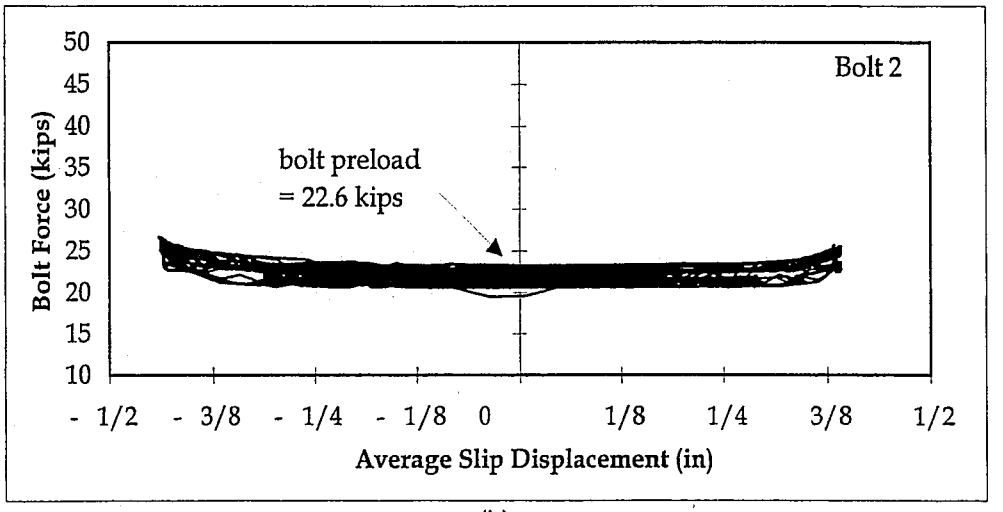

(b)

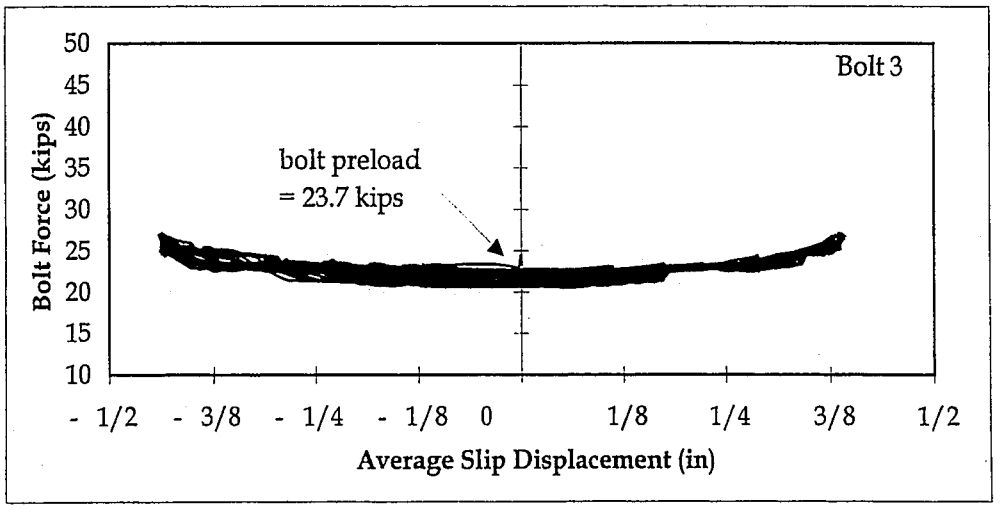

(c)

Figure 5.30. Clamping Bolt Force vs. Average Slip Displacement
Test F3: (a) Bolt 1; (b) Bolt 2; and (c) Bolt 3

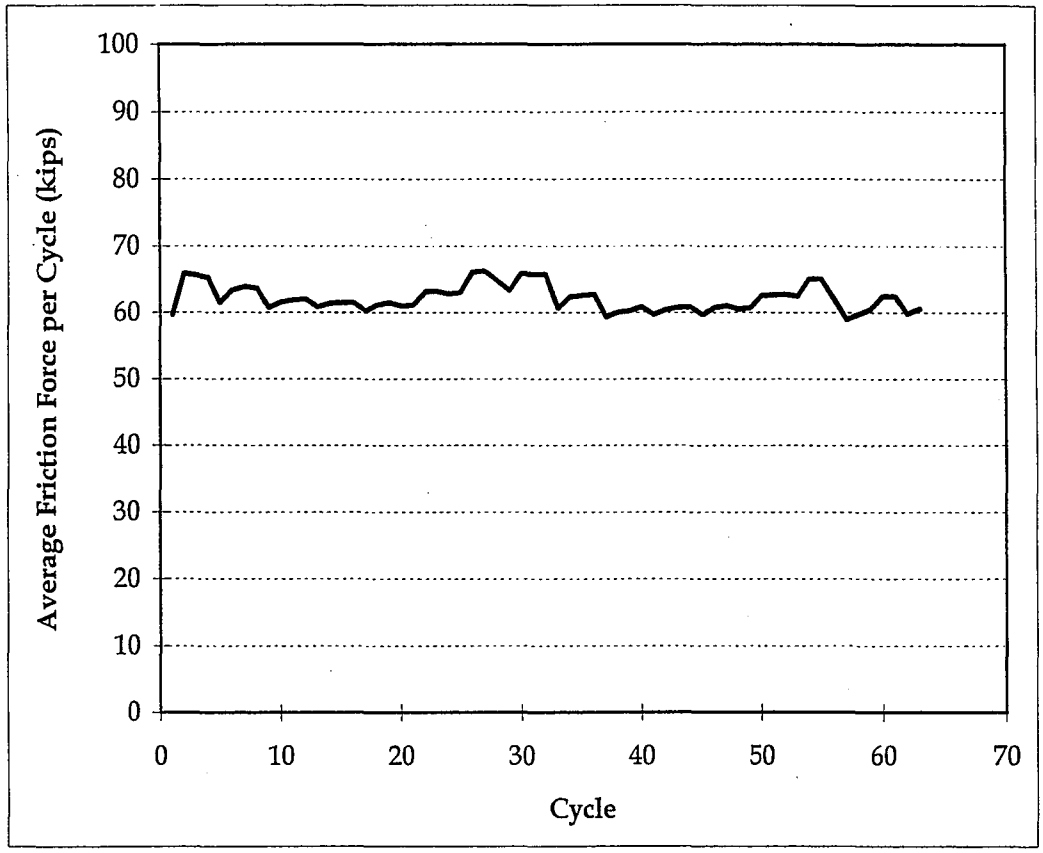

Figure 5.31. Average Friction Force per Cycle for Test F3

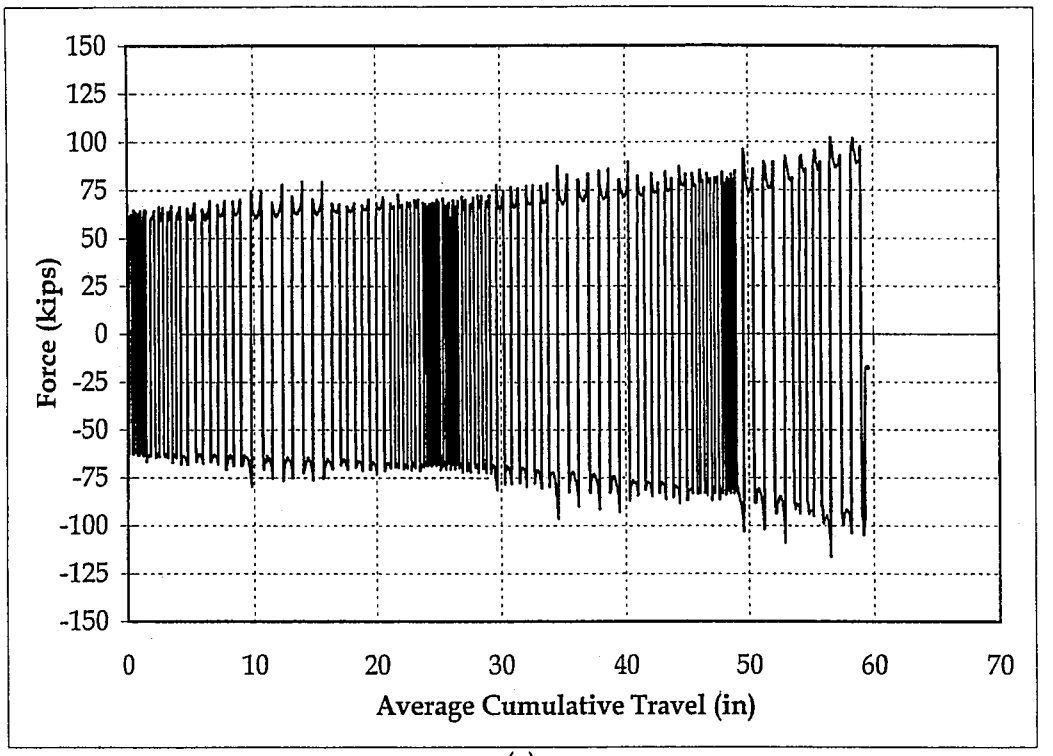

(a)

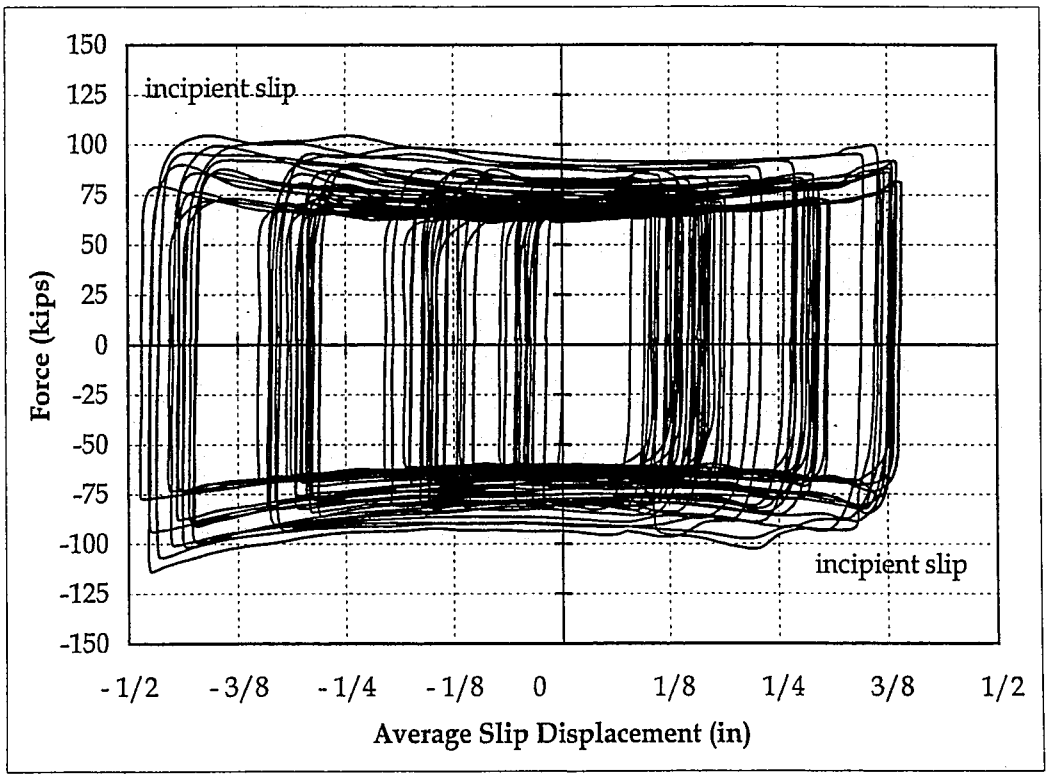

(b)

Figure 5.32. (a) Force vs. Average Cumulative Travel for Test F4; and
(b) Force vs. Average Slip Displacement for Test F4

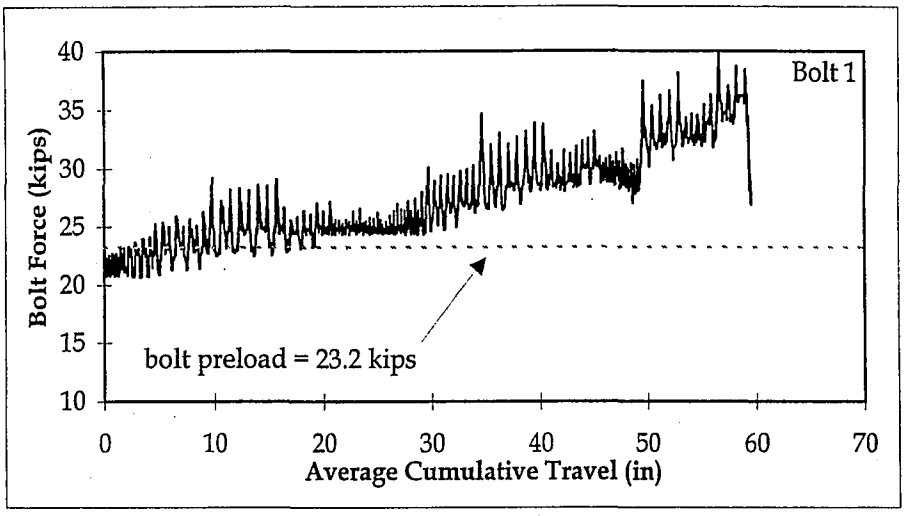

(a)

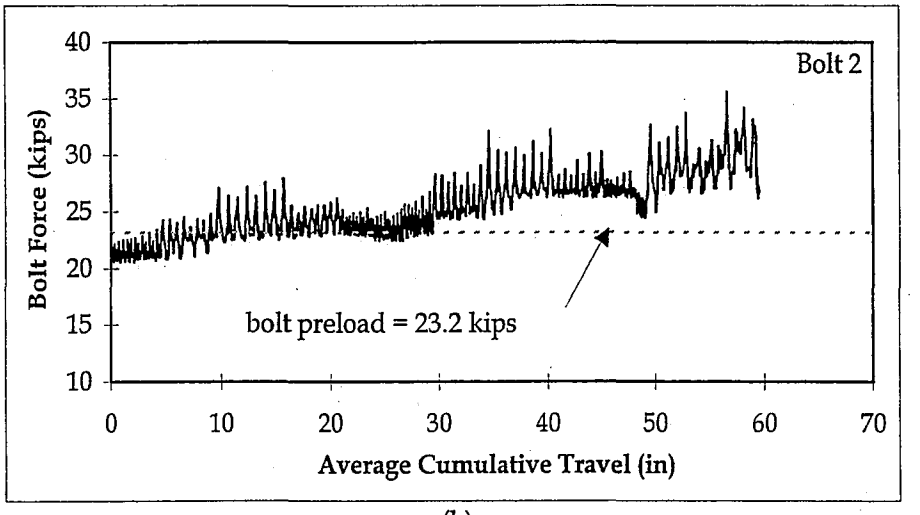

(b)

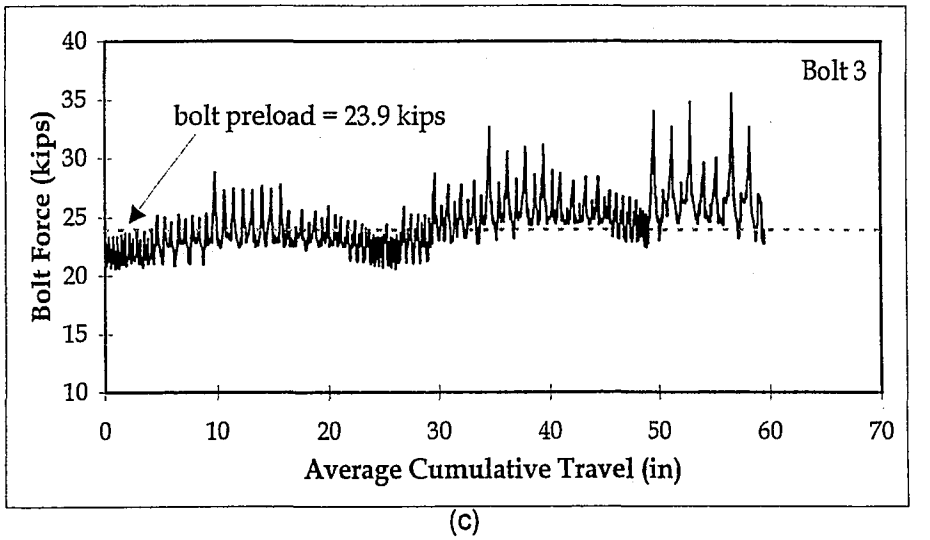

(c)

Figure 5.33. Clamping Bolt Force vs. Average Cumulative Travel for Test F4: (a) Bolt 1; (b) Bolt 2; and (c) Bolt 3

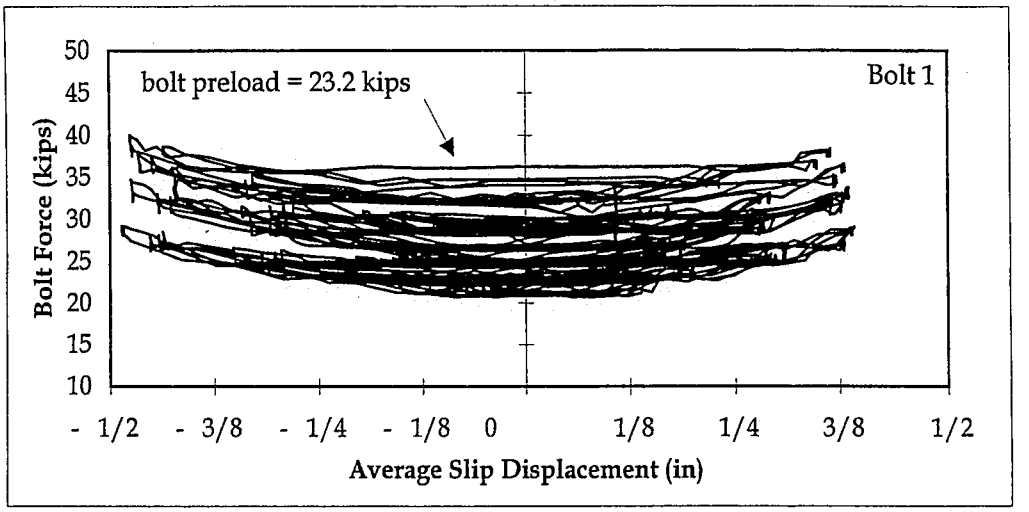

(a)

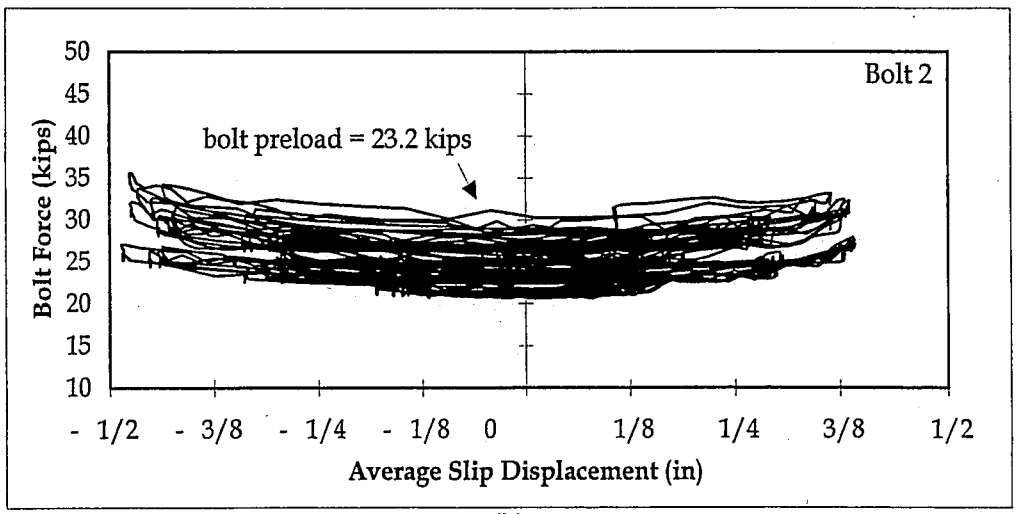

(b)

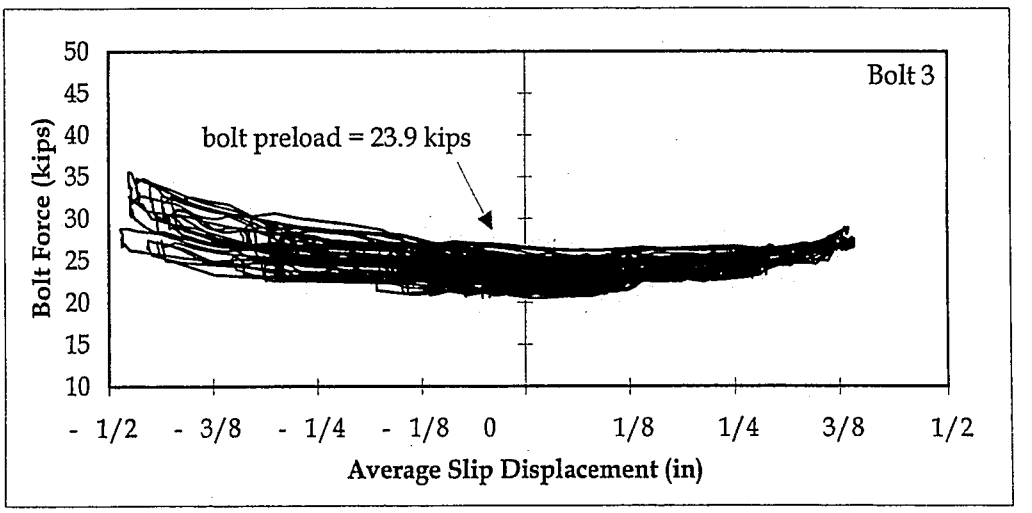

(c)

Figure 5.34. Clamping Bolt Force vs. Average Slip Displacement
Test F4: (a) Bolt 1; (b) Bolt 2; and (c) Bolt 3

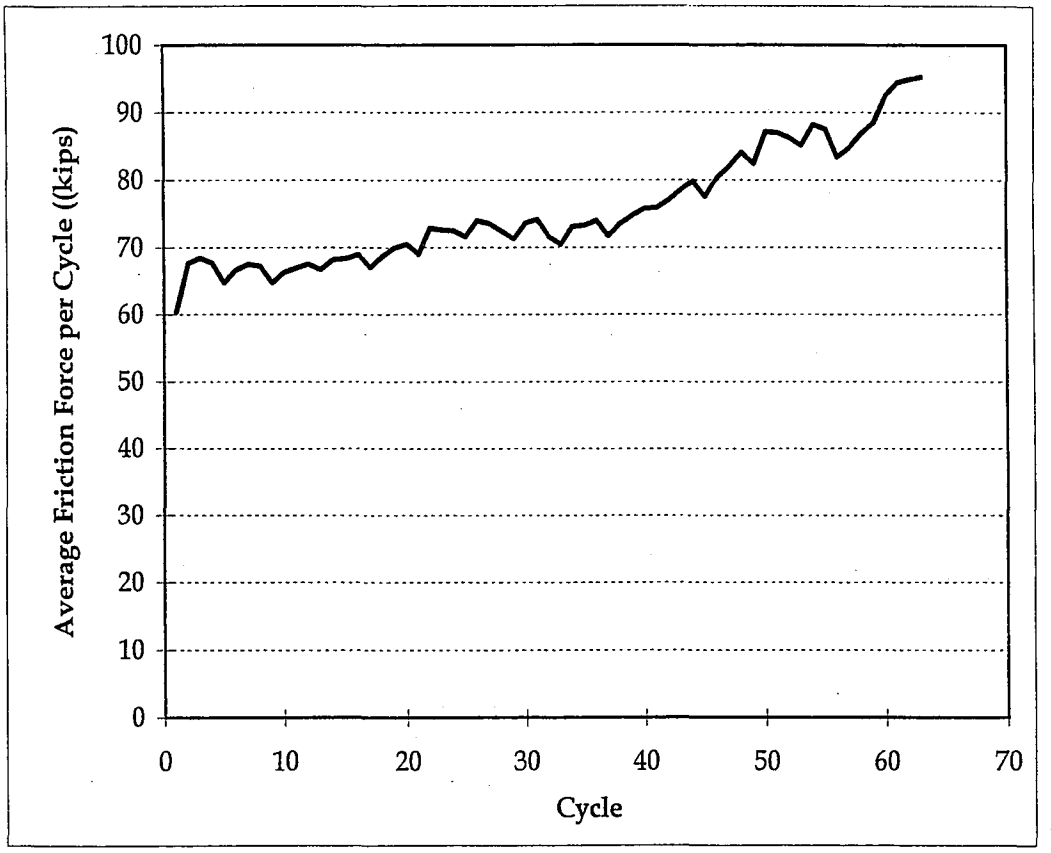

Figure 5.35. Average Friction Force per Cycle for Test F4

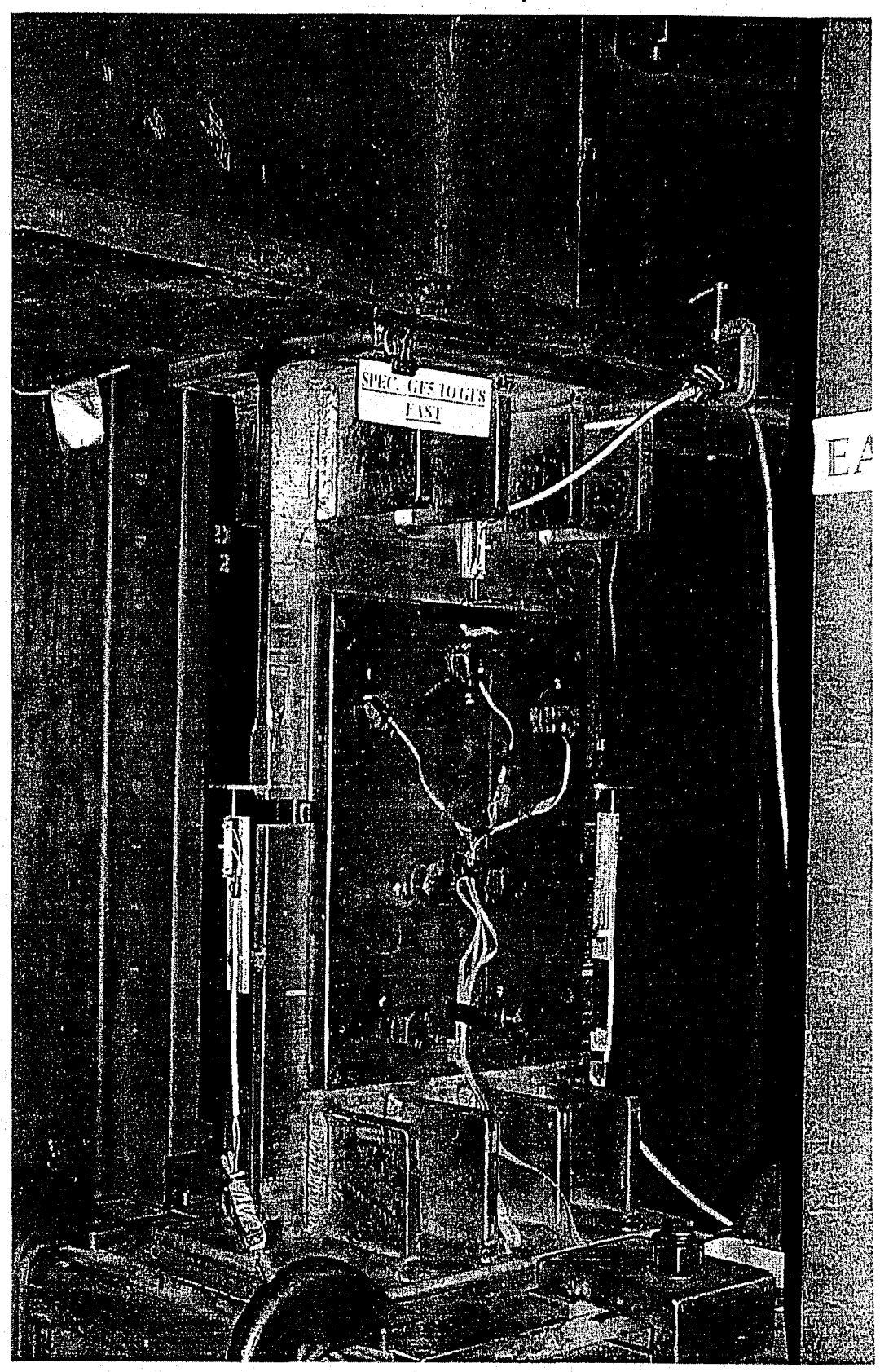

Figure 5.36. Photo of Double Plate Test Specimen for Tests F5 to F8

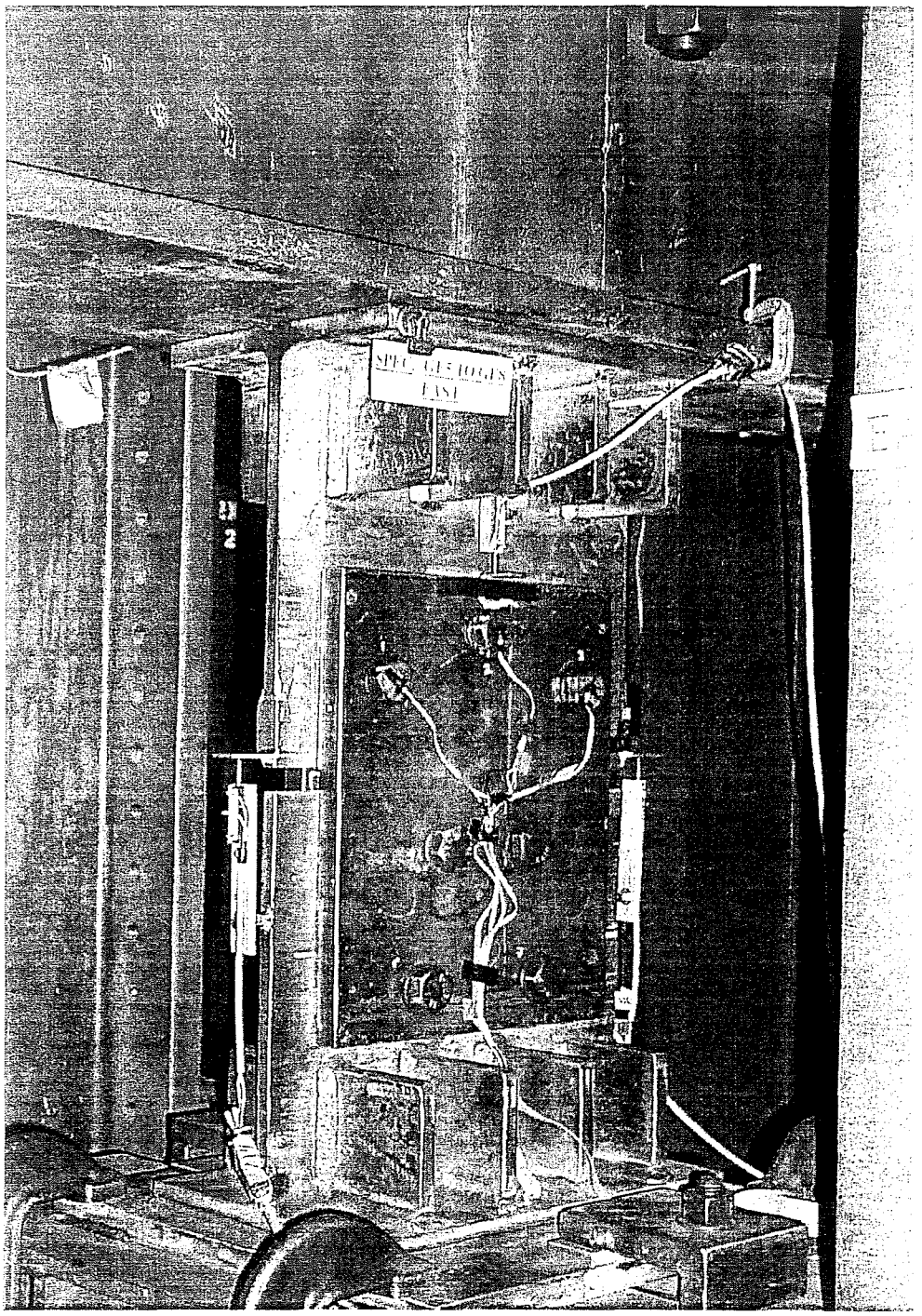

Figure 5.36. Photo of Double Plate Test Specimen for Tests F5 to F8

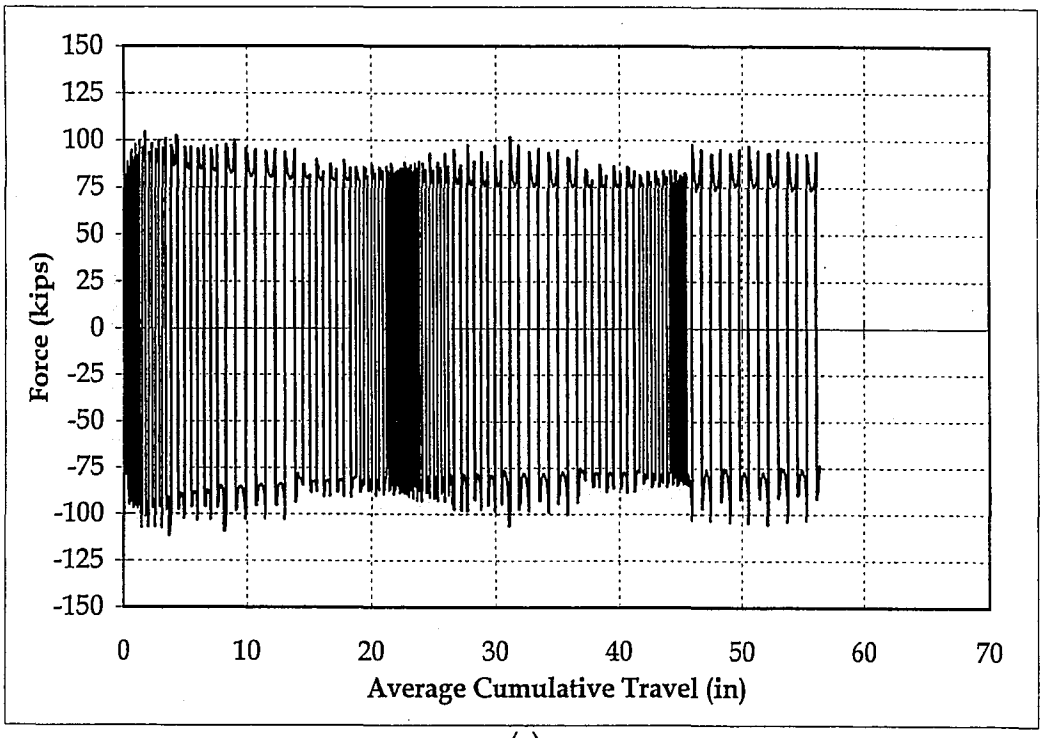

(a)

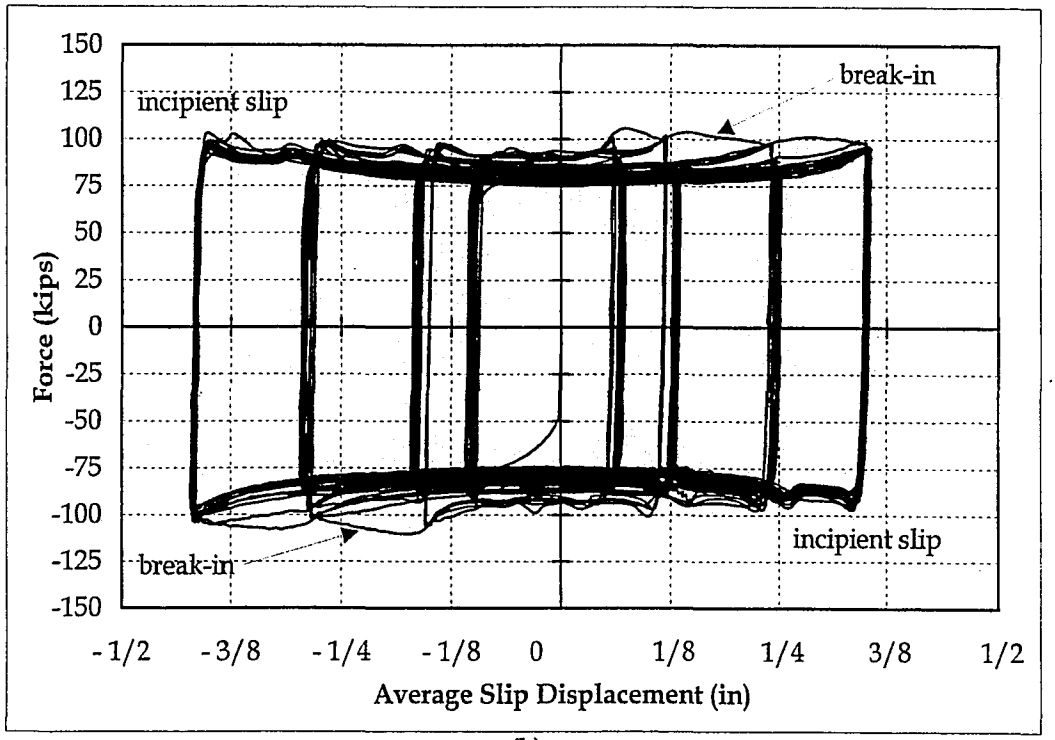

(b)

Figure 5.37. (a) Force vs. Average Cumulative Travel for Test F5; and
(b) Force vs. Average Slip Displacement for Test F5

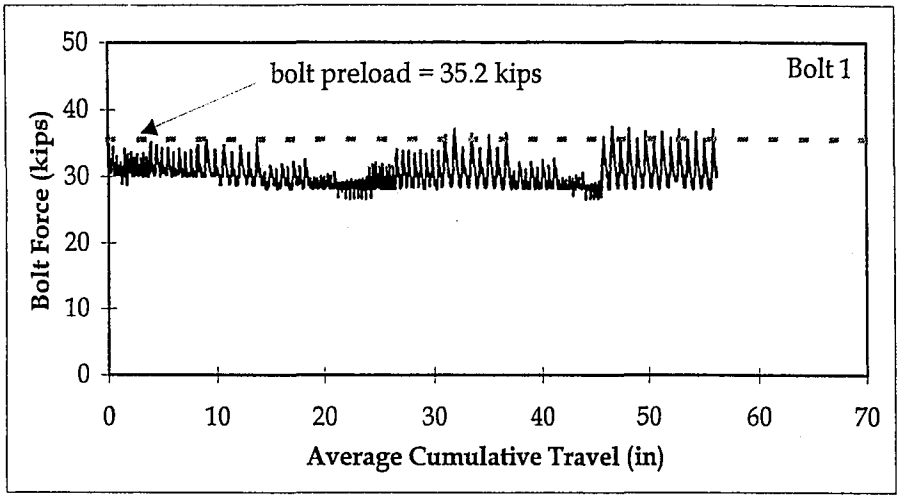

(a)

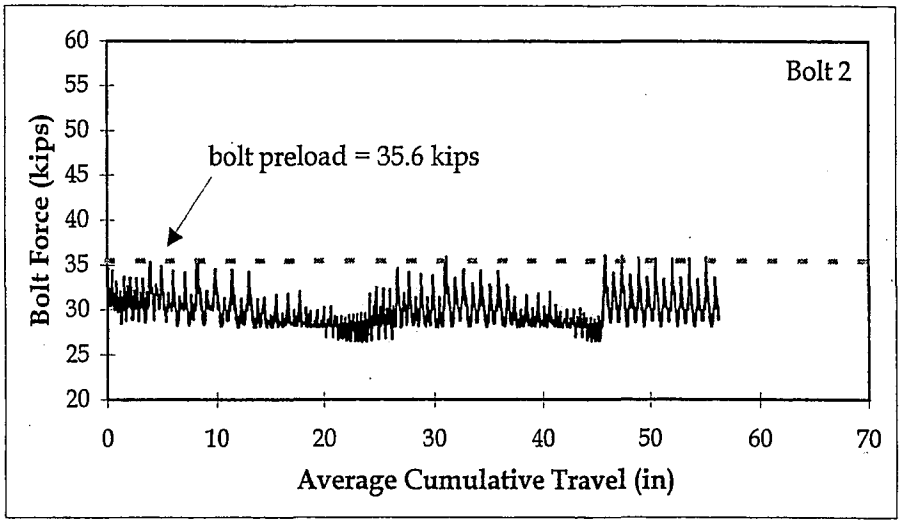

(b)

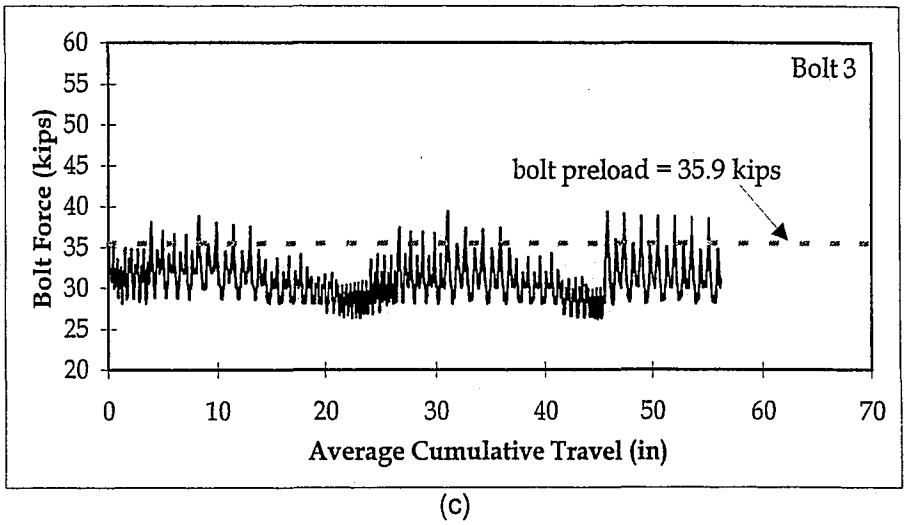

(c)

Figure 5.38. Clamping Bolt Force vs. Average Cumulative Travel for Test F5: (a) Bolt 1; (b) Bolt 2; and (c) Bolt 3

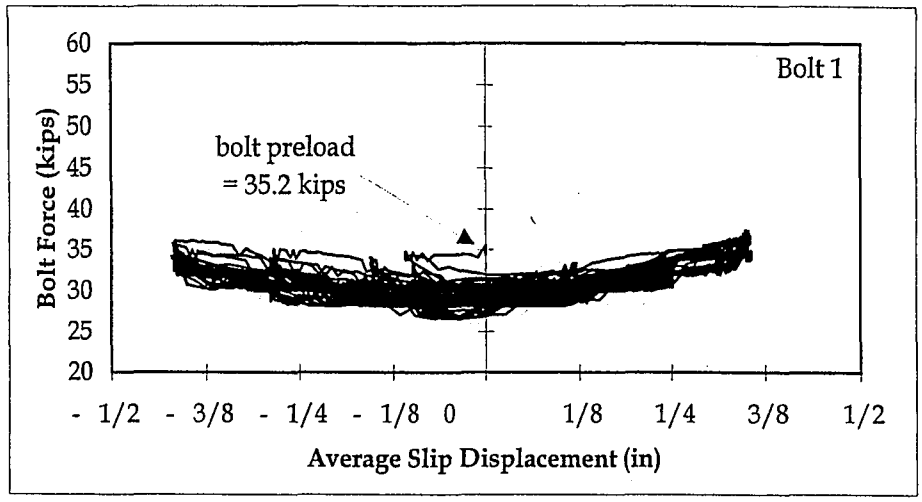

(a)

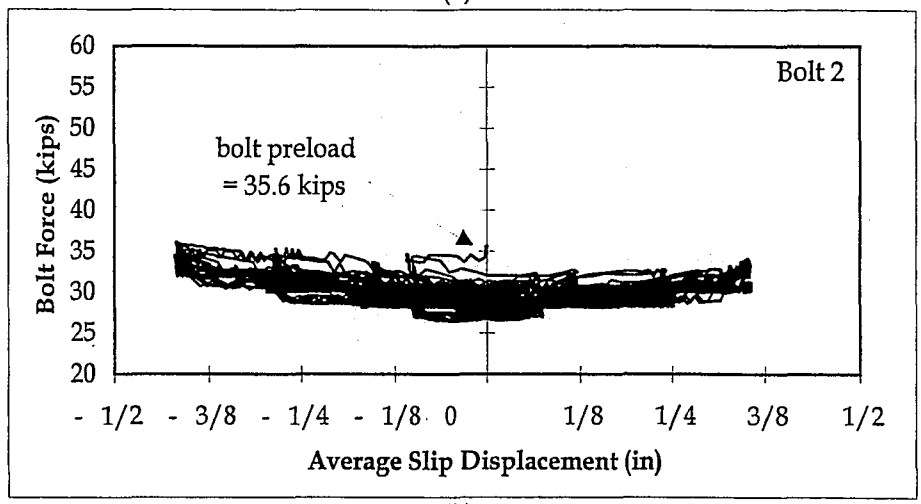

(b)

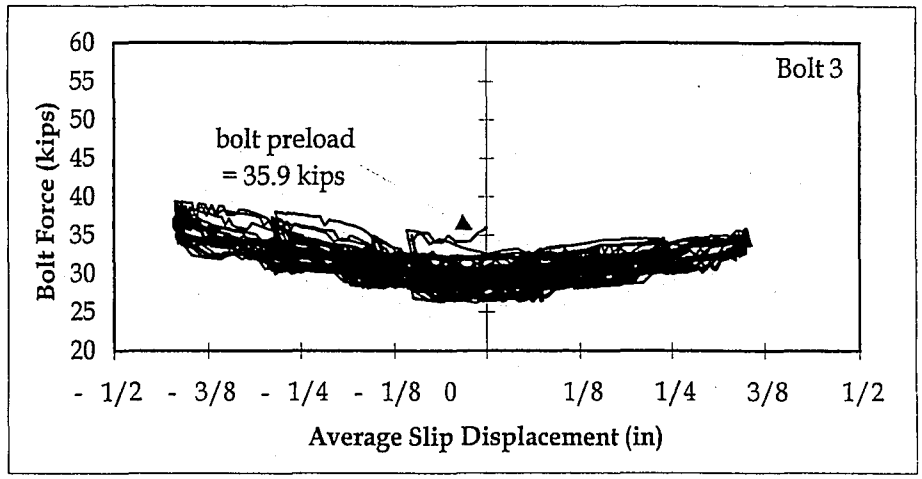

(c)

Figure 5.39. Clamping Bolt Force vs. Average Slip Displacement for Test F5: (a) Bolt 1; (b) Bolt 2; and (c) Bolt 3

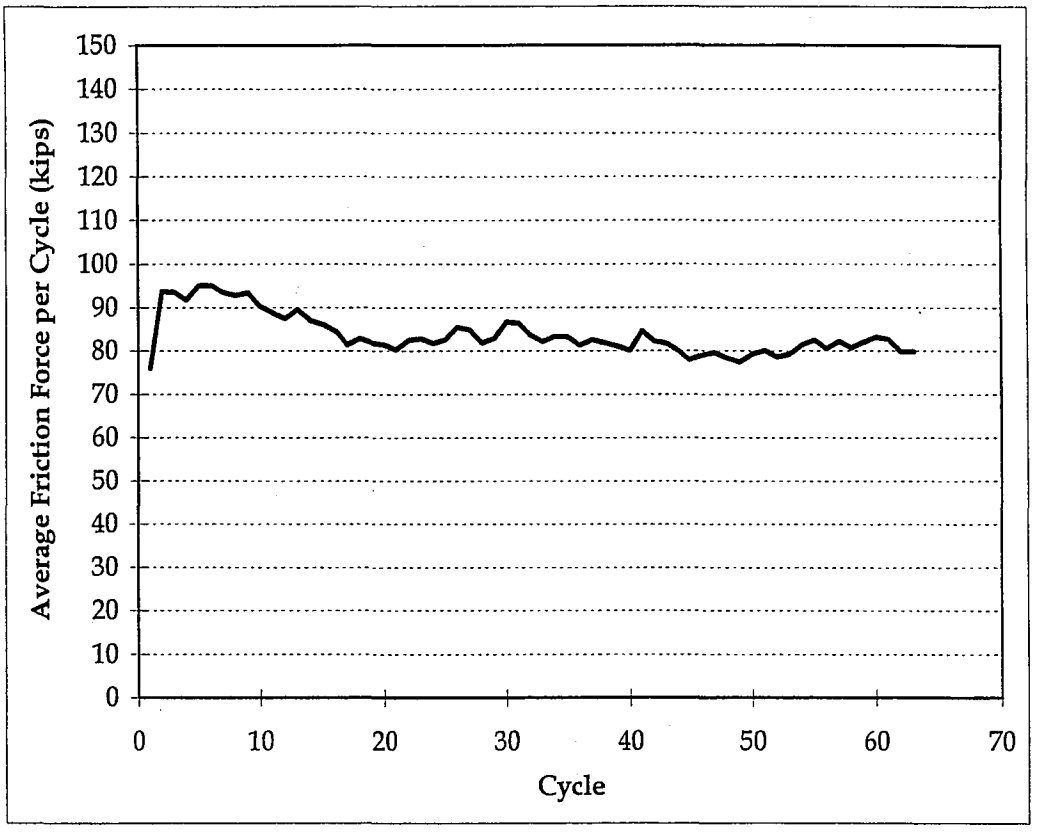

Figure 5.40. Average Friction Force per Cycle for Test F5

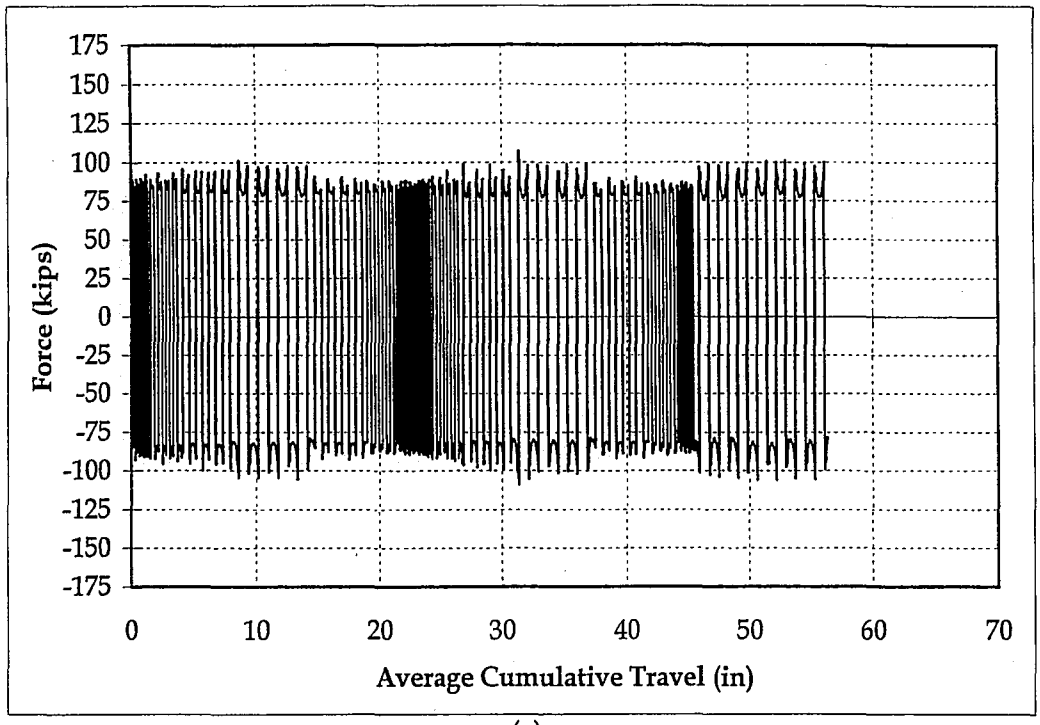

(a)

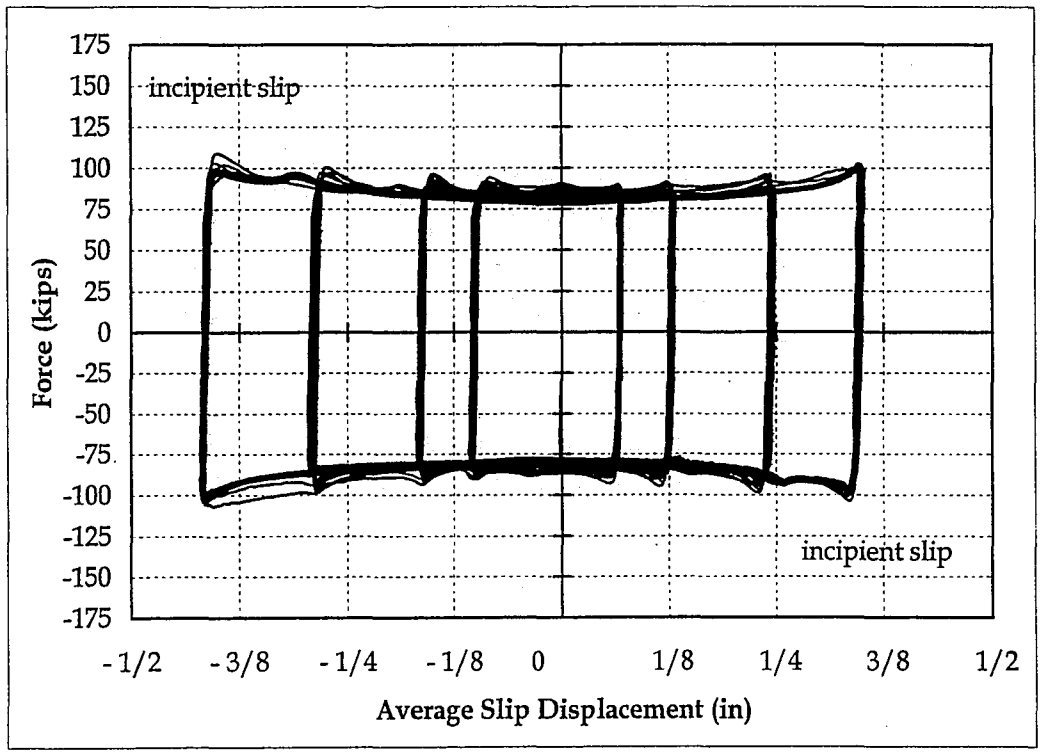

(b)

Figure 5.41. (a) Force vs. Average Cumulative Travel for Test F6; and
(b) Force vs. Average Slip Displacement for Test F6

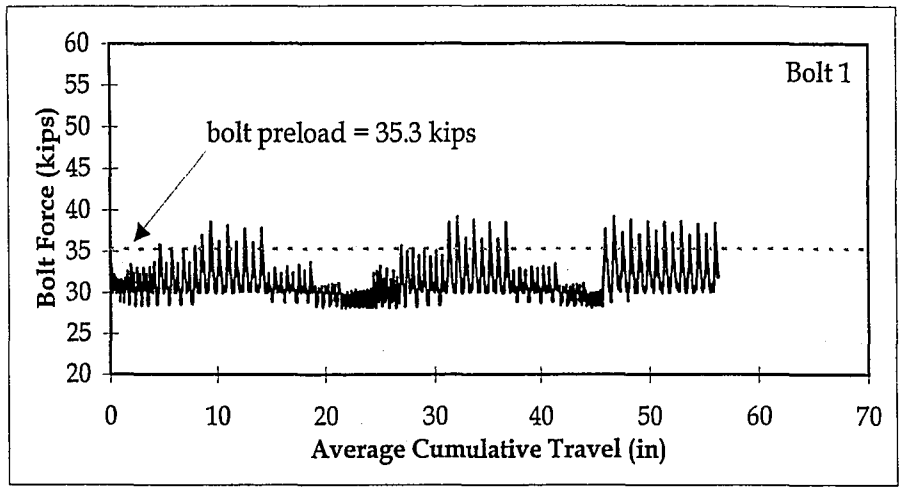

(a)

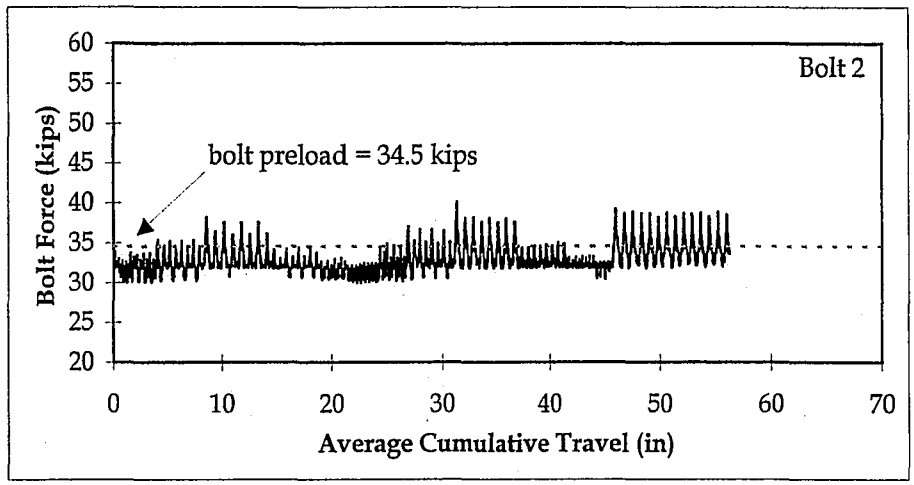

(b)

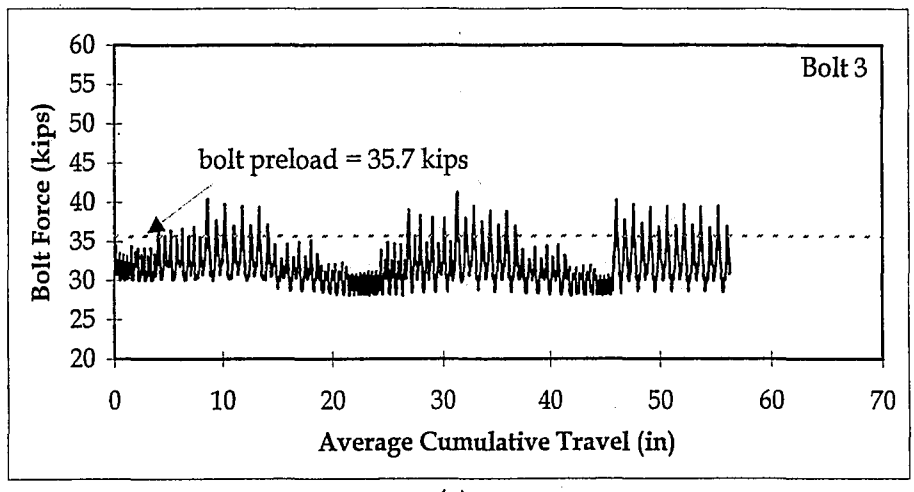

(c)

Figure 5.42. Clamping Bolt Force vs. Average Cumulative Travel for Test F6: (a) Bolt 1; (b) Bolt 2; and (c) Bolt 3

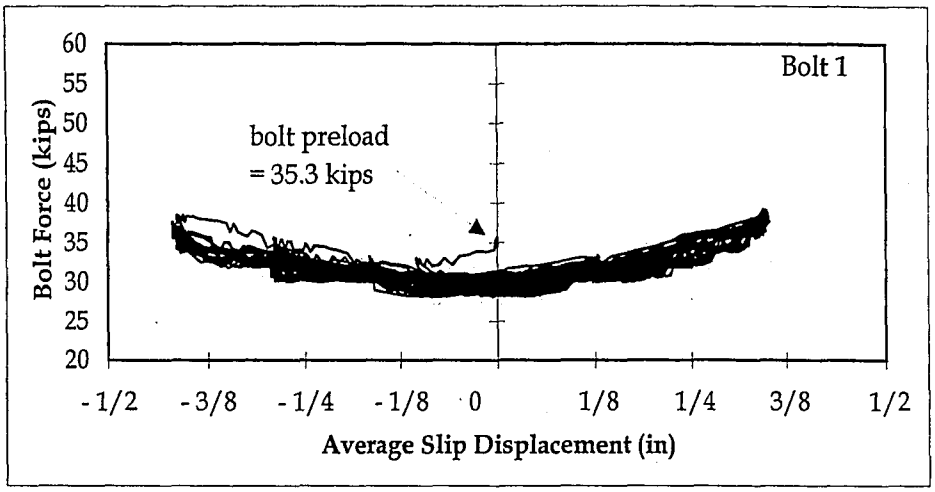

(a)

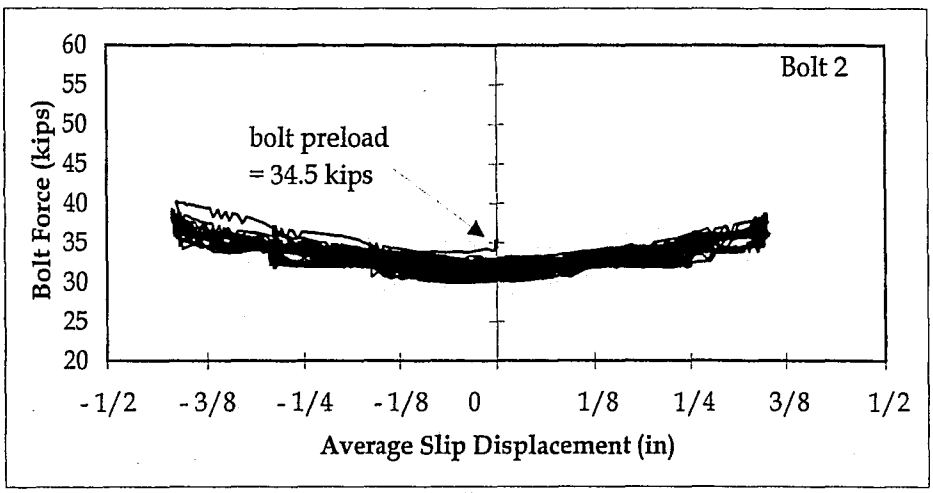

(b)

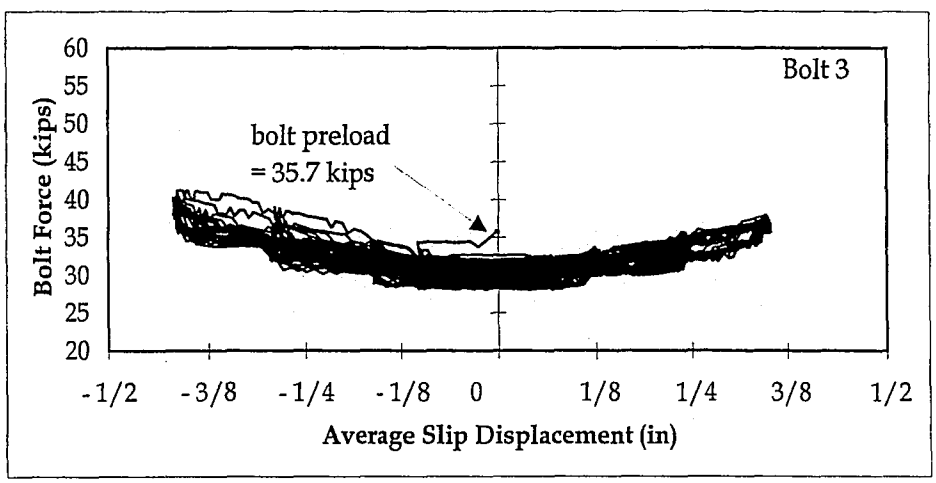

(c)

Figure 5.43. Clamping Bolt Force vs. Average Slip Displacement for Test F6: (a) Bolt 1; (b) Bolt 2; and (c) Bolt 3

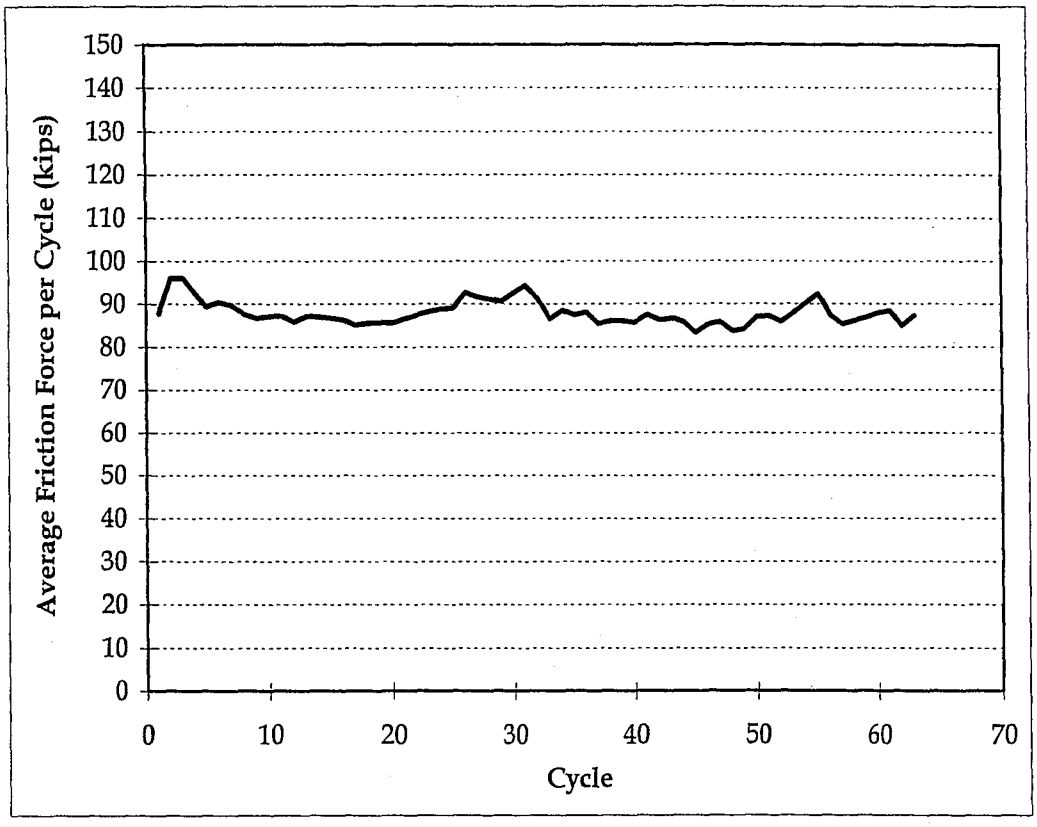

Figure 5.44. Average Friction Force per Cycle for Test F6

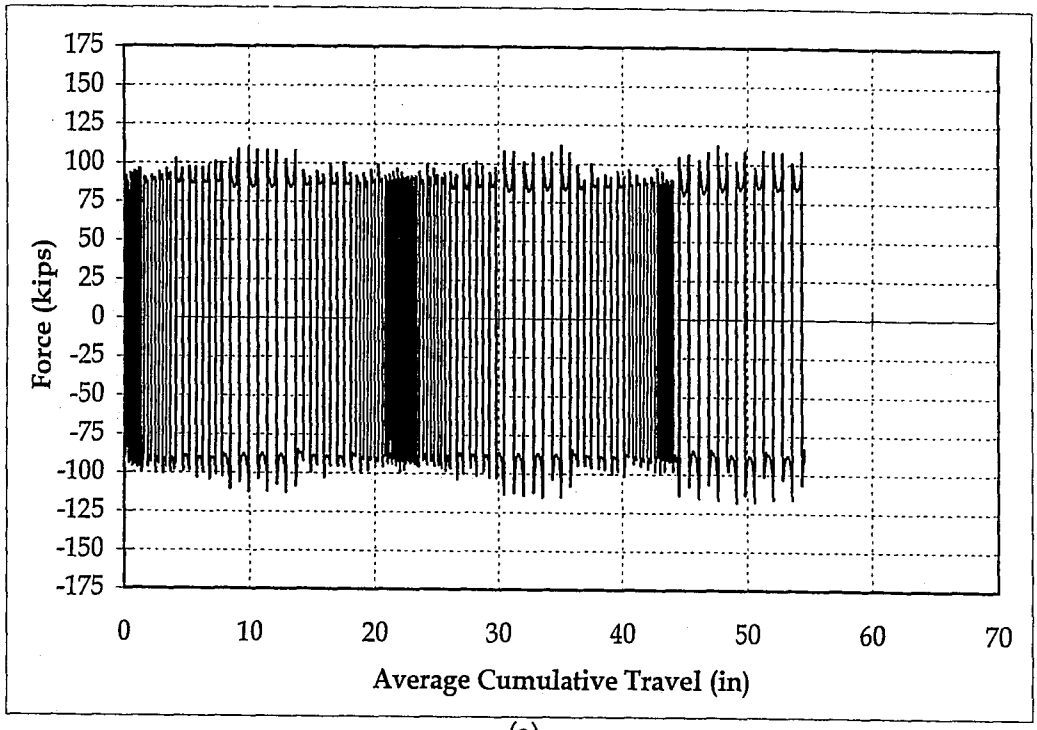

(a)

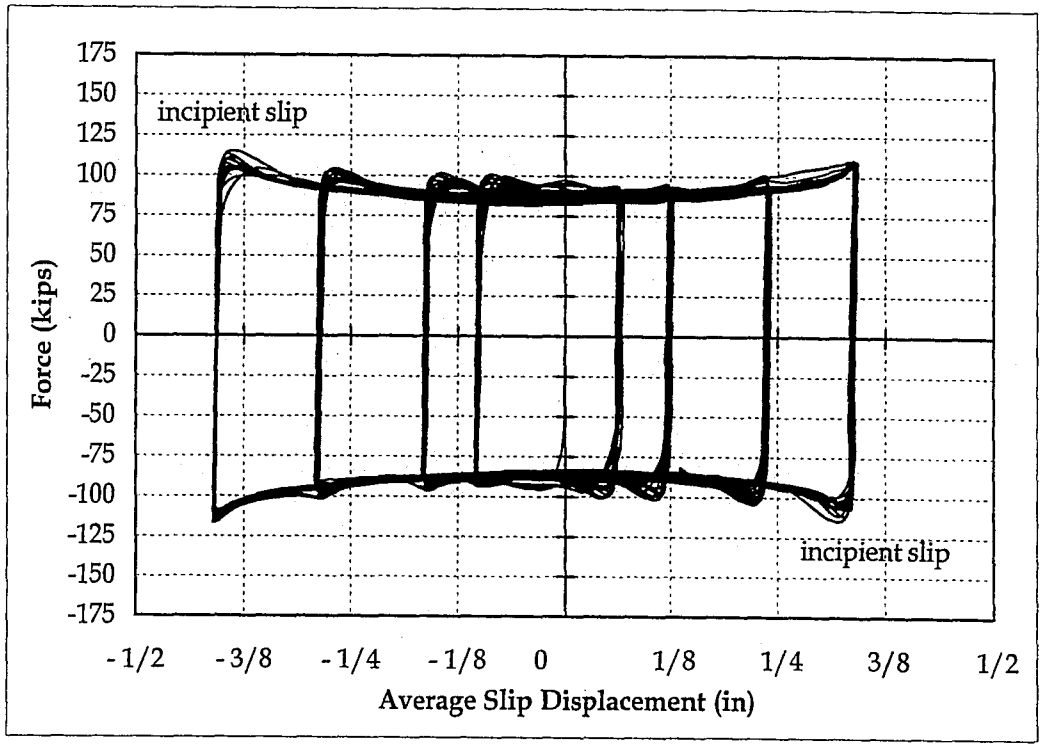

(b)

Figure 5.45. (a) Force vs. Average Cumulative Travel for Test F7; and
(b) Force vs. Average Slip Displacement for Test F7

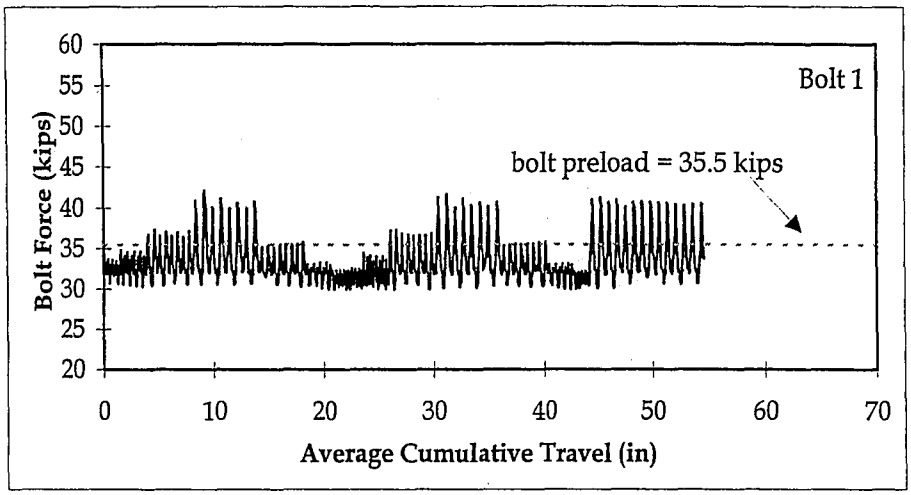

(a)

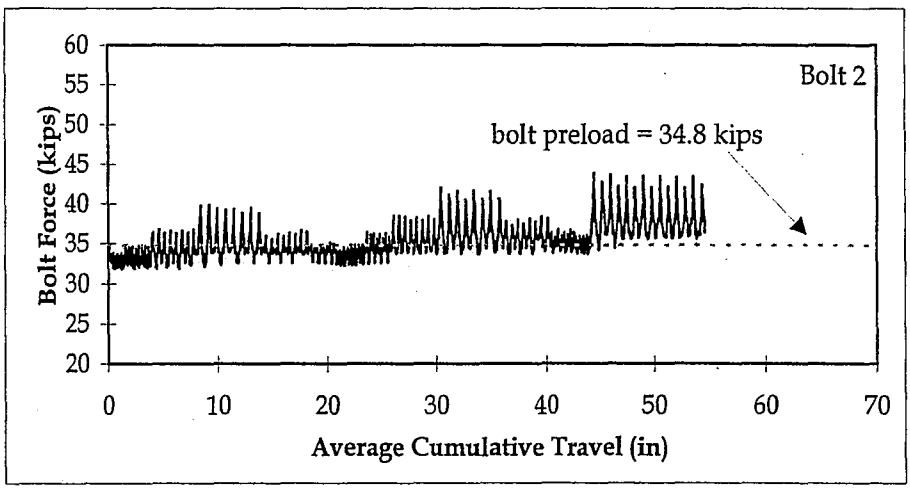

(b)

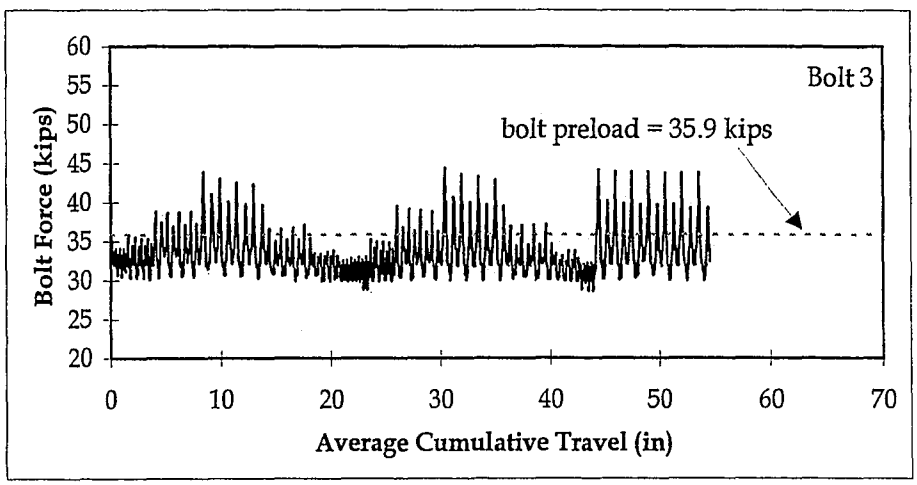

(c)

Figure 5.46. Clamping Bolt Force vs. Average Cumulative Travel for Test F7: (a) Bolt 1; (b) Bolt 2; and (c) Bolt 3

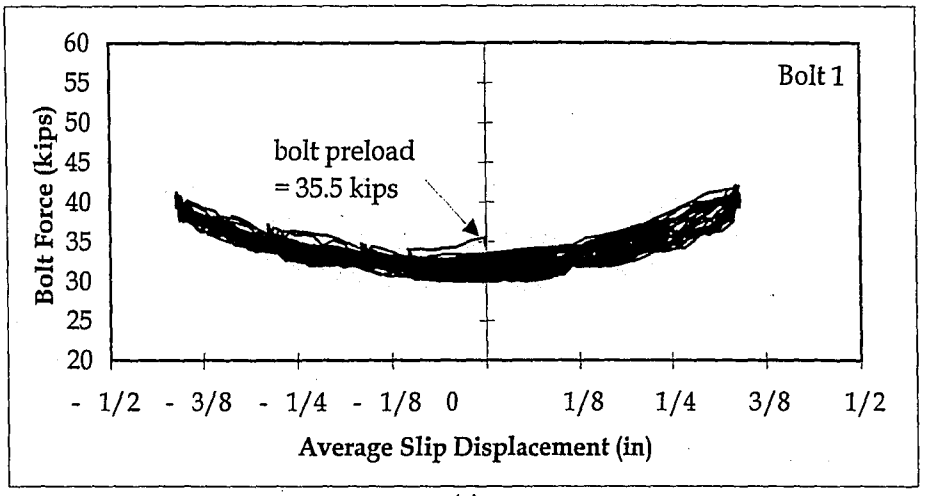

(a)

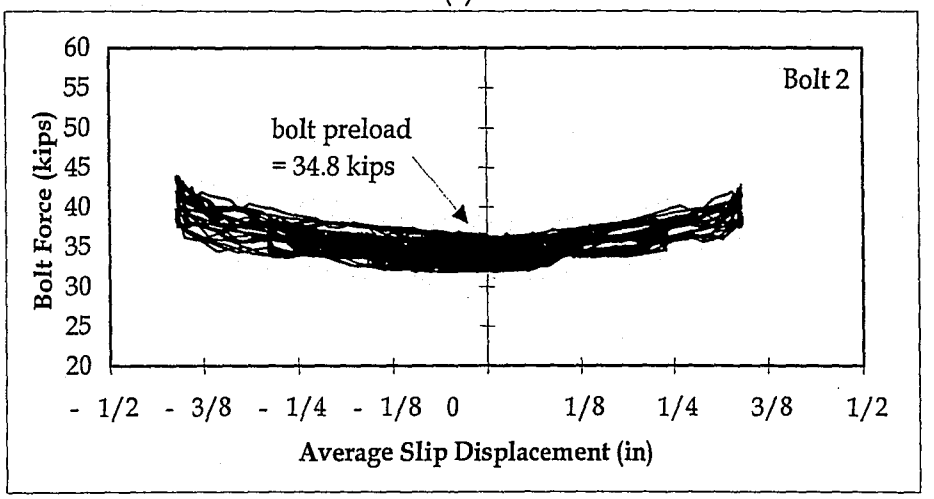

(b)

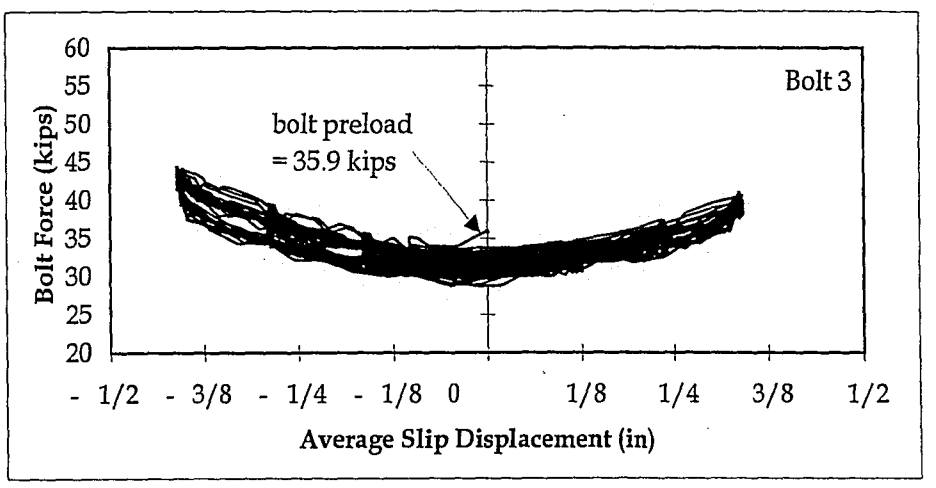

(c)

Figure 5.47. Clamping Bolt Force vs. Average Slip Displacement for Test F7: (a) Bolt 1; (b) Bolt 2; and (c) Bolt 3

Figure 5.48. Average Friction Force per Cycle for Test F7

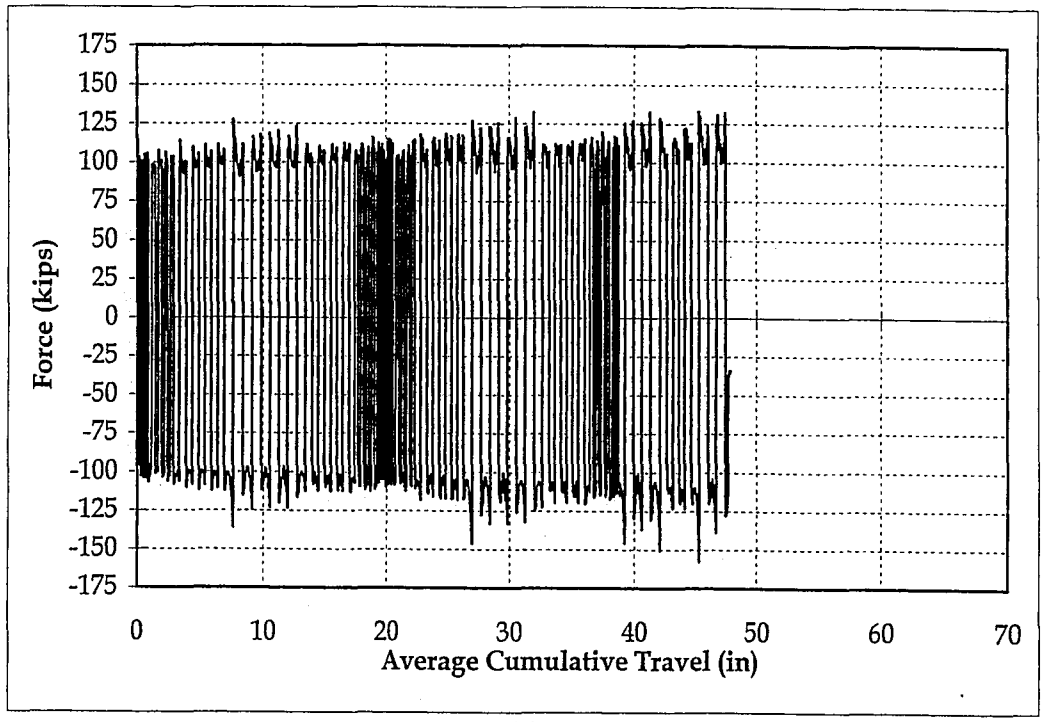

(a)

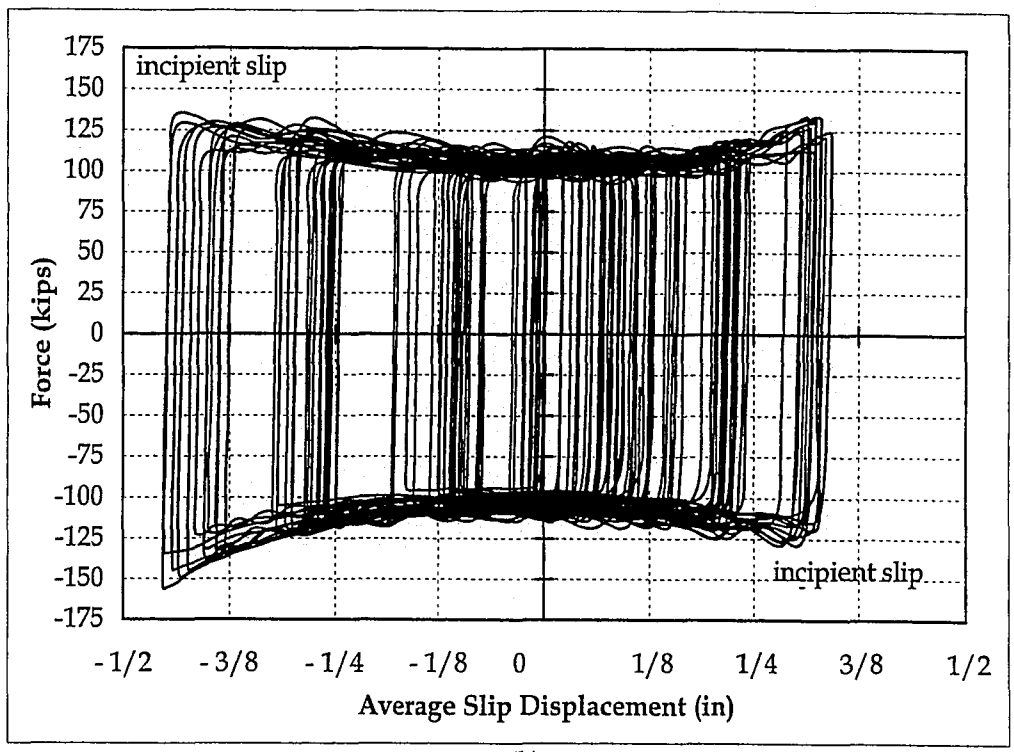

(b)

Figure 5.49. (a) Force vs. Average Cumulative Travel for Test F8; and
(b) Force vs. Average Slip Displacement for Test F8

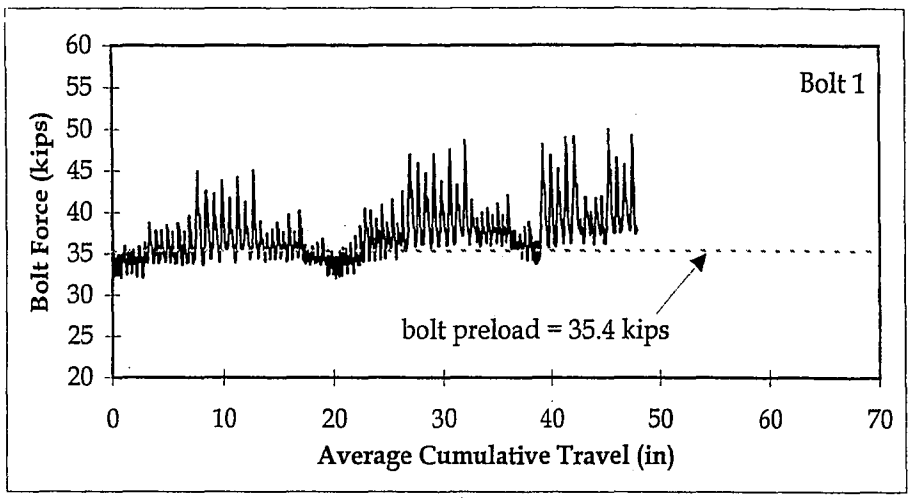

(a)

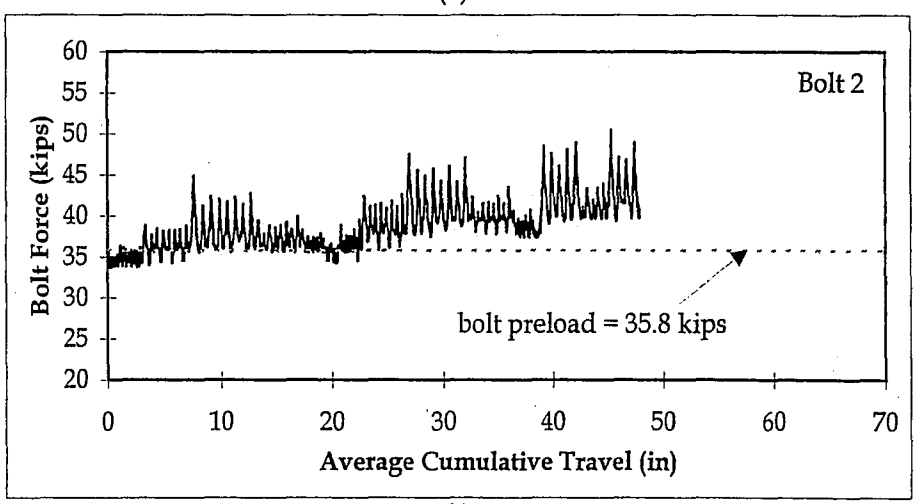

(b)

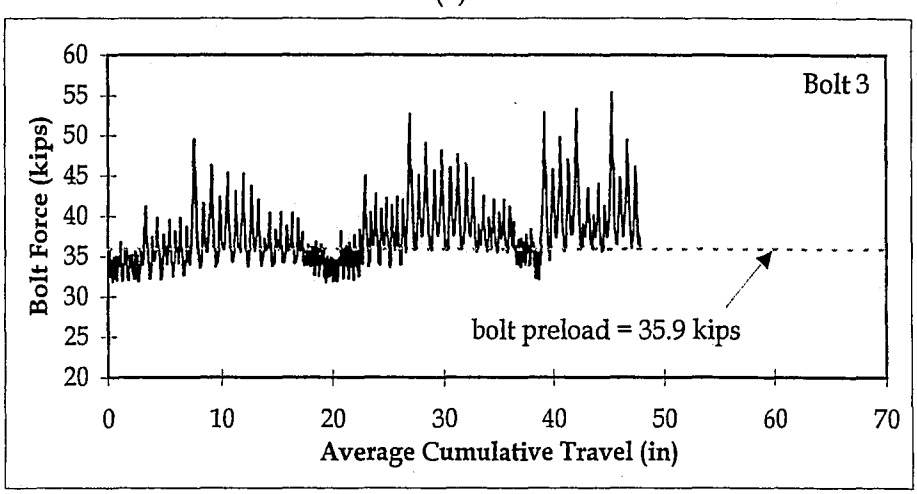

(c)

Figure 5.50. Clamping Bolt Force vs. Average Cumulative Travel for Test F8: (a) Bolt 1; (b) Bolt 2; and (c) Bolt 3

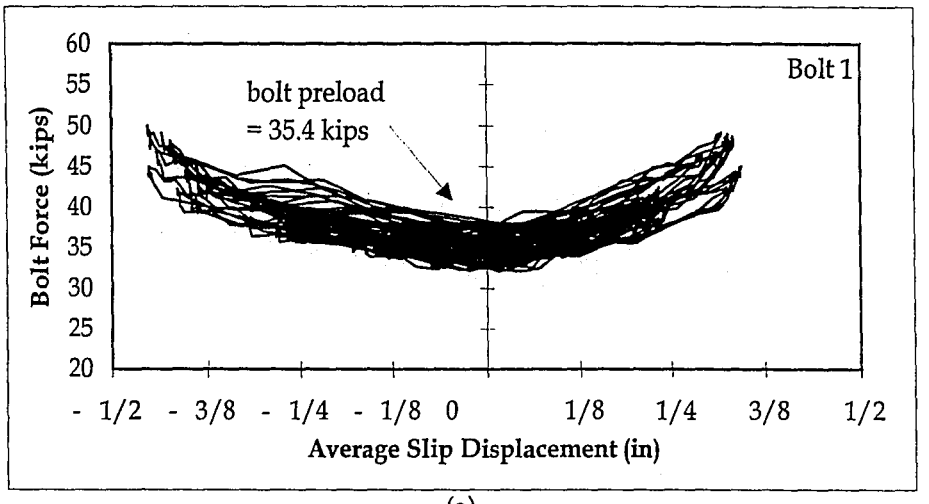

(a)

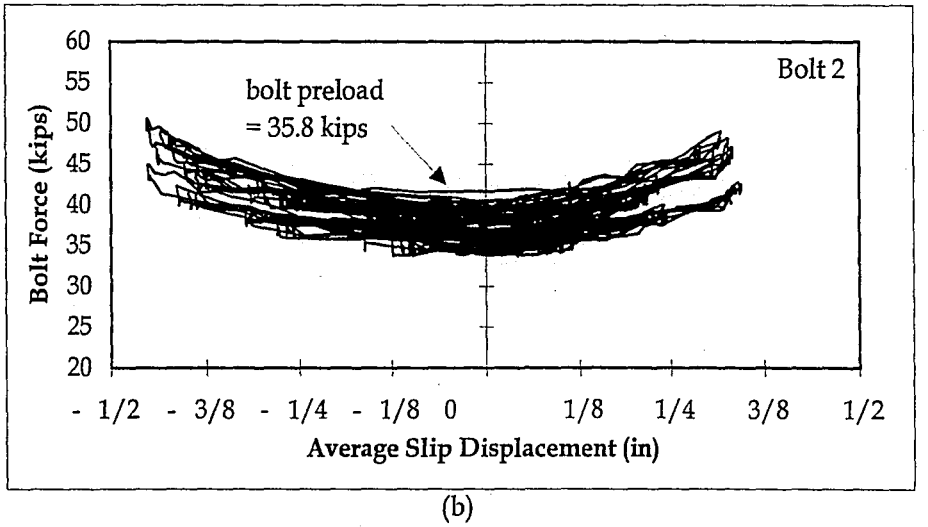

(b)

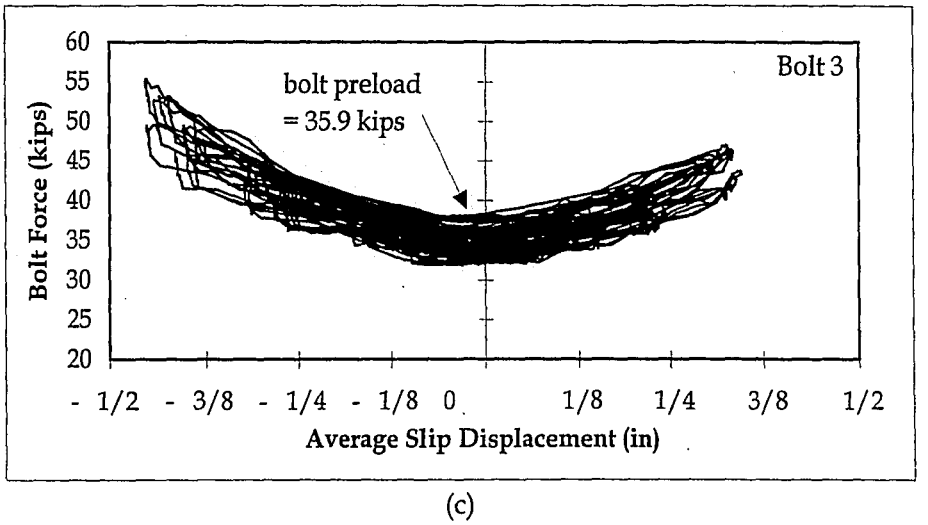

(c)

Figure 5.51. Clamping Bolt Force vs. Average Slip Displacement for Test F8: (a) Bolt 1; (b) Bolt 2; and (c) Bolt 3

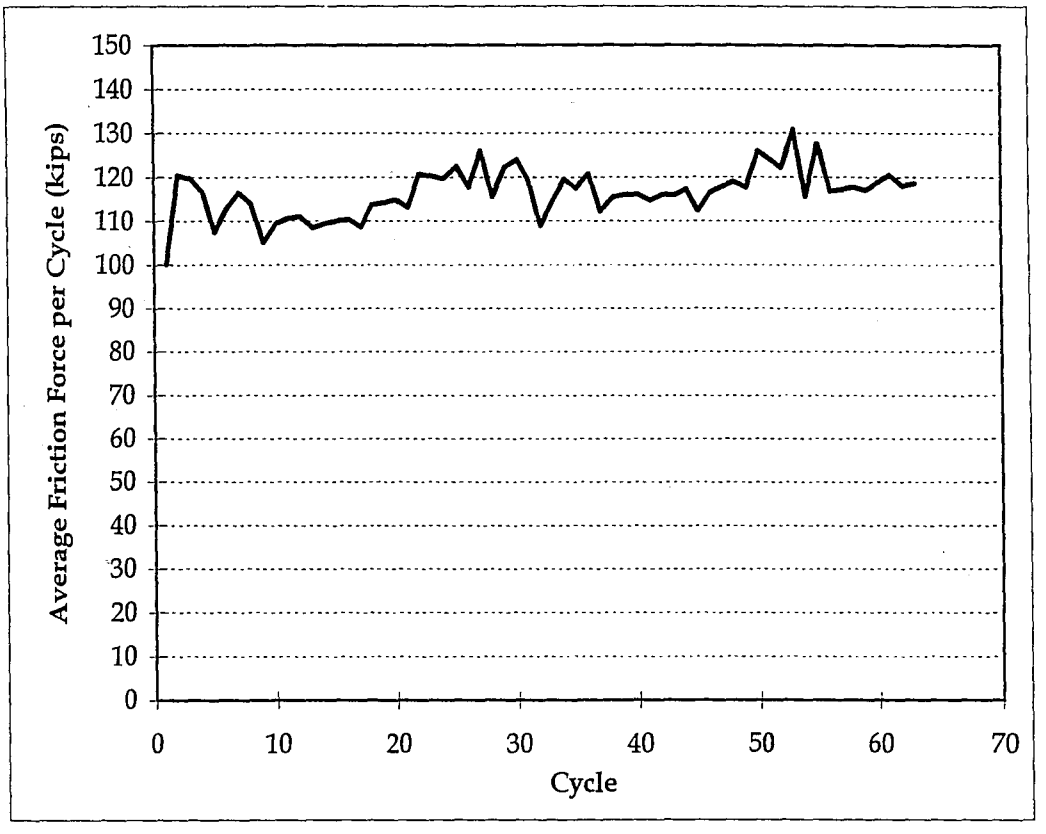

Figure 5.52. Average Friction Force per Cycle for Test F8

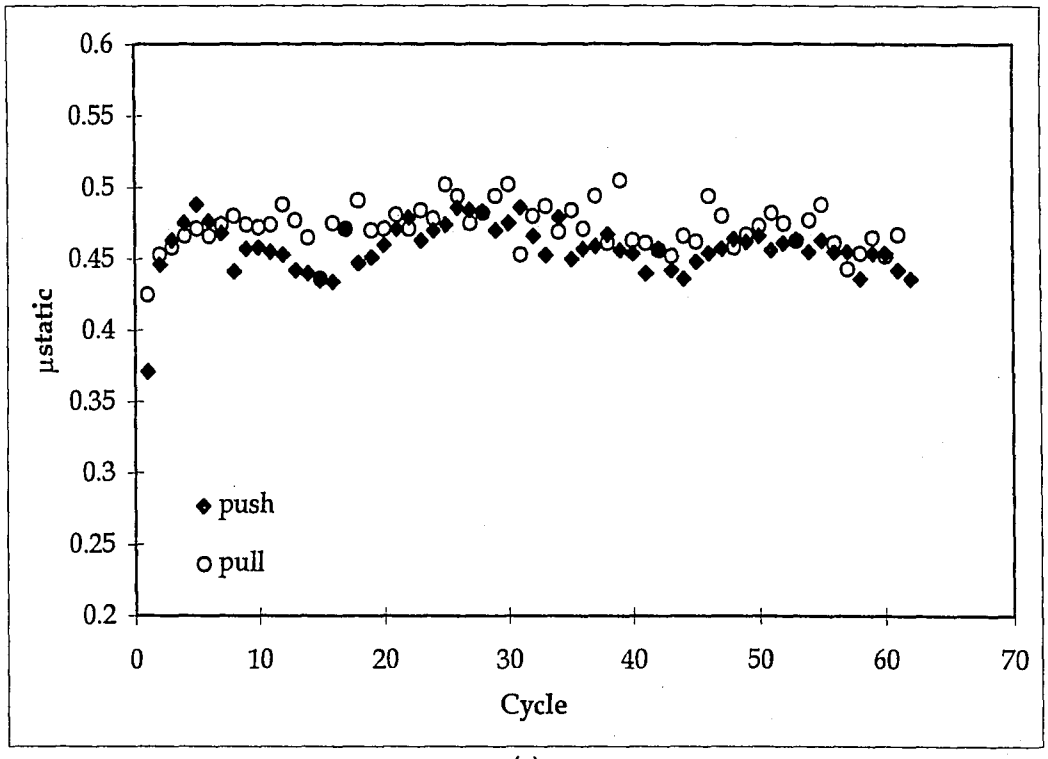

(a)

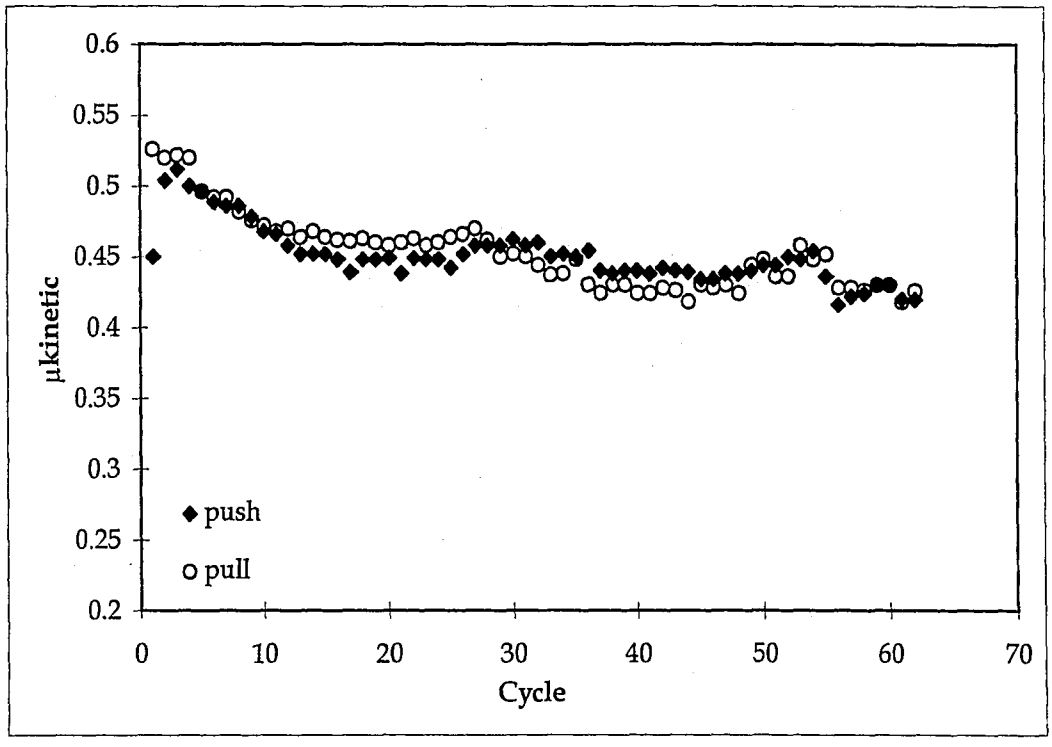

(b)

Figure 5.53. Coefficients of Friction in Each Cycle of Test F1:
(a) Static; and (b) Kinetic

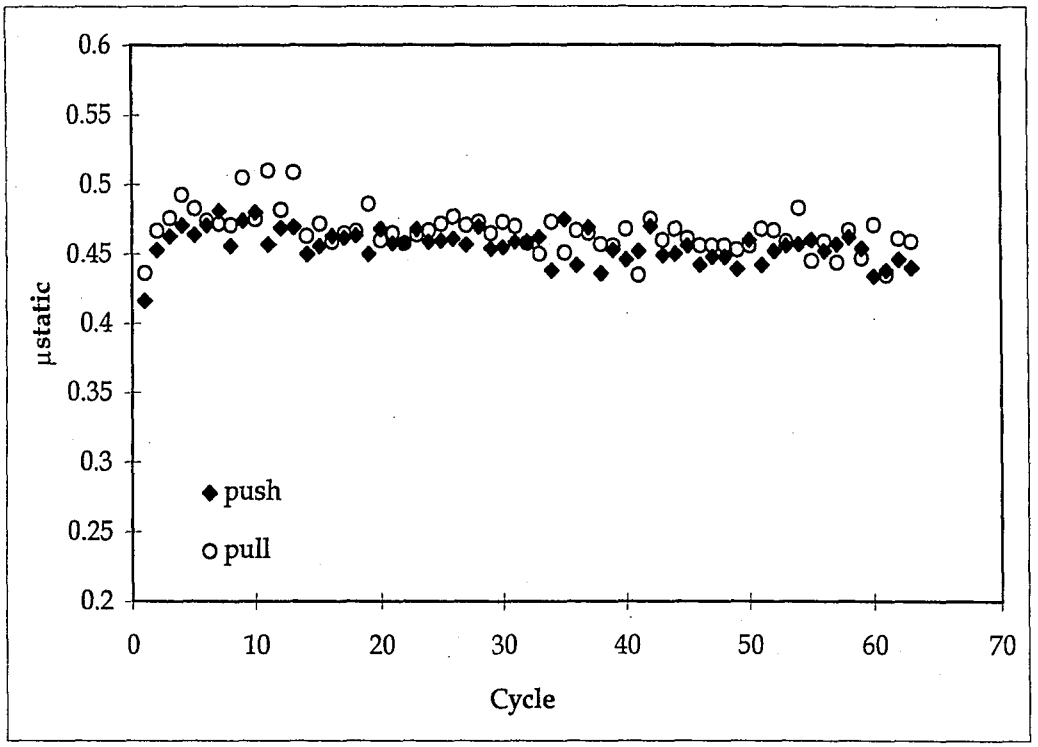

(a)

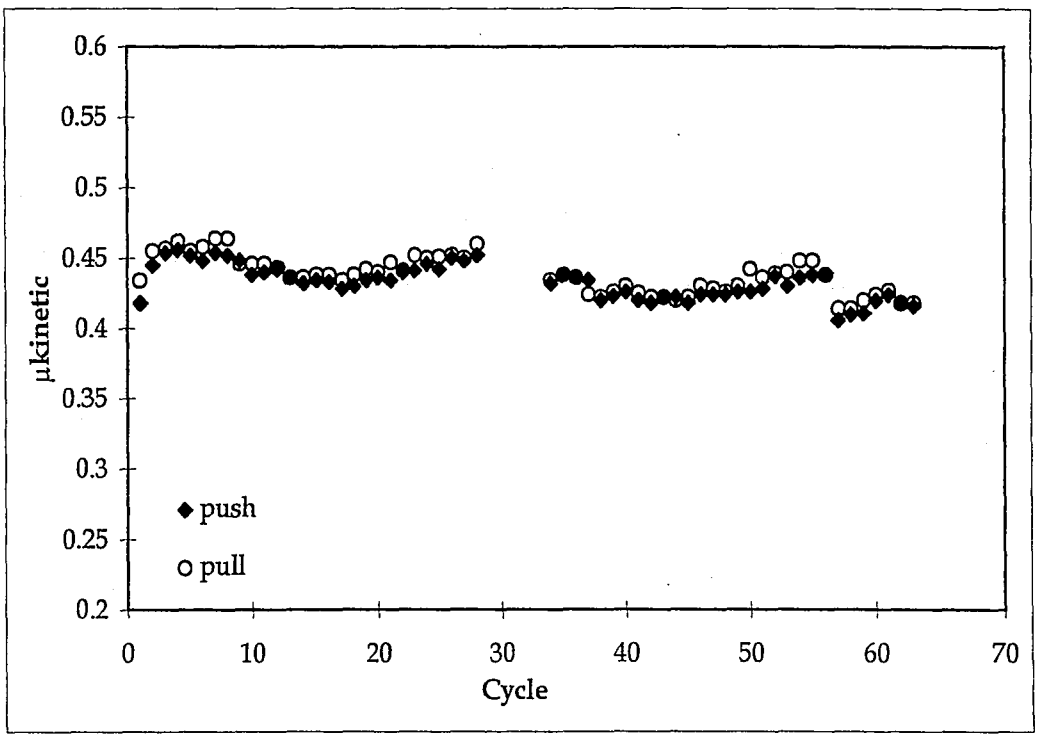

(b)

Figure 5.54. Coefficients of Friction in Each Cycle of Test F2:
(a) Static; and (b) Kinetic

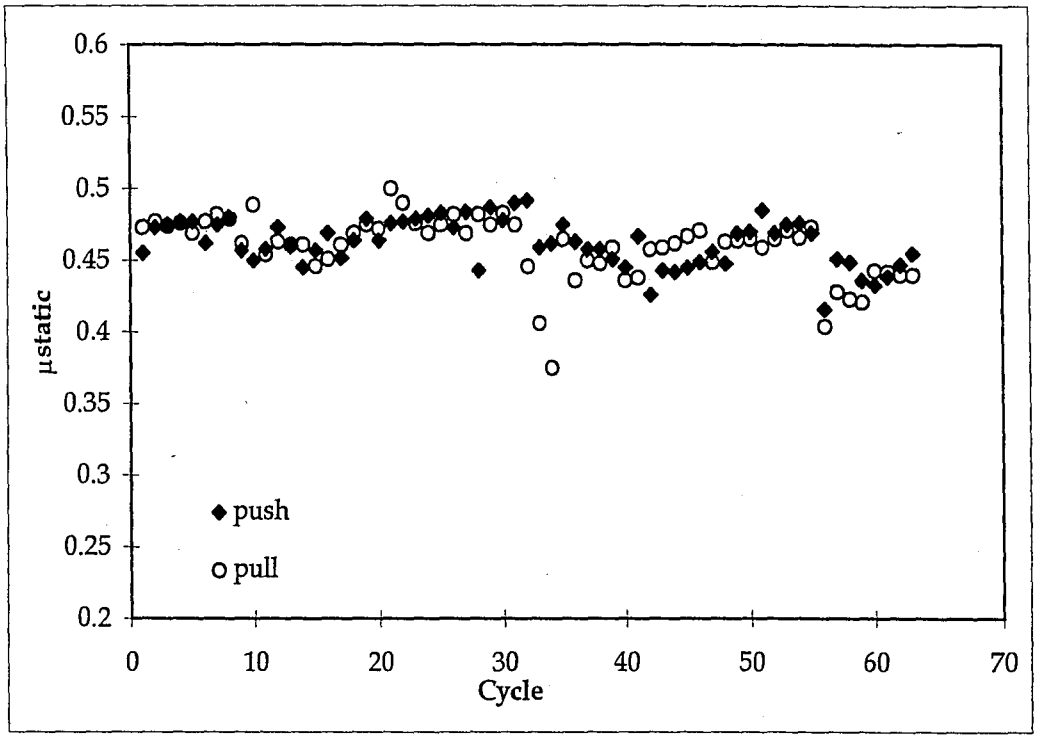

(a)

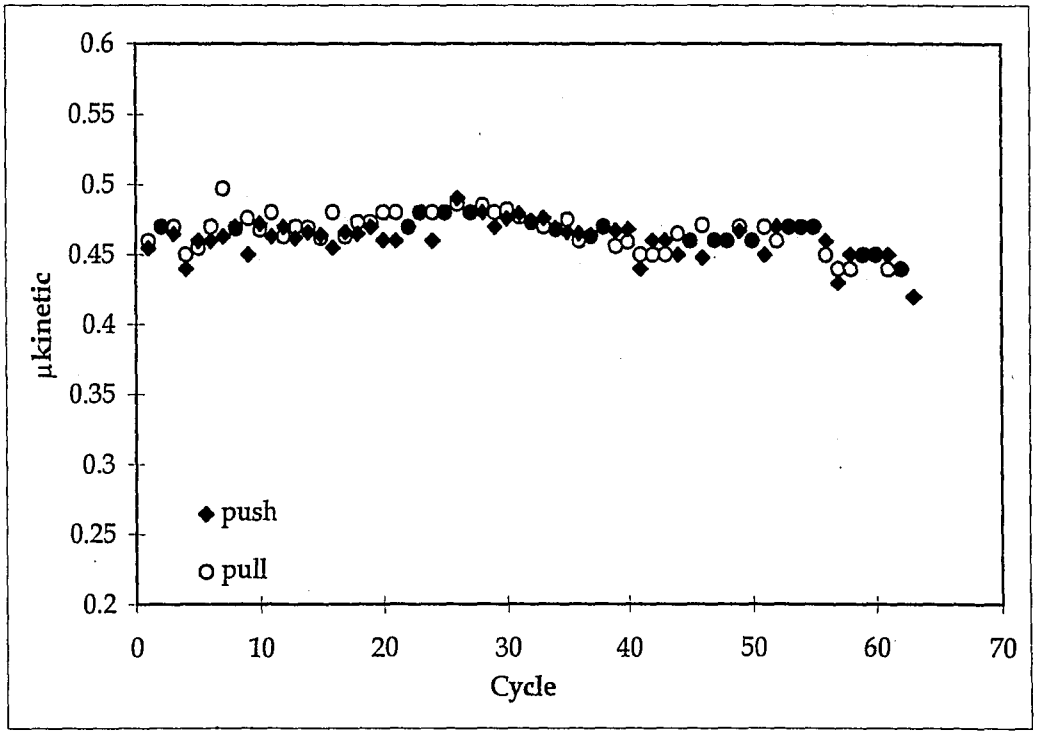

(b)

Figure 5.55. Coefficients of Friction in Each Cycle of Test F3:
(a) Static; and (b) Kinetic

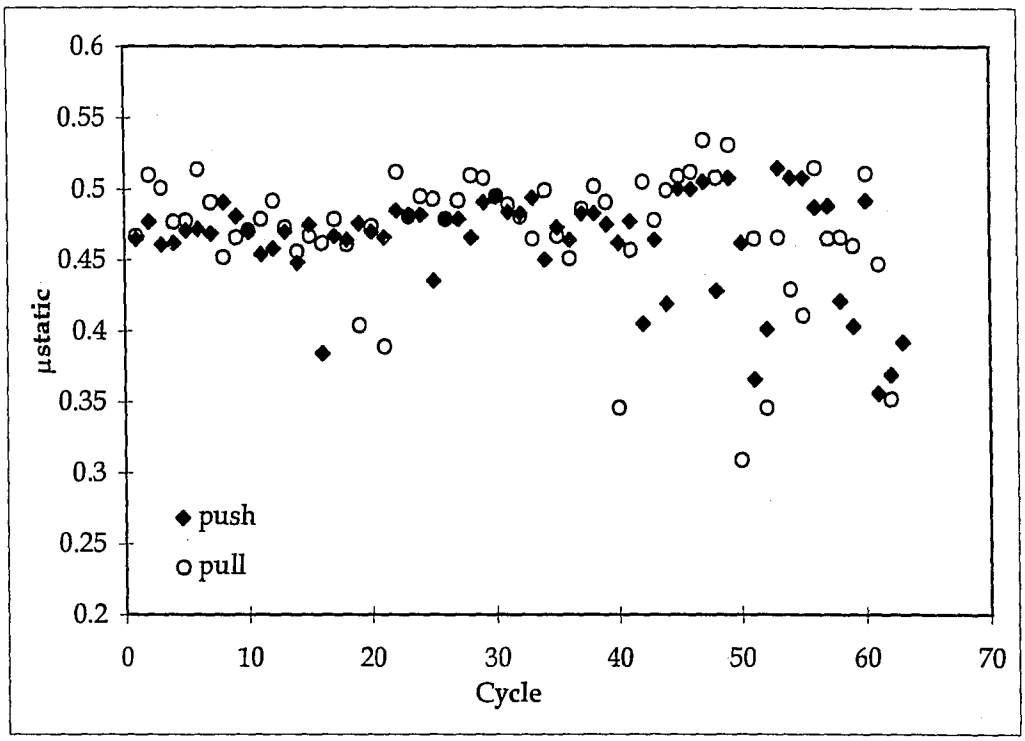

(a)

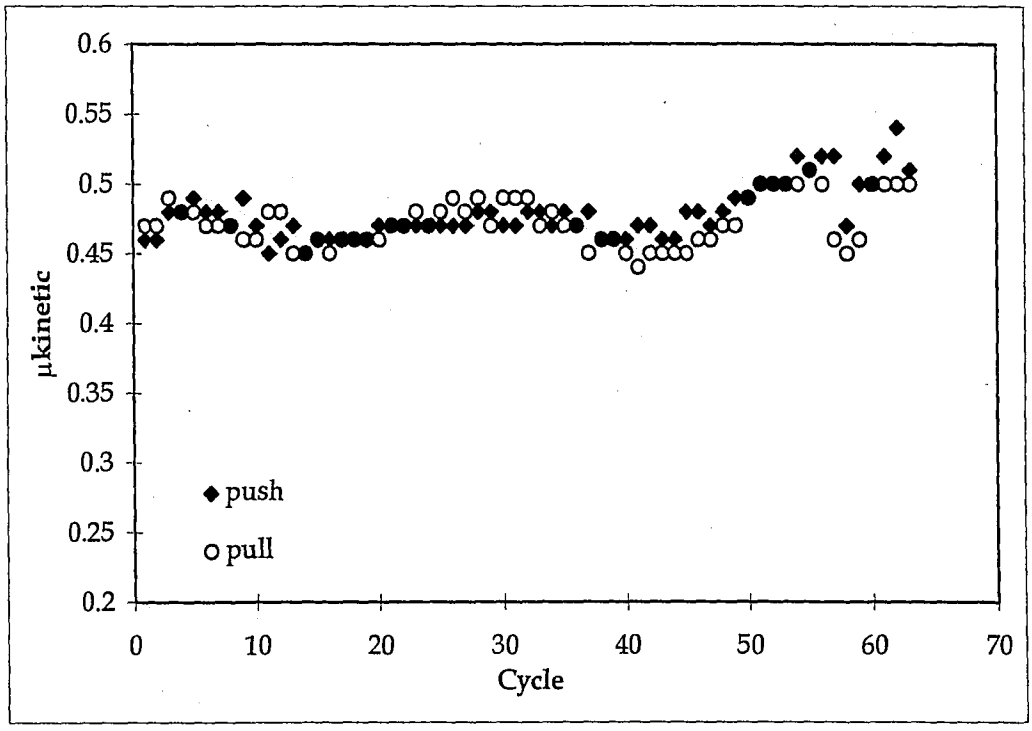

(b)

Figure 5.56. Coefficients of Friction in Each Cycle of Test F4:
(a) Static; and (b) Kinetic

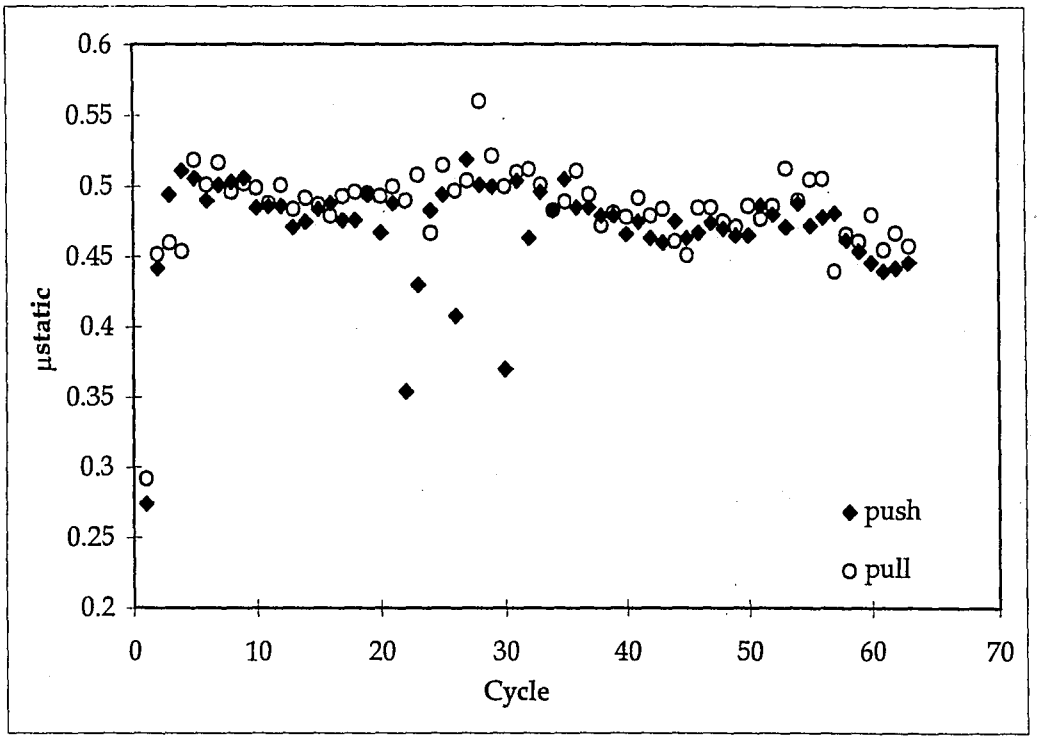

(a)

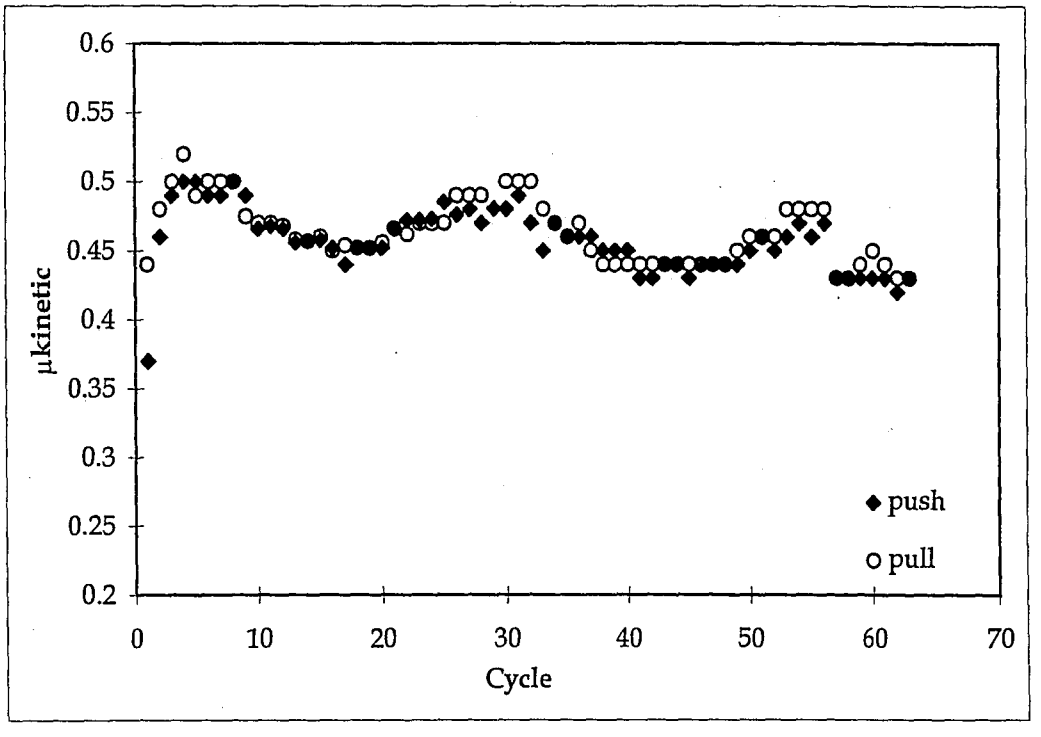

(b)

Figure 5.57. Coefficients of Friction in Each Cycle of Test F5:
(a) Static; and (b) Kinetic

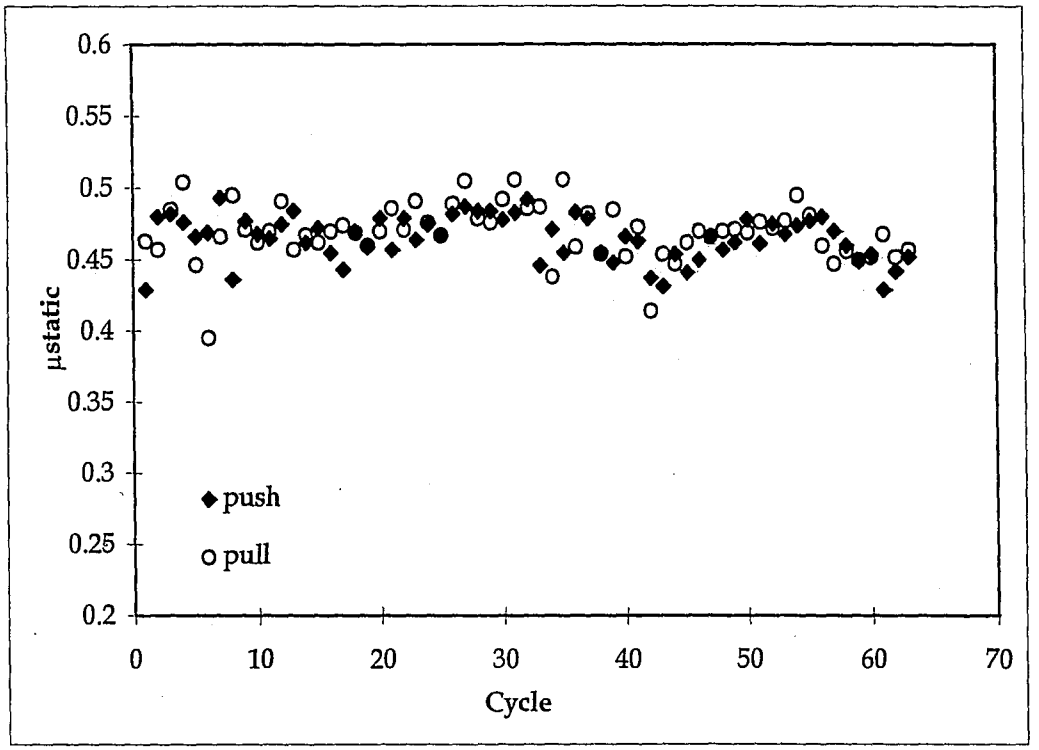

(a)

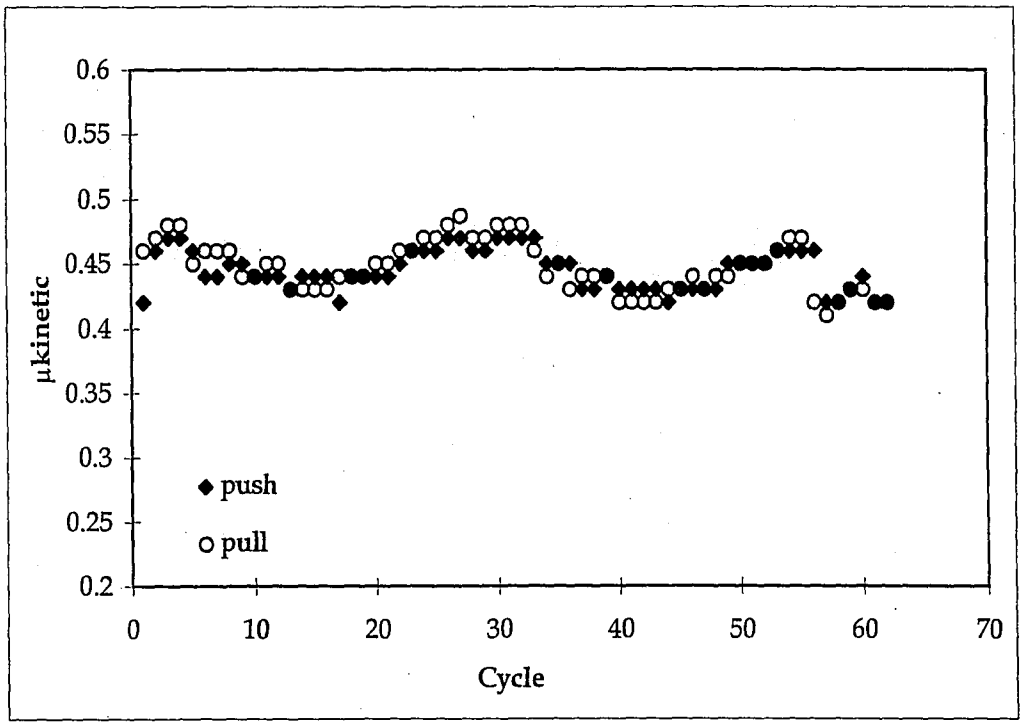

(b)

Figure 5.58. Coefficients of Friction in Each Cycle of Test F6;
(a) Static; and (b) Kinetic

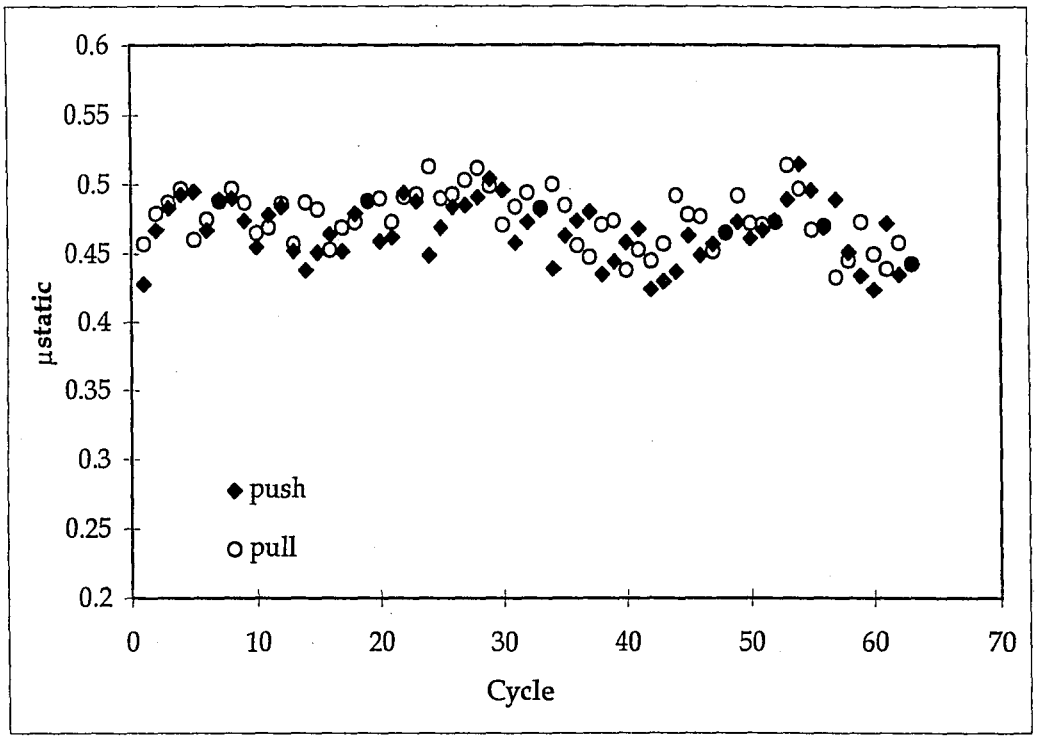

(a)

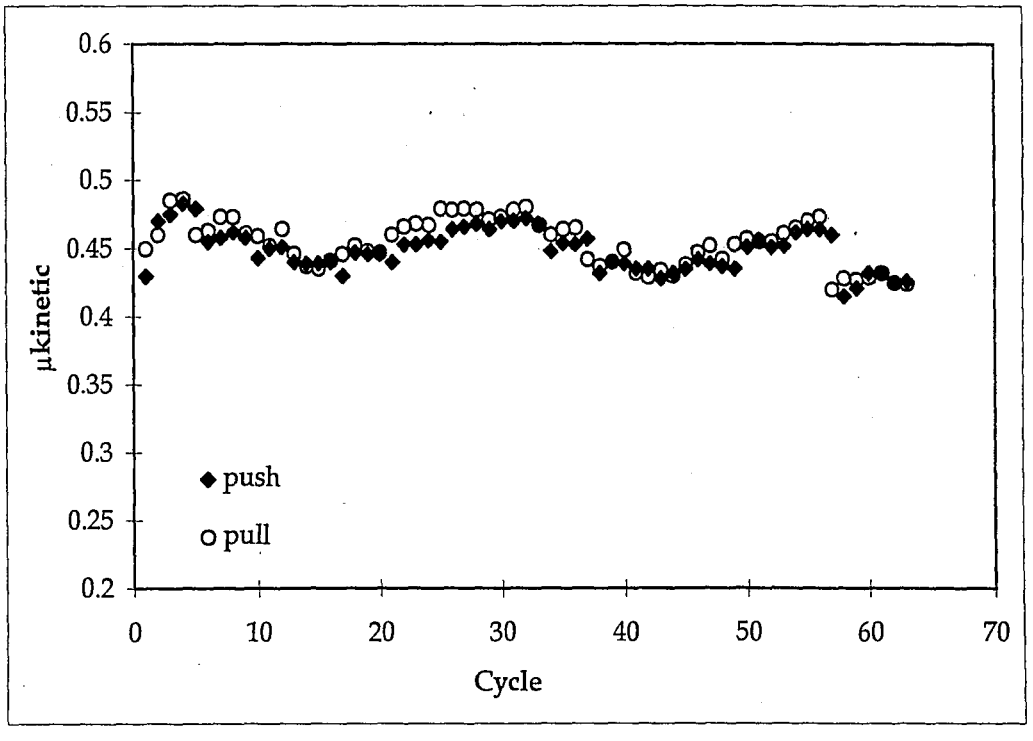

(b)

Figure 5.59. Coefficients of Friction in Each Cycle of Test F7:
(a) Static; and (b) Kinetic

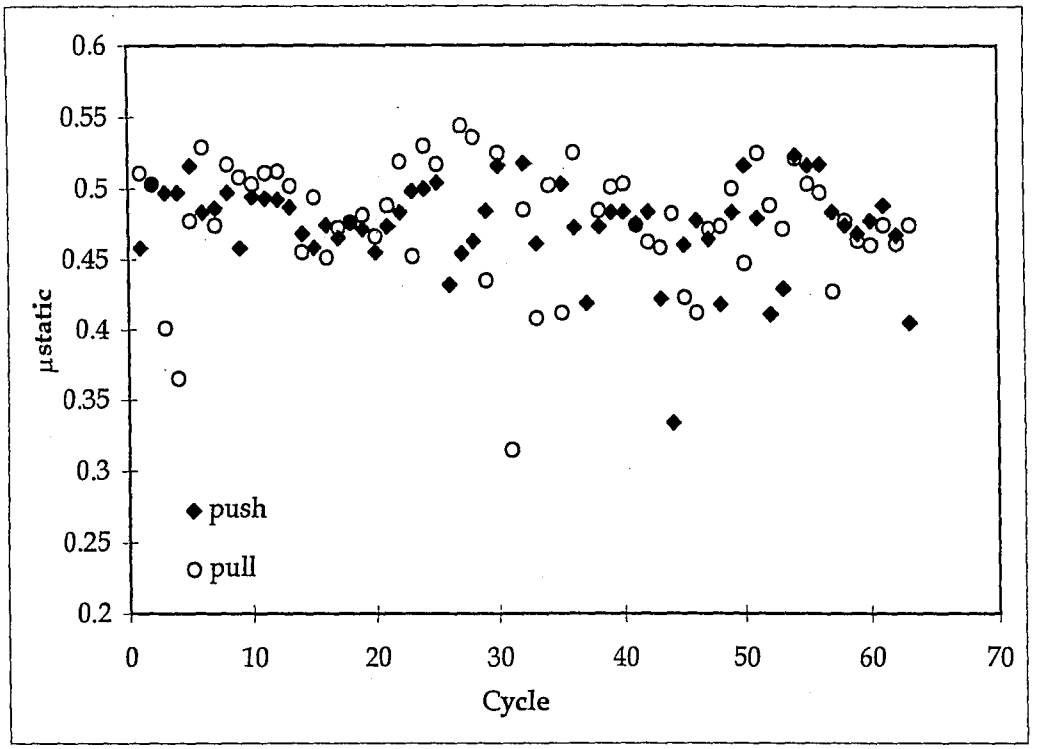

(a)

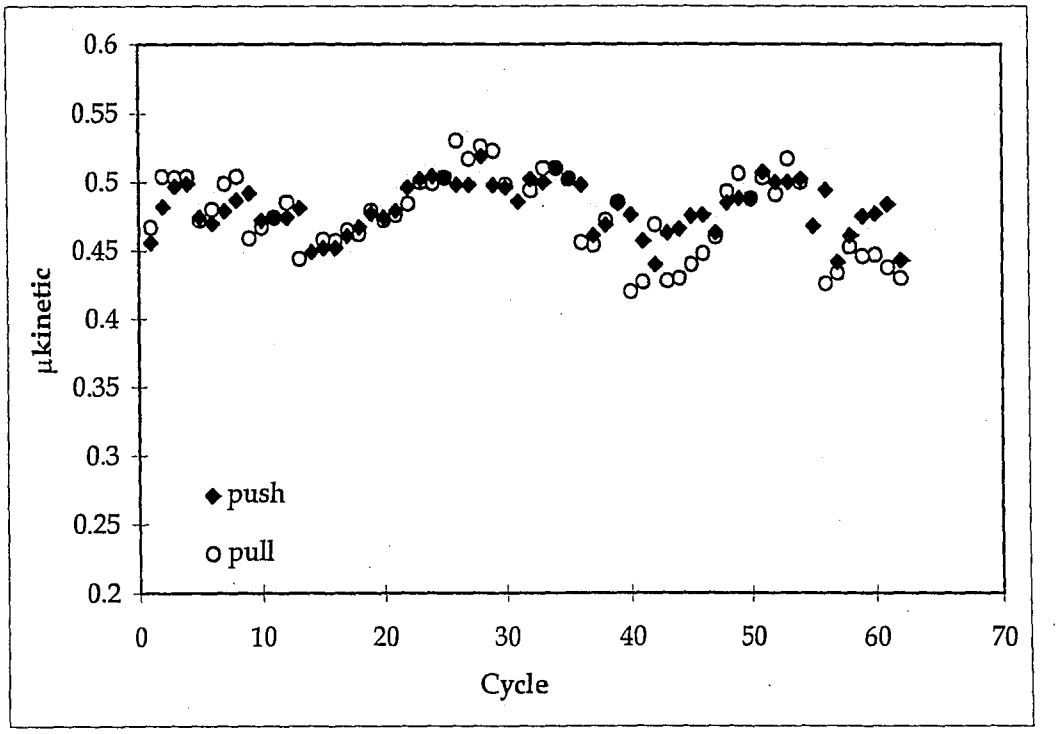

(b)

Figure 5.60. Coefficients of Friction in Each Cycle of Test F8:
(a) Static; and (b) Kinetic

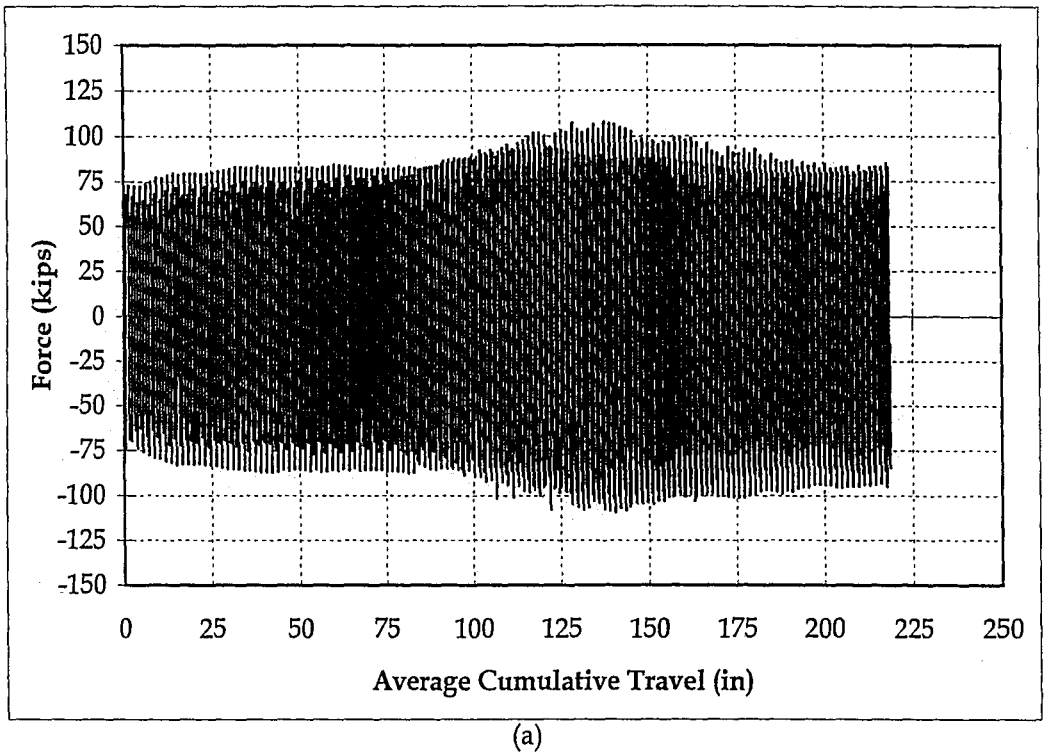

(a)

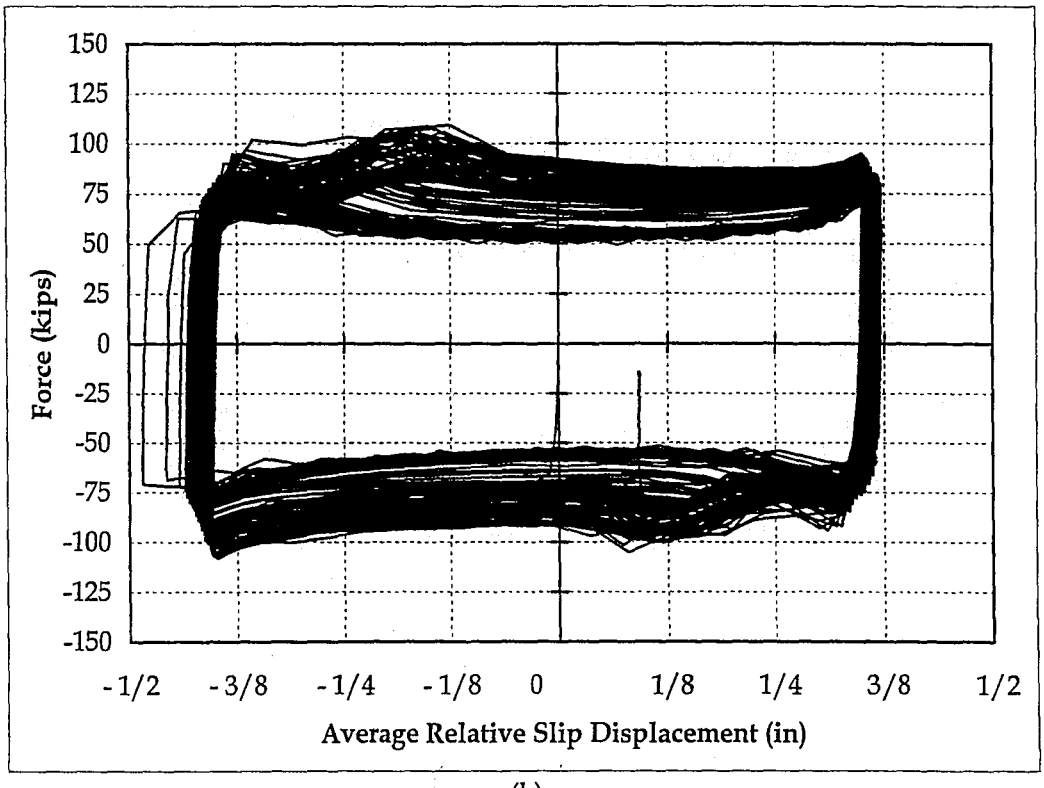

(b)

Figure 5.61. (a) Force vs. Average Cumulative Travel for Test F9; and
(b) Force vs. Average Slip Displacement for Test F9

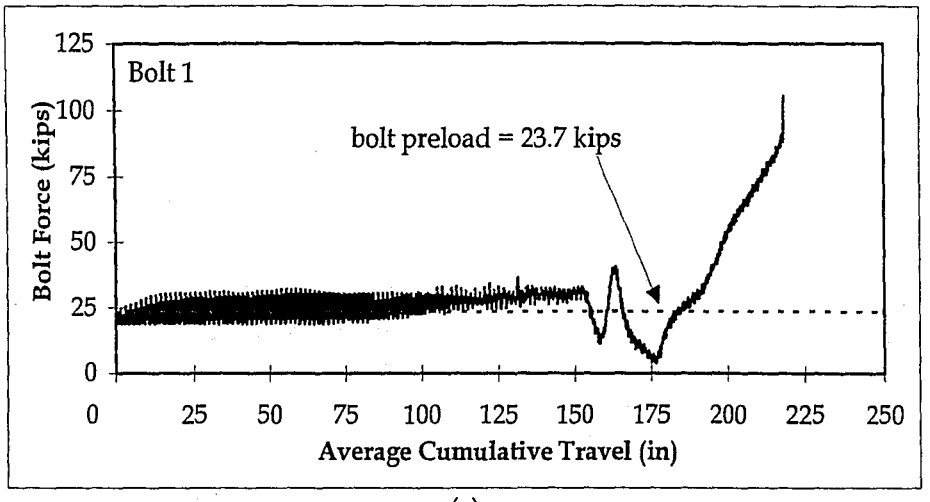

(a)

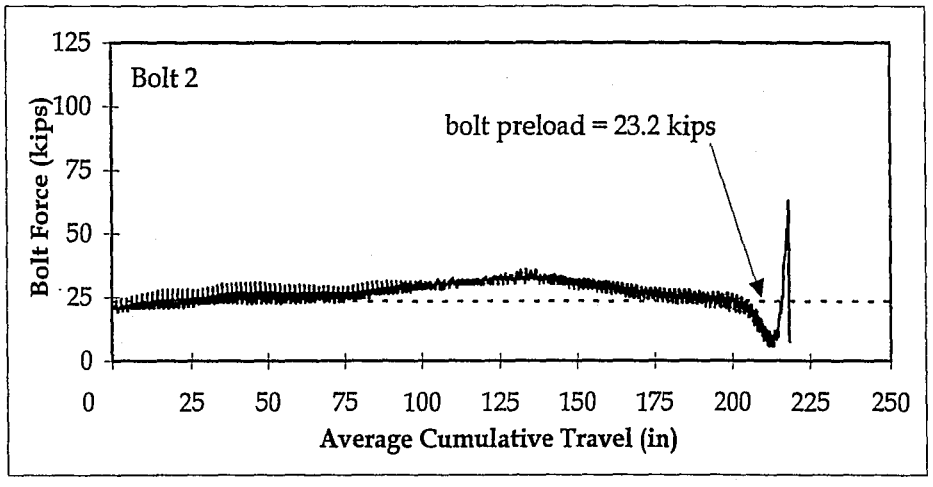

(b)

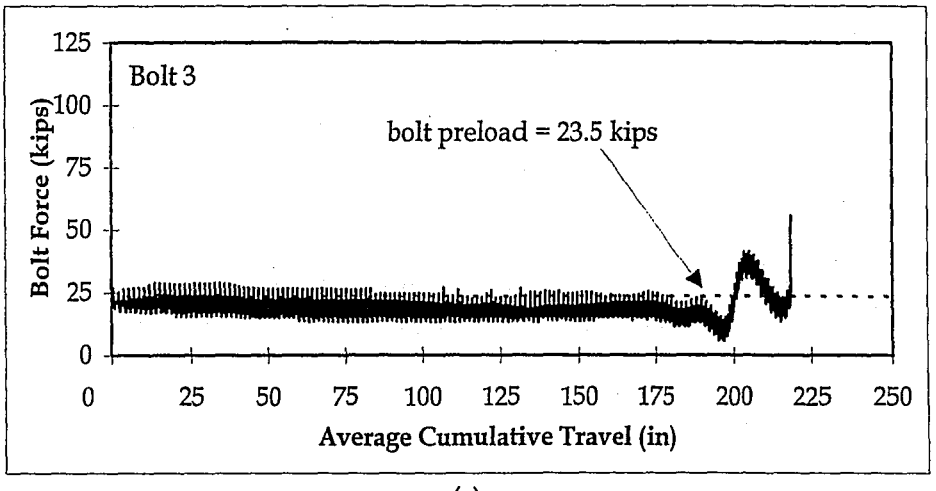

(c)

Figure 5.62. Clamping Bolt Force vs. Average Cumulative Travel for Test F9: (a) Bolt 1; (b) Bolt 2; and (c) Bolt 3

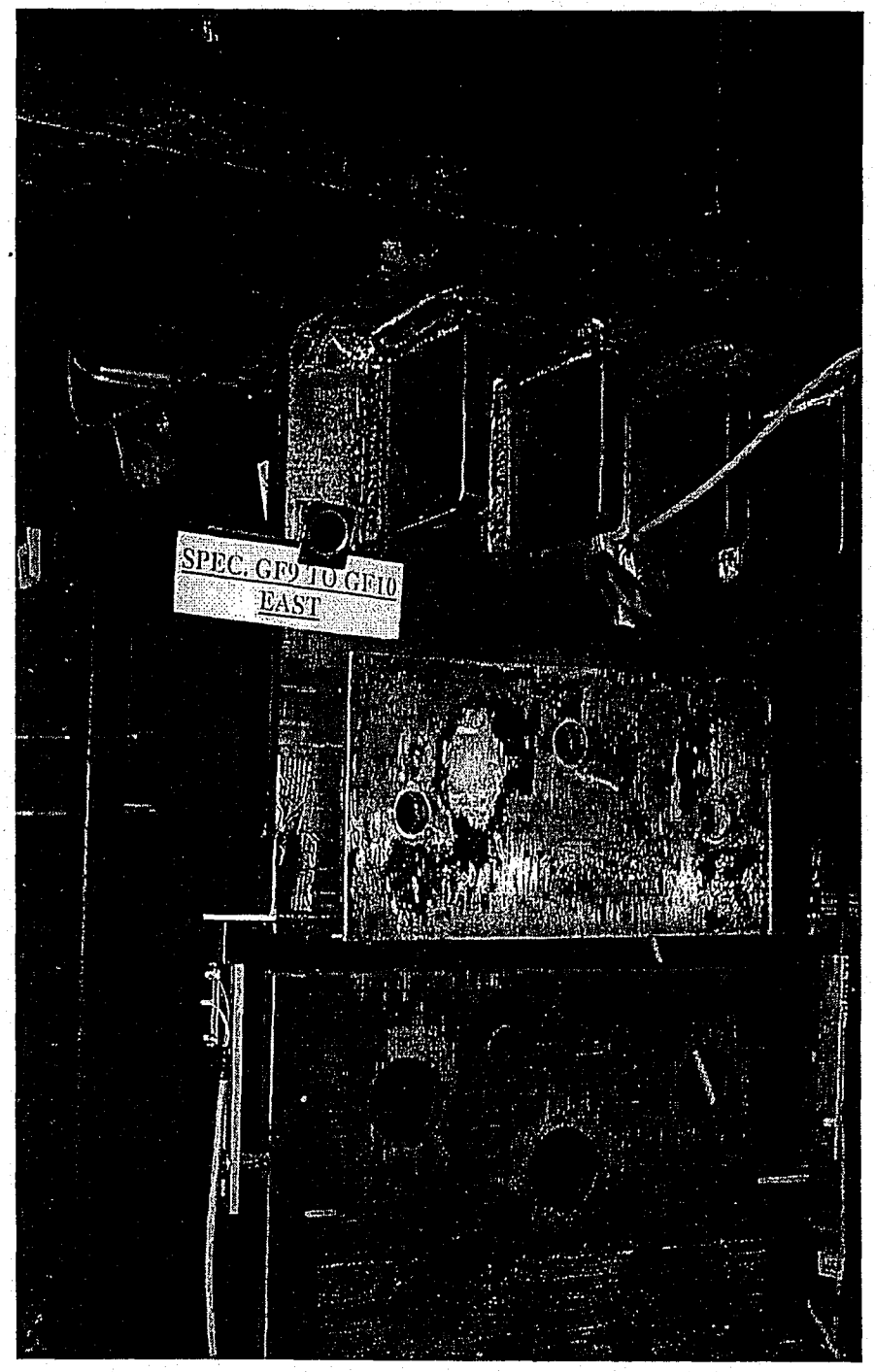

Figure 5.63. Fusing of the Brass-Steel Tribo Surface during Test F9

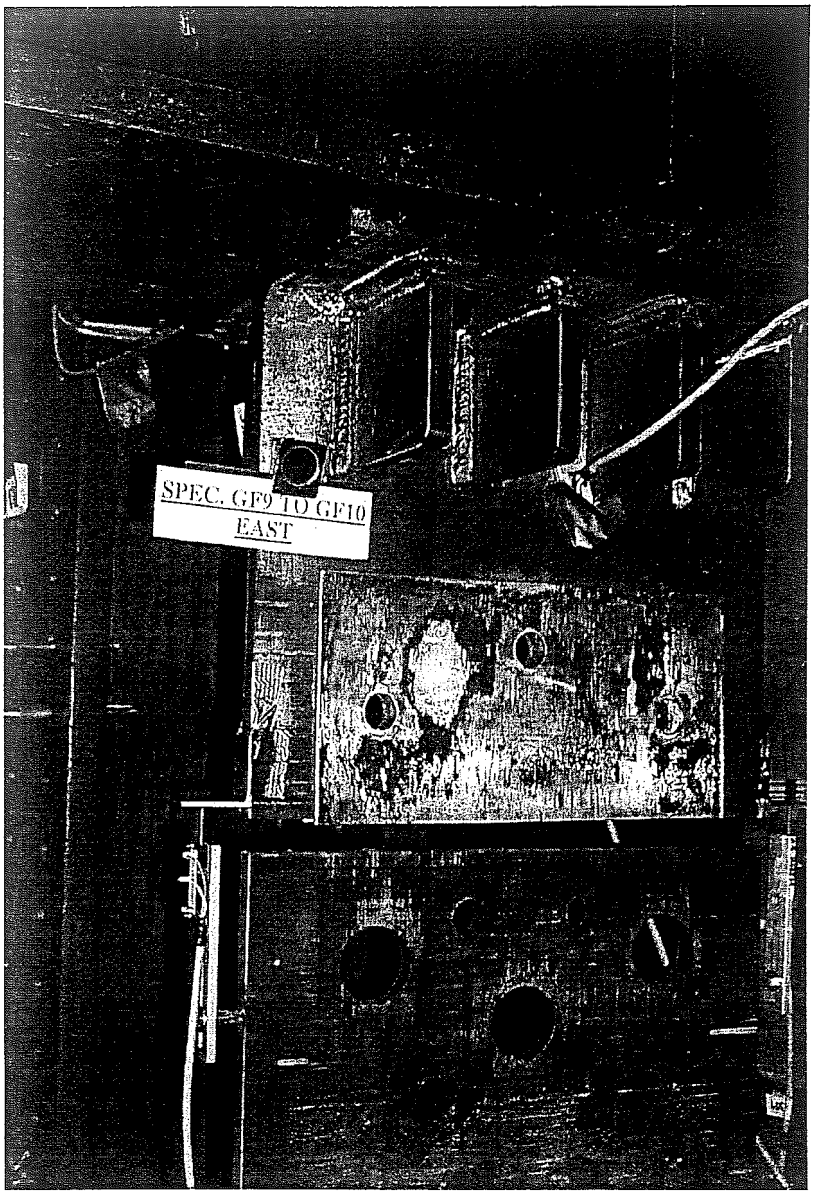

Figure 5.63. Fusing of the Brass-Steel Tribo Surface during Test F9

6. Double Angle Friction Connection Component Tests

This chapter presents results of the double angle friction connection component (FCC) tests. A total of sixteen brass-steel FCC tests were conducted as shown in Table 6.1. The tests studied: (1) the friction behavior of the double angle FCC; (2) the repeatability of the friction behavior; (3) the effects of the displacement (i.e., slip) rate on the friction behavior; (4) and the durability of the brass-steel tribo surfaces. Possible assembly sequences of the FCC were also studied based on typical steel frame erection procedures used in practice. The procedures described in Section 4.5 were used in the tests. Figure 6.1 shows the FCC assembled in the test frame at the beginning of the tests.

The double angle FCC tests were similar to the double plate friction tests. One series of tests was conducted using clamping bolt preloads of 23 kips/bolt, and one series of tests was conducted using clamping bolt preloads of 35 kips/bolt. Other test investigated the effects of the assembly sequence. For the first test of each group, tests FCC2 and FCC5, unworn brass shims were used. The second test in each group, tests FCC2A and FCC6, studied possible variations in the friction behavior due to wearing of the brass shim tribo surfaces. The average displacement rate for these tests was constant at 0.00625 inch/second. The third test of each group, tests FCC3 and FCC7, had a displacement rate twice the displacement rate used in the previous tests (i.e., FCC2, FCC2A, FCC5 and FCC6). This allowed for study of the changes in the friction behavior due to the increase in displacement

rate. Test FCC4 studied the friction behavior of the FCC with a clamping bolt preload of 35 kips/bolt after prior wearing of the brass shims under a bolt preload of 23 kips/bolt. Test FCC8 studied the durability of the tribo surfaces and the consistency of the friction behavior under a continuous sinusoidal displacement with an average displacement rate of 0.00625 inch/second. For Tests FCC9 and FCC10A, stiffeners were added to the double angles of the FCC, and the resulting friction behavior evaluated. The shim material was unworn for Test FCC9 and reused for FCC10A. Test FCC10 was stopped prematurely due to a technical error and therefore is excluded from the discussion. Test FCC1 was the pilot test for the double angle FCC tests.

6.1 Study of Friction Connection Component Assembly Sequences

The double angle friction component may be assembled in various ways as part of the erection of a steel frame. Three possible assembly sequences were examined to determine their effects on the friction behavior.

6.1.1 Friction Connection Component Assembly Sequences

Assembly sequence 1 models conditions that occur when the second of two double angle FCCs located at opposite ends of a single beam is attached to the column. The double angles are shop-bolted to the beam web, and field-bolted to the column flanges as shown by steps 1 and 2 in Figure 6.2(a). After the fastening the first FCC, the horizontal displacement of the beam with respect to the column is restricted due

to the restraint provided by the first FCC. Clearance, due to erection tolerances, exists between the angles of the second, unattached FCC and the column flange as shown in Figure 6.2(a). The clearance is removed as the bolts compress the angle leg against the column flange as shown in Figure 6.2(b). During the tightening of the bolts, the angles deform. Due to the deformation in each angle, only a portion of the angle leg around the support bolts may be compressed against the column flange. The final deformed shape of the angles depends on the initial clearance of the angles.

In assembly sequence 2 the angles are bolted to the flanges of the column first, and are then bolted to the beam web, as shown in Figure 6.3(a). The assembly sequence occurs as follows. One angle is shop-bolted to the column flange as shown by step 1 in Figure 6.3(a). The remaining angle must be bolted in the field, because the beam flanges cannot be coped. The beam is positioned with respect to the shop-bolted angle, and the second angle is fastened to the column, which results in sandwiching of the beam as shown by step 2 in Figure 6.3(a). The angle legs are then bolted to the beam as shown by step 3 in Figure 6.3(a). Before the tightening of the clamping bolts, the angles are not fully compressed against the beam, and therefore a clearance exists between the angles and beam as shown in Figure 6.3(a). The angle leg is deformed as the angle is compressed against the beam web as shown in Figure 6.3(b). The degree of deformation in the angles is dependent on the initial clearance between the angles and the beam.

Assembly sequence 3 is similar to assembly sequence 1 except that assembly sequence 3 models conditions that occur as the first of two double angle FCCs located at opposite ends of a single beam is bolted to the column. The connection is again shop-bolted to the beam web (step 1) and field-bolted to the column flange (step 2) as shown in Figure 6.4(a). The displacement of the beam with respect to the column is not restrained because the FCC at the far end of the beam is not bolted to the column. Therefore, the deformation of the angles is minimal as the angles are compressed against the column flange, as shown in Figure 6.4(b).

To test the influence of these three assembly sequences on the behavior of the FCC, the test specimens were assembled in one of the aforementioned assembly sequences in the test frame described in Chapter 4. A displacement history consisting of two sets of four sinusoidal cycles (Figure 6.5) was applied. The average displacement rate was 0.00625 inch/second.

6.1.2 Effects of Assembly Sequence on Friction Behavior

Assembly Test AS1

Test AS1 used assembly sequence 2, shown in Figure 6.3. The support bolts fastening the angles to the lower spreader beam were tightened. The preloads in support bolts 4, 5, 6 and 7 were 52.9, 52.4, 50.6, and 51.8 kips, respectively. The clamping bolts were then tightened. The corresponding clamping bolt preloads in bolts 1, 2, and 3 were 24.2, 24.9, 24.2 kips. The values of the friction force (F_f) at

incipient slip in the pull and push directions were 31 and 36 kips, respectively. The hysteresis loops were repeatable as shown in Figure 6.6(a), which plots the applied force versus the average slip displacement. The average slip displacement is the average of the displacements measured by the tribo surface slip potentiometers located on both faces of the T-stub web.

Assembly Test AS2

Test AS2 used assembly sequence 1 shown in Figure 6.2. The clamping bolts were fastened first. The clamping bolt preloads in bolts 1, 2, and 3 were 24.0, 23.6, and 23.2 kips, respectively. The restrained displacement of the beam was simulated by the actuator holding the upper T-stub in position during assembly. The support bolts were then tightened. The preloads in support bolts 4, 5, 6, and 7 were 50.9, 51.5, 50.1, and 54.2 kips, respectively. As the support bolts were tightened, a tensile (i.e., upward) force of 28 kips developed in the actuator. This force corresponds the forces developing at the brass-steel tribo surfaces as the angles were fastened to the lower spreader beam. This force is a function of the clearance between the double angles and the lower spreader beam, and the required angle deformation needed to compress the angles against the lower spreader beam. Although slip displacement did not occur on the tribo surfaces, it is believed that slip would occur for larger clearances.

The values of the friction force (F_f) at incipient slip during the pull and push cycles were 55 kips and 71, respectively, as shown in Figure 6.6(b). F_f was very repeatable, and an increase in F_f occurred as the edge of the oversized hole in the T-stub web was pushed toward the bolt. The increase in F_f was between 2 and 3 kips, which was less than that observed in the double plate friction tests discussed in Chapter 5.

Assembly Test AS3

Test AS3 used assembly sequence 3, shown in Figure 6.4. The clamping bolts were tightened first. The preloads in clamping bolts were 23.2, 23.8, and 23.3 kips for bolts 1, 2, and 3, respectively. To simulate the unrestrained displacement of the beam with respect to the column, the actuator was allowed to move as the angles of the test specimen were compressed (pulled down) on the lower spreader beam during the tightening of the support bolts. To accomplish this, the bolts which fastened the upper T-stub to the upper spreader beam were loosened to provide approximately 1/8 inch of unrestrained movement between the lower actuator clevis and the upper spreader beam. The test specimen was supported using straps hung from an overhead crane. The straps were positioned at both ends of the upper spreader beam, and attached to the crane directly above the test specimen. The support bolts were then tightened without restraint from the actuator. The preloads in support bolts 4, 5, 6, and 7 were 54.5, 54.2, 52.1, and 52.7 kips, respectively. After the support bolts were tightened, the lower clevis of the actuator

was repositioned above the upper spreader beam. The bolts in the lower clevis were re-tightened, and the crane straps were removed to complete the assembly.

The values of the friction force (F_f) at incipient slip ranged between 49 kips during the pull cycles and 60 kips during the push cycles, as shown in Figure 6.6(c). A consistent 10 kips difference existed in the friction force between the pull and push cycles.

Fastening the clamping bolts first produced a greater value of F_f. F_f is a function of the assembly sequence and the initial deformation of the angle due to the assembly sequence. F_f is also a function of angle deformation during loading as discussed later. The difference in F_f for Test AS3 (10 kips) was greater than the difference in F_f for Test AS1 (5 kips), but the magnitude of F_f was 20 to 30 kips less for Test AS1. Assembly sequence 3 (Test AS3) was used for all of the double angle FCC tests, except Test FCC1 (the pilot test) which used assembly sequence 1 (Test AS2)

6.2 Experimental Observations

6.2.1 Observed Phenomena Repeated from Double Plate Friction Tests

Phenomena which occurred during the double plate friction tests were also observed during the double angle friction connection component (FCC) tests. These phenomena are: (1) wear of the brass-steel tribo surfaces; (2) deformation of the outer steel plates; and (3) variations in the force of the clamping bolts. For the

double angle FCC tests, the vertical legs of the double angles are initially deformed inward at the locations of the oversized holes in the T-stub web, and are then pushed outward during cyclic displacement of the T-stub web, causing the variations in the clamping bolt force. Thus the angle vertical legs behave similar to the outer plate in the double plate friction tests. In the double angel FCC tests, conclusive evidence of thermal effects was not observed due to the slower displacement rates of 0.00625 and 0.0125 inch/second used in the FCC tests, as compared with the dynamic displacement rate of 0.5 inch/second used during the double plate friction tests, which produced noticeable thermal effects.

6.2.2 Effects of Double Angle Deformation

As the double angle friction connection component (FCC) was subjected to imposed displacements, it appears that elastic deformation of the double angles occurred. The deformation of the angles explains why the friction force varied from the expected value of μ times the sum of the forces in the clamping bolts times two tribo surfaces ($\mu \bullet \Sigma P_{bolt} \bullet 2$). An analytical study was conducted to understand the effects of deformation of the angles on the behavior of the double angle FCC.

Pull Cycle

The pull cycle refers to the part of the imposed displacement cycles when the upper T-stub is moving upward relative to the double angles as discussed in Chapter 4. The friction force that develops pulls the double angles away from the lower

spreader beam. During the pull cycles, the deformation of the angles causes a reduction in the normal force on the tribo surface which reduces the friction force. The deformation in the angles is small and difficult to observe by visual inspection. The deformation is assumed to be similar to (but much smaller in magnitude than) the deformation that occurred during the tests of angles conducted by Garlock (1989), as shown in Figure 6.7.

The expected friction force, based on Coulomb friction theory is equal to μ times the normal force, where the normal force is expected to be equal to the sum of the forces in the clamping bolts (ΣP_{bolt}). As shown in Figure 6.8, the preload of the clamping bolts produces a normal force on the tribo surfaces. As deformation occurs during the pull cycles, the vertical angle leg pulls away from the web of the T-stub as shown in Figure 6.9, and an internal shear force (V) is produced in the vertical angle leg as shown in Figure 6.10. This internal shear force reduces the normal force on the tribo surface and the resulting friction force for the FCC is as follows:

$$F_f = (\mu \cdot N) \cdot 2 = [\mu \cdot (\Sigma P_{bolt} - V)] \cdot 2 \qquad (6.1)$$

An analysis of the double angles was conducted to develop estimates of the internal shear force, and corresponding normal force and friction force that developed during the tests. Free body diagrams (FBDs) of the deformed angle were developed by breaking the angle into three critical segments as shown in Figure 6.11. The three critical segments are: (1) the angle vertical leg between the clamping bolts and

fillet region; (2) the angle fillet region; and (3) the angle horizontal leg between the support bolts and fillet region. The segments of the angle legs within the bolt regions (i.e., where the bolt force resultant is shown to act) are not critical in determining V, but are used to show equilibrium of the angle.

Based on the FBDs, equations were developed for the internal forces on the three critical segments. A FBD of the fillet region is shown in Figure 6.12. The fillet region is assumed to be rigid. A summation of moments taken about point 0 results in the following equation:

$$m_1 + V \cdot \left(k - \frac{t}{2}\right) - m_2 - \left[(\mu \cdot N1) \cdot \left(k - \frac{t}{2}\right)\right] = 0 \qquad (6.2)$$

where: m_1 = the internal moment in the angle vertical leg,

m_2 = the internal moment in the angle horizontal leg,

k = the length of the angle fillet region,

t = the thickness of the angle,

N1 = the normal force on the tribo surfaces, and

μN1 = the friction force on the tribo surfaces.

The assumed deformed shape of the vertical leg segment between the clamping bolt and fillet region is shown in Figure 6.9. Assuming that this segment is deformed due to a rotation (θ) of the rigid fillet region without horizontal deflection, as shown in Figure 6.9, V and m_1, shown in Figure 6.13(a), are as follows:

$$V = \left(\frac{6 \cdot E \cdot I}{L1^2}\right) \cdot \theta \tag{6.3}$$

$$m_1 = \left(\frac{4 \cdot E \cdot I}{L1}\right) \cdot \theta \tag{6.4}$$

where: L1 = the length of the angle vertical leg decompressed during deformation

The assumed deformed shape for the horizontal leg segment between the fillet region and the support bolts is shown in Figure 6.9. It is assumed that the deformation of this segment is caused by a vertical deflection (Δ) and rotation (θ) of the segment end adjacent to the fillet region, as shown in Figure 6.13(b). The internal shear and moment, acting on the horizontal leg segment are as follows:

$$\mu N1 = \left[\left(\frac{12 \cdot E \cdot I}{L2^3}\right) \cdot \Delta\right] - \left[\left(\frac{6 \cdot E \cdot I}{L2^2}\right) \cdot \theta\right] \tag{6.5}$$

$$m_2 = \left[\left(\frac{6 \cdot E \cdot I}{L2^2}\right) \cdot \Delta\right] - \left[\left(\frac{4 \cdot E \cdot I}{L2}\right) \cdot \theta\right] \tag{6.6}$$

where: L2 = the length of the angle horizontal leg decompressed during deformation, and

Δ = the vertical displacement of the angle horizontal leg segment.

Equations 6.3, 6.4, and 6.6 are substituted into 6.2 to develop Equation 6.7, as follows:

$$\left\{\left[\left(\frac{4\cdot E\cdot I}{L1}\right)+\left(\frac{6\cdot E\cdot I\cdot\left(k-\frac{t}{2}\right)}{L1^2}\right)+\left(\frac{4\cdot E\cdot I}{L2}\right)\right]\cdot\theta\right\}+\left[\left(\frac{-6\cdot E\cdot I}{L2^2}\right)\cdot\Delta\right]=\mu N1\cdot\left(k-\frac{t}{2}\right) \quad (6.7)$$

Equations 6.5 and 6.7 can be solved for θ as follows:

$$\theta=\frac{\mu N1\cdot\left[\left(k-\frac{t}{2}\right)+\left(\frac{L2}{2}\right)\right]}{\left[\left(\frac{4\cdot E\cdot I}{L1}\right)+\left(\frac{6\cdot E\cdot I\left(k-\frac{t}{2}\right)}{L1^2}\right)+\left(\frac{4\cdot E\cdot I}{L2}\right)-\left(\frac{3\cdot E\cdot I}{L2}\right)\right]} \quad (6.8)$$

Substituting Equation 6.8 into Equation 6.3, V is determined as follows:

$$V=\left(\frac{6\cdot E\cdot I}{L1^2}\right)\cdot\left\{\frac{\mu N1\cdot\left[\left(k-\frac{t}{2}\right)+\left(\frac{L2}{2}\right)\right]}{\left[\left(\frac{4\cdot E\cdot I}{L1}\right)+\left(\frac{6\cdot E\cdot I\left(k-\frac{t}{2}\right)}{L1^2}\right)+\left(\frac{4\cdot E\cdot I}{L2}\right)-\left(\frac{3\cdot E\cdot I}{L2}\right)\right]}\right\} \quad (6.9)$$

Similarly Equations 6.5 and 6.7 can be solved for Δ, which is the vertical displacement (or uplift) of the angle fillet region, as follows:

$$\Delta = \frac{\mu N1 \cdot \left[\frac{\left(\frac{6 \cdot E \cdot I \cdot \left(k - \frac{t}{2} \right)}{L2^2} \right)}{\left(\left(\frac{4 \cdot E \cdot I}{L1} \right) + \left(\frac{6 \cdot E \cdot I \left(k - \frac{t}{2} \right)}{L1^2} \right) + \left(\frac{4 \cdot E \cdot I}{L2} \right) \right)} + 1 \right]}{\frac{12 \cdot E \cdot I}{L2^3} - \left[\frac{\frac{\left(36 \cdot E^2 \cdot I^2 \right)}{L2^4}}{\left(\left(\frac{4 \cdot E \cdot I}{L1} \right) + \left(\frac{6 \cdot E \cdot I \left(k - \frac{t}{2} \right)}{L1^2} \right) + \left(\frac{4 \cdot E \cdot I}{L2} \right) \right)} \right]} \tag{6.10}$$

An iterative process is used to calculate V. As shown in Equation 6.1, N is equal to ΣP_{bolt} - V, and therefore both V and N are unknown. N1 is an assumed value of N. Initially, N1 is assumed equal to ΣP_{bolt}. V is then determined using Equation 6.9. A new N is calculated as ΣP_{bolt} - V (i.e., the new N = ΣP_{bolt} - V). N should equal N1. If this is not true, another iteration is performed, using the calculated N as N1. This is repeated until N is approximately equal to N1. Δ is determined from the final value of N1 using Equation 6.10. L1 and L2 are assumed with the distance from the bolt centerline to the exterior face of the angle leg being the upper bound. The upper bounds for L1 and L2 for the double angles that were tested are 3-1/4 inches and 3-1/8 inches, respectively.

After N is estimated, the corresponding friction force (F_f) is estimated from Equation 6.1. The analytical estimates of F_f are compared with the applied force during the tests (taken to be the measured friction force) in Figures 6.14(a), 6.15(a), 6.16(a), 6.17(a), 6.18(a), and 6.19(a) for Tests FCC2, FCC2A, FCC3, FCC5, FCC6, and FCC7, respectively. The measured friction force (F_f) in these figures is from the pull cycle portion of one cycle during cycle set 1, with a displacement amplitude of 7/16 inch. For each measured friction force data point in the figures, a corresponding analytical estimate of F_f is determined using Equation 6.1 and 6.9 including the effect of shear in the angle vertical leg. The corresponding analytical estimates are based on the measured bolt forces and a μ of 0.45. For comparison, values of $(\mu \bullet \Sigma P_{bolt}) \bullet 2$, with μ equal to 0.4 and 0.5 are also shown in the figures.

For the tests with a clamping bolt preload of 23 kips/bolt, L1 and L2 values of 2.2 and 1 inches, respectively, were assumed in the analytical estimates. For Test FCC2 (Figure 6.14(a)), the measured friction force (F_f) is between the two curves for $(\mu \bullet \Sigma P_{bolt}) \bullet 2$ with μ equal to 0.4 and 0.5. The analytical estimates of F_f (i.e., $F_f = (\mu \bullet \Sigma P_{bolt} - V) \bullet 2$) are less than the measured F_f. However, the measured data is taken from the break-in cycles where the friction force is typically higher. The calculated values of V were between 12 and 13 kips, the calculated values of N were between 60 and 64 kips, and the values of ΣP_{bolt} were between 73 and 77 kips. Δ was calculated to be approximately 0.0005 inch. For Tests FCC2A and FCC3 (Figures 6.15(a) and 6.16(a)), the measured F_f is consistently less than $(\mu \bullet \Sigma P_{bolt}) \bullet 2$ with μ

equal to 0.4. The analytical estimates are close to the measured values of F_f as shown in Figure 6.14(a) and 6.15(a). The calculated values of V were between 11 and 12 kips, the calculated values of N were between 55 and 62 kips, and the values of ΣP_{bolt} were between 66 and 75 kips. Δ was approximately 0.0005 inch.

For the tests with a clamping bolt preload of 35 kips/bolt, L1 and L2 values of 3 and 1.3 inches, respectively, were assumed in the analytical estimates. For Test FCC5 (Figure 6.17(a)), the measured F_f is less than $(\mu \cdot \Sigma P_{bolt}) \cdot 2$ with μ equal to 0.4. The analytical estimates are close to the measured values of F_f for when the slip displacements is near zero, but the analytical estimates differ from the measured values when the slip displacement is near 7/16 inch. For FCC5, the calculated values of V were between 16 and 18 kips, the calculated values for N were between 91 and 98 kips, and the values of ΣP_{bolt} were between 108 and 116 kips. Δ was approximately 0.0017 inch. For Tests FCC6 and FCC7 (Figures 6.18(a) and 6.19(a), respectively), the calculated values of V were between 19 and 23 kips. For Test FCC6, the calculated values of N were between 88 to 103 kips, and for Test FCC7, the calculated values of N were between 92 to 102 kips. For both tests, the values of ΣP_{bolt} were between 107 and 126 kips. For Tests FCC6 and FCC7, the measured values and analytical estimates of F_f were comparable.

The ratio of the measured F_f to $(\mu \cdot \Sigma P_{bolt}) \cdot 2$, with μ equal to 0.45, is shown in Table 6.2. During the pull cycles, the measured F_f was at most 1.05 times $(\mu \cdot \Sigma P_{bolt}) \cdot 2$, and at least 0.80 times $(\mu \cdot \Sigma P_{bolt}) \cdot 2$ for the unstiffened angle tests, excluding Test FCC1, which used assembly sequence 1 instead of assembly sequence 3 (i.e., including Tests FCC2 to FCC8).

Push Cycle

The push cycle refers to the part of the imposed displacement cycles when the upper T-stub is moving downward as discussed in Chapter 4. During the push cycles, the heels of the angles were expected to bear against the steel plate that is attached to the lower spreader beam, and the measured friction force (F_f) was expected to be proportional to the clamping bolt forces (i.e., $(\mu \cdot \Sigma P_{bolt}) \cdot 2$). As shown in Figures 6.14(b), 6.15(b), and 6.16(b), the measured F_f is approximately equal $(\mu \cdot \Sigma P_{bolt}) \cdot 2$ with a μ equal to 0.45 during the push cycles of Tests FCC2, FCC2A, and FCC3, with a clamping bolt preload of 23 kips/bolt. However, as shown in Figures 6.17(b), 6.18(b), and 6.19(b), the measured F_f is greater than $(\mu \cdot \Sigma P_{bolt}) \cdot 2$ for μ equal to 0.5 during the push cycles of Tests FCC5, FCC6, and FCC7 with a clamping bolt preload of 35 kips/bolt. The difference in the results for the tests with a preload of 23 kips/bolt and the results for the tests with a preload of 35 kips/bolt could not be explained. It is believed that, under a preload of 35 kips/bolt, a deformation develops in the angles that results in an internal shear (V) in the vertical legs of the angles. This internal shear increases the normal force (N) on the tribo surfaces.

However, an analysis of the deformation in the angles, and the related internal shear force (V), that accounts for the differences between the results for the tests with a preload of 23 kips/bolt and the results for the tests with a preload of 35 kips/bolt could not be developed, and this analysis is left for future research.

6.3 Experimental Results

A total of 13 test were conducted on the friction connection component as shown in Table 6.1. Test FCC4A and FCC10 are not included in the following discussion because the tests were not completed due to technical errors. As in the previous chapter, the test results are presented for two series of test according to the clamping bolt preload. For the first series of test (FCC1 to FCC3), the clamping bolt preload was 23 kips/bolt. For the second series of test (FCC4 to FCC10A), the clamping bolt preload was 35 kips/bolt. The following plots were created to show the experimental results: (1) the applied force versus the average cumulative travel; (2) the applied force versus the average slip displacement; (3) the clamping bolt force versus the average cumulative travel, (4) the bolt force versus average slip displacement for the clamping bolts and the support bolts. A summary of the FCC experimental results is given in Table 6.2.

6.3.1. Friction Connection Component Tests FCC1 to FCC3

Tests FCC1 to FCC3 used a clamping bolt preload of 23 kips/bolt. Test FCC1 was similar to the remaining tests (Tests FCC2, FCC2A, and FCC3), except for the

assembly sequence. Also, Test FCC1 was the pilot test for the double angle FCC tests. The friction behavior in Tests FCC1, FCC2, FCC2A, and FCC3 is shown in Figures 6.20, 6.24, 6.28, and 6.32, which show the applied force versus the average cumulative travel, and the applied force versus the average slip displacement. The applied force versus the average cumulative travel plots show the applied force as the average slip displacement is accumulated from the beginning to the end of each test. The average slip displacements are the average of the displacements measured by the tribo surface slip linear potentiometers located on both faces of the T-stub web.

Tests FCC1 and FCC2 begin with unworn brass shims and used the same displacement rate. For both tests, the friction force (F_f) was lower throughout the first cycles. For Test FCC1 (Figure 6.20(a)), during the first cycle, the value of F_f at incipient slip was 40 kips in the pull cycles and 45 kips during the push cycles. For Test FCC2 (Figure 6.24(a)) during the first cycle, F_f at incipient slip in the pull and push cycles was 53 and 39 kips, respectively. During Test FCC1 after break-in, F_f at incipient slip was between 50 and 55 kips in the pull direction, and 72 and 82 kips in the push direction. During Test FCC2 after break-in, F_f at incipient slip during the pull cycles ranged between 53 and 65 kips, and during the push cycles ranged between 55 and 68 kips. Test FCC2A used the same brass shims as Test FCC2 and the same displacement rate (0.00625 inch/second). During Test FCC2A (Figure 6.28), F_f at incipient slip ranged between 49 and 51 kips during the pull cycles and

between 59 and 62 kips during the push cycles. The values of F_f at incipient slip for Test FCC2A were similar to Test FCC2. Test FCC3 was similar to Test FCC2A, except the displacement rate used in Test FCC3 was two times the rate used in Test FCC2A. The brass shims used in FCC2A were reused in FCC3. During Test FCC3 (Figure 6.32), Ff at incipient slip ranged from 49 to 51 kips during the pull cycles and 57 to 64 kips during the push cycles. Although the displacement rates vary between Tests FCC2A and FCC3, the values of F_f at incipient slip are similar.

The clamping bolt force versus the average cumulative travel is shown in Figures 6.21, 6.25, 6.29, and 6.33 for Tests FCC1, FCC2, FCC2A, and FCC3. This figure shows the clamping bolt force plotted from the beginning to the end of each test. The average cumulative travel is the average slip displacement accumulated from the beginning to the end of each test. For Test FCC1, the force in bolt 2 and 3 (Figure 6.21(b) and 6.21(c), respectively) declined as slip began due to the yielding of the asperity peaks placed in contact during assembly. In addition to the typical cyclic variations in bolt force discussed previously, a continual drop in the bolt force occurred throughout cycle set 1. Steady state appears to have been reached towards the end of cycle set 1. At this point, the force in each bolt remained relatively constant throughout the remainder of the test with only the cyclic variations occurring. The total decline in bolt force from the preload was 3 to 4 kips in bolts 2 and 3. Bolt 1 (Figure 6.21(a)) exhibited an increase in bolt force as slip occurred during beginning of the test. The bolt force remained greater than the

preload for most of cycle set 1, then dropped below the preload at the end of cycle set 1. The final bolt force was about 2 kips less than the preload.

During Test FCC2 (Figure 6.25), the clamping bolt behavior for each bolt was similar to that of bolt 1 in Test FCC1 (Figure 6.21(a)). The bolt force increased during the cycle set 1 above the preload, and dropped below the preload towards the end of cycle set 1. Except for the cyclic variations, the bolt force remains constant from the beginning of cycle set 2 to the end of the test. The final bolt force, when the bolt is near the center of the oversized hole, is approximately 22 kips in each bolt.

The clamping bolt force versus the average cumulative travel for Tests FCC2A and FCC3 is shown in Figures 6.29 and 6.33, respectively. For these tests, unlike the previous tests which began with unworn brass shims, the bolt force did not decline below the preload. For both tests FCC2A and FCC3, bolts 1 and 2 retained their preload throughout the test. The behavior of bolt 3 was similar for both tests. The bolt force gradually increased during the test. This behavior is similar to the behavior of the bolts in the double plate friction tests when thermal effects were observed (Figure 5.29). Bolt force increases due to thermal effects were not evident in bolts 1 and 2 for either test. Therefore, this increase in bolt force may be to a malfunction of the bolt gauge.

Figures 6.21, 6.25, 6.29, and 6.33 show the typical cyclic variations in bolt forces observed in the friction connection component tests. These figures show that a larger variation occurred in the force in bolt 2. This may be due to deformation of the angle, The cyclic variation of the force in the clamping bolts is also shown in Figures 6.22, 6.26, 6.30, and 6.34 (clamping bolt force vs. average slip displacement) for Tests FCC1, FCC2, FCC2A, and FCC3 respectively. These figures show the bolt force for specific slip displacement throughout the each test. The concave upward shape in some of the figures corresponds to the displacement amplitude dependent increases in bolt force caused by deformation of the angle vertical leg at the location of the oversized hole in the T-stub web. The increase in the force in bolt 2 is greater than that of bolts 1 and 3 for Tests FCC2, FCC2A, and FCC3 (Figure 6.26(b), 6.30(b) and 6.34(b)). The concave upward shape was not noticeable for Test FCC1 (Figure 6.22).

The bolt force versus the average slip displacement for the support bolts is shown in Figures 6.23, 6.27, 6.31, and 6.35 for Tests FCC1, FCC2, FCC2A, and FCC3, respectively. These figures show the bolt force in the support bolts for specific slip displacements. During Test FCC2, an approximate 3 kip variation in the force in bolt 6 was observed as shown in Figure 6.23. The bolt force increased during the pull cycles and decreased during the push cycles. This pattern was most evident in bolts 4 and 6 of all tests. The variation in force in the support bolts was generally small as shown in the figures.

6.3.2. Friction Connection Component Tests FCC4 to FCC8

Tests FCC4, FCC5, FCC6 and FCC7 were conducted with an approximate clamping bolt preload of 35 kips/bolt. The figures used to show the experimental results are similar to those used for the tests with a bolt preload of 23 kips/bolt. A summary of the test results is given in Table 6.2.

The friction force behavior for Tests FCC4, FCC5, FCC6 and FCC7 is shown in Figures 6.36, 6.40, 6.44 and 6.48, in which the applied force versus the average cumulative travel and the applied force versus the average slip displacement are given. Test FCC4 reused the worn brass shims from Tests FCC2 to FCC3. The displacement rate was 0.00625 inch/second. During Test FCC4 (Figure 6.36), F_f at incipient slip was between 73 and 77 kips during the pull cycles and 93 to 102 kips during the push cycles. For Test FCC5, an unworn set of brass shims was used. The displacement rate for the test was 0.00625 inch/second. During FCC5 (Figure 6.40), F_f at incipient slip was between 83 and 91 kips in the pull cycles and between 112 and 127 kips in the push cycles. For Test FCC6, the worn brass shims used in Test FCC5 were reused. The displacement rate was consistent with the rate used in Tests FCC4 and FCC5 (0.00625 inch/second). During Test FCC6 (Figure 6.44), F_f at incipient slip ranged between 76 and 84 kips during the pull cycles and 116 and 123 kips during the push cycles. The values of F_f at incipient slip during the pull cycles were similar for Tests FCC4, FCC5 and FCC6. The values of F_f at incipient slip

during the push cycles for Tests FCC5 and FCC6 were similar, while the values for Test FCC4 were slightly lower.

For Test FCC7, the worn shims used in Tests FCC5 and FCC6 were reused. The displacement rate was 0.0125 inch/second which was twice the displacement rate used in Tests FCC4 to FCC6. The range of F_f values at incipient slip for Test FCC7 (Figure 6.48) were between 81 and 92 during the pull cycles and 113 to 128 during the push cycles. F_f values for Tests FCC7 were similar to those from Tests FCC5 and FCC6.

The hysteresis loops for Tests FCC5, FCC6 and FCC7 (Figures 6.40(b), 6.44(b), and 6.48(b), respectively) show the effects of the unequal stroke of the actuator discussed in Chapter 4. The bow-tie shape of the hysteresis curves is very evident for Tests FCC5, FCC6, and FCC7, reflecting the amplitude displacement dependent bolt force variation which results from deformation of the angle vertical leg at the location of the oversized holes in the T-stub web.

The clamping bolt force versus the average cumulative travel for Tests FCC4, FCC5, FCC6 and FCC7 is shown in Figures 6.37, 6.41, 6.45 and 6.49, respectively. The behavior of the clamping bolts is similar for each test. As the test began, the bolt force dropped below the preload due to yielding of the asperities. The minimum bolt force was highest during the cycles with a slip displacement amplitude of 7/16

inch, and lowest at during the cycles with a slip displacements amplitude of 1/8 inch. The bolt forces for each test were fairly stable and consistent with the preload. The bolt force at the end of each test was above the preload, except for Test FCC4 (Figure 6.37) in which the bolt force decreased slightly below the preload. The force in bolt 3 increased gradually during Tests FCC5, FCC6 and FCC7 as shown in Figures 6.41(c), 6.45(c) and 6.49(c), respectively. It is not clear if this increase in force was due to thermal effects or possible due to a malfunction in the bolt gauge because thermal effects are not visible in the behavior of bolts 1 and 2.

The consistency of the bolt force for the clamping bolts is shown in Figures 6.38, 6.42, 6.46, and 6.50, which shows the clamping bolt force versus average slip displacement for Tests FCC4, FCC5, FCC6 and FCC7, respectively. The behavior in the bolts for each test is similar. A small variation in bolt force is visible for each bolt, but the bolt force is very consistent throughout the entire test. The concave upward shape of the curve shows the increase in bolt force as slip displacement increases. Thus the effects of deformation of the angle vertical leg at the location of the oversized hole in the T-stub was evident.

The force in the support bolts for Tests FCC4, FCC5, FCC6 and FCC7 is shown in Figures 6.39, 6.43, 6.47 and 6.51, respectively. The behavior of the support bolts is similar to that described for the previous tests with a clamping bolt preload of 23 kips/bolt, except the variation in force is greater due to the increase in F_f.

Durability of Brass-Steel Tribo System

The purpose of Test FCC8 was to evaluate the durability of the brass-steel tribo surfaces by subjecting the specimen to 144 cycles at a displacement amplitude of 7/16 inch. The displacement rate was 0.00625 inch/second. The total expected travel was 245 inches (20.4 feet). The figures used to show the experimental results are similar to those used for the previous tests with a bolt preload of 23 and 35 kips/bolt. The figures showing the force in the support bolts were excluded because the results are similar to those shown for the tests with a clamping bolt preload of 23 kips/bolt.

The friction force behavior for Test FCC8 is shown in Figure 6.52. F_f was consistent throughout the test. F_f at incipient slip for the pull cycles ranged between 82 and 99 kips and for the push cycles varying between 126 and 131 kips, as shown in Figure 6.52(a). The consistency of F_f is also evident by the overlapping of loops in the applied force versus the average slip displacement plot (Figure 6.52(b)).

The clamping bolt force versus the average cumulative travel is shown in Figure 6.53. Bolts 1 and 2 display a stable response for the entire test. The bolt force in these clamping bolts, when they were centered in the oversized bolt hole, was close to the preload, as shown in Figures 6.53(a) and 6.53(b) respectively. A slight decline in bolt force occurred after a travel of 150 inches for bolt 2 (Figure 6.53(b)). The force in bolt 3 (Figure 6.53) increased throughout the test. The increase in bolt force

may be due to a malfunction of the gauge and not thermal effects, because the increase began at the initiation of the test. The consistency of the bolt force for bolts 1 and 2 throughout the test is shown in Figure 6.54.

6.3.3 Stiffened Angle Tests FCC9 to FCC10A

Stiffeners were added to the ends of the angles to restrict the deformation of the angles as shown in Figure 6.55. The specimen was assembled according to assembly sequence 3. The tribo surfaces were assumed to be fully-compressed after assembly. This was followed by the addition of 1/2 inch stiffeners welded to the exterior edges of the angle. It was assumed that distortion due to welding would be minimal, because the angles were initially compressed against the web of the T-stub. Three tests were conducted, FCC9, FCC10 and FCC10A, at a displacement rate of 0.0625 inch/second. Unworn shims were used for FCC9, and re-used for FCC10A. Test FCC10 was not completed and therefore the results are not discussed.

The friction force behavior for Tests FCC9 and FCC10A is shown in Figures 6.56 and 6.60, respectively. F_f, at incipient slip after break-in, for FCC9 (Figure 6.56), varied between 54 and 80 kips for both cycles. F_f peaked at the end of the slip displacement for both the pull cycles and push cycles, rising to 90 kips for the pull cycles and 125 kips for the push cycles. As shown in Figures 6.56 and 6.60 for Tests FCC9 and FCC10A, respectively, F_f at incipient slip was similar for both the push

and pull cycles. The reason for the increase in F_f at the end of the slip displacement for the push and pull cycles is unclear.

The force in the clamping bolts for Test FCC9 (Figure 6.57) decreased during cycle set 1 for each bolt. This behavior resembles that observed for Test FCC1 (Figure 6.25). The bolt force was relatively constant, after a slight decline, for FCC10A (Figure 6.61). The clamping bolt force versus the average slip displacement for Tests FCC9 and FCC10A is shown in Figures 6.58 and 6.62, respectively.

The force in the support bolts is shown in Figure 6.59 for Tests FCC9, and Figure 6.63 for Test FCC10A. The behavior of the support bolts was similar in both tests. The force in the exterior support bolts (bolts 4 and 6) varies with respect to the direction of applied force. The forces in the interior support bolts (bolts 5 and 7) remain relatively constant.

6.3.4 Energy Dissipation

Table 6.3 shows the accumulated energy dissipation for each experimental test. Due to variations in the displacement history imposed during the constant amplitude cycles for Test FCC2, the accumulated energy dissipation shown for Tests FCC2, FCC2A and FCC3 is determined at the end of cycle set 2. The energy dissipated for Test FCC1 is greater than Tests FCC2, FCC2A, and FCC3. All of these tests have the same bolt preload. This is because the displacement history of FCC1

differed slightly from the remaining test due to errors in the sinusoidal displacements that manually imposed. The energy dissipated for Tests FCC2, FCC2A and FCC3 is very consistent. The energy dissipated for Tests FCC4, FCC5, FCC6, and FCC7 is also similar. Thus the reliability of the energy dissipating capacity of the FCC is evident. The energy dissipation for Tests FCC9 and FCC10A is less than Tests FCC4, FCC5, FCC6, and FCC7 although the clamping bolts preloads were approximately the same. This is due to a reduction in F_f which was caused by the stiffeners.

Table 6.1. Double Angle Friction Connection Component Test Matrix

Test	Tribo Surface Area	Parameter	Initial Brass Shim Condition	Clamping Bolt Preload (kips)	Assembly Sequence*	μ (Assumed)**	Friction Force [(μ•N)•2***] (kips)	Displacement Rate (in/sec)
FCC1	7.25x14"	F_f	Unworn	23	Sequence 1	0.45	62.1	0.00625
AS1	7.25x14"	Assembly	Worn	23	Sequence 2	0.45	62.1	0.00625
AS2	7.25x14"	Assembly	Worn	23	Sequence 1	0.45	62.1	0.00625
AS3	7.25x14"	Assembly	Worn	23	Sequence 3	0.45	62.1	0.00625
FCC2	7.25x14"	F_f	Unworn	23	Sequence 3	0.45	62.1	0.00625
FCC2A	7.25x14"	Repeatability	Worn	23	Sequence 3	0.45	62.1	0.00625
FCC3	7.25x14"	Rate Effects	Worn	23	Sequence 3	0.45	62.1	0.0125
FCC4	7.25x14"	F_f	Worn	35	Sequence 3	0.45	94.5	0.00625
FCC4A^	7.25x14"	Repeatability	Worn	35	Sequence 3	0.45	94.5	0.00625
FCC5	7.25x14"	F_f	Unworn	35	Sequence 3	0.45	94.5	0.00625
FCC6	7.25x14"	Repeatability	Worn	35	Sequence 3	0.45	94.5	0.00625
FCC7	7.25x14"	Rate Effects	Worn	35	Sequence 3	0.45	94.5	0.0125
FCC8	7.25x14"	Durability	Worn	35	Sequence 3	0.45	94.5	0.00625
FCC9	7.25x14"	Stiffened Angles	Unworn	35	Sequence 3	0.45	94.5	0.00625
FCC10^	7.25x14"	Stiffened Angles	Worn	35	Sequence 3	0.45	94.5	0.00625
FCC10A	7.25x14"	Stiffened Angles	Worn	35	Sequence 3	0.43	90.3	0.00625

* assembly sequences

sequence 1: horizontal bolts, vertical bolts

sequence 2: vertical bolts, horizontal bolts

sequence 3: horizontal bolts, loosen actuator clevis, vertical bolts, tighten actuator clevis

** based on double plate friction test

*** $N = \Sigma P_{bolt}$ and 2 tribo surfaces

^ test not completed

Table 6.2. Double Angle Friction Connection Component Test Results

Test	Clamping Bolt Preload (kips)	Range of Measured F_f from Test		F_f** $[\mu \cdot \Sigma P_{bolt} \cdot 2]$	Max. Measured F_f $\mu \cdot \Sigma P_{bolt} \cdot 2$		Min. Measured F_f $\mu \cdot \Sigma P_{bolt} \cdot 2$		ΔT
		Push Cycle (kips)	Pull Cycle (kips)	(kips)	Push Cycle ---	Pull Cycle ---	Push Cycle ---	Pull Cycle ---	(°F)
FCC1^^	23	45* to 82	40* to 55	62.1	1.32	0.89	0.72*	0.64*	8
ES1	23	---	---	62.1	---	---	---	---	---
ES2	23	---	---	62.1	---	---	---	---	---
ES3	23	---	---	62.1	---	---	---	---	---
FCC2	23	39* to 68	53* to 65	62.1	1.10	1.05	0.63*	0.85*	16
FCC2A	23	59 to 62	49 to 51	62.1	1.00	0.82	0.95	0.79	18
FCC3	23	57 to 64	49 to 51	62.1	1.03	0.82	0.92	0.79	19
FCC4	35	93 to 102	73 to 77	94.5	1.08	0.81	0.98	0.77	31
FCC4A^	35	---	---	94.5	---	---	---	---	---
FCC5	35	112 to 127	83 to 91	94.5	1.34	0.96	1.19	0.88	36
FCC6	35	116 to 123	76 to 84	94.5	1.30	0.89	1.23	0.80	25
FCC7	35	113 to 128	81 to 92	94.5	1.35	0.97	1.20	0.86	38
FCC8	35	126 to 131	82 to 99	94.5	1.39	1.05	1.31	0.87	43
FCC9	35	43 to 65	31 to 80	94.5	0.69	0.85	0.46	0.33	19
FCC10^	35	---	---	94.5	---	---	---	---	---
FCC10A	35	67 to 96	61 to 78	94.5	1.02	0.83	0.71	0.65	22

* F_f of initial cycle with unworn shims

** $\mu_{assumed} = 0.45$

^ Test not completed

^^ Manual displacement control

Table 6.3. Accumulated Energy Dissipation during Friction Connection Component Tests

Test	Accumulated Energy Dissipation (kips•in)
FCC1*	3688
FCC2**	2564
FCC2A**	2414
FCC3**	2539
FCC4	4222
FCC5	4272
FCC6	4250
FCC7	4263
FCC9	3818
FCC10A	3852

* displacement history varied from remaining tests

** accumulated energy dissipation at the end of cycle set 2

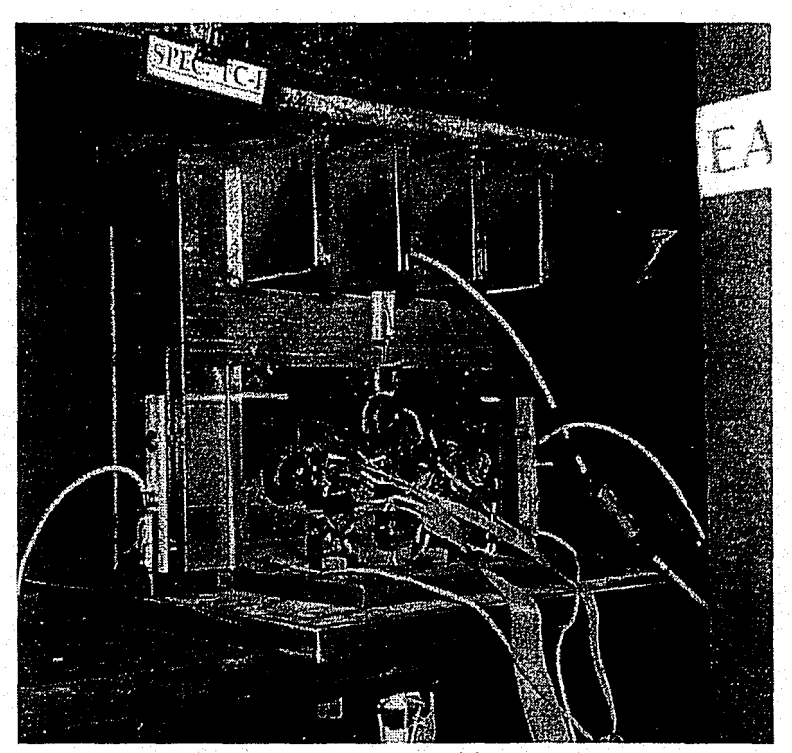

(a) East Elevation Oblique View

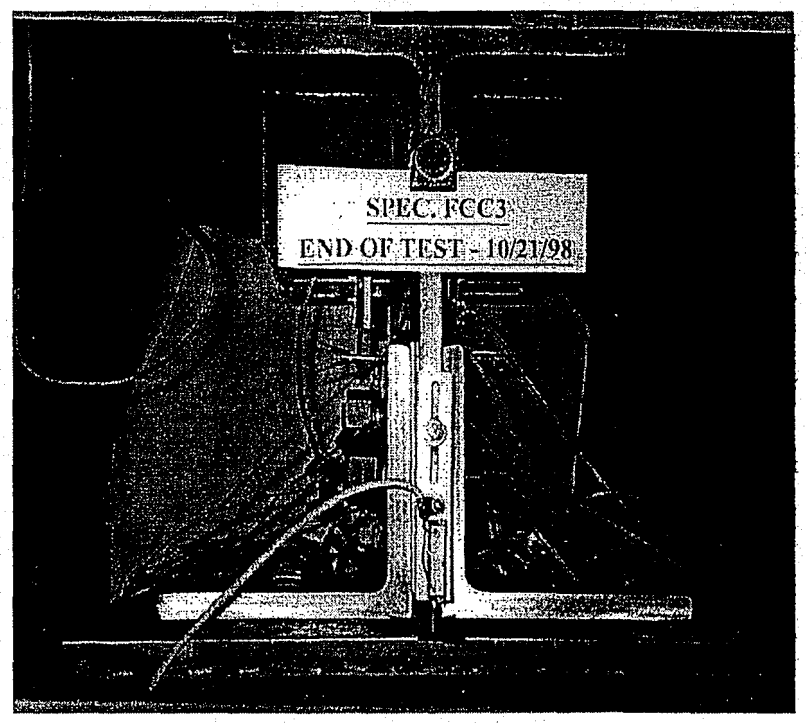

(b) Section View

Figure 6.1. Friction Connection Component (FCC) Test Specimen

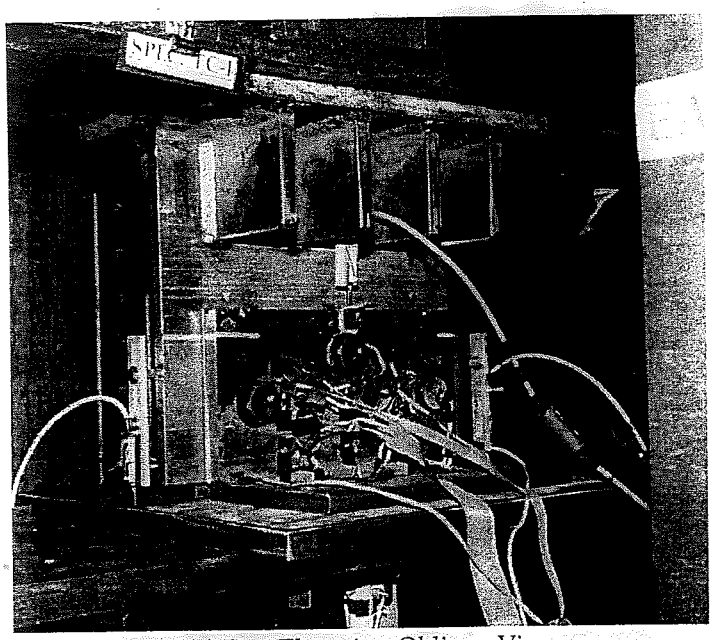

(a) East Elevation Oblique View

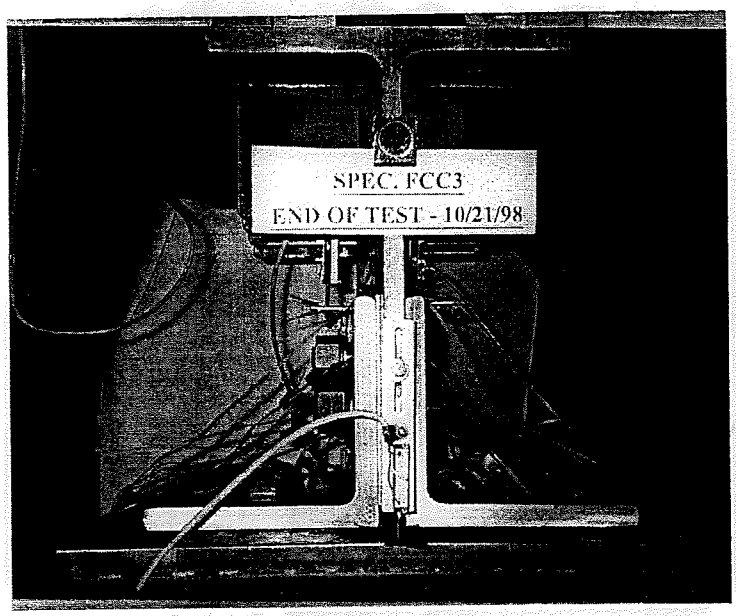

(b) Section View

Figure 6.1. Friction Connection Component (FCC) Test Specimen

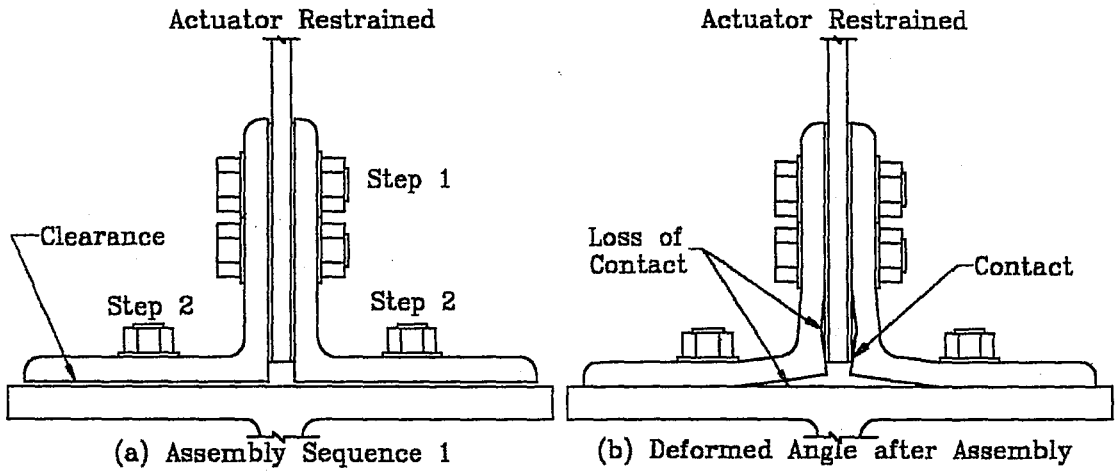

Figure 6.2. Assembly Sequence 1 for Test AS2

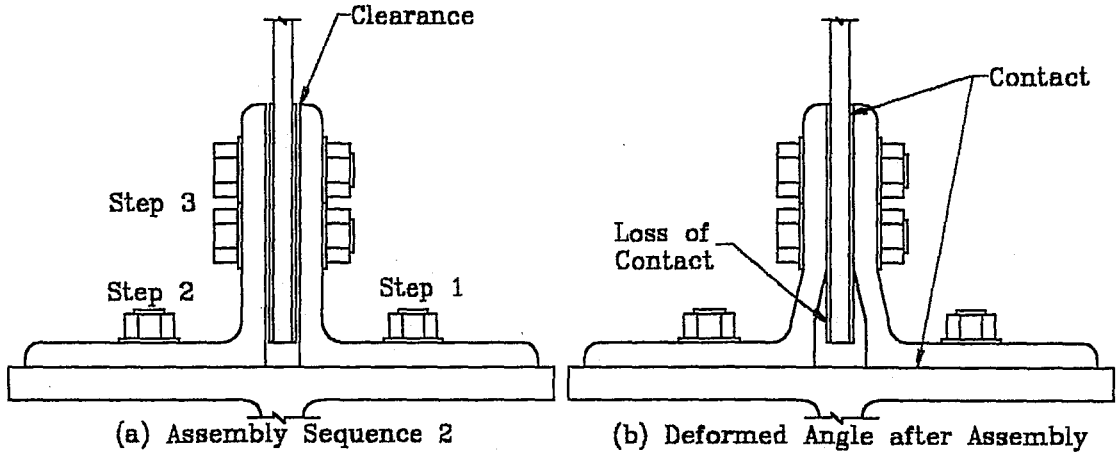

Figure 6.3. Assembly Sequence 2 for Test AS1

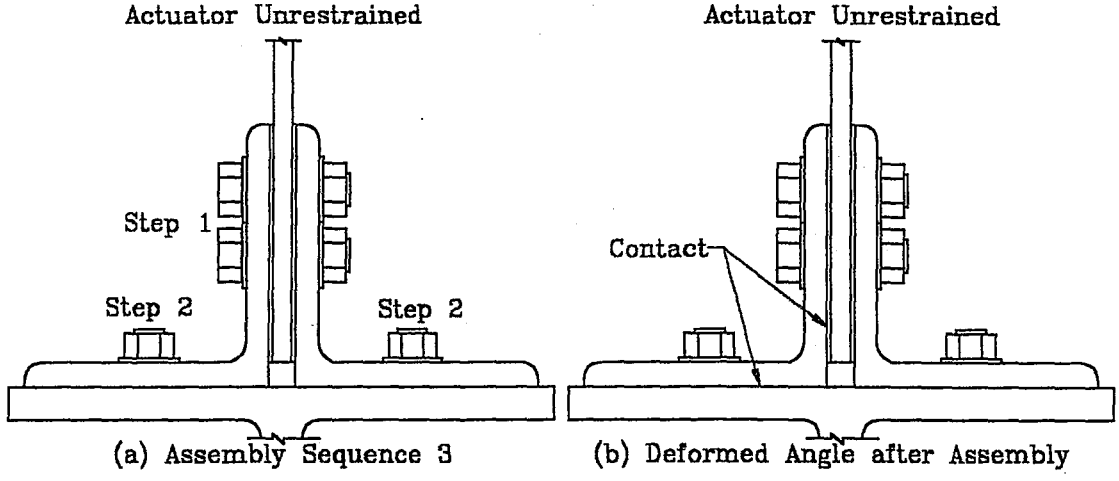

Figure 6.4. Assembly Sequence 3 for Test AS3

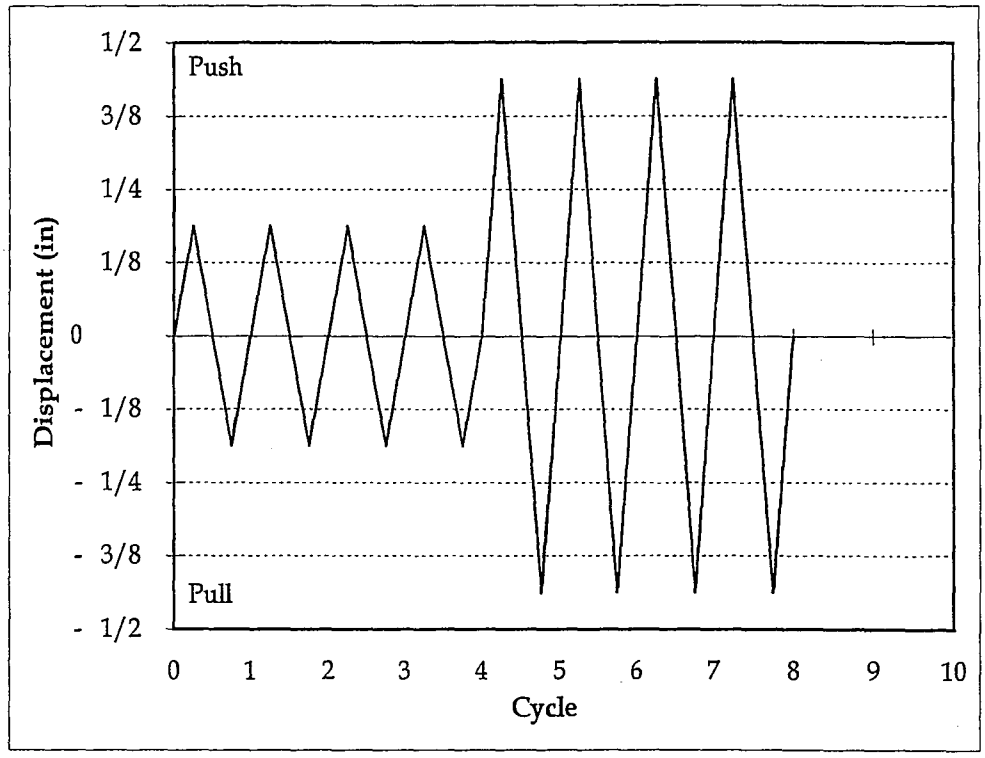

Figure 6.5. Displacement History for Typical Assembly Sequence Test

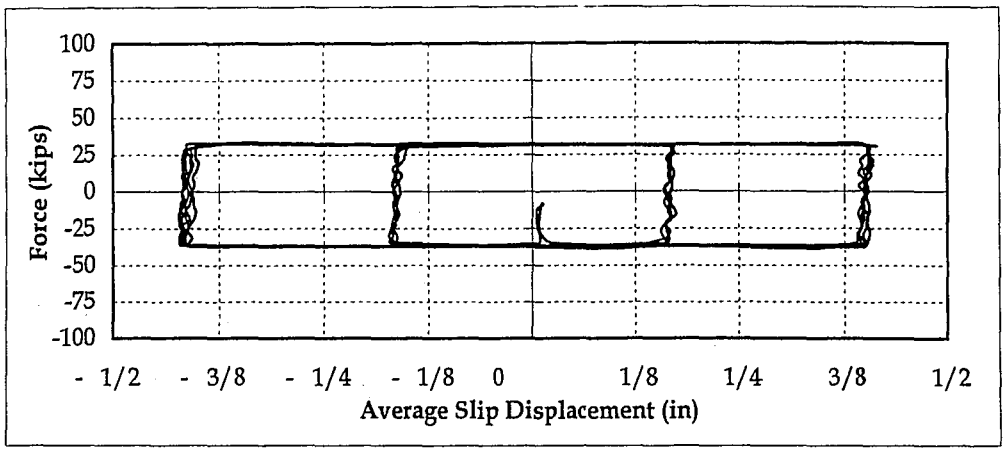

(a)

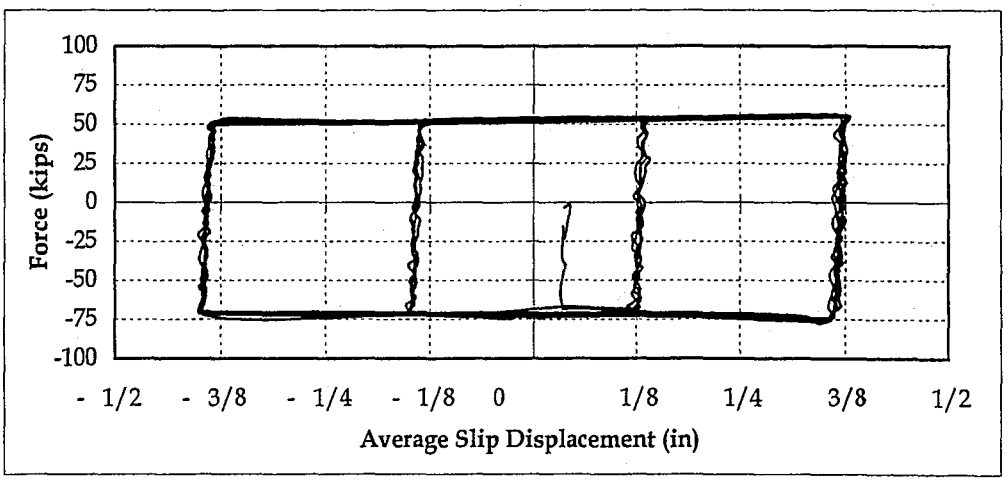

(b)

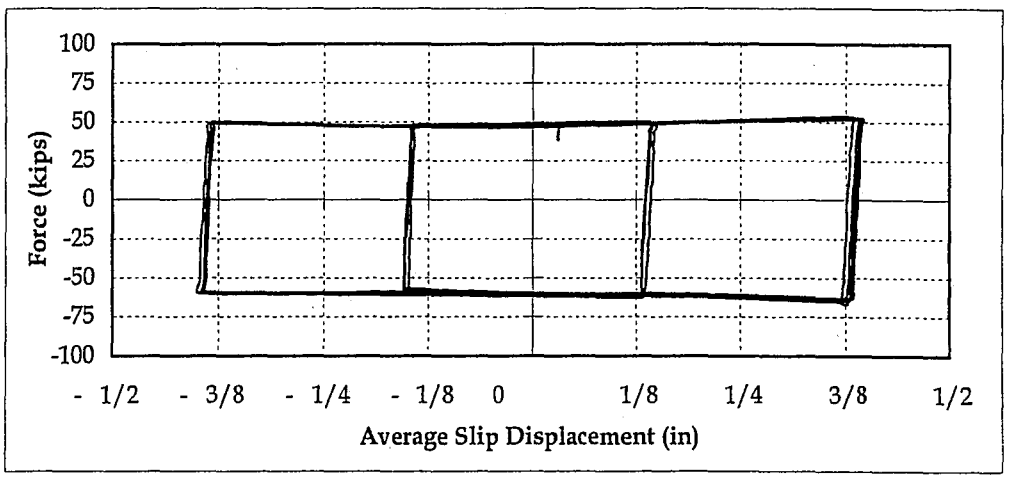

(c)

Figure 6.6. Assembly Sequence Test Hysteresis Loops:
(a) Test AS1; (b) Test AS2; and (c) Test AS3

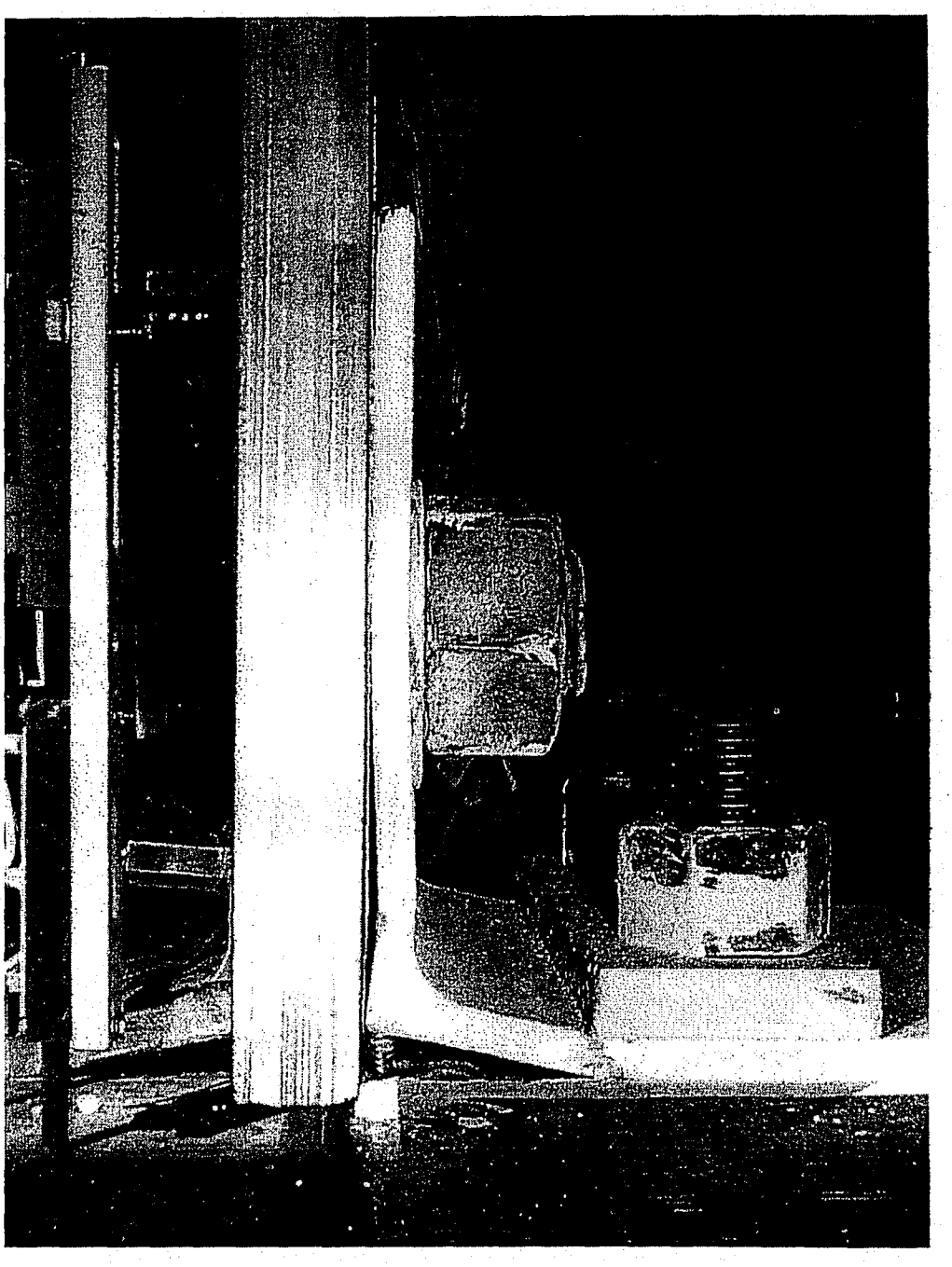

Figure 6.7. Assumed Deformed Shape of Angle (Garlock et al., 1989)

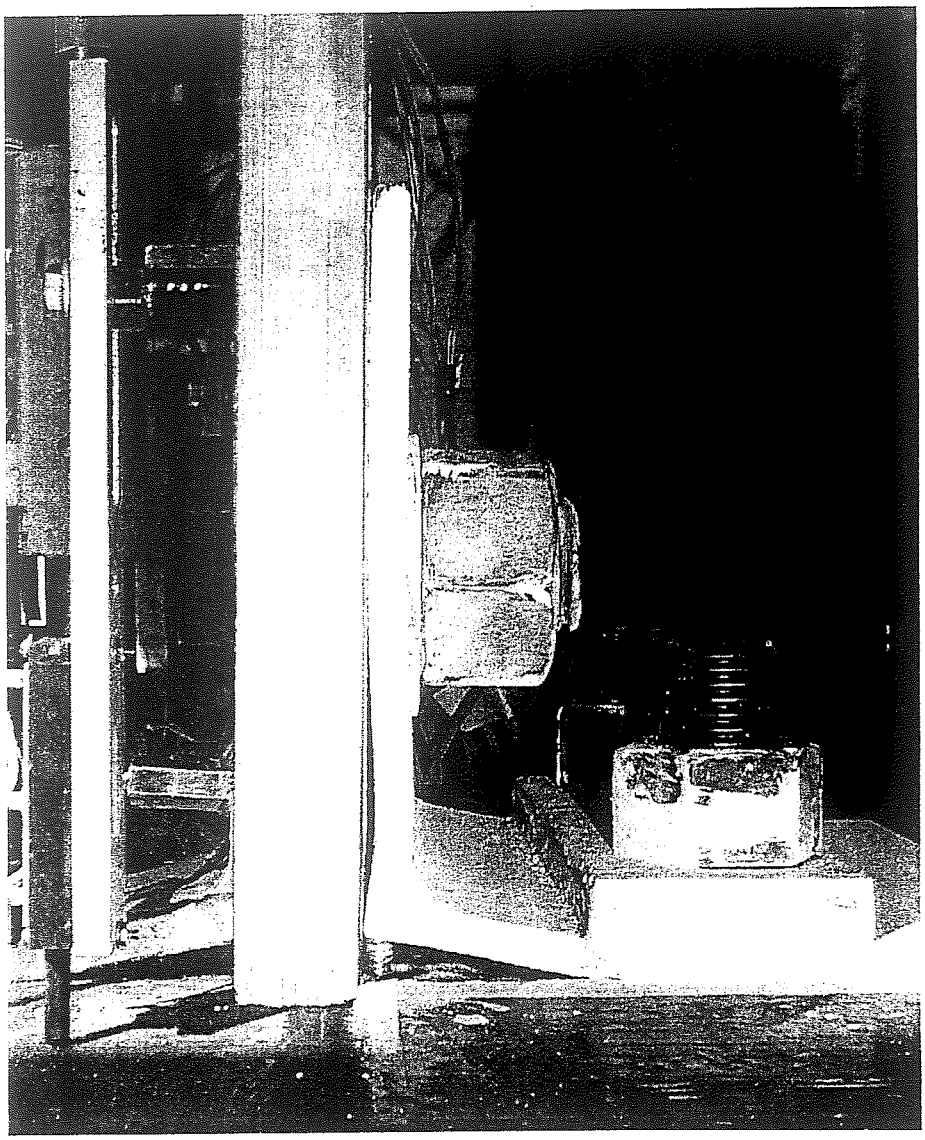

Figure 6.7. Assumed Deformed Shape of Angle (Garlock et al., 1989)

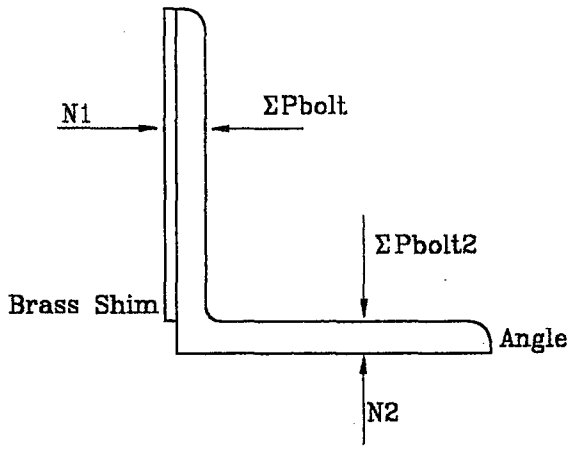

Figure 6.8. Undeformed Angle with External Forces After Assembly

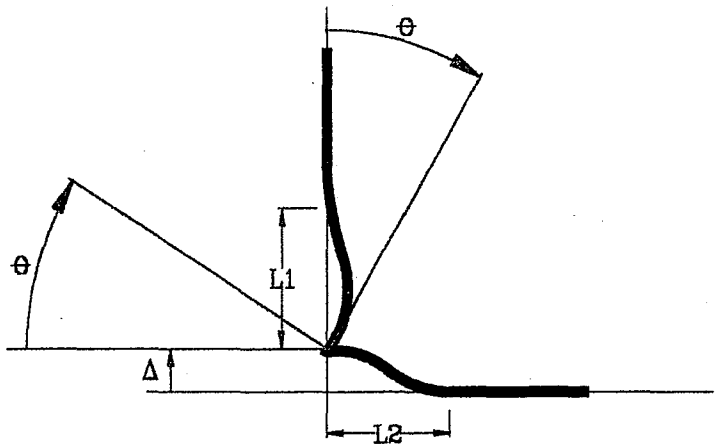

Figure 6.9. Deformed Shape of Angle

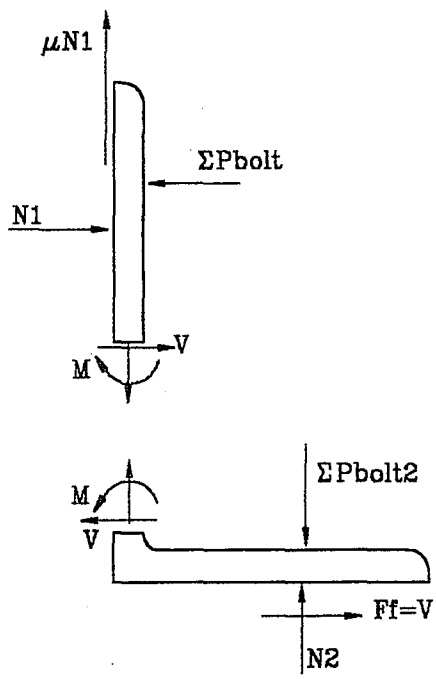

Figure 6.10. Angle Internal Shear Force (V)

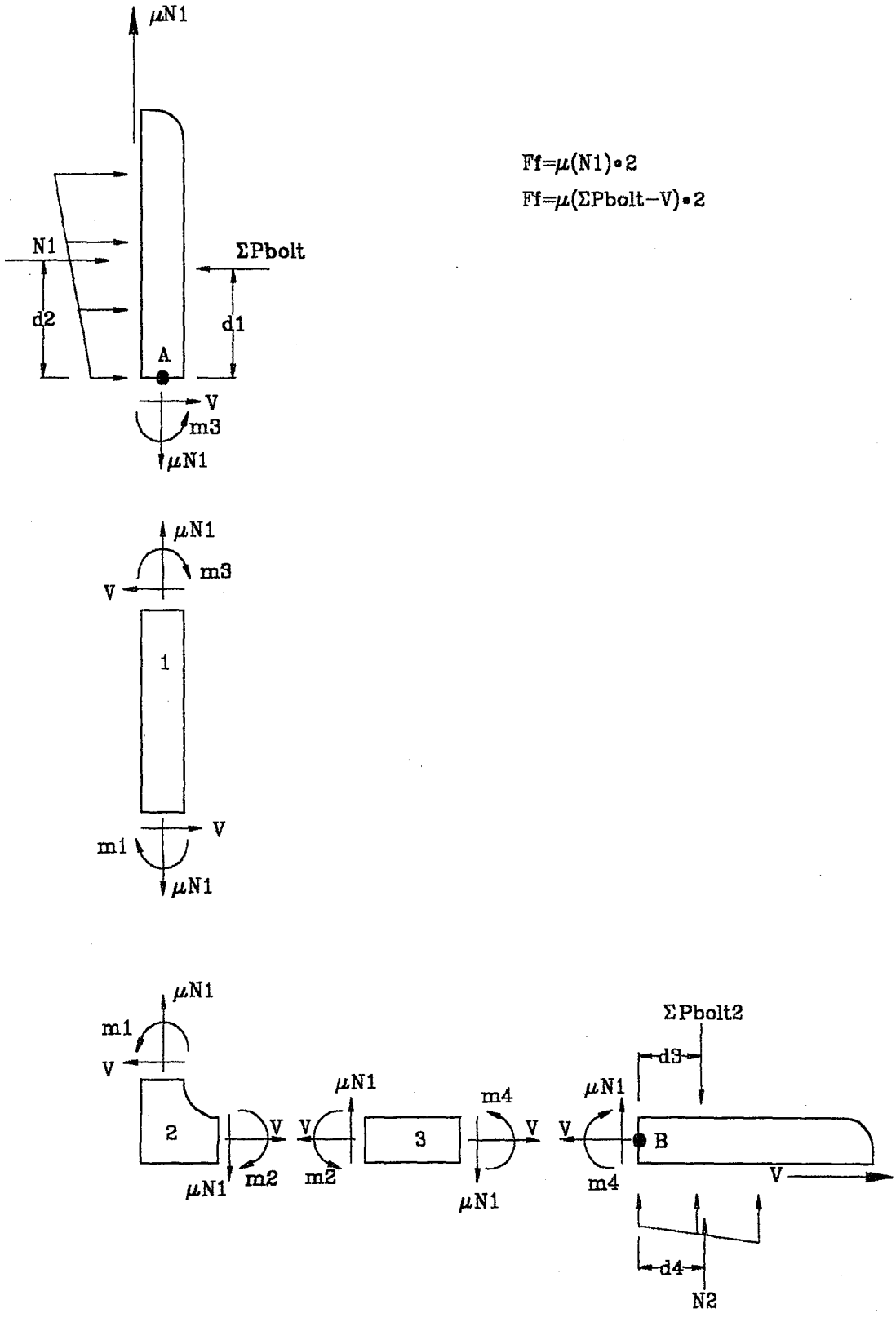

Figure 6.11. FBD of Angle during Pull Cycle

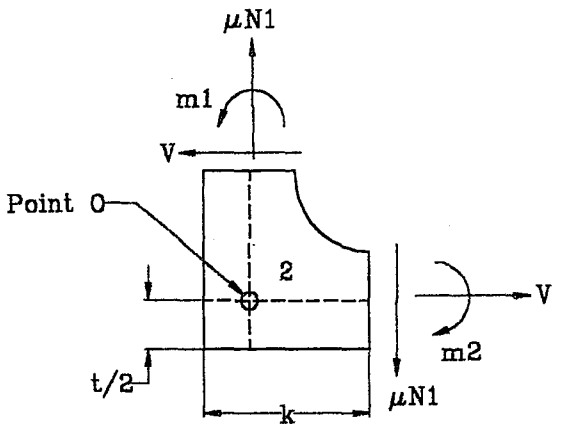

Figure 6.12. FBD of Angle Fillet Region during Pull Cycle

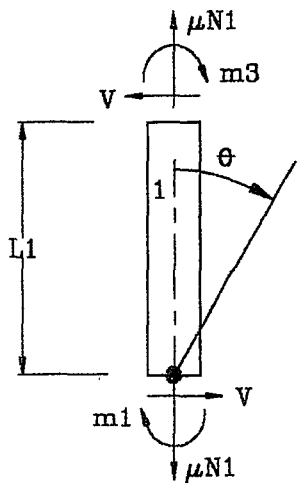

(a) FBD of Vertical Leg Segment

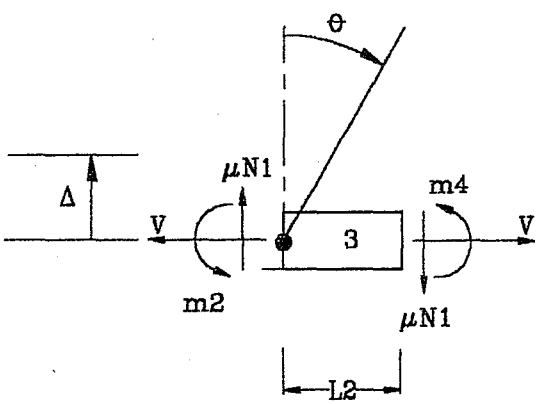

(b) FBD of Horizontal Leg Segment

Figure 6.13. FBD of Angle Vertical and Horizontal Legs Segments during Pull Cycle

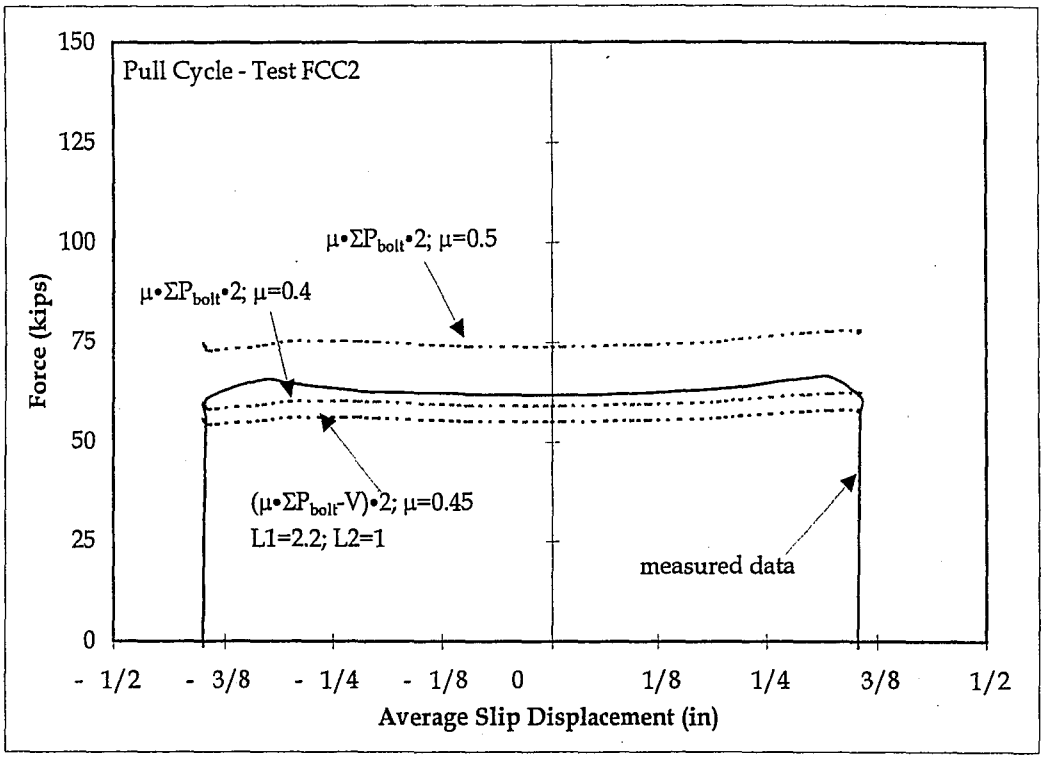

(a) Pull Cycle

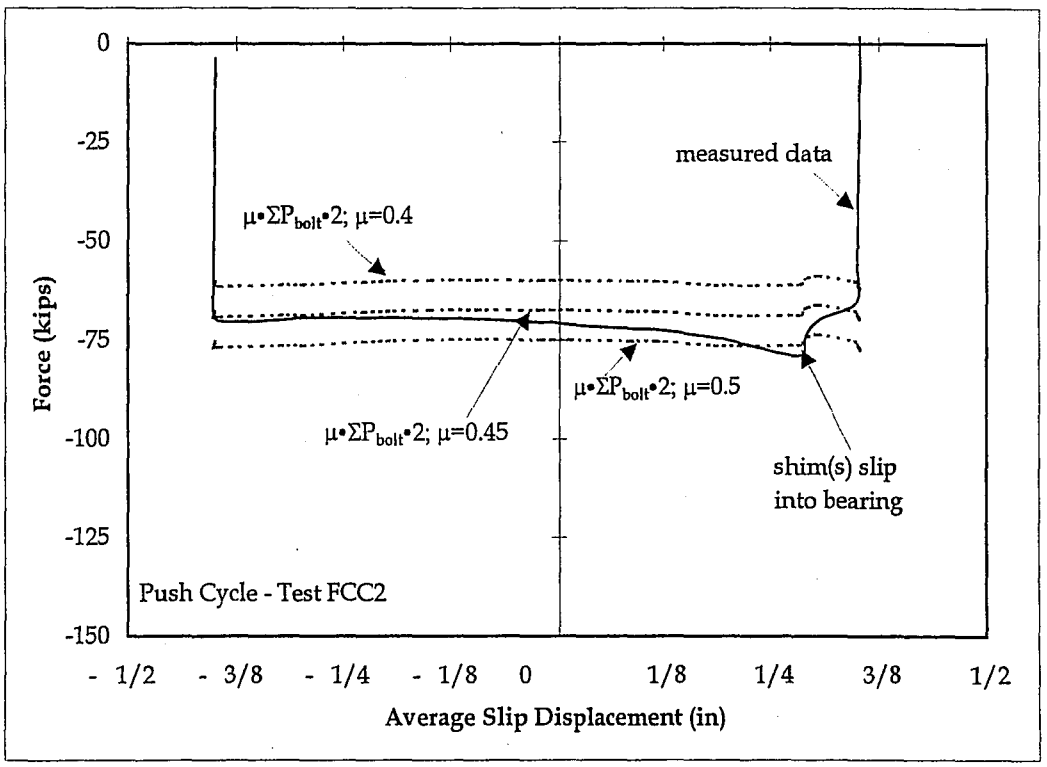

(b) Push Cycle

Figure 6.14. Test FCC2 - Comparison of Analytically Estimated Friction Force including Angle Deformation with Test Results

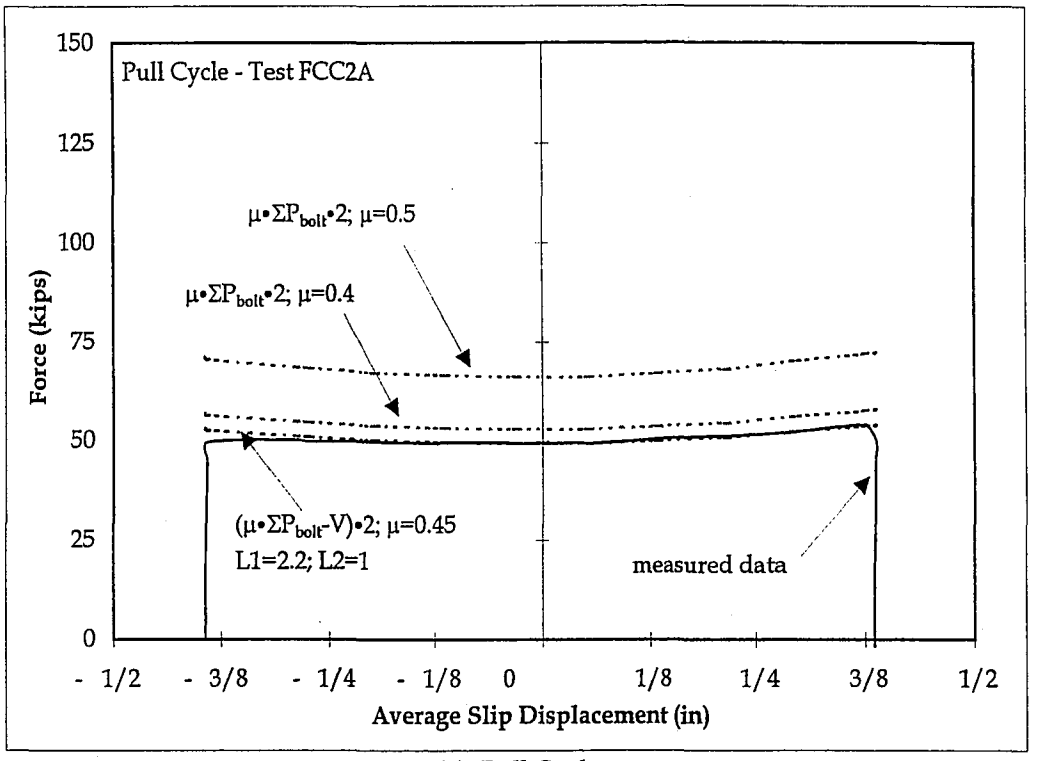

(a) Pull Cycle

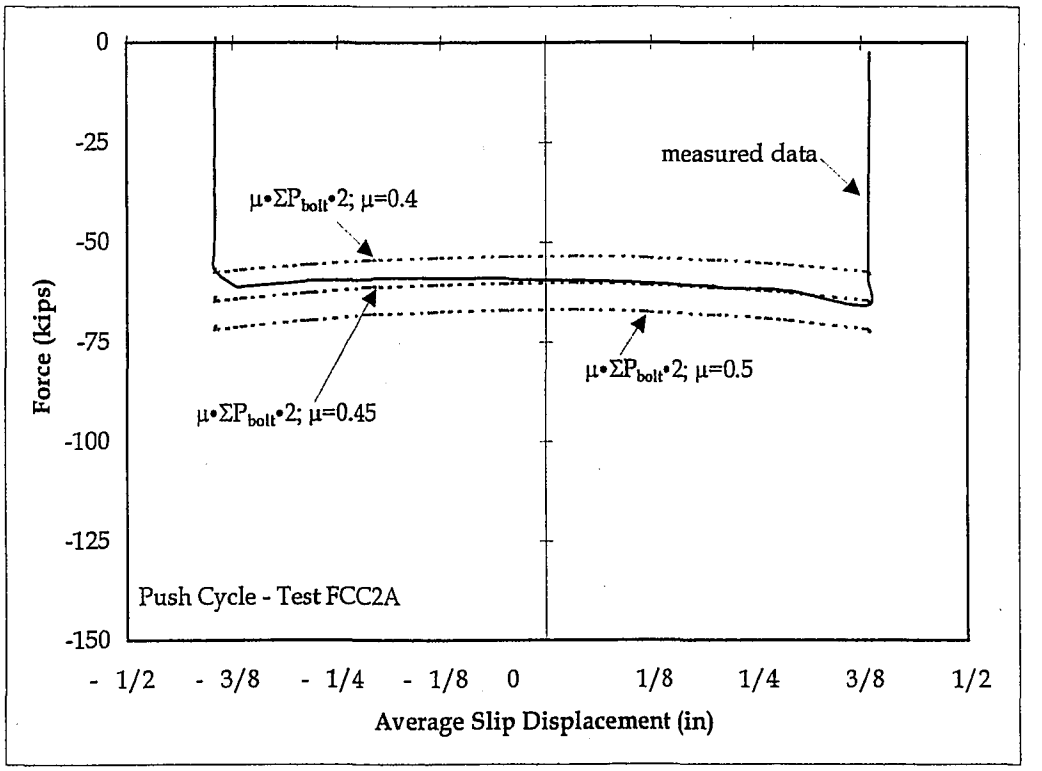

(b) Push Cycle

Figure 6.15. Test FCC2A - Comparison of Analytically Estimated Friction Force including Angle Deformation with Test Results

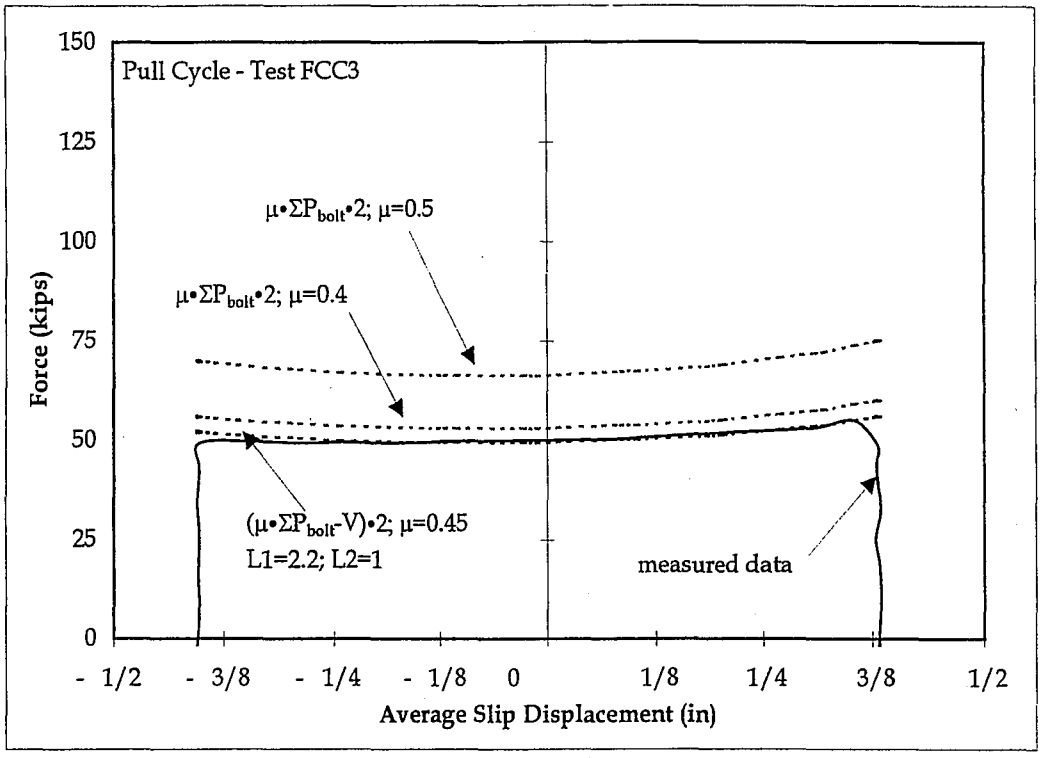

(a) Pull Cycle

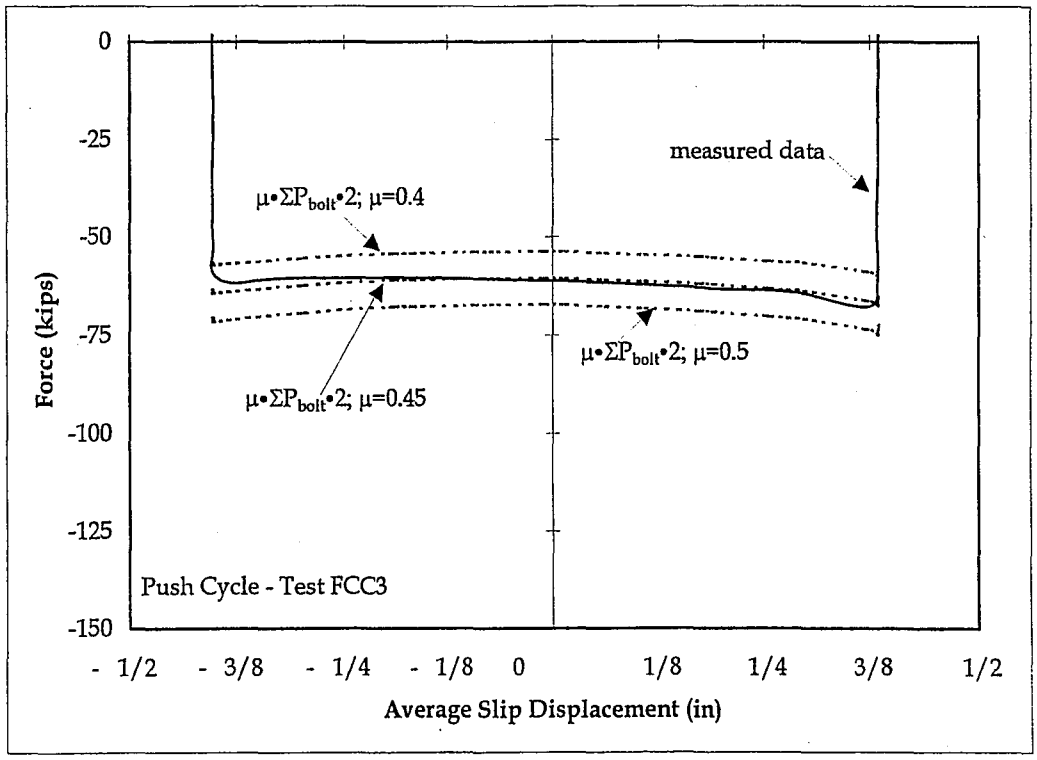

(b) Push Cycle

Figure 6.16. Test FCC3 - Comparison of Analytically Estimated Friction Force including Angle Deformation with Test Results

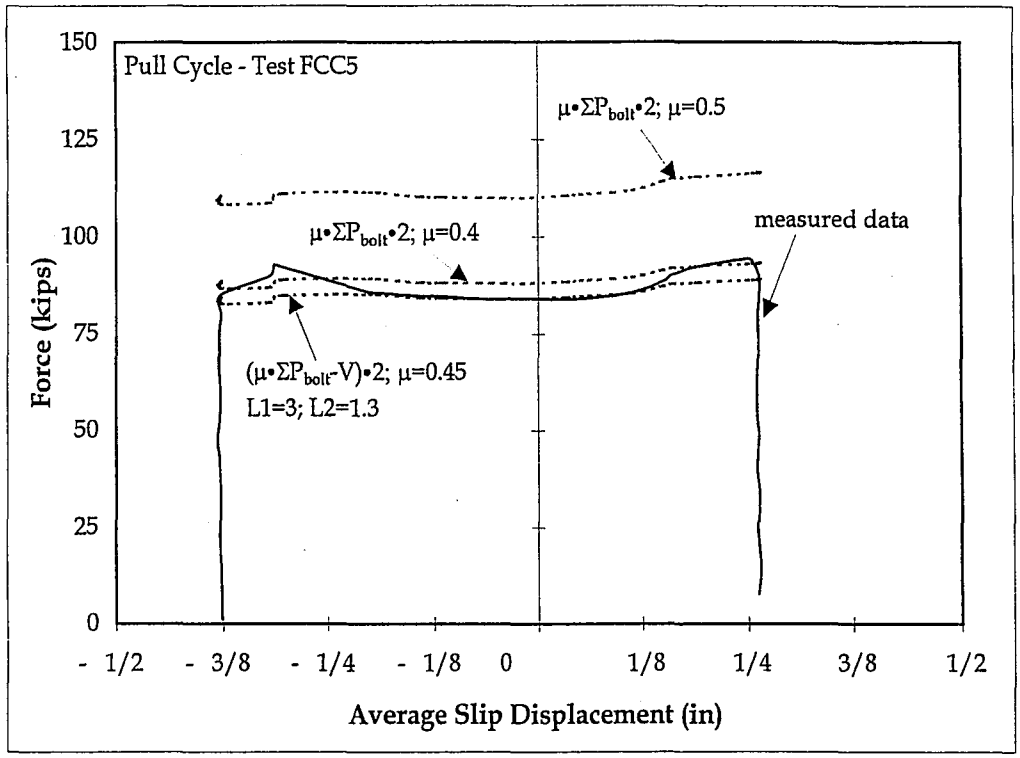

(a) Pull Cycle

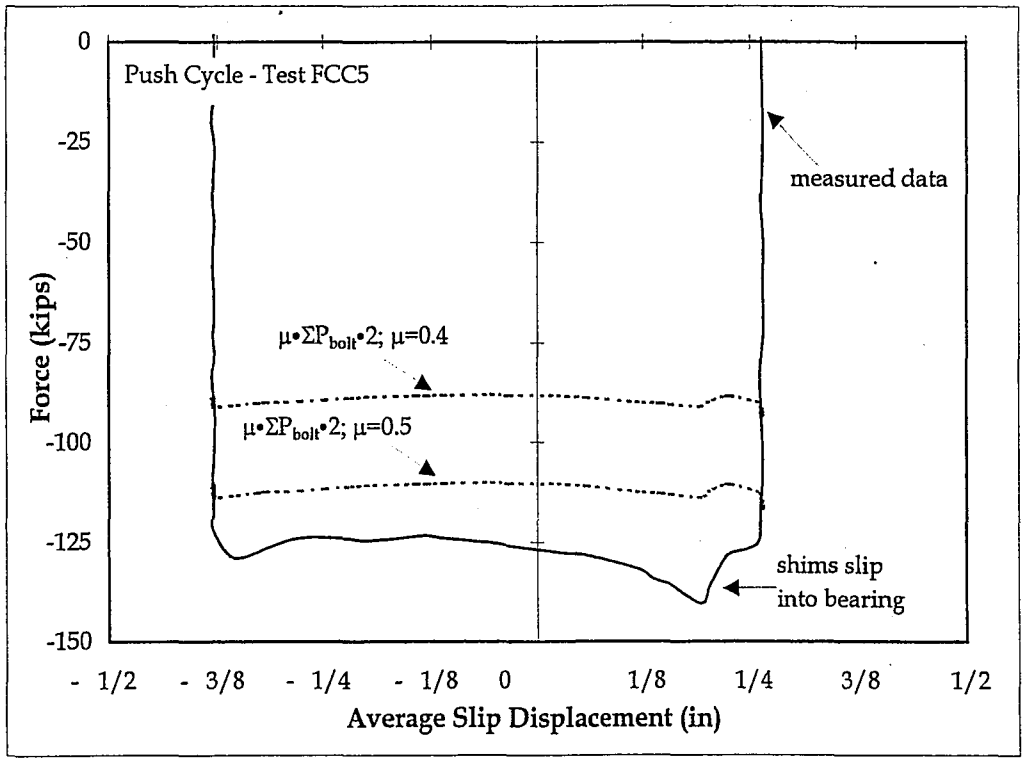

(b) Push Cycle

Figure 6.17. Test FCC5 - Comparison of Analytically Estimated Friction Force including Angle Deformation with Test Results

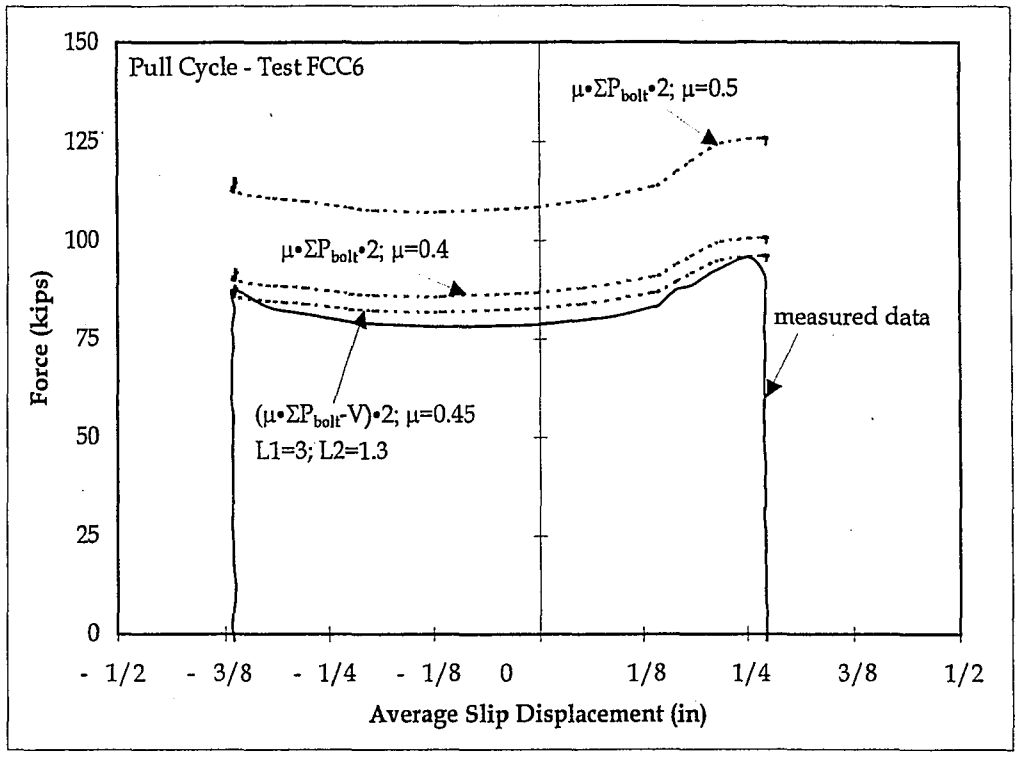

(a) Pull Cycle

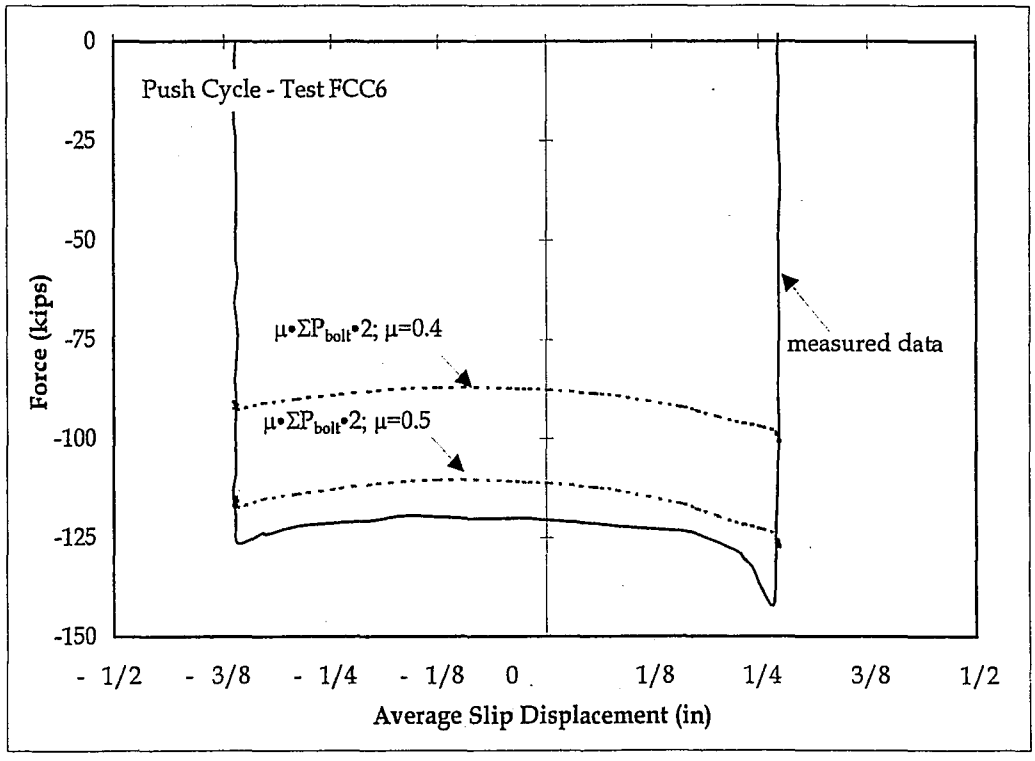

(b) Push Cycle

Figure 6.18. Test FCC6 - Comparison of Analytically Estimated Friction Force including Angle Deformation with Test Results

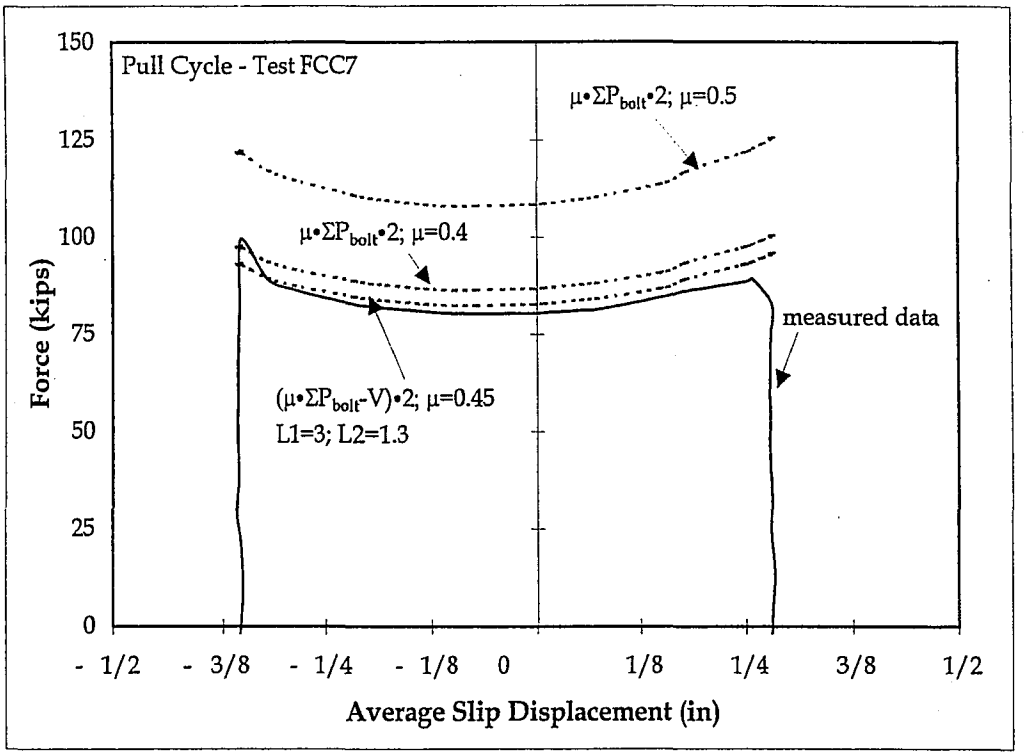

(a) Pull Cycle

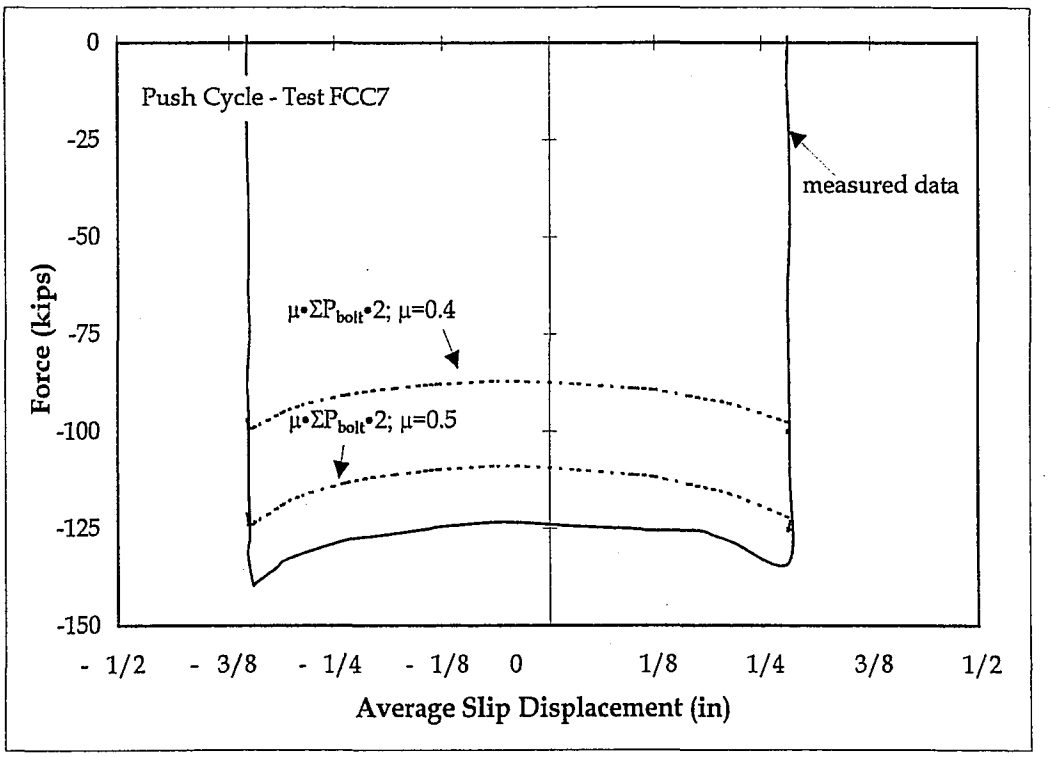

(b) Push Cycle

Figure 6.19. Test FCC7 - Comparison of Analytically Estimated Friction Force including Angle Deformation with Test Results

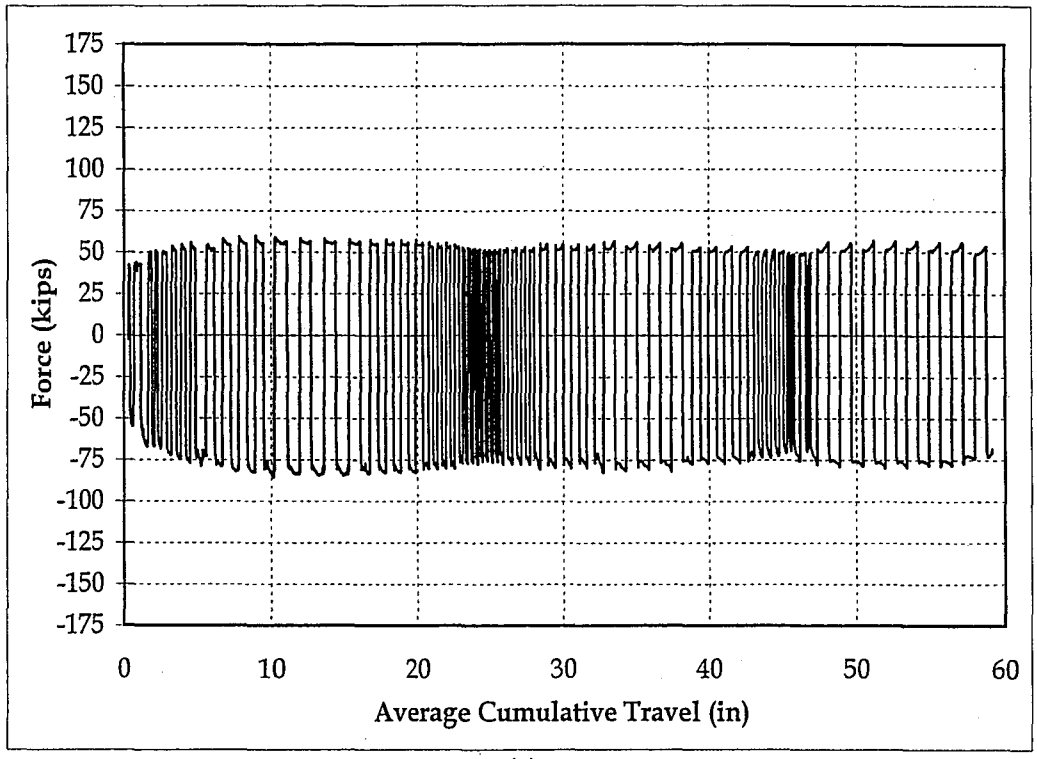

(a)

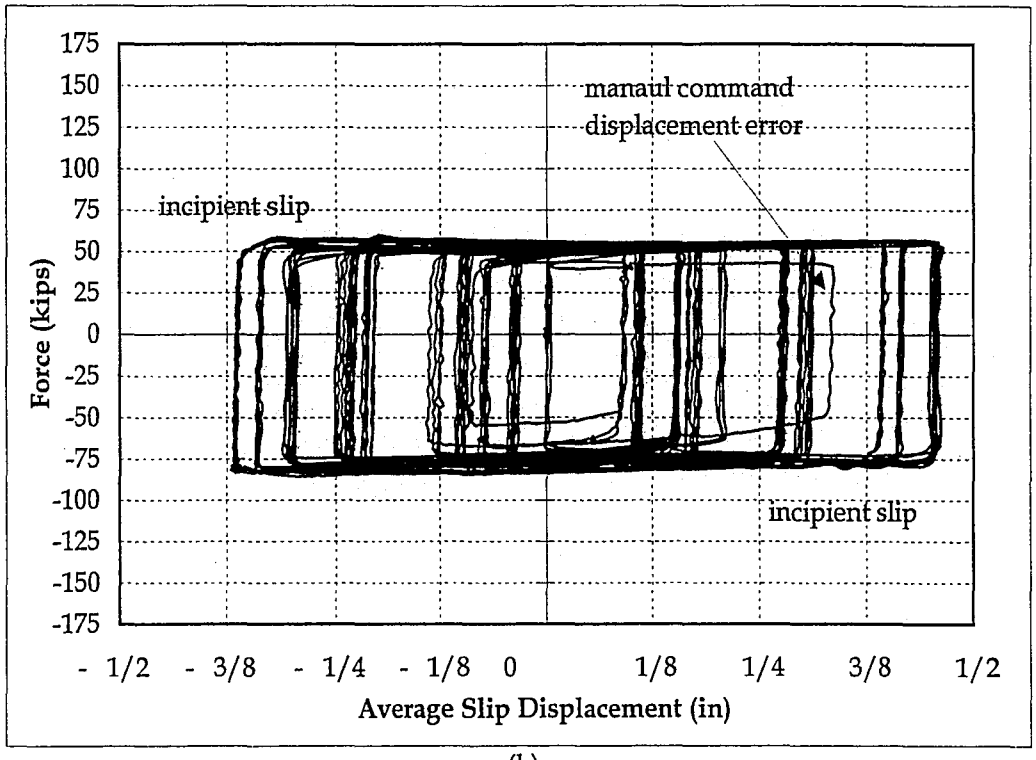

(b)

Figure 6.20. Friction Behavior for Test FCC1:
(a) Force vs. Average Cumulative Travel; and
(b) Force vs. Average Slip Displacement

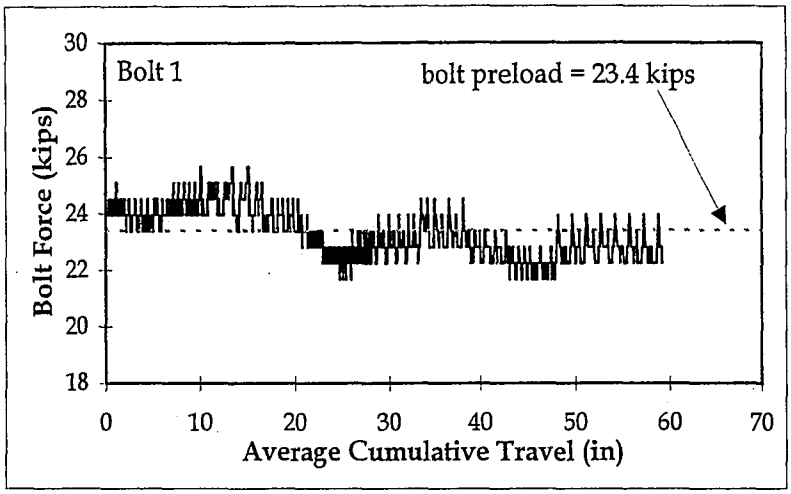

(a)

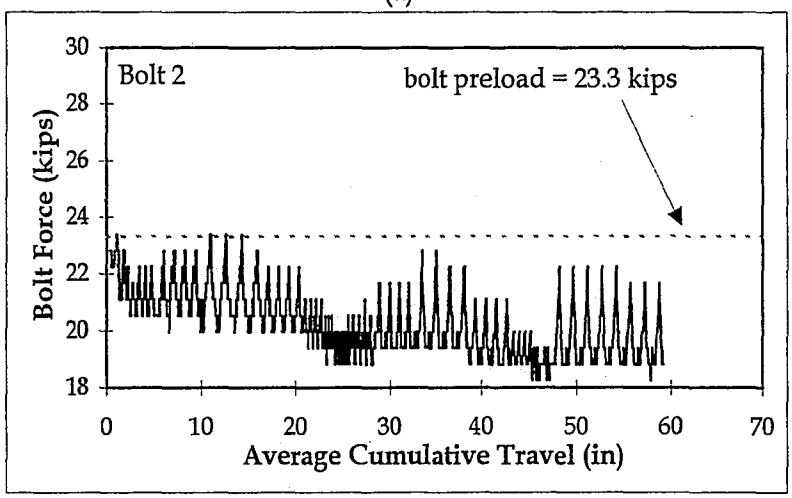

(b)

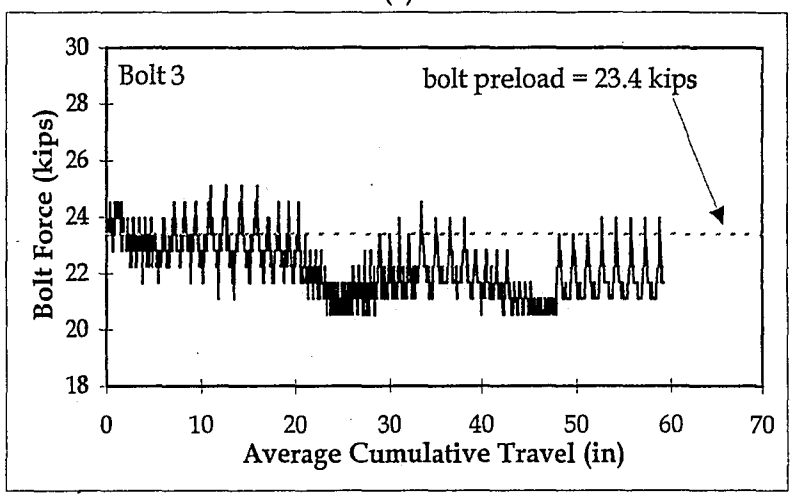

(c)

Figure 6.21. Clamping Bolt Force vs. Average Cumulative Travel for Test FCC1: (a) Bolt 1; (b) Bolt 2; and (c) Bolt 3

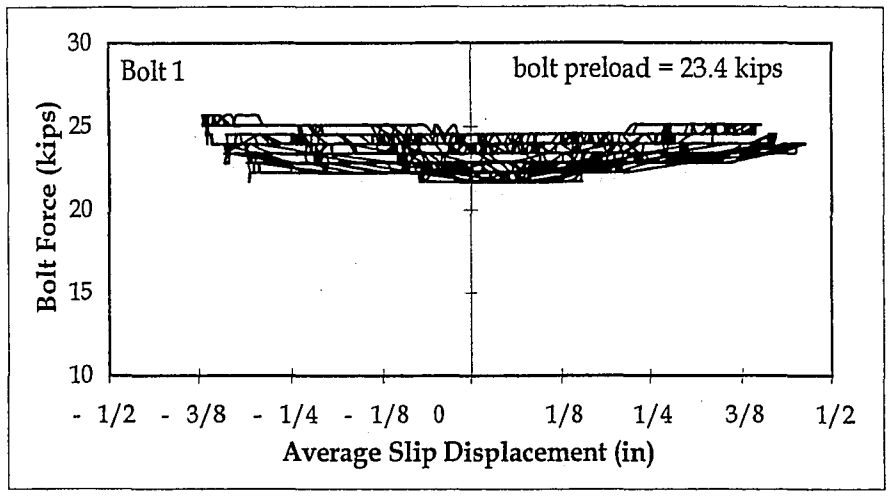

(a)

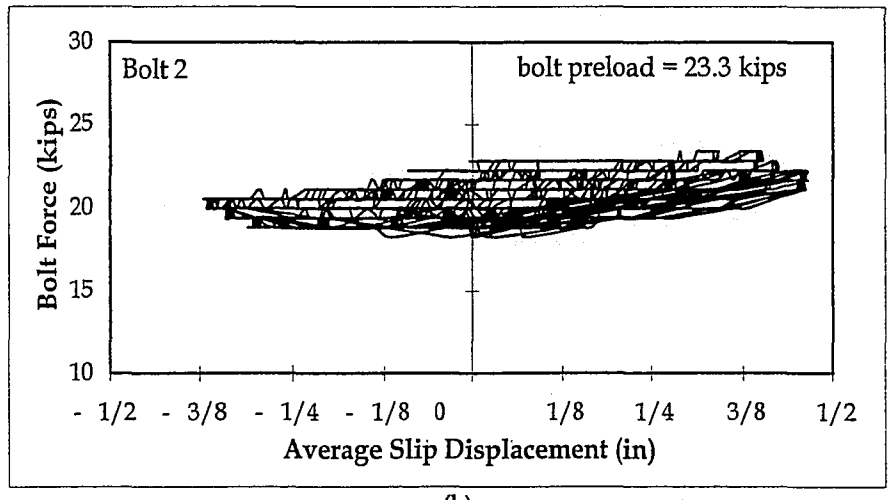

(b)

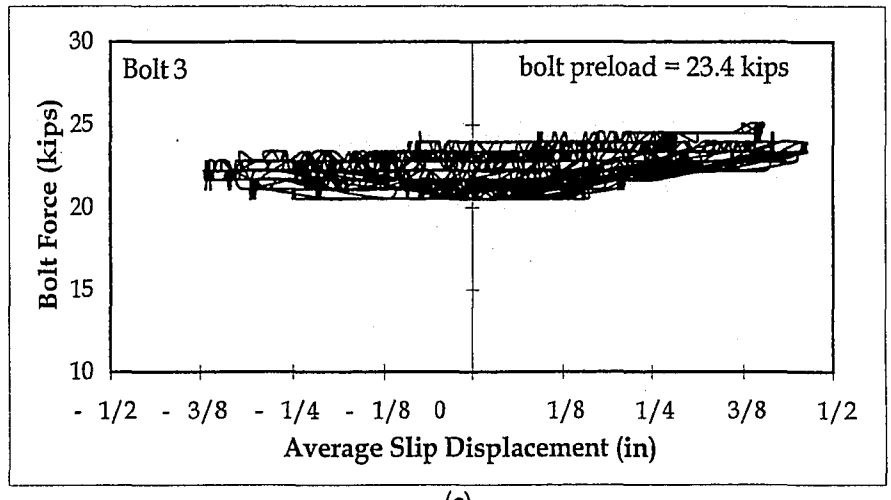

(c)

Figure 6.22. Clamping Bolt Force vs. Average Slip Displacement for Test FCC1: (a) Bolt 1; (b) Bolt 2; and (c) Bolt 3

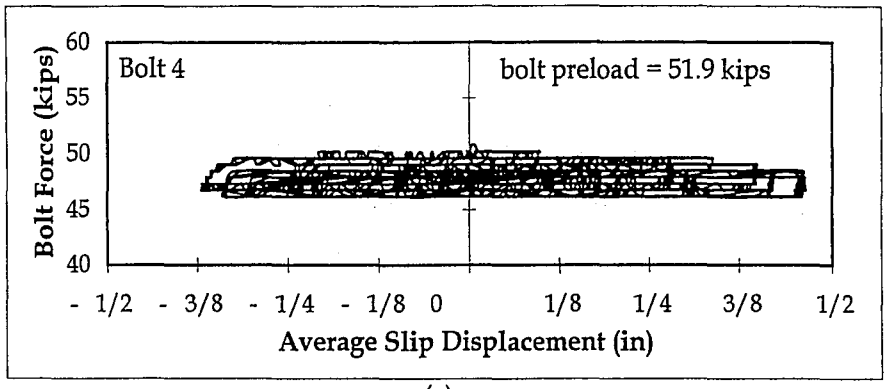

(a)

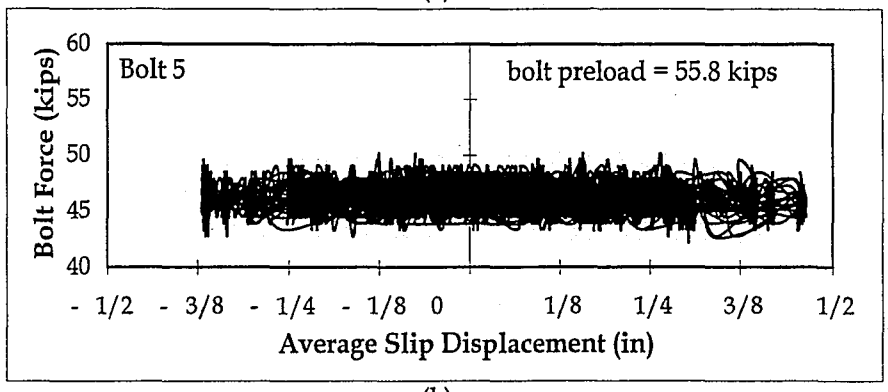

(b)

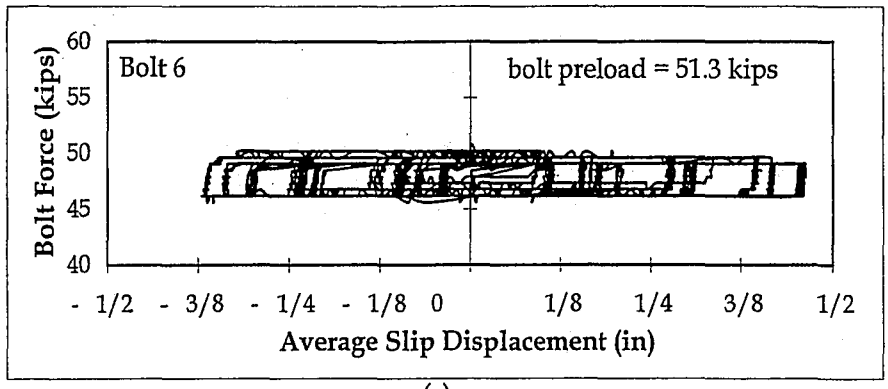

(c)

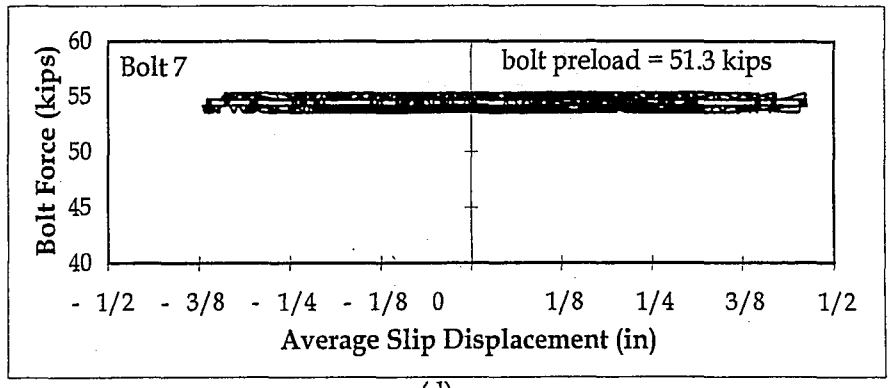

(d)

Figure 6.23. Support Bolt Force vs. Average Slip Displacement for Test FCC1: (a) Bolt 4; (b) Bolt 5; (c) Bolt 6; and (d) Bolt 7

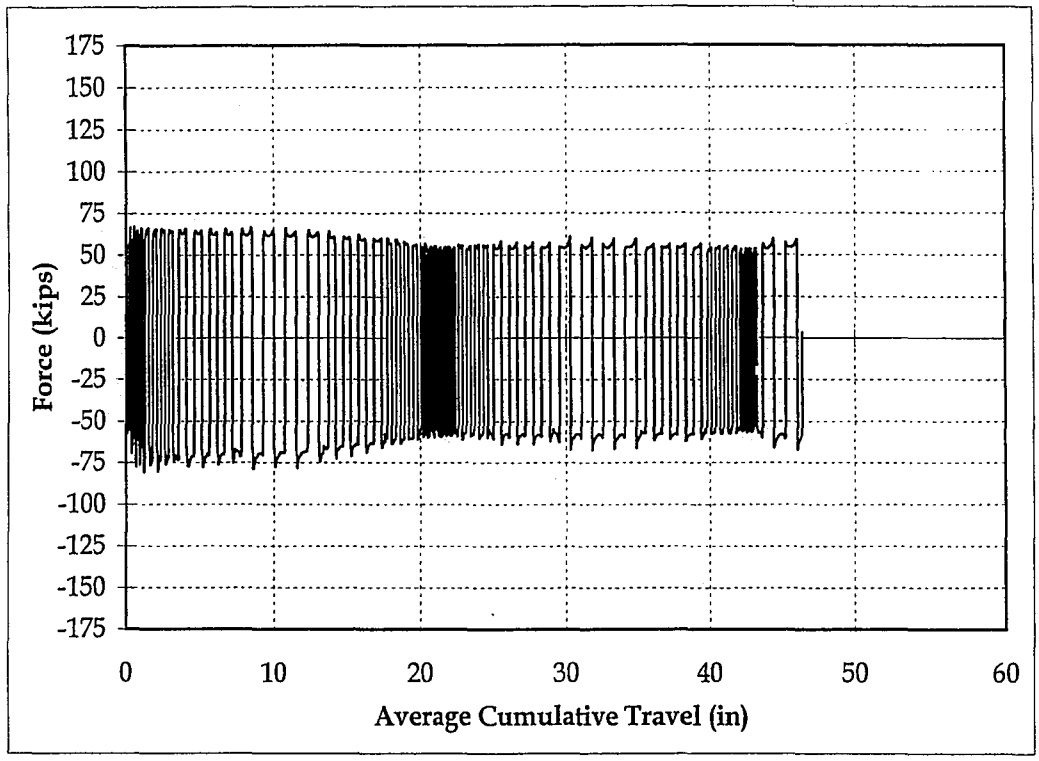

(a)

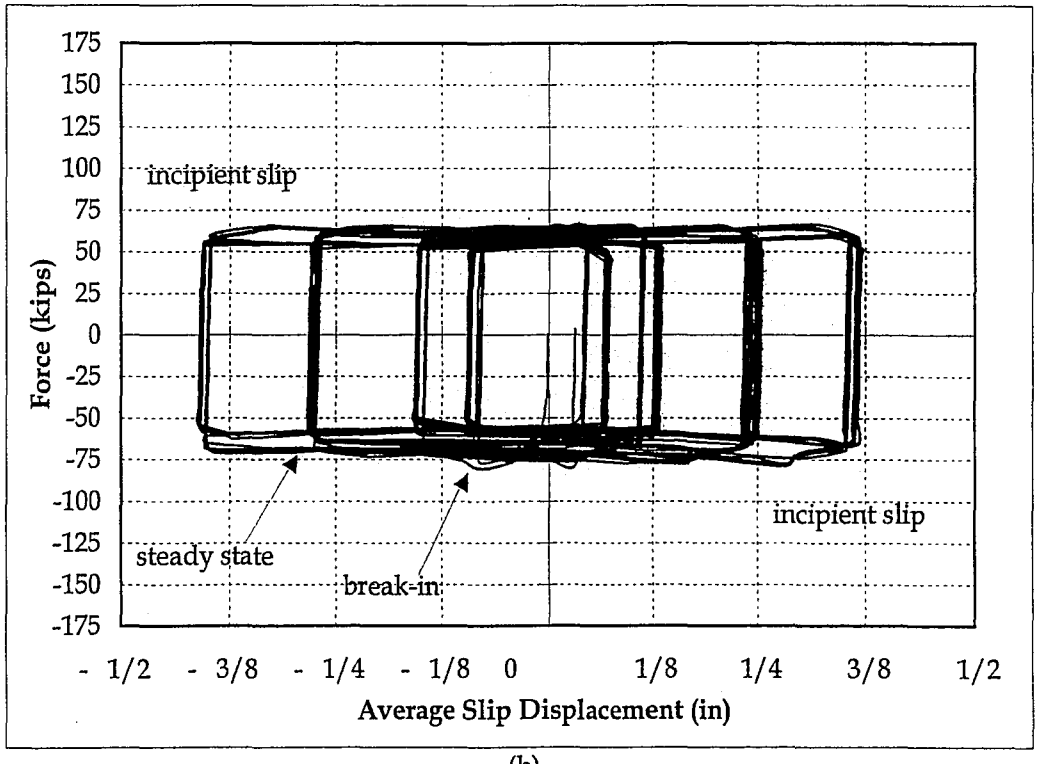

(b)

Figure 6.24. Friction Behavior for Test FCC2:
(a) Force vs. Average Cumulative Travel; and
(b) Force vs. Average Slip Displacement

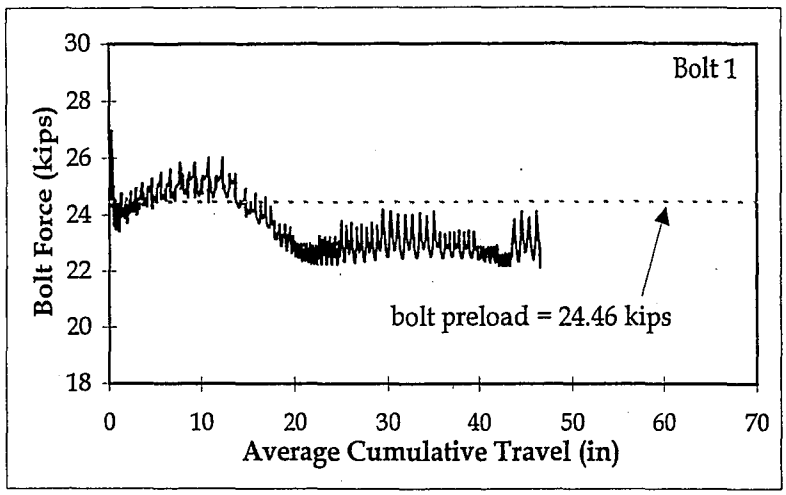

(a)

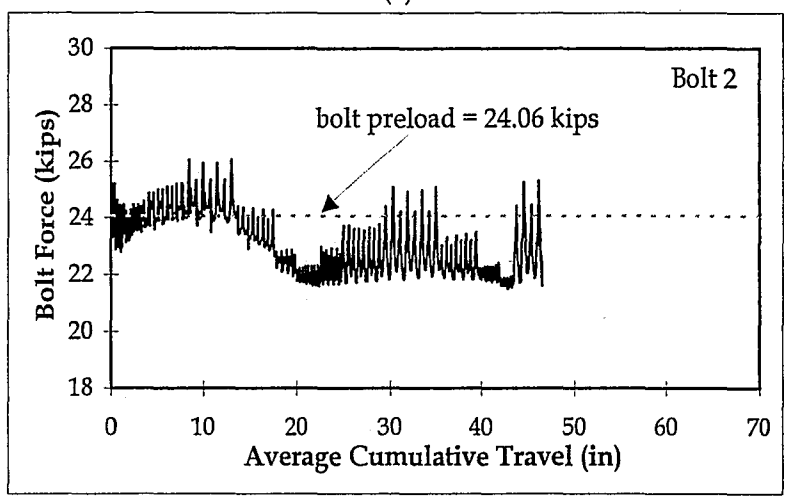

(b)

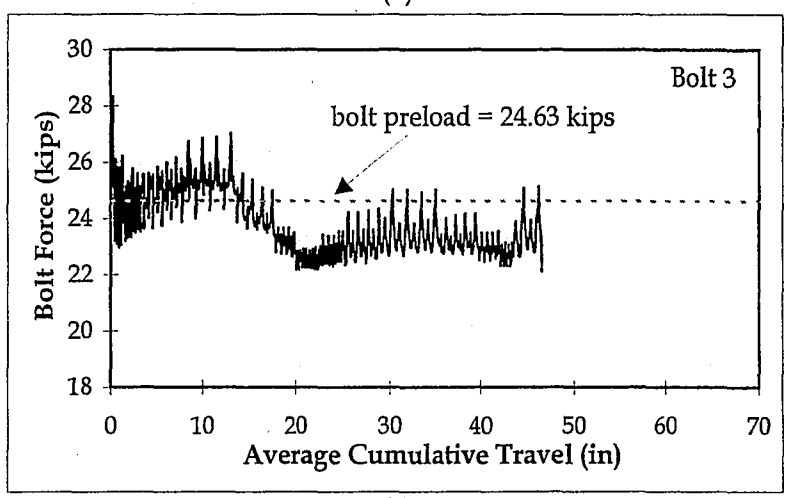

(c)

Figure 6.25. Clamping Bolt Force vs. Average Cumulative Travel for Test FCC2: (a) Bolt 1; (b) Bolt 2; and (c) Bolt 3

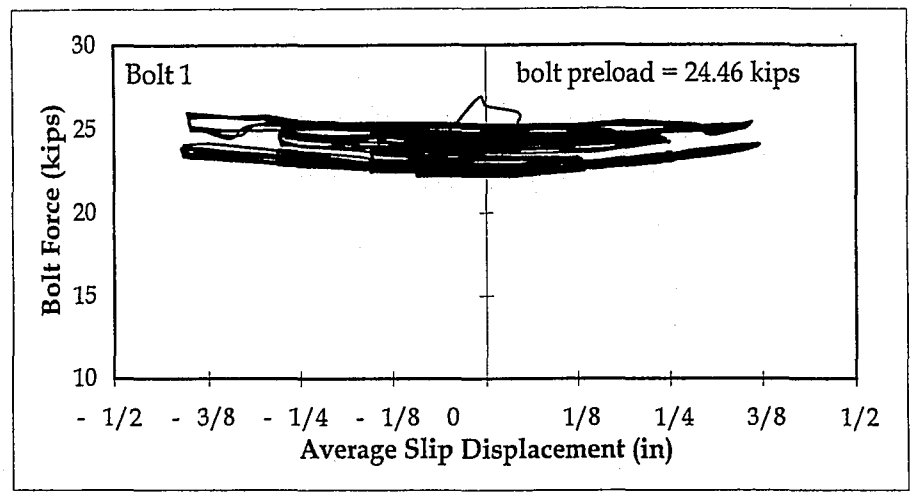

(a)

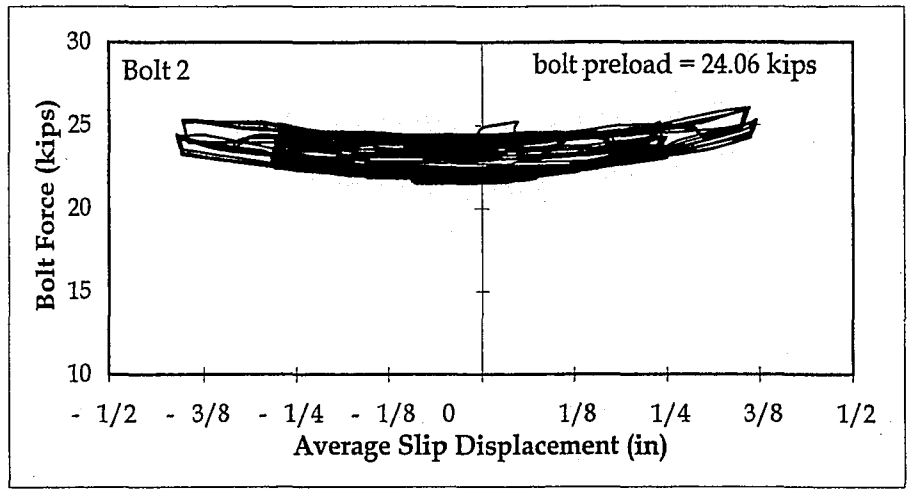

(b)

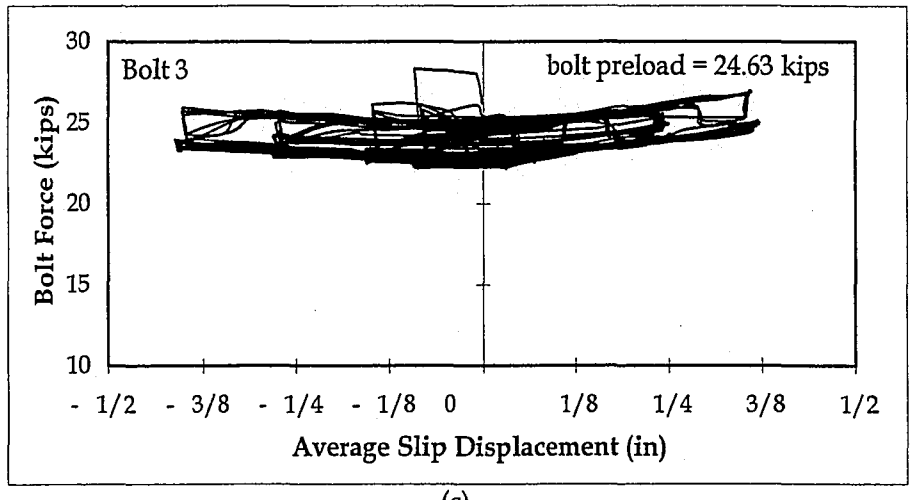

(c)

Figure 6.26. Clamping Bolt Force vs. Average Slip Displacement for Test FCC2: (a) Bolt 1; (b) Bolt 2; and (c) Bolt 3

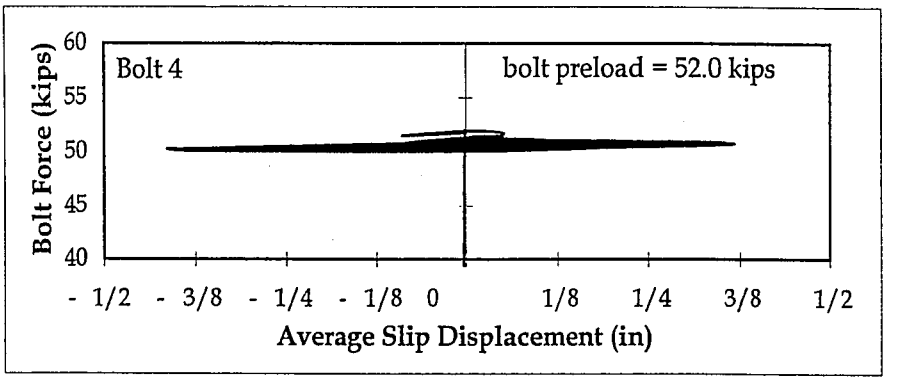

(a)

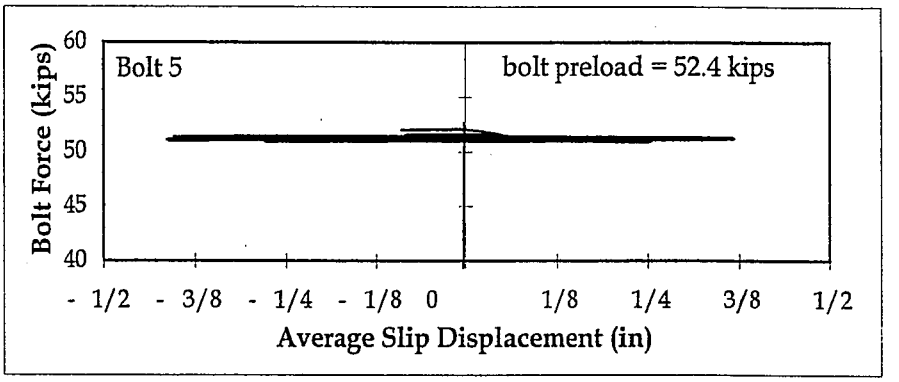

(b)

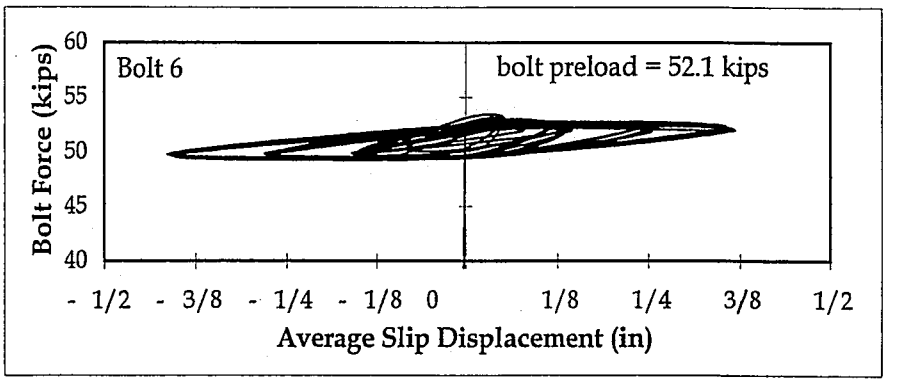

(c)

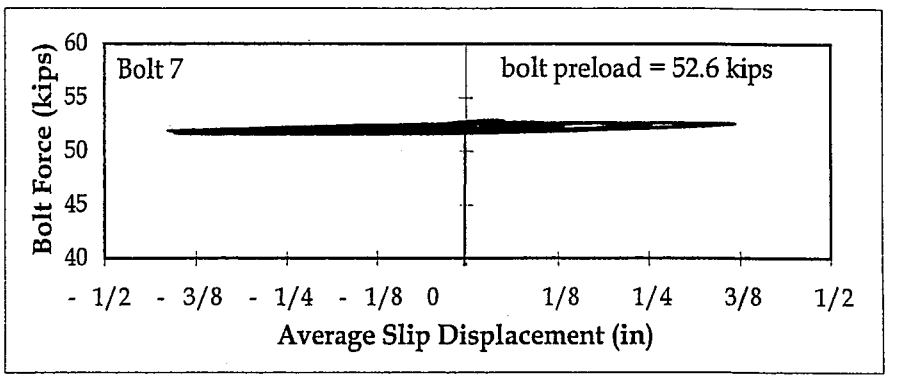

(d)

Figure 6.27. Support Bolt Force vs. Average Slip Displacement for Test FCC2: (a) Bolt 4; (b) Bolt 5; (c) Bolt 6; and (d) Bolt 7

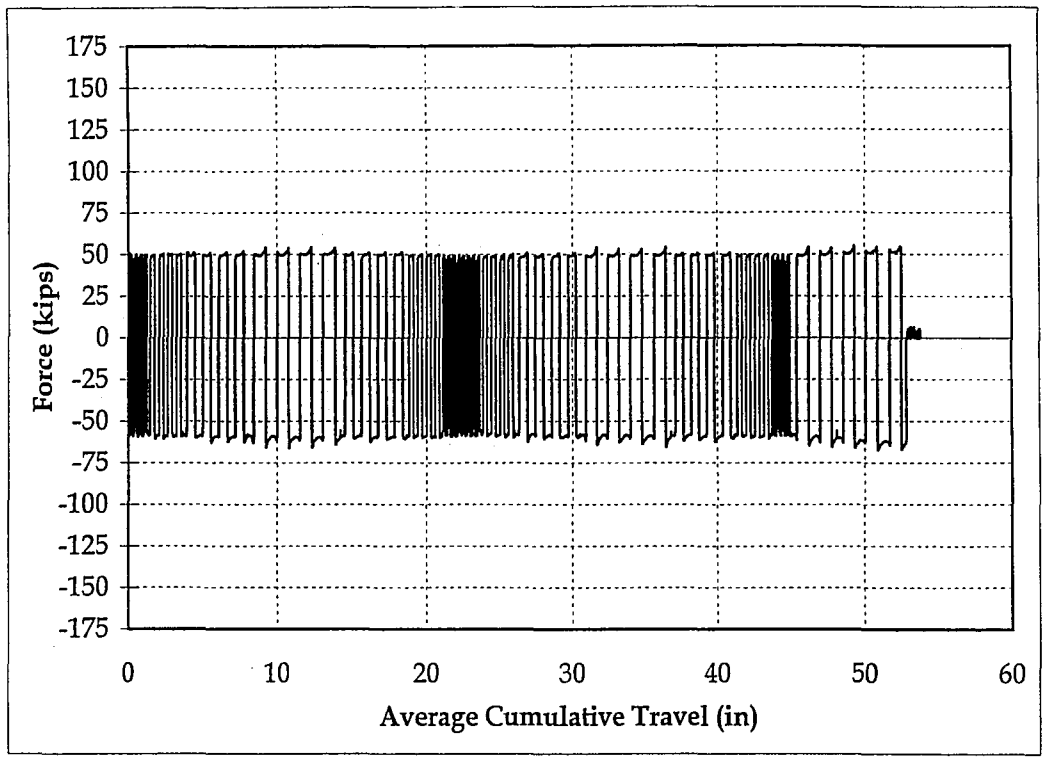

(a)

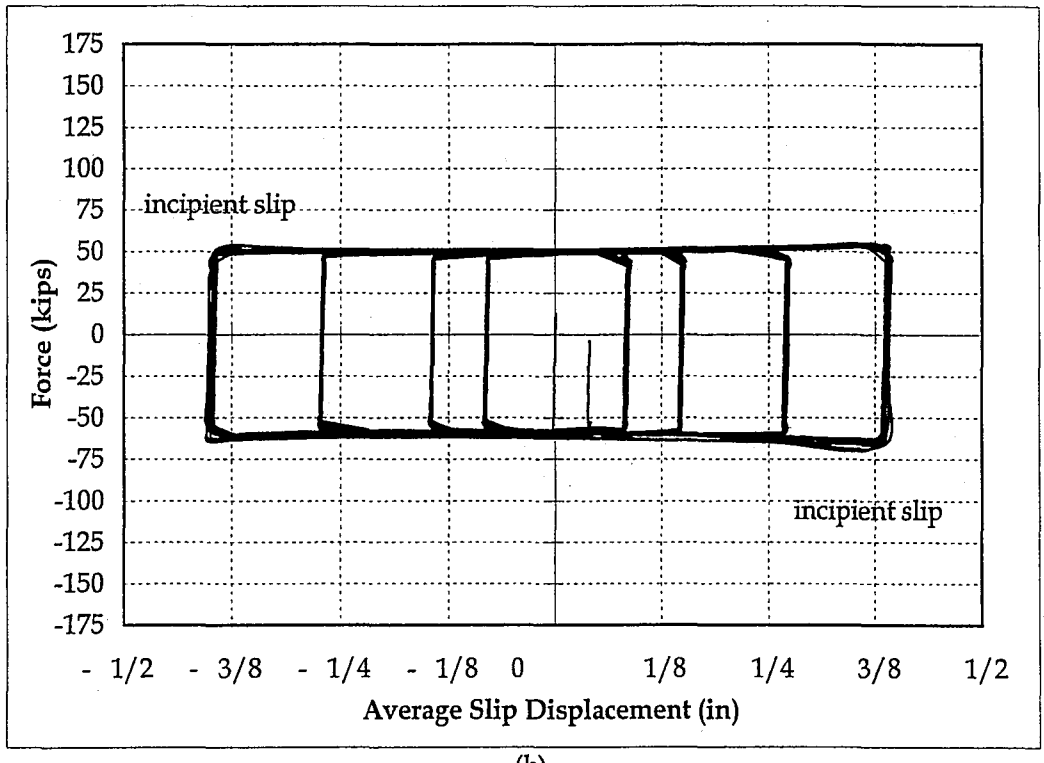

(b)

Figure 6.28. Friction Behavior for Test FCC2A:
(a) Force vs. Average Cumulative Travel; and
(b) Force vs. Average Slip Displacement

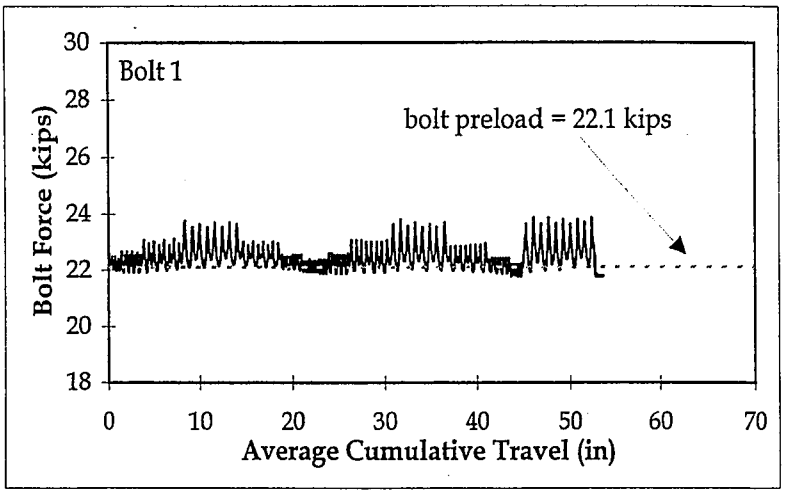

(a)

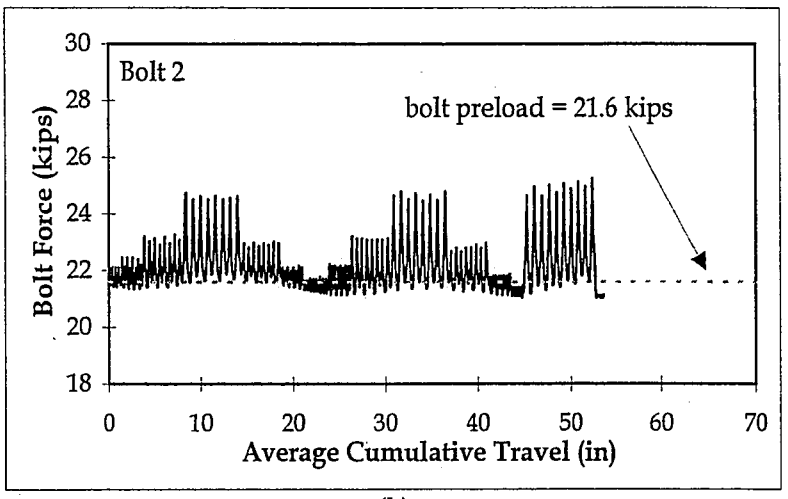

(b)

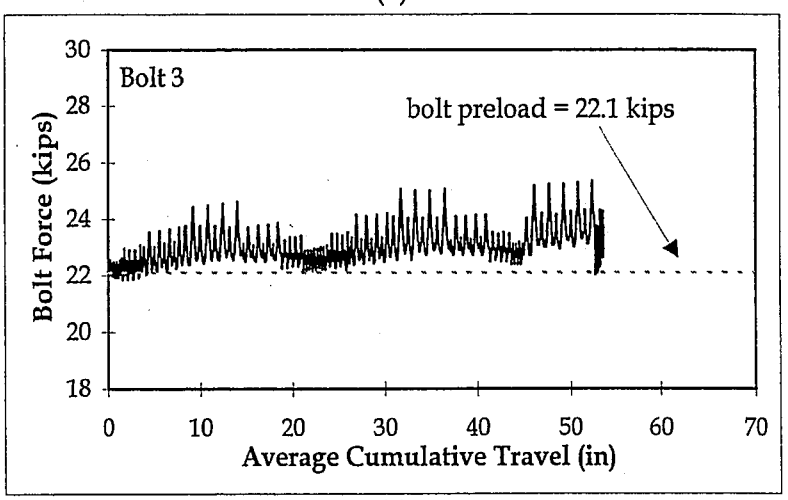

(c)

Figure 6.29. Clamping Bolt Force vs. Average Cumulative Travel for Test FCC2A: (a) Bolt 1; (b) Bolt 2; and (c) Bolt 3

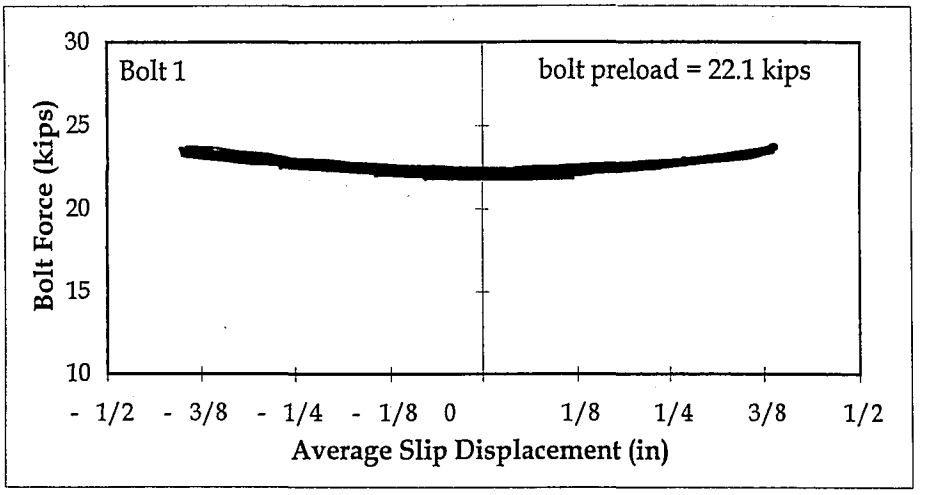

(a)

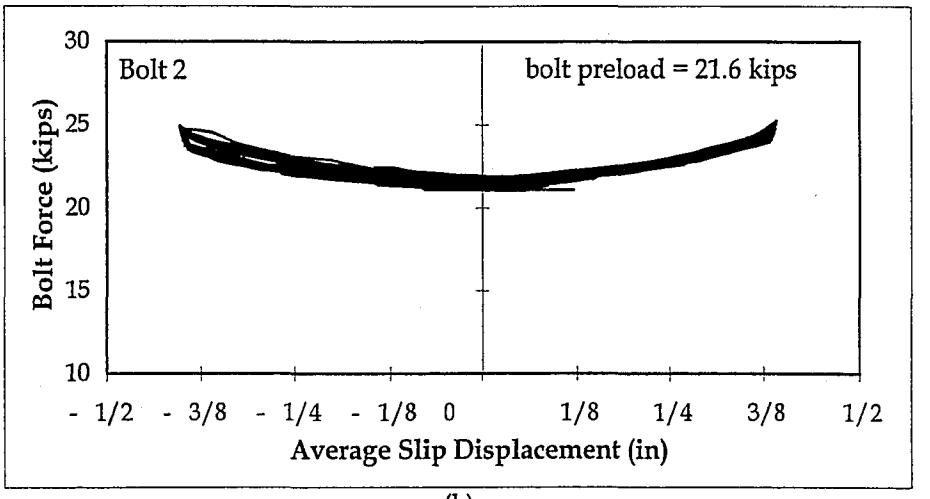

(b)

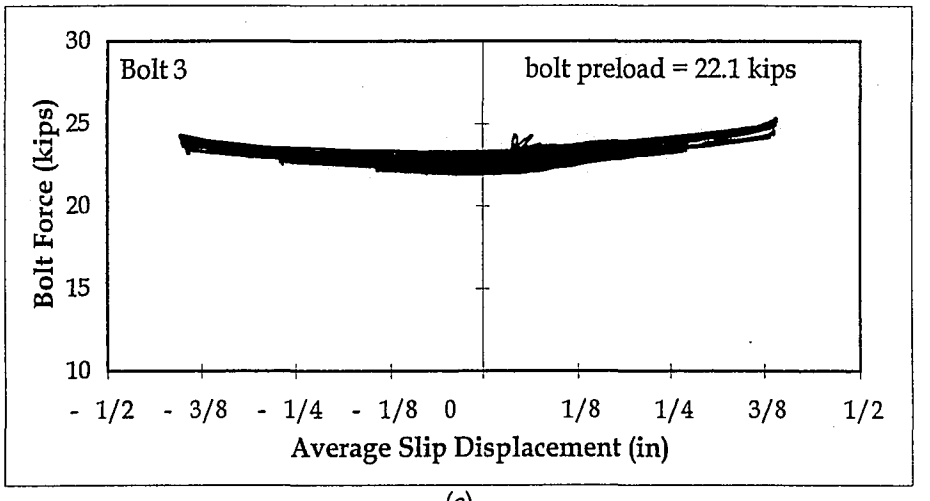

(c)

Figure 6.30. Clamping Bolt Force vs. Average Slip Displacement for Test FCC2A: (a) Bolt 1; (b) Bolt 2; and (c) Bolt 3

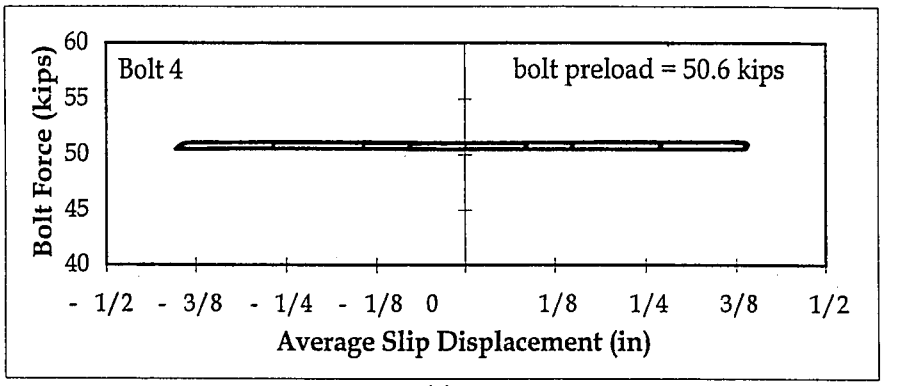

(a)

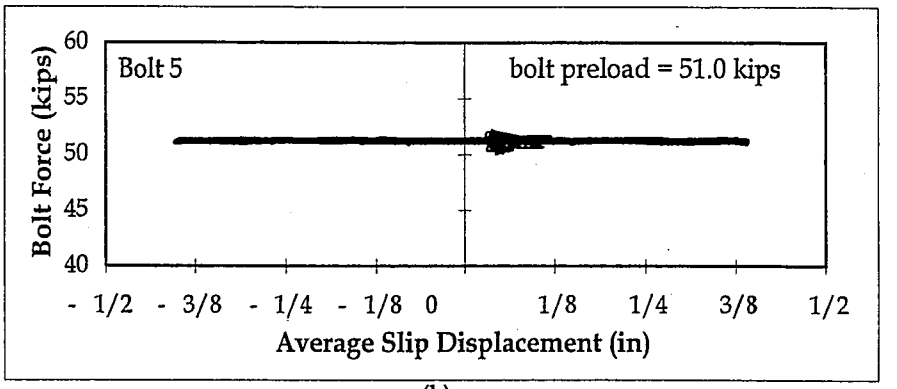

(b)

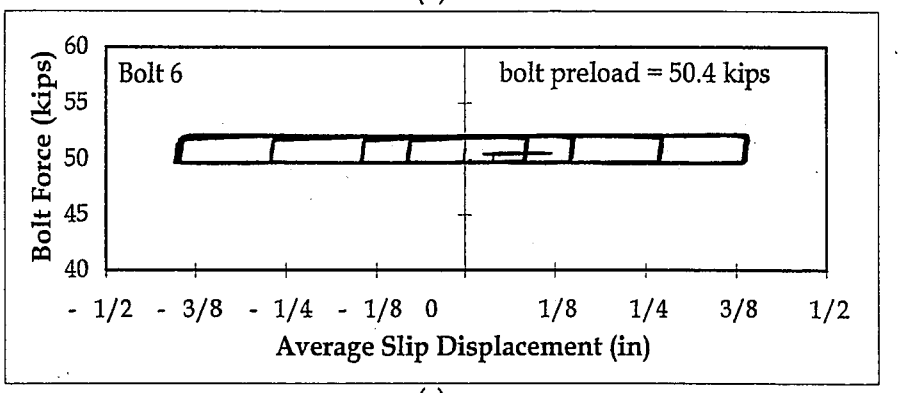

(c)

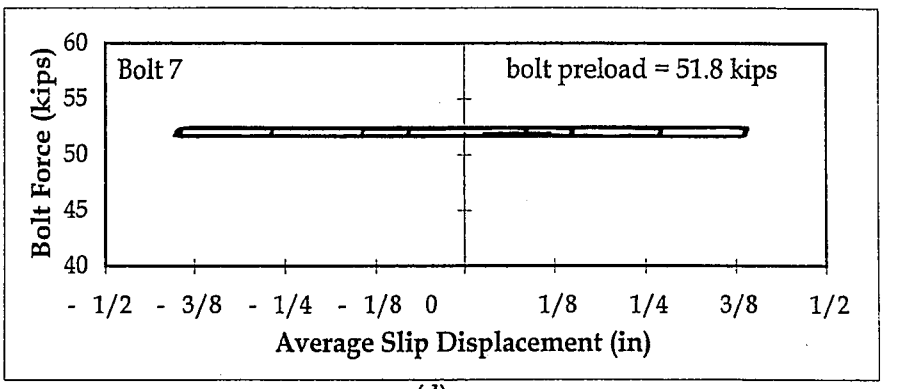

(d)

Figure 6.31. Support Bolt Force vs. Average Slip Displacement for Test FCC2A: (a) Bolt 4; (b) Bolt 5; (c) Bolt 6; and (d) Bolt 7

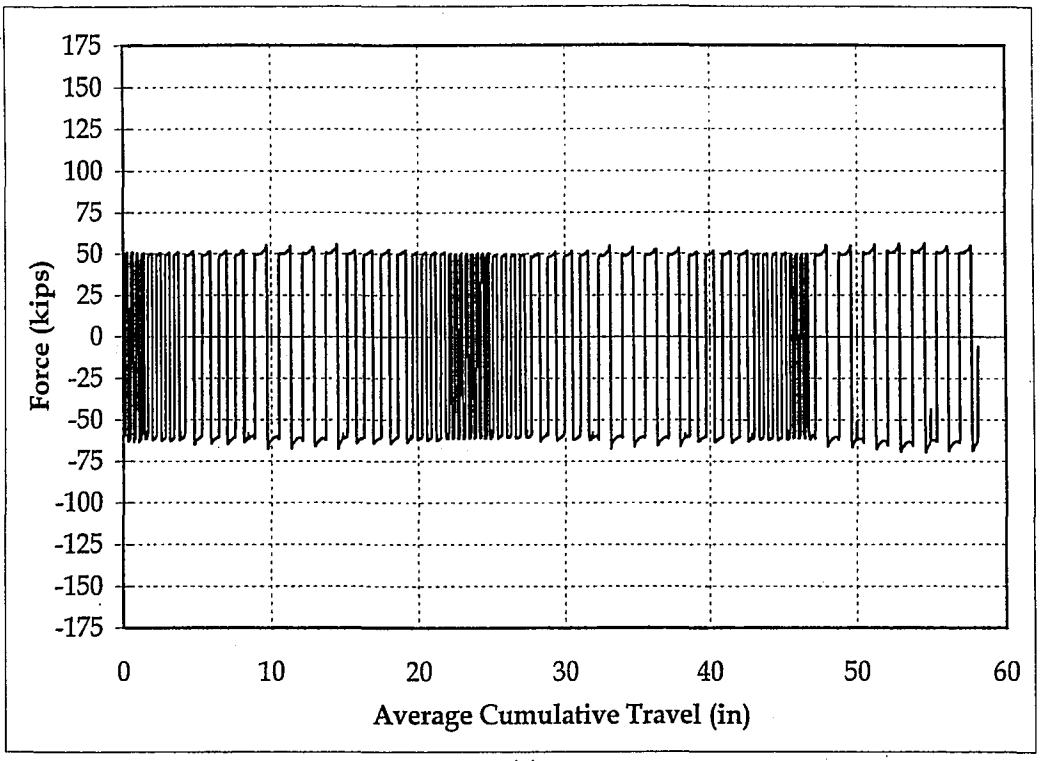

(a)

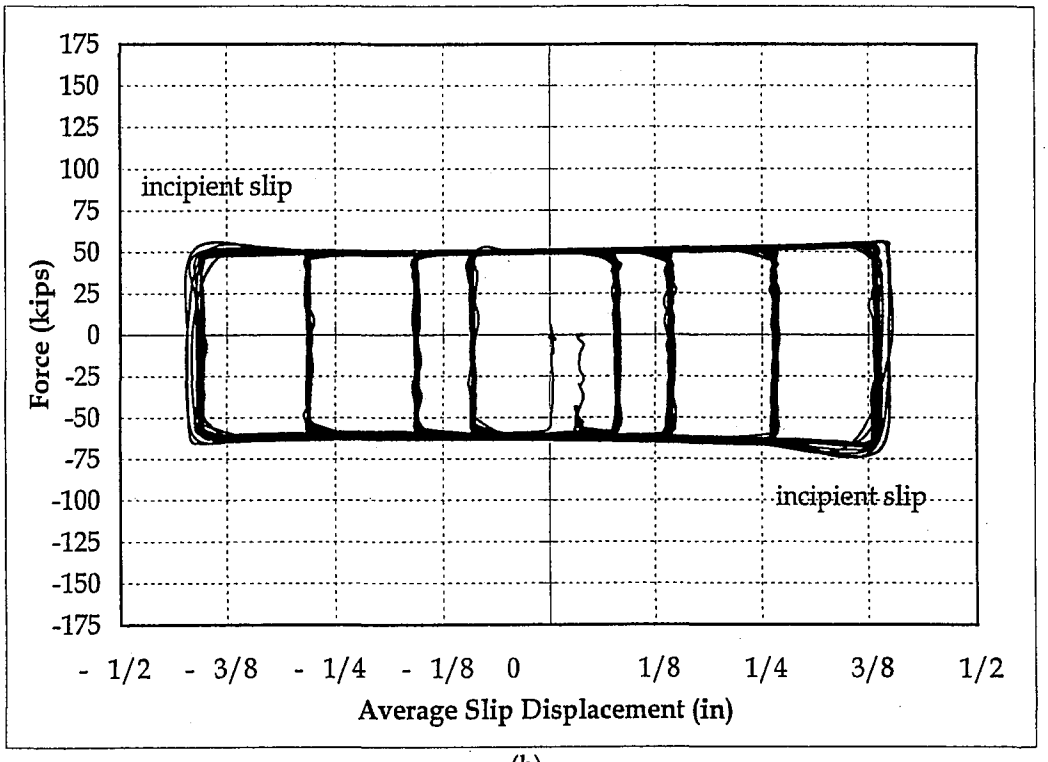

(b)

Figure 6.32. Friction Behavior for Test FCC3:
(a) Force vs. Average Cumulative Travel; and
(b) Force vs. Average Slip Displacement

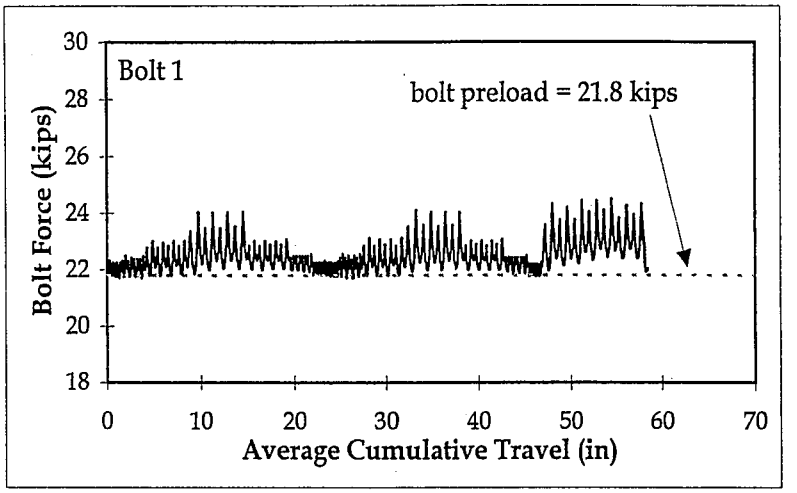

(a)

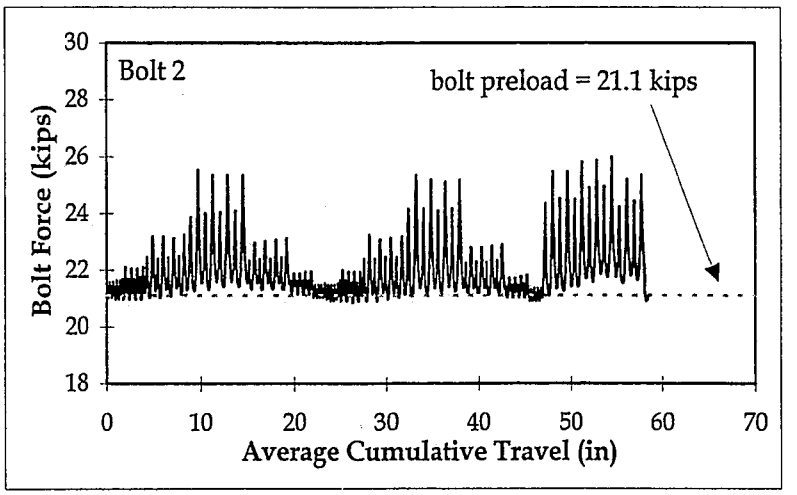

(b)

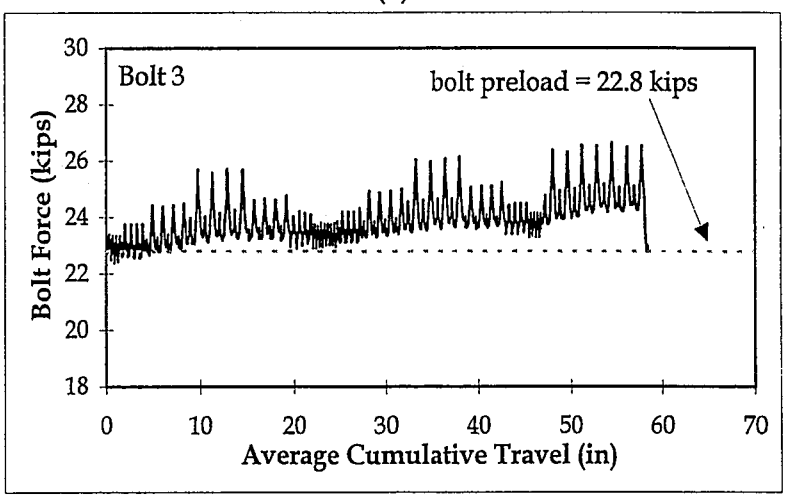

(c)

Figure 6.33. Clamping Bolt Force vs. Average Cumulative Travel for Test FCC3: (a) Bolt 1; (b) Bolt 2; and (c) Bolt 3

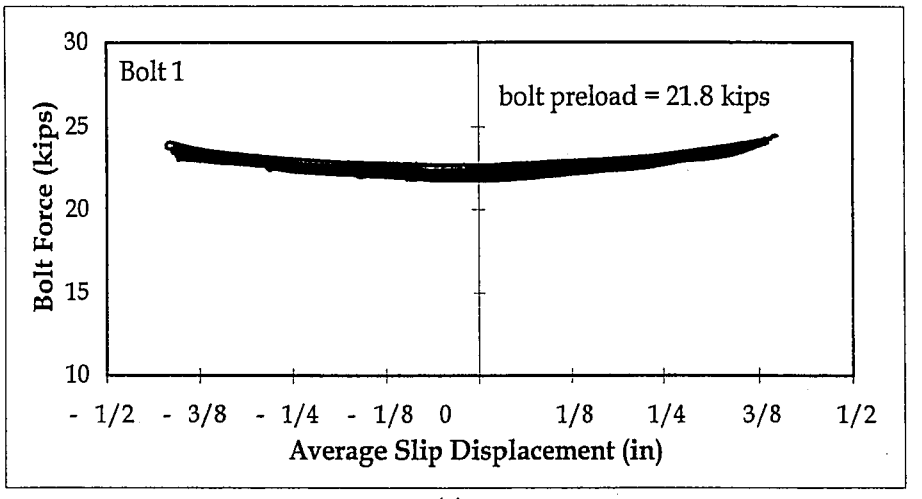

(a)

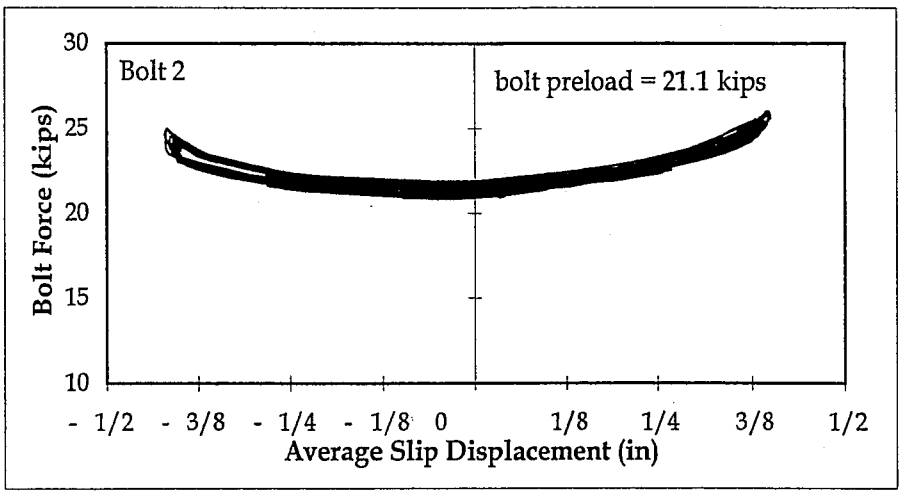

(b)

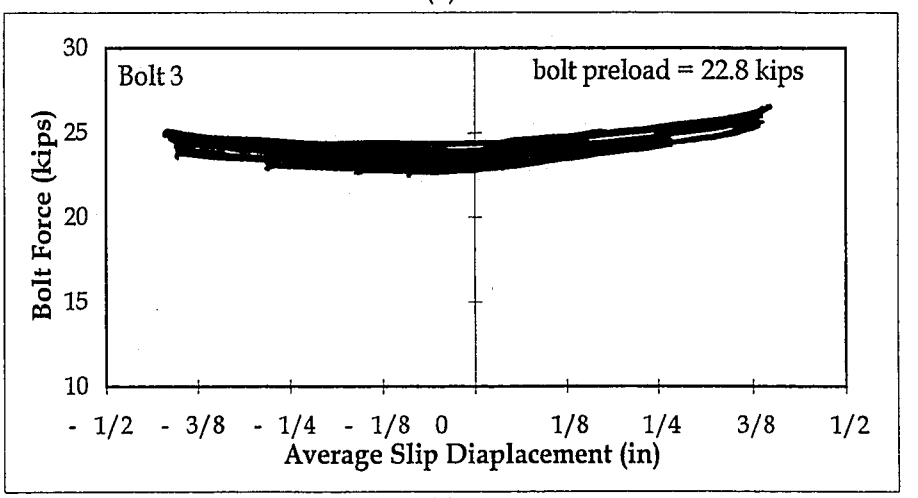

(c)

Figure 6.34. Clamping Bolt Force vs. Average Slip Displacement for Test FCC3: (a) Bolt 1; (b) Bolt 2; and (c) Bolt 3

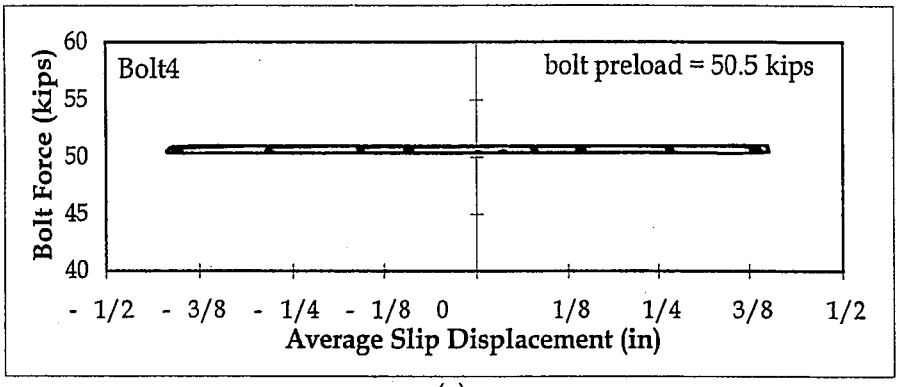

(a)

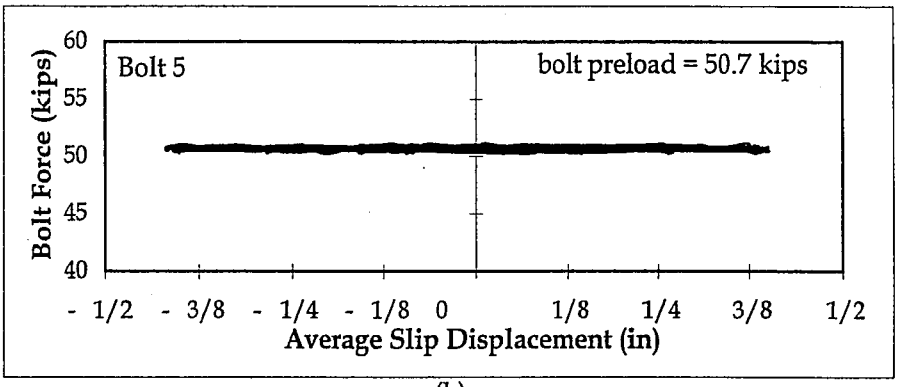

(b)

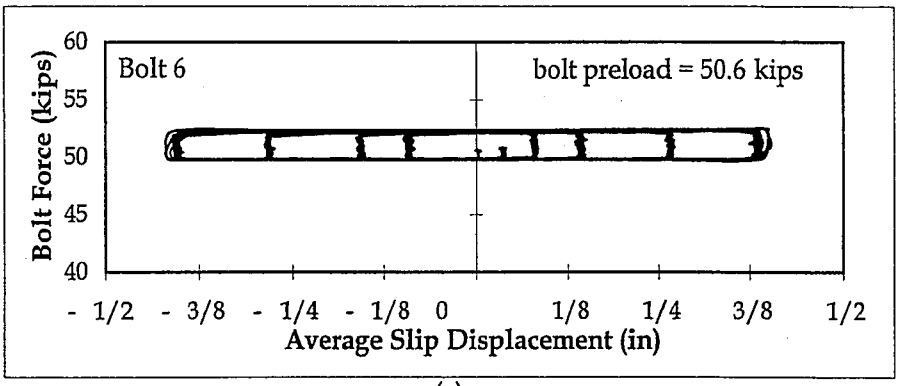

(c)

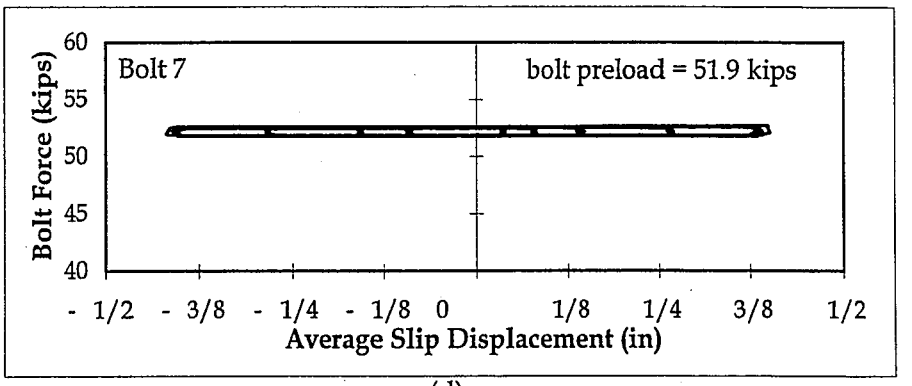

(d)

Figure 6.35. Support Bolt Force vs. Average Slip Displacement for Test FCC3: (a) Bolt 4; (b) Bolt 5; (c) Bolt 6; and (d) Bolt 7

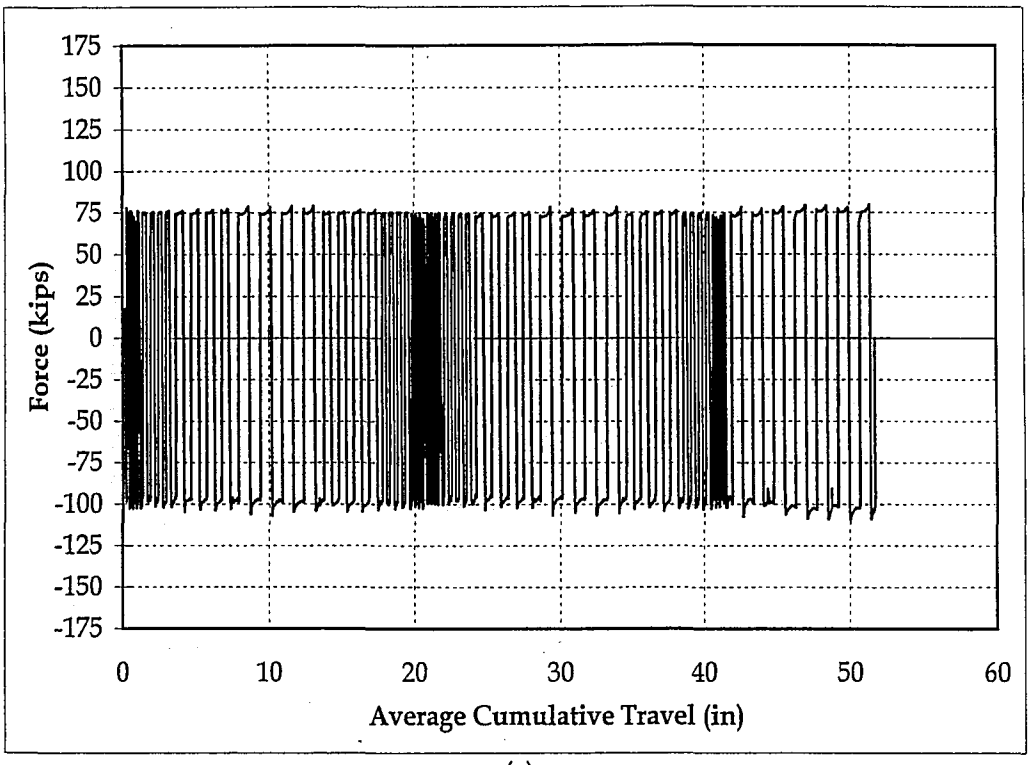

(a)

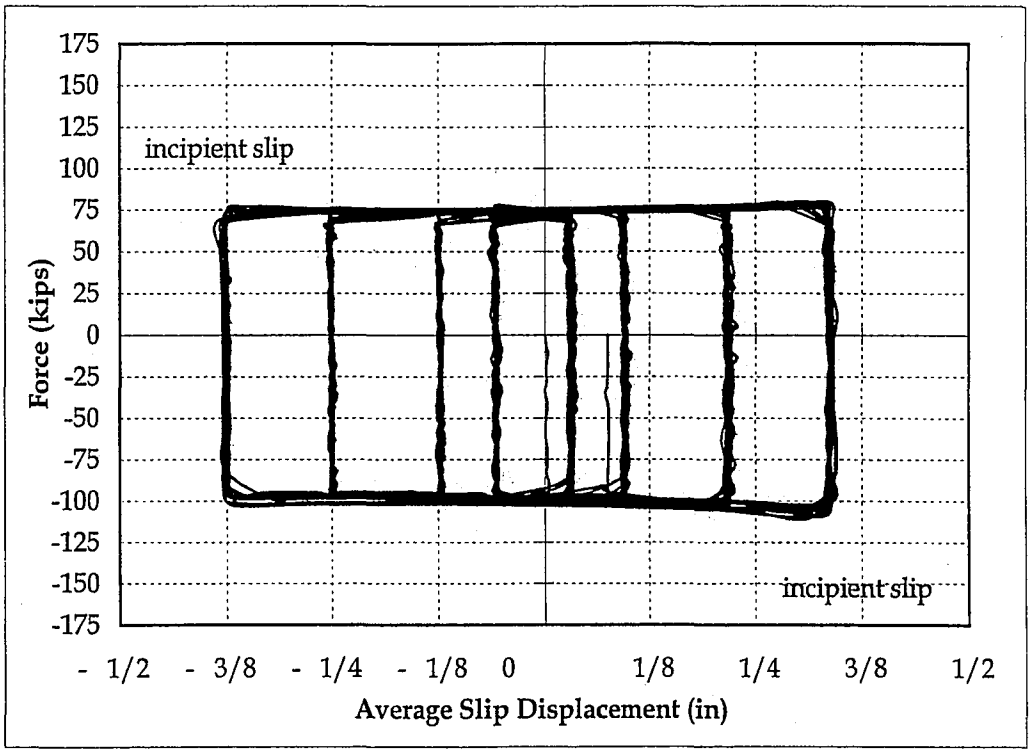

(b)

Figure 6.36. Friction Behavior for Test FCC4:
(a) Force vs. Average Cumulative Travel; and
(b) Force vs. Average Slip Displacement

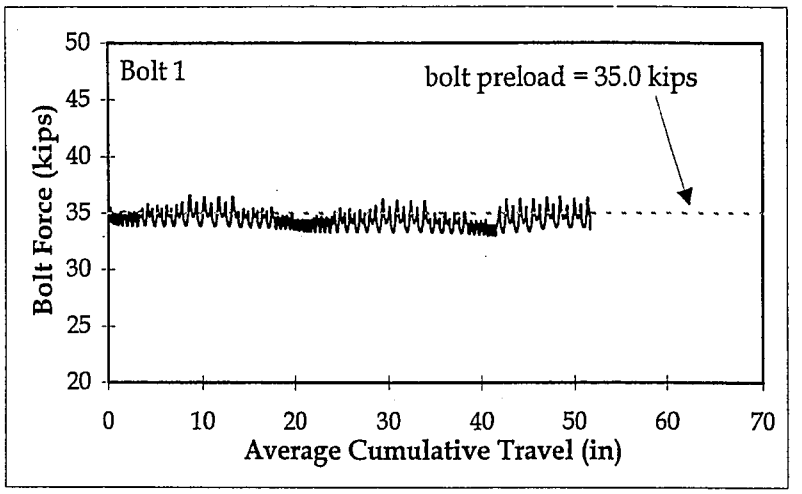

(a)

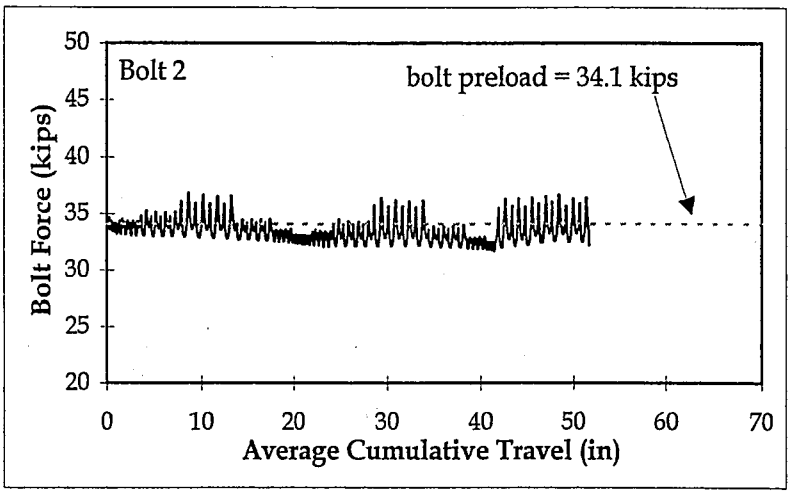

(b)

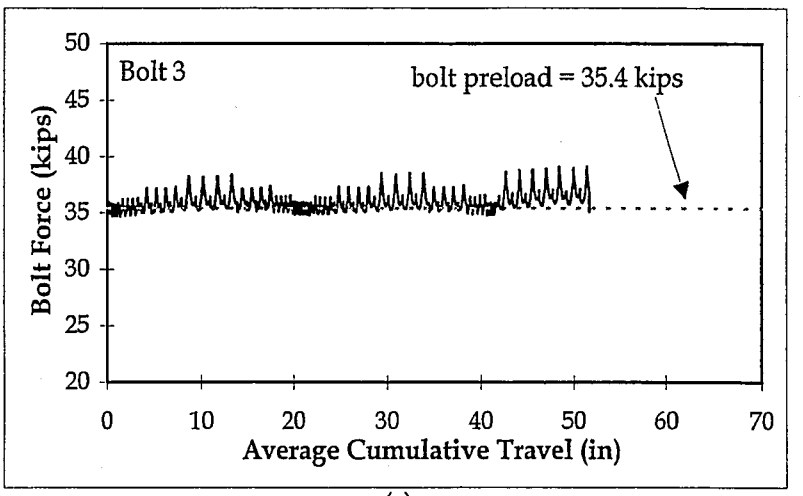

(c)

Figure 6.37. Clamping Bolt Force vs. Average Cumulative Travel for Test FCC4: (a) Bolt 1; (b) Bolt 2; and (c) Bolt 3

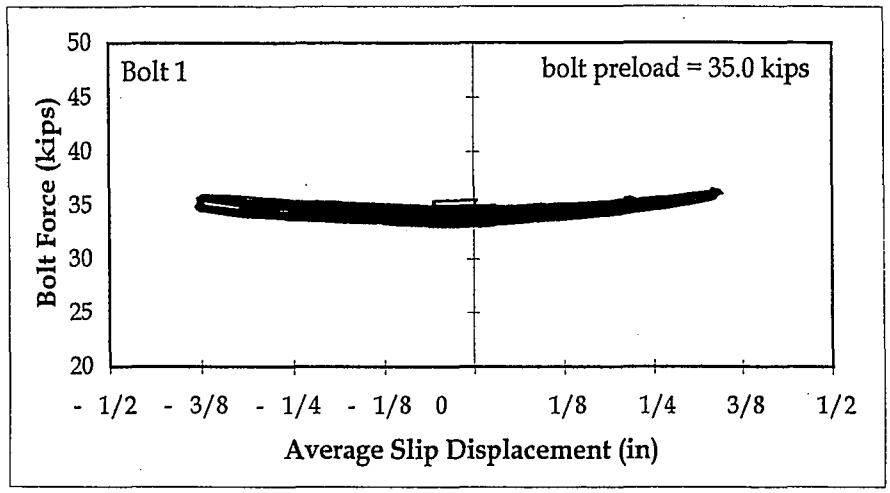

(a)

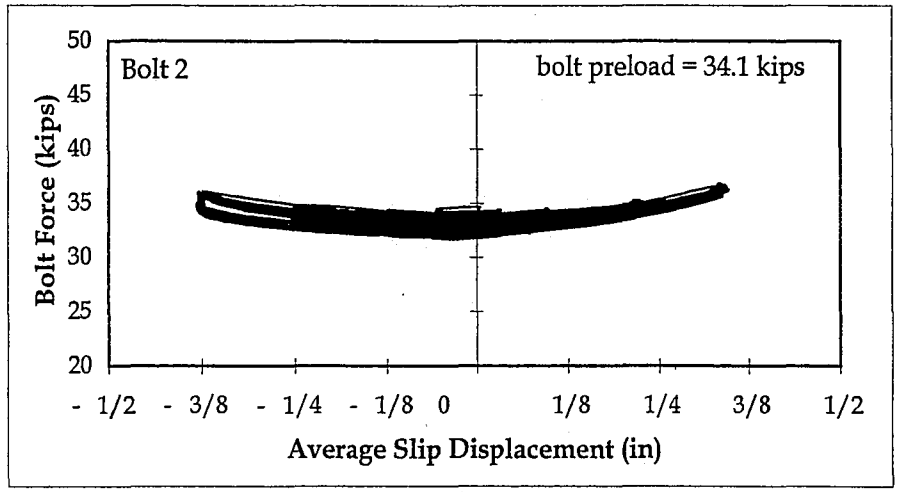

(b)

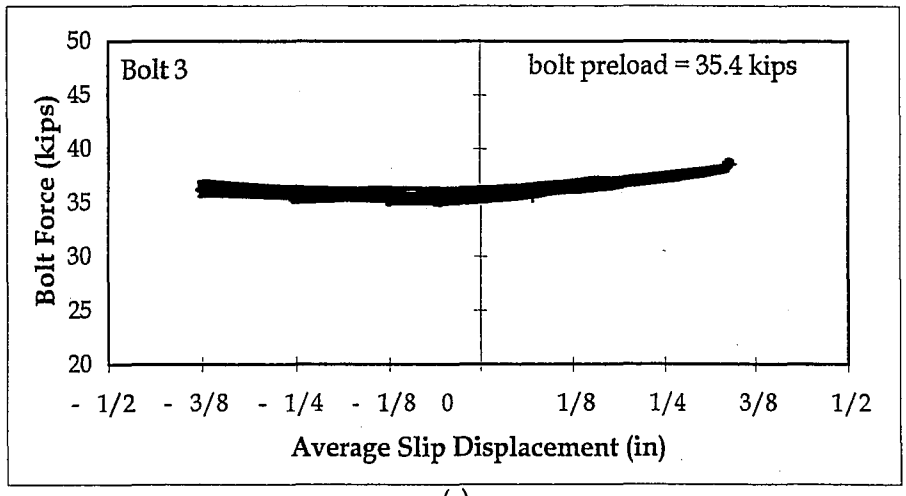

(c)

Figure 6.38 Clamping Bolt Force vs. Average Slip Displacement for Test FCC4: (a) Bolt 1; (b) Bolt 2; and (c) Bolt 3

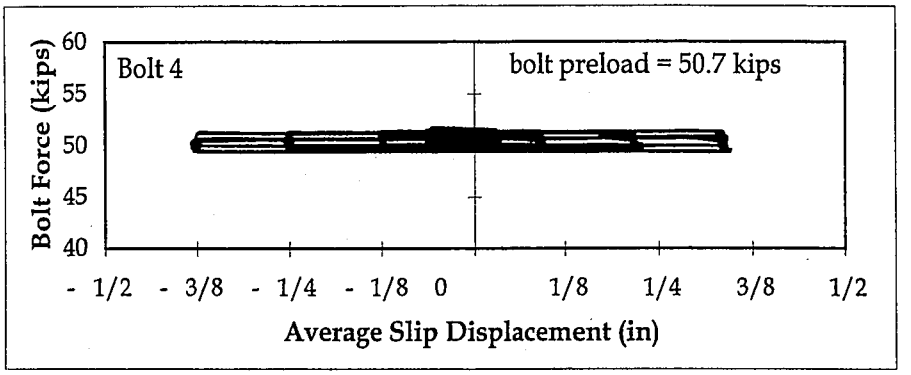

(a)

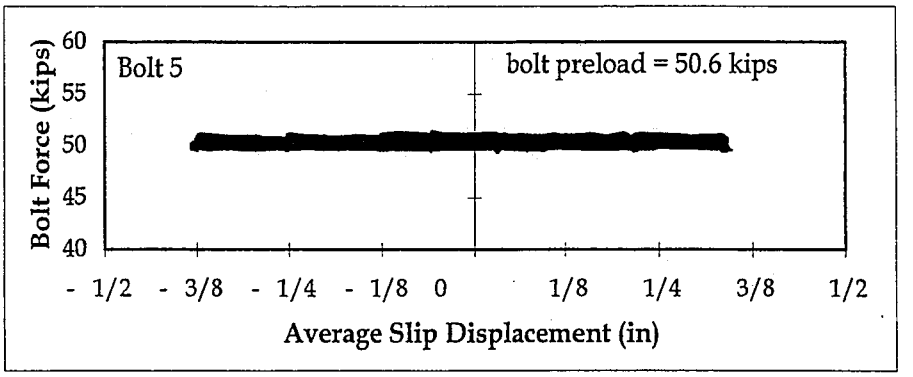

(b)

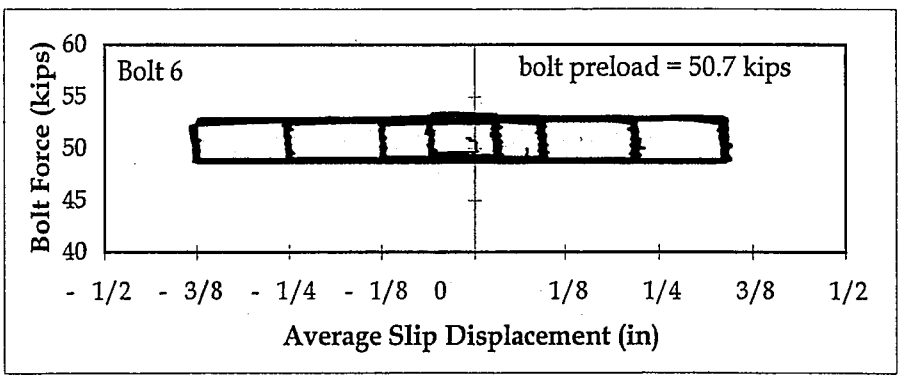

(c)

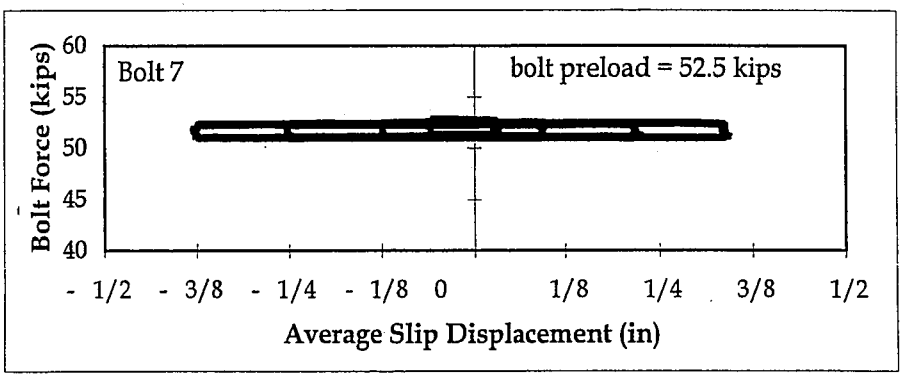

(d)

Figure 6.39. Support Bolt Force vs. Average Slip Displacement for Test FCC4: (a) Bolt 4; (b) Bolt 5; (c) Bolt 6; and (d) Bolt 7

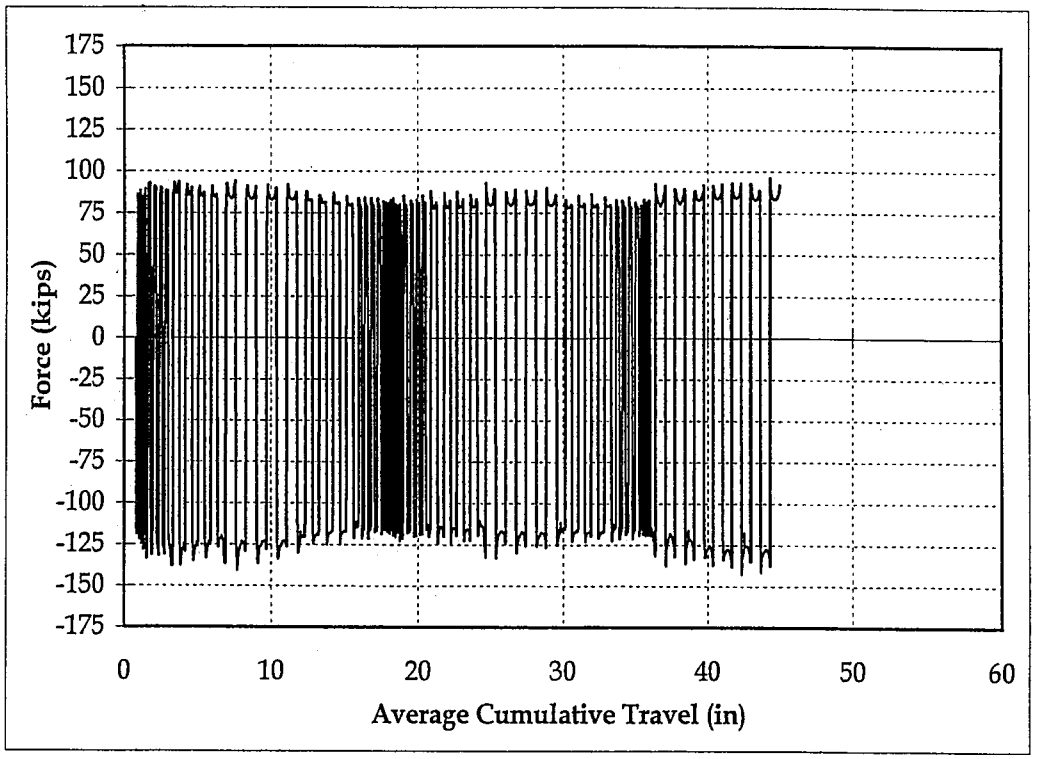

(a)

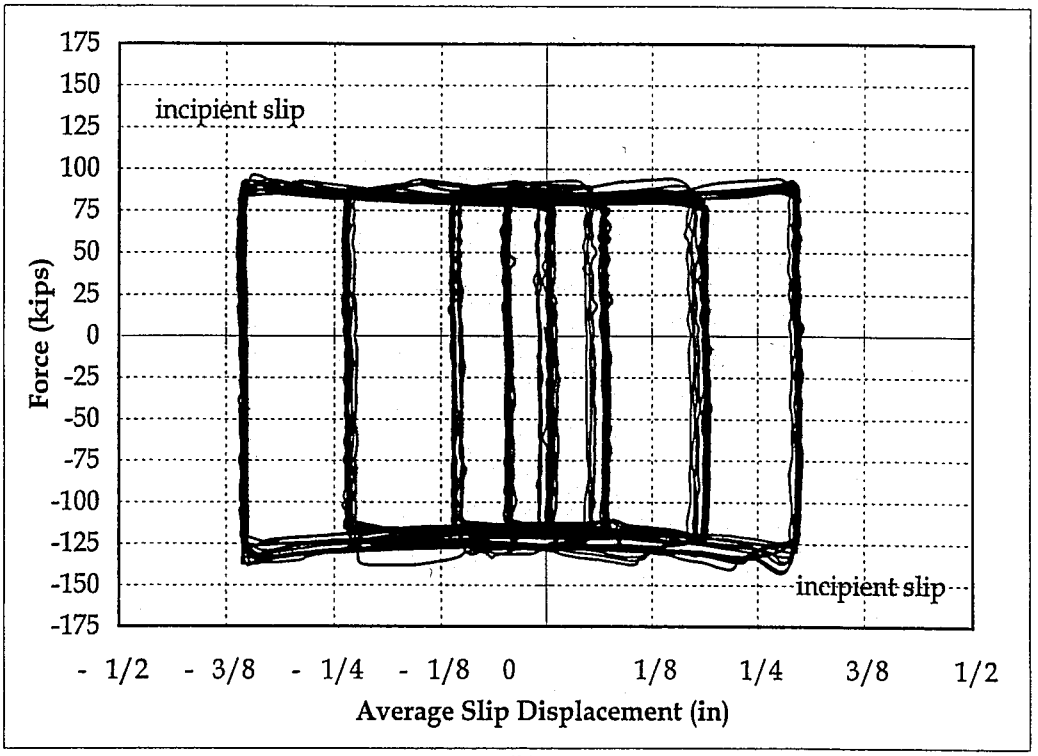

(b)

Figure 6.40. Friction Behavior for Test FCC5:
(a) Force vs. Average Cumulative Travel; and
(b) Force vs. Average Slip Displacement

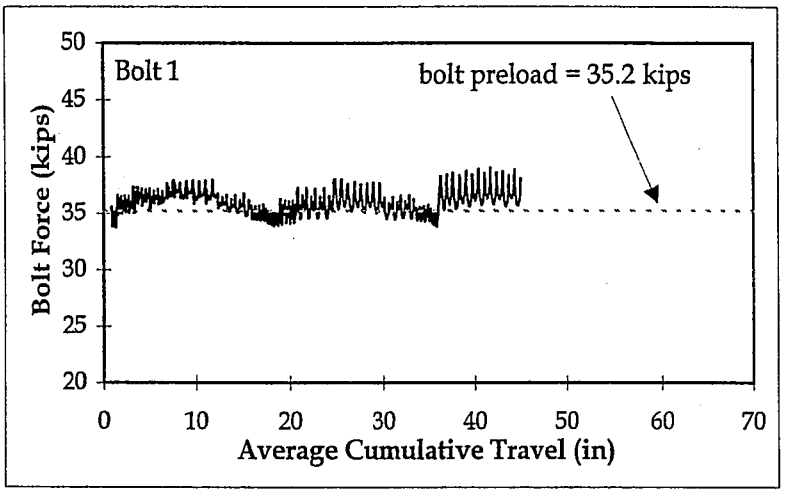

(a)

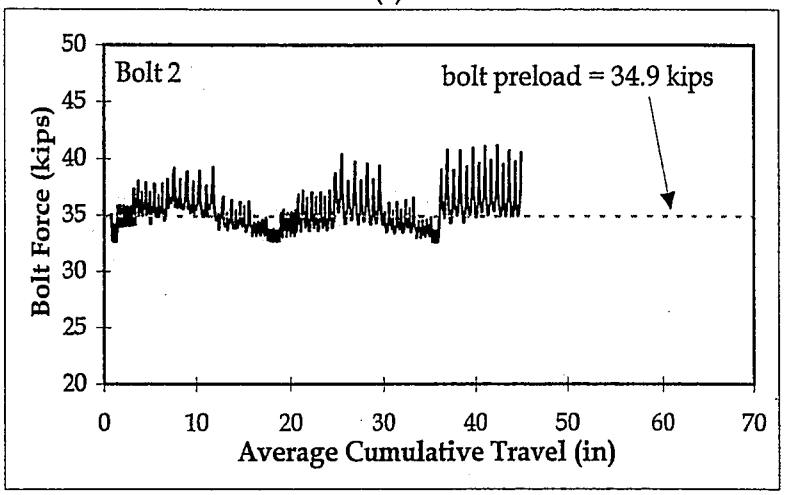

(b)

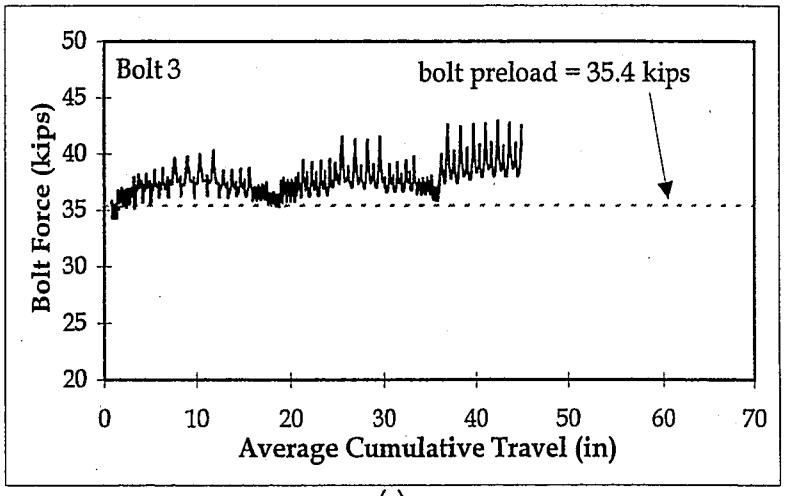

(c)

Figure 6.41. Clamping Bolt Force vs. Average Cumulative Travel for Test FCC5: (a) Bolt 1; (b) Bolt 2; and (c) Bolt 3

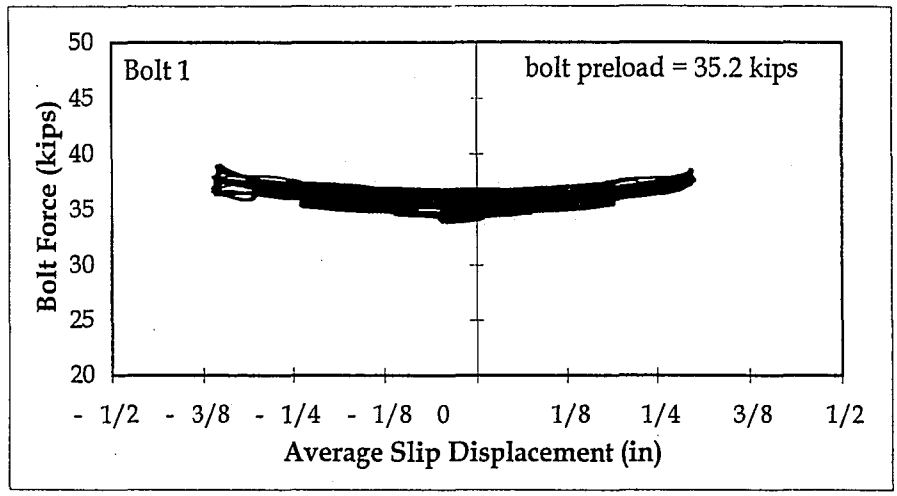

(a)

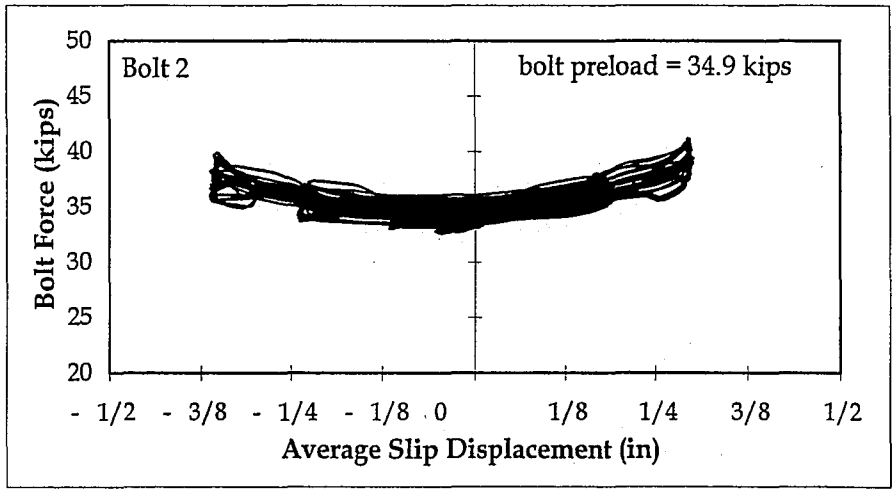

(b)

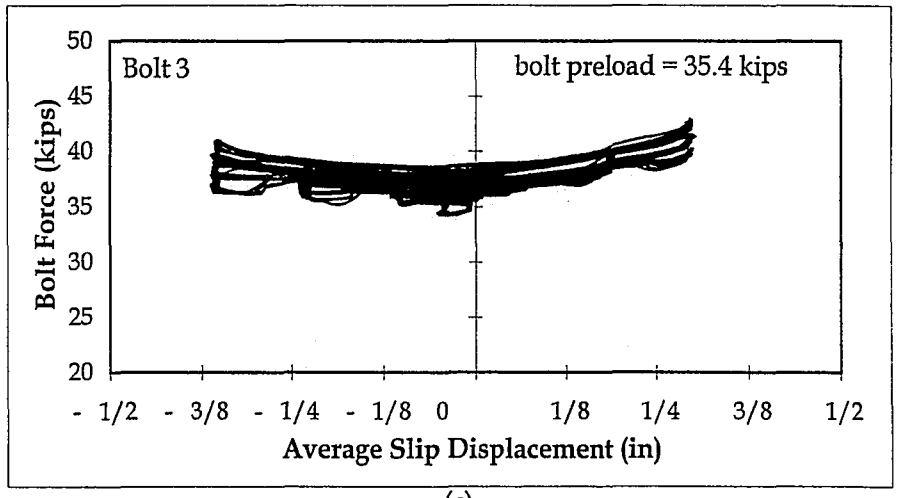

(c)

Figure 6.42. Clamping Bolt Force vs. Average Slip Displacement for Test FCC5: (a) Bolt 1; (b) Bolt 2; and (c) Bolt 3

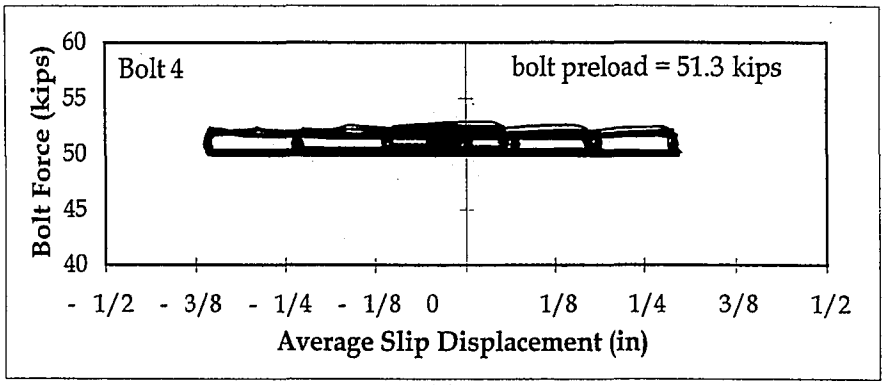

(a)

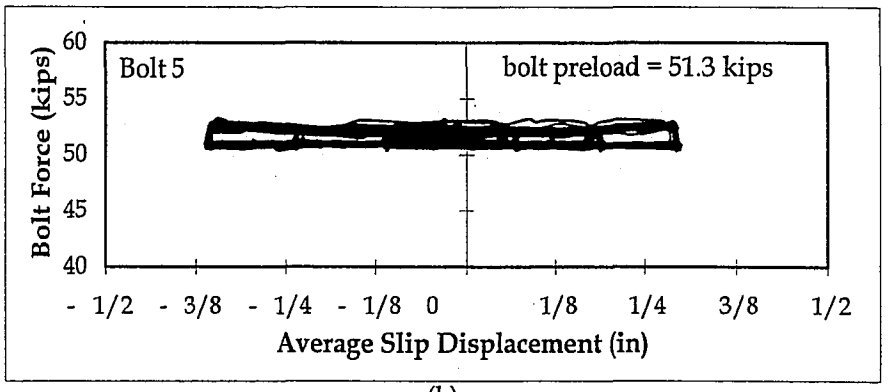

(b)

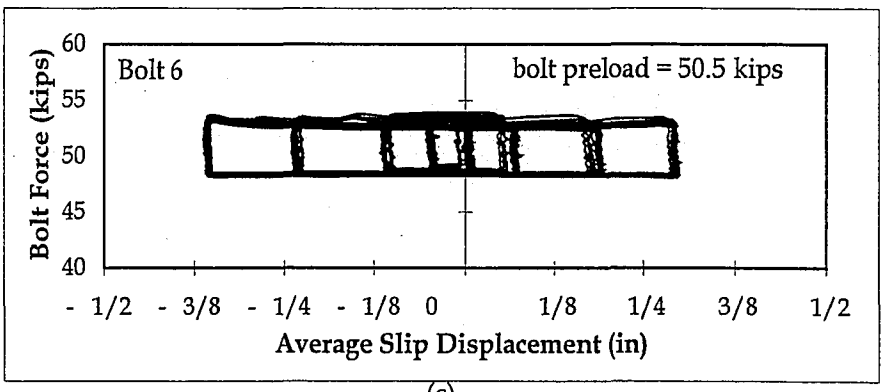

(c)

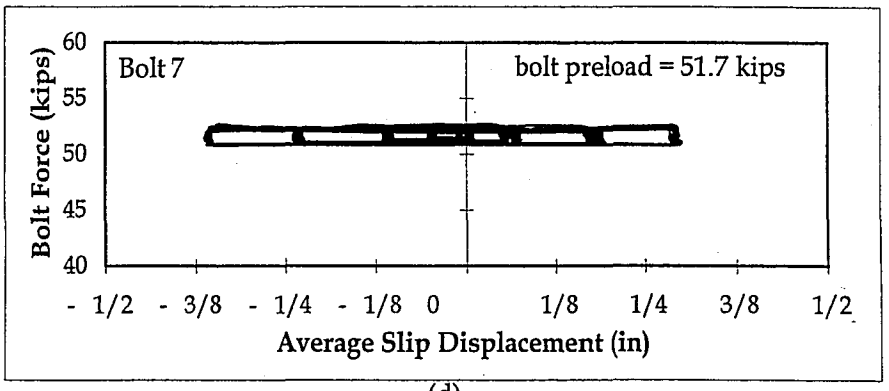

(d)

Figure 6.43. Support Bolt Force vs. Average Slip Displacement for Test FCC5: (a) Bolt 4; (b) Bolt 5; (c) Bolt 6; and (d) Bolt 7

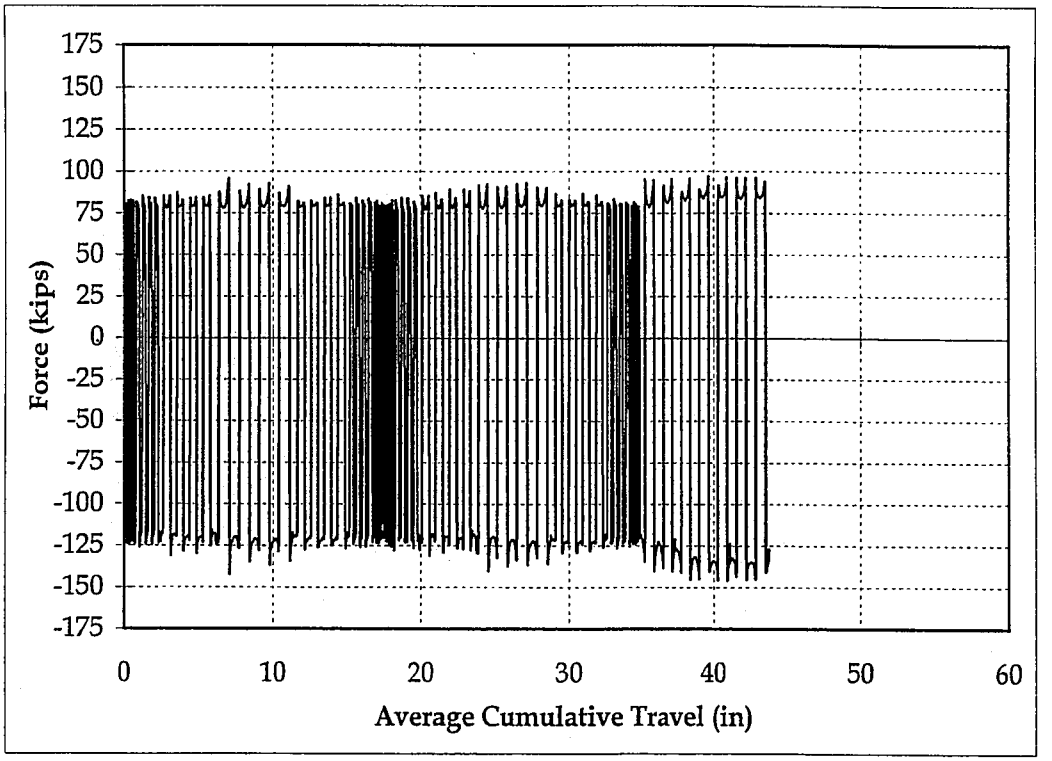

(a)

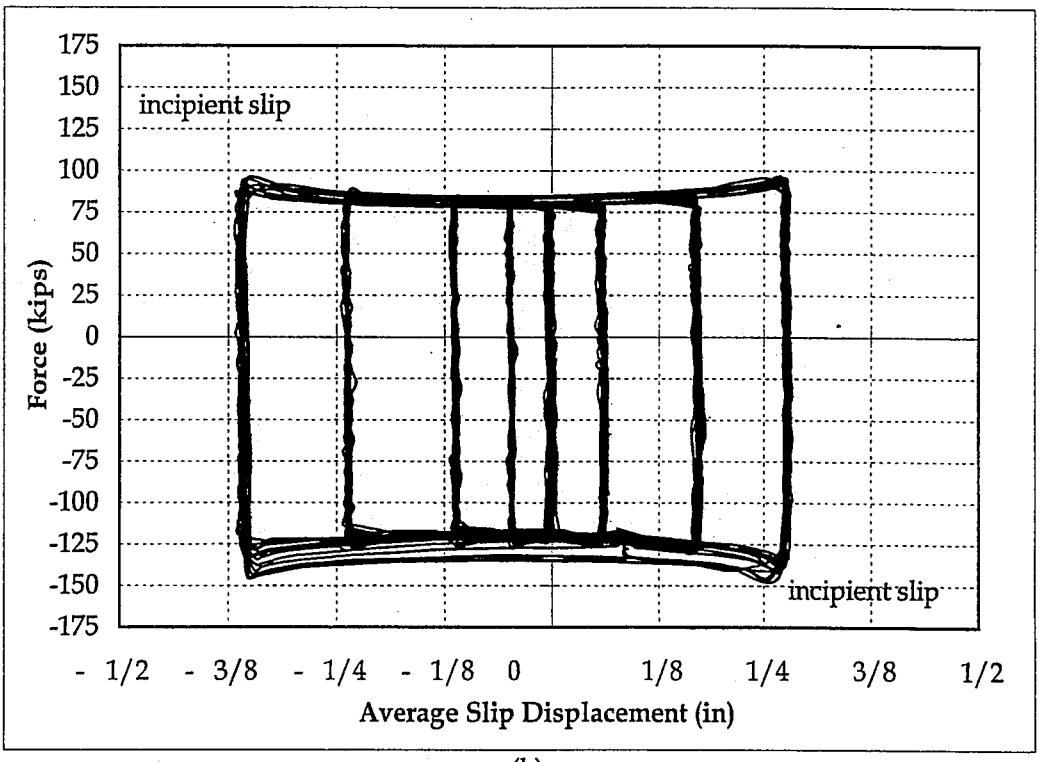

(b)

Figure 6.44. Friction Behavior for Test FCC6:
(a) Force vs. Average Cumulative Travel; and
(b) Force vs. Average Slip Displacement

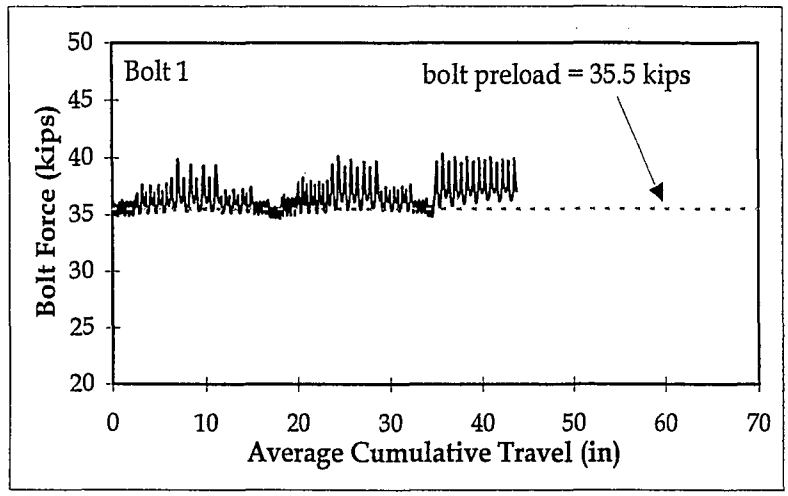

(a)

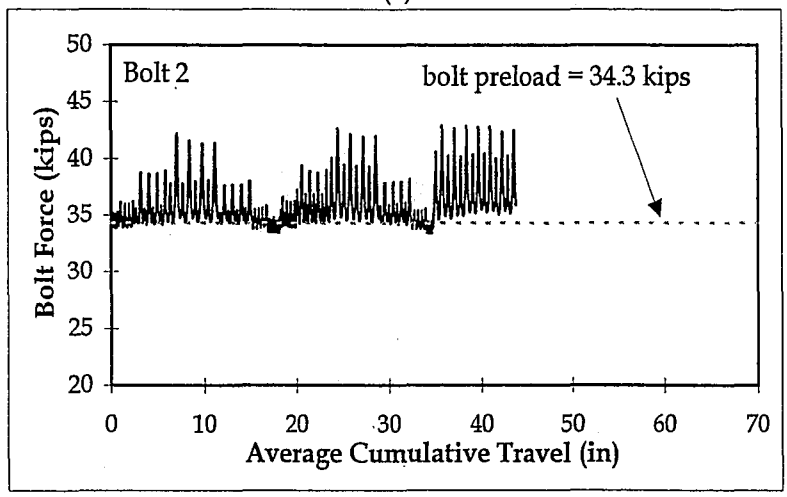

(b)

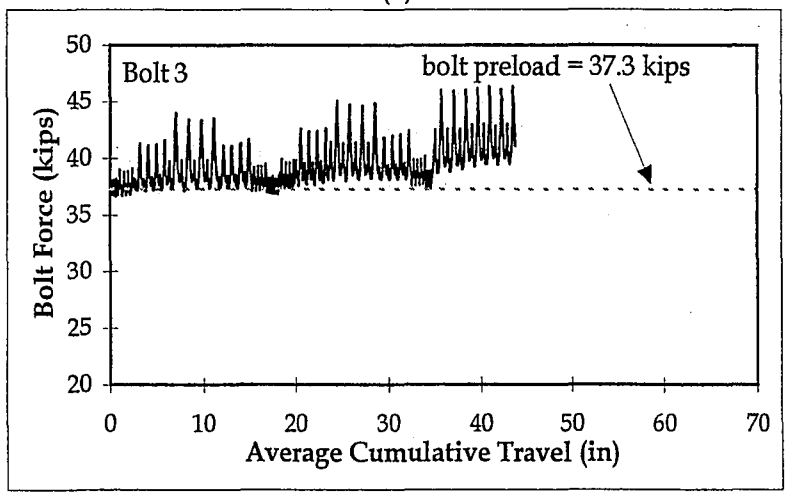

(c)

Figure 6.45. Clamping Bolt Force vs. Average Cumulative Travel for Test FCC6: (a) Bolt 1; (b) Bolt 2; and (c) Bolt 3

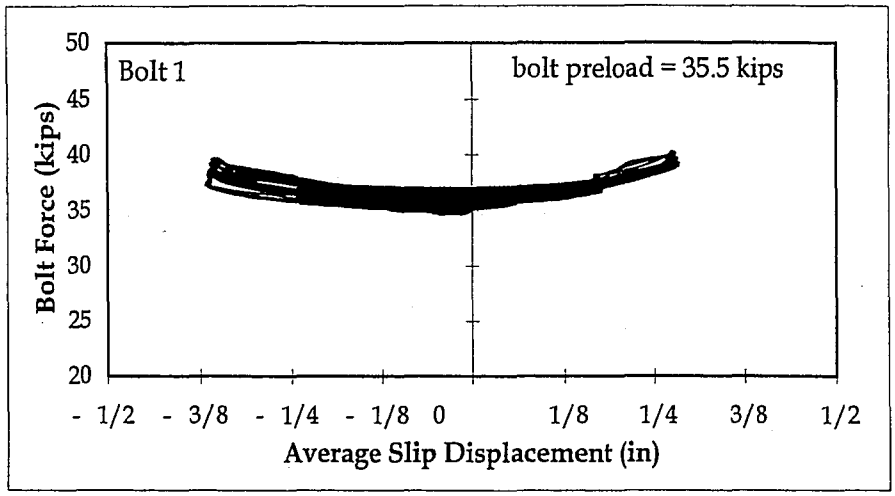

(a)

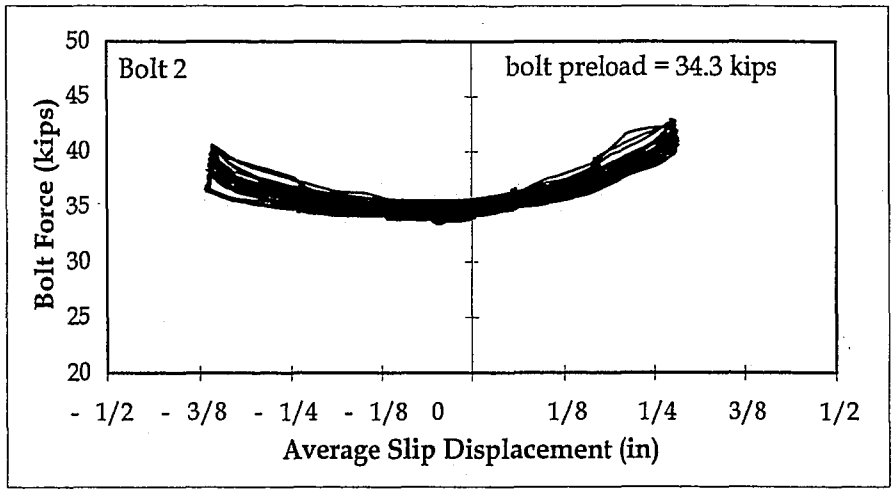

(b)

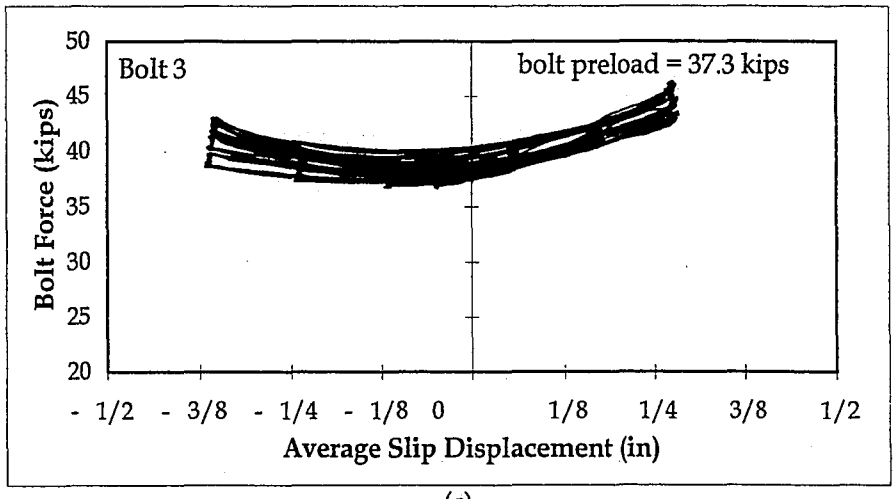

(c)

Figure 6.46. Clamping Bolt Force vs. Average Slip Displacement for Test FCC6: (a) Bolt 1; (b) Bolt 2; and (c) Bolt 3

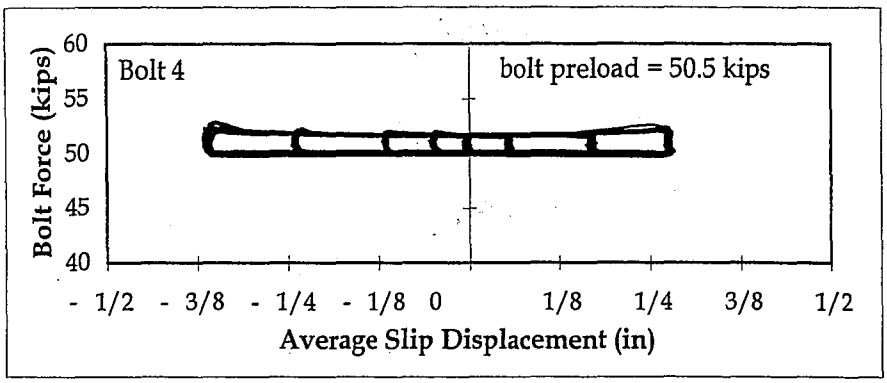

(a)

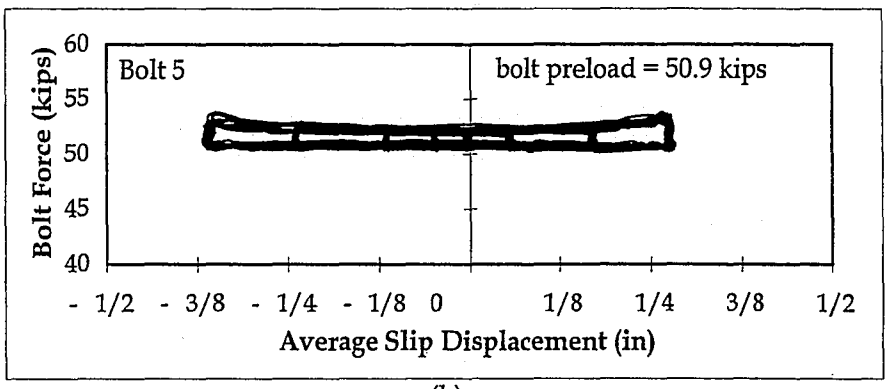

(b)

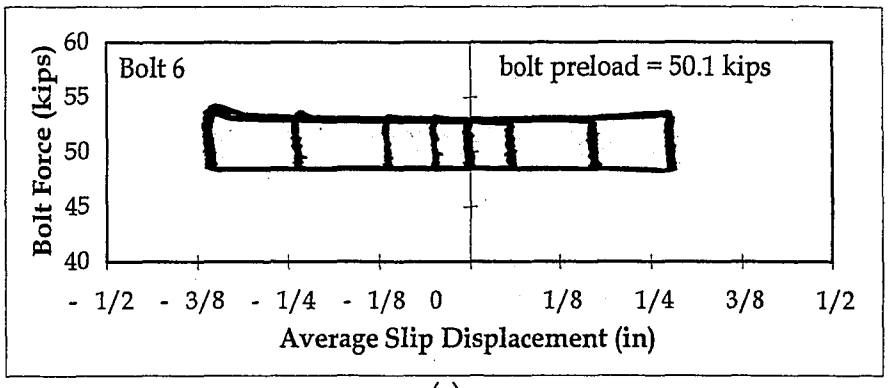

(c)

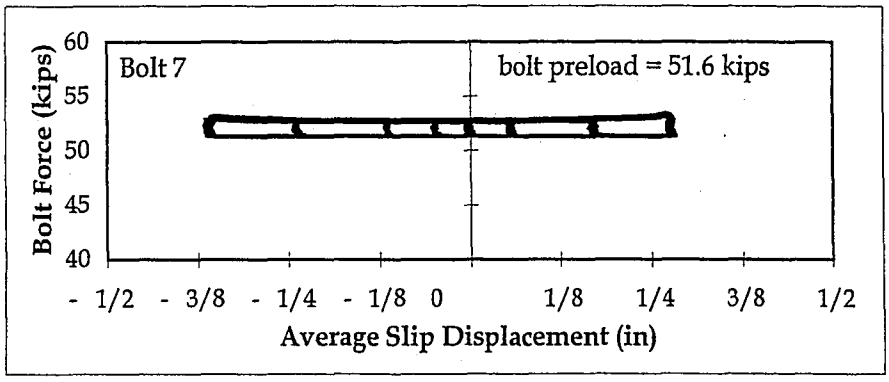

(d)

Figure 6.47. Support Bolt Force vs. Average Slip Displacement for Test FCC6: (a) Bolt 4; (b) Bolt 5; (c) Bolt 6; and (d) Bolt 7

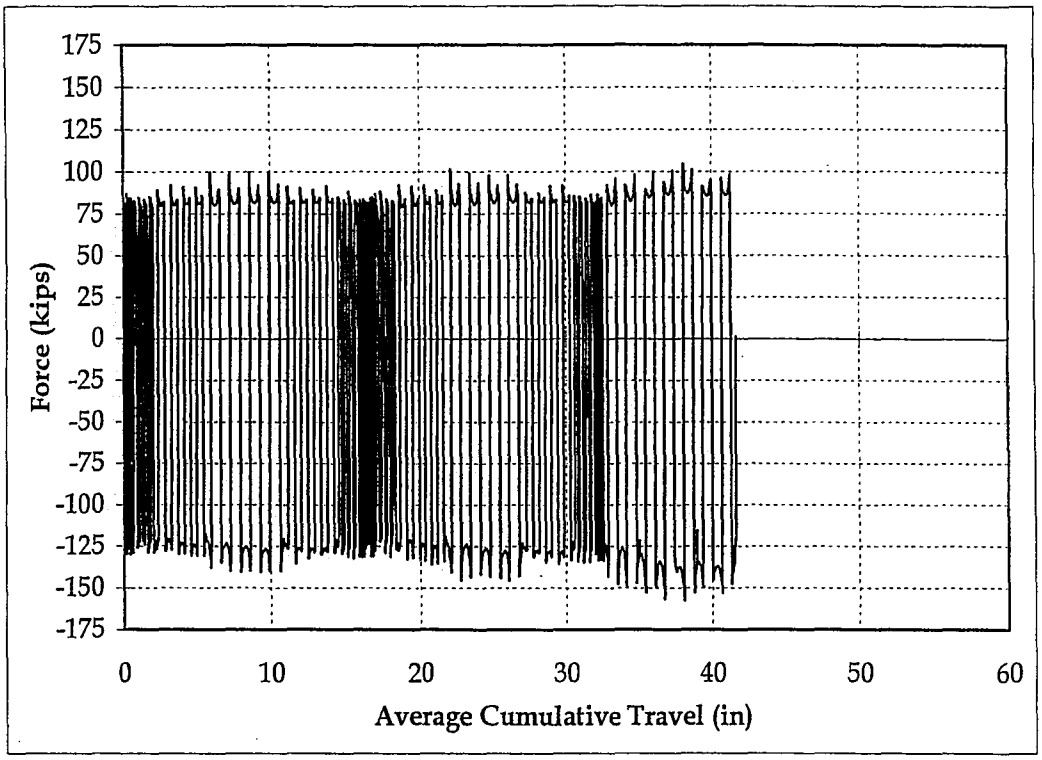

(a)

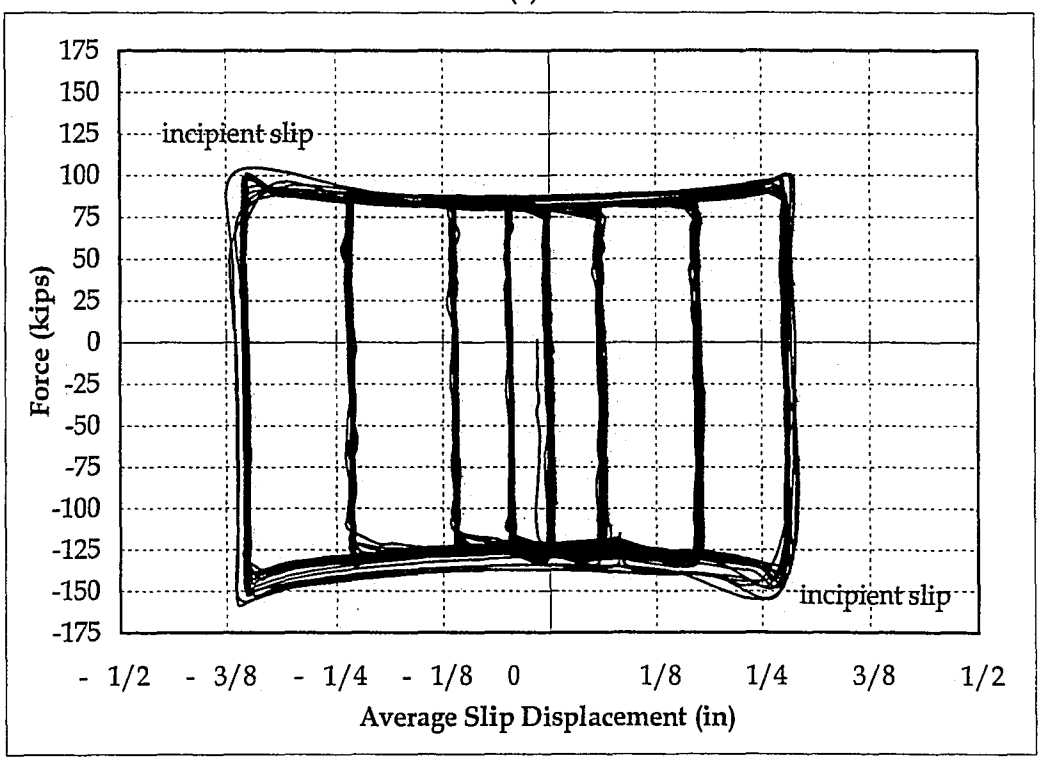

(b)

Figure 6.48. Friction Behavior for Test FCC7
(a) Force vs. Average Cumulative Travel; and
(b) Force vs. Average Slip Displacement

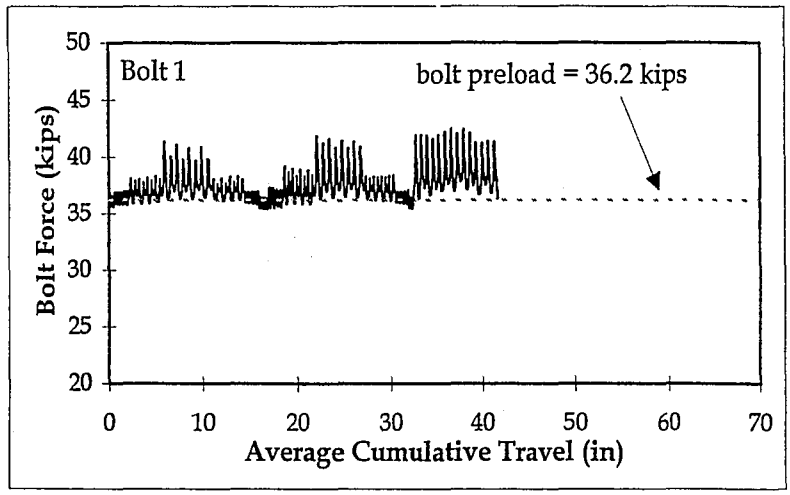

(a)

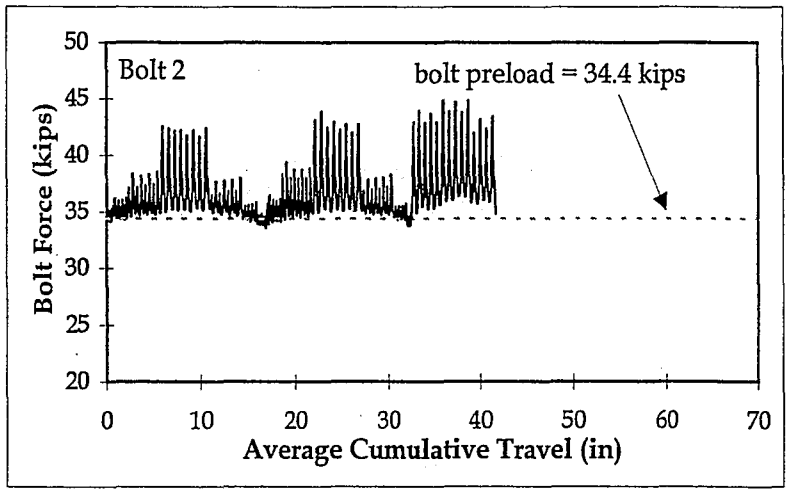

(b)

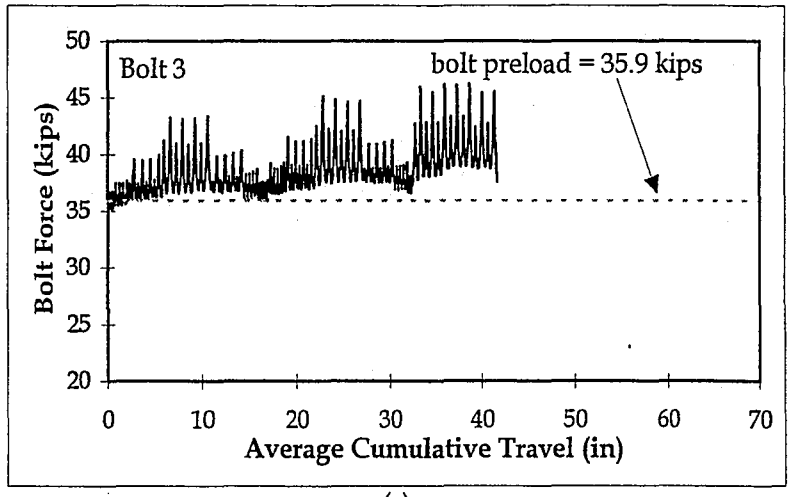

(c)

Figure 6.49. Clamping Bolt Force vs. Average Cumulative Travel for Test FCC7: (a) Bolt 1; (b) Bolt 2; and (c) Bolt 3

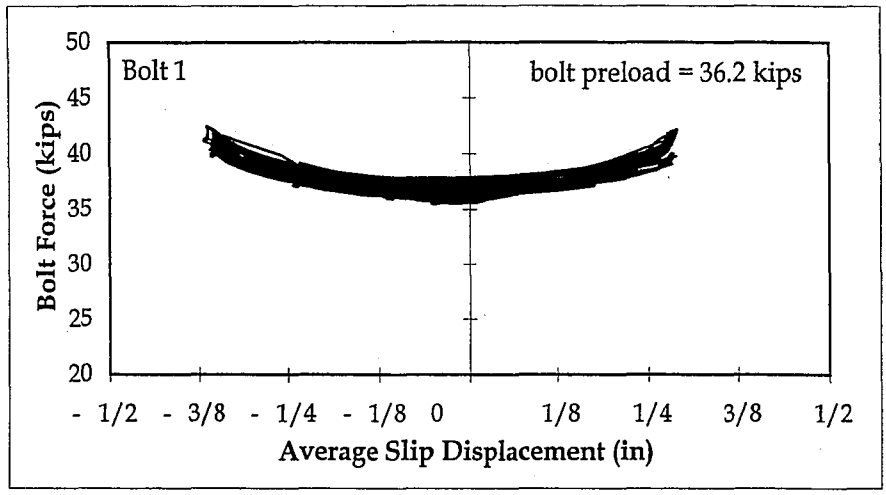

(a)

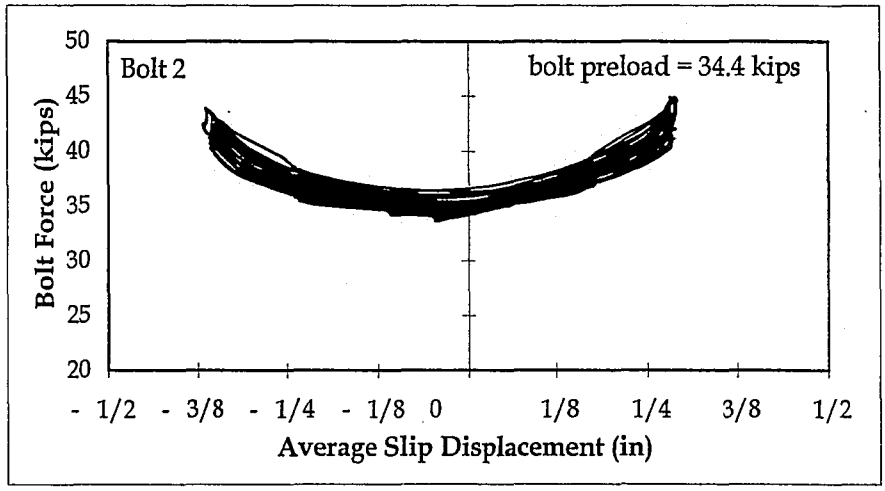

(b)

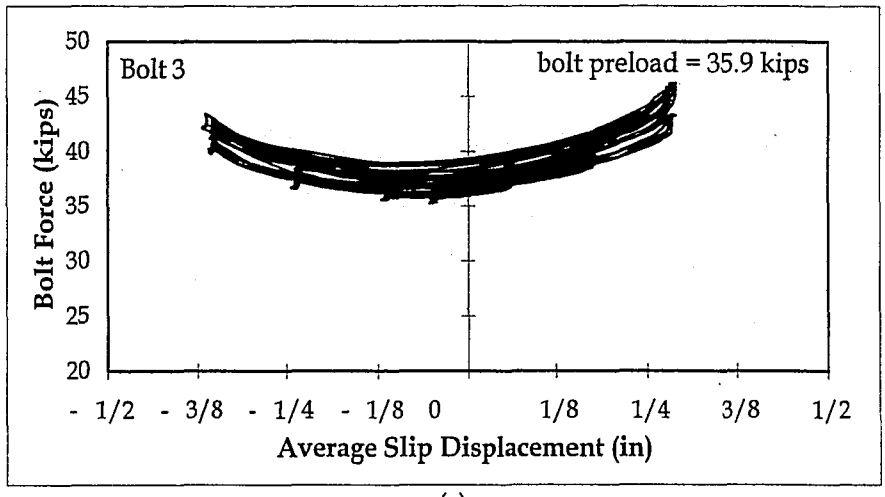

(c)

Figure 6.50. Clamping Bolt Force vs. Average Slip Displacement Test FCC7: (a) Bolt 1; (b) Bolt 2; and (c) Bolt 3

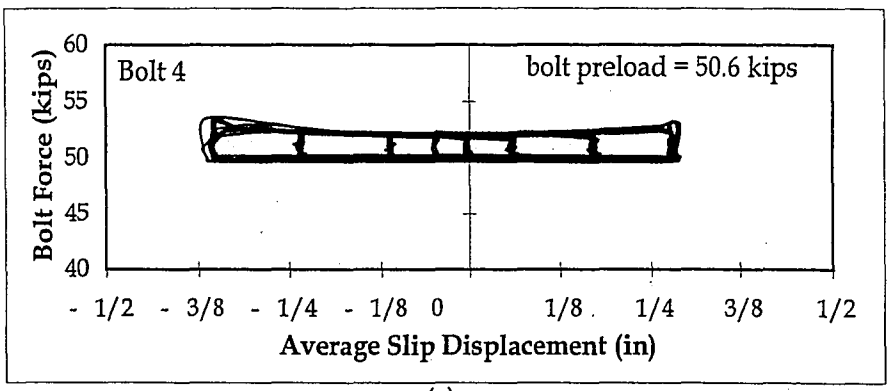

(a)

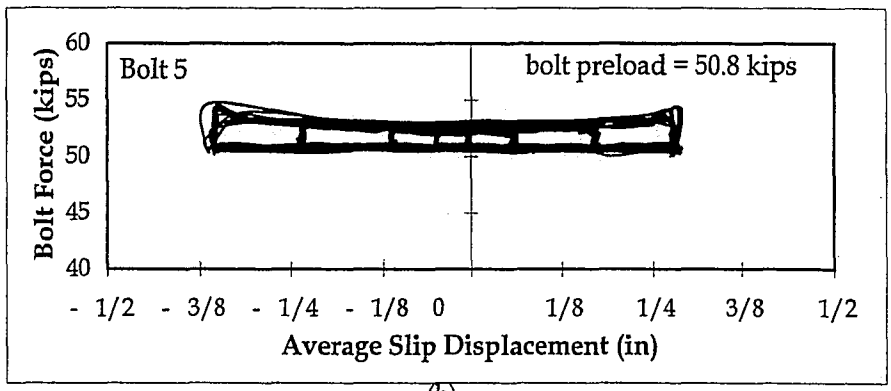

(b)

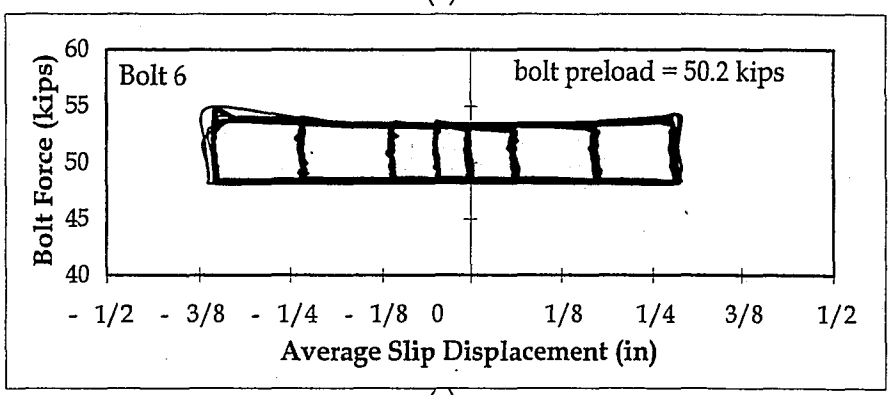

(c)

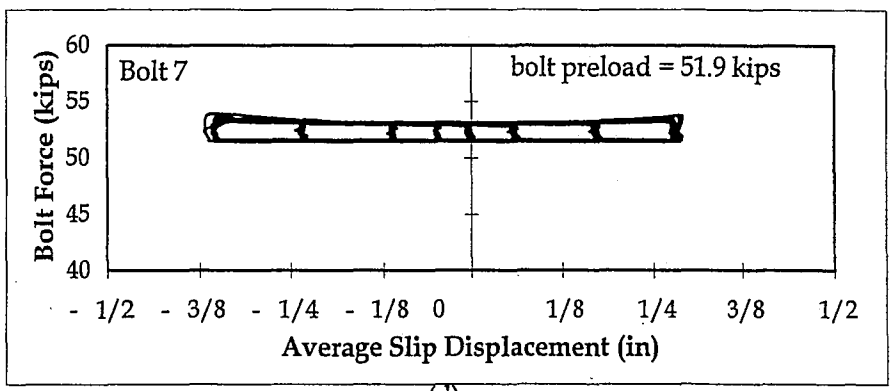

(d)

Figure 6.51. Support Bolt Force vs. Average Slip Displacement for Test FCC7: (a) Bolt 4; (b) Bolt 5; (c) Bolt 6; and (d) Bolt 7

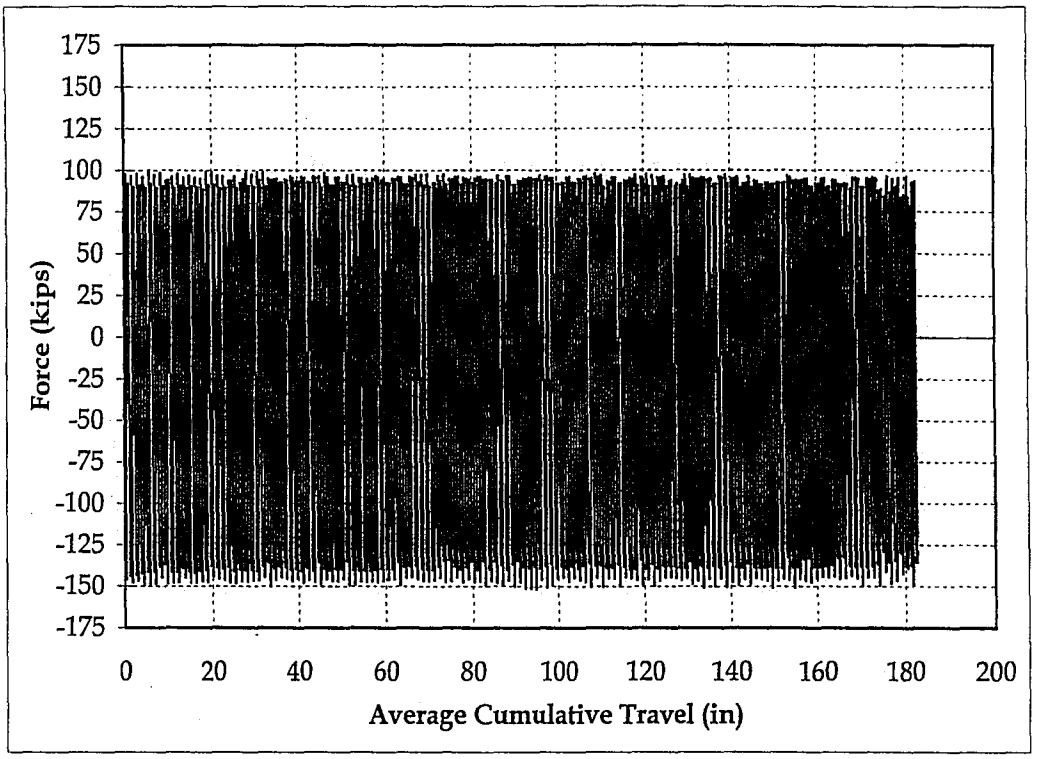

(a)

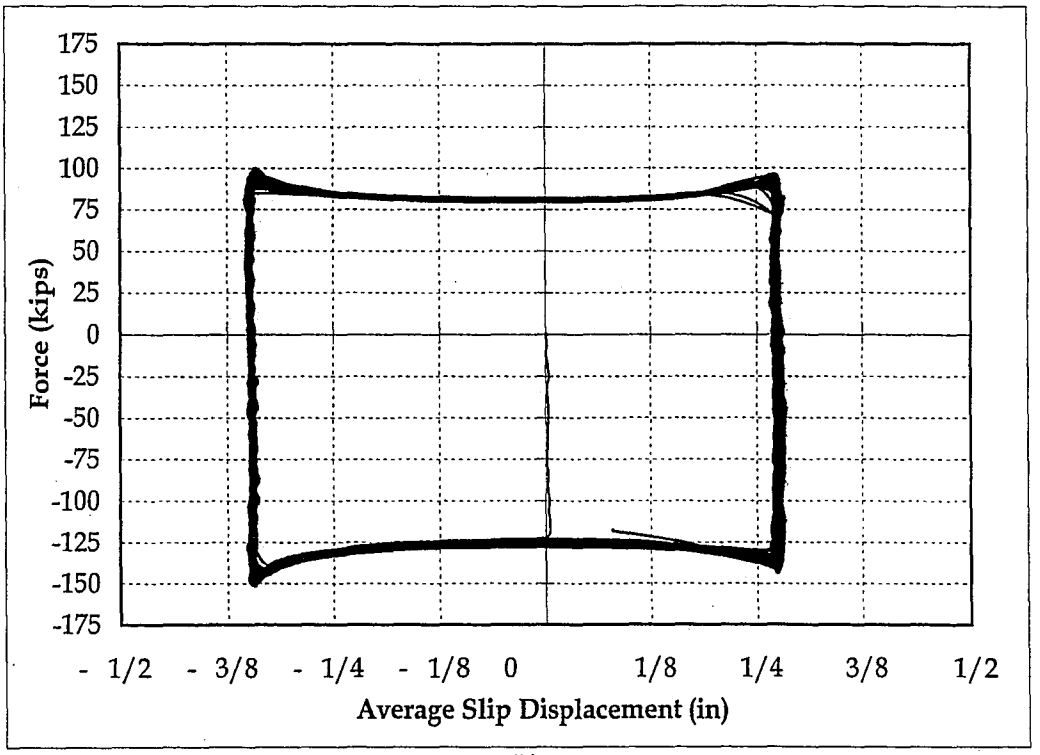

(b)

Figure 6.52. Friction Behavior for Test FCC8:
(a) Force vs. Average Cumulative Travel; and
(b) Force vs. Average Slip Displacement

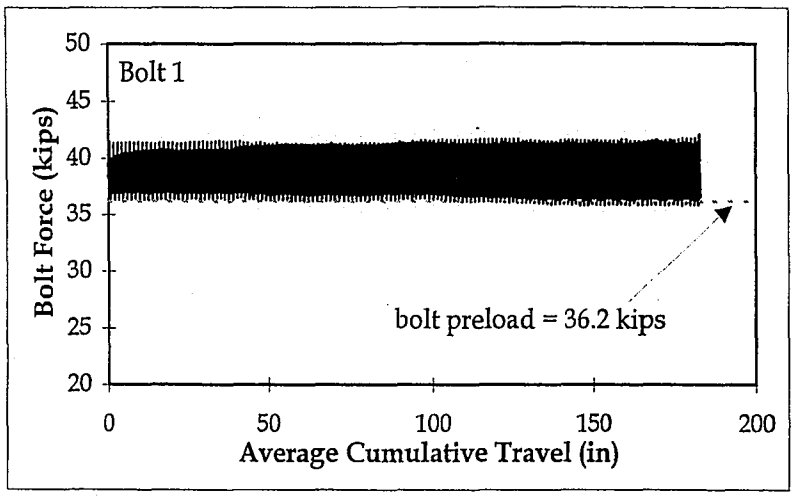

(a)

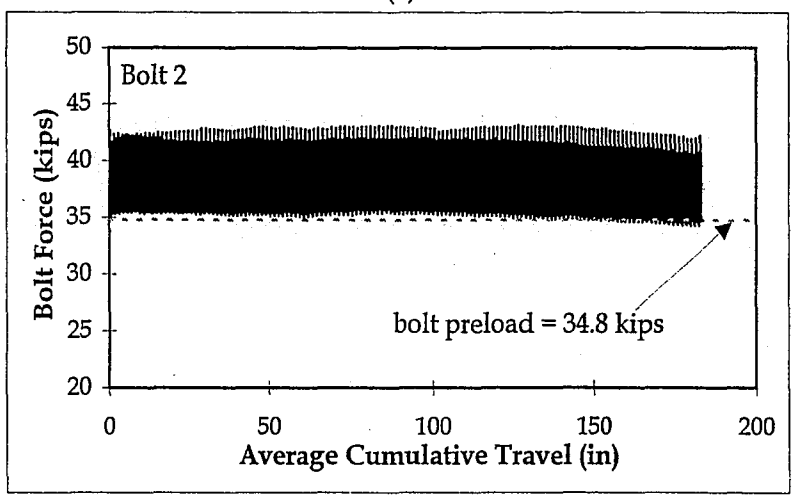

(b)

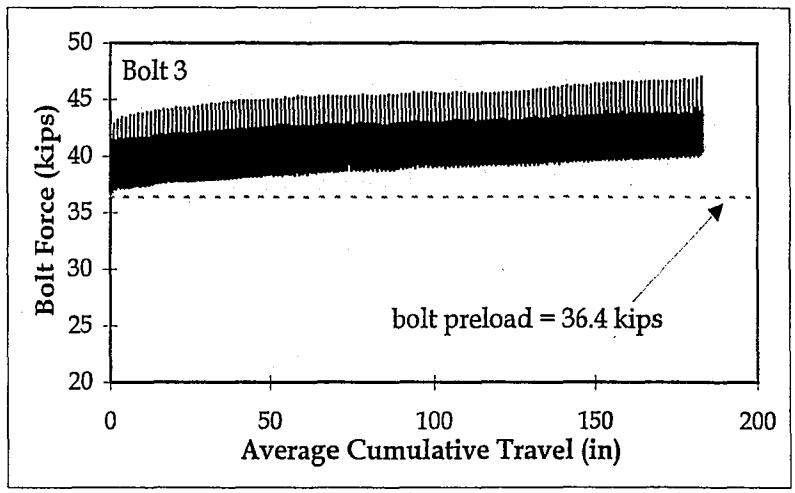

(c)

Figure 6.53. Clamping Bolt Force vs. Average Cumulative Travel for Test FCC8: (a) Bolt 1; (b) Bolt 2; and (c) Bolt 3

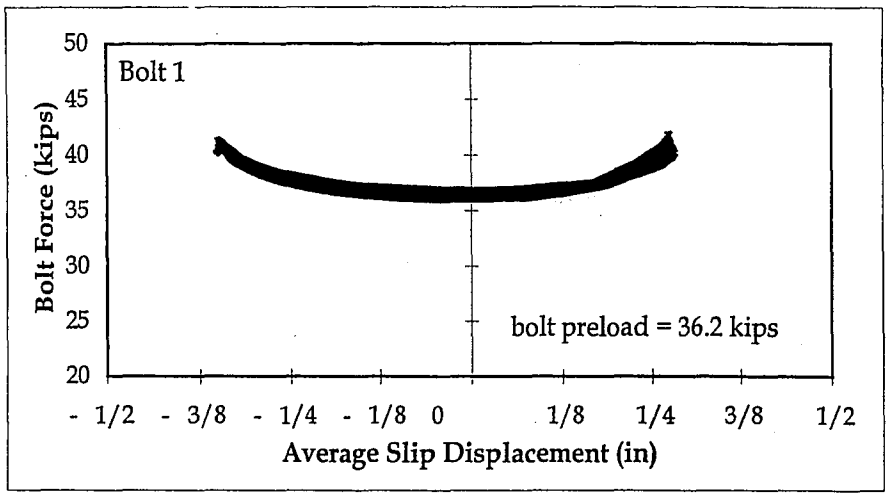

(a)

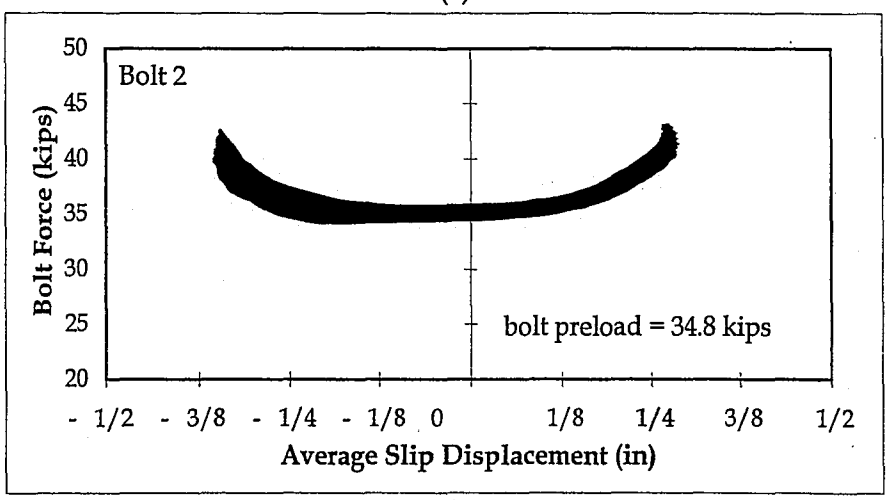

(b)

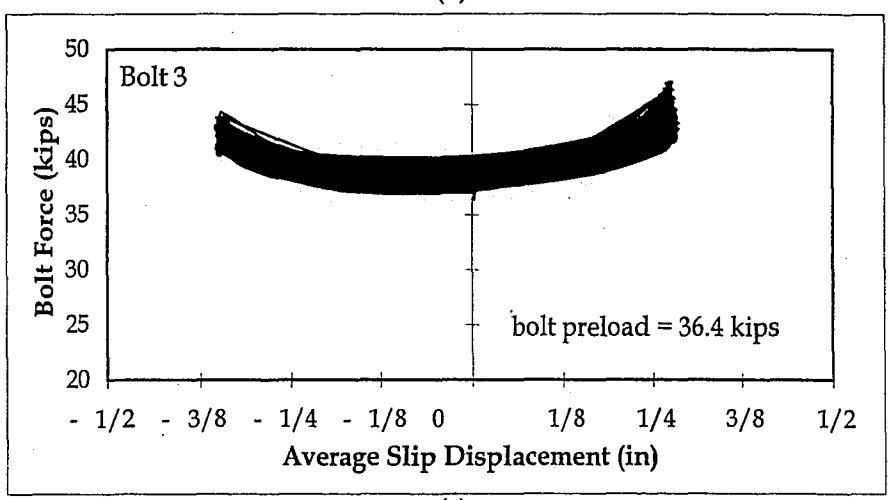

(c)

Figure 6.54. Clamping Bolt Force vs. Average Slip Displacement for Test FCC8: (a) Bolt 1; (b) Bolt 2; and (c) Bolt 3

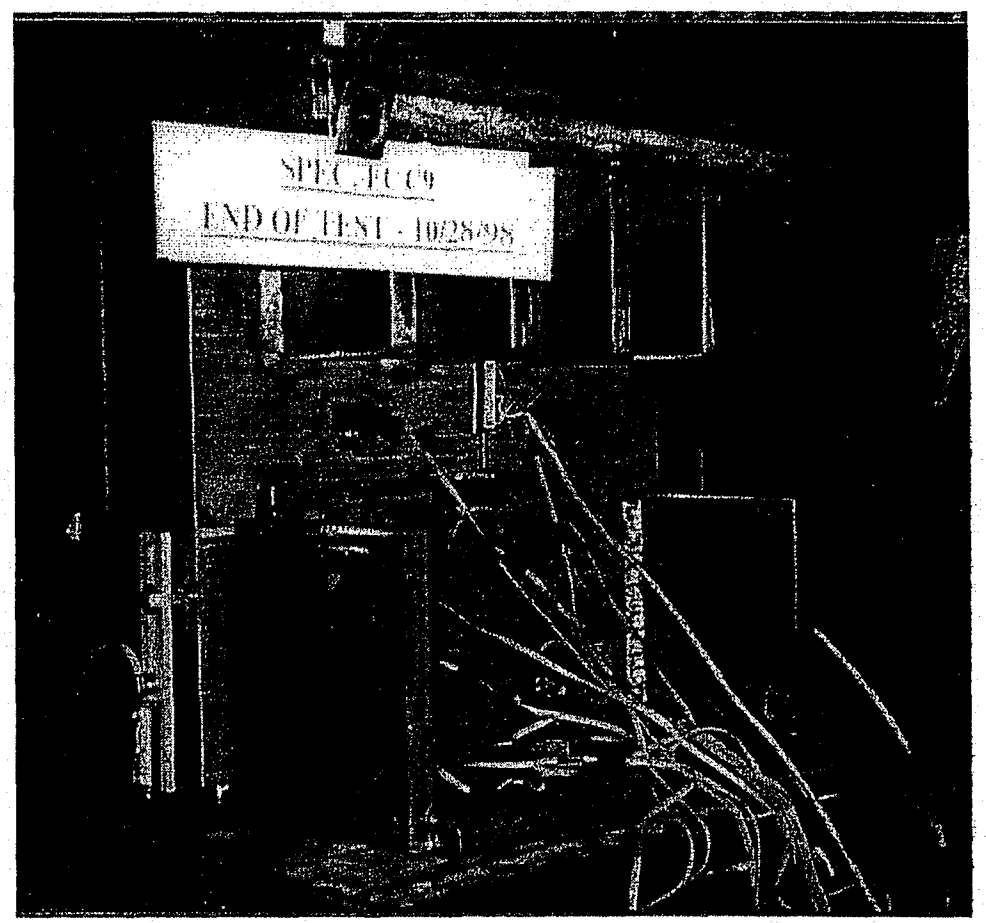

Figure 6.55. Stiffened Double Angle Friction Connection Component Test Specimen

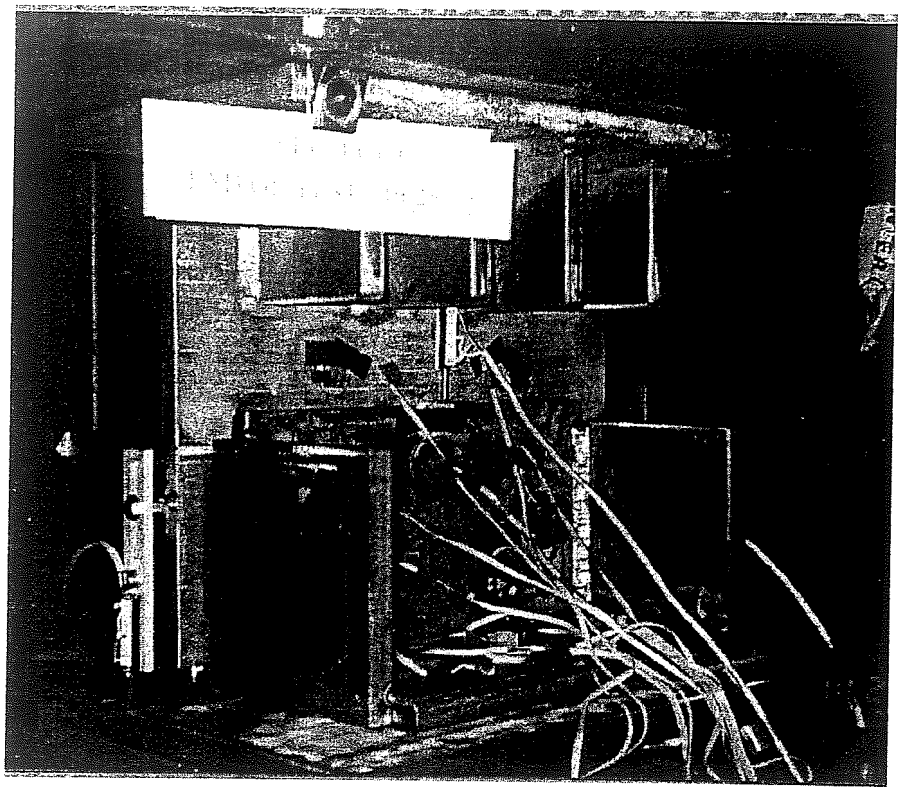

Figure 6.55. Stiffened Double Angle Friction Connection Component Test Specimen

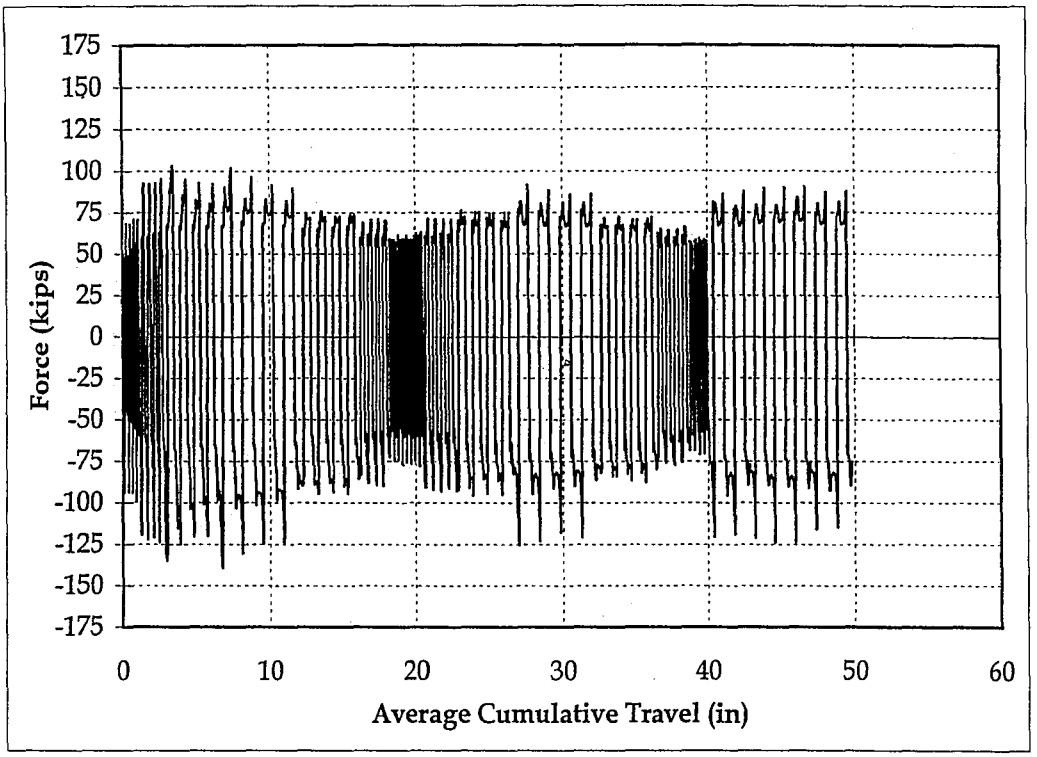

(a)

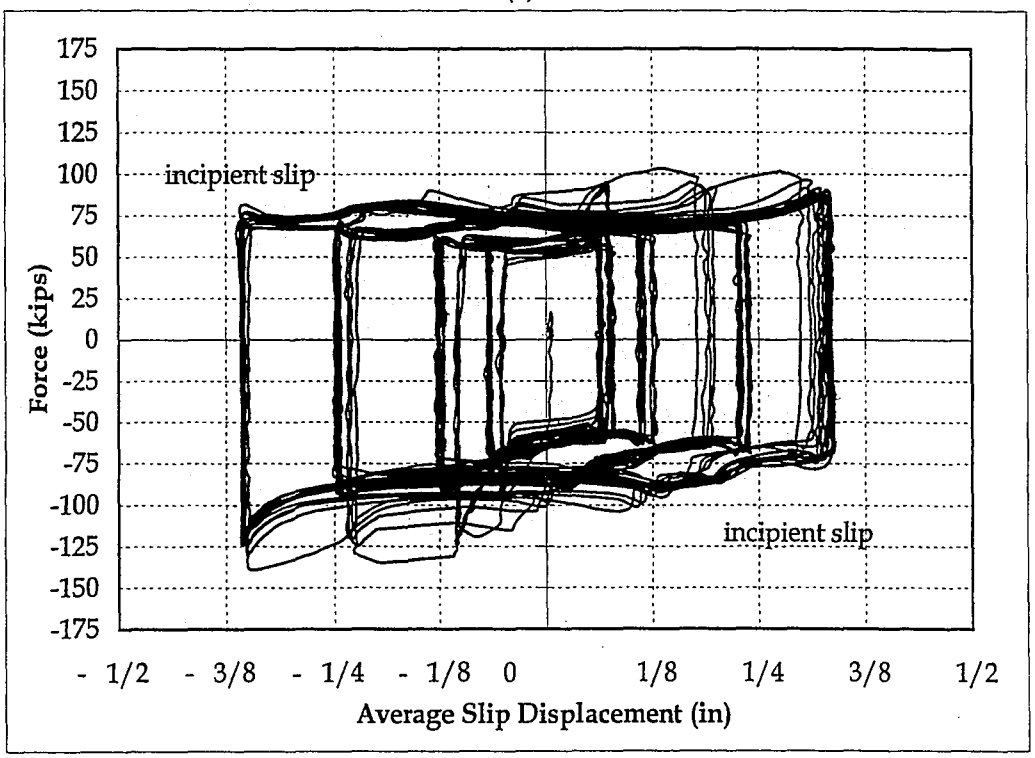

(b)

Figure 6.56. Friction Behavior for Test FCC9:
(a) Force vs. Average Cumulative Travel; and
(b) Force vs. Average Slip Displacement

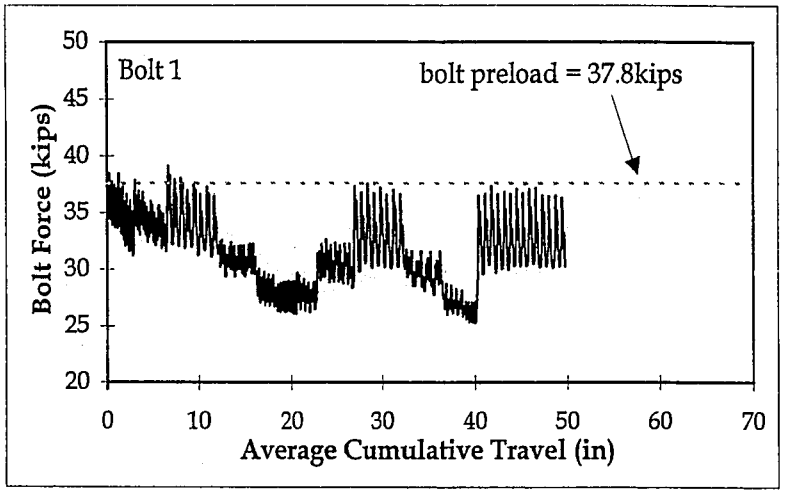

(a)

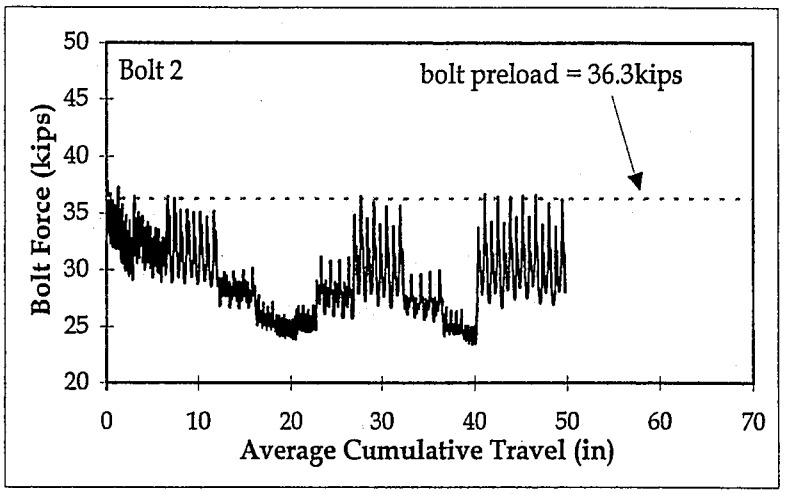

(b)

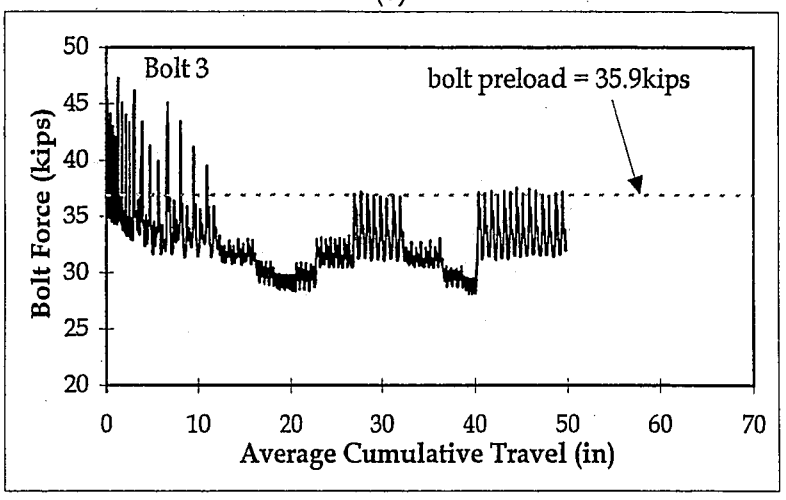

(c)

Figure 6.57. Clamping Bolt Force vs. Average Cumulative Travel for Test FCC9: (a) Bolt 1; (b) Bolt 2; and (c) Bolt 3

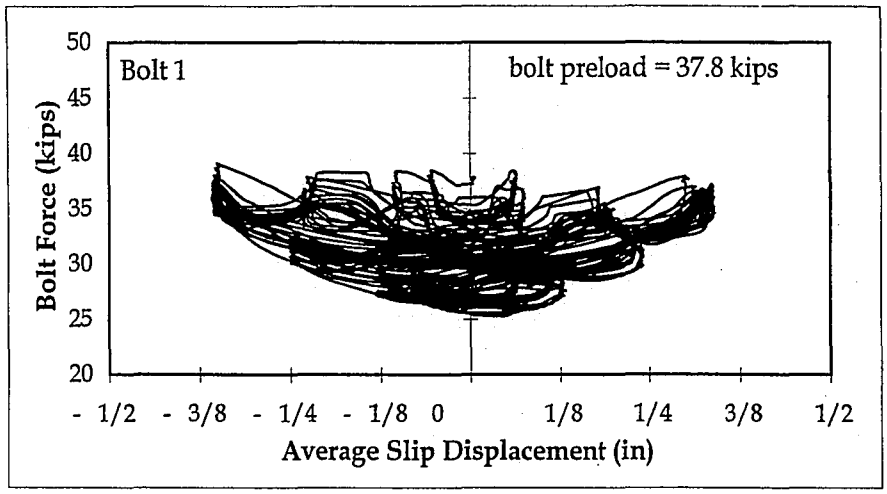

(a)

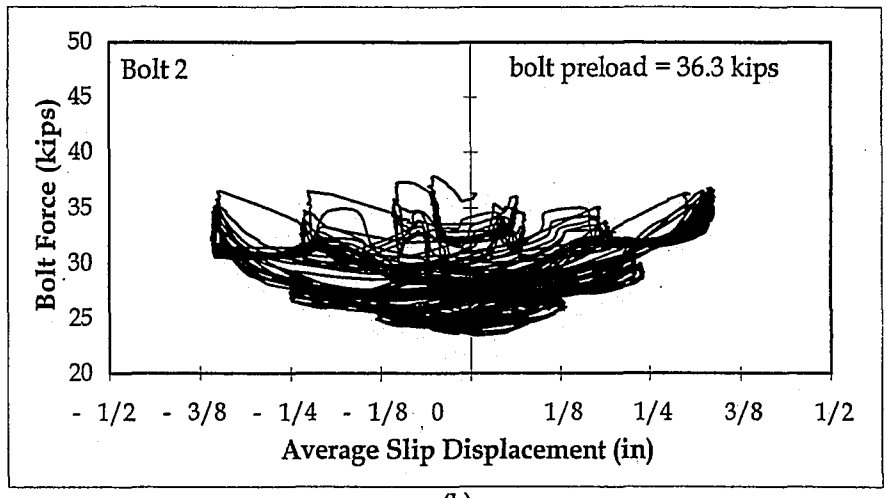

(b)

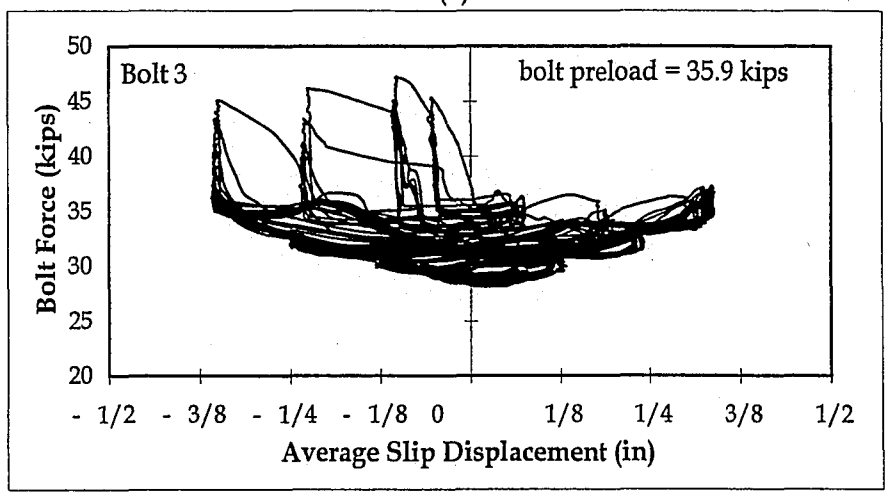

(c)

Figure 6.58. Clamping Bolt Force vs. Average Slip Displacement for Test FCC9: (a) Bolt 1; (b) Bolt 2; and (c) Bolt 3

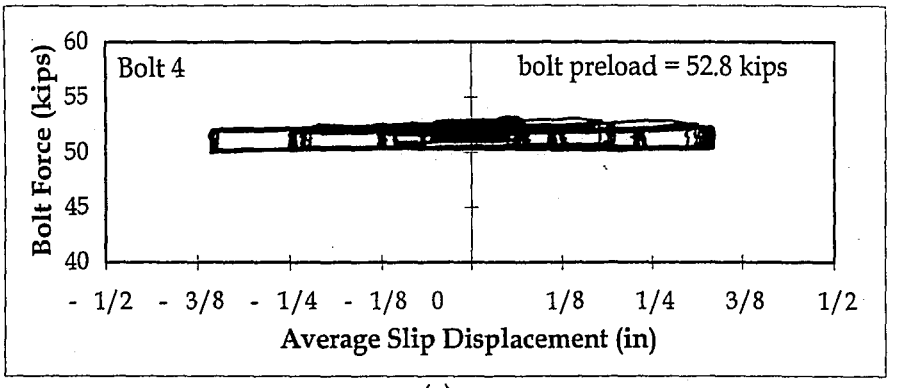

(a)

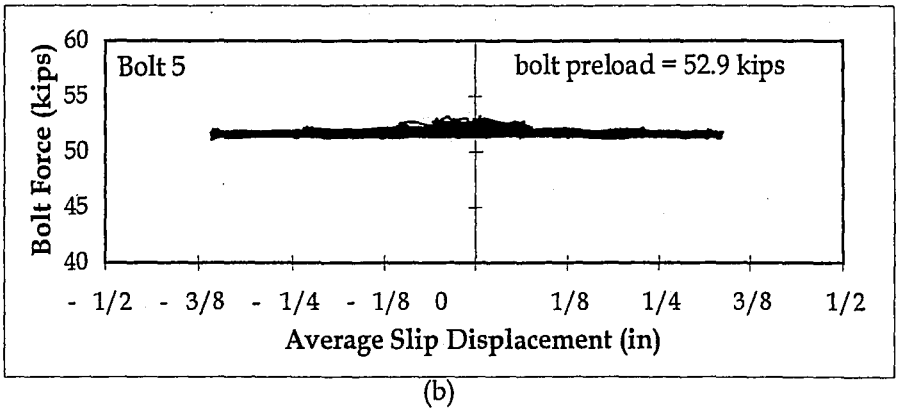

(b)

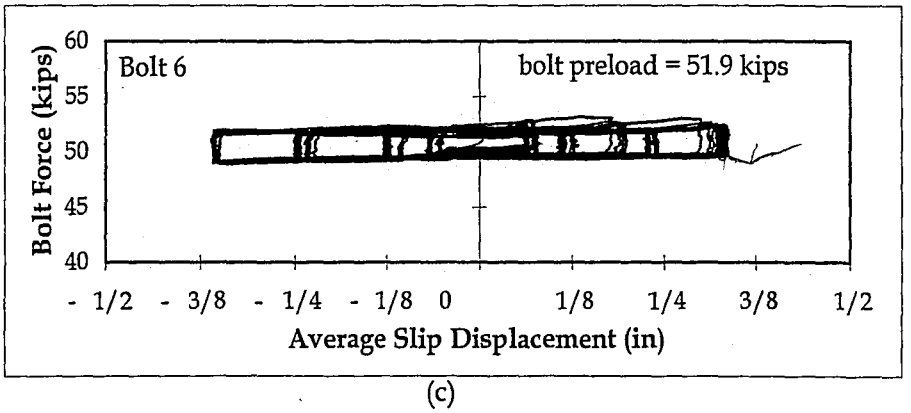

(c)

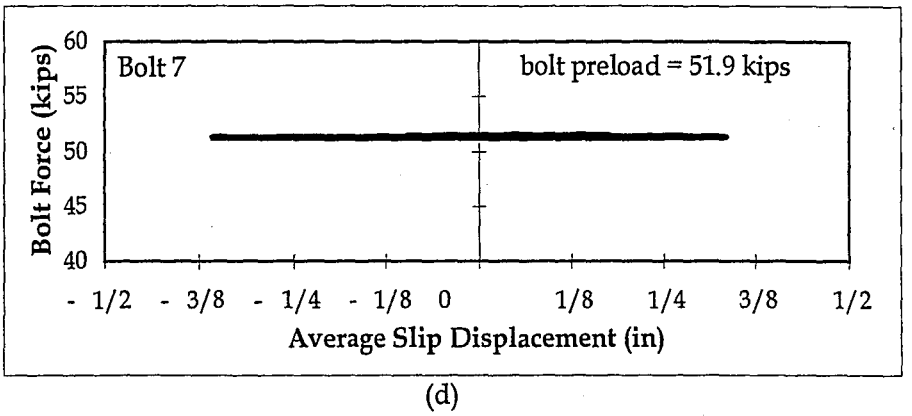

(d)

Figure 6.59. Support Bolt Force vs. Average Slip Displacement for Test FCC9: (a) Bolt 4; (b) Bolt 5; (c) Bolt 6; and (d) Bolt 7

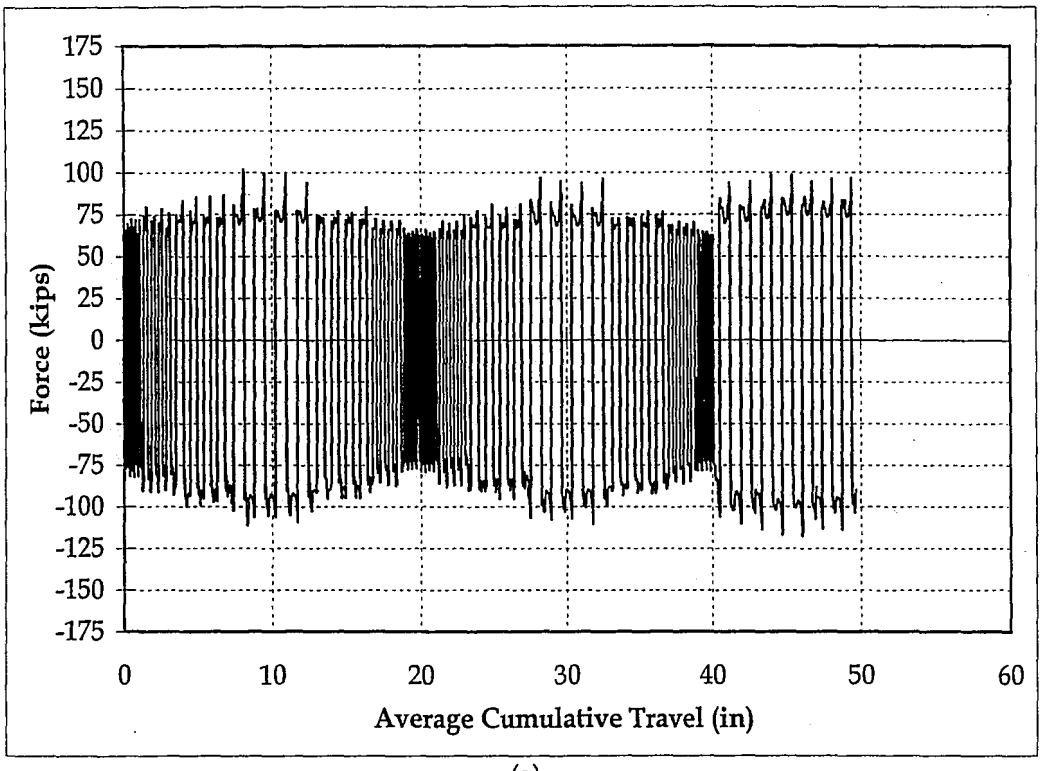

(a)

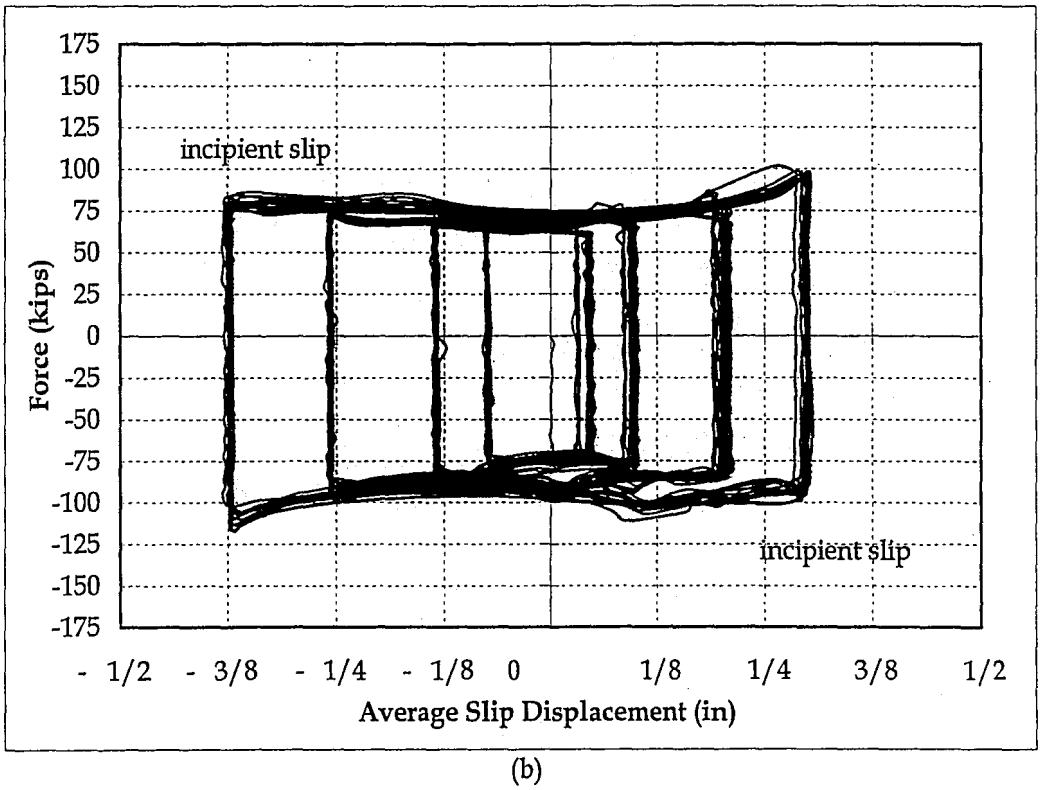

(b)

Figure 6.60. Friction Behavior for Test FCC10A:
(a) Force vs. Average Cumulative Travel; and
(b) Force vs. Average Slip Displacement

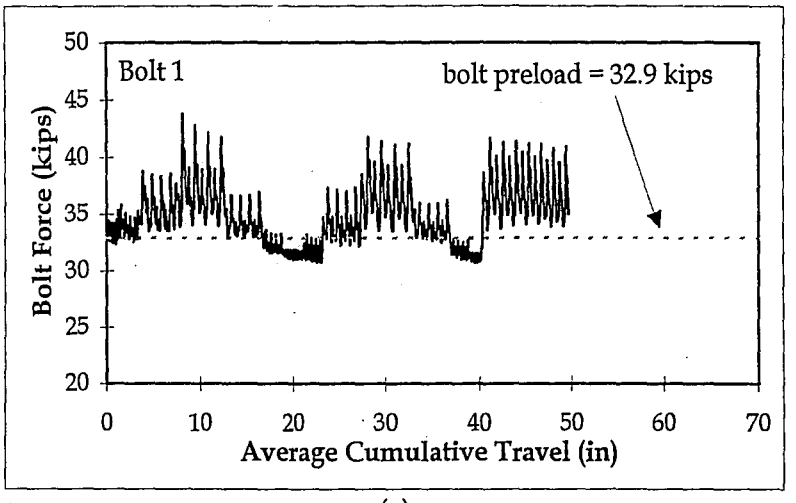

(a)

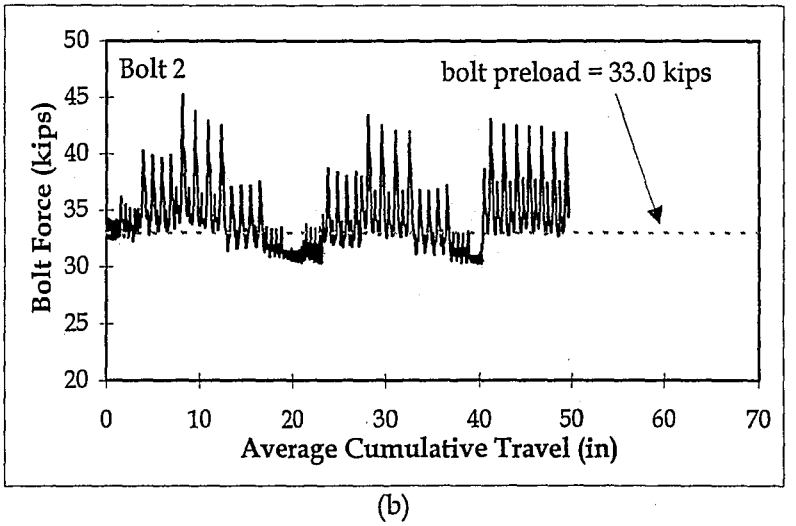

(b)

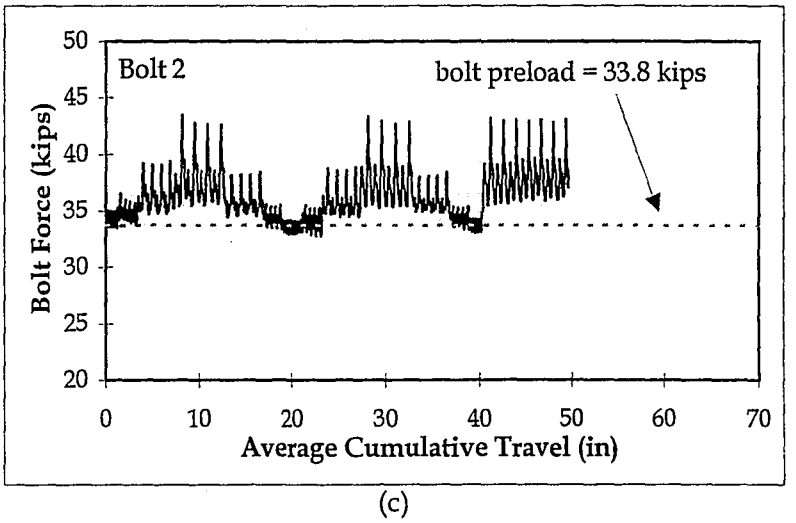

(c)

Figure 6.61. Clamping Bolt Force vs. Average Cumulative Travel for Test FCC10A: (a) Bolt 1; (b) Bolt 2; and (c) Bolt 3

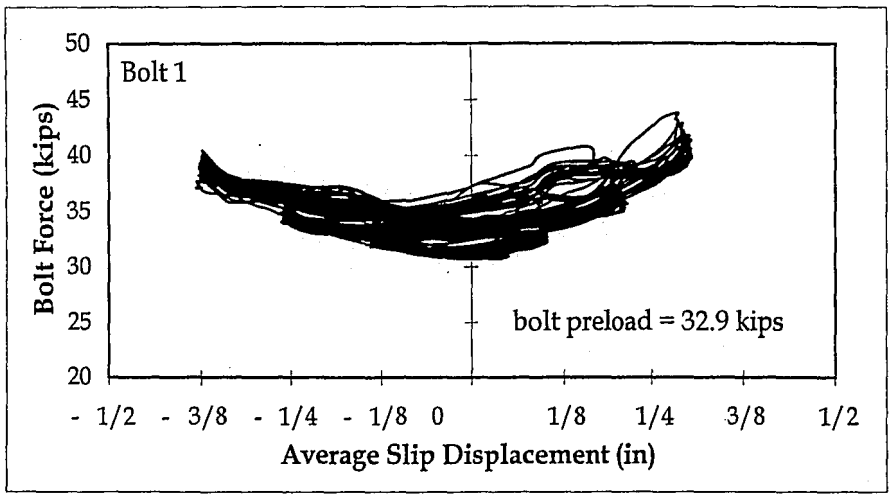

(a)

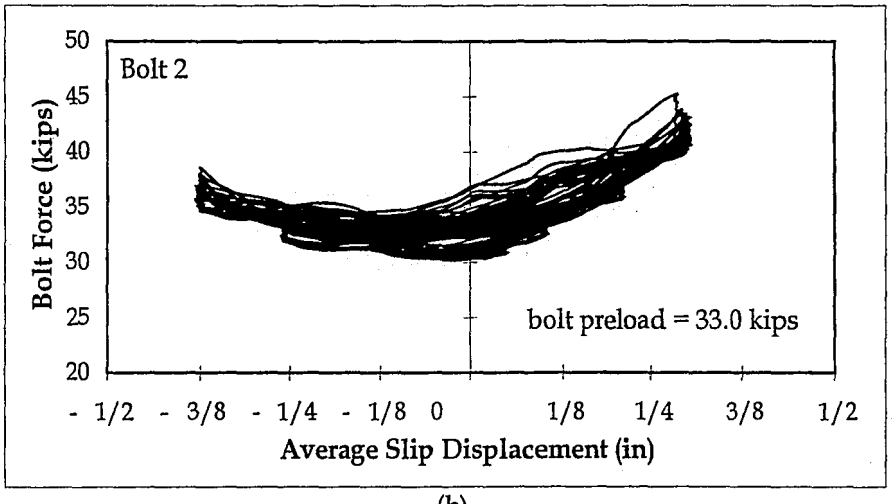

(b)

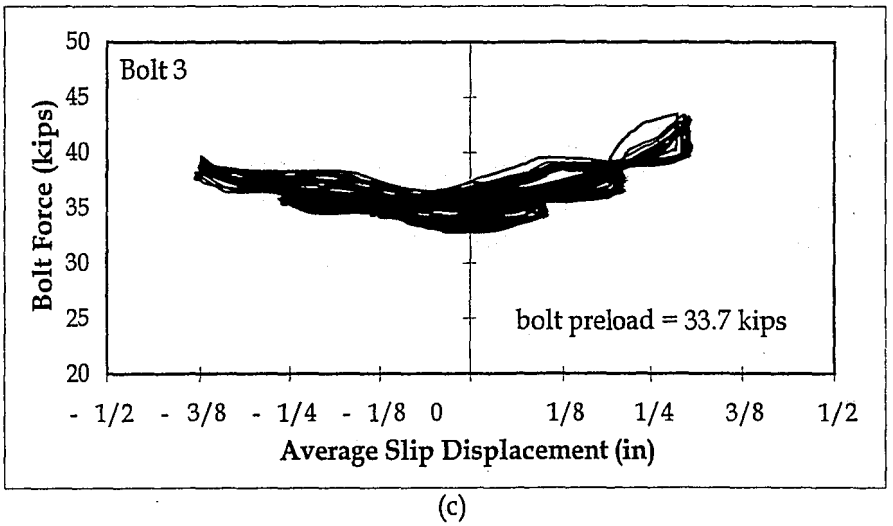

(c)

Figure 6.62. Clamping Bolt Force vs. Average Slip Displacement for Test FCC10A: (a) Bolt 1; (b) Bolt 2; and (c) Bolt 3

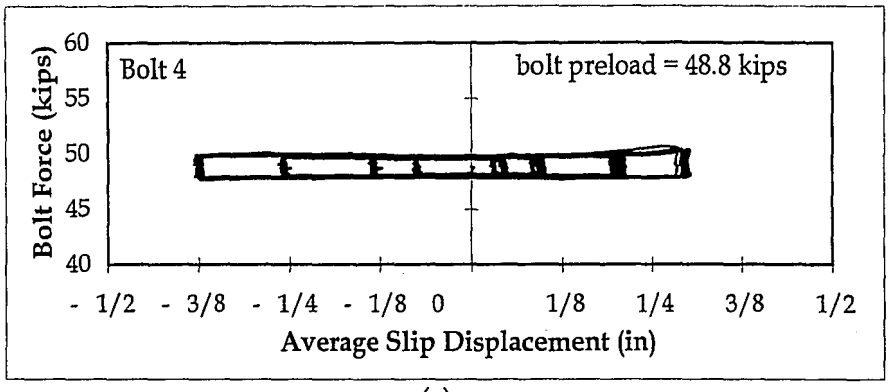

(a)

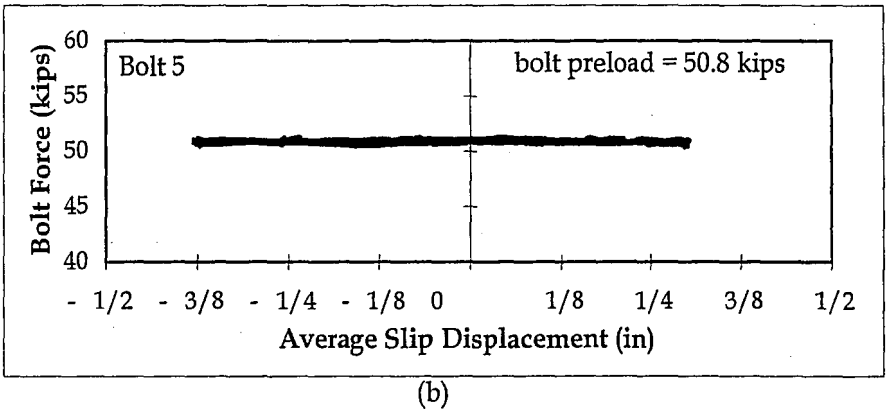

(b)

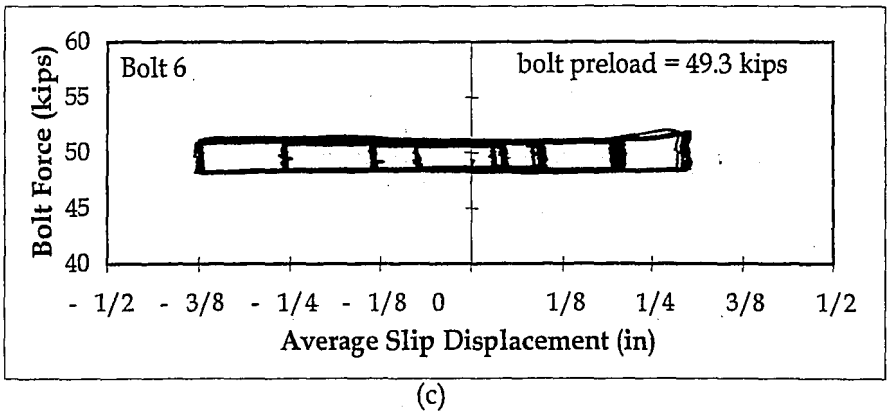

(c)

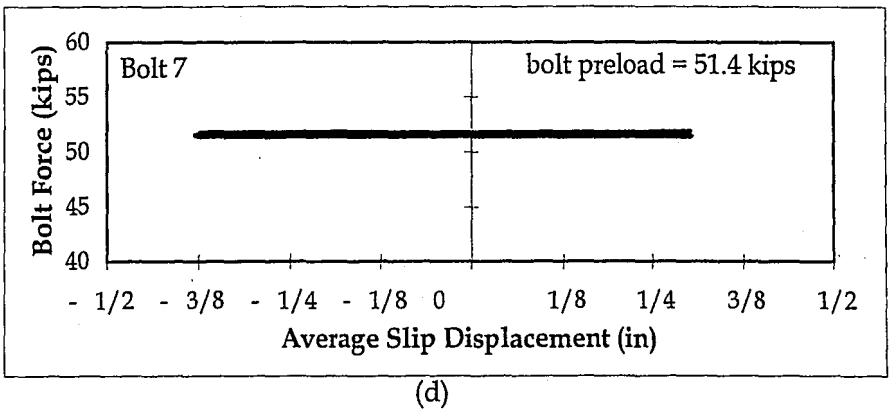

(d)

Figure 6.63. Support Bolt Force vs. Average Slip Displacement for Test FCC10A: (a) Bolt 4; (b) Bolt 5; (c) Bolt 6; and (d) Bolt 7

7. Summary and Conclusions

7.1 Summary

The research presented in this thesis focused on an experimental evaluation of the friction component of an innovative connection for seismic-resistant steel moment resisting frames, called the post-tensioned friction-damped connection (PFC). The objectives of this research were: (1) to develop preliminary analytical and design procedures for a post-tensioned steel connection with a friction damping component; and (2) to evaluate the friction connection component as an energy dissipater for the post-tensioned steel connection.

The research involved two types of tests. The first series of tests (double plate friction tests) was intended to evaluate the brass-steel tribo surfaces used in the friction component of the PFC. Nine of these tests were conducted. The parameters varied were the initial wear of the brass tribo surface and the imposed displacement rate. The second series of tests was conducted on double angle friction connection components. Sixteen tests were conducted. The parameters varied were the assembly sequence, initial wear of the brass tribo surface, the imposed displacement rate, and the use of stiffeners on the angles.

The motivation for developing the PFC is presented in Chapter 1. An overview of recent problems with welded moment resisting frame (MRF) connections is given.

The post-tensioned steel connection is introduced as an alternative moment resisting connection that provides the stiffness of a fully-restrained connection, and the deformation capacity required to perform properly during major seismic events. The chapter also introduces the use of a friction component as an energy dissipater for post-tensioned steel connections.

Chapter 2 discusses models for predicting the moment-rotation (M-θ) behavior of the PFC. The M-θ behavior is based on the M-θ behavior of its two components: (1) the post-tensioned strands; and (2) the friction connection component. Simple models are used to present the individual M-θ behavior of each component. These models are combined to develop simple models for the PFC M-θ behavior. A more comprehensive analysis of the moment developed in a PFC due to the friction connection component is presented.

Chapter 3 discusses the preliminary design of the friction connection component (FCC) of a PFC. The selection of the elements of the FCC and a preliminary design of these elements is discussed. A previously designed post-tensioned connection was used as the basis for the design for the FCC.

Chapter 4 discusses the experimental procedures used in this research. This discussion includes a description of: (1) the test frame used in the experiments; (2) the double plate friction tests; (3) the double angle friction connection component

tests; (4) the corresponding instrumentation for each set of tests to measure strains and displacements; (5) the material properties of the clamping bolts and double angles used in the tests; and (6) the displacement history and displacement rates used for the tests.

Chapter 5 presents results and observations from the double plate friction tests. Phenomena that were observed during the tests are discussed. Simple analyses to support the observations are also provided, and the effects of the observed phenomena on the test results are discussed. A detailed discussion of the results of each test is given. Based on the test results, a coefficient of friction for the brass-steel tribo surfaces of the FCC of 0.45 was selected for the remaining parts of the research.

Chapter 6 presents results and observations from the double angle friction connection component (FCC) tests. Observed phenomena from the FCC tests are discussed. Simple analyses to support the observations of angle deformation and its effects on the friction behavior of the FCC are provided. A detailed discussion of the results of each FCC test is given.

7.2 Summary of Findings

During the double plate friction tests and the double angle friction connection component tests, the following phenomena and associated effects on the test results were observed.

Friction wear was observed on the brass and steel tribo surfaces. Abrasive wear, gouging wear, and adhesive wear were observed. Wear of the brass shim was more significant, however, the friction force was not influenced by the wear phenomena. Test F9 showed that high temperature abrasive wear can melt the brass surface and result in fusing the brass and steel tribo surfaces together as the melted surface cools. However, this high temperature abrasive wear and subsequent fusing of the brass surface to the steel surface only occurred when the test specimen was continuously cycled through a displacement history much more demanding than that expected during a typical seismic event.

Deformation of the outer steel plates into the oversized holes in the T-stub web (which simulated the beam web) was observed in the double plate friction tests. A similar deformation of the angle legs was observed in the double angle friction connection component tests. The deformation developed when the preload of the tribo surface clamping bolts compressed the outer steel plates (or angle legs) and the brass shims into the oversized hole. Although this deformation was very small, reversal of this deformation as the clamping bolts approached the edge of the

oversized hole during loading resulted in variations in the clamping bolt forces and also assisted in gouging wear of the brass shim.

Variations of the clamping bolt force were observed in both the double plate friction tests and the double angle friction connection component tests. The variation in the bolt force was caused by the deformation of the outer steel plates (or angle legs). The magnitude of the variation in the bolt force depended on the amplitude of the slip displacement. The bolt force increased as the clamping bolts approached the edges of the oversized holes and returned to a relatively constant minimum force as the clamping bolts approached the center of the oversized holes. The bolt force cycled up and down, approximately 3 to 5 kips, with respect to the minimum force. Corresponding increases in the friction force were observed.

Thermal effects were observed during the double plate friction tests with average displacement rates of 0.5 inch/second. Heat was generated from the friction on the brass-steel tribo surfaces. This heat caused thermal expansion of the layers of (brass and steel) material between the clamping bolts to occur, which in turn increased the clamping bolt force. The friction force increased as the bolt force increased.

Deformation of the angles was observed during the double angle friction connection component tests. Elastic deformation of the angles, and the resulting internal forces, influenced the normal force on the tribo surfaces. As a result, the

angle deformation caused decreases, and, in some cases, increases in the friction force on the tribo surfaces. The magnitude of the elastic deformation, and the resulting internal forces, depend on the magnitude of the friction force, which was most strongly influenced by the clamping bolt preload. Thus, for the tests with the larger clamping bolt preload, the decreases (or increases) in friction force caused by elastic deformation of the angles were larger.

7.3 Conclusions

From the evaluation of the brass-steel tribo surfaces using the results of the double plate friction tests, the following conclusions can be drawn:

- The static coefficient of friction is generally in the range of 0.45 to 0.50.
- The kinetic coefficient of friction is generally in the range of 0.43 to 0.50.
- The difference between the static and kinetic coefficients of friction is considered negligible when determining the friction force of a double angle FCC. However, the kinetic coefficient of friction is more appropriate for use in analyzing the behavior of a MRF with post-tensioned friction-damped connections under seismic loading.
- The friction force could be estimated based on Coulomb friction theory, using the preload of the clamping bolts as the normal force.
- The friction force (and friction coefficient) is higher for the brass-steel tribo surface during initial wearing of the brass shim (i.e., during the break-in cycles).

- The friction force (and friction coefficient) after break-in (i.e., during the steady state cycles) is nearly constant.
- Little variation in the friction force occurred between tests in which previously worn brass shims were subjected to displacement cycles at the same displacement rate (e.g., 0.00625 inch/second).
- Little variation in the friction force occurred between tests in which previously worn brass shims were subjected to displacement cycles at different displacement rates when the two slow rates (i.e., 0.00625 and 0.0125 inch/second) were used.
- The friction forces during a slow displacement rate (i.e., 0.00625 inch/second) test and those during a dynamic displacement rate (i.e., 0.5 inch/second) test are similar during the initial cycles of the dynamic rate test. As thermal effects influence the test with the dynamic displacement rate, the friction force increases

From the evaluation of the double angle friction connection component (FCC) using the results of the double angle FCC tests, the following conclusions can be drawn:

- The friction force obtained for a given clamping bolt preload varies with the assembly sequence of the FCC.
- Deformation of the angles during assembly of the double angle FCC occurs as the bolts compress the angle legs to the T-stub web (simulating the beam web) and the lower spreader beam (simulating the column flange).

- The friction force is reduced if some of the clamping bolt force is required to deform the angles as they are compressed against the T-stub web. That is, tightening of the angles to the column first and then to the beam web may reduce the friction force for a given clamping bolt force.
- Based on current MRF erection procedures, if the FCC is shop-bolted to the beam web, the first FCC at one end of a beam can be bolted to the column flange with minimal angle deformation. More angle deformation will occur in when the second FCC at the other end of the beam is bolted to the column flange because of required erection clearances.
- Elastic deformation of the double angles, and the resulting internal forces, influenced the normal force on the tribo surfaces, causing decreases (or increases) in the friction force. The magnitude of the elastic deformation and internal forces, depend on the magnitude of the friction force, which is strongly influenced by the clamping bolt preload. Thus, with a larger clamping bolt preload, larger decreases (or increases) in friction force are expected.
- The results of the tests show that the double angle FCC is a viable way to dissipate energy in a PT steel connection. A relatively consistent and durable friction behavior was obtained

Appendix 1. Wear and Friction Terminology

Tribology -	"The science and technology of interacting surfaces in relative motion, or (with the present approach) the science and technology of tribo systems" (Vingsbo, 1988).
Tribo -	Friction
Tribo System -	"Any system comprising (two or more) tribo surfaces. (Vingsbo, 1988).
Tribo Surfaces -	"Surfaces in mechanical contact under relative motion". (Vingsbo, 1988).
Contact Surfaces -	A specific area on the tribo surfaces in which friction is generated during relative motion.
Friction -	"Force, acting against relative sliding of tribo surfaces" (Vingsbo, 1988).
Asperity -	"High points" or surface irregularities found on material surfaces (Flaherty and Petach, 1957)
Asperity Junction -	"...the formation of interatomic bonds, extending from each of the two mating surface elements into the other. ...the nature of bonding... is generally referred to as adhesive, but may as well be of a cohesive character" (Vingsbo, 1988).
Wear Mechanism -	"micromechanism by which wear (or loss of material) takes place (at the tribo surface)" (Vingsbo, 1988).
Wear Fragments -	"loose material that has been removed from its parent tribo surface" (Vingsbo, 1988).
Tribo Fracture -	"a wear mechanism in which wear fragment are broken free from their tribo surface by means of compressing and shearing forces acting at the tribo surface." (Vingsbo, 1988).
Abrasive Wear -	"ploughing of asperities and the cutting action of either entrapped or free-rolling grit particles (wear fragments) between the surfaces" (Petach and White, 1957).

Adhesive Wear - "based on proposed weld theory by Bowden, Tabor and others" - wearing of a surface due to the local welding of asperities from on surface as a result of local normal and shearing forces at the asperities (Petach and White, 1957).

Wear - removal of materials from solid surfaces as a result of mechanical action. (Grigorian and Popov, 1994)

Gouging Wear - a form of wear in which "abrasive lumps or particles rub against a surface with sufficient force to gouge out material" (Lansdown and Price, 1986)

Break-in - "those processes which occur prior to steady state when two or more solid surfaces are brought together under load and moved relative to another. This process is usually accompanied by changes in macroscopic friction force and/or rates of wear" (Grigorian and Popov, 1994).

Steady state - "condition of a given tribo system (tribological system) wherein the average kinetic friction coefficient, wear rate, and/or other specified parameters have reached and maintained a relatively constant level". (Grigorian and Popov, 1994).

References

AISC-LRFD, (1995) *Manual of Steel Construction: Load Resistance Factor Design Volume II - Connections,* 2nd Edition, American Institute of Steel Construction, Chicago, IL.

ASTM E8-83, (1997) "Standard Methods of Tension Testing of Metallic Materials", American Society for Testing and Materials Standard E8-83, Philadelphia.

Chen, T. (1998) "An Experimental Evaluation of A Post Tensioned Moment Connection for Steel Frames in Seismic Zones," Research Report, Department of Civil and Environmental Engineering, Lehigh University.

El-Sheikh, M., Sause, R., Pessiki, S., Lu, L.W., and Kurama, Y. (1997) "Seismic Analysis, Behavior, and Design of Unbonded Post-Tensioned Precast Concrete Frames," Earthquake Engineering Research Report, Report No. EQ-97-02, Department of Civil and Environmental Engineering, Lehigh University.

FEMA 267 (1995) "Interim Guidelines: Evaluation, Repair, Modification and Design of Welded Steel Moment Resisting Frame Structures," *Bulletin No. 267,* FEMA, Washington, DC

Flaherty, J.W., and Petach, S. (1957) "Fundamental Aspects of Friction and Wear," *Corrosion and Wear Handbook,* United States Atomic Energy Commission, New York.

Galambos, T.V. (1998) *Guide to Stability Design Criteria for Metal Structures,* 5th Edition, Structural Stability Research Council, Lehigh University, Bethlehem, PA.

Garlock, M.M., Peng, S.W., Ricles, J.M., Sause, R., Zhao, C., & Lu, L.W. (1998) "Post-Tensioned Seismic Resistant Connections for Steel Frames," *Proceedings of 1998 SSRC Annual Technical Session and Meeting,* Structural Stability Research Council, Atlanta, GA.

Grigorian, C.E., and Popov, E.P. (1994) "Energy Dissipation with Slotted Bolted Connections," Earthquake Engineering Research Center (EERC), Report No. UBC/EERC-94/02, University of California, Berkeley.

INCO (1968) *Properties of Some Metals and Alloys,* 3rd Edition, International Nickel Company, New York.

Lansdown, A.R., and Price, A.L. (1986) *Materials to Resist Wear: A Guide to their Selection and Use,* Pergamon Press, Elmsford, New York.

Peng, S.W. (1997) "Results of 5 inches long x 1 inch Diameter A325 Bolt Testing," ATLSS Research Center, Lehigh University.

Peng, S.W., Chen, T.W., Ricles, J.M., Sause, R., and Lu, L.W. (1999) "An Experimental Evaluation of a Post-Tensioned Moment Connection for Steel Frames in Seismic Zones," paper in preparation, Lehigh University.

Rabinowicz, E. (1991) "Friction Fluctuations," *Fundamentals of Friction: Macroscopic and Microscopic Processes, Proceedings of the NATO Advanced Study Institute on Fundamentals of Friction*, Braunlage, Harz, Germany.

Tabor, D. (1991) "Friction as a Dissipative Process," *Fundamentals of Friction: Macroscopic and Microscopic Processes, Proceedings of the NATO Advanced Study Institute on Fundamentals of Friction*, Braunlage, Harz, Germany.

Vingsbo, O. (1988) "Fundamentals of Friction and Wear," *Proceedings of an International Conference, Engineered Materials for Advanced Friction and Wear Applications*, Gaithersburg, MD.

Young, W.C. (1989) *Roark's Formulas for Stress and Strain*, McGraw-Hill, New York.

Vita

Garrick D. Petty was born on June 4th 1974 in Atlanta, Georgia. He is the proud son of Donald K. Petty and Leola J. Tanks. Garrick earned his Bachelor of Science degree in Architectural Engineering at the North Carolina Agricultural and State Technical University in Greensboro, North Carolina in May 1997. During his undergraduate studies, Garrick was inducted in Phi Alpha Epsilon, the Architectural Engineering Honorary, and Tau Beta Pi, the National Engineering Honor Society. Garrick continued his education by pursuing his Master of Science in Civil and Environmental Engineering at Lehigh University in Bethlehem, Pennsylvania. Garrick will receive his degree in January 2000. After graduation, Garrick will be working as a structural engineer for Jacobs-Sverdrup in St. Louis, Missouri.

END OF TITLE